Durham University

Durham E-Theses

Hydrocarbon Upgrading and Co-processing by Metal-modified Zeolites and Zincosilicates

RYAN KERRIGAN

How to cite:

KERRIGAN, RYAN (2024) Hydrocarbon Upgrading and Co-processing by Metal-modified Zeolites and Zincosilicates. Doctoral thesis, Durham University.

Use policy

The full-text may be used and/or reproduced, and given to third parties in any format or medium, without prior permission or charge, for personal research or study, educational, or not-for-profit purposes provided that:

- a full bibliographic reference is made to the original source
- a https://etheses.durham.ac.uk/id/eprint/15736/ is made to the metadata record in Durham E-Theses
- the full-text is not changed in any way

The full-text must not be sold in any format or medium without the formal permission of the copyright holders.

Please consult the full Durham E-Theses policy for further details.

Academic Support Office, The Palatine Centre, Durham University, Stockton Road, Durham, DH1 3LE
e-mail: e-theses.admin@durham.ac.uk Tel: +44 0191 334 6107
https://etheses.durham.ac.uk

Hydrocarbon Upgrading and Co-processing by Metal-modified Zeolites and Zincosilicates

This thesis is submitted in partial fulfilment for the degree of PhD at the University of Durham

Ryan Kerrigan

Supervisor: Dr. Russell A. Taylor

December 2023

Statement of Originality

The work contained within this thesis was conducted by the author within the Department of Chemistry at Durham University, between the period of October 2019 and December 2022. All work described within this thesis is original, unless acknowledged as being otherwise in the text or in the references supplied. No work contained within this thesis has been submitted for any other degree at this or at any other University. The ownership of this work rests with Durham University and Johnson Matthey.

Signed: Ryan Kerrigan

December 2023.

Acknowledgements

To finally achieve a completed thesis for a PhD that has endured the COVID pandemic, with a laboratory that has withstood numerous sporadic indoor rainy seasons amongst several other testing endeavours, were a task that could only be risen to through the immense help of others.

I must first acknowledge my PhD supervisor, Dr Russell Taylor, from whom I received first class guidance, support and technical knowledge throughout my time at and beyond Durham. I will always be thankful for being given the opportunity to be part of the RAT group, where I could always learn new things and build the confidence to push myself further than ever before. A special mention must go out to the members of the research group past and present, in particular Meera, Sam R, Irene, Sam M, Abdul and Catherine, for sharing your knowledge, sharing a laugh, sharing a bag of wasabi nuts with a pint and for being a pleasure to work alongside and share an office with.

I must also acknowledge Dr Ronan Bellabarba, my industrial supervisor from Johnson Matthey during my time at Durham, alongside colleagues Dr Nicolas Bats and Dr Raquel Garcia. The expert support and guidance that was provided throughout was invaluable.

Furthermore, I would like to thank the members of Durham University who were present during my time, in particular those who have collected data for the project or supported us with equipment from the various workshops. I've lost count of the number of favours called upon for a quick quartz u-tube fix.

Finally, I have to thank my family who have supported me unconditionally and without them I would not be here today. Last, but not least, Amy. From whom the love and support has been the rock that has carried me through the long evenings and weekends of writing.

Generous funding from Johnson Matthey and Durham University's EPSRC Doctoral Training Partnership is also very gratefully acknowledged.

Hasta la vista,

silver.

Table of Contents

Chapter One – Extracting Hydrocarbons for Fuels and Fine Chemicals 13

1.1 It's Raw: Producing Chemicals using Raw Materials originating from Renewable and Non-Renewable Sources 13

1.1.1 Meeting Energy Demands is a Tireless Task 14

1.2 Economic Viability of Associated Natural Gas Capture and Conversion 17

1.2.1 Routes to Indirect and Direct Conversion of Methane – Heterogeneous 19

1.2.2 Routes to Indirect and Direct Conversion of Methane - Homogeneous 21

1.3 A Quest for the Holy Grail: Direct Methane to Methanol Conversion 22

1.3.1 Direct Methane-to-Methanol Conversion (dMtM) using Methane Monooxygenase 23

1.3.2 Direct Methane-to-Methanol Conversion (dMtM) using Zeolite Catalysts 24

1.3.3 Routes to Establishing a Methanol Economy 25

1.4 Silver: One Metal for Money, Medicine, and Methanol Dehydrogenation 31

1.5 Chapter One Bibliography 33

Chapter Two – Zeolites: Natures Solid Acid Catalyst 41

2.1 Zeolites and Zeotypes: Factors Affecting Hydrothermal Synthesis 42

2.2 Zeolites and Zeotypes: Topology, Dimensionality and Acidity of Solid Acid Catalysts 47

2.2.1 CHA: A Small Pore Topology 55

2.2.2 MFI: A Medium Pore Topology 56

2.2.3 MOR: A pseudo-1D Topology of Mixed Channels 57

2.2.4 FER and TON: Frameworks with no 4MR 59

2.3 Silver-exchanged Zeolites: Auto Reduction and Other Reported Phenomena 60

2.3.1 Irreversible Silver Redox Chemistry in Zeolites Following Oxygen Evolution 62

2.4 Conclusion of Zeolites, Zeotypes and Silver-exchanged Catalysts 65

2.5 Chapter Two Bibliography 66

Chapter Three – Experimental Details and Characterisation Methods 74

3.1 Characterisation Techniques 75

3.1.1 Solid-state NMR Spectroscopy 75

3.1.2 X-Ray Analytical Techniques 86

3.1.2.1 Powder X-Ray Diffraction (pXRD) 86

3.1.2.2 Electron Microscopy 90

3.1.2.2.1 Scanning Electron Microscopy (SEM) 90

3.1.2.2.2 Transmission electron microscopy (TEM) 91

3.1.3 Energy-Dispersive X-Ray Fluorescence (ED-XRF) 94

3.1.4 X-ray Absorption Near Edge Structure (XANES) 95

3.1.4.1 Extended X-ray Absorption Fine Structure (EXAFS) 97
3.1.5 ICP-OEs 97
3.1.6 DRIFTS 98
3.1.7 Brunauer-Emmett-Teller Theory (BET) 100
3.1.8 Gas Chromatography-Mass Spectrometry 101

3.2 Experimental Methods 104
3.2.1 Zeolite Dehydration 104
3.2.2 Pressing and Sieving 105
3.2.3 Calcination 105
3.2.4 Aqueous Ion-Exchange 106
3.2.5 Centrifugation 107
3.2.6 Powder X-Ray Diffraction Experimental Method 108
3.2.7 SEM Experimental Method 108
3.2.8 TEM Experimental Method 108
3.2.9 ED-XRF Experimental Method 109
3.2.10 XAS Experimental Method 110
3.2.11 ICP-OEs Experimental Method 112
3.2.12 DRIFTS Experimental Method 112
3.2.13 BET Experimental Method 113
3.2.14 HEL FlowCAT Flow Reactor Experimental Method 114
3.2.15 GC-MS Experimental Method 114
3.2.16 Experimental Methods for Solid-state NMR Spectroscopy 115

3.3 Chapter Three Bibliography 119

Chapter Four – Project Aims 125

4.1 Project Aims 125

4.2 Chapter Four Bibliography 127

Chapter Five – Hydrothermal Synthesis of Zeolites and Silver Ion-exchange 128

5.1 Silver Ion-exchange of Zeolites 128
5.1.1 Aqueous Ion-exchange with Silver 128
5.1.2 Solid Mixing for Ion-exchange with Silver 133
5.1.3 Analysis of Silver-exchanged Materials 133
5.1.4 Conclusion of Silver Ion-exchange 148

5.2 Hydrothermal Synthesis and Characterisation of CHA Zeolites 149
5.2.1 Hydrothermal Synthesis of Chabazite 151
5.2.2 Powder X-ray Diffraction of Hydrothermally Synthesized CHA 154
5.2.3 FT-IR spectroscopy of Hydrothermally Synthesized CHA 156
5.2.4 Solid-state NMR spectroscopy of Hydrothermally Synthesized CHA 162
5.2.5 Electron Microscopy of Hydrothermally Synthesized CHA 168
5.2.6 Brunauer-Emmett-Teller Theory on Hydrothermally Synthesized CHA 170
5.2.7 Conclusion of Hydrothermal Synthesis of Chabazite 171

5.3 Chapter Five Bibliography 172

Chapter Six – Hydrothermal Synthesis of Zincosilicates and Subsequent Silver Ion-exchange..... 178

6.1 Hydrothermal Synthesis and Characterisation of Zincosilicate CHA 178

6.1.1 Hydrothermal Synthesis of Zincosilicate Chabazite 180

6.2 Characterisation of Synthesized Zincosilicate CHA 185

6.2.1 Powder X-ray Diffraction of Hydrothermally Synthesized Zincosilicate CHA 185

6.2.2 FT-IR spectroscopy of Hydrothermally Synthesized Zincosilicate CHA 186

6.2.3 Solid-state MAS NMR of Hydrothermally Synthesized Zincosilicate CHA 192

6.2.4 Electron Microscopy of Hydrothermally Synthesized Zincosilicate CHA 202

6.2.5 X-ray Absorption Spectroscopy of Hydrothermally Synthesized Zincosilicate CHA 205

6.2.6 Brunauer-Emmett-Teller theory of Hydrothermally Synthesized Zincosilicate CHA 208

6.2.7 Conclusion of Hydrothermal Synthesis of Zincosilicate CHA 210

6.3 Analysis of Silver-exchanged zincosilicates 211

6.3.1 Powder X-ray Diffraction of Silver-exchanged ZnCHA 213

6.3.2 Transmission Electron Microscopy of Silver-exchanged ZnCHA 214

6.3.3 X-Ray Absorption Spectroscopy of Silver-exchanged ZnCHA 219

6.3.4 Conclusion of Zincosilicate Hydrothermal Synthesis and Characterization 223

6.4 Chapter Six Bibliography 224

Chapter Seven – Hydrocarbon Upgrading over Metal-Modified Zeolites and Zincosilicates 228

7.1 Hydrocarbon Upgrading Reactions 228

7.2 Accurate Determination of Catalyst Activity by In-Line GC-MS-BID Monitoring .. 230

7.3 Ethanol Upgrading Reactions 232

7.3.1 Ethanol Upgrading Reactions over Metal-exchanged Protic Zeolites 234

7.3.2 Ethanol Upgrading Reactions over Metal-exchanged Zincosilicates 246

7.3.3 Conclusion of Ethanol Upgrading Reactions 273

7.4 Methanol Upgrading Reactions 274

7.4.1 Methanol Upgrading over Silver-exchanged Zeolites and Zincosilicates 276

7.4.2 Methanol Upgrading over Indium-exchanged Zeolites 280

7.4.3 Conclusion: Methanol Upgrading Reactions 289

7.5 It's a Gas, Gas, Gas: Methane Co-processing with Methanol, Ethanol and Ethylene. 290

7.5.1 Methane/Methanol Co-processing Reactions 290

7.5.2 Methane/Ethanol Co-processing Reactions 296

7.5.3 Methane/Ethylene Co-processing Reactions 308

7.6 Conclusion of Upgrading Reactions 312

7.7 Chapter Seven Bibliography 313

Chapter Eight – Pretty Vacant: Silver Auto Reduction, Surface Clustering and Framework Oxidation 319

8.1 The Effects of Dehydration on Silver-exchanged Zeolites and Zincosilicates 319

8.1.1 Conclusion of Silver Auto Reduction in Silver-exchanged Zeolites and Zincosilicates 336

8.2 Effects of Hydrocarbon Upgrading on Metal-exchanged Zeolites and Zincosilicates 338

8.2.1 Spent Catalyst Characterisation Following Hydrocarbon Upgrading Reactions 338

8.2.2 Spent Metal-Exchanged Zincosilicate CHA following Ethanol Upgrading 357

8.2.3 Conclusion of the Effects of Hydrocarbon Upgrading on Metal-exchanged Zeolites and Zincosilicates 365

9. Chapter Nine – Project Outlook and Conclusions 370

9.1 Project Conclusion 370

9.1.1 Hydrothermal Synthesis of CHA and ZnCHA 370

9.1.2 Silver Exchanged Materials 371

9.1.3 Hydrocarbon Upgrading and Co-processing 372

9.1.4 Spent Material Characterisation 373

9.2 Future Work 375

9.3 Chapter Nine Bibliography 376

10. Appendix 379

10.1 Further Characterisation of Hydrothermally Synthesized CHA 379

10.2 GC-MS-BID Calibration 382

10.2.1 MS Calibration 383

10.2.2 GC-BID calibration 388

10.3 Chemicals Used in Project 392

10.4 Project Material ED-XRF Results 394

10.5 Appendix Bibliography 399

Abbreviations

BAS – Brønsted Acid Sites

BEA – Beta topology material

BET – Brunauer-Emmett-Teller theory

BF – Bright Field (STEM)

BID – Barrier Ionisation Discharge detector

BTX – Benzene, Toluene and Xylenes

BP – British Petroleum

CBU – Composite Building Unit

CHA – Chabazite topology material

COP26 – 2021 United Nations Climate Change Conference of Parties

COVID – Corona Virus Disease

CP – Cross-Polarisation (NMR)

DE – Direct Excitation

DF – Dark-Field (STEM)

DI water – De-ionised water

DME – Dimethyl ether

dMtM – direct Methane to Methanol conversion

deNOx – Nitrogen Oxide removal (emissions control process)

DW – Debye-Waller factor

DRIFTS – Diffuse Reflectance Infrared Fourier Transform Spectroscopy

DQSQ (NMR) – Double-Quantum Single-Quantum (NMR)

ED-XRF – Energy-Dispersive X-Ray Fluorescence

EDS – Energy Dispersive X-Ray Spectroscopy

EO – Ethylene Oxide

EXAFS – Extended X-Ray Absorption Fine Structure

FA - Formaldehyde

FAU – Faujasite topology material

FCC – Fluid Catalytic Cracking

FER – Ferrierite topology material

FID –Flame Ionisation Dectector

FT – Fisher-Tropsch

FT-IR – Fourier Transform Infrared Spectroscopy

GC – Gas Chromatography

GC-MS – Gas Chromatography-Mass Spectroscopy (tandem analysis)

HC – Hydrocarbon Cracking

HETCOR – Two-dimensional Heteronuclear Correlation (NMR)

HPDEC – High-Power Proton Decoupling (NMR)

HPLC – High-Performance Liquid Chromatography

ICP-OEs – Inductively Coupled Plasma Optical Electron Spectroscopy

IPA – Isopropyl alcohol

IUPAC – International Union of Pure and Applied Chemistry

IZA – International Zeolite Association

IZC – Inter-zeolite Conversion

KBr – Potassium bromide

kHz – kilohertz

LCF – Linear combination fitting

LNG – Liquified Natural Gas

LPG – Liquified Petroleum Gas

MAS – Magic Angle Spinning

MDH – Methanol Dehydrogenase

MeCN-d_3 - Deuterated acetonitrile

MFC – mass flow controller

MFI – Zeolite Socony Mobil - Five (ZSM-5 (five)) topology material

MMO – Methane Monooxygenase

MOR – Mordenite topology material

MR – Membered Ring

MS – Mass Spectroscopy

MTG – Methanol-to-Gasoline

MTH – Methanol-to-Hydrocarbons

MTO – Methanol-to-Olefins

MTP – Methanol-to-Propylene

NMR – Nuclear Magnetic Resonance spectroscopy

NNN – Next-Nearest Neighbour Conformation

NNNN – Next-Next-Nearest Neighbour Conformation

NOx – Nitrogen Oxides

NP(s) – Nanoparticle(s)

OSDA – Organic Structural Directing Agent

PBU – Primary Building Unit

pMMO – Particulate Methane Monooxygenase

POM – Partial Oxidation of Methane

pXRD – powder X-Ray Diffraction

RRT – Relative Retention Time

RT – Retention Time

SABIC – Saudi Basic Industries Corporation

SAF – Sustainable Aviation Fuel

SAPO – Silicoaluminophosphate

SBU – Secondary Building Unit

SCR – Selective Catalytic Reduction

SDA – Structural Directing Agent

SEM – Scanning Electron Microscopy

STEM – Scanning Transmission Electron Microscopy

sMMO – Soluble Methane Monooxygenase

SOx – Sulphur Oxides

Syngas – Synthesis Gas

T atom – Tetrahedral atom (of a zeolite framework structure)

TEM – Transmission Electron Microscopy

TEM-EDS – Transmission Electron Microscopy with Energy Dispersive X-Ray Spectroscopy

TMS – Tetramethylsilane

TON – Theta One topology material

TS – Transition State

US – United States

XANES – X-Ray Absorption Near-Edge Structure

XAS – X-Ray Absorption Spectroscopy

XPS – X-Ray Photoelectron Spectroscopy

ZnCHA – Zincosilicate Chabazite topology material

ZnMFI – Zincosilicate MFI topology material

Chapter One – Extracting Hydrocarbons for Fuels and Fine Chemicals

It would in fact be a reasonable hypothesis to assume that every synthetic object surrounding us today began life in a hole in the ground. Crude chemicals, first extracted from an oil or gas well are transformed by the oil and gas industry. The transport of these raw materials is facilitated by long pipelines, carrying them to a refinery so they can finally be transformed into a spectacular array of fuels, bulk chemicals, solvents, plastics, fine chemicals and fibres. This chapter aims to explore a select few of these diverse processes and the catalysts behind them.

1.1 It's Raw: Producing Chemicals using Raw Materials originating from Renewable and Non-Renewable Sources

In 2014 alone, the chemical industry worldwide reported a gargantuan record revenue of 5.4 trillion US dollars, with it having decreased to a still vast 3.9 trillion US dollars in 2019.[1] As the petrochemical industry is so far-reaching, it can be argued that major disruptions can cause drastic changes throughout industry or even in our day-to-day life.[2] Petrochemicals are a group of chemical products that originate from the oil and gas industry. Refining is a chemical process that converts the raw material, for example crude oil, into the commercial product. The first step of refining crude oil is fractional distillation, which separates crude oil into several fractions based on their based on their boiling point and vapour pressure. Fractions with long chain molecules undergo fluid catalytic cracking (FCC) or hydrocracking (HC) to break long chain molecules into more valuable, shorter chain products. FCC and HC are commercial processes that are facilitated by zeolite solid-acid catalysts. The reasoning for why these are so effective is discussed in further detail in Section 2.1

FCC produces an array of petrochemicals. It is projected that global ethylene production will reach over 200 million tonnes by 2026, driven by increasing demand for food packaging, beverages, personal care, healthcare and consumer electronics.[3,4] Petrochemicals also see use as feedstocks that undergo further refinement, feedstocks including polyesters, butadiene, benzene, toluene, xylenes and (poly)styrenes, that when refined even further, and adding to the diverse applications mentioned earlier, can be found in clothing, stationery, synthetic rubber and paints.[2]

The drive to decarbonise the oil industry consists of several complex factors, however, the shift from producing fuels to bulk chemicals continues to be driven by a long-term decrease in fuel demand in developed economies, naturally lowering the industries carbon footprint. The need for petrochemicals is offset by the improving efficiency of transportation and its electrification, the use of sustainable aviation fuel (SAF), and the use of H-fuels, ammonia, methanol, and biodiesel, for marine fuels.[5,6] Declining demand for single use plastics, moving towards sustainable alternatives such as biopolymers and biodegradable materials for packaging have also contributed towards the shift away from oil.[7]

1.1.1 Meeting Energy Demands is a Tireless Task

Due to an ever-increasing demand being placed on our natural resources that shows no signs of halting, creative and innovative ways of maximising our finite resources are constantly explored. One major talking point around our environmental impact is in our use of fossil fuels. This non-renewable energy source is a major constituent in fuels for transportation, chemical feedstocks, and energy generation. Energy generation from the combustion of non-renewable resources, such as fossil fuels, is referred to as primary energy. Our total primary energy consumption dropped during the COVID-19 pandemic in 2020, however, it still matched that of 2015 even after a profound investment in renewable energy sources in recent years.[8] Even so, our reliance on finite, non-renewable sources such as coal and natural gas continues to grow.[8] This insatiable consumption of finite non-renewable sources means that the pipelines carrying them will one day run dry. Although the exact date at which we deplete all resources is highly debated, a reasonable estimate would place it within this century, so the need to maximise our use of finite resources has never been greater. The BP Energy Outlook for 2022 reported that our habits changed rapidly as we continued to emerge from the COVID-19 pandemic, observing a sharp rise in oil demand that rose to levels higher those seen pre-COVID-19.[9] Since the worldwide economy recovered and activity returned to levels saw previously, our demand on resources continued to follow the expected trends.

Major global events have had a huge impact on the price of energy, often dictated by the stability of supply. Europe's dependence on natural gas resources originating in Russia, outlined in Figure 1.1, total 169.3 billion cubic metres for both liquified and natural gas combined.[8] Gas prices soared across the continent following the rapidly rising tensions internationally with the war in Ukraine. This uncertainty, coupled with the

ever-increasing crude brent oil prices, led to some drastic changes in energy policies, shifting our focus evermore towards renewable sources for the generation of our energy. Further efforts to move towards full electrification of personal transport has shifted the focus of the petrochemical industry, who now focus on producing petrochemicals from oil rather than fuels for transport.[9] For the year to date in 2022, 14% of all new vehicles purchased in the UK were battery electric vehicles, running entirely from the electric energy stored onboard, whilst around 50% of the vehicles sold so far have been hybrid, running from a mixture of electric energy and conventional fuels.[10] As a result of this changing marketplace, Aramco and SABIC now focus their plant designs for newly built and future chemical plants specifically around the production of petrochemicals and no longer towards fuels.[3]

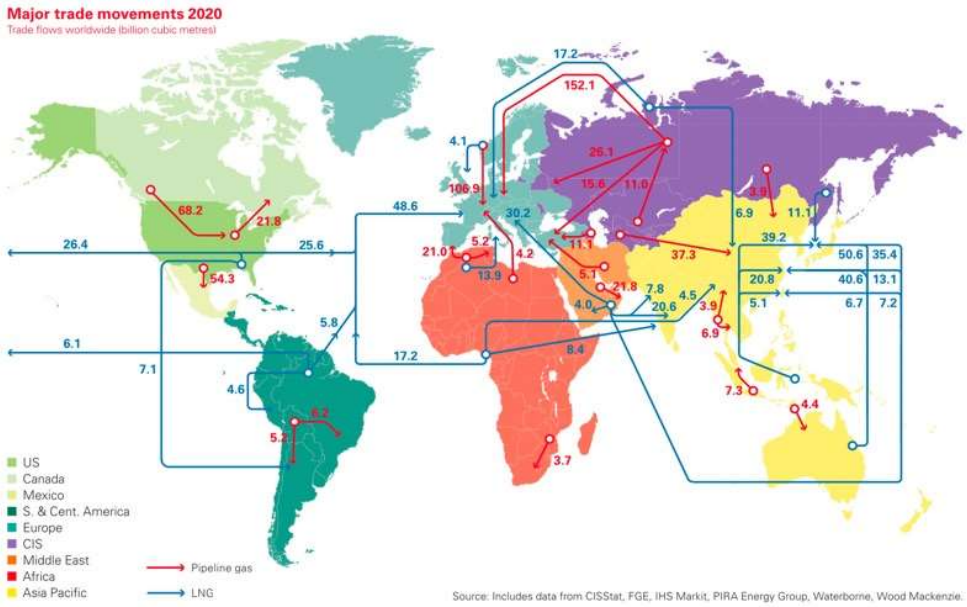

Figure 1.1: Figure reported in the BP Statistical Review 2021 containing the world trade movements of gas to and from regions during the year 2020, for both pipeline gas and LPG (units: billion cubic metres).[8]

Uncertainty provided us with an even greater motivation to invest in renewable energy sources, such as solar, wind and nuclear, or towards renewable carbon-based sources, such as biomass. However, whilst global investment in energy generation via renewables has increased in recent years, a lot more is required to meet global demand.[9] At present, we fall short of achieving our climate goals set out in the Paris agreement, which limited average global temperatures warming less than 2 ˚C, with carbon-neutral emissions being achieved globally by 2050.[11] Achieving this now requires a drop in carbon emissions equal to those observed during the first lockdown of the

COVID-19 pandemic, a drop of 6.3% of carbon emissions from energy generation alone, for every year between now and 2050.[8]

In the US, propane continues to be touted as the next big renewable gas resource, facilitated by the ability to substitute conventional gas for renewable propane in many applications. Renewable propane is produced as a by-product during the production of biodiesel and sustainable aviation fuel (SAF), both derived from renewable sources. One process to produce propane from renewable sources utilises transesterification of triglycerides, which originate in fats, oils and greases.[12] Transesterifcation is carried out using methanol in the presence of sodium or potassium hydroxide, facilitating the cleavage of triglycerides at the C–O bond of the ester. Each triglyceride results in one molecule of glycerol and three molecules of fatty acid methyl esters, referred to commonly as biodiesel.[12] The hydrogenation of glycerol produces propane.

However, whilst it is far from being carbon neutral at present, renewable propane reduces the carbon footprint of conventional propane sources which it may be blended with, which in-turn reduces the footprint of the application it is used in. The World LP Gas Association state that renewable propane could meet half of the worlds gas demands by 2050, should sufficient investment and adoption of the fuel source be undertaken. In addition, the California Air Resources Board claim that renewable propane has a footprint around a quarter of the size of conventional natural gas, and around a fifth of that of gasoline, as shown in Figure 1.2.[13]

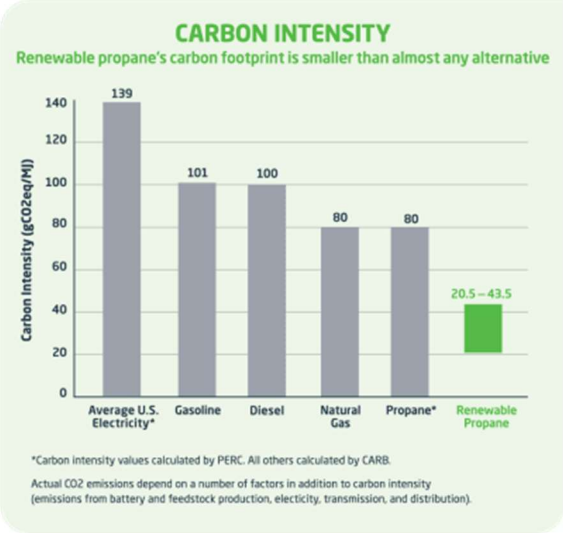

Figure 1.2: Graphic showing the carbon footprints reported by the California Air Resources Board for several conventional energy and fuel sources in the US, compared with the carbon footprint of renewable propane.[13]

1.2 Economic Viability of Associated Natural Gas Capture and Conversion

The discovery of gas within an oil well is certainly not uncommon. The petrochemical industry refers to the gas found with oil as associated natural gas, which predominantly consists of methane. Methane is an incredibly potent greenhouse gas, associated natural gas is flared at source rather than released to the atmosphere. In 2020, global flaring consumed 142 billion cubic metres of associated natural gas, comparable to the combined gas demands of Central and South America.[14] The resultant emissions of gas flaring released 265 mega tonnes (Mt) of CO_2 and 8 Mt of methane. Due to the potency of methane as a greenhouse gas, around 30-fold more potent than CO_2 over a 100-year timescale, the methane emission alone was equivalent to the emission of an additional 240 Mt extra CO_2 into the atmosphere over the 100-year time frame. As a result, COP26 saw over 100 countries sign up to the global methane pledge, to reduce worldwide methane emissions by 30% by 2030.

Capturing associated natural gas, found alongside oil as shown in Figure 1.3, rarely proves economically viable due to the inherent costs associated with transporting it from gas source to refinery, which are often hundreds of miles apart. Valorising associated natural gas has captured a huge amount of interest from both industry and academia, as the valorisation of methane – direct methane to methanol (dMtM) in particular – would prove to be hugely beneficial towards the efficient use of finite resources, whilst also a financially lucrative opportunity.

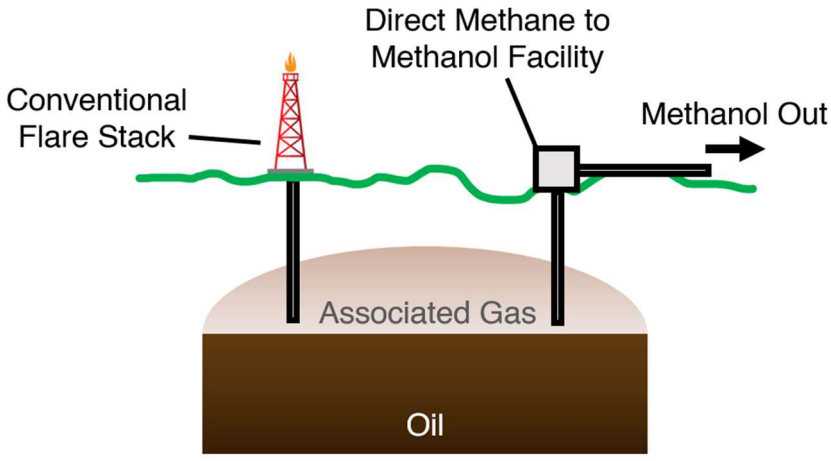

Figure 1.3: A graphic showing a simplified and idealised direct method of methane conversion at source. Methane (associated natural gas in an oil well) is converted directly to methanol, a functionalisation and liquification step that facilitates the capture of and further upgrading of a hugely abundant carbon feedstock whilst avoiding the wasteful methane flaring process.

Methane has the highest bond dissociation enthalpy of any alkane, one of the reasons leading to its characteristic stability.[15] As such, the design of processes that facilitate the easy capture and transport of methane at source, have eluded scientists thus far, although it is undeniable that methane could play a crucial role as a carbon feedstock in the future for upgrading hydrocarbon streams, providing us with an opportunity to directly valorise this incredibly cheap and abundant material.

Liquified natural gas (LNG) is one route for condensing methane into a liquid form, with the density of liquid methane being 640-times that of gaseous methane. LNG has been produced at commercial plants in the US since 1941, although the history of LNG stretches back to the start of the 20th century.[16] The required storage conditions for LNG are the main concern. To maximise the profitability and return on investment, LNG plants must be produced on as large a scale as possible. Transportation on large scale wasn't achieved until 1959, 18 years after the first commercial plant opened. This saw the ocean-going vessel, the Methane Pioneer, carry LNG from the US to the UK. However, the cost of designing and running these carriers is immense. Typically, modern carriers have a cargo capacity between 125,000 and 150,000 m^3 and are designed for transporting LNG at temperatures below −162 °C.[17] This need for expensive transportation methods led to the creation of facilities like the Gulf Gateway Energy Bridge in 2005, which was the first to combine floating storage and re-gasification, so LNG could be vapourised directly onto a docked ship, whilst also having two separate pipeline connections the grid. Nevertheless, these solutions to provide LNG still proved too costly to design and maintain, with ventures into the use of shale gas causing numerous facilities to be decommissioned.

At atmospheric pressures, methane has a boiling point of −161.5 °C, requiring a great deal of energy to condense large volumes.[15] It is therefore not unreasonable to postulate the application of high pressure methane storage. Pressurised methane in storage vessels may eventually lead to methane liquification at temperatures close to ambient, which is understood to emulate how LNG pipelines operate when they carry natural gas to the grid.[16] Whilst this avoids the use of cryogenic temperatures, this does not remove the need of an energy intensive process, whilst also introducing the safety hazard of working with high pressures. The feasibility of carrying out methane liquefication on the scale required to avoid flaring would arguably require a colossal investment in facilities to handle the energy requirements and for the storage of the liquid product. However, as shown in Figure 1.1, the trade of both pipeline gas and LNG occurs world-wide on the billions of cubic metres scale each year.

In addition to the sources of methane of discussed thus far, shale gas has seen a huge rise in popularity in recent years. Shale gas is known to be like other unconventional natural gas sources like coalbed methane, tight sandstones, and methane hydrates, albeit with a higher percentage of ethane and propane constituents. What makes these methane sources so unconventional is their lack of practical access to evolve methane or natural gas. Extraction from rocks buried deep below the ground requires hydraulic fracturing, a politically fraught topic, much like coalbed techniques, capturing methane evolved during the extraction of coal, in what is now a deeply undesirable mining industry.

1.2.1 Routes to Indirect and Direct Conversion of Methane – Heterogeneous

Indirect methane conversion heavily relies on energy intensive processes. One route that has seen commercial success requires methane gasification to produce synthesis gas (syngas). Syngas is composed from a mixture of carbon monoxide and hydrogen, with some carbon dioxide present, and following its formation it is subsequently used as a feedstock for the Fischer-Tropsch (FT) reaction and for methanol formation. Syngas can be produced through either steam reforming (SR) or autothermal reforming (ATR). The reactions shown in Equations 1.1 and 1.2 show steam reforming and water gas shift respectively. SR is very endothermic, requiring the generation of temperatures exceeding 1000 K and pressures greater than 20 atm.[18,19] This is known to consume somewhere in the region of 20–50 % of the methane feedstock to reach and sustain reaction conditions.[20] The process behind methane to methanol conversion using FT is shown in Equation 1.3.

$$[1.1]\ CH_4 + H_2O \rightarrow CO + 3H_2 \quad \Delta G^0_{298K} = 142.1\ kJ/mol$$

$$[1.2]\ CO + H_2O \rightarrow CO_2 + H_2 \quad \Delta G^0_{298K} = 28.6\ kJ/mol$$

$$[1.3]\ CO + 2H_2 \rightarrow CH_3OH \quad \Delta G^0_{298K} = 29.4\ kJ/mol$$

ATR on the other hand is a combination of SR and the partial oxidation of methane, which can require temperatures in excess of 1000 K, although this process has an overall reaction enthalpy close to zero.

Furthermore, producing a plant capable of handling the conditions required for FT on a bulk scale is expensive and utilises catalysts that are prone to deactivation, either through sintering or from an excess build-up of carbonaceous deposits.[21] As a result, both syngas and FT plants are built on large scales to maximise their efficiency and to maximise return on investment. Indirect methane upgrading therefore requires two

chemical processing facilities to work in tandem, with the syngas producing facility often being the major investment.

There are several reasons to why methane is inherently stable. Methane has very low acidity due to the similar electronegativity of carbon and hydrogen, whilst also having poor HOMO and LUMO accessibility making the C–H bonds of methane resistant to attack, making the four equivalent bonds very strong, each requiring over 400 kJ/mol to break.[15] As a result, very few hydrocarbons have a higher bond dissociation enthalpy, causing further difficulty for selective isolation of products following methane upgrading, where there are endless possibilities for end products after methane functionalisation. Olivos-Suarez *et al.* produced an overview of different possible routes for methane upgrading, shown in Figure 1.4.[19]

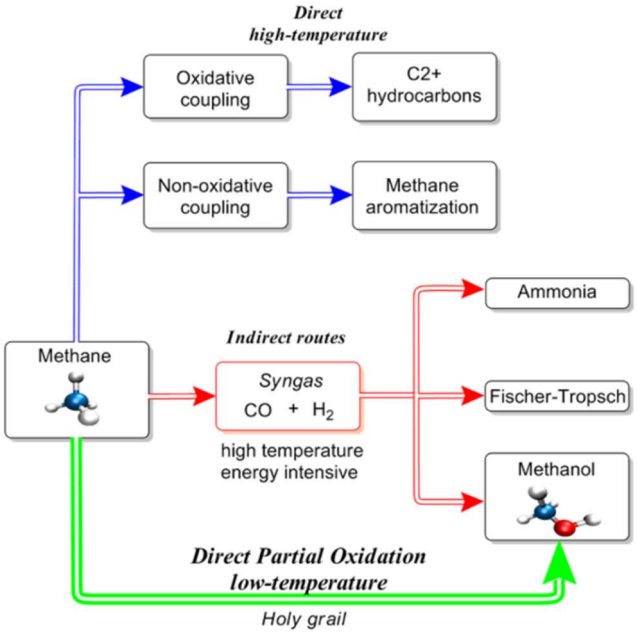

Figure 1.4: Olivos-Suarez et al. report on the known routes for direct and indirect methane conversion, where methane goes via intermediate products to the final products for the given process. Reprinted with permission from A. I. Olivos-Suarez et al., ACS Catal., 2016, 6, 2965–2981. Copyright 2023 American Chemical Society.

POM has been touted as a potential route to produce syngas under milder conditions, over a range of metal or metal-oxide containing catalysts.[22–25] Kobayashi *et al.* report POM over Re doped Ru/Al_2O_3, which was noted to be more efficient at producing syngas when compared to ATR or SR through the use of reduced temperatures and pressures.[26] An additional benefit of the reduced temperature comes from the use of conventional stainless steel reactors, reducing the capital cost when designing commercial plants.

1.2.2 Routes to Indirect and Direct Conversion of Methane - Homogeneous

Bone *et al.* performed one of the earliest demonstrations of methane conversion by homogeneous catalysis, to produce CO by partial oxidation of methane (POM) and even since the early 20th century, research into methane conversion by homogeneous catalysis has remained an active area.[27] However, there are several common limitations that prove to be difficult to overcome. A prerequisite for many homogeneous processes is the use of strong acids, which are very corrosive, require extensive safety measures and additional personnel training, leading to an increased initial outlay when designing a plant. Homogeneous catalysts tested for their capability of functionalising methane are often expensive or incredibly toxic metals, adding further to the capital outlay.[28] Although homogeneous catalysts often deliver high selectivity through the careful design of ligands to produce reactions with high chemoselectivity, regioselectivity or enantioselectivity.[29,30] However, their homogenous nature creates difficulty when trying to separate catalyst and reaction media. Several approaches have been devised to immobilise the catalysts, such as the use of biphasic systems,[29] to keep the catalyst separate from the products, or by binding the catalyst to a support.[31]

One example of homogeneous conversion of methane to higher products is through the oxidation of methane to methyl bisulphate and methyl trifluoroacetate, both of which can be achieved with excellent yields.[32–38] Whilst some these approaches make use of toxic metals, such as mercury, thallium and lead, some make use of expensive, precious metals, such as platinum and palladium. Another route for methane valorisation is through the use of superacid catalysts.[39,40] Superacids are acids which have a proton with a higher chemical potential than that of pure sulfuric acid, making them stronger than any conventional mineral acid. Superacids facilitate stoichiometric oxidation of methane at temperatures around 200 ˚C, but the implementation of super acids once again limits the feasibility of scaling the process commercially.

In respect to the shale gas industry mentioned earlier, direct conversion of mixed gas sources could allow for higher conversion than just methane alone. Methane lacks a functional group, whereas ethane and propane contain both C–C and C–H bonds. Periana *et al.* report how homogeneous catalysis of methane, ethane and propane mixtures using main group elements, thallium and lead, allows for highly selective, stoichiometric oxidation at only 180 ˚C.[37] Selectivity reportedly is greater than 95% for esters of methanol and ethanol, ethylene glycol, propylene glycol and isopropanol. However, whilst this process proves to be very efficient at taking a gas mixture with a similar composition to shale gas, oxidising them at temperatures far lower than those found for POM, the major drawback to scaling up and commercialisation comes once

again from the metals and reagents required to facilitate the reaction. The use of copious amounts of trifluoroacetic acid and thallium or lead for the catalyst, creates safety concerns and subsequently higher costs, which alongside the sub-par catalytic performance renders this process unfeasible for the scales required.

1.3 A Quest for the Holy Grail: Direct Methane to Methanol Conversion

Developing direct methane conversion would allow us to avoid the capital investment required by indirect commercial upgrading routes. One chemical transformation that has garnered a huge amount of attention is direct methane-to-methanol (dMtM) conversion, regarded as the 'Holy Grail of Catalysis.'[41–44] Transporting methane from source to refinery has huge costs associated with capture and carriage. dMtM has the potential to convert this raw, gaseous feedstock into a functionalised, liquid product in a single step. Methanol density at room temperature is around 1200-times that of methane and is a feedstock for commercial processes, such as the production of formaldehyde and acetic acid, as well as the emerging processes such as methanol-to-gasoline (MTG) and methanol-to-olefins (MTO). However, the difficulty lies in preserving and isolating methanol under the conditions required to functionalise methane. Referring to Equations 1.4 to 1.6, only the initial step to activate methane was enthalpically unfavourable, with all subsequent steps leading to products being enthalpically favoured. Hence, achieving high selectivity for dMtM has proved challenging thus far.

$$[1.4]\ CH_4 + \frac{1}{2}O_2 \rightarrow CH_3OH \quad \Delta H^0_{298K} = -126\ kJ/mol$$

$$[1.5]\ CH_4 + \frac{3}{2}O_2 \rightarrow CO + H_2O \quad \Delta H^0_{298K} = -437\ kJ/mol$$

$$[1.6]\ CH_3OH + \frac{3}{2}O_2 \rightarrow CO_2 + 2H_2O \quad \Delta H^0_{298K} = -387 kJ/mol$$

Methanol C–H bonds are approximately 40 kJ/mol weaker than in methane, as shown in Figure 1.5, making methanol more susceptible to further transformations under reaction conditions, with oxidative conditions eventually leading to the production of carbon dioxide as the end product.[43,45–50]

Figure 1.5: Comparison between the bond strengths of the four equivalent C–H bonds found in methane, and the bond strengths of the three equivalent C–H bonds and the O–H bond found in methanol, values provided by Hudgens and Gutman.[47,49]

Methanol oxidation is a facile process in comparison to methane oxidation, due to the polarity of methanol and the lone pairs on oxygen allowing it to bind at Lewis acid sites. As a result, methanol will readily adsorb to the surface of a catalyst making activation and subsequent oxidation easier.

However, no routes for dMtM have been successfully commercialised to date.[51] Even with the difficulties faced, the potential of direct methane valorisation maintains dMtM as an incredibly active area of research within both industry and academia, seeing a wide-range of catalytic systems employed for their activity and selectivity in this process.[19,27,28,43,52–57]

1.3.1 Direct Methane-to-Methanol Conversion (dMtM) using Methane Monooxygenase

Another route that has been known in nature for the functionalisation of methane is the Partial oxidation of methane (POM) to methanol, shown in Equation 1.4. However, over-oxidation can readily occur during POM, as the reaction conditions required facilitates the oxidation of methanol to carbon oxides, highlighted in Equation 1.6. Nature on the other hand does not require such harsh conditions to achieve POM. A unique class of Proteobacteria known as methanotrophs use methane monooxygenase (MMO) enzymes to convert methane to methanol with oxygen at physiological conditions.[58] MMO are typically found in sediments, such as soil, and oxidise the methane emitted from the environment with a stoichiometric amount of oxygen. Methanol dehydrogenase (MDH) is typically employed after methanol formation to afford formaldehyde, a compound of major importance to methanotroph metabolism. MMO can be classified as one of two types, particulate methane monooxygenase (pMMO) and soluble methane

monooxygenase (sMMO). pMMO consists of a membrane-bound copper, with its structural unit having been determined and included in Figure 1.6.[59] pMMO is reported to be the most efficient methane oxidiser known and capable of catalysing POM so efficiently that one molecule of methane is converted every second.[60] sMMO are a water-soluble iron containing enzyme and are less efficient than their pMMO counterpart. The ability of MMO's to conduct POM at ambient temperatures and pressures has attracted widespread interest, with numerous attempts to replicate their activity towards methane through mimicking their active site.[58,61–66]

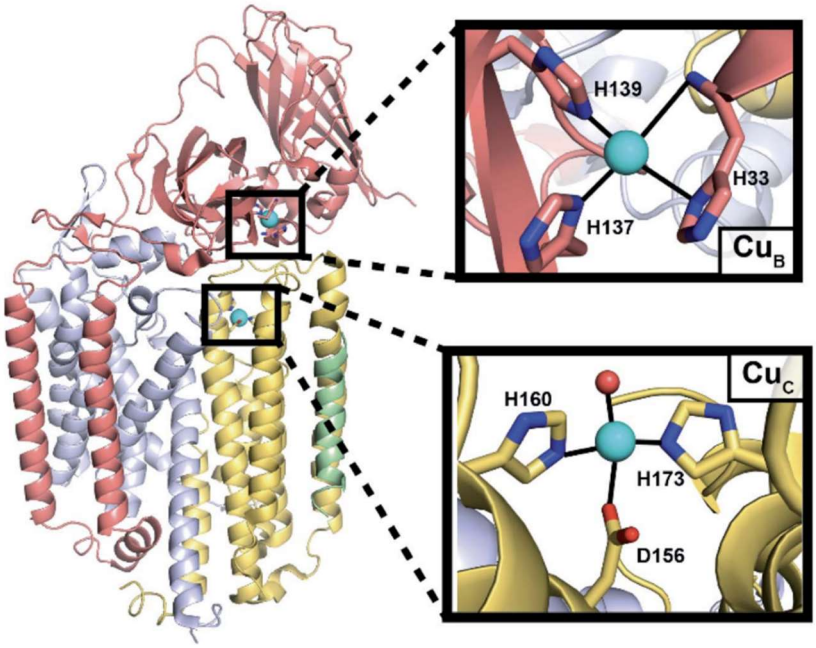

Figure 1.6: Rosenzweig reported the structure for particulate methane monooxygenase (pMMO) to reveal the arrangement of a multinuclear copper active site; copper are teal spheres and oxygen red.[59] In focus are the Cu_B and Cu_C sites (right). Reproduced from G. E. Cutsail, M. O. Ross, A. C. Rosenzweig and S. DeBeer, Chem. Sci., 2021, 12, 6194–6209 with permission from the Royal Society of Chemistry.

1.3.2 Direct Methane-to-Methanol Conversion (dMtM) using Zeolite Catalysts

Solid acid catalysts have been used since the turn of the 20th century for the direct transformation of methane into functionalised products.[67–69] The desire to develop a direct method to transform methane at source has gathered a huge environmental drive, boosting the incentive of transforming an undesirable waste product to valorous chemicals. In particular, ion-exchanged zeolites with iron, cobalt and nickel have displayed favourable properties towards dMtM under ambient conditions.[70–72] One of the most widely studied zeolites for this purpose is copper-exchanged ZSM-5, where a dimeric active site has been proposed following extensive use of experimental data and computational modelling.[73,74] The activation of copper-exchanged zeolites under raised temperatures and in an O_2 containing atmosphere can lead to the dimeric Copper oxo

species, $[Cu–O–Cu]^{2+}$, which is believed to be responsible for the dMtM ability of the catalyst. Schoonheydt *et al.* report the observation of methanol being produced by dMtM over Cu/ZSM-5 and Cu/MOR at temperatures as low as 120 ˚C and at an atmospheric pressure of methane.[74] Although dMtM was carried out at greatly reduced temperatures, catalyst activation was carried out in a flow of pure O_2 at 450 ˚C. Extracting the methanol produced during the reaction required the flushing of the micropores with a mixture of water and acetonitrile. The need for these steps enormously hinders the practicality of a copper-oxo-containing zeolite framework, rendering them hugely unattractive for their use on an industrial scale, and a process that will prove difficult for methanol recovery.

1.3.3 Routes to Establishing a Methanol Economy

Chang *et al.* reported on the first developments of methanol-to-olefin processes (MTO) that were developed at Mobil.[75] MTO is used to convert methanol to olefins, such as ethylene and propylene, both widely useful plastics that are produced on the thousands of kiloton scale each year.[76] Following its early success, it was predicted that MTO would dominate any future methanol-based chemical economy, however, that is yet to be seen. They were not alone in foreseeing the importance of methanol. Nobel laureate George Olah dedicated a large section of his life's work to describe how the chemical economy of the future could become hugely reliant on methanol, and making changes to chemical processes to use methanol as a feedstock would slowly wean our reliance away from oil and gas.[77] Not only would this prove beneficial in reducing carbon emissions, but also allow for the utilisation of renewable bio-methanol sources for a wider array of end products.

Methanol conversion can lead to a wide array of products, with those produced wholly dependent on the reaction conditions chosen. Methanol-to-hydrocarbons (MTH) is an overarching banner given to denote the upgrading of methanol to higher products, although product distribution can be changed by varying reaction conditions, through raised or lowered reaction temperatures and pressures, with oxidative or non-oxidative conditions and changing the catalyst used. As a result, methanol conversion to a range of valorous fine chemicals or feedstocks occurs through MTH processes such as methanol-to-propylene (MTP), methanol-to-olefins (MTO) and methanol-to-gasoline (MTG). However, the isolation of products under oxidative conditions could prove incredibly difficult, with products consumed by over-oxidation to carbon monoxide/dioxide.[78–80] Tatibouët reports that hydrogen generation is never observed for methanol conversion that includes an oxygen containing feed with water detected as a byproduct.[81] Equation 1.7 and Equation 1.8 show that when considering methanol upgrading to methyl formate, the use of oxygen in the feed leads to the production of

water as a by-product, but makes the process exothermic, whereas the conversion of methanol to methyl formate under non-oxidative conditions is an endothermic process with a by-product of hydrogen.

$$[1.7]\ 2\ CH_3OH + O_2 \rightarrow HCOOCH_3 + 2\ H_2O \qquad \Delta H^0_{298K} = -358\ kJ/mol$$

$$[1.8]\ 2\ CH_3OH \rightarrow HCOOCH_3 + 2\ H_2 \qquad \Delta H^0_{298K} = 151\ kJ/mol$$

MTO has shown good selectivity towards to the production of methyl formate when carried out over mixed-metal oxides such as V–Ti, Sn–Mo and Bi, as shown in Figure 1.7.[78,80,82–85] Selective production of formaldehyde from methanol over materials with amphoteric properties, particularly weak acid and weak base sites reduce the residence time of formaldehyde due to the weaker interaction of formaldehyde with the catalyst, lowering the chances of further H-abstraction. A second H-abstraction – producing a dioxy-methylene species – has been attributed to the formation of dimethoxy methane, produced when the dioxy-methylene reacts with a neighbouring methoxy or an adsorbed methanol on the catalyst.

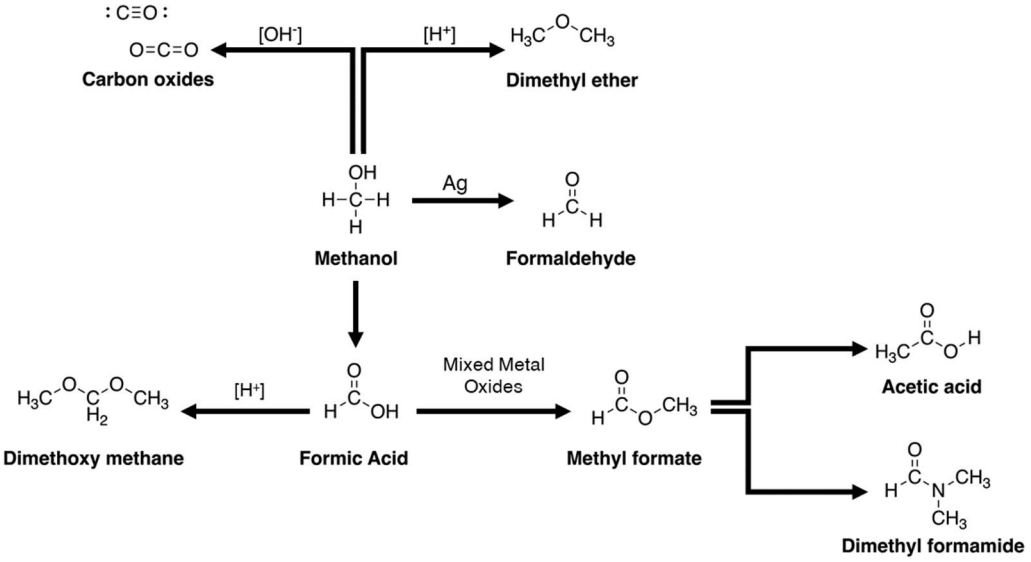

Figure 1.7: Methanol conversion roadmap showing various routes to reported products for methanol upgrading reactions. Additionally, the conversion conditions, such as acidic or basic conditions, and two major products that can be produced from methyl formate.[81]

It could be said that the production of biofuels for a methanol-based economy through biomass could become even more important in years to come. Not only would this lessen our demand on oil and gas further, but also impact on global warming, with further reduced greenhouse gas production. Biomass sources are renewable, with the ability to

produce fuels and fine chemicals from maize, sugar cane, soybeans and vegetable oils.[86] Biomass can undergo gasification into syngas if it has a moisture content lower than 30 %, into a fuel gas by partial combustion, into a bio-gas by fermentation, into bio-diesel or even be transformed into bio-oil.[87–89]

Biomass sources for biofuel production are split into three main classifications: those with high sugar content, such as sugar cane; those with high starch content, such as corn and wheat; or cellulosic biomass, such as woods or grasses. One key biofuel component is bioethanol. 80% of the world's bioethanol production comes from the USA and Brazil, with corn to ethanol being the dominant process in the US and sugarcane to ethanol being the favoured process in Brazil. To give an idea of scale, around 40% of corn produced in the US is consumed to produce around 95% of the total ethanol production in the USA, which exceeded 15 billion litres in 2021 and 2022.[90,91] Total ethanol production worldwide in 2023 exceeded 112 billion litres.[91,92] Preparation of biomass sources requires either wet milling or dry grinding, before converting the extracted starches or sugars into ethanol over several steps, as shown in Figure 1.8.

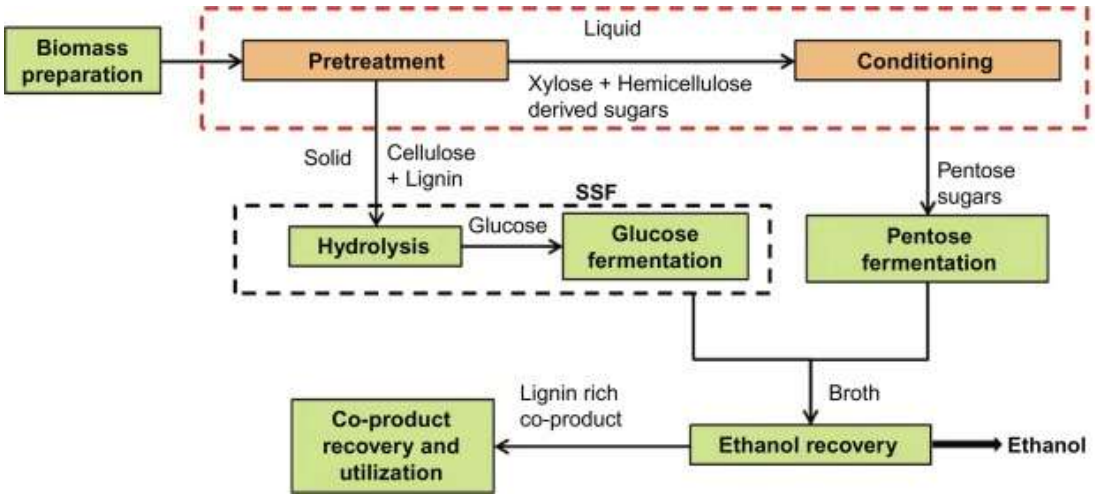

Figure 1.8: Kumar reported this schematic outlining the steps to transform lignocellulosic biomass (dry plant matter), such as corn, into bioethanol. Reprinted with permission from D. Kumar and V. Singh, ed. S. Serna-Saldivar, AACC International Press, Oxford, 2019, pp. 615–631. Copyright 2019 AACCI and published by Elsevier Inc.

Following the extraction of starch, the successive steps focus on breaking down the long chains to glucose which is subsequently transformed into bio alcohols. This contrasts with ethanol production from crude oil sources using the hydrolysis method. This process requires the cracking of long chain hydrocarbons to produce ethylene, which is

hydrated to produce ethanol. Efficient hydrolysis requires the use of high temperatures and phosphoric acid as a catalyst.

Biomass to bioethanol is becoming increasingly important for fuel production, with bioethanol now widely used as a drop in fuel for personal transportation.[93,94] Fuel blends have shifted from containing 5% renewable ethanol (E5 gasoline) to 10% (E10 gasoline) in recent years. This facilitates a reduction in greenhouse gas emissions of personal transport, reducing the reliance on crude oil. A number of harmful compounds, including formaldehyde, acetaldehyde and benzaldehyde, have been found in exhaust gas emissions since the inclusion of bioethanol, which is of particular concern for urban environments.[95]

Bio alcohols are an especially useful as a cost-effective feedstock in the production of chemicals like acetaldehyde, ethyl acetate, propylene and butadiene. Weber *et al.* produced an excellent review that reported average prices for several potential upgrading products for bio alcohols over a three-year span (2015–2018) in the US, to gauge their profitability as a target molecule.[96] Figure 1.9 highlights not only their profitability, but also the scale on which they are consumed globally per annum.

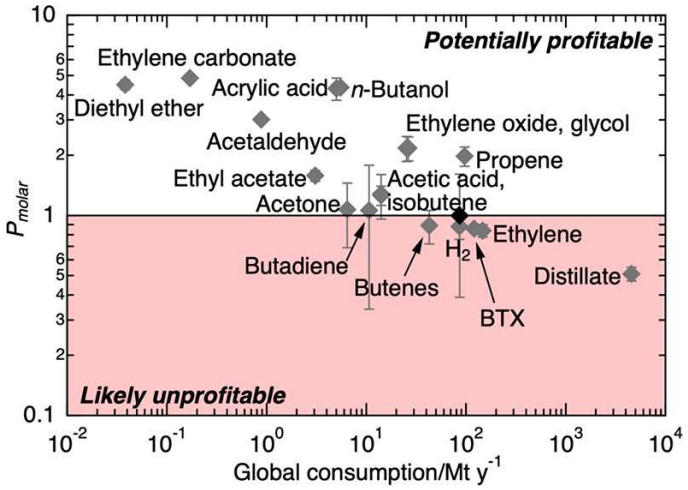

Figure 1.9: Weber et al. reported this graphic to highlight the potential profitability of products produced by bioethanol conversion. An Approximate indicator of operating costs, Pmolar is equal to the ratio of product price divided by the stoichiometric cost of ethanol to produce it. Ethanol lies on the horizontal line, dividing profitable and unprofitable zones. Ethanol is given as the black diamond, products given as grey diamonds. Reprinted with permission from R. S. Weber et al., Ind. Eng. Chem. Res. 2020, 59, 11, 4843–4853. Copyright 2023 American Chemical Society.[96]

Understanding the routes required to transform bio alcohols into higher value chemicals are hugely important, to ensure the reaction is selectively producing profitable products. One example is the use of alumina catalysts to perform ethanol dehydration, affording ethylene and diethyl ether. This process readily occurs over solid-acid catalysts and is

carried out on an industrial scale.[96,97] MTP is a process that is currently seeing a huge shift in focus towards. Historically, propylene production has been achieved using naphtha cracking, allowing propylene to be one of the largest volume organic chemicals produced per annum. However, changing demands in recent years has led to the requirements of new approaches for propylene production, with declining gasoline demand expected to continue to fall. Chemical transformations such as propane dehydrogenation (PDH), using propane captured in natural gas, is one approach that could be used, although a major drawback of PDH is the high selectivity towards CO and CO_2 production if conducted under oxidative conditions.

Grant *et al.* report that boron nitride, formally an unreactive material used for applications that require excellent thermal and chemical stability, has been found to be catalytically active towards PDH and enhance the overall selectivity towards propylene.[98] At 14% propane conversion, they obtain a maximum selectivity of 79% propylene and 12% ethylene. As shown in Figure 1.9, Weber et al. categorise propylene as a profitable chemical, although ethylene is likely unprofitable.[96]

Improving selectivity for MTH and MTP required the use of zeolite solid acid catalysts, with several frameworks having been reported to display very high conversion of methanol, even approaching 100% conversion at 370 ˚C, with a single product selectivity of 41.4% (isobutane) at 370 ˚C.[99] To understand why zeolites displayed such high conversion, as well their selectivity towards certain products, computational modelling has been applied to determine how confinement and interactions with the channels affect transition states during upgrading.[100] To gain a handle on the products from MTH reactions, Weber *et al.* produced the pathway shown in Figure 1.10 for the upgrading of ethanol. Whilst the concept that the petrochemical industry has been involved in some stage of producing all synthetic objects that surround us, the seemingly infinite possibilities that ethanol can be converted into certainly gives further evidence to the claim.

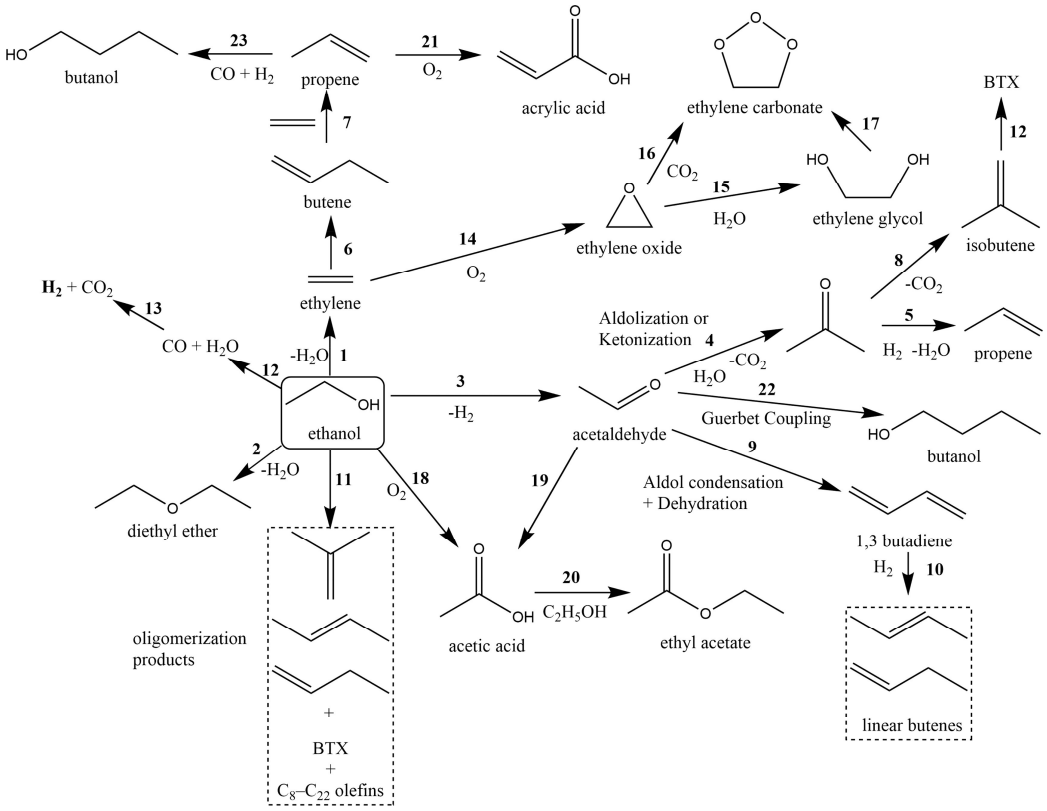

Figure 1.10: Weber et al. reported this graphic as a simplified collection of pathways to products from bioethanol conversion. BTX is an abbreviation of benzene, toluene and xylenes. Reprinted with permission from R. S. Weber et al., Ind. Eng. Chem. Res. 2020, 59, 11, 4843–4853. Copyright 2023 American Chemical Society.[96]

One pathway on Figure 1.10, transforming ethanol to butadiene, is known as the Lebedev process and has seen great interest since it was first reported by Lebedev in 1928.[101–106] Interest waned as availability of butadiene via petrochemical routes usurped Lebedev's ethanol based production process, although changing focuses driven by economic and environmental concerns, along with the availability of bioethanol, have revived interest in this chemical transformation. This process requires a catalyst that is capable of ethanol dehydrogenation, forming acetaldehyde, before subsequent coupling and dehydration of two acetaldehyde molecules to form a single molecule of butadiene, a compound of huge importance in synthetic rubber production.[103,106] Dehydrogenation of ethanol occurs over catalysts containing Lewis acid sites, with coupling and dehydration occurring over metals and/or Brønsted acidic sites.[107]

As alluded to, the requirement for such catalysts led to the development of processes incorporating zeolites since the mid-20th century, which have now become processes that are carried out on the mega ton scale each year. The zeolite framework chosen is only one of the crucial characteristics of the catalyst for the transformations taking place, with the factors surrounding these solid-acid catalysts discussed in detail in Chapter 2.

1.4 Silver: One Metal for Money, Medicine, and Methanol Dehydrogenation

Whilst it has been known about since ancient times and is one of the seven metals of antiquity, silver's name is derived from its Latin name of Argentum, meaning 'shiny' or 'white,' from which its chemical symbol Ag is derived. Silver has the highest reflectivity, highest thermal conductivity, and highest electrical conductivity of any metallic element, and as a result, silver has seen use in a wide range of applications.[108–112] Due to its high electrical conductivity, even when tarnished, silver can be found in high-end electronic equipment and components and in solar power equipment; silver's anti-bacterial properties has led to its use in bandages and dressings, and in water purification; the light sensitive nature of silver has led to widespread use in photographic equipment, specifically films and lenses; but also in tableware and jewellery due to its appearance amongst numerous other applications not listed, such as electrically conductive adhesive materials.[113,114]

There are two main isotopes of silver, ^{107}Ag and ^{109}Ag, which are split 48:52 for their natural abundance and are both a spin-½ nucleus. Whilst NMR spectroscopy of silver has been explored, one major limitation for the observation of either silver isotopes via NMR spectroscopy is that both have a very low sensitivity leading to the requirement of very long experiment times, or the use of very high field instruments.[115]

Silver is a lustrous, white metal that is typically found in its pure, elemental form in the Earth's crust, or as an alloy, typically with gold as electrum. Silver resides in group 11 along with copper and gold and have the trivial group name of 'coinage metals.' The common oxidation state of silver is +1, with the closed shell electron configuration $4d^{10}$. Silver has the lowest first ionisation energy of group 11 elements, and the highest second and third ionisation energies, however, several compounds containing silver with an oxidation state of +2 are known, although Ag^{2+} is strongly oxidising.[116,117] Silver (II) compounds typically react violently when exposed to moisture or air, with silver (III) even more so. As a result, silver (I) compounds are stable and are typically covalent in character. However, the coordination number and stereochemistry around silver can vary throughout the wide number of complexes known, as shown in Table 1.1.[118]

Table 1.1: Table containing a selection of silver containing compounds over the various oxidation states known for silver with differing coordination numbers and stereochemistry around the silver centre[116–118]

Oxidation State of Silver	Coordination Number of Silver	Stereochemistry	Representative Compound
Ag^0 ($d^{10}s^1$)	3	Trigonal Planar	$Ag(CO)_3$
Ag^I (d^{10})	2	Linear	$[Ag(CN)_2]^-$
	3	Trigonal Planar	$AgI(PEt_2Ar)_2$
	4	Tetrahedral	$[Ag(diars)_2]^+$
	6	Octahedral	AgX[a]
Ag^{II} (d^9)	4	Square Planar	$[Ag(py)_4]^{2+}$
	6	Octahedral (distorted)[117]	AgF_2
Ag^{III} (d^8)	4	Square Planar	$[Ag_2(ptp)_2](CF_3SO_3)_2$
	6	Octahedral	$[AgF_6]^{3-}$

[a] X denotes fluoride, chloride and bromide

Silver has the capacity to destroy infectious micro-organisms, making it one of the most powerful antimicrobial agents known. This is especially attractive towards fighting 'super-bugs' that are resistant to antibiotics. In addition, silver has plasmonic properties that facilitate useful biosensing and bioimaging agent properties, assisted by the biocompatibility of silver within the human body.[119] However, the toxicity of silver has been claimed to have a direct relationship to the silver particle size. Small silver cationic particles and metallic silver particles are claimed to be highly toxic, whilst becoming increasingly less toxic as they increase in size, although changes to the physicochemical properties of silver particles through the use of capping and reducing agents can affect their toxicity also.[120,121]

Nanoparticles (NPs) of silver can enter the body through the skin, respiratory or digestive systems, which can occur involuntarily with silver nanoparticles being used in applications such as air purification filters. This is facilitated by the leaching or sintering of the silver nanoparticles, factors which affect this undesirable property of cationic silver include temperature, the presence of organic matter, the pH and interactions between any applied surface coatings and the silver cations. Sintering is one factor which a particular challenge when working with silver-based catalysts, as reactions are typically carried out with raised temperatures and a constant flow of material over the catalyst.

However, whilst silver does have a wide-ranging set of applications, the catalytic activity towards hydrocarbon upgrading is of great interest here. Pioneering work carried out by Baba showed that for zeolites with equal amounts of different metals impregnated, silver came out on top for methane conversion, at 13.2%, when carrying out methane–ethylene co-processing reactions at 400 ˚C.[122] Not only that, but compared to other metals tested, silver impregnated zeolites showed suppressed C–C bond cleavage during upgrading reactions.

Two very well documented catalytic processes that occur over silver-based catalysts in-flow are ethylene epoxidation to ethylene oxide over Ag/α-Al_2O_3, and methanol dehydrogenation to formaldehyde over silver crystals.[123–125] The silver crystalline catalyst sinters during methanol dehydrogenation due to the high reaction temperatures used for the process (600 – 720 ˚C), leading to a reduced pressure across the reaction bed which causes a drop in activity and ultimately catalyst deactivation.

The process of silver sintering is what drives NP agglomeration to occur during reactions carried over silver catalysts, leading to reduced catalyst lifetime and reducing activity over time until eventual deactivation. Ostwald ripening of the AgNPs leads to the growth of larger species until they eventually display the properties of bulk silver, which directly correlates with reduced catalyst activity.[126] Another issue is catalyst poisoning. Silver catalysts used for ethylene can become poisoned by the undesired formation of acetylene. This deactivation process is a major issue, as the silver acetylide (Ag_2C_2) formed is a highly explosive compound.

As a result of these undesirable factors leading to the premature deactivation of silver catalysts, industrial processes are often designed to maximise output at the expense of catalyst lifetime, with the benefits outweighing the cost of needing to replace the spent silver catalyst. It can be postulated that having silver cations highly dispersed throughout a zeolite framework could minimize the risk of forming compounds like silver acetylide due to the conferment of the micropores, whilst also delivering the possibility of slowing silver sintering through restricting mobility. The ability to negate both effects will be crucial in developing a silver-based catalyst that displays both good activity and a longer lifetime than those reported in literature.[127]

1.5 Chapter One Bibliography

1 L. Fernandez, Revenue of the global chemical industry 2005-2019, https://www.statista.com/statistics/302081/revenue-of-global-chemical-industry/#statisticContainer.

2 Petrochemical Trends H_2 2021, https://www.spglobal.com/commodity-insights/PlattsContent/_assets/_files/en/specialreports/petrochemicals/global-petrochemical-supply-racing-to-keep-up-post-covid.html.

3 Executive Summary, Ethylene: A litmus test for the chemical industry, https://www.gpca.org.ae/wp-content/uploads/2020/04/Ethylene-A-Litmus-Test-for-the-Chemical-Industry_ES.pdf.

4 Koncept Analytics, Global Ethylene Market (By Production Capacity & Demand): Insights & Forecast with Potential Impact of COVID-19 (2022-2026), 2022.

5 B. P. Sandaka and J. Kumar, Chem. Eng. J. Adv., Alternative vehicular fuels for environmental decarbonization: A critical review of challenges in using electricity, hydrogen, and biofuels as a sustainable vehicular fuel, 2023, 14, 100442.

6 M. Braun, W. Grimme and K. Oesingmann, J. Air Transp. Manag., Pathway to net zero: Reviewing sustainable aviation fuels, environmental impacts and pricing, 2024, 117, 102580.

7 I. D. Ibrahim, Y. Hamam, E. R. Sadiku, J. M. Ndambuki, W. K. Kupolati, T. Jamiru, A. A. Eze and J. Snyman, Polymers (Basel)., Need for Sustainable Packaging: An Overview., , DOI:10.3390/polym14204430.

8 BP Statistical Review of World Energy - 70th edition, https://www.bp.com/content/dam/bp/business-sites/en/global/corporate/pdfs/energy-economics/statistical-review/bp-stats-review-2021-full-report.pdf.

9 BP Energy Outlook 2022, https://www.bp.com/content/dam/bp/business-sites/en/global/corporate/pdfs/energy-economics/energy-outlook/bp-energy-outlook-2022.pdf.

10 SMMT, UK car market - SMMT, https://www.smmt.co.uk/vehicle-data/car-registrations/, (accessed 10 September 2022).

11 United Nations Framework Convention on Climate Change, The Paris Agreement, https://unfccc.int/process-and-meetings/the-paris-agreement/the-paris-agreement.

12 R. M. Baldwin, M. R. Nimlos and Y. Zhang, Techno-Economic, Feasibility, and Life Cycle Analysis of Renewable Propane (Final Report), United States, 2022.

13 Renewable Propane, https://propane.com/about-propane/renewable-propane/, (accessed 7 October 2022).

14 IEA, Flaring Emissions, Paris, 2021.

15 D. R. Lide, Ed., CRC Handbook of Chemistry and Physics, CRC Press, Boca Raton, 85th edn., 2005.

16 M. S. Mannan, Lees' Loss Prevention in the Process Industries, Butterworth-Heinemann, 2012.

17 Y. Bai and W.-L. Jin, Eds., Marine Structural Design, Butterworth-Heinemann, Oxford, 2nd edn., 2016.

18 W. L. and G. S. R. Reimert, F. Marschner, H.-J. Renner, W. Boll, E. Supp, M. Brejc, in Ullmann's Encyclopedia of Industrial Chemistry, Wiley-VCH Verlag GmbH & Co. KGaA, 2011.

19 A. I. Olivos-Suarez, A. Szecsenyi, E. J. M. Hensen, J. Ruiz-Martinez, E. A. Pidko and J. Gascon, Acs Catal., Strategies for the Direct Catalytic Valorization of Methane Using Heterogeneous Catalysis: Challenges and Opportunities, 2016, 6, 2965–2981.

20 K. Aasberg-Petersen, J.-H. Bak Hansen, T. S. Christensen, I. Dybkjaer, P. S. Christensen, C. Stub Nielsen, S. E. L. Winter Madsen and J. R. Rostrup-Nielsen,

Appl. Catal. A Gen., Technologies for large-scale gas conversion, 2001, 221, 379–387.

21 K. Aasberg-Petersen, I. Dybkjær, C. V Ovesen, N. C. Schjødt, J. Sehested and S. G. Thomsen, J. Nat. Gas Sci. Eng., Natural gas to synthesis gas – Catalysts and catalytic processes, 2011, 3, 423–459.

22 R. C. Ramaswamy, P. A. Ramachandran and M. P. Dudukovic, Ind. Eng. Chem. Res., Modeling Catalytic Partial Oxidation of Methane to Syngas in Short-Contact-Time Packed-Bed Reactors, 2007, 46, 8638–8651.

23 K. Li, H. Wang, Y. Wei and D. Yan, Chem. Eng. J., Partial oxidation of methane to syngas with air by lattice oxygen transfer over ZrO_2-modified Ce–Fe mixed oxides, 2011, 173, 574–582.

24 Z. Ma, P. Ouzilleau, C. Trevisanut, C. Neagoe, S. Lotfi, D. C. Boffito and G. S. Patience, Can. J. Chem. Eng., Partial oxidation of methane to syngas over Pt/Rh/MgO catalyst supported on FeCralloy woven fibre, 2016, 94, 642–649.

25 C. Cheephat, P. Daorattanachai, S. Devahastin and N. Laosiripojana, Appl. Catal. A Gen., Partial oxidation of methane over monometallic and bimetallic Ni-, Rh-, Re-based catalysts: Effects of Re addition, co-fed reactants and catalyst support, 2018, 563, 1–8.

26 L. Li, N. H. MD Dostagir, A. Shrotri, A. Fukuoka and H. Kobayashi, ACS Catal., Partial Oxidation of Methane to Syngas via Formate Intermediate Found for a Ruthenium–Rhenium Bimetallic Catalyst, 2021, 11, 3782–3789.

27 W. A. Bone and R. V Wheeler, J. Chem. Soc. Trans., LVIII.—The slow oxidation of methane at low temperatures, 1902, 81, 535–549.

28 N. J. Gunsalus, A. Koppaka, S. H. Park, S. M. Bischof, B. G. Hashiguchi and R. A. Periana, Chem. Rev., Homogeneous Functionalization of Methane, 2017, 117, 8521–8573.

29 D. J. Cole-Hamilton, Science., Homogeneous Catalysis - New Approaches to Catalyst Separation, Recovery, and Recycling, 2003, 299, 1702–1706.

30 R. Rinaldi and F. Schüth, Energy Environ. Sci., Design of solid catalysts for the conversion of biomass, 2009, 2, 610–626.

31 A. Corma and H. Garcia, Adv. Synth. Catal., Silica-Bound Homogenous Catalysts as Recoverable and Reusable Catalysts in Organic Synthesis, 2006, 348, 1391–1412.

32 R. A. Periana, D. J. Taube, E. R. Evitt, D. G. Löffler, P. R. Wentrcek, G. Voss and T. Masuda, Science, A mercury-catalyzed, high-yield system for the oxidation of methane to methanol, 1993, 259, 340–343.

33 C. E. Taylor, R. R. Anderson and R. P. Noceti, Catal. Today, Activation of methane with organopalladium complexes, 1997, 35, 407–413.

34 R. A. Periana, D. J. Taube, S. Gamble, H. Taube, T. Satoh and H. Fujii, Science, Platinum Catalysts for the High-Yield Oxidation of Methane to a Methanol Derivative, 1998, 280, 560–564.

35 M. Muehlhofer, T. Strassner and W. A. Herrmann, Angew. Chemie Int. Ed., New Catalyst Systems for the Catalytic Conversion of Methane into Methanol, 2002, 41, 1745–1747.

36 M. Soorholtz, R. J. White, T. Zimmermann, M.-M. Titirici, M. Antonietti, R. Palkovits and F. Schüth, Chem. Commun., Direct methane oxidation over Pt-modified nitrogen-doped carbons, 2013, 49, 240–242.

37 B. G. Hashiguchi, M. M. Konnick, S. M. Bischof, S. J. Gustafson, D. Devarajan, N. Gunsalus, D. H. Ess and R. A. Periana, Science, Main-Group Compounds

Selectively Oxidize Mixtures of Methane, Ethane, and Propane to Alcohol Esters, 2014, 343, 1232.

38 M. Ravi and J. A. van Bokhoven, ChemCatChem, Homogeneous Copper-Catalyzed Conversion of Methane to Methyl Trifluoroacetate in High Yield at Low Pressure, 2018, 10, 2383–2386.

39 G. A. Olah and R. H. Schlosberg, J. Am. Chem. Soc., Chemistry in super acids. I. Hydrogen exchange and polycondensation of methane and alkanes in FSO_3H-SbF_5 ('magic acid') solution. Protonation of alkanes and the intermediacy of CH_5^+ and related hydrocarbon ions. The high chemical reactivity of 'paraffins', 1968, 90, 2726–2727.

40 S. Vasireddy, S. Ganguly, J. Sauer, W. Cook and J. J. Spivey, Chem. Commun., Direct conversion of methane to higher hydrocarbons using AlBr3–HBr superacid catalyst, 2011, 47, 785–787.

41 N. R. Foster, Appl. Catal., Direct catalytic oxidation of methane to methanol — a review, 1985, 19, 1–11.

42 B. Han, Y. Yang, Y. Xu, U. J. Etim, K. Qiao, B. Xu and Z. Yan, Chinese J. Catal., A review of the direct oxidation of methane to methanol, 2016, 37, 1206–1215.

43 M. Ravi, M. Ranocchiari and J. A. van Bokhoven, Angew. Chemie Int. Ed., The Direct Catalytic Oxidation of Methane to Methanol—A Critical Assessment, 2017, 56, 16464–16483.

44 S. Raynes, M. A. Shah and R. A. Taylor, Dalt. Trans., Direct conversion of methane to methanol with zeolites: towards understanding the role of extra-framework d-block metal and zeolite framework type, 2019, 48, 10364–10384.

45 C. W. Bauschlicher, S. R. Langhoff and S. P. Walch, J. Chem. Phys., Theoretical study of the bond dissociation energies of methanol, 1992, 96, 450–454.

46 C. W. Bauschlicher and H. Partridge, J. Phys. Chem., Heat of Formation of CH2OH, 1994, 98, 1826–1829.

47 J. Berkowitz, G. B. Ellison and D. A. Gutman, J. Phys. Chem., Three methods to measure RH bond energies, 1994, 98, 2744–2765.

48 Y. Li and J. N. Amor, in Natural Gas Conversion II, eds. H. E. Curry-Hyde and R. Howe, Elsevier, 1994, vol. 81, pp. 103–113.

49 R. D. Johnson and J. W. Hudgens, J. Phys. Chem., Structural and Thermochemical Properties of Hydroxymethyl (CH_2OH) Radicals and Cations Derived from Observations of $\tilde{B}$ 2A'(3p) ← $\tilde{X}$ 2A'' Electronic Spectra and from ab Initio Calculations, 1996, 100, 19874–19890.

50 J. A. Labinger, J. Mol. Catal. A Chem., Selective alkane oxidation: hot and cold approaches to a hot problem, 2004, 220, 27–35.

51 J. H. Lunsford, Catal. Today, Catalytic conversion of methane to more useful chemicals and fuels: a challenge for the 21st century, 2000, 63, 165–174.

52 R. G. W. Norrish and S. G. Foord, Proc. R. Soc. London. Ser. A - Math. Phys. Sci., The kinetics of the combustion of methane, 1936, 157, 503–525.

53 US-2493038-A, 1950.

54 H. D. Gesser, N. R. Hunter and C. B. Prakash, Chem. Rev., The direct conversion of methane to methanol by controlled oxidation, 1985, 85, 235–244.

55 J. A. Labinger, Fuel Process. Technol., Methane activation in homogeneous systems, 1995, 42, 325–338.

56 W. Ding, S. Li, G. D Meitzner and E. Iglesia, J. Phys. Chem. B, Methane Conversion to Aromatics on Mo/H-ZSM5: Structure of Molybdenum Species in

Working Catalysts, 2001, 105, 506–513.

57 V. R. Choudhary, K. C. Mondal and S. A. R. Mulla, Angew. Chemie Int. Ed., Simultaneous Conversion of Methane and Methanol into Gasoline over Bifunctional Ga-, Zn-, In-, and/or Mo-Modified ZSM-5 Zeolites, 2005, 44, 4381–4385.

58 L. Nazaries, J. C. Murrell, P. Millard, L. Baggs and B. K. Singh, Environ. Microbiol., Methane, microbes and models: fundamental understanding of the soil methane cycle for future predictions, 2013, 15, 2395–2417.

59 G. E. Cutsail, M. O. Ross, A. C. Rosenzweig and S. DeBeer, Chem. Sci., Towards a unified understanding of the copper sites in particulate methane monooxygenase: an X-ray absorption spectroscopic investigation, 2021, 12, 6194–6209.

60 J. D. Semrau, A. A. DiSpirito and S. Yoon, FEMS Microbiol. Rev., Methanotrophs and copper, 2010, 34, 496–531.

61 H. Dalton, D. D. S. Smith and S. J. Pilkington, FEMS Microbiol. Lett., Towards a unified mechanism of biological methane oxidation, 1990, 87, 201–207.

62 A. C. Rosenzweig, C. A. Frederick, S. J. Lippard, P. auml and r Nordlund, Nature, Crystal structure of a bacterial non-haem iron hydroxylase that catalyses the biological oxidation of methane, 1993, 366, 537–543.

63 D. A. Kopp and S. J. Lippard, Curr. Opin. Chem. Biol., Soluble methane monooxygenase: activation of dioxygen and methane, 2002, 6, 568–576.

64 R. L. Lieberman and A. C. Rosenzweig, Crit. Rev. Biochem. Mol. Biol., Biological Methane Oxidation: Regulation, Biochemistry, and Active Site Structure of Particulate Methane Monooxygenase, 2004, 39, 147–164.

65 K. T. Dinh, M. M. Sullivan, P. Serna, R. J. Meyer, M. Dincă and Y. Román-Leshkov, ACS Catal., Viewpoint on the Partial Oxidation of Methane to Methanol Using Cu- and Fe-Exchanged Zeolites, 2018, 8, 8306–8313.

66 R. Banerjee, J. C. Jones and J. D. Lipscomb, Annu. Rev. Biochem., Soluble Methane Monooxygenase, 2019, 88, 409–431.

67 Patent No 352,687, 1905.

68 US1565345A, 1925.

69 WO1983000859A1, 1982.

70 N. V Beznis, B. M. Weckhuysen and J. H. Bitter, Catal. Letters, Partial Oxidation of Methane Over Co-ZSM-5: Tuning the Oxygenate Selectivity by Altering the Preparation Route, 2010, 136, 52–56.

71 J. Shan, W. Huang, L. Nguyen, Y. Yu, S. Zhang, Y. Li, A. I. Frenkel and F. (Feng) Tao, Langmuir, Conversion of Methane to Methanol with a Bent Mono(μ-oxo)dinickel Anchored on the Internal Surfaces of Micropores, 2014, 30, 8558–8569.

72 E. V Starokon, M. V Parfenov, L. V Pirutko, S. I. Abornev and G. I. Panov, J. Phys. Chem. C, Room-Temperature Oxidation of Methane by α-Oxygen and Extraction of Products from the FeZSM-5 Surface, 2011, 115, 2155–2161.

73 A. A. Arvidsson, V. P. Zhdanov, P.-A. Carlsson, H. Grönbeck and A. Hellman, Catal. Sci. Technol., Metal dimer sites in ZSM-5 zeolite for methane-to-methanol conversion from first-principles kinetic modelling: is the $[Cu–O–Cu]^{2+}$ motif relevant for Ni, Co, Fe, Ag, and Au?, 2017, 7, 1470–1477.

74 M. H. Groothaert, P. J. Smeets, B. F. Sels, P. A. Jacobs and R. A. Schoonheydt, J. Am. Chem. Soc., Selective Oxidation of Methane by the Bis(μ-oxo)dicopper Core Stabilized on ZSM-5 and Mordenite Zeolites, 2005, 127, 1394–1395.

75 C. D. Chang, C. T.-W. Chu and R. F. Socha, J. Catal., Methanol conversion to olefins over ZSM-5: I. Effect of temperature and zeolite SiO2Al2O3, 1984, 86, 289–296.

76 TechnipFMC, Ethylene Production, 2017.

77 G. A. Olah, Angew. Chemie Int. Ed., Beyond Oil and Gas: The Methanol Economy, 2005, 44, 2636–2639.

78 M. Ai, J. Catal., Catalytic activity for the oxidation of methanol and the acid-base properties of metal oxides, 1978, 54, 426–435.

79 Y. C. Liu, G. L. Griffin, S. S. Chan and I. E. Wachs, J. Catal., Photo-oxidation of methanol using MoO_3TiO_2: Catalyst structure and reaction selectivity, 1985, 94, 108–119.

80 G. Busca, J. Mol. Catal., On the mechanism of methanol oxidation over vanadia-based catalysts: a FT-IR study of the adsorption of methanol, formaldehyde and formic acid on vanadium, 1989, 50, 241–249.

81 J. M. Tatibouët, Appl. Catal. A Gen., Methanol oxidation as a catalytic surface probe, 1997, 148, 213–252.

82 M. Ai, J. Catal., The reaction of formaldehyde on various metal oxide catalysts, 1983, 83, 141–150.

83 G. Busca, P. Tittarelli, E. Tronconi and P. Forzatti, J. Solid State Chem., Evidence for the formation of an antase-type VTi oxide solid-state solution, 1987, 67, 91–97.

84 G. Busca, A. S. Elmi and P. Forzatti, J. Phys. Chem., Mechanism of selective methanol oxidation over vanadium oxide-titanium oxide catalysts: a FT-IR and flow reactor study, 1987, 91, 5263–5269.

85 I. E. Wachs, J.-M. Jehng, G. Deo, H. Hu and N. Arora, Catal. Today, Redox properties of niobium oxide catalysts, 1996, 28, 199–205.

86 D. Debnath, eds. D. Debnath and S. C. B. T.-B. Babu Bioenergy and Food Security, Academic Press, 2019, pp. 45–60.

87 C. Briens, J. Piskorz and F. Berruti, Int. J. Chem. React. Eng., Biomass Valorization for Fuel and Chemicals Production -- A Review, , DOI:10.2202/1542-6580.1674.

88 H. Y. Lim and S. Yusup, eds. B. Gurunathan, R. Sahadevan and Z. A. Zakaria, Elsevier, 2022, pp. 25–40.

89 M. Ram and M. K. Mondal, eds. B. Gurunathan, R. Sahadevan and Z. A. Zakaria, Elsevier, 2022, pp. 253–276.

90 D. Kumar and V. Singh, ed. S. Serna-Saldivar, AACC International Press, Oxford, 2019, pp. 615–631.

91 RFA - Annual Ethanol Production, https://ethanolrfa.org/markets-and-statistics/annual-ethanol-production, (accessed 3 August 2024).

92 N. Koehler, J. Mccaherty, C. W. Rfa and G. Cooper, Renew. Fuels Assoc, Ethanol industry outlook: powered with renewed energy, 2019, 1–40.

93 M. Balat, H. Balat and C. Öz, Prog. Energy Combust. Sci., Progress in bioethanol processing, 2008, 34, 551–573.

94 C. Manochio, B. R. Andrade, R. P. Rodriguez and B. S. Moraes, Renew. Sustain. Energy Rev., Ethanol from biomass: A comparative overview, 2017, 80, 743–755.

95 S. Manzetti and O. Andersen, Fuel, A review of emission products from bioethanol and its blends with gasoline. Background for new guidelines for emission control, 2015, 140, 293–301.

96 R. A. Dagle, A. D. Winkelman, K. Ramasamy, V. L. Dagle and R. S. Weber, Ind. Eng. Chem. Res., Ethanol as a Renewable Building Block for Fuels and Chemicals, 2020, 59, 4843–4853.

97 I. Takahara, M. Saito, M. Inaba and K. Murata, Catal. Letters, Dehydration of Ethanol into Ethylene over Solid Acid Catalysts, 2005, 105, 249–252.

98 J. T. Grant, C. A. Carrero, F. Goeltl, J. Venegas, P. Mueller, S. P. Burt, S. E. Specht, W. P. McDermott, A. Chieregato and I. Hermans, Science, Selective oxidative dehydrogenation of propane to propene using boron nitride catalysts, 2016, 354, 1570–1573.

99 G. J. Hutchings, P. Johnston, D. F. Lee, A. Warwick, C. D. Williams and M. Wilkinson, J. Catal., The Conversion of Methanol and Other O-Compounds to Hydrocarbons over Zeolite β, 1994, 147, 177–185.

100 H. Xia, ACS Omega, Monomolecular Dehydration of Ethanol into Ethylene over H-MOR Studied by Density Functional Theory, 2020, 5, 9707–9713.

101 FR665917A, 1928.

102 GB331482A, 1929.

103 A. Talalay and L. Talalay, Rubber Chem. Technol., The Russian Synthetic Rubber from Alcohol. A Survey of the Chemistry and Technology of the Lebedev Process for Producing Sodium-Butadiene Polymers, 1942, 15, 403–429.

104 Compr. Org. Name React. Reagents, 2010, 1728–1730.

105 V. F. Tret'yakov, R. M. Talyshinskii, A. M. Ilolov, A. L. Maksimov and S. N. Khadzhiev, Pet. Chem., Initiated conversion of ethanol to divinyl by the Lebedev reaction, 2014, 54, 195–206.

106 G. Pomalaza, P. Arango Ponton, M. Capron and F. Dumeignil, Catal. Sci. Technol., Ethanol-to-butadiene: the reaction and its catalysts, 2020, 10, 4860–4911.

107 A. Kumar, Ind. Eng. Chem. Res., Ethanol Decomposition and Dehydrogenation for Hydrogen Production: A Review of Heterogeneous Catalysts, 2021, 60, 16561–16576.

108 J. Burgess and P. J. Steel, Coord. Chem. Rev., Is the silver–alkene interaction a useful new supramolecular synthon?, 2011, 255, 2094–2103.

109 T. Bruna, F. Maldonado-Bravo, P. Jara and N. Caro, Int. J. Mol. Sci., 2021, 22.

110 M. A. Islam, M. V Jacob and E. Antunes, J. Environ. Manage., A critical review on silver nanoparticles: From synthesis and applications to its mitigation through low-cost adsorption by biochar, 2021, 281, 111918.

111 N. Ibrahim, J. O. Akindoyo and M. Mariatti, J. Sci. Adv. Mater. Devices, Recent development in silver-based ink for flexible electronics, 2022, 7, 100395.

112 Z. Sun, J. Li, M. Yu, M. Kathaperumal and C.-P. Wong, Chem. Eng. J., A review of the thermal conductivity of silver-epoxy nanocomposites as encapsulation material for packaging applications, 2022, 446, 137319.

113 C. Li, Q. Li, X. Long, T. Li, J. Zhao, K. Zhang, S. E, J. Zhang, Z. Li and Y. Yao, ACS Appl. Mater. Interfaces, In Situ Generation of Photosensitive Silver Halide for Improving the Conductivity of Electrically Conductive Adhesives, 2017, 9, 29047–29054.

114 W.-T. Cheng, Y.-W. Chih and W.-T. Yeh, Int. J. Adhes. Adhes., In situ fabrication of photocurable conductive adhesives with silver nano-particles in the absence of capping agent, 2007, 27, 236–243.

115 K. Zangger Armitage, I. M., Met. Based. Drugs, Silver and gold NMR, 1999, 6,

239–245.

116 N. N. Greenwood and A. Earnshaw, Chemistry of the Elements, Elsevier Science, 2012.

117 I. Sánchez-Movellán, J. Moreno-Ceballos, P. García-Fernández, J. A. Aramburu and M. Moreno, Chem. – A Eur. J., New Ideas for Understanding the Structure and Magnetism in AgF_2: Prediction of Ferroelasticity, 2021, 27, 13582–13590.

118 A. G. Young and L. R. Hanton, Coord. Chem. Rev., Square planar silver(I) complexes: A rare but increasingly observed stereochemistry for silver(I), 2008, 252, 1346–1386.

119 G. A. Sotiriou and S. E. Pratsinis, Curr. Opin. Chem. Eng., Engineering nanosilver as an antibacterial, biosensor and bioimaging material, 2011, 1, 3–10.

120 A. Huk, E. Izak-Nau, B. Reidy, M. Boyles, A. Duschl, I. Lynch and M. Dušinska, Part. Fibre Toxicol., Is the toxic potential of nanosilver dependent on its size?, 2014, 11, 65.

121 J. Pulit-Prociak, K. Stokłosa and M. Banach, Environ. Chem. Lett., Nanosilver products and toxicity, 2015, 13, 59–68.

122 T. Baba and H. Sawada, Phys. Chem. Chem. Phys., Conversion of methane into higher hydrocarbons in the presence of ethylene over H-ZSM-5 loaded with silver cations, 2002, 4, 3919–3923.

123 M. Lamoth, T. Jones, M. Plodinec, A. Machoke, S. Wrabetz, M. Krämer, A. Karpov, F. Rosowski, S. Piccinin, R. Schlögl and E. Frei, ChemCatChem, Nanocatalysts Unravel the Selective State of Ag, 2020, 12, 2977–2988.

124 N. Y. Usachev, I. Krukovsky and S. A. Kanaev, Pet. Chem., The nonoxidative methanol dehydrogenation to formaldehyde: (A review), 2004, 44, 379–394.

125 G. J. Millar and M. Collins, Ind. Eng. Chem. Res., Industrial Production of Formaldehyde Using Polycrystalline Silver Catalyst, 2017, 56, 9247–9265.

126 J. K. Lee, X. E. Verykios and R. Pitchai, Appl. Catal., Support and crystallite size effects in ethylene oxidation catalysis, 1989, 50, 171–188.

127 Y. Ono and T. Baba, Phys. Chem. Chem. Phys., Unique properties of silver cations in solid-acid catalysis by zeolites and heteropolyacids, 2015, 17, 15637–15654.

Chapter Two – Zeolites: Natures Solid Acid Catalyst

The first reports of zeolites in nature came from the mid-18th century. Discovered by Cronstedt, a famous Swedish minerologist, he was the first to describe the physical properties of zeolites, discovered by heating his samples in a blow-pipe flame.[1,2] Taken from the Ancient Greek words for “to boil” (ζέω) and “stones” (λίθος), zéo líthos, or zeolites, were observed to release bubbling water after the application of heat, leading to their representation as ‘boiling stones’ and an early indication of their microporosity.

This characteristic of zeolites arises from their ordered arrangement of tetrahedrally arranged units of alumina and silica, where Al^{3+} and Si^{4+} tetrahedral atoms (T atoms) are interconnected by shared oxygen atoms, generating a three-dimensional microporous framework of uniformly sized channels on the molecular dimension scale. Entry to the framework through pores at the channel ends allow for molecules small enough to fit to diffuse through the framework, whilst those too large are simply excluded from entering the micropores.

Zeolites are split into two classifications, with ‘natural’ zeolites and ‘synthetic’ zeolites. Natural zeolites are those found in the Earth’s crust and are extracted by mining operations which were carried out on an estimated 1.6 million tonnes scale worldwide in both 2020 and 2021.[3] Following the pioneering work by Barrer to produce the first synthetic zeolite, an array of novel zeolites frameworks have been produced through hydrothermal synthesis.[4–10] However, both natural and synthetic zeolites have found use in a wide range of applications owing to their excellent ion-exchange properties, favourable catalytic activity, low cost and their frameworks robustness, and as such have been used for cleaning radioactive waste streams and water streams, as de-NOx catalysts in emissions systems and their largest scale use, in laundry detergents, due to their water softening properties with their affinity for Ca^{2+} and Mg^{2+}.[11–15] As alluded to in Section 1.3.3, the catalytic properties of zeolites originate from the Brønsted acid sites present on the framework, facilitating processes such as Fluid Catalytic Cracking (FCC) and Hydrocracking (HC).[16]

Zeolites display varying chemical and physical properties due to differences in their crystal structure and chemical composition. This leads to varying ion-exchange isotherms, molecular pore dimensions and both the number and strength of Brønsted acid sites present on the zeolite framework. At the T atom sites that include Al^{3+}, a

charge-balancing cation is required to balance the charge deficit of the $[AlO_4]^-$ unit, preserving the overall neutral charge of the zeolite framework, as shown in Figure 2.1.

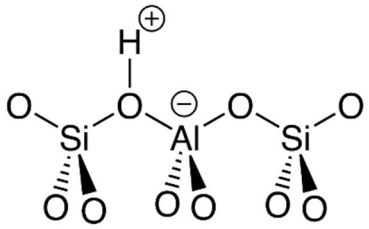

Figure 2.1: Due to the charge deficit of the $[AlO_4]^-$ unit of the zeolite framework, a cation, in this case a proton, is required to balance the overall charge of the material. This site is commonly referred to as a Brønsted acid site.

To date, the IZA database contains 246 fully ordered framework types and 9 partially disordered framework types. Whilst this collection of framework topologies is diverse, only 17 of these frameworks have found use in industry.[17–19] Natural zeolites are often found within a limited range of silicon-to-aluminium ratio, with Na^+, K^+, Ca^{2+} and Mg^{2+} counterions. These limited properties of natural zeolites restrict their applications. Synthetic zeolites can be tuned to have specific properties and are reported with widely varying counterions and silicon-to-aluminium ratio, with further modification possible using post-synthetic treatment.[20]

2.1 Zeolites and Zeotypes: Factors Affecting Hydrothermal Synthesis

Ever since the first synthetic zeolites were produced, hydrothermal synthesis has been utilised to produce zeolites and zeotypes with targeted characteristics to provide enhanced properties for their specific catalytic applications.[8,21–24] Routine hydrothermal synthesis is carried out in batches, requiring the preparation of a synthesis gel that is transferred to an autoclave, typically PTFE-lined due to the corrosive nature of the gel. A synthesis gel consists of several parts, which are zeolite precursors in set ratios. Once these precursors are thoroughly mixed into a free-flowing gel, the application of heat and pressure results in their crystallisation and the growth of the crystalline zeolite framework.

Synthesis gels for zeolites consist of only a few components: the silicon source, the aluminium source, a mineralising agent, structural directing agent (SDA) and water. The SDA can be inorganic or organic and is used to direct the crystallisation growth around a fixed shape. Quaternary ammonium cations are commonly used for this purpose and are commonly referred to as organic structural directing agents (OSDA). The use of

quaternary ammonium cations facilitates for the easy removal of the OSDA post-synthesis with a calcination under air at elevated temperatures proving sufficient to initiate both Hofmann elimination and oxidation. The mechanism of elimination proceeds to eliminate the ammonium cation as an olefin and tertiary amine, which diffuse out of the micropores and leave behind a Brønsted acid site.[25,26] Another route into directing the growth of zeolite crystals is to use seeds. Seeds are previously formed zeolite materials, which facilitate the crystallisation of the synthesis gel mixture by giving the gel a template on which to grow which facilitates faster nucleation times. This epitaxial growth relies on the seed material having a very high degree of crystallinity, for which the new material mimics as it grows. As these direct the shape of the newly formed materials, it is essential that the crystals of the seed used are as defect free as possible.

The silicon and aluminium sources used in the synthesis gel guide the final ratio of silicon-to-aluminium in the synthesised material, although a wide range of sources for both are regularly used in the literature surrounding hydrothermal synthesis of zeolites, including colloidal silicas, fumed silicas, aluminium salts and oxides, and alkoxides of both silicon and aluminium.[7,27–30] The adaptation of zeolite synthesis methods allow for the production of zeotype materials by hydrothermal synthesis.[31] Zeotypes can be produced from either partial or complete substitution of aluminium in the synthesis gel and therefore in the final product. Or a post-synthetic modification can be carried out on zeolites, consisting of de-alumination before insertion of the metal of choice into the framework vacancy. In academia, metals used in zeotype materials is limited only by their efficiency, however, in terms of scaling for commercialisation and adoption on an industrial scale, choices must be made considering practicality, economics and yield. A good example of this is TEOS, a silicon alkoxide commonly used in academia for the synthesis of zeolites, although the high reagent cost and need for large volumes of ethanol removal post-synthesis make it economically unsuitable for industrial applications. Another synthesis gel component that is commonly plagued by similar issues is the organic structural directing agent. Hence, research is ever active around synthesising zeolites using cheaper and more sustainable silica sources.[32,33]

Many silicon precursors are poorly soluble in aqueous conditions and to produce a homogenous synthesis gel, the use of mineralising agents must be employed. Mineralising agents carry out multiple roles in the gel. Firstly, they improve the transport of and accessibility to metal precursors. Silica species are broken down by the mineralising agent to leave them in their monomeric form which can be crystallised during the growth phase to become part of the zeolite framework. Mineralising agents for zeolite synthesis are commonly hydroxide (OH^-) or fluoride (F^-) based and very rarely

would another mineralising agent be used.[33,34] The choice of mineralising agent can often limit the feasibility of synthesis scale-up for zeolites and zeotypes.

Synthesis gel pH is normally alkaline, resulting from the choice of the mineralising agent. Choosing the mineralising agent often requires careful consideration as gel pH can have a major effect on the final silicon-to-aluminium ratio of the synthesized zeolite, whilst some frameworks are sensitive towards specific pH ranges and only in those can stable phases of zeolite crystal successfully form.[35] One thing to note, is that fluoride based mineralising agents allow for the use of acidic gels or even non-aqueous media, although these often require longer synthesis times.

Considering the green chemistry aspects of zeolite synthesis gels, water is the classic solvent of choice whilst using components that are soluble to varying degrees within water. The ease of water removal, wide range of sources and its ability to be recycled, very low cost and availability make it an economic and environmentally excellent choice.[32] However, the volume of water used in the gel requires careful control as this affects both reagent concentration and gel viscosity. As water can enter and fill the voids and micropores formed during the growth phase, which potentially impacts pore diameter, this can also cause the gel to become de-homogenised, changing reagent concentration and affecting overall growth of the zeolite. Gel viscosity affects the diffusion rate of reactants during hydrothermal synthesis, whilst the addition of alcohols can add further control to the rate of hydrolysis of silicon from alkoxide sources.[36] However, routes to produce solvent-free hydrothermal synthesis methods have also been explored.[37]

Time and temperature are two more factors that are important to consider. The synthesis time of zeolites can be sped up; however, each framework is known to have different rates of crystallisation.[38] Hydrothermal synthesis temperature has a direct influence on the gel viscosity, changing the reagent diffusion rates and also the nucleation rate, affecting both the crystallinity and the crystal size of the zeolites formed.[38] Not only this, but also the heating application used can have a major impact on the final product, as zeolites synthesized under microwave or ultrasonic treatment can display improved crystallinity, reduced crystal size and increased surface area when compared to conventional oven heating.[39,40]

Post-synthetic modifications allow for a wide range of tuned properties, including the incorporation of metals into the framework itself to create a zeotype, which can display changed acid strength or acid type.[20] Post-synthetic modification can also be used to introduce mesopores, which facilitate processes via a ‘ship in a bottle’ approach.[20,41,42]

One common post-synthesis modification is to exchange the extra-framework cations to tune the zeolites properties for a specific application, which can be achieved through aqueous ion-exchange, incipient wetness impregnation, solid mixing or by vapour deposition.

Zeolite frameworks can also have their T atoms selectively removed using acid or base treatments, to remove aluminium or silicon T atoms respectively.[43–46] This produces vacancies in the framework that allow for the incorporation of new metals into the framework positions or the production of topologies that have silicon-to-aluminium ratios that fall outside of the range typically allowed from hydrothermal synthesis. Following the dealumination or desilication of a zeolite framework, the vacancies left behind by the removed T atom can be filled using a suitable metal of choice, as shown in Figure 2.2. What factors make these metals suitable are that they are similar in both size and charge to those removed, with Ga^{3+}, Sn^{4+}, Ti^{4+} and Zn^{2+} and Zr^{4+} being commonly used.[47–52]

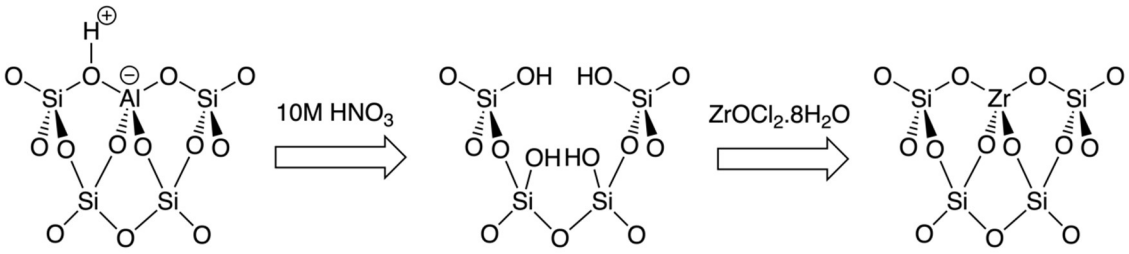

Figure 2.2: Graphic showing a simplified mechanism for the de-alumination of a zeolite framework using nitric acid, followed by the metal impregnation step, incorporating zirconium into the framework. Reagents taken from work reported by Ivanova.[52]

One example of a material prepared this way was reported by Ivanova, who investigated ethanol to butadiene over a series of Zr impregnated zeolite Beta frameworks, which were also doped using 1 wt% of Ag.[52] The highest activity towards ethanol conversion was reported as 15.9%, whilst the highest butadiene selectivity was reported at 67.1%, albeit for two different materials, although all results fell in a similar range for conversion and selectivity values. Incorporation of zirconium into the framework was achieved following dealumination in 10M HNO_3, before impregnation of Zr into the framework using a zirconium chloride solution in DMSO. Silver was introduced through incipient wetness impregnation using $AgNO_3$ solution. Whilst these catalysts do show promising results for this process, considering the requirements of scale for catalyst synthesis, the materials are likely to remain of an academic interest for the foreseeable future.

Initial nanosized zeolite syntheses were first reported in the early 1990s, where varied preparation methods from the use of colloidal suspensions to clear precursor

suspensions.[53–55] By the late 1990s, the zeolite frameworks of industrial importance were available in their nanosized forms, although it has taken almost another decade since before research targeting the optimisation of nanocrystal synthesis was carried out.[56,57] It was found that in order to favour the formation of nanocrystals, low temperatures are required for hydrothermal synthesis. Low temperatures benefit nucleation rate whilst hindering the rate of growth, leading to small crystal sizes being obtained. Valtchev *et al.* achieved the synthesis of zeolite A under room temperature conditions and without the use of an organic template.[58]

Alkali metal content can cause notable differences in the aggregation of gel particles in synthesis gel, so the use of low quantities of alkali metals became favoured. Ultimately, this leads to a reduced amount of alkali cations for charge balancing the final product, however, this is compensated for through an abundant use of organic cations.

Direct synthesis of metal-exchanged CHA has been reported as a route to introduce metals into exchangeable framework positions during synthesis. Haldor Topsøe were amongst the first to record this route, filing a patent (EP2931406A1) for a one-pot method to synthesize Cu-SSZ-13. Wei *et al.* reported the hydrothermal synthesis of Fe-SSZ-13 after addition of iron (II) sulphate to the synthesis gel.[59] Whilst this idea certainly proves to be an interesting concept, the potential to incorporate metals of choice during synthesis could prove to be extremely difficult to carry out successfully with silver. Seff *et al.* reported that silver can auto reduce under raised temperature conditions, leading to framework oxidation to produce oxygen vacancies in the framework and reducing overall crystallinity.[60] During calcination, raised temperatures are required to decompose the OSDA which can facilitate silver auto reduction, causing extensive framework damage that may even lead to complete framework collapse. This effect is discussed further in Section 2.3.

2.2 Zeolites and Zeotypes: Topology, Dimensionality and Acidity of Solid Acid Catalysts

Löwenstein's rule is fundamental in how aluminium T atoms are arranged within a zeolite framework. That is because Löwenstein's rule states that zeolite frameworks cannot have an oxygen atom being shared by adjacent Al T atoms, so Al–O–Al sequences are not allowed. One sequence that is commonly reported as the most stable for 6 MR configurations are Al–O–(Si–O)$_2$–Al sequences, denoting an Al pair commonly referred to as a next-next-nearest neighbour (NNNN) conformation. Another common sequence is Al–O–Si–O–Al, denoting an Al pair that is one silicon T atom closer than the previous, which is commonly referred to as a next-nearest neighbour (NNN) conformation. These are shown in Figure 2.3.

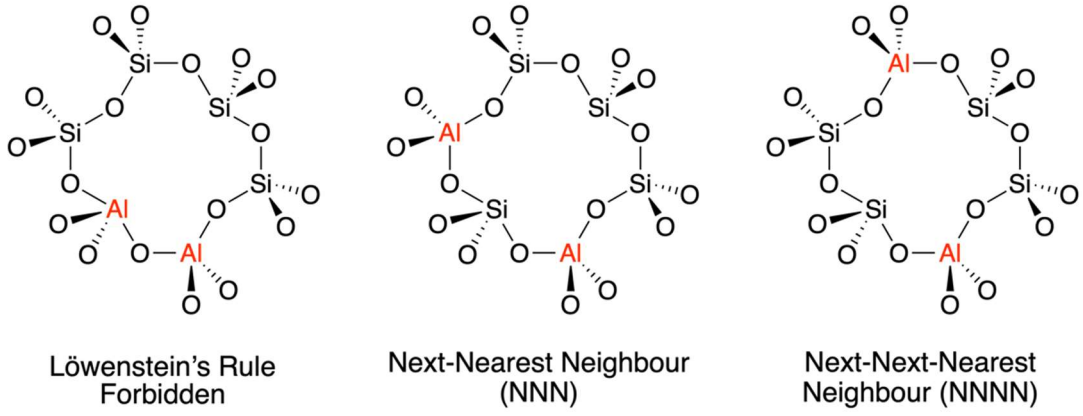

Figure 2.3: A simplified graphic of a zeolite 6 MR (absence of charge balancing cations for clarity) showing the three potential conformations for 6 MR's containing two Al T atoms, with both neighbouring configurations and the Löwenstein's rule forbidden adjacent Al T atoms

Since zeolite frameworks can have widely varying silicon-to-aluminium ratios, as well as the potential to contain defect sites and extra framework atoms, defining the exact positions for T atoms proves to be a major challenge. Adding to this is the number of possible configurations for each unit cell of a framework. For example, the zeolite material SSZ-13 is of the CHA topology with a strict silicon-to-aluminium ratio of 17 and would be expected to have two Al atoms per unit cell. Through the use of computational modelling, it is possible to calculate the stability of different unit cell conformations, giving insight into which T atom sites contribute towards framework stability.[61,62] When modelling the unit cell, Löwenstein's rule forbidden sequences can be modelled. Following placement of the first Al T atom, a total of 35 possible T-atom positions are available for the second Al T atom to be located, giving a total of 560 unique

combinations for the positions of T atoms and extra-framework cations. However, only 33 positions are available for the second Al T atom to not violate Löwenstein's rule.

Making changes to the synthesis conditions can alter the final position of Al within the framework. Fletcher *et al.* calculated a difference for Al T atom position favourability between chabazite synthesized with H^+ and Na^+ cations.[61] In the sodium form, Al T atoms preferred the NNNN conformation, whilst in the proton form the NNN conformation was preferred. This is in close agreement with experimental results, where hydrothermal synthesis was sensitive towards the extra-framework cations used, with Li^+ found to promote aluminium pairing the most out of alkali metal cations due to the reduced cationic radius.[30,63] However, materials with aluminium pairing as NNN do not conform with Dempsey's rule, which would predict from the electrostatics alone that Al atoms would prefer to be positioned as far apart as possible. Aluminium pairing in the zeolite framework allows for the exchange of doubly or even triply charged extra-framework cations to counterbalance the framework charge deficit, as shown in Figure 2.4.

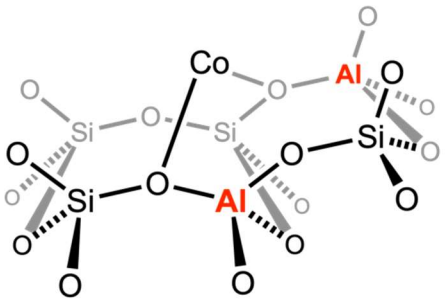

Figure 2.4: Image showing the next-nearest neighbour (NNN) arrangement of aluminium pairs in a zeolite framework, capable of being charge balanced by the Co^{2+} doubly charged cation

Wendelbo *et al.* reported the distribution of Al atoms in both natural and synthetic chabazite materials through the use of NMR spectroscopy.[64] This work built upon previously reported studies for Al distribution in the faujasite structure.[65,66] Without careful control of hydrothermal synthesis by choosing components that facilitate aluminium pairing, chabazite will typically be synthesized in a conformation where NNN are the least common conformation when analysed by ^{29}Si MAS NMR spectroscopy.[64] This result reflects directly with naturally occurring chabazite. This inclination to avoid NNN conformations suggests the validity of Dempsey's rule.

Careful control of the counterions used in hydrothermal synthesis unlocks new synthetic routes to produce zeolites with tuned catalytic properties, enhancing selectivity and stability through careful control of both silicon-to-aluminium ratio and Al positioning.[24,63]

For example, carrying out hydrothermal synthesis to produce the lithium form would facilitate closer Al pairing within the structure, which can be followed by a post-synthetic treatment to exchange the lithium extra-framework counterions for whatever may be desired. In addition, the synthetic route and reagents used in the synthesis can be crucial to introducing desired characteristics to a material. Inter-zeolite conversion (IZC) is a process that utilises a parent zeolite as the alumina source in the process of creating a daughter zeolite, although the exact mechanism remains unclear.[67]

Dědeček reported a straightforward technique involving Co^{2+} titration to probe the approximate aluminium distribution of the CHA framework.[68] The Co^{2+} ion facilitates accurate determination of the sites accessible for aqueous ion-exchange, which can be of particular interest in the preparation of polyvalent metal-exchanged frameworks.

Reports of zeolites used in catalytic applications were first announced in 1960, with zeolites X and Y demonstrating isomerisation of paraffin and molecular cracking.[69] The first commercial catalytic process was gas–oil cracking, reported to have a worldwide capacity for processing over 40 million barrels per day by 1962.[70] In the early 1960's, the phrase 'shape selectivity' was coined by Weisz and Frilette to describe the unique catalytic properties observed for small pore frameworks, although this quickly expanded to medium pore frameworks.[71] Size exclusion effects are a major factor arising from the microporous dimensions of zeolite frameworks, affecting both reactant and product selectivity, restricting the possible transition states (TS) and molecule conformations found within the micropores.[72] However, this also gives rise to the confinement effect which promotes reaction activity through the stabilisation of TS from interactions in the micropores. The result of these factors have a direct effect on the catalytic activity of zeolites, their sorption properties and even on their overall acidity.[73]

Unit cells are the repeating atomic arrangements that are unique to each zeolite framework topology, where zeolite frameworks can be thought of as being comprised of infinite or a finite number of component units. These component units are secondary building units (SBU) and composite building units (CBU), where the primary building units (PBU) consist of the TO_4 tetrahedra themselves. SBU's contain up to 16 T-atoms and work under the assumption that the entire framework consists solely of one SBU. In addition, unit cells contain an integral number of SBU's. CBU's however can appear in several different framework topologies and are occasionally referred to as tertiary structure units. Common CBU's include sodalite cages, double 4, double 6 and double-8 rings, α-cavities, pentasil rings and mordenite units.[74,75] The difference between the building units, as well as common CBUs are shown in Figure 2.5.

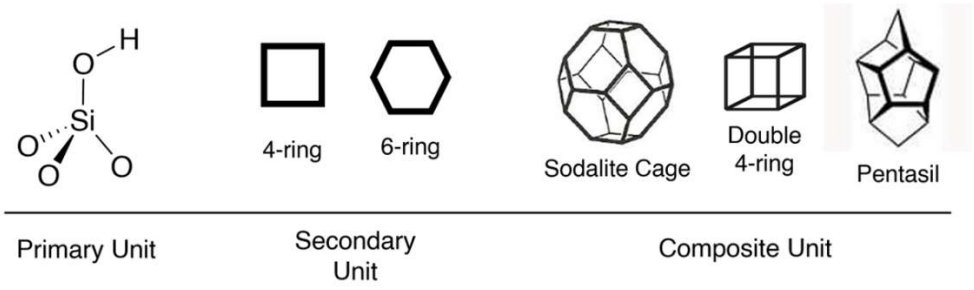

Figure 2.5: Graphic displaying the different levels of building unit that zeolite frameworks are comprised of, from a primary building unit (Silica, SiO_4), secondary building unit (single six-ring) and a tertiary (composite) building unit (Sodalite cage).

Some zeolite framework topologies have diverse silicon-to-aluminium ratios whilst others have fixed silicon-to-aluminium ratios and changing this requires post synthetic modification. Modification also facilitates changed T atoms being incorporated into the framework. T atoms can vary significantly and their suitability is dependent on their size and charge, however, phosphorous, tin, titanium, gallium and zinc are all commonly used when creating zeolite-like (zeotype) materials.[76]

The different classifications and properties for zeotypes are ultimately diverse, the most widely used being aluminophosphates (ALPO) and silicoaluminophosphates (SAPO), whilst others like titanosilicates, the most common material being TS-1, have been widely studied for their use in epoxidation reactions.[23–25] In zeolites, where T atoms consist of Si^{4+} and Al^{3}, the charge deficit of aluminium requires a single charge-balancing cation, typically H^{+}, NH_4^{+} or Na^{+}. With materials like zincosilicates, the T atom of Al^{3+} is replaced by Zn^{2+} and requires either two cations or a doubly charged cation for charge-balancing, such as Ca^{2+}. Other Zeotypes include the fully-silica zeolites, such as silicalite-1, which is of an MFI topology. Each zeotype displays its own distinct properties, such as changed acidity and acid strength. Some pure silica zeolites display hydrophobic properties, whilst titanosilicates display Lewis acidity rather than the Brønsted acidity of zeolites, as shown in Figure 2.6.[23,77–80]

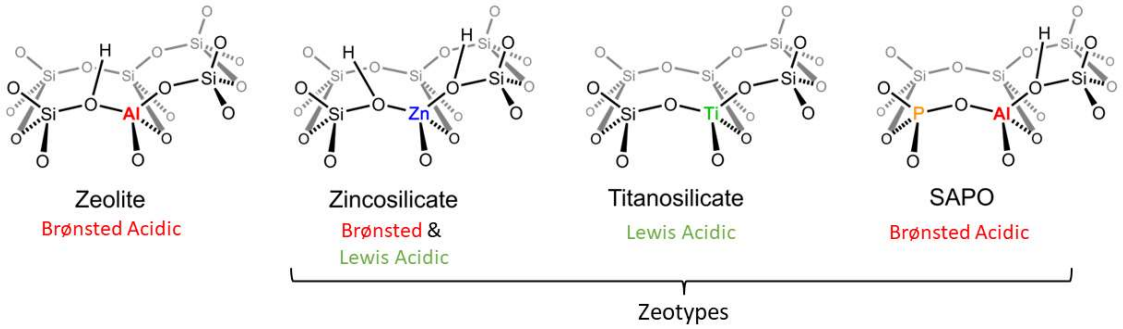

Figure 2.6: Image displaying a simplified version of a zeolite, zincosilicate, titanosilicate and silicoaluminophosphate (SAPO) to highlight the different elements found in the framework and the requirement of charge balancing counterions.[23,79,80]

Lewis acid and Brønsted acid sites are found at varying locations on zeolite and some zeotype frameworks. Sites which display strong Brønsted acidity in zeolites are what facilitate the catalytic activity that is responsible for isomerisation, dehydration, decarbonylation and cracking reactions.[69,70,81,82] Brønsted acidic sites in zeolites can be present due to defects in the framework or naturally from the Al^{3+} T atom in the framework, creating an overall charge deficit of the framework requiring a cation counterbalance the charge and bring overall neutrality. A proton (H^+) is what counterbalances the charge at Brønsted acid sites (BAS), which have been shown to be proton-donating in nature. The strength of a materials Brønsted acidity can be directly associated with the angle of the Al–O(H)–Si bond of the BAS, as shown in Figure 2.7.[80]

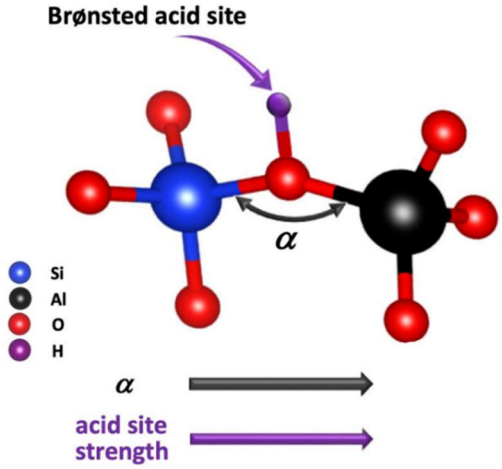

Figure 2.7: Graphic that displays the changing Brønsted acid site strength of zeolites as a function of the T−O−T bond angle. Figure has been reprinted from Analysis and control of acid sites in zeolites, 606, A. Palčić and V. Valtchev, 117795, Copyright (2020), with permission from Elsevier.[80]

As the angle of the Al–O(H)–Si bond at the BAS increases to approach 180°, the acid site strength increases. This effect is caused by the proton becoming more labile as the energy of the O–H interaction is decreased which is postulated as having an effect on the possible structures formed by TS during reactions.[80,83] The tunability of zeolites allows for control of both acid site strength and their density, which is achieved through tuning the silicon-to-aluminium ratio, which delivers optimisation for a respective process.[63] In addition, the introduction of changed extra-framework cations, Na^+ and K^+ in place of H^+, will not only reduce the strength of BAS but also introduce Lewis acidity to the framework.

Lewis acidity in zeolites can arise through various sources, but the common species responsible are extra framework moieties, whether at the surface or at channel intersections or channel wall positions. The species are typically extra-framework aluminium present within the micropores, defect sites within the framework which display resonance between groups (Al and Si–O^-), extra-framework charge balancing cations or between coordinatively unsaturated species which can accept electron donation from a Lewis base.[84–86] Charge balancing extra-framework cations are capable of exhibiting Lewis acidity and their location was found to determine their inherent Lewis acid strength.[87] Being located at channel intersections led to the highest Lewis acid strength being observed for cations, whilst being positioned on channel walls displayed weaker Lewis acidity. However, as the channel dimensions decreased, the Lewis acidity displayed increased accordingly. Lewis acid strength was also found to be driven by coordination and accessibility, with extra-framework cations showing stronger Lewis acidity and better accessibility with weaker coordination to the framework.[87]

The micropores of the framework leads to the generation of channels that run through the length of a zeolite crystal. Dimensionality is a major aspect of framework topology. Materials can be one-dimensional (1D), in which channels run along a single axis (x or y); two-dimensional (2D), in which the channels go along two axes (x and y), although the two channels are not interconnected; three-dimensional (3D), where channels interconnect with one another and are formed along multiple axes (x, y and z).

As the channels of the framework are on the molecular scale, diffusion limitations become a real issue. This could lead to a reduction in observed reaction rates, possibly leading to further (and potentially undesired) reactions taking place. For applications where coking can become an issue, such as methanol-to-gasoline (MTG), activity can be quickly lost for 1D materials due to excessive coke build-up blocking micropores. Materials that are 3D tend to be the most resilient to deactivation, as channels have

multiple openings for molecules to diffuse through. However, the removal of carbonaceous deposits typically requires thermal or chemical treatments to remove the coke ex-situ, which must be carefully applied to avoid damaging effects to the framework.

Pore-sizes are a critical factor for framework characteristics, as highlighted earlier with the shape selectivity that zeolites exhibit in the micropores.[70–72] Zeolites are classified as small, medium, large, and ultra-large pore materials. Small pore frameworks, where the largest T atom rings are 8 membered rings (MR), so can exclude bulky molecules from diffusing into their micropores as the molecules are too large to fit. However, they may display the greatest confinement effects within the micropores due to the proximity of the channel walls. Medium pore zeolites contain 10 MR as their largest ring size, whilst large pore zeolites contain 12 MR as their largest ring, with ultra-large frameworks containing 14, 18 or 20 MR.[88] In order to be classified as microporous, the pores of the material must be less than 2 nm in size, with materials containing pores of 2 – 50 nm classified as mesoporous. Examples of common zeolite topologies have been included in Table 2.1.

Table 2.1: Table containing commonly used zeolite frameworks found in commercial and industrial applications for separation, adsorption, emission control and fuel upgrading. Frameworks shown here cover those talked about within the work contained in this thesis. Zeolite framework data taken from IZA Database.[15]

Framework	Dimensionality	Ring sizes (# of T atoms)	Pore Diameter (Å)	Accessible Volume
BEA	3D	12 6 5 4	12-ring [100] ~7.3 x 6.6 12-ring [001] 5.6 x 5.6	20.52 %
CHA	3D	8 6 4	8-ring [001] 3.8 x 3.8	17.27 %
FAU	3D	12 6 4	12-ring [111] 7.4 x 7.4	27.42 %
FER	2D	10 8 6 5	10-ring [001] 5.4 x 4.2 8-ring [010] 4.8 x 3.5	10.01 %
MFI	3D	10 6 5 4	10-ring [100] 5.1 x 5.5 10-ring [010] 5.3 x 5.6	9.81 %
MOR	1D[a]	12 8 5 4	12-ring [001] 7.0 x 6.5 8-ring [001] 5.7 x 2.6	12.27 %
TON	1D	10 6 5	10-ring [001] 4.6 x 5.7	8.04 %

a – MOR considered as a pseudo-1D framework due to the side channels only facilitating the mobility of single He atoms and are not large enough for the entry or diffusion of larger molecules.

2.2.1 CHA: A Small Pore Topology

Small-pore zeolites have seen a surge in interest after exhibiting excellent performance towards applications such as methanol-to-olefins (MTO), ethene-to-propene (ETP) reactions and for gas separation.[89–92] Materials of the CHA topology, shown in Figure 2.8, are well documented, with zeolite SSZ-13 and silicoaluminophosphate SAPO-34 regarded as highly effective catalysts for MTO and ETP respectively, with both on their way to established commercial scale applications.[89] However, the most common commercial application for CHA materials are deNOx catalysts for the control of diesel engine exhaust gas emissions. This is achieved by selective catalytic reduction (SCR), a process that continues to be widely studied throughout industry and academia and widely makes use of Cu/SSZ-13 and Cu/SAPO-31.[13,22,93,94] Although copper-exchanged zeolites such as ZSM-5 and beta have shown excellent conversion and selectivity for SCR, they lack the thermal stability and steaming resistance exhibited by CHA temperatures exceeding 700 ˚C.[95,96]

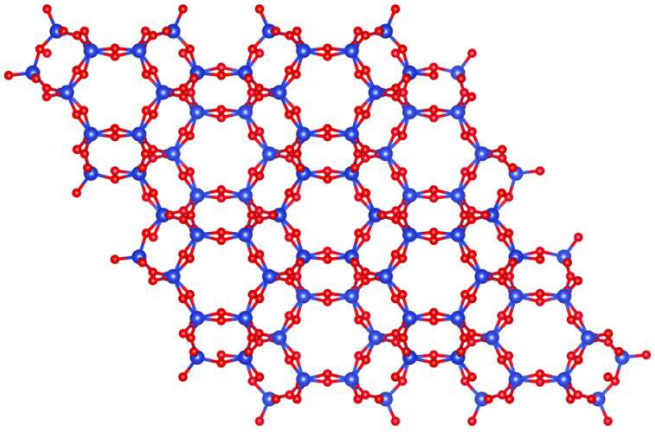

Figure 2.8: A 3D ball and stick model of the chabazite structure, which consists of double 6-rings and chabazite cage composite building units. The small pore topology is a 3D framework that contains a small pore (8MR) channel, leading to a cage. T atoms in this model are blue, whilst connecting oxygen atoms are red.

Due to these promising reports for hydrocarbon upgrading, it became apparent that CHA was a good candidate as a small pore topology for hydrocarbon upgrading, especially when coupled with the future potential of scaling to commercial scale, as CHA has already been established on the commercial scale due to its aforementioned deNOx applications. The deNOx capabilities are facilitated by CHA's proven excellent thermal stability and resistance to steaming, both of which could prove especially useful towards achieving extended catalytic lifetimes during upgrading reactions and resist framework damage during time on-stream.

2.2.2 MFI: A Medium Pore Topology

Materials which are of the medium pore MFI topology, shown in Figure 2.9, are renowned for their use in two of the largest catalytic applications in industry, which are fluid catalytic cracking (FCC) and hydrocarbon cracking (HC).[70,97] Alongside ultra-stable zeolite Y, the use of a second co-catalyst, in the case ZSM-5, allows the FCC process to see a significant uplift in the selectivity towards light olefins (C_3–C_5), whilst also a reduction towards gasoline selectivity.[98] This implies that the ZSM-5 co-catalyst would facilitate C–C cracking of the longer C_6–C_9 linear and branched chain olefins, improving the gasoline octane rating through enrichment with aromatic and isopentane products.[99] Typically for these applications, the catalysts would be exchanged with sodium or rare earth metals, or in their synthesized H form. The drive towards cleaner fuels, reaching the desired octane ratings without the inclusion of tetraethyl lead, and free from both sulphur and aromatics, has driven the widespread ZSM-5 adoption in FCC applications. Those reasons coupled with the increasing demand for propylene has also made the light olefin selectivity even more desirable for the FCC process.

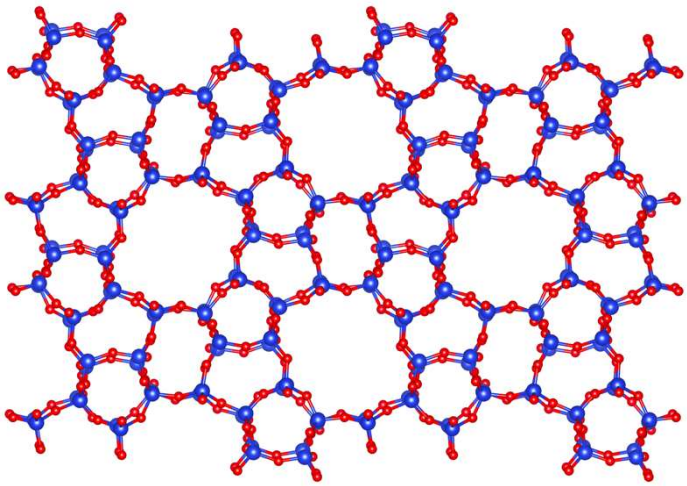

Figure 2.9: A 3D ball and stick model of the MFI topology, which consists of four CBU's and a chain consisting of pentasil units. MFI is a medium pore 3D topology that contains medium pore (10MR) channels that are sinusoidal in nature. T atoms in this model are blue, whilst connecting oxygen atoms are red.

ZSM-5 displays a high hydrothermal stability, which has led to applications such as deNOx catalysts, however, the activity of the material can be lost during high temperature applications at a rapid rate through its susceptibility to dealumination, which has been combatted in FCC through the formation of aluminium-phosphate complexes in the micropores.[100,101]

2.2.3 MOR: A pseudo-1D Topology of Mixed Channels

Mordenite is an important catalyst used in disproportionation, trans-alkylation, hydro isomerisation and decarbonylation reactions.[102] It is referred to as a pseudo-1D framework as it contains two channels of different sizes, a small 8 MR channel and a large 12 MR main channel, which run parallel to one another down the [100] plane, as shown in Figure 2.10. The main channel has 8MR side pockets which interconnect the 12MR channels, however, the accessibility of these is limited to only the smallest of molecules, such as O_2 or N_2, and as such are not classed as channels, limiting the material to being 1D. Mordenite has been shown to exhibit good chemical resistance, thermal stability, a large surface area and pore volume.[102] As with all zeolite frameworks, the silicon-to-aluminium ratio will affect these attributes, with higher Si/Al ratios offering increased acidity, better shape selectivity and increased resistance to dealumination.[103]

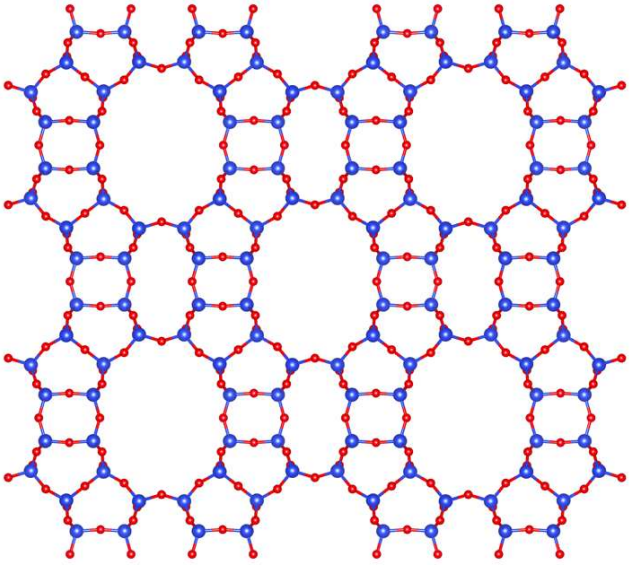

Figure 2.10: A 3D graphic showing the MOR framework structure, consisting of the mor CBU connected by 4-membered rings. This mixed small and large pore topology is a pseudo 1D framework that contains small pore (8MR) and large pore (12MR) channels that run parallel. T atoms in this model are blue, whilst connecting oxygen atoms are red.

Semagina *et al*. investigated the dealumination of the MOR framework, in which they discussed the stability exhibited by the four-membered rings and the observed selectivity towards their dealumination.[41] These four-membered rings are a double 4-ring (D4R), shown in Figure 2.2, which is positioned between the 8 MR channel and 12 MR channel. This builds upon work carried out by Jacobs *et al*. who investigated the mechanism of dealumination in mordenite frameworks of varying SAR.[44] Typically, the D4R of mordenite was found to contain two Al atoms which were simultaneously extracted, resulting in the formation silanol defects at the newly created Al vacancies. It

has also been shown that Al is preferentially included within the 4-rings positions of the framework structure during hydrothermal synthesis of MOR.[44,104–106] We therefore postulated that these positions could therefore be a 'weak-spot' of the zeolite lattice and any breakdown of the structure could occur from these positions.

Changing the counterion of mordenite can display a noticeable change in the accessibility for molecules within the micropores. Ripmeester *et al*. characterised the micropore size for various mordenite frameworks via the use of ^{129}Xe MAS NMR.[46] The MOR frameworks were modified post-synthesis to be in their NH_4, Na, K and Cs form and observed that the main channels and side pockets were available for Xe to freely diffuse into for the NH_4, Na and K forms, however, for Cs-MOR only the main channels were available.

Coke formation on mordenite was reported to be initially rapid, with the rate dropping off exponentially following initial coke formation.[107] Catalytic activity was reportedly improved following a mild acid treatment to remove extra-framework species, although it was reported that going further to also reduce crystal size, increase porosity and reduce defects would inhibit coke formation to improve stability.[43,107] Semagina *et al*. observed that removal of Al from 4-membered ring sites was not responsible for activity loss and catalyst deactivation, instead leading to a changed selectivity being observed for DME carbonylation. Instead, the Al situated in 5-membered ring sites were ultimately responsible for deactivation and total loss of activity during DME carbonylation.[43]

2.2.4 FER and TON: Frameworks with no 4MR

The major difference between the aforementioned topologies and FER and TON, is the smallest ring size. CHA, MFI and MOR have a 4 MR as the smallest ring in the framework, whereas FER and TON have a 5 MR as the smallest ring. Semagina provided evidence to suggest MOR dealumination could be selective towards the removal of Al T-atoms located in the 4-membered rings, as discussed in Section 2.1. It was postulated that silver auto reduction and subsequent framework oxidation could facilitate this process and lead to loss of framework crystallinity. FER and TON topologies were investigated to determine whether the reportedly susceptible 4-membered ring sites were more susceptible in comparison with 5-membered ring sites. Discussion around silver auto reduction, facilitating conditions and the potential impact on the framework is contained in Chapter 2.3.

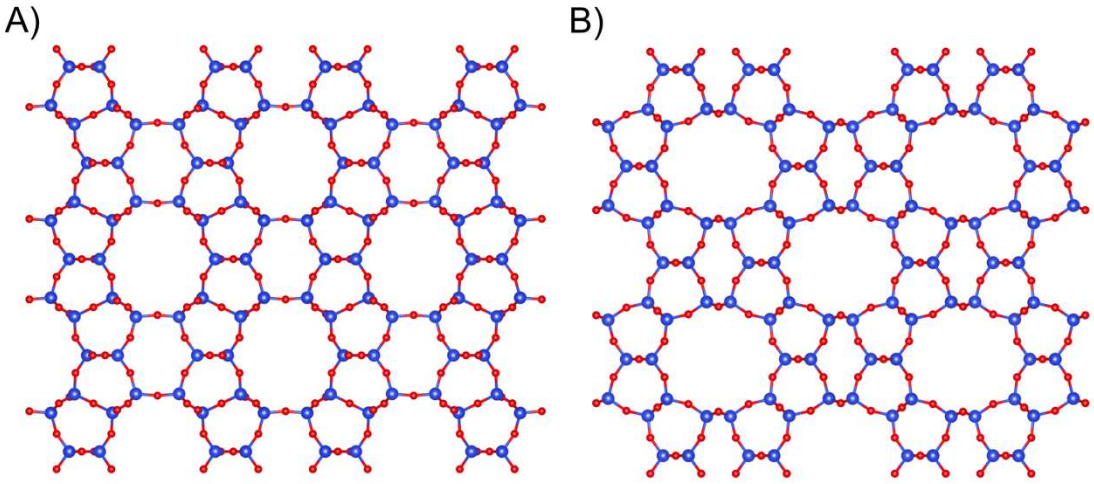

Figure 2.11: A ball and stick model for both the FER framework structure (A) and the TON framework structure (B). A – the FER framework consists of three CBU's and is a 2D framework that contains small pore (8MR) and medium pore (10MR) channels. B – the TON framework consists of four CBU's and is a 1D framework that contains medium pore (10MR) channels. T atoms in this model are blue, whilst connecting oxygen atoms are red.

Ferrierite has found uses in applications such as dewaxing, a process used to improve the cold flow properties of distillate fuels. Ferrierite displayed favourable hydrocracking and hydro isomerisation properties to converts the n-paraffins in the distillate to i-paraffins.[108–110] Skeletal isomerisation of butenes is another established chemical process that is facilitated by ferrierite.[111,112] TON has seen use in several petrochemical applications, with its ability in petrochemical refining being most explored. Favourable results have been reported for n-heptane cracking over TON, facilitated by its excellent hydrothermal stability, well suited acidity and selectivity for the reaction.[112,113]

2.3 Silver-exchanged Zeolites: Auto Reduction and Other Reported Phenomena

Rálek *et al.* was among the first to report on the unexpected physical properties of silver-exchanged zeolite LTA as far back as 1962, where the material was found to change colour based on the level of hydration.[114] Fully dehydrated Ag/LTA zeolites were reported to be brick red in colour, before the addition of water led them through a gradient of orange, yellow and finally white, for their fully hydrated form. At the time of reporting, the reason behind why silver-exchanged LTA materials displayed sensitivity to their hydration level was unknown, however, Seff *et al.* reported that silver clusters were formed simultaneously alongside the colour change in LTA.[115] Seff *et al.* utilised single crystal X-ray diffraction studies to determine that silver-exchanged LTA displayed an auto reductive process during dehydration under reduced pressure, where the activation of silver led to the formation of silver clusters.[115] It was determined that auto reduction of silver cations occurred during the dehydration of fully silver-exchanged LTA under reduced pressures at elevated temperatures, leading to the formation of mixed species within the sodalite cages.[116] Seff *et al.* report the observation of octahedrally shaped metallic silver clusters, Ag_6, that are located within cationic, cube-shaped Ag_8^{n+} clusters, as shown in Figure 2.12. This however is not a unique characteristic to silver-exchanged zeolites, as copper-exchanged zeolites had been previously observed, reporting of copper auto reduction occurring within zeolite Y.[117]

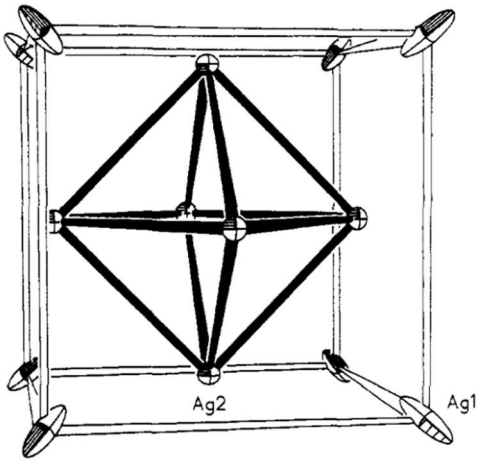

Figure 2.12: Graphic reported by Seff et al. representing an $(Ag^+)_8(Ag_6)$ cluster found within sodalite cages for FAU type zeolite frameworks

It has been understood since the mid-20th century that transition metal ions found within zeolite micropores continue to exhibit redox properties. This was typically observed and reported by those whose aim it was to produce highly dispersed metal clusters in zeolites or during preparation of bi-functional zeolites. As such, the observation of several transition metal cations exchanged in zeolite Y, such as Ni,[118–120] Hg, Cd and Zn,[121] and Cu,[122] were reduced after heating the exchanged forms of zeolite Y in hydrogen, with lower temperatures required than for their respective oxides in powder form.[118,123–125]

The work reported by Seff built upon the pioneering work carried out by Beyer *et al.* for the determination of silver cluster formation in zeolites.[126] Beyer *et al.* reported silver clustering would occur in silver-exchanged zeolite Y using both high and low temperature procedures, although the reduction would produce different species, with low temperature reduction resulting in the formation of mixed metal-cationic species of $Ag^0(Ag_3)^+$.[126]

Beyer *et al.* reported that silver reduction was fully reversible in silver-exchanged zeolites, although this process was once again reported to be temperature dependent.[126] It was observed that low temperature oxidative treatments would lead to the oxidation of only highly dispersed silver clusters found within the cages of zeolite Y, whilst the reoxidation of surface clusters required temperatures exceeding 500 K, which would also result in the migration of silver cations back into the zeolite matrix. In addition to the migration of silver metallic and cationic species, Beyer *et al.* reported 'other peculiarities' for silver-exchanged zeolites, not only with the colour changing due to hydration levels but also the observation that water was cleaved under oxidative thermal desorption of both $Ag(0.71),Na(0.29)/Y_{2.5}$ and $Ag(0.85),Na(0.15)/MOR_{5.3}$ producing hydrogen.[127]

However, through experimental observations, it was noticed by both Beyer and Reikert that the reversibility of silver reduction and oxidation was not 100%. Materials displayed an irreversible colour change to grey, slight decrease in the materials water balance alongside a noted decrease to the oxygen consumed for repeated redox cycles.[128,129] Equations 2.1 and 2.2 show the consumption of hydrogen and oxygen for the redox cycle for silver cations.

$$[2.1]\ 2\,Ag^+ + H_2 \rightarrow 2\,Ag^0 + 2\,H^+$$

$$[2.2]\ 2\,Ag^0 + \tfrac{1}{2}O_2 + 2\,H^+ \rightarrow 2\,Ag^+ + H_2O$$

2.3.1 Irreversible Silver Redox Chemistry in Zeolites Following Oxygen Evolution

Seff *et al.* reported that silver auto reduction leads to irreversible framework damage under raised temperature conditions.[60] Extra-framework silver cations which are located in framework charge balancing positions are responsible for the loss of oxygen, leading to the generation of oxygen vacancies and loss of framework crystallinity. This agrees with the original conclusions that lattice destruction or dealumination were caused by an interzeolitic process.[60,116,127–129] Reports of silver auto reduction under reduced pressures with raised temperature has to led to the observation of oxygen evolution from silver-exchanged materials, facilitated by the formation of oxygen vacancies in the framework, shown in Figure 2.13. The loss of long-range crystallinity in the zeolite leads to a dramatic change in the pXRD pattern, where no phases are typically observed.

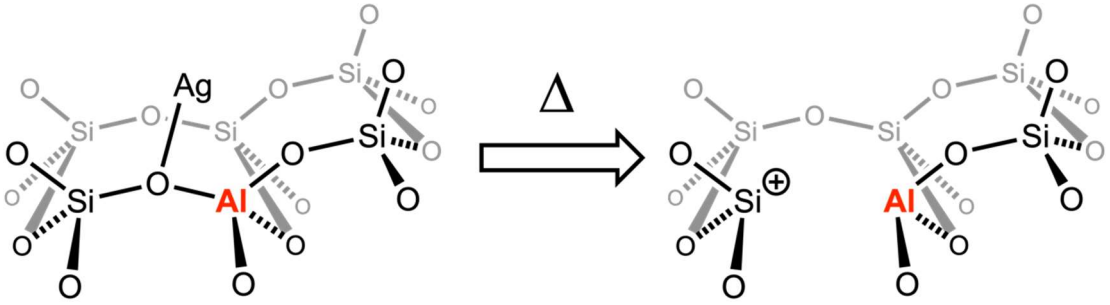

Figure 2.13: Graphic showing the auto reduction of silver in a silver-exchanged zeolite leading to the loss of oxygen from the framework, generating an oxygen vacancy.

However, whilst it has been reported that oxidative treatments are capable of re-oxidising silver metallic species, they are also capable of restoring crystallinity to the damaged framework, returning oxygen atoms to the vacant sites.[130] Murata *et al.* used XAFS to study the temperature dependence of regenerative oxidative treatments to spent silver-exchanged zeolites.[131] It was discovered that temperatures below 773 K were sufficient to re-oxidise the silver metallic species formed by reduction during upgrading reactions, whilst temperatures above 773 K were required to combust the coke formed on the surface of the zeolite. Therefore, it was postulated that the most effective way of regenerating silver-exchanged zeolites to extend their lifetime to the fullest, would be to carry out a two-stage oxidative regeneration. This would allow for low temperature redispersion of silver cations throughout exchangeable framework positions inside the micropores, before a second high temperature coke combustion. However, successful redispersion would require the catalyst to not be coked excessively, or diffusion into the micropores could be severely hindered. In addition,

framework requires the presence of negatively charged labile sites to exchange with the re-oxidised silver cations.

One route that has been reportedly capable of avoiding the requirement for oxidative post-reaction treatment is the incorporate of oxygen into the feed of the reaction or to dehydrate the material under flowing O_2. Seff *et al.* reported dehydration of silver-exchanged zeolite X under flowing O_2 and under reduced pressure at 673 K, reporting a visible colour change for the reduced pressure sample from white to dark grey, indicative of silver reduction to form metallic Ag^0 species on the surface.[132] In contrast, there was no reported colour change observed for the sample dehydrated under flowing O_2 and no unwanted framework damage was observed for the sample dehydrated under flowing O_2. Silver-exchanged zeolites with higher silver loading levels that were dehydrated in the absence of oxygen were noted for forming a greater number of oxygen vacancies in the framework and subsequently a more profound crystallinity loss.[132]

Kuroda *et al.* and Yang *et al.* have both reported on the potential application of silver-exchanged ZSM-5 for oxidation reactions.[133,134] Kuroda *et al.* explored the possibility of Ag/ZSM-5 as a catalyst for partial oxidation of methane to form methanol. Yang *et al.* explored the possibility of using Ag/ZSM-5 for complete ethylene oxidation at room temperature to produce CO_2. Both cases give further evidence to suggest that oxidative conditions are required to avoid undesirable framework damage caused by silver auto reduction. Texter *et al.* determined that silver auto reduction was a two-electron process, facilitated by two silver cations for each oxygen atom vacancy produced.[135] Using ESR to observe framework oxidation, it was determined that O_2 evolution following framework oxidation was a result of four silver cations being reduced to silver metallic species. Equations 2.3, 2.4 and 2.5 show the processes that occur during framework oxidation, with Equation 2.6 showing a full balanced equation for silver auto reduction that leads to the evolution of O_2 from the zeolite framework.

$$[2.3]\quad 2\,ZO^- \rightarrow 2\,O^- + 2\,Z^+ + 2\,e^-$$

$$[2.4]\quad 2\,O^- \rightarrow O_2 + 2\,e^-$$

$$[2.5]\quad 4\,Ag^+ \rightarrow 4\,Ag^0 + 4\,e^-$$

$$[2.6]\quad 4\,Ag^+ + 2\,ZO^- \rightarrow 4\,Ag^0 + 2\,Z^+ + O_2$$

As described by Seff *et al.*, auto reduction of silver under reduced pressure leads to the loss of framework crystallinity through the formation of oxygen vacancies.[60] As a result of this phenomena being reported, dehydration under gas flow was always carried out for silver-exchanged materials used in upgrading applications in this project. However, dehydration *in vacuo* was used when investigating the activity of silver-exchanged materials towards methane by solid-state NMR spectroscopy, which was also the case for their characterisation by this analytical method. Materials would be dehydrated under reduced pressure at elevated temperatures, conditions which were favourable towards silver auto reduction, even though the conditions are a requirement of dehydration and desorption of undesired molecules present in the micropores. We therefore explored the effects of dehydration over a range of silver-exchanged frameworks, to determine the difference between dehydration under reduced pressure, nitrogen flow and argon flow at raised temperatures in Chapter 8.

2.4 Conclusion of Zeolites, Zeotypes and Silver-exchanged Catalysts

Zeolites are natures solid acid catalysts, however, since Barrers discovery of hydrothermal synthetic routes to produce synthetic zeolites, an array of different framework types are now known.[4–10,17–19] Producing zeolites with tuned properties has provided materials with enhanced characteristics towards their specific catalytic applications.[8,11–13,16,21–24] Materials can have their properties tuned through the use of targeted hydrothermal synthesis. Hydrothermal synthesis is sensitive to a number of different parameters, such as the choice of silicon and aluminium source,[7,27–30] the mineralising agent,[33,34] synthesis gel pH,[35] duration of synthesis and the type of heating applied,[38–40] with each of the aforementioned factors displaying a major effect on the final material. However, tuning a materials properties are not restricted to hydrothermal synthesis, but can also be achieved through post-synthetic treatments.[20] Acidic and basic treatments can facilitate the removal of aluminium or silicon T atoms from the framework,[43–46] leaving behind vacancies for metals that are similar in both size and charge, facilitating the generation of zeotypes like stannosilicates, gallosilicates and zincosilicates, with Sn^{4+}, Ga^{3+} and Zn^{2+} in the framework.[47,49–51]

Zeolites contain Brønsted acid sites which are responsible for their ability to catalyse isomerisation, dehydration, decarbonylation and cracking reactions.[69,70,81,82] These BAS arise naturally at Al^{3+} T atom positions, where an extra-framework cation is required to restore overall charge neutrality. The exchange of silver cations has led to the observation some surprising behaviour, including undesirable silver auto reduction and subsequent framework oxidation.[116] The effects of this undesired redox chemistry was deemed to be reversible, following oxidative treatments at raised temperature.[130,131] Even with their potential difficulty, silver-exchanged zeolites have shown very favourable properties towards methane conversion under co-processing conditions.[136,137]

Hydrothermal synthesis of zincosilicate materials in the topology of industrially relevant zeolites,[138] would facilitate the direct comparison between catalysts with the same topology but with Brønsted or Lewis acidity. This change in acidity would provide a changed reaction pathway, with addition of the potential for pairing effects between closely positioned BAS and Lewis acid sites.[139] In addition, the activity of zincosilicates can be tuned and enhanced further through the careful inclusion of extra-framework cations.[140]

2.5 Chapter Two Bibliography

1 A. F. Cronstedt, *Kongl Vetenskaps Acad. Handl. Stock.*, A. F. Cronstedt, Kongl Vetenskaps Academiens Handlingar Stockholm, 1756, 17, 120., 1756, **17**, 120.

2 C. Colella and A. Gualtieri, *Microporous Mesoporous Mater.*, Cronstedt's zeolite, 2007, **105**, 213–221.

3 R. D. Crangle Jr., *Mineral Commodity Summaries - Zeolites (Natural)*, 2022.

4 R. M. Barrer, *J. Chem. Soc.*, 33. Synthesis of a zeolitic mineral with chabazite-like sorptive properties, 1948, 127–132.

5 D. W. Breck, W. G. Eversole, R. M. Milton, T. B. Reed and T. L. Thomas, *J. Am. Chem. Soc.*, Crystalline Zeolites. I. The Properties of a New Synthetic Zeolite, Type A, 1956, **78**, 5963–5972.

6 S. A. I. Barri, G. W. Smith, D. White and D. Young, *Nature*, Structure of Theta-1, the first unidimensional medium-pore high-silica zeolite, 1984, **312**, 533–534.

7 J. Li, A. Corma and J. Yu, *Chem. Soc. Rev.*, Synthesis of new zeolite structures, 2015, **44**, 7112–7127.

8 C. S. Cundy and P. A. Cox, *Microporous Mesoporous Mater.*, The hydrothermal synthesis of zeolites: Precursors, intermediates and reaction mechanism, 2005, **82**, 1–78.

9 E. T. C. Vogt, G. T. Whiting, A. Dutta Chowdhury and B. M. Weckhuysen, in *Advances in Catalysis*, ed. F. Jentoft, Academic Press, Cambridge, MA, 2015, vol. 58, pp. 143–314.

10 Y. Guo, P. Li, Z. Wei, G. Wu and L. Li, *Dalt. Trans.*, Facile synthesis of aluminosilicate zeolites with STT, CHA and MWW topology structures, 2023, **52**, 9398–9405.

11 M. B. Hafez, A. F. Nazmy, F. Salem and M. Eldesoki, *J. Radioanal. Chem.*, Fixation mechanism between zeolite and some radioactive elements, 1978, **47**, 115–119.

12 B. S. Sekhon and M. K. Sangha, *Resonance*, Detergents — Zeolites and enzymes excel cleaning power, 2004, **9**, 35–45.

13 U. Deka, I. Lezcano-Gonzalez, S. J. Warrender, A. Lorena Picone, P. A. Wright, B. M. Weckhuysen and A. M. Beale, *Microporous Mesoporous Mater.*, Changing active sites in Cu–CHA catalysts: deNOx selectivity as a function of the preparation method, 2013, **166**, 144–152.

14 A. J. W. Physick, D. J. Wales, S. H. R. Owens, J. Shang, P. A. Webley, T. J. Mays and V. P. Ting, *Chem. Eng. J.*, Novel low energy hydrogen–deuterium isotope breakthrough separation using a trapdoor zeolite, 2016, **288**, 161–168.

15 J. Zhang, J. Liang, H. Peng, Y. Mi, P. Luo, H. Xu, M. He and P. Wu, *Appl. Catal. B Environ.*, Cost-effective fast-synthesis of chabazite zeolites for the reduction of NOx, 2021, **292**, 120163.

16 A. Kumar, *Ind. Eng. Chem. Res.*, Ethanol Decomposition and Dehydrogenation for Hydrogen Production: A Review of Heterogeneous Catalysts, 2021, **60**, 16561–16576.

17 Ch. Baerlocher and L. B. McCusker, Database of Zeolite Structures, http://www.iza-structure.org/databases/.

18 H. van Bekkum, E. M. Flanigen, P. A. Jacobs and J. Jansen, Eds., *Introduction to Zeolite Science and Practice*, Elsevier, Amsterdam, 2nd edn., 2001, vol. 137.

19 Y. Li and J. Yu, *Chem. Rev.*, New Stories of Zeolite Structures: Their Descriptions, Determinations, Predictions, and Evaluations, 2014, **114**, 7268–7316.

20 V. Valtchev, G. Majano, S. Mintova and J. Perez-Ramirez, *Chem. Soc. Rev.*, Tailored crystalline microporous materials by post-synthesis modification, 2013, **42**, 263–290.

21 Y. Kunitake, T. Takata, Y. Yamasaki, N. Yamanaka, N. Tsunoji, Y. Takamitsu, M. Sadakane and T. Sano, *Microporous Mesoporous Mater.*, Synthesis of titanated chabazite with enhanced thermal stability by hydrothermal conversion of titanated faujasite, 2015, **215**, 58–66.

22 S. Zhang, L. Pang, Z. Chen, S. Ming, Y. Dong, Q. Liu, P. Liu, W. Cai and T. Li, *Appl. Catal. A Gen.*, Cu/SSZ-13 and Cu/SAPO-34 catalysts for deNOx in diesel exhaust: Current status, challenges, and future perspectives, 2020, **607**, 117855.

23 J. Yao, H. Tian, F. Zha, S. Ma, X. Tang, Y. Chang and X. Guo, *New J. Chem.*, Regulating the size and acidity of SAPO-34 zeolites using dual templates to enhance the selectivity of light olefins in MTO, 2021, **45**, 11812–11822.

24 J. Li, M. Gao, W. Yan and J. Yu, *Chem. Sci.*, Regulation of the Si/Al ratios and Al distributions of zeolites and their impact on properties, 2023, **14**, 1935–1959.

25 Z. Wang, in *Comprehensive Organic Name Reactions and Reagents*, 2010, pp. 1451–1456.

26 H. Chen and O. A. Abdelrahman, *ACS Catal.*, Cooperative Adsorption: Solvating the Hofmann Elimination of Alkylamines, 2021, **11**, 6416–6430.

27 B. O. Hincapie, L. J. Garces, Q. H. Zhang, A. Sacco and S. L. Suib, *Microporous Mesoporous Mater.*, Synthesis of mordenite nanocrystals, 2004, **67**, 19–26.

28 P. M. Piccione, S. Yang, A. Navrotsky and M. E. Davis, *J. Phys. Chem. B*, Thermodynamics of Pure-Silica Molecular Sieve Synthesis, 2002, **106**, 3629–3638.

29 S. Li, J. Li, M. Dong, S. Fan, T. Zhao, J. Wang and W. Fan, *Chem. Soc. Rev.*, Strategies to control zeolite particle morphology, 2019, **48**, 885–907.

30 J. R. Di Iorio and R. Gounder, *Chem. Mater.*, Controlling the Isolation and Pairing of Aluminum in Chabazite Zeolites Using Mixtures of Organic and Inorganic Structure-Directing Agents, 2016, **28**, 2236–2247.

31 N. Koike, K. Iyoki, S. H. Keoh, W. Chaikittisilp and T. Okubo, *Chem. – A Eur. J.*, Synthesis of New Microporous Zincosilicates with CHA Zeolite Topology as Efficient Platforms for Ion-Exchange of Divalent Cations, 2018, **24**, 808–812.

32 A. Khaleque, M. M. Alam, M. Hoque, S. Mondal, J. Bin Haider, B. Xu, M. A. H. Johir, A. K. Karmakar, J. L. Zhou, M. B. Ahmed and M. A. Moni, *Environ. Adv.*, Zeolite synthesis from low-cost materials and environmental applications: A review, 2020, **2**, 100019.

33 S. Gao, H. Peng, B. Song, J. Zhang, W. Wu, J. Vaughan, P. Zardo, J. Vogrin, S. Tulloch and Z. Zhu, *J. Environ. Chem. Eng.*, Synthesis of zeolites from low-cost feeds and its sustainable environmental applications, 2023, **11**, 108995.

34 A. Kuperman, S. Nadimi, S. Oliver, G. A. Ozin, J. M. Garces and M. M. Olken, *Nature*, Non-aqueous synthesis of giant crystals of zeolites and molecular sieves, 1993, **365**, 239–242.

35 Y. Wang, C. Wang, J. Wang, J. Wang, L. Wang, C. Xu and M. Shen, *Mater. (Basel, Switzerland)*, Efficient Hydrothermal Synthesis of SSZ-13 with Variable Grain Size., DOI:10.3390/ma13081829.

36 R. Mallada, eds. E. Drioli and L. Giorno, Springer Berlin Heidelberg, Berlin, Heidelberg, 2016, pp. 1005–1006.

37 S. Al-Nahari, D. Laurencin and B. Alonso, *Microporous Mesoporous Mater.*, Solvent-free synthesis of zeolites: New insights into the mechanism and non-

mechanochemical route, 2023, **350**, 112445.

38 R. Lima, L. Bieseki, P. Melguizo and S. Pergher, 2019, pp. 65–91.

39 N. Salahudeen, *Chem. Africa*, A Review on Zeolite: Application, Synthesis and Effect of Synthesis Parameters on Product Properties, 2022, **5**, 1889-1906.

40 A. Deneyer, Q. Ke, J. Devos and M. Dusselier, *Chem. Mater.*, Zeolite Synthesis under Nonconventional Conditions: Reagents, Reactors, and Modi Operandi, 2020, **32**, 4884–4919.

41 K. J. Balkus, A. K. Khanmamedova, K. M. Dixon and F. Bedioui, *Appl. Catal. A Gen.*, Oxidations catalyzed by zeolite ship-in-a-bottle complexes, 1996, **143**, 159–173.

42 L. Dong, D. Hu, Y. Wang, Z. Sheng, M. Hong and S. Yang, *Nanoscale Adv.*, A zeolite-based ship-in-a-bottle route to ultrasmall carbon dots for live cell labeling and bioimaging, 2020, **2**, 5803–5809.

43 A. A. C. Reule, J. A. Sawada and N. Semagina, *J. Catal.*, Effect of selective 4-membered ring dealumination on mordenite-catalyzed dimethyl ether carbonylation, 2017, **349**, 98–109.

44 P. Bodart, J. B. Nagy, G. Debras, Z. Gabelica and P. A. Jacobs, *J. Phys. Chem.*, Aluminum siting in mordenite and dealumination mechanism, 1986, **90**, 5183–5190.

45 V. Paixão, R. Monteiro, M. Andrade, A. Fernandes, J. Rocha, A. P. Carvalho and A. Martins, *Appl. Catal. A Gen.*, Desilication of MOR zeolite: Conventional versus microwave assisted heating, 2011, **402**, 59–68.

46 H. Sammoury, J. Toufaily, K. Cherry, T. Hamieh, Y. Pouilloux and L. Pinard, *Microporous Mesoporous Mater.*, Desilication of *BEA zeolites using different alkaline media: Impact on catalytic cracking of n-hexane, 2018, **267**, 150–163.

47 C.-F. Cheng and J. Klinowski, *J. Chem. Soc. Faraday Trans.*, Synthesis and characterization of the mesoporous galloaluminosilicate molecular sieve MCM-41, 1996, **92**, 289–292.

48 S. Dzwigaj, Y. Millot, J.-M. Krafft, N. Popovych and P. Kyriienko, *J. Phys. Chem. C*, Incorporation of silver atoms into the vacant t-atom sites of the framework of SiBEA zeolite as mononuclear Ag(I) Evidenced by XRD, FTIR, NMR, DR UV-vis, XPS, and TPR, 2013, **117**, 12552–12559.

49 P. Wolf, C. Hammond, S. Conrad and I. Hermans, *Dalt. Trans.*, Post-synthetic preparation of Sn-, Ti- and Zr-beta: a facile route to water tolerant, highly active Lewis acidic zeolites, 2014, **43**, 4514–4519.

50 T. Yan, W. Dai, G. Wu, S. Lang, M. Hunger, N. Guan and L. Li, *ACS Catal.*, Mechanistic Insights into One-Step Catalytic Conversion of Ethanol to Butadiene over Bifunctional Zn–Y/Beta Zeolite, 2018, **8**, 2760–2773.

51 P. I. Kyriienko, O. V Larina, N. D. Scherban, I. M. Remezovskyi, L. M. Alekseenko, P. S. Yaremov, S. O. Soloviev and S. M. Orlyk, *Theor. Exp. Chem.*, Catalytic Properties of ZnLaZrSi-Oxide Systems in the Process of Obtaining 1,3-Butadiene from Ethanol–Aqueous Mixtures, 2020, **56**, 329–337.

52 V. L. Sushkevich and I. I. Ivanova, *ChemSusChem*, Ag-Promoted ZrBEA Zeolites Obtained by Post-Synthetic Modification for Conversion of Ethanol to Butadiene, 2016, **9**, 2216–2225.

53 M. Tsapatsis, *AIChE J.*, 2-dimensional zeolites, 2014, **60**, 2374–2381.

54 W. J. Roth, P. Nachtigall, R. E. Morris and J. Cejka, *Chem. Rev.*, Two-Dimensional Zeolites: Current Status and Perspectives, 2014, **114**, 4807–4837.

55 X. Zhang, D. Liu, D. Xu, S. Asahina, K. A. Cychosz, K. V. Agrawal, Y. Al Wahedi,

A. Bhan, S. Al Hashimi, O. Terasaki, M. Thommes and M. Tsapatsis, *Science*, Synthesis of Self-Pillared Zeolite Nanosheets by Repetitive Branching, 2012, **336**, 1684–1687.

56 K. Varoon, X. Zhang, B. Elyassi, D. D. Brewer, M. Gettel, S. Kumar, J. A. Lee, S. Maheshwari, A. Mittal, C.-Y. Sung, M. Cococcioni, L. F. Francis, A. V McCormick, K. A. Mkhoyan and M. Tsapatsis, *Science*, Dispersible Exfoliated Zeolite Nanosheets and Their Application as a Selective Membrane, 2011, **334**, 72–75.

57 M. Choi, K. Na, J. Kim, Y. Sakamoto, O. Terasaki and R. Ryoo, *Nature*, Stable single-unit-cell nanosheets of zeolite MFI as active and long-lived catalysts, 2009, **461**, 246–249.

58 V. Valtchev, L. Tosheva and K. N. Bozhilov, *Langmuir*, Synthesis of zeolite nanocrystals at room temperature., 2005, **21 23**, 10724–10729.

59 K. Niu, G. Li, J. Liu and Y. Wei, *J. Solid State Chem.*, One step synthesis of Fe-SSZ-13 zeolite by hydrothermal method, 2020, **287**, 121330.

60 N. H. Heo, Y. Kim, J. J. Kim and K. Seff, *J. Phys. Chem. C*, Surprising Intrazeolitic Chemistry of Silver, 2016, **120**, 5277–5287.

61 R. E. Fletcher, S. Ling and B. Slater, *Chem. Sci.*, Violations of Löwenstein's rule in zeolites, 2017, **8**, 7483–7491.

62 S. Li, H. Li, R. Gounder, A. Debellis, I. B. Müller, S. Prasad, A. Moini and W. F. Schneider, *J. Phys. Chem. C*, First-Principles Comparison of Proton and Divalent Copper Cation Exchange Energy Landscapes in SSZ-13 Zeolite, 2018, **122**, 23564–23573.

63 J. Bae and M. Dusselier, *Chem. Commun.*, Synthesis strategies to control the Al distribution in zeolites: thermodynamic and kinetic aspects, 2023, **59**, 852–867.

64 D. E. Akporiaye, I. M. Dahl, H. B. Mostad and R. Wendelbo, *J. Phys. Chem.*, Aluminum Distribution in Chabazite: An Experimental and Computational Study, 1996, **100**, 4148–4153.

65 G. Engelhardt, U. Lohse, E. Lippmaa, M. Tarmak and M. Mägi, *Zeitschrift für Anorg. und Allg. Chemie*, 29Si-NMR-Untersuchungen zur Verteilung der Silicium- und Aluminiumatome im Alumosilicatgitter von Zeolithen mit Faujasit-Struktur, 1981, **482**, 49–64.

66 S. Ramdas, J. M. Thomas, J. Klinowski, C. A. Fyfe and J. S. Hartman, *Nature*, Ordering of aluminium and silicon in synthetic faujasites, 1981, **292**, 228–230.

67 J. Devos, M. A. Shah and M. Dusselier, *RSC Adv.*, On the key role of aluminium and other heteroatoms during interzeolite conversion synthesis, 2021, **11**, 26188–26210.

68 J. Dědeček, Z. Sobalík and B. Wichterlová, *Catal. Rev.*, Siting and Distribution of Framework Aluminium Atoms in Silicon-Rich Zeolites and Impact on Catalysis, 2012, **54**, 135–223.

69 J. A. Rabo, P. E. Pickert, D. N. Stamires and J. E. Boyle, *Paris*, Actes du deuxième congrès international de Catalyse.

70 W. O. Haag, in *Zeolites and Related Microporous Materials: State of the Art 1994 - Proceedings of the 10th International Zeolite Conference, Garmisch-Partenkirchen, Germany, 17-22 July 1994*, eds. J. Weitkamp, H. G. Karge, H. Pfeifer and C. Hölderich, Elsevier, 1994, vol. 84, pp. 1375–1394.

71 V. J. Frilette, P. B. Weisz and R. L. Golden, *J. Catal.*, Catalysis by crystalline aluminosilicates I. Cracking of hydrocarbon types over sodium and calcium "X" zeolites, 1962, **1**, 301–306.

72 S. M. Csicsery, *Pure Appl. Chem.*, Catalysis by shape selective zeolites-science

and technology, 1986, **58**, 841–856.

73 E. Grifoni, G. Piccini, J. A. Lercher, V.-A. Glezakou, R. Rousseau and M. Parrinello, *Nat. Commun.*, Confinement effects and acid strength in zeolites, 2021, **12**, 2630.

74 J. Zhang, Y. Chu, F. Deng, Z. Feng, X. Meng and F.-S. Xiao, *Inorg. Chem. Front.*, Evolution of D6R units in the interzeolite transformation from FAU, MFI or *BEA into AEI: transfer or reassembly?, 2020, **7**, 2204–2211.

75 C. Li, M. Moliner and A. Corma, *Angew. Chemie Int. Ed.*, Building Zeolites from Precrystallized Units: Nanoscale Architecture, 2018, **57**, 15330–15353.

76 J. W. Harris, J. S. Bates, B. C. Bukowski, J. Greeley and R. Gounder, *ACS Catal.*, Opportunities in Catalysis over Metal-Zeotypes Enabled by Descriptions of Active Centers Beyond Their Binding Site, 2020, **10**, 9476–9495.

77 Y. G. Bushuev, G. Sastre, J. V. de Julián-Ortiz and J. Gálvez, *J. Phys. Chem. C*, Water–Hydrophobic Zeolite Systems, 2012, **116**, 24916–24929.

78 D. S. Wragg, R. E. Morris and A. W. Burton, *Chem. Mater.*, Pure Silica Zeolite-type Frameworks: A Structural Analysis, 2008, **20**, 1561–1570.

79 B. Wang, Y. Guo, J. Zhu, J. Ma and Q. Qin, *Coord. Chem. Rev.*, A review on titanosilicate-1 (TS-1) catalysts: Research progress of regulating titanium species, 2023, **476**, 214931.

80 A. Palčić and V. Valtchev, *Appl. Catal. A Gen.*, Analysis and control of acid sites in zeolites, 2020, **606**, 117795.

81 A. Corma, J. Mengual and P. J. Miguel, *Appl. Catal. A Gen.*, IM-5 zeolite for steam catalytic cracking of naphtha to produce propene and ethene. An alternative to ZSM-5 zeolite, 2013, **460**–**461**, 106–115.

82 A. Corma, J. Mengual and P. J. Miguel, *J. Catal.*, Catalytic cracking of n-alkane naphtha: The impact of olefin addition and active sites differentiation, 2015, **330**, 520–532.

83 X. Li, W. Shen and A. Zheng, *Microporous Mesoporous Mater.*, The influence of acid strength and pore size effect on propene elimination reaction over zeolites: A theoretical study, 2019, **278**, 121–129.

84 G. Busca, *Microporous Mesoporous Mater.*, Acidity and basicity of zeolites: A fundamental approach, 2017, **254**, 3–16.

85 M. Ravi, V. L. Sushkevich and J. A. van Bokhoven, *J. Phys. Chem. C*, Lewis Acidity Inherent to the Framework of Zeolite Mordenite, 2019, **123**, 15139–15144.

86 T. T. Le, A. Chawla and J. D. Rimer, *J. Catal.*, Impact of acid site speciation and spatial gradients on zeolite catalysis, 2020, **391**, 56–68.

87 H. V. Thang, K. Frolich, M. Shamzhy, P. Eliasová, M. Rubeš, J. Cejka, R. Bulanek and P. Nachtigall, *Phys. Chem. Chem. Phys.*, The effect of the zeolite pore size on the Lewis acid strength of extra-framework cations, 2016, **18**, 18063–18073.

88 A. Tavolaro and E. Drioli, *Adv. Mater.*, Zeolite Membranes, 1999, **11**, 975–996.

89 M. Moliner, C. Martinez and A. Corma, *Chem. Mater.*, Synthesis Strategies for Preparing Useful Small Pore Zeolites and Zeotypes for Gas Separations and Catalysis, 2014, **26**, 246–258.

90 B. Liu, Y. Zheng, N. Hu, T. Gui, Y. Li, F. Zhang, R. Zhou, X. Chen and H. Kita, *Microporous Mesoporous Mater.*, Synthesis of low-silica CHA zeolite chabazite in fluoride media without organic structural directing agents and zeolites, 2014, **196**, 270–276.

91 W. Dai, X. Sun, B. Tang, G. Wu, L. Li, N. Guan and M. Hunger, *J. Catal.*, Verifying

the mechanism of the ethene-to-propene conversion on zeolite H-SSZ-13, 2014, **314**, 10–20.

92 M. Dusselier and M. E. Davis, *Chem. Rev.*, Small-Pore Zeolites: Synthesis and Catalysis, 2018, **118**, 5265–5329.

93 S. J. Schmieg, S. H. Oh, C. H. Kim, D. B. Brown, J. H. Lee, C. H. F. Peden and D. H. Kim, *Catal. Today*, Thermal durability of Cu-CHA NH_3-SCR catalysts for diesel NOx reduction, 2012, **184**, 252–261.

94 J.-H. Park, H. J. Park, J. H. Baik, I.-S. Nam, C.-H. Shin, J.-H. Lee, B. K. Cho and S. H. Oh, *J. Catal.*, Hydrothermal stability of CuZSM-5 catalyst in reducing NO by NH_3 for the urea selective catalytic reduction process, 2006, **240**, 47–57.

95 K. C. C. Kharas, H. J. Robota and D. J. Liu, *Appl. Catal. B Environ.*, Deactivation in Cu-ZSM-5 lean-burn catalysts, 1993, **2**, 225–237.

96 S. A. Gomez, A. Campero, A. Martinez-Hernandez and G. A. Fuentes, *Appl. Catal. A Gen.*, Changes in Cu^{2+} environment upon wet deactivation of Cu-ZSM-5 deNOx catalysts, 2000, **197**, 157–164.

97 K. Kubo, H. Iida, S. Namba and A. Igarashi, *Catal. Commun.*, Ultra-high steaming stability of Cu-ZSM-5 zeolite as naphtha cracking catalyst to produce light olefin, 2012, **29**, 162–165.

98 M. S. Rigutto, R. van Veen and L. Huve, in *Introduction to Zeolite Science and Practice*, eds. J. Cejka, H. van Bekkum, A. Corma and F. Schuth, Elsevier, 2007, **168**, 855.

99 Y. G. Adewuyi, D. J. Klocke and J. S. Buchanan, *Appl. Catal. A Gen.*, Effects of high-level additions of ZSM-5 to a fluid catalytic cracking (FCC) RE-USY catalyst, 1995, **131**, 121–133.

100 T. F. Degnan, G. K. Chitnis and P. H. Schipper, *Microporous Mesoporous Mater.*, History of ZSM-5 fluid catalytic cracking additive development at Mobil, 2000, **35**–**36**, 245–252.

101 E. T. C. Vogt and B. M. Weckhuysen, *Chem. Soc. Rev.*, Fluid catalytic cracking: recent developments on the grand old lady of zeolite catalysis, 2015, **44**, 7342–7370.

102 S. Narayanan, P. Tamizhdurai, V. L. Mangesh, C. Ragupathi, P. Santhana krishnan and A. Ramesh, *RSC Adv.*, Recent advances in the synthesis and applications of mordenite zeolite – review, 2021, **11**, 250–267.

103 N. Kordala and M. Wyszkowski, *Molecules*, 2024, 29.

104 E. García-Pérez, D. Dubbeldam, B. Liu, B. Smit and S. Calero, *Angew. Chemie Int. Ed.*, A Computational Method To Characterize Framework Aluminum in Aluminosilicates, 2007, **46**, 276–278.

105 G. Debras, J. B. Nagy, Z. Gabelica, P. Bodart and P. A. Jacobs, *Chem. Lett.*, Determination of silicon-aluminium orderings in mordenite and its aluminium deficient forms using high-resolution magic-angle-spinning 29Si NMR, 1983, **12**, 199–202.

106 T. I. Korányi and J. B. Nagy, *J. Phys. Chem. B*, Distribution of Aluminum in Different Periodical Building Units of MOR and BEA Zeolites, 2005, **109**, 15791–15797.

107 N. Chaouati, A. Soualah and L. Pinard, *React. Kinet. Mech. Catal.*, Coke toxicities, descriptors of the deactivating effect of coke on microporous and desilicated mordenite zeolite, 2023, **136**, 2243–2257.

108 A. Corma and A. Martínez, in *Zeolites and Ordered Mesoporous Materials: Progress and Prospects*, eds. J. Čejka and H. van Bekkum, Elsevier, 2005, vol.

157, pp. 337–366.

109 European Patent Office, EP0236590A1, 1986.

110 H. Xu, J. Zhu, L. Zhu, E. Zhou and C. Shen, *Molecules*, 2020, 25.

111 P. Mériaudeau, C. Naccache, H. N. Le, T. A. Vu and G. Szabo, *J. Mol. Catal. A Chem.*, Selective skeletal isomerisation of n-butenes over ferrierite catalyst: Further studies on the possible mechanisms, 1997, **123**, L1–L4.

112 W. Vermeiren and J.-P. Gilson, *Top. Catal.*, Impact of Zeolites on the Petroleum and Petrochemical Industry, 2009, **52**, 1131–1161.

113 L. V. de Sousa Júnior, T. R. S. Ribeiro, B. J. B. Silva, P. H. L. Quintela, S. L. Alencar, J. G. A. P. Filho and A. O. S. Silva, *Res. Soc. Dev.*, Different approaches to the synthesis of ZSM-22 zeolite with application in n-heptane cracking, 2022, **11**, 1–18.

114 M. Rálek, P. Jírů, O. Grubner and H. Beyer, *Collect. Czechoslov. Chem. Commun.*, Molekularsiebe mit farbiger Indizierung des Wassergehaltes, 1962, **27**, 142–146.

115 Y. Kim and K. Seff, *J. Am. Chem. Soc.*, Structure of a very small piece of silver metal. The octahedral silver (Ag_6) molecule. Two crystal structures of partially decomposed vacuum-dehydrated fully silver(1+) ion-exchanged zeolite A, 1977, **99**, 7055–7057.

116 T. Sun and K. Seff, *Chem. Rev.*, Silver Clusters and Chemistry in Zeolites, 1994, **94**, 857–870.

117 P. A. Jacobs, W. de Wilde, R. A. Schoonheydt, J. B. Uytterhoeven and H. Beyer, *J. Chem. Soc. Faraday Trans. 1 Phys. Chem. Condens. Phases*, Redox behaviour of transition metal ions in zeolites. Part 3.—Auto-reduction of cupric ions in Y zeolites, 1976, **72**, 1221–1230.

118 J. A. Rabo, C. L. Angell, P. H. Kasai and V. Schomaker, *Discuss. Faraday Soc.*, Studies of cations in zeolites: adsorption of carbon monoxide; formation of Ni ions and Na centres, 1966, **41**, 328–349.

119 M. Selenina, *Zeitschrift für Anorg. und Allg. Chemie*, Untersuchungen an Nickel-Zeolith-Trägerkatalysatoren. I. Herstellung und Charakterisierung von Nickel-Zeolith-Trägerkatalysatoren, 1972, **387**, 179–189.

120 W. Romanowski, in *Metal Microstructures in Zeolites*, eds. P. A. Jacobs, N. I. Jaeger, P. Jírů and G. Schulz-Ekloff, Elsevier, 1982, vol. 12, pp. 213–219.

121 D. J. C. Yates, *J. Phys. Chem.*, The Stability of Metallic Cations in Zeolites, 1965, **69**, 1676–1683.

122 C. M. Naccache and Y. Ben Taarit, *J. Catal.*, Oxidizing and acidic properties of copper-exchange Y zeolite, 1971, **22**, 171–181.

123 B. Janković, B. Adnađević and S. Mentus, *Chem. Eng. Sci.*, The kinetic study of temperature-programmed reduction of nickel oxide in hydrogen atmosphere, 2008, **63**, 567–575.

124 D. S. Lee and D. J. Min, *Met. Mater. Int.*, A Kinetics of Hydrogen Reduction of Nickel Oxide at Moderate Temperature, 2019, **25**, 982–990.

125 J. Y. Kim, J. A. Rodriguez, J. C. Hanson, A. I. Frenkel and P. L. Lee, *J. Am. Chem. Soc.*, Reduction of CuO and Cu_2O with H_2: H Embedding and Kinetic Effects in the Formation of Suboxides, 2003, **125**, 10684–10692.

126 H. Beyer, P. A. Jacobs and J. B. Uytterhoeven, *J. Chem. Soc. Faraday Trans. 1 Phys. Chem. Condens. Phases*, Redox behaviour of transition metal ions in zeolites. Part 2. Kinetic study of the reduction and reoxidation of silver-Y zeolites, 1976, **72**, 674–685.

127 P. A. Jacobs, J. B. Uytterhoeven and H. K. Beyer, *J. Chem. Soc. Faraday Trans. 1 Phys. Chem. Condens. Phases*, Redox behaviour of transition metal ions in zeolites. Part 6. Reversibility of the reduction reaction in silver zeolites, 1977, **73**, 1755–1762.

128 P. A. Jacobs, J. B. Uytterhoeven and H. K. Beyer, *J. Chem. Soc. Faraday Trans. 1 Phys. Chem. Condens. Phases*, Some unusual properties of activated and reduced AgNaA zeolites, 1979, **75**, 56–64.

129 L. Riekert, *Ber. Bunsenges. Phys. Chem.*, 1973, **73**, 331.

130 H. K. Beyer and P. A. Jacobs, in *Metal Microstructures in Zeolites*, eds. P. A. Jacobs, N. I. Jaeger, P. Jírů and G. Schulz-Ekloff, Elsevier, 1982, vol. 12, pp. 95–102.

131 K. Murata, J. Ohyama and A. Satsuma, *Catal. Sci. Technol.*, Kinetic analysis of Ag particle redispersion into ZSM-5 in the presence of coke usingin situXAFS, 2021, **11**, 506–515.

132 S. H. Lee, Y. Kim and K. Seff, *Microporous Mesoporous Mater.*, Weak Ag+–Ag+ bonding in zeolite X. Crystal structures of $Ag_92Si_{100}Al_{92}O_{384}$ hydrated and fully dehydrated in flowing oxygen, 2000, **41**, 49–59.

133 Y. Kuroda, T. Mori, H. Sugiyama, Y. Uozumi, K. Ikeda, A. Itadani and M. Nagao, *J. Colloid Interface Sci.*, On the possibility of AgZSM-5 zeolite being a partial oxidation catalyst for methane, 2009, **333**, 294–299.

134 H. L. Yang, C. Y. Ma, Y. Li, J. H. Wang, X. Zhang, G. Wang, N. L. Qiao, Y. G. Sun, J. Cheng and Z. P. Hao, *Chem. Eng. J.*, Synthesis, characterization and evaluations of the Ag/ZSM-5 for ethylene oxidation at room temperature: Investigating the effect of water and deactivation, 2018, **347**, 808–818.

135 J. Texter, R. Kellerman and T. Gonsiorowski, *J. Phys. Chem.*, Formation of charged silver clusters and their reversible silver ion desorption in zeolite A, 1986, **90**, 2118–2124.

136 T. Baba and H. Sawada, *Phys. Chem. Chem. Phys.*, Conversion of methane into higher hydrocarbons in the presence of ethylene over H-ZSM-5 loaded with silver cations, 2002, **4**, 3919–3923.

137 A. G. Wang, P. He, M. Yung, H. B. Zeng, H. Qian and H. Song, *Appl. Catal. B-Environmental*, Catalytic co-aromatization of ethanol and methane, 2016, **198**, 480–492.

138 A. Katovic, E. Szymkowiak, G. Giordano, S. Kowalak, A. Fonseca and J. B. Nagy, in *Zeolites and Mesoporous Materials at the dawn of the 21st century*, eds. A. Galarneau, F. Fajula, F. Di Renzo and C. Vedrine, Elsevier, 2001, vol. 135, p. 337.

139 M. W. Schreiber, C. P. Plaisance, M. Baumgärtl, K. Reuter, A. Jentys, R. Bermejo-Deval and J. A. Lercher, *J. Am. Chem. Soc.*, Lewis–Brønsted Acid Pairs in Ga/H-ZSM-5 To Catalyze Dehydrogenation of Light Alkanes, 2018, **140**, 4849–4859.

140 N. Koike, K. Iyoki, B. Wang, Y. Yanaba, S. P. Elangovan, K. Itabashi, W. Chaikittisilp and T. Okubo, *Dalton Trans.*, Increasing the ion-exchange capacity of MFI zeolites by introducing Zn to aluminosilicate frameworks., 2018, **47**, 9546–9553.

Chapter Three – Experimental Details and Characterisation Methods

Accurately measuring, observing, and characterising materials used in this project, for their chemical properties and catalytic activity, required a wide range of different analytical techniques. Each zeolite framework topology has a unique overall structure, leading to varying surface areas, pore volumes and pore dimensionalities, a decisive set of characteristics that define the overall performance of the catalyst during reactions. Each analytical technique provides a different insight into the material composition.

Chapter three aims to show how several complimentary analytical techniques used in tandem provides information into the degree of zeolite framework crystallinity. This is achieved through observing defect sites, collecting data on their nature and determining the species responsible for a signal to determine their location in the framework and the associated acidity. Characterisation techniques were used to provide information as varied as the position of functional groups, whether in the framework itself or an extra-framework moiety, to measure the average crystal size or even the accessible surface area of the zeolite framework itself. The ability to accurately determine and observe changes to any one of these characteristics can give us a greater understanding of the chemical and catalytic properties of zeolites and zeotypes, allowing us to tune them and further improve their overall catalytic activity. Analysis can also provide suggestions to why some pathways are favoured during upgrading reactions, or to why some T atom positions in zeolite frameworks are more susceptible towards attack, leading to crystallinity loss and ultimately a zeolite framework collapse.

3.1 Characterisation Techniques

3.1.1 Solid-state NMR Spectroscopy

Solid-state nuclear magnetic resonance (ssNMR) spectroscopy is an analytical technique that is used to characterise and provide insight into the atomic level structure revealing the chemical environments present in a material by exploiting the magnetic properties of nuclei when they are exposed to an external magnetic field.[1–3] The magnetic properties of a nucleus consist of nuclear spin quantum number, *(I)*, which can take on any value that is an integer, half-integer or zero. The magnetic quantum number, (m), can be any value between *+I* and *-I*, in integral steps, with a total of *(2I + 1)* values. In nuclear magnetic resonance (NMR) spectroscopy, nuclear spin is a vector quantity and takes on a value for both magnitude and direction, contrasting with classical angular momentum in physics. As nuclear spin is quantised, the magnitude is calculated by Equation 3.1, where ħ is Planck's reduced constant, which is Planck's constant, h, divided by 2π.

$$[3.1]\ \sqrt{I(I+1)}\hbar$$

Two values associated closely to nuclear spin are spin angular momentum, *(J)*, and the magnetic moment, *(μ),* the latter of which can be parallel or antiparallel to *I*, with a constant of proportionality known as the gyromagnetic ratio, *(γ),* an intrinsic value unique to each element. NMR spectroscopy can only exploit isotopes that are referred to as 'spin active', where $I \neq 0$. In the absence of a magnetic field, the *(2I + 1)* states of a nucleus are degenerate. The application of an external magnetic field, B_0, to a spin-active nucleus, causes *μ* to align with the magnetic field and produces a projection on the B_0 axis, also referred to as the z axis. The magnetic field perturbs the degenerate energy levels, splitting them into *(2I + 1)* energy levels, m, which are split by a uniformly sized energy gap, ∆E. The nucleus can spin-flip or transition between being aligned parallel or antiparallel to B_0, as shown in Figure 3.1.

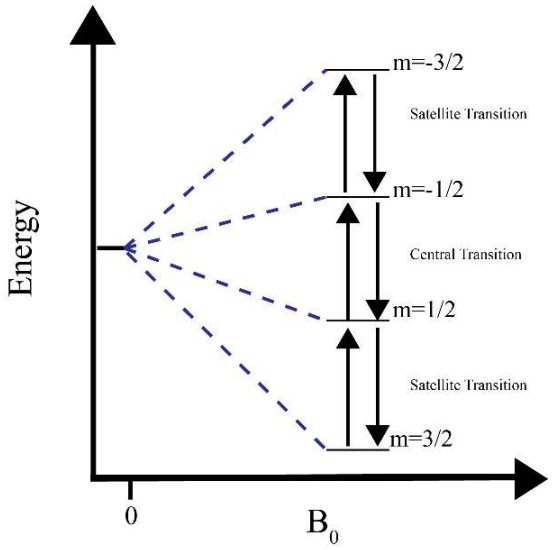

Figure 3.1: A graphic representation showing the loss of degeneracy following the application of a magnetic field, B_0, to a nucleus with a spin quantum number (I) = $^3/_2$.

Additionally, the magnetic moment of a nucleus will now precess after the magnetic field has been applied, the frequency of the precesses is referred to as the Larmor frequency. The Larmor frequency is proportional to the energy gaps between values of *m*. The application of stronger magnetic field, B_0, leads to a larger gap between levels, as shown by Equation 3.2.

$$[3.2]\ \Delta E = \hbar \gamma B_0$$

An NMR signal is obtained using a second magnetic field, B_1, used in a frequency equal to the Larmor frequency (radio frequency range), that interacts with the nucleus, exciting it and changing the orientation, before allowing it to relax to its previous state with the release of energy. The recording of these frequencies produces an NMR signal that can be processed into an NMR spectrum.

Solid state NMR spectroscopy differs greatly to conventional liquid-state NMR spectroscopy. Unlike with liquid-state NMR spectroscopy, where molecular tumbling averages out many of the spin interactions that occur, no tumbling or molecular movement occurs for ssNMR. Therefore, we observe several effects that influence the acquired spectrum, arising from anisotropic interactions such as chemical shift anisotropy and dipolar coupling. Several of the major interactions and their effects on ssNMR spectra have been listed:

- Magnetic dipole moments of nuclei, which can cause small, localised magnetic fields within the system by through-space dipole-dipole interactions. These interactions vary in strength and have directional dependence. This effect ultimately leads to peak broadening in the spectrum.
- Chemical shift anisotropy is caused by the electron distribution being anisotropic arising from the electron density and subsequent shielding of a nucleus not being equal in all orientations. This ultimately affects the chemical shift value, which is mathematically comprised from an isotropic component and an anisotropic component and failing to remove this element causes the recorded spectrum to have an orientational dependence.
- Quadrupolar interactions are one of the most important factors for nuclei with a spin quantum number, *I*, greater than ½. These interactions cause peak splitting due to the non-spherical distribution of charge around a nucleus, meaning its local environment lacks symmetry when exposed to an electric field. This is one of the major interactions in solid state NMR that needs to be overcome for many nuclei. As a result, magic angle spinning (MAS) is required, in which the NMR rotor and sample is spun at 54.736˚ with respect to B_0, allowing us to overcome the first order interaction of this effect. In some cases, this completely removes the effect of quadrupolar interactions, whilst only minimising it in others.
- Paramagnetic interactions that arise from hyperfine interactions between atoms, which result in a loss of sensitivity and a subsequent loss of resolution.

As a result of these complications, solid state NMR spectroscopy uses a rotor which can be spun quickly and is positioned at the magic angle of 54.736° to B_0. Spin-rate is dependent on rotor size and sample mass, but commonly for a 4 mm rotor, a spin-rate of 10 kHz is used. This setup allows for an average reading across the sample with minimised quadrupolar interactions, leading to spectra that are isotropic in nature, meaning they have no orientational dependence and as a result, they can display scalar couplings.

Characterisation of zeolites can be achieved using solid state NMR spectroscopy. As zeolites consist of TO_4 tetrahedra, containing silicon or aluminium as the tetrahedral atom, ^{27}Al and ^{29}Si NMR spectroscopy can distinguish between T atom environments in the framework, indicating the level of order through the detection of defect sites present in the framework. However, various nuclei can be observed within zeolites and zeotypes to provide both structural information, and to identify reaction products and pathways, especially through isotopic labelling studies. The differences between common nuclei observed in the zeolites and zeotypes used in this project is included in Table 3.1.

Table 3.1: Nuclear magnetic properties for the nuclei observed using solid-state NMR spectroscopy, showing natural abundance, spin quantum number, frequency and gyromagnetic ratio, along with relative receptivity, a factor of abundance and sensitivity, when compared with ^{1}H (D^{P}) and ^{13}C (D^{C}).[4]

Isotope	Natural Abundance (%)	Spin	Frequency (MHz at 9.4T)	Gyromagnetic Ratio ($\gamma/10^7$ rads s^{-1} T^{-1})	Relative Receptivity D^P	Relative Receptivity D^C
^{1}H	99.99	$^{1}/_{2}$	400.02	26.752	1.00	$5.87x10^{3}$
^{2}H	0.01	1	61.43	4.107	$1.11x10^{-6}$	$6.52x10^{-3}$
^{13}C	1.07	$^{1}/_{2}$	100.63	6.728	$1.70x10^{-4}$	1.00
^{27}Al	100.00	$^{5}/_{2}$	104.31	6.976	0.21	$1.22x10^{-3}$
^{29}Si	4.68	$^{1}/_{2}$	79.53	-5.319	$3.68x10^{-4}$	2.16
^{67}Zn	4.10	$^{5}/_{2}$	25.09	1.677	$1.18x10^{-4}$	0.692

Some NMR experiments carried out in this project used direct excitation (DE) experiments. In these, the nucleus of interest is direct irradiated by the pulse sequence used. Other experiments made use of cross-polarisation (CP) experiments. CP operates by indirectly irradiating the nucleus of interest through initially irradiating a more abundant and more sensitive nucleus (commonly ^{1}H), which transfers the magnetisation to our nucleus of interest through dipolar coupling. CP experiments enhance the signal intensity of fixed groups whilst reducing acquisition time. DE experiments provide quantitative spectra, whilst CP experiments tend to be only qualitative.[3]

Zeolites are known for being solid-acid catalysts, which can be host to both Brønsted acid sites and Lewis acid sites within a single framework. The IUPAC 'Gold Book' defines Brønsted acid sites as a "molecular entity capable of donating a proton to a base," whilst Lewis acid sites are "a molecular entity and the corresponding chemical species, that is an electron-pair acceptor and therefore able to react with a Lewis base to form a Lewis adduct."[5] A zeolite can host both types of acid site within the framework.

Characterization of Brønsted acid sites in zeolites using ^{1}H solid-state NMR spectroscopy can give insight into the nature and environment of the BAS following initial dehydration of the material. The strength of an acid site is indicated through the shift value at which it appears, with strong acid sites appearing at higher shift values, weaker acid sites at lower shift values. If materials are not sufficiently dehydrated, the presence of water in the micropores of the framework overlaps and obscures the peaks of the

other species present within the broad chemical shift, as shown in Figure 3.2.[6,7]This effect arises from the timescale difference of NMR spectroscopy as a relatively slow process compared with the labile exchange processes occurring between water and the framework species.[6] Dehydration at raised temperatures, paired with reduced pressure or dry gas flow is sufficient at removing water from the micropores.

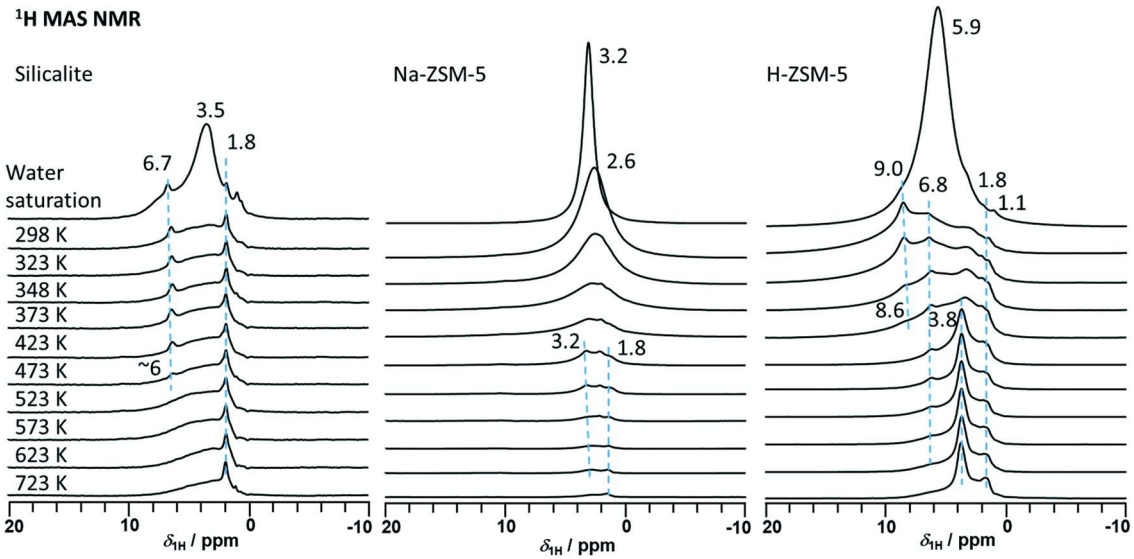

Figure 3.2: Dyballa et al. reported this series of 1H MAS NMR spectra of hydrated and dehydrated MFI topology materials with changed functional groups. Reproduced from Ref. Z. Li, D. Dittmann, C. Rieg, M. Benz and M. Dyballa, Catal. Sci. Technol., 2022, 12, 5189–5202 with permission from The Royal Society of Chemistry.

Not only Brønsted acid sites, but also hydroxyl sites or terminal framework silanol groups can also be observed. Strong hydrogen interactions between sites on the framework can cause peaks to shift downfield for species like Al–O(H)–Si, when interacting with neighbouring oxygen atoms.[8,9] These interactions typically lead to the broadening of peaks, requiring cooling of the sample to produce sharp peaks. However, the complexity of defining shifts for ssNMR in zeolites becomes apparent due to the potential number of different environments present in any zeolite framework. Defining the location of defect sites can prove difficult, requiring additional NMR experiments or analytical techniques to be conducted.[9,10] NMR experiments observing additional nuclei are commonly used in determining both the number and nature of defects. Common shift values for the environments typically observed within zeolite frameworks by ^{1}H ssNMR spectroscopy is shown in Figure 3.3:

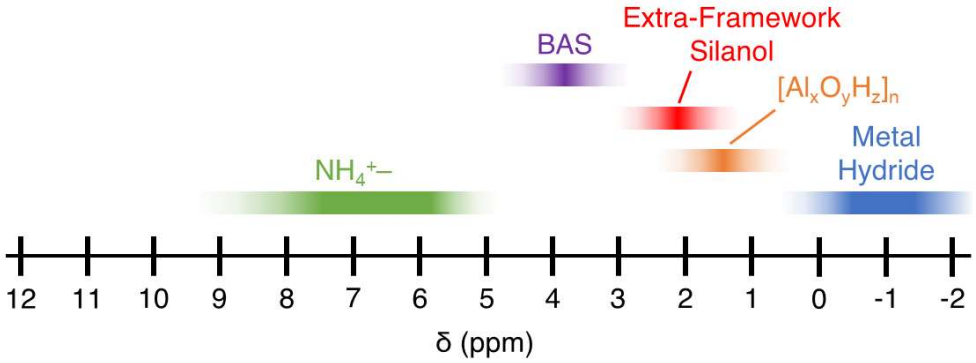

Figure 3.3: Graphic showing a range of example shift values for proton environments typically found during characterisation of the zeolite frameworks used in this project.

Deuterium was another nuclei of interest during this project as through the use of ^{2}H ssNMR spectroscopy, the lability of species present in the framework could be determined by observing changes in signal intensity caused by H/D exchange. The exchangeability of a species can help to determine its location within a framework.

13-Carbon is a common nucleus to observe in liquid-state NMR spectroscopy, although the use of ^{13}C ssNMR spectroscopy for zeolites is typically restricted to isotopically labelled studies to discern reaction pathways and products.[11–13] Table 3.1 highlights the low natural abundance of ^{13}C. This coupled with the low abundance of species and intermediates relative to the high fraction of solid in an NMR rotor that is zeolite framework, restricts the suitability of the ssNMR experiments towards isotopically enriched experiments.

Qualitatively observing the activation of methane via this analytical technique would prove difficult unless at high concentrations, which is why methane activation work in this project utilised ^{13}C-methane. Whilst isotopically enriched materials are a powerful tool in enabling new analytical routes, their cost and availability can prove to be limiting factors. However, they can prove to be very powerful when trying to establish the upgrading products from hydrocarbon upgrading in zeolites.[14] Examples of species observed within this project for ^{13}C ssNMR spectroscopy are shown in Figure 3.4. The zinc-methyl shift appears at 0 to −20 ppm, which is now well known[15–17] alongside some higher products such as methoxy and formate groups.[14]

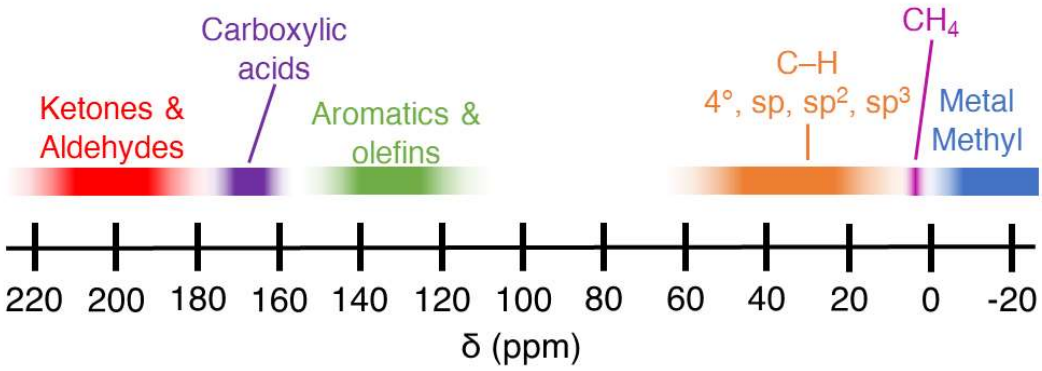

Figure 3.4: Graphic showing a range of example shift values for carbon environments typically found within zeolite frameworks following methane activation or after OSDA removal from calcination.

Whilst the aluminium environment can be changed by using post-synthetic treatments to the zeolite framework, the nature and activity of octahedral aluminium causes much debate and to define the exact Al species present with confidence requires multiple analytical techniques.[18,19]

Tetrahedrally co-ordinated aluminium consists of an Al atom bound to four O atoms. However, these O atoms do not necessarily bridge to adjacent T atoms. Tetrahedral Al atoms give rise to BAS in the zeolite framework when the charge balancing cation is a proton. The need for charge balancing on the framework is due to the charge deficit for the aluminium unit, $[AlO_4]^-$. However, for Al T atoms that are located at the edge of a framework, or situated at a defect site, Al–O–H species can form. These will appear at a different chemical shift value in the ^{1}H MAS NMR spectrum to BAS, however, this highlights the necessity for multiple NMR experiments when aiming to define what species are present in a material.

Penta-co-ordinated aluminium environments are less commonly observed with zeolites, however, post-synthesis thermal treatments such as calcination at temperatures exceeding 600 °C have been shown to lead to the emergence of penta-co-ordinated aluminium environments in the zeolite framework.[20–23] It is believed that thermal treatments cause the tetrahedral environment to distort, going from the thermodynamically stable Al^{IV} environment to the metastable Al^{V}.[20] Routes that avoid lengthy calcination times and cooling are thought to be required if these environments, reported to have excellent activity in several processes, are to become an industrially viable option.[21]

Octahedral aluminium environments consist of an aluminium atom that has changed its geometry, often following ejection from the zeolite framework, creating what is referred to as either a defect site or framework vacancy and changing the type of acidity displayed by the Al atom itself. Octahedral aluminium atoms are considered as a non-framework species, instead considered as extra-framework. Lewis acidity in zeolites can be attributed to the generation of octahedrally co-ordinated aluminium species, however, the geometry of aluminium can be reversibly switched between tetrahedral and octahedral, allowing for the tuning of zeolite acid sites.[18]

Stepanov reports in detail how ^{27}Al ssNMR spectroscopy can be used quantitatively for zeolites to calculate the silicon-to-aluminium ratio, as long as we remember to observe Löwenstein's rule.[24] Löwenstein's rule states that Al–O–Al linkages are forbidden, so any aluminate tetrahedra (AlO_4) must be connected to four silicate tetrahedra, as shown in Table 3.2. Hence, no aluminium analogues to Q^1 to Q^4 environments shown in Table 3.3 can exist. Drawing comparisons between ^{27}Al and ^{29}Si MAS solid-state NMR spectroscopy, it can be argued that observing ^{27}Al is simpler than ^{29}Si due to the lack of adjacent T atom positions in zeolites – not the case for zeotypes, however – with their shifts and species shown in Table 3.4.

The quadrupolar coupling constant for ^{27}Al is highly sensitive to any distortion in the symmetry around the aluminium environments, making ^{27}Al ssNMR spectroscopy a useful technique for detecting structural changes in the material, however, this also has the potential to cause complications from signal overlap in the spectrum.[25,26] Observing tetrahedral aluminium species in hydrated zeolites by solid-state NMR spectroscopy would show a reasonably sharp, single line centred at around 60 ppm. However, for dehydrated zeolites the quadrupolar interactions would heavily distort the line shape, potentially broadening the shift beyond the shift region that can be observed.

Table 3.2: Aluminium environments typically observed in zeolite frameworks and their name denoting the geometry at the aluminium atom, which a typical chemical shift value that these Al environments are observed at in ^{27}Al NMR spectroscopy.

Al environment	Chemical Shift (ppm)	Example Species
Tetrahedral	55	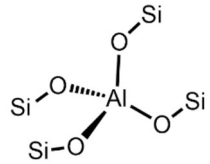
Penta-co-ordinated	30	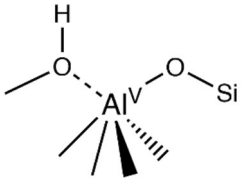
Octahedral	0	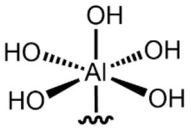

^{29}Si ssNMR spectroscopy was carried out using both direct-excitation (HPDEC) and CP (cross-polarisation) experiments. Quantitative analysis is only achieved when carrying out HPDEC experiments, however, the use of ^{1}H-^{29}Si CP MAS NMR spectroscopy allows for the enhancement of ^{29}Si species signals, which provide an important insight into the presence of structural defects. Silicon T atoms have five possible configurations in the framework, with each of these units denoted by a unique code, as shown in Table 3.3, each of which appears within a specific range of chemical shift values. Q^0 would not be observed for zeolites as this indicates an $SiOH_4$ species. Q^1 is the most 'open' site here that can be observed for zeolites, containing only one O atom that bridges the Si T atom with the rest of the framework. Q^4 is referred to as a 'closed' site, with all four O atoms of the tetrahedra being connected with the rest of the framework. If there are no sites other than Q^4 sites detected in ^{29}Si solid state NMR spectroscopy, then the framework is said to be defect free, however, you must bear in mind that silicon positioned at the terminating edges of a zeolite crystal are Q^3 in nature, so detection of defects, particularly through CP will occur.

Table 3.3: Tetrahedral silicon environments typically observed within zeolite frameworks, each with a unique code denoting the nature of the site and the typical chemical shift range they are observed for ^{29}Si ssNMR spectroscopy.[27]

Code	Chemical Shift (ppm)	Example Species
Q^0	−60 to −80	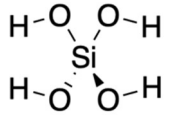
Q^1	−70 to −90	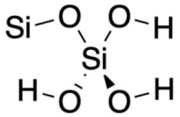
Q^2	−80 to −100	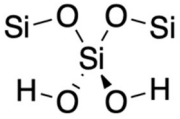
Q^3	−90 to −110	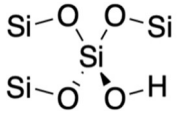
Q^4	−100 to −120	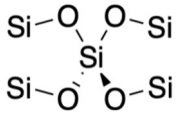

Characterisation of zeolite and zeotype materials by ^{29}Si ssNMR spectroscopy has the potential of displaying multiple silicon environments with T atoms other than silicon positioned adjacent to silicon within the framework. Shown in Table 3.4 are the possible Q^4 silicon environments with chemical shift values for T = Al.[27] The chemical shift value for the silicon environment changes when a T atom other than silicon is adjacent due to either reduced or increased shielding based on their relative electronegativity. For zincosilicates, the chemical shift value for each environment is expected to be downfield of the corresponding aluminium environment, due to zinc being more electronegative than aluminium.

Table 3.4: Tetrahedral silicon environments connected to a varying number of heteroatoms that are typically observed within zeotype frameworks, with the chemical shift range stated for T = Al for ^{29}Si ssNMR spectroscopy.[27]

Code	Chemical Shift (ppm)	Example Species
Q^4 (0T)	-100 to -120	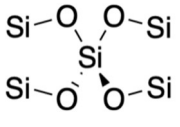
Q^4 (1T)	-90 to -120	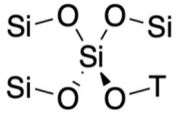
Q^4 (2T)	-80 to -110	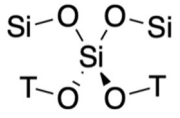
Q^4 (3T)	-70 to -100	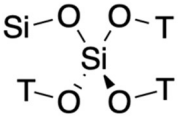
Q^4 (4T)	-60 to -90	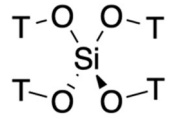

One final application of ^{27}Al and ^{29}Si ssNMR spectroscopy is following dealumination, to remove aluminium from the zeolite framework and desilication, to remove silicon from the zeolite framework. In each case, either strong acid or strong base is used as a post-synthesis treatment, for which the respective ssNMR spectroscopic technique can be used to confirm their removal from the framework.[28–30]

As discussed, solid-state NMR spectroscopy is a very powerful analytical tool for the characterisation of zeolites and zeotypes.[1–3] This technique allows for the determination of material crystallinity and order through the presence or absence of defect sites,[31] T atom positioning in framework or extra-framework positions,[32] observing methane activation with subsequent products within the micropores,[14,15,33] and even the determination of acid site type and strength through the use of probe molecules, such as phosphine oxides, pyrrole and pyridine.[34–37]

3.1.2 X-Ray Analytical Techniques

X-ray based analytical techniques are capable of providing accurate qualitative and quantitative information about the surface composition, crystal structure and surface structure of zeolites. X-rays have a wavelength ranging from 0.01 nm to 10 nm, allowing them to penetrate solids and interact with the atoms inside. Depending on the technique, a wide range of information can be obtained. X-ray techniques are sensitive as they can detect small changes in the energy of the X-rays that interact with the sample.

X-ray techniques that have been applied to zeolites and zeotypes in this project include powder X-ray diffraction (pXRD), electron microscopy, X-ray fluorescence (XRF), and two X-ray absorption spectra (XAS) techniques of X-ray absorption near edge structure (XANES) and extended X-ray absorption fine structure (EXAFS).

3.1.2.1 Powder X-Ray Diffraction (pXRD)

Powder X-ray Diffraction (pXRD) is a non-destructive technique used to observe the phase purity of a crystalline solid through the generation of a diffraction pattern. The pattern is generated from the interaction between an incident X-ray beam and the crystalline lattice structure of a material. Incident X-rays are those emitted from a detector and directed towards the sample of interest and can interact in several different ways with a solid sample. X-rays may be ‘transmitted’ by the crystalline solid, in which they traverse through the solid in their original direction, or they may be ‘scattered’ by the electrons of the atoms present. As the X-rays pass through the layers of the crystal, the scattered X-rays can be collected to generate a diffraction pattern. The pattern contains information about the crystal structure, the lattice parameters, the phase composition, and preferred orientation of the solid.[38–41]

The type of interaction that is most useful to us is referred to as constructive interference. Constructive interference occurs when two X-ray waves have phases that are separated by an integer number of wavelengths combine to create a single wave with a greater amplitude (Figure 3.5). This is achieved when two parallel X-rays are scattered from a source that contains two adjacent planes and the path difference of these two waves is an integer number of wavelengths. The opposite of constructive is destructive interference, whereby the X-rays in adjacent planes are of different phases to one another, causing reduced amplitude or total signal loss.

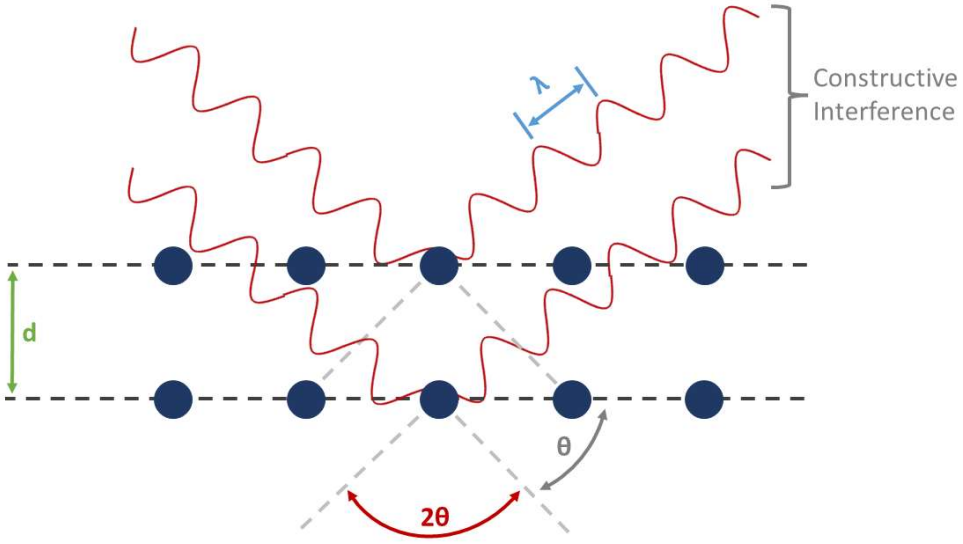

Figure 3.5: Graphic of a lattice arrangement and the interaction between the atoms and the incident X-ray beam creating constructive interference.

As shown in Figure 3.5, the angle between the transmitted beam and the Bragg diffracted beam, the X-ray beam diffracted from the solid, is always given as 2θ (two theta). Results of analysis by X-ray diffraction (XRD) are commonly given in 2θ. The wavelength or the angles for coherent scattering of X-rays from a crystal lattice structure can be calculated with the Bragg equation, Equation 3.3 given below. For the equation, n = order of diffraction, relating to the diffraction grating spacing and angle, given as integer values.

$$\text{Path difference} = n\,\lambda$$

$$n\lambda = 2d\sin(\theta)$$

$$[3.3]\ \lambda = 2d_{hkl}\sin(\theta)_{hkl}$$

Applying the Bragg equation with the use of Bragg's Law, it is possible to calculate lattice spacings of crystal lattices. Crystalline materials in their perfect form have a repeating structure running throughout the material, for which it is possible to derive a unit cell representation describing the overall structure in the smallest number of atoms possible. There are a total of 14 different arrangements known for atoms in a repeating unit, which can be represented by the Bravais lattices or crystallographic planes, which can be described using the Miller index (Figure 3.6) To generate a pattern, the radiation beam requires a wavelength that will interact constructively with the crystal planes in the crystalline solid. Planes are on the atomic scale, separated by only a few angstroms,

making X-rays the perfect radiation source for this technique due to their wavelength being on the pico or nanometre scale.

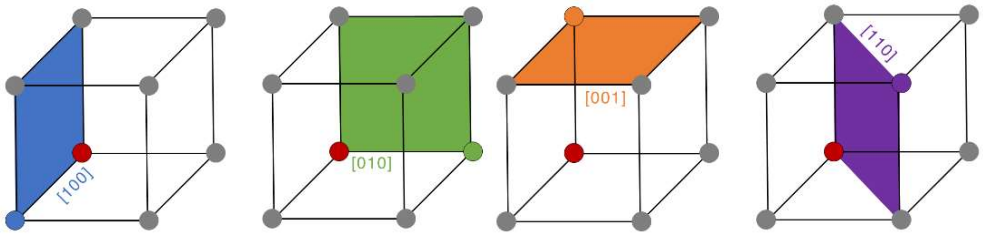

Figure 3.6: Simplified graphic describing the Miller index notation system for planes found in crystalline materials with respect of the red marked atom, describing lattice plane direction using the integer values for h, k and l.

Preparation of powder materials like zeolites requires them to be loaded onto an XRD disc, which can be packed with the sample, or for discs fitted with a silicon wafer the sample can be loaded using petroleum jelly. The disc is rotated in the beam path and the rotation of the sample coupled with the movement of both the X-ray source and the X-ray detector, as shown in Figure 3.7. This captures a diffraction pattern which is an average of the crystal structure due to the directional dependence of crystallographic planes present in the zeolite framework.

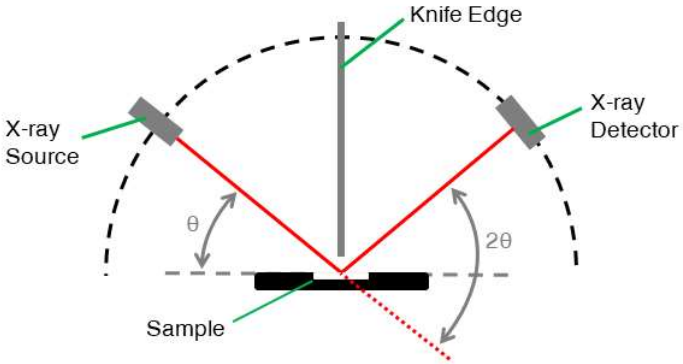

Figure 3.7: A simplified graphic showing how pXRD analysis is conducted, with a dotted path showing the rotation of both the x-ray source and detector as it revolves around the rotating sample, centre.

Due to the use of low angles of 2θ values, the primary beam can become scattered by the surface of the material when collecting data. This can lead to unwanted background signals appearing in the pXRD pattern. To negate this negative effect, we make use of a knife edge attachment to block this scattering from being observed. X-rays lead to the acquisition of surface information for a material, neutrons penetrate deep into the

framework of crystalline materials, leading to generating information about the bulk zeolite material. However, this technique requires the generation of a neutron beam, which typically comes from a source such as a nuclear reactor or particle accelerator, and access to facilities with this capability are limited.

Peak intensity is dependent on the atomic arrangement of the atoms in the unit cells, which is caused by differences in the interaction of the radiation with an atom's electron cloud. These phases reflect the beam efficiently to a detector, leading to a series of peaks in the recorded pXRD pattern, allowing us to qualitatively determine how the degree of crystallinity in the material. Broad peaks occur through crystal defects, inhomogeneity or stacking faults, whereas sharp peaks are indicative of a highly ordered material. The intensity of signals is only qualitative for pXRD, as atoms do not all diffract with equal efficiency.

Application of the Scherrer equation, named after Swiss physicist Paul Scherrer, facilitated the calculation of the approximate crystallite size of our materials based on the peak width observed in the diffraction pattern. The Scherrer equation is shown in Equation 3.4.

$$[3.4]\ D = \frac{k\,\lambda}{\beta\cos(\theta)}$$

D = crystal size (in nanometres) in given direction (hkl)

k = Shape constant, 0.9 implies a good shape fit

λ = X-ray wavelength

β = Observed peak full-width half maximum

θ = Bragg angle for peak of interest

However, there are limitations to the use of the Scherrer equation for determining crystallite size. Whilst there are no hard size limits, the upper limit is generally accepted to be between 100 – 200 nm, with the accuracy depending on several factors, such as the instrument, the sample of interest and signal-to-noise for the acquired pattern.[42] The lower limit has been determined to be around 4 nm.[43] As the crystallite size increases the peak width decreases, and conversely, peak width increases with decreased crystallite size. However, as the crystallite size approaches the aforementioned limits, factors such as lattice imperfections, inhomogeneity of the material, thermal movement of the atoms and even optical aberrations can affect the measured peak width, leading to inaccurate size determination.

3.1.2.2 Electron Microscopy

Electron microscopy is a powerful technique for obtaining high resolution images of crystalline materials like zeolites, whose crystal sizes are on the micro and nanometre scale.[44,45] With a powerful electron beam and incredibly high magnification, detailed images of single crystals can be produced, capturing detail on the nanometre scale. Whilst regular microscopy makes use of visible light even the best optics limit magnification of an image to around 1000x, whereas an atom is too small to observe as its size is far smaller than even the shortest visible light wavelength at around 400 nm. Electron microscopes can achieve 300,000x and above, allowing direct observation of the micromolecular scale. However, some materials display sensitivity towards high energy beams of electrons, which cause damage to the sample.[46,47]

3.1.2.2.1 Scanning Electron Microscopy (SEM)

Scanning Electron Microscopy (SEM) is a technique that utilises an electron microscope to produce highly magnified images of a materials surface. This is achieved using a focused beam of electrons, which are fired at the surface of a solid material, and from the interaction with the surface atom a signal is produced that is detected by a detector utilising a raster scan pattern. The intensity of the signal is combined with the position of the beam to produce an image. Due to the use of a high energy electron beam, several phenomena may be observed, including secondary electron emission, back-scattered electrons, and characteristic X-ray emission leading to photon emission. Secondary electrons are produced when the primary electron beam transfers energy to a core shell electron of an atom located at the surface, with the electron being ejected and subsequently observed by the detector. The generation of secondary electrons produces high-resolution image data for a material surface, making this the most common mode of SEM operation. Another mode is to observe back scattering electrons, which occurs when the primary beam is reflected from the atoms on the surface.[48] A blown-up graphic displaying the components of an SEM microscope is shown below in Figure 3.8.

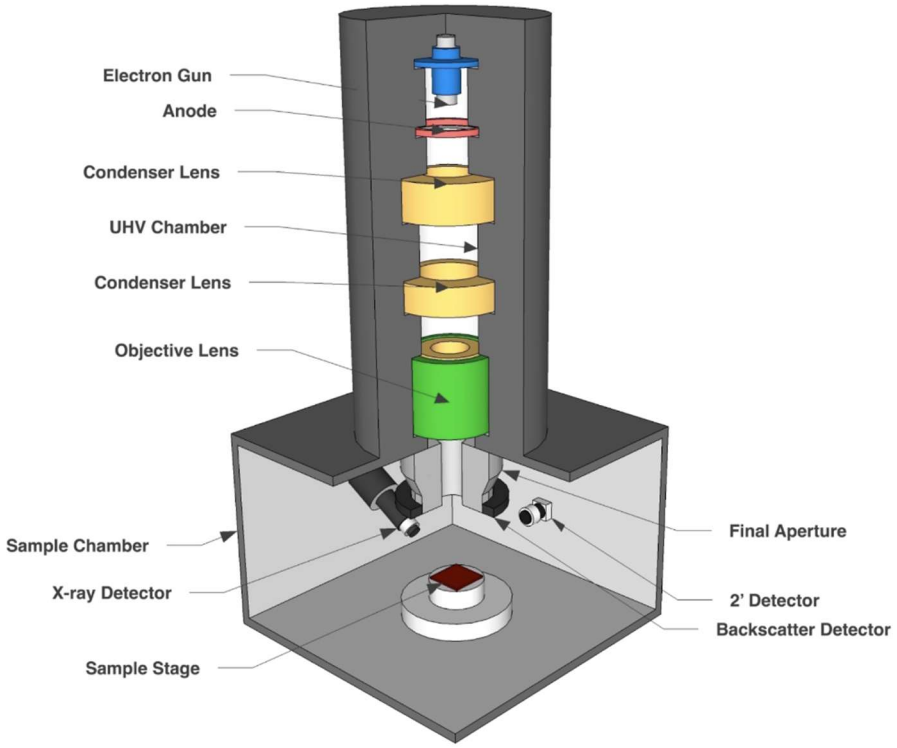

Figure 3.8: A graphic displaying an SEM microscope, with the focusing of the electron beam via lenses before hitting the sample, showing the various types of detector present for the multiple operating modes to capture scattered electrons and x-ray emission. Figure has been reproduced with permission from P. J. D. Whiteside, J. A. Chininis and H. K. Hunt, Coatings, 2016, ***6****, 35.*[49]

SEM is a powerful technique for zeolites, capable of producing 3D images with a magnification up to around 1 - 2 million times. The resolution for SEM is restricted to around 0.5 nm, however advancements in the field can reach as low as 50 pm. Zeolites between 20 nm and 20 μm can be observed using SEM, providing information about crystal morphology and dimensions, which is an indicator of zeolite framework and an indication into the quality/defective nature of the material, which can be determined via the uniformity of the zeolite crystals.[50]

3.1.2.2.2 Transmission electron microscopy (TEM)

Like SEM, transmission electron microscopy (TEM) functions by firing a focused beam of electrons at the surface of a solid, however, the difference is that electrons now transmit through the material to a detector, which forms an image. A simplified graphic to display the components present inside of a TEM microscope is shown in Figure 3.9.

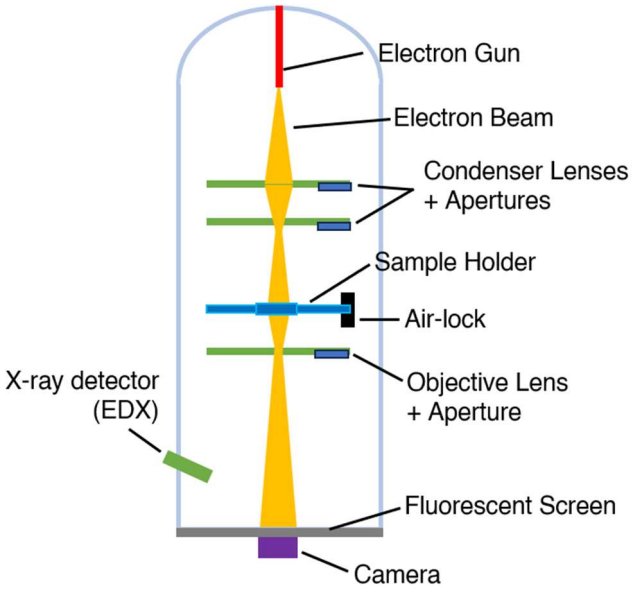

Figure 3.9: A graphic displaying the major components of a TEM microscope, with beam focusing achieved through the use of several lenses placed before the sample in the beam path, showing the positioning of both the camera and EDX detector.

For TEM, the sample must be less than 100 nm thick and in either a pellet form or dispersed onto a thin, suspended grid. The detector produces an image following the interaction of the electrons from an electron beam with a sample, however, unlike SEM the beam is transmitted directly through the material before reaching the detector. Consequently, this makes TEM an incredibly sensitive microscopy technique when observing the structure of a material, allowing for the capture of details down to the atomic scale, with images produced at magnifications of over 50 million times. To achieve this, an initial image is created which then undergoes magnification, before being focused by optics onto an image capture device, which consists of a fluorescent screen, a film or even a sensor, such as a charge-coupled device, CCD. As a result, TEM can observe the structure of zeolites in incredibly high resolution.[45]

However, due to the high energy electron beam used, zeolites can be particularly susceptible to damage and charging by the electron beam. A common observation during TEM is secondary electron beam damage appearing on the grids used to suspend samples, as the carbon film layer darkens, however, after extended exposure of a zeolite sample to the high energy electron beam, it is possible to observe the zeolite framework ‘melt’ with a loss of observable detail.

The thickness of the sample being observed can negatively impact the quality of images produced as the beam must travel through the material to the detector. For frameworks

with at least medium-pore channels, such as MFI, and when observing regions which are of the right thickness, it is possible to directly observe the channels that run through the framework in a series of regular arrays. An example of this is shown below, in Figure 3.10. The observation of the micropores is possible for medium or larger pore materials by TEM, however, some smaller pored materials can begin to reach the limits of the detectors used, requiring high-resolution TEM to image these clearly.[51]

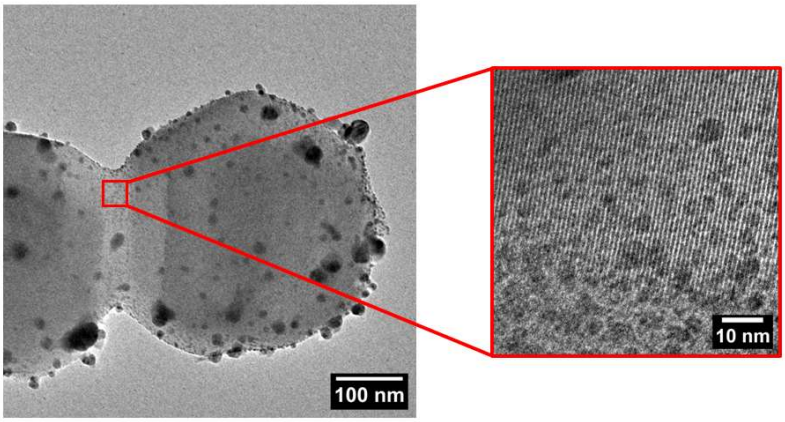

Figure 3.10: BF-STEM images of a silver-exchanged zincosilicate MFI, with a high-resolution capture of a region that displayed the regular arrangement of microporous channels that run through the material, as well as the silver nanoparticles that have formed on the materials surface indicated by the dark spots.

Initial TEM measurements investigated whether the preparation steps caused any significant changes to the materials. A typical preparation of a TEM grid would consist of dispersing a chosen solid in isopropanol (IPA), assisted by ultrasonic waves. Three drops of the suspended solid would be placed on the grid and allowed to dry. However, it was postulated that IPA could be causing a chemical effect with some materials. Therefore, TEM grids were prepared for silver-exchanged ZSM-5 using IPA, methanol, and de-ionised water to observe any potential chemical interactions would occur between zeolite and solvent. However, this study showed that there were no observable chemical effects on the silver-exchanged materials when choosing to use any of the aforementioned solvents, so for convenience of sample preparation, IPA was used throughout.

Energy dispersive X-ray spectroscopy (EDS) systems are commonly found attached to both SEM and TEM microscopes. The incorporation of EDS into TEM imaging allows for the generation of either qualitative elemental maps of materials, or for point analysis of a specific region of a material. Although, EDS maps are low resolution when compared against SEM and TEM images.[52] Accurate determination of elements and

their approximate quantities requires proper calibration, with a reasonable input count rate from the sample with an absence of interference.[53] The overlap of X-ray transition energies between elements can cause issues with false positives being reported for elements that are not present, with it noted that grids themselves can be detected as they are comprised of copper, nickel or gold, using a layer of graphene, carbon film or holey carbon, so care must be taken when interpreting sample data. The ability of EDS-TEM to highlight areas of low and high density of an element was of particular use when observing silver sintering in spent silver-exchanged zeolites and zeotypes, especially following hydrocarbon upgrading reactions.

3.1.3 Energy-Dispersive X-Ray Fluorescence (ED-XRF)

Energy-dispersive X-ray fluorescence (ED-XRF) is a non-destructive analytical technique requiring little sample preparation and utilises an X-ray beam source to bombard a material with high-energy X-rays. These high energy X-rays perturb electrons in the inner shells of atoms causing them to become excited. This excitation requires a high amount of energy and the relaxation of the excited electron can lead to its ejection from the inner shell to leave behind a gap, allowing an electron from a higher energy level to relax and occupy the inner shell position. Relaxation causes the release of energy as a photon corresponding to the energy gap between the two energy levels of an atom, which is unique to each element, meaning the element responsible can be identified from the observed fluorescence.[54] However, fluorescence is an inefficient secondary radiation produced by atoms, which is weaker than the primary radiation from the X-ray source of the instrument and can become obscured. Issues with accuracy when observing light elements can arise, as the energy required to excite the core electrons of light elements is much lower than that of heavy elements, making accurate determination of light elements more difficult. A graphic of an ED-XRF spectrometer is shown in Figure 3.11.

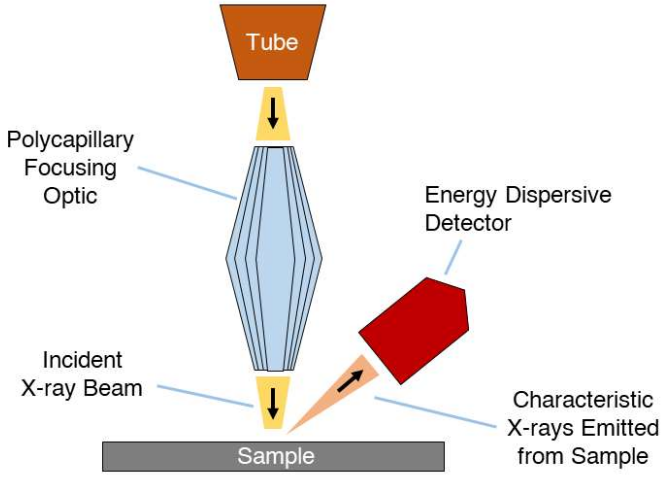

Figure 3.11: A graphic displaying how ED-XRF analysis is conducted, with the X-Ray beam focused directly onto the sample, before its emission is detected by an adjacent detector.

3.1.4 X-ray Absorption Near Edge Structure (XANES)

X-ray absorption near edge structure (XANES) is one of the X-ray absorption spectroscopy (XAS) techniques used in this project to provide information about the electronic structure of a materials surface.

XAS techniques investigate several different interactions between incident X-rays are they pass through and interact with a material. Whilst some X-rays are scattered (elastic scattering), some are absorbed (inelastic scattering) and lead to electron excitation. Following excitation of an atoms core election (1s or 2p shell) after interaction from an incoming X-ray photon (in the range of 100 eV to 10 keV), the excited core electron leave behind a core electron hole. The excited electron either occupies a previously unoccupied higher energy state or is ejected into the continuum and becomes unbound. The core electron hole of each atom has an energy that is both element specific and local-bonding environment specific, however, core holes are extremely short lived as they are highly unstable. Relaxation of the excited core electrons from a higher energy level to a lower energy state leads to the generation of a photoelectron, with the fluorescence emission giving information about the element and local structure.

For XANES, neighbouring atoms affect the electronic transitions that occur following excitation, as excited core electrons can bounce between the neighbouring atoms before returning to the absorbed atom. Localised bonding affects the energy levels and electronic states of the core electron, with the energy levels influenced by the local symmetry, coordination environment and oxidation state to produce features at specific energies in the XANES region.

XAS can be applied *ex-situ* or *in-situ* and is a powerful technique for understanding heterogenous catalyst structure and active site.[55–59] A recent example of *in-situ* XAS of ZSM-5 supported Pt NPs applied to understand catalyst performance under process relevant conditions.[60]

An example XAS spectrum is shown in Figure 3.12, which can be broken down into three separate parts. XANES is interested in the pre-edge absorption, which is 10 eV below and 50 eV above the edge jump, as well as the edge absorption itself, highlighted in blue in Figure 3.12. The extended edge, highlighted in green in Figure 3.12, is analysed using extended edge X-ray absorption fine structure (EXAFS) and is discussed in Chapter 3.1.4.1. XANES provides information about the electronic structure of a material whereas EXAFS provides details about the local atomic environment at a specific element of interest.

Linear combination fitting (LCF) can be applied to an acquired XAS spectrum to compare it against a set of known 'standard' XAS spectra and identify the chemical species or environments present in a material. These spectra can be combined in varied proportions to estimate the composition of an unknown material and identify the species responsible for the features present in the experimental XAS spectrum. Conducting LCF is an iterative process, requiring an initial set of standards which can be refined following the initial fitting. LCF provide a reasonable estimation for the amount of each elemental state present in the material, however, uncertainty errors are similar to typical XAS analysis and are assumed be around 5 – 10%.

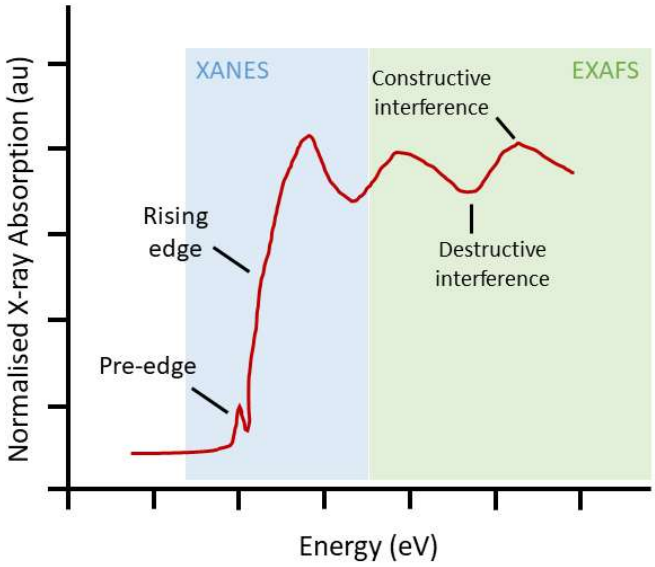

Figure 3.12: Graph showing a simulated XAS spectrum to highlight the individual features typically observed for materials, with a pre-edge and a rising edge for XANES, and an oscillating extending edge region consisting of destructive and constructive interference for EXAFS.

3.1.4.1 Extended X-ray Absorption Fine Structure (EXAFS)

Extended X-ray absorption fine structure (EXAFS) is an XAS technique that is used in partnership with XANES and is interested in the extended edge region of the XAS spectrum, highlighted in green in Figure 3.12. The extended edge describes the oscillating region of the XAS spectrum that appears 50 eV to 1000 eV above the edge jump. The oscillating increase and decrease in X-ray absorption observed in EXAFS region corresponds to constructive and destructive interference in the scattered waves. Oscillations occur when the X-rays interact with the material, inducing oscillations in the electron cloud around the nucleus of the atoms. When these scattered waves align in phase when they reach the detector, they produce constructive interference. In contrast, when they arrive at the detector out of phase, they produce destructive interference.

EXAFS can be used to determine the state of elements present in a material, even at very low concentrations and provides structural information about the neighbouring atoms, facilitating the determination of bond lengths, coordination numbers and local atomic arrangements.[61–63] This is achieved through LCF, providing an accurate estimation of coordination number to nucleus of interest, the disorder of the neighbouring atoms and the radial distance between neighbouring atoms. However, LCF of the EXAFS region requires the use of the Debye-Waller (DW) factor to account for fluctuations in interatomic distances that arise due to the thermal vibrations of atoms. DW factors quantify the range of distances between the neighbouring atoms and the absorbing atom, ultimately improving the reliability of LCF.

3.1.5 ICP-OEs

Inductively coupled plasma optical emission spectroscopy (ICP-OEs) is a destructive technique used to analyse several elements simultaneously and is capable of measuring trace levels of metals and other elements, allowing for high levels of precision due to the inherent sensitivity and destructive nature of the technique. Zeolite samples were digested prior to their analysis, so they could be introduced in the liquid phase. ICP-OEs functions through the interaction of heat and light energy. By generating an argon gas plasma approaching temperatures of 10,000 K, when an analyte interacts with the high energy of the plasma the energy is transferred to the analyte and causes an excitation of the atoms. When the excited atoms relax to a low energy position, emission rays are released as photons which have a specific wavelength and is unique to each element. Detection is carried out by an optical spectrometer, to produce a spectrum, which when integrated will produce a concentration for each element observed.[64]

ICP-OEs was used in tandem with ED-XRF to distinguish the accuracy of data during the analysis of samples using the non-destructive ED-XRF technique.

3.1.6 DRIFTS

Diffuse reflectance infrared Fourier transform spectroscopy (DRIFTS) is a form of infrared (IR) spectroscopy that facilitates the analysis of solid samples that can be ground into a fine powder, often mixed with an IR inactive material such as potassium bromide (KBr), through which the IR beam can be reflected and transmitted. DRIFTS requires minimum sample preparation other than the sample being a powder with good homogeneity, uniform particle sizing and loose packing into the sample cup, which ensures the maximum IR beam penetration and the best representation of the overall bulk material. The cup requires aligning for its positioning (X, Y, Z) with the IR beam, to ensure maximum transmission of the signal to the detector also. A graphic displaying a generic DRIFTS cell setup is shown in Figure 3.13.

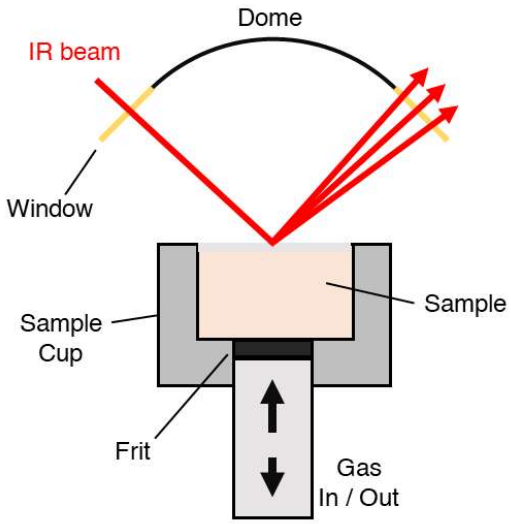

Figure 3.13: Simplified graphic displaying the individual components of a DRIFTS cell, the IR beam path through the cell and how gases are introduced to or removed from the cell.

DRIFTS IR spectroscopy allows for the characterization and quantification of acid sites in zeolites, following their dehydration under reduced pressures at raised temperatures. In addition, the introduction of probe molecules can also distinguish between the location and strength of acid sites.[65,66] Pyridine is a popular probe molecule and interacts with both BAS and Lewis acid sites as shown in Figure 3.14. Pyridine has a kinetic diameter of 5.7 Å, which is too large to enter small-pore zeolites, which means it can be used selectively to probe surface acidity with a smaller molecule like ammonia to probe

internal acid sites.[65] Temperature is another important factor for the acquisition of spectra and especially so when using probe molecules, as temperature changes can move peak intensities by 15% and wavenumbers by up to 4cm^{-1} per 100 °C.[66] By not conducting experiments at a fixed temperature, comparison between materials is compromised as peaks appear at changed wavenumbers or may not be observed due to decreased intensity.

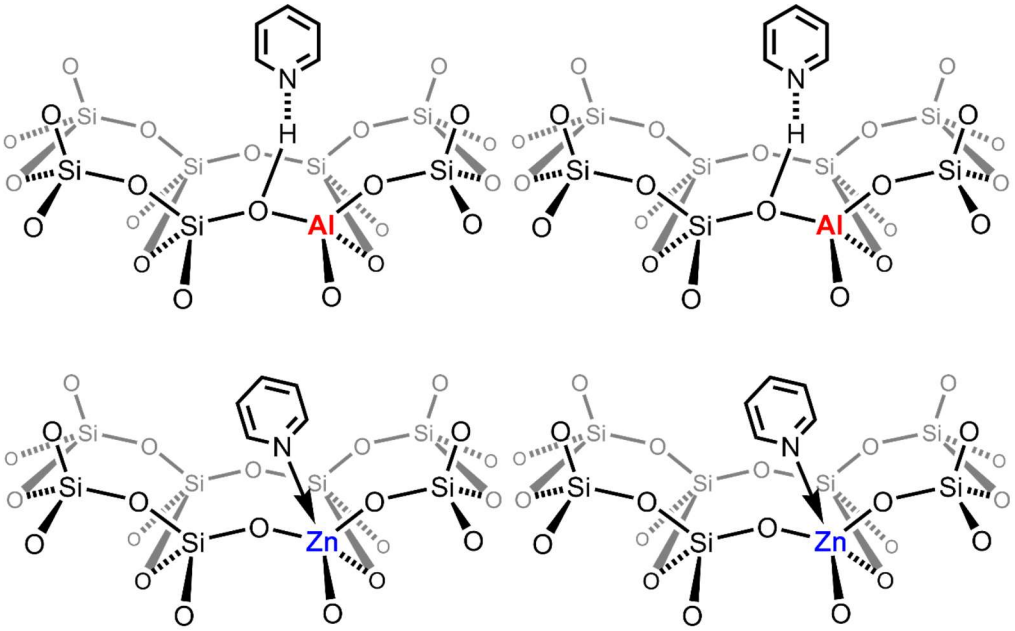

Figure 3.14: Two proposed interactions between pyridine and zeolite/zincosilicate frameworks, for binding to Brønsted and Lewis acid sites.[66]

A wide range of chemical species can be present within zeolite frameworks and these fall within the 4000 – 600 cm^{-1} wavenumber range. Bands of particular interest for determining zeolite order fall between 3800 – 3400 cm^{-1}, which are closely associated with alumina or silica species.[66] Isolated external silanol (Si–OH) species are reported to appear around 3750 cm^{-1}, with isolated internal silanol species appearing around 3735 cm^{-1}.[67] Several kinds of undefined defect sites can be observed around 3700 – 3650 cm^{-1}, with bridging OH groups appearing around 3600 cm^{-1}.[67] Silanol nests and adsorbed water can lead to a broad peak centred between 3400 – 3700 cm^{-1}. Brønsted acid sites appear between 3600 – 3400 cm^{-1}, depending on the level of interaction with their local environment. Acid sites at lower wavenumbers are weaker and less isolated, as they interact with a higher number of groups in the framework. Acid sites which are more isolated appear at higher wavenumbers and are stronger acids.

The region around 2400 cm^{-1} is typically indicative of CO_2 being present. Medin *et al.* reason that a broad band around 2400 cm^{-1} can be attributed to an O–C–H bending

vibration overtone from chemisorbed olefins, with the fundamental vibration for the species around 1200 cm^{-1} not being observed.[68] The reason the band at 1200 cm^{-1} cannot be observed is due to complete light absorption from zeolite framework lattice vibrations, corresponding to a series of T–O–T vibrations, which appear between 2000 and 800 cm^{-1} and obscure any smaller bands below them.

Pyridine can probe the strength of BAS and Lewis acid sites present in the framework. For BAS, the bands associated with BAS species will decrease in intensity whilst new bands appear at ~1545 cm^{-1} and ~1637 cm^{-1}. Lewis acid sites lead to the evolution of bands at ~1456 cm^{-1} and ~1622 cm^{-1}, due to the co-ordination of pyridine with Lewis acid sites and overlapping signals centred around 1490 cm^{-1} from pyridine on Lewis and Brønsted acid sites.[66] Acetonitrile was another probe molecule chosen as it is capable of probing both Brønsted and Lewis acid sites and is small enough to enter the micropores of small pore zeolites. However, deuterated acetonitrile (MeCN-d_3) was chosen as the probe molecule as acetonitrile can introduce several strong Fermi resonances that will unnecessarily complicate the IR spectrum.[69]

3.1.7 Brunauer-Emmett-Teller Theory (BET)

Brunauer-Emmett-Teller (BET) theory was produced to rationalize the adsorption of gas molecules on solid surfaces and is an important technique for the measurement of a materials surface area. BET measurements are referred to as physical adsorption, or physisorption and are of great importance to meso and microporous materials like zeolites, as the specific surface area can determine catalytic activity differences between materials with different composition, topology, and extra-framework cations, allowing for the refinement of materials to enhance their catalytic activity further. BET theory itself is an extension of the Langmuir adsorption model, which is a theory for monolayer adsorption of molecules. BET theory extends this to multilayer adsorption of molecules, with the following mathematical assumptions:

- Gas molecules are physically adsorbed onto layers of solids indefinitely, and only interact with adjacent layers of gas molecules.
- Enthalpy of adsorption is highest for the first layer, decreasing with each additional layer.
- Enthalpy of adsorption for the second layer and above is equal to the enthalpy of liquefaction for the gas used.
- To each layer of gas molecules adsorbed, the Langmuir theory can be applied.

Following these assumptions, BET theory also assumes that adsorption can only occur on well-defined sites, with the only interaction coming between the site and a single molecule per site being adsorbed. Also assumed is that the uppermost layer is in equilibrium with the gas phase, at saturation the molecular layer number tends to infinity – akin to being surrounded by a liquid phase – and that desorption of a gas is a kinetically controlled process. Several models, or isotherms, have been created to explain the behaviour of adsorption on materials. These are given as an isotherm type, with microporous materials such as zeolites typically being type I, shown in Figure 3.15. This arises from the initial adsorption forming a monolayer on the material, prior to the delayed multilayer formation at higher pressure. This can be explained from the gas molecules having a higher affinity for the material surface than towards one another, hence the rapid formation of a monolayer and the delayed formation of the multilayer adsorbate. The observed adsorption and desorption curves do not overlap, highlighting capillary condensation in the micropores, described as an H4 hysteresis. Even with the limitations, BET remains a widely used technique for both meso and microporous materials.[70–72]

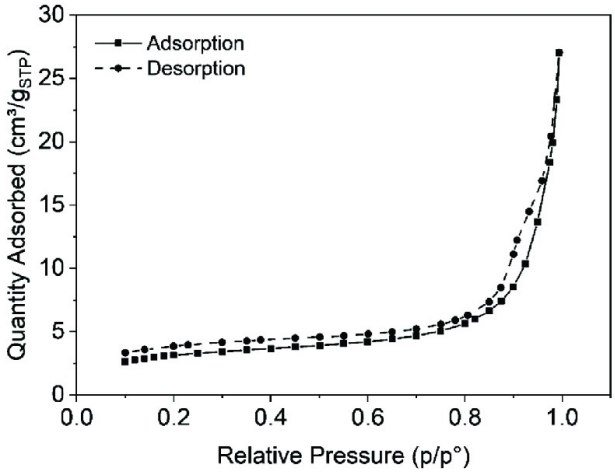

Figure 3.15: An example of a BET isotherm type I + H4 hysteresis, typically observed for microporous materials like zeolites, where the initial monolayer adsorption is fast, with a delay until higher partial pressure before multilayer adsorption.[73]

3.1.8 Gas Chromatography-Mass Spectrometry

Gas Chromatography (GC) is analogous to other forms of chromatography, using a gaseous mobile phase to separate the components of a gaseous mixture as they pass along and interact with a narrow column due to an applied gas pressure.[74] GC can be a very sensitive technique for the separation and detection of trace amounts of low weight compounds and requires a mobile phase of very high purity. Samples can be introduced

as gases or as liquids, which are vaporised upon injection. One key aspect that affects resolution in GC comes from the choice of column. Separation of the components is dependent on the affinity the component has towards the stationary phase and the mobile phase. Compounds with a greater affinity towards the stationary phase elute later giving them a longer retention time (RT). A materials affinity towards the column is dependent on the strength of the intermolecular interaction between components.

There are a wide variety of GC columns, with the most common being packed or capillary columns, as shown in Figure 3.16. Packed columns are commonly 2-6 metres in length with internal diameters between 2-4 mm, walls made from glass, aluminium, copper or steel, and packed with porous, high surface area silica particles. Capillary columns are constructed from fused silica, coated with a protective polymer layer on the inner wall and are often also referred to as wall-coated columns. These columns are much longer, ranging from 15-100 metres in length, with internal diameters of 150-300 µm.[75]

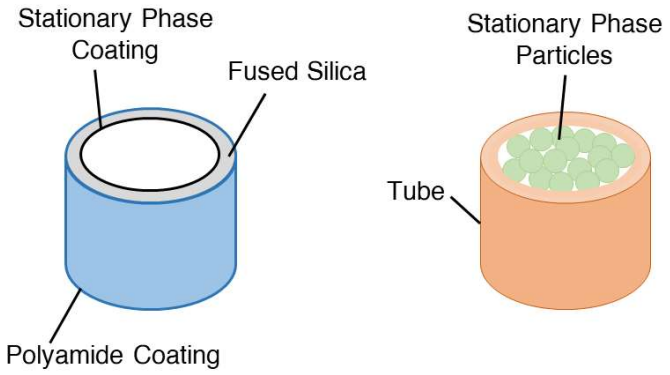

Figure 3.16: A simplified graphic displaying the difference between wall-coated capillary columns and packed columns, two of the most commonly used types of gas chromatography (GC) column.

Mass-Spectroscopy (MS) is an analytical method used to accurately determine the molecular mass of a compound for identification, generally from a combination of molecular fragment pattern, isotopic ratios and a molecular ion peak present in the mass spectrum. In MS, a sample is introduced to the mass spectrometer, then vaporised and ionised by an electron beam, typically an electron gun, to provide a molecular ion from either removing or adding an electron. This bombardment of high energy electrons causes molecules to fragment; however, the parent can often be easily recognised. After ionisation, the charged ions are accelerated by an electric field to form a focused beam of ions, to give them all identical kinetic energy. The ions are then deflected by a magnetic field according to their mass and charge, those with the lightest mass or greatest charge are deflected more strongly, before then being detected by an electric

current to produce a mass spectrum. The mass spectrum shows the relative abundance of each ion detected as well as the mass-to-charge ratio for each fragment.[76] Peak intensity can be strongly affected by the electrostatics of a molecule, with the molecular peak being much more intense for: aromatic molecules, due to the π-conjugation in the system; and in conjugated olefins and unsaturated compounds, due to their π-electron system and the delocalisation and stabilisation of charges.

Both Gas Chromatography (GC) and Mass Spectroscopy (MS) are common laboratory analytical techniques in their own right, but through their combined application as a tandem analytical technique, Gas Chromatography-Mass Spectroscopy (GC-MS) has the capability to separate, quantify and identify constituents in an analyte mixture. GC-MS proved particularly useful when needing to identify an array of products during trial runs of hydrocarbon upgrading reactions, so calibration these newly identified products could be carried out. This facilitated accurate comparison between catalysts, allowing us to discern which properties are beneficial towards catalytic activity.

3.2 Experimental Methods

3.2.1 Zeolite Dehydration

The dehydration of zeolites is a crucial step for several processes, including multiple forms of characterisation and when carrying out upgrading reactions. Dehydration and desorption were crucial in preparing the materials for characterisation using NMR spectroscopy, or prior to reagent vapor-deposition or methane activation.

Vacuum dehydration was performed in a quartz u-tube attached to Schlenk line (vacuum provided by an Edwards RV8 rotary vacuum pump) using a Carbolite EVA 12/150B (1200 °C) tube furnace. Zeolite powder was sandwiched between two plugs of quartz wool, holding the zeolite in the centre of the muffle furnace heating zone, as shown in Figure 3.17. The u-tube would be connected via one tap to the Schlenk line, which was connected to dry nitrogen, methane and to the vacuum pump, whilst the other u-tube tap would be connected to a gas bubbler. Calcination could therefore be achieved under reduced pressure, dry nitrogen flow or argon flow.

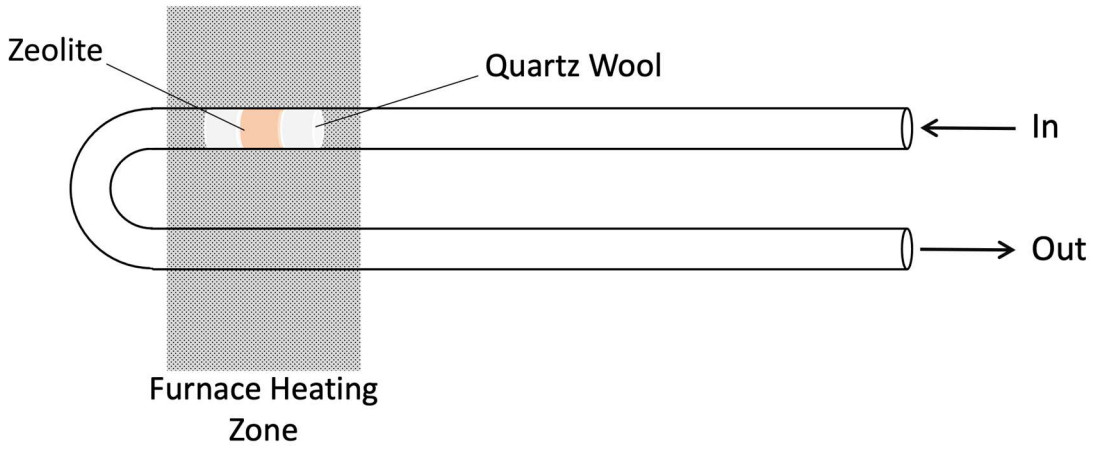

Figure 3.17: Simplified graphic showing a quartz u-tube loaded with zeolite between two quartz wool plugs and gas flow controlled by Young's taps.

The muffle furnace was heated to 400 °C to provide milder dehydration and desorption conditions for silver-exchanged materials, minimising the risk of auto reduction. Reduced pressures of below 5 x 10^{-2} mbar whilst at raised temperature were deemed to be sufficient for complete desorption and activation of the materials. The calcination profile for this method is included in Figure 3.18, showing a subsequent step with methane activation carried out at 250 °C.

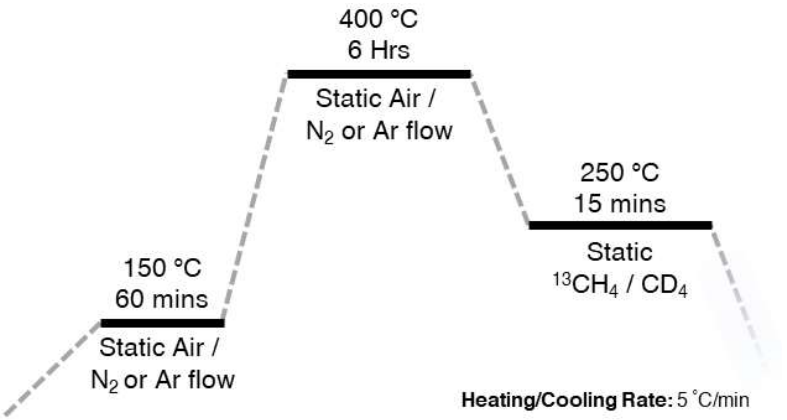

Figure 3.18: A simplified graphic showing a mild calcination profile used for materials more susceptible to framework damage that was used in this project in conjunction with a Schlenk line, that allowed for reduced pressure, nitrogen flow or argon flow during calcination, before subsequent exposure to methane to assess the materials ability to activate methane.

3.2.2 Pressing and Sieving

A Specac hydraulic press (set to 10 ton) and an Apollo Scientific XRF die fitted with KBX-320 pellets (32 mm). The materials were loaded into the die and pressed at 10 ton for 1 minute, forming a solid 32 mm pellet of the material, which was then pressed by hand through a 40-mesh (400 µm) stainless steel sieve. The pressed particles that passed through the 40-mesh sieve and were captured by a 60-mesh (250 µm) sieve were retained, whilst those which passed through were deemed too small and underwent the process again.

Materials whose particle size was between 250 and 400 µm were used for flow chemistry, as particles of this size gives a good balance between interacting with the gas feed through the reactor, whilst not causing a sufficient restriction to the gas flow through the reactor and causing a build-up of excess backpressure in the system. Particles which are well under 250 µm in size also have the propensity to pass the filter and travel along the pipework, which not only contaminates the system but can lead to increased levels of backpressure or ultimately a system blockage.

3.2.3 Calcination

Zeolites were calcined under static air using: Carbolite CWF 11/13 (1100 °C), Carbolite HTC 16/3 (1600 °C) or a Carbolite RHF14/3 (1400 °C) muffle furnace.

Calcinations were routinely carried out using the following calcination profile, unless stated: Ramp to 150 °C (ramp rate: 5 °C/min), 1 hour dwell at 150 °C, ramp to 550 °C (ramp rate: 5 °C/min), 5 hour dwell at 550 °C, cool to ambient temperature.

Zincosilicates require a more gentle calcination method, to avoid undesirable framework damage and crystallinity loss. Additionally, silver-exchanged materials were never routinely subjected to calcination conditions due to their susceptibility for silver to undergo autoreduction at raised temperatures, which can lead to autoreduction and subsequent framework damage.[77–82]

3.2.4 Aqueous Ion-Exchange

Aqueous ion-exchange of zeolites and zincosilicates was the default method employed for the introduction of changed extra-framework cations, such as silver, at exchanged framework sites. Both vapor deposition and solid ion-exchanges were also conducted during this project, however, in both cases this will be stated alongside experimental parameters.

Aqueous ion-exchange was routinely conducted when preparing metal-exchanged zeolites and zincosilicates. It was of upmost importance when selecting a silver reagent that it was widely available and cost-effective and readily soluble in water. This was due to the widespread use of silver-exchanged materials in this project. Silver (I) nitrate was an easy choice when deciding on silver reagent for aqueous ion-exchange of zeolites, due to fitting all three requirements and was used for exchanges throughout the project.

One major concern of the use of silver comes from the known photosensitivity of silver (I) salts, in which silver cations are reduced to silver metal, a well-known example of which is silver chloride.[83–85] To avoid light exposure, ion-exchanges involving silver were carried out using opaque, black centrifuge tubes (shown in Figure 3.19) rather than the standard clear tubes. Handling silver-exchanged materials was carried out whilst avoiding direct sunlight, keeping light-exposure to a minimum, with the materials stored under darkness in foil-wrapped vials.

Figure 3.19: Light protective centrifuge tubes used when handling silver-exchanged zeolites/zeotypes or carrying out silver-exchange of zeolites/zeotypes.

Unless stated otherwise, routine aqueous ion-exchange was conducted throughout this project for all materials unless stated, using the following method:

Exchange was carried out with the zeolite (2.0 g) suspended into an aqueous solution (0.1M, 35 mL) into a 50 mL centrifuge tube and allowed to mix for 1 hour on a tube roller. Solids were separated by centrifugation and washed with deionised water (3 x 35 mL), before being dried at 80 °C in an oven for 16 hours.

Zeolite framework, reagent and solution molarity were changed throughout the project, with the changes made to the generic method stated. For materials that were not silver-exchanged, calcination was carried out following overnight drying of the material.

Other silver reagents were used, such as silver sulphate, silver carbonate and silver chloride. Aqueous ion-exchange was used where possible, with solid-state mixing used for ion-exchange for those insoluble in water.

3.2.5 Centrifugation

Centrifugation of samples was performed on a Heraeus™ Megafuge™ from Thermo Scientific. A centrifuge tube was charged with an aqueous suspension of zeolite (10-40 mL) and centrifuged at 4500 RPM for 5-10 minutes, with supernatant liquid removed and solid dried in air at 80 °C.

Samples which were light-sensitive required protective measures. Opaque, black centrifuge tubes were used in place of clear tubes and covered with perforated foil during the drying phase.

3.2.6 Powder X-Ray Diffraction Experimental Method

Samples were prepared on XRD slides fitted with a thin, low background [911] silicon wafer, over which petroleum jelly was thinly spread. The sample was evenly scattered until the jelly layer was covered, with the loose material removed and the sample submitted for analysis. This was required for materials which were pressed to 40-60 mesh or static in nature to stop mobility of the sample during acquisition. Alternatively, ground, non-static powders were packed onto XRD slides without a silicon wafer by flattening until a homogenous sample was achieved.

pXRD patterns were acquired using a Bruker AXS D8 Advance diffractometer, fitted with a Lynxeye Soller PSD detector and controlled by Diffrac and XRD commander software. Copper $K\alpha_1$ (λ = 1.5406 Å) and $K\alpha_2$ (λ = 1.5444 Å) radiation was used. Patterns were recorded with a range of 5 – 60° (2θ), with 0.02° spacing and a knife edge in place to reduce background scattering at low 2θ values. Scan durations were 25 minutes.

Data was kindly collected by Gary Oswald of Durham University.

3.2.7 SEM Experimental Method

SEM analysis TEM was carried out at the GJ Russell Electron Microscopy facility located here at Durham University. SEM was performed using powder samples that were initially dispersed in isopropanol, before a single drop of the dispersion deposited onto a silicon [100] wafer (Agar Scientific, wafer thickness: 460-530 μm, polished), dried in air and placed onto a microscope stub. The microscope stub was transferred and coated with approximately 20 nm of a gold using a sputter coater and subsequently analyzed. Images were acquired using a FEI Helios Nanolab microscope operated at 5 kV on samples which had been coated with a 20 nm gold layer using a Cressington sputter coater 108 Auto.

Sample preparation and image acquisition was kindly carried out by both Dr Irene Mazzei and Miss Catherine Crockett.

3.2.8 TEM Experimental Method

TEM was carried out at the GJ Russell Electron Microscopy facility located here at Durham University. TEM was performed using powder samples that were dispersed in isopropanol, assisted with ultrasonic waves. Three drops of the dispersion were applied to 300 mesh copper grids covered with carbon film and left to dry in air. Images were acquired using a JEOL JEM-2100F Field Emission Electron Microscope (fitted with a

Schottky field emitter), operating voltage was set at 200 kV. A GATAN Orius SC1000 CCD camera fitted with a Gatan tridiem (imaging filter) was used for imaging, with image resolution set to 4096x4096 (4K x 4K) resolution for all acquired images. Chemical analysis was obtained using an Oxford Instruments INCAx-sight Si(Li) detector for EDX (50 mm^2 area detector, 25° take off angle providing 130 eV energy resolution). Piezo-driven stage for precision sample movement for X, Y and Z axis, with EDS-TEM acquired at x = 15° to maximise signal intensity. Sample chamber temperature was set to 10.0 °C for all acquisitions. Images were obtained using Cmos Rio16 imaging software, with elemental composition mapping obtained in Oxford Instruments Aztec software. Further image manipulation and measurement of crystal size and nanoparticle size was carried out using ImageJ.[86]

3.2.9 ED-XRF Experimental Method

Energy-dispersive X-ray fluorescence (ED-XRF) spectroscopy measurements were acquired using a benchtop Malvern Panalytical Epsilon 1 ED-XRF analyser, equipped with a 50 kV Ag anode X-ray tube and calibrated using zeolite standards. Samples were analyzed as powders, requiring 0.2g to 1g for analysis. Samples were loaded into polypropylene cups fitted with a thin 4 mm polypropylene film at their base, before being gently compacted by hand to give a homogenous, free of intraparticle voids sample, for which mass was recorded. The XRF spectrum was acquired using a program that collected an unfiltered XRF spectra alongside 3 filtered XRF spectra using Ag, Cu and Al filters, taking around 20 minutes per acquisition. Three spectra were acquired for each sample with 120° clockwise rotation carried out between acquisitions to record an average of each material.

Samples were analyzed using the Malvern Panalytical's proprietary 'Omnian' calibration, to which additional zeolite derived standards had been added to it to improve accuracy for zeolite specific elements, such as Si and Al.

All samples for which elemental composition has been stated, with wt% and elemental ratio, have been acquired by ED-XRF.

Results recorded using the Epsilon 1 were compared against those recorded by ICP-OEs, a departmental service ran by Dr Emily Unsworth of Durham University. The technique is discussed in Chapter 3.1.5 and the experimental detail in Chapter 3.2.1.7. Table 3.5 shows an example material that was analysed using both ED-XRF and ICP-OEs, for which the wt% values acquired agreed across the measured elements.

Table 3.5: Table comparing the results obtained for a potassium exchanged ZSM-5 analysed by ED-XRF and ICP-OEs, to highlight any discrepancy between the two analytical methods.

Material	Technique	Al	Si	K	Si/Al	K/Al
RK-2-41 K/ZSM-$5_{13.5}$	ED-XRF	2.69 ±0.02	32.95 ±0.36	6.69 ±0.09	11.76	1.72
	ICP-OEs	2.65 ±0.07	31.03 ±0.14	6.49	11.25	1.69

3.2.10 XAS Experimental Method

Samples were supplied as fine, homogenous powders. A known mass of sample was mixed with cellulose (Avicel® PH-101) and the diluted sample was pressed into 13 mm diameter pellet using a die cast and a hydrolytic press (both supplied by Specac). *Ex-situ* Zn K-edge XAFS on pellets were conducted. Pellets were placed onto spectrometer using polymer containing adhesive tape (Scotch® Magic™ Invisible Tape). Experiments were performed on 4 samples and three zinc references, as shown in Table 3.6.

Experiment was conducted on the EasyXAFS300+ laboratory-scale spectrometer (easyXAFS, WA), which uses a Rowland circle optical geometry.[87,88] Zn K-edge XAFS were acquired using a Si (733) spherically bent crystal analyser (SBCA) and an Ag anode X-ray tube at 40 kV. The X-ray current was varied between 4 to 24 mA (160 – 960 W), depending on the sample to maintain a collection deadtime of < 30 %. Four consecutive scans were performed for each sample, collecting the intensity of the transmitted beam (I_t) for each sample, and incident beam only (I_0), with the total times shown in **Error! Not a valid bookmark self-reference.**. Scan parameters used are shown below in 3.7. EXAFS were collected to a K range of 12 $Å^{-1}$.

Data collection and processing incorporates a deadtime correction, which is performed by the silicon drift detector (SSD) and multiple component analyser (MCA) within the instrument. Background correction and energy shifts were conducted on EasyXAFS software. Sample energies were calibrated using a Zn foil standard. The processing of EXAFS and XANES data was performed using IFEFFIT with the demeter package (Athena and Artemis).[89]

Data processing conducted for XAS was as follows:

- X-ray absorption near edge structure **(XANES)** – Linear combination fitting (LCF)
- Extended X-ray absorption fine structure **(EXAFS)** – used for modelling the K-space of the system.

Table 3.6: Sample details for samples submitted for XAFS analysis with sample ID, material name, mass and exposure time.

Sample number	Sample ID	Sample name	Edge and experiment	Amount used /mg	Time per sample*
1	IM153(5)	K/ZnMFI	Zn K-edge XAFS	106	2h 20
2	RK-2-132	Ag/ZnMFI	Zn K-edge XAFS	106	2h 20
3	RK-2-118(5)	H,K/ZnCHA	Zn K-edge XAFS	77	2h 20
4	RK-2-124	Ag,K/ZnCHA	Zn K-edge XAFS	81	2h 20
5	ZnO	ZnO (ref)	Zn K-edge XAFS	10	2h 20
6	ZnAc	Zn acetate (ref)	Zn K-edge XAFS	20	2h 20
7	Zn foil	Zn^0 (ref)	Zn K-edge XAFS	n/a	2h 20

*Time does not include the collection of the incident beam (I_0) scan. I_0 scan was conducted, taking 2h 20 min using the same X-ray source at 40 kV and 4 mA.

Table 3.7: Scanning parameters used for XAFS experiments.

Energy range /eV	Step size / eV $step^{-1}$	Duration per step /s
9560 – 9644	2	1
9644 – 9699	0.25	3
9699 – 10200	2.85*	3

*Derived via the K Step Zone, shown below:

Energy range /eV	K Max / Å	K step / Å	K weight	Duration per step /s
9699 – 10200	12.0	0.05	1.0	3.0

I must acknowledge Dr Monik Panchal of Durham University for his help in sample preparation, data acquisition and data interpretation for the XAS data included in this report.

3.2.11 ICP-OEs Experimental Method

Samples were supplied as fine, homogenous powders of 20 to 25 mg in mass. Zeolites were initially wetted using 2–3 drops of DI water before addition of 2.5 mL UA–1 (Inorganic Ventures™ acid dissolution reagent) and 0.1 mL 70% HNO_3. The vessel was sealed and shaken for 1–3 minutes before addition of 10 mL UNS–1 (Inorganic Ventures™ stabilization reagent). The solution was adjusted to a final weight of 25 to 125 g with deionized water and thoroughly mixed, before a further five-fold dilution with DI water to reduce viscosity and improve plasma stability.

ICP-OES analysis was performed using a Jobin Yvon Horiba Ultima 2. Instrument was equipped with a radial torch, sequential monochromater, cyclonic spray chamber and concentric nebulizer. Sequential monochromator average wavelengths were:

- 224.641 nm and 328.068 nm for Ag species
- 394.401 nm and 396.152 nm for Al species
- 766.490 nm and 769.896 nm for K species
- 588.995 nm and 589.592 nm for Na species
- 251.611 nm and 288.158 nm for Si species
- 213.856 nm and 334.502 nm for Zn Species

Samples were kindly ran by Dr Emily Unsworth of Durham University on a sample submission basis, who also handled both sample dissolution and data collection.

3.2.12 DRIFTS Experimental Method

DRIFTS measurements were acquired using a Bruker Invenio-R FT-IR spectrometer controlled by Bruker OPUS software, fed by a constant flow of dry N_2 (0.6 litres per hour) to ensure no moisture build-up in the detectors or sample chamber. The spectrometer was fitted with a Harrick Praying Mantis cell with high temperature reaction chamber, equipped with a Harrick ATK controlled heating element. To provide cooling to the cell and extend the lifetime of the chamber seal, a Haake F3 was attached to circulate room temperature water as a coolant to the chamber. Vacuum was provided by a Pfeiffer Duo 3 rotary pump for the initial pump down (pressures greater than $1x10^{-2}$ mbar), before a Pfeiffer HiCube 80 eco turbopump was used to reduce pressures further. Pressure measurements were taken using a Pfeiffer PKR360C gauge located closest to the sample cell.

Dehydration of the material for characterisation was achieved by loading the high temperature reaction chamber with a fresh 80-mesh stainless steel gauze into the

sample cup before the zeolite was loaded as a fine powder. The top of the sample was gently pressed flat by hand before sealing the chamber and fitting into the Praying Mantis cell. The reaction chamber was pumped down using the Pfeiffer Duo 3 rotary pump whilst at room temperature, whilst the cell was purged by a constant flow of dry N_2 to remove atmospheric moisture from the beam path during the experiment. Once at pressures lower than $1x10^{-2}$ mbar, the vacuum was switched to the Pfeiffer HiCube 80 eco turbopump, and the reaction chamber was heated from room temperature to 500 °C at 5 °C/min ramp rate, holding at 500 °C for at least 2 hours until the pressure for the cell gauge would read below $1x10^{-4}$ mbar. The sample was then cooled to room temperature and a spectrum collected for material characterisation.

Probe experiments would follow the dehydration protocol, before introducing deuterated acetonitrile or pyridine in small doses through the vacuum system. Extreme caution was used as not to disturb or bump the loaded sample. The pressures inside the chamber were stated using the Pfeiffer PKR360C gauge located closest to the sample cell.

Backgrounds were collected following the dehydration protocol, only using potassium bromide in place of a sample. It was important to use identical handling of sample and background to maximise the accuracy of the background subtraction.

3.2.13 BET Experimental Method

Samples were supplied as fine, homogenous powders, with surface area measured by nitrogen adsorption at 77 K on a Micromeritics ASAP 2020 gas adsorption analyser, operating in a pressure range of P/P_0 = 0.005-1.00. Prior to nitrogen adsorption, samples were degassed at 623K for 4 hours. The total surface area was calculated using the Brunauer-Emmett-Teller equation within a pressure range of P/P_0 = 0.005-0.300.

Data was kindly collected by Dr Abdul-Lateef Adedigba or Miss Catherine Crockett.

3.2.14 HEL FlowCAT Flow Reactor Experimental Method

Flow chemistry was carried out using a HEL FlowCAT flow reactor paired with on-line GC-MS-BID analysis, discussed in Chapter 3.2.15. All reaction parameters, such as temperature, gas and liquid flow rate, along with analytical parameters, were controlled independently using an external PC. Materials were prepared as outlined in Chapter 3.2.2. The catalyst bed was prepared as follows: 300 mg of prepared material (40-60 mesh) was diluted with 1.2 g of carborundum (80 grit) and packed between a pre- and post-bed of carborundum (2 x 1.5 g, 80 grit) in a stainless-steel reactor (I.D. = 4 mm). The reactor was fitted into a vertical clam-shell furnace, with temperature monitoring provided by an internally positioned thermocouple. Gas flow was controlled using an integrated mass flow controller, whilst liquid feeds were delivered by an Eldex HPLC pump.

3.2.15 GC-MS Experimental Method

Analysis of the upgrading reaction products was carried out using the on-line GC-MS-BID connected to the HEL FlowCAT via insulated, trace heated lines kept at 170 °C. Two samples were taken as the effluent passed through two Vici valves (6-port design, heated at 180 °C) fitted to the system, each fitted with a sample loop of 500 µL capacity. One valve fed sample 1 into the injection port of the GC-BID (heated to 200 °C) and the other sample 2 into the injection port of the MS (heated to 220 °C). GC-BID analysis used a Thames Restek RTX-VMS (length: 30 m, I.D. = 0.25 mm, film thickness = 0.25 µm) fused silica capillary column, whilst for MS a Restek Shincarbon ST column (length: 2 m, I.D. = 1 mm, 100-120 mesh packing). Each column was housed in the same oven and underwent identical thermal treatment during the course of the analytical method, which was: Oven set to hold at 80 °C for 7 minutes, before heating to 250 °C (ramp rate: 30°C/min), oven set to hold at 250 °C for 18 minutes, giving a total run time of 30 minutes per injection. Sample 1 was analysed using a Shimadzu GC-MS-QP2010 SE mass spectrometer, with interface temperature (220 °C) and ion source temperature (200 °C) held throughout. MS was collected during the entirety of the GC program (0.1 min – 30 min), events occurring every 0.3 s. Ions were detected over m/z range: 10 – 200, with a scan speed of 666 ms. Sample 2 was analysed using a Shimadzu BID-2010 Plus detector, with the He plasma set to 300 °C. Analysis was performed during the entirety of the GC program (0.1 min – 30 min), with a sampling rate of 40 ms.

Calibration results for the GC-MS system are included in Section 10.

3.2.16 Experimental Methods for Solid-state NMR Spectroscopy

This section outlines the experimental methods designed to acquire information on the species present in the framework used in the characterisation of zeolites and zeotypes for the aforementioned nuclei. In addition, experiments were conducted to determine activity towards methane and identify further products. For the ssNMR work, I must give acknowledgement to both Dr David Apperley of Durham University and Dr Sam Page of Durham University for their expertise, their assistance in the acquisition and interpretation of NMR spectra and for conducting the NMR experiments.

^{1}H ssNMR Spectroscopy experimental method

^{1}H Solid-state NMR direct-excitation (DE) spectra were recorded using a Bruker Avance III HD spectrometer operating at 400 MHz. They were obtained using a 4 mm rotor (outside diameter) in a magic-angle spinning probe at a spin rate of 10 kHz at ambient temperature. Spectra were obtained using DEPTH background suppression with a contact time of 3.8 μ s (equivalent to a pulse angle of 90°), with a recycle delay of 10 s and 160 repetitions. Spectral referencing is with respect to external, neat tetramethylsilane (TMS), carried out by setting the signal from an external sample of adamantane to 1.9 ppm.

Note: Some specific experiments were conducted using a 3.2 mm rotor (outside diameter) in a magic-angle spinning probe at a spin rate of 20 kHz at either ambient temperature or – 20 °C. This was the only deviation from the standard experimental procedure and was used to provide line sharpening to the acquired spectrum. This deviation will be referred to at the relevant spectra.

^{2}H ssNMR spectroscopy experimental method

^{2}H Solid-state NMR DE spectra were recorded using a Bruker Avance III HD spectrometer operating at 61.43 MHz. They were obtained using a 4 mm rotor (outside diameter) in a magic-angle spinning probe at a spin rate of 10 kHz at ambient temperature. Spectra were obtained using a pulse-acquire experiment with a contact time of 4.2 μ s (equivalent to a pulse angle of 45°), with a recycle delay of 4 s and 128 repetitions. Spectral referencing is with respect to $CDCl_3$ at 7.24 ppm or set using D_2O at 4.81 ppm.

^{2}H Solid-state NMR CP spectra were recorded using a Bruker Avance III HD spectrometer operating at 61.43 MHz. They were obtained using a 4mm rotor (outside diameter) in a magic-angle spinning probe at a spin rate of 10 kHz at ambient temperature. Spectra were obtained using a pulse-acquire experiment, utilising the

transfer of magnetisation from proton to deuterium using the cp pulse with a contact time of 7 ms, a recycle delay of 2 s and 10000 repetitions. Spectral referencing is with respect to $CDCl_3$ at 7.24 ppm or set using D_2O at 4.81 ppm.

^{13}C ssNMR Spectroscopy experimental method

^{13}C Solid-state NMR DE spectra were recorded using a Bruker Avance III HD spectrometer operating at 100.63 MHz. They were obtained using a 4 mm rotor (outside diameter) in a magic-angle spinning probe at a spin rate of 10 kHz at ambient temperature. Spectra were obtained using DEPTH background suppression with a contact time of 3.3 μ s and a recycle delay of 0.5 s for 13000 repetitions. Spectral referencing is with respect to neat tetramethylsilane (TMS), carried out by setting the high-frequency signal from an external sample of adamantane to 38.5 ppm.

^{13}C Solid-state NMR CP spectra were recorded using a Bruker Avance III HD spectrometer operating at 100.63 MHz. They were obtained using a 4 mm rotor (outside diameter) in a magic-angle spinning probe at a spin rate of 10 kHz at ambient temperature. Spectra were obtained using cross-polarisation, utilising the transfer of magnetisation from proton to carbon using the cp pulse, with TOSS spinning sideband suppression with a 1 s recycle delay and 4 ms contact time and 1080 repetitions. Spectral referencing is with respect to neat tetramethylsilane, carried out by setting the high-frequency signal from an external sample of adamantane to 38.5 ppm.

^{27}Al ssNMR Spectroscopy experimental method

^{27}Al Solid-state NMR spectra were recorded using a Bruker Avance III HD spectrometer operating at 104.28 MHz. They were obtained using a 4 mm rotor (outside diameter) in a magic-angle spinning probe at a spin rate of 10 kHz at ambient temperature. Spectra were obtained using direct excitation and high-powered ^{1}H decoupling. Spectra were typically obtained using a recycle delay of 1 s for 3600 repetitions. Spectral referencing is with respect to an aqueous standard of 1.0 M $Al(NO_3)_3$ with a shift of 0.0 ppm.

^{29}Si ssNMR Spectroscopy experimental method

Solid-state NMR ^{29}Si (DE) spectra were recorded using a Bruker Avance III HD spectrometer operating at 79.44 MHz. They were obtained using a 4 mm rotor (outside diameter) in a magic-angle spinning probe at a spin rate of 10 kHz at ambient temperature. Spectra were obtained using a recycle delay of 30 s for 400 repetitions. Spectral referencing is with respect to neat tetramethylsilane (TMS), carried out by setting the high-frequency signal from an external sample of tetrakis(tetramethylsilyl)silane to - 9.9 ppm.

Solid-state NMR ^{29}Si (CP) spectra were recorded using a Bruker Avance III HD spectrometer operating at 79.44 MHz. They were obtained using a 4 mm rotor (outside diameter) in a magic-angle spinning probe at a spin rate of 10 kHz at ambient temperature. Spectra were obtained using a pulse-acquire experiment, utilising the transfer of magnetisation from proton to silicon using the cp pulse sequence and a recycle delay of 1 s, contact time of 3.4 μ s and 3600 repetitions. Spectral referencing is with respect to neat tetramethylsilane (TMS), carried out by setting the high-frequency signal from an external sample of tetrakis(tetramethylsilyl)silane to – 9.9 ppm.

The ^{29}Si ssNMR spectroscopy CP experiments carried out were not quantitative, only qualitative and provided information into the presence of defect sites in both synthesized zeolites and zeotypes.

2D NMR Experimental Methods

^{1}H–^{27}Al ssNMR Spectroscopy REAPDOR experimental method

^{1}H–^{27}Al ssNMR Spectroscopy REAPDOR experiments were conducted using a Bruker Avance III HD spectrometer operating at 400 MHz. They were obtained using a 4mm rotor (outside diameter) in a magic-angle spinning probe at a spin rate of 10 kHz at ambient temperature. Spectra were obtained using the REAPDOR sequence, utilising the dipolar coupling between proton and aluminium, with a recycle delay of 4 s, contact time of 3.7 μ s and 400 repetitions. Spectral referencing is with respect to external, neat tetramethylsilane (TMS), carried out by setting the signal from an external sample of adamantane to 1.9 ppm.

The REAPDOR NMR sequence is used to measure the distance separating a spin-$^{1}/_{2}$ nucleus and a quadrupolar nucleus, such as ^{1}H and ^{27}Al. The experiment operates by transferring magnetisation between the two nuclei using dipolar coupling.

^{1}H–^{29}Si ssNMR Spectroscopy HETCOR experimental method

^{1}H–^{29}Si ssNMR HETCOR experiments were conducted using a Bruker Avance III HD spectrometer operating at 400 MHz. They were obtained using a 4mm rotor (outside diameter) in a magic-angle spinning probe at a spin rate of 10 kHz at ambient temperature. Spectra were obtained using the lghetfq sequence, which utilises spin-spin coupling of two nuclei connected by a single bond to provide information on nuclei that are spatially close and interacting. HETCOR experiments used a recycle delay of 1 s, a contact time of 3.0 μ s and 3584 repetitions. Spectral referencing is with respect to external, neat tetramethylsilane (TMS), carried out by setting the signal from an external sample of adamantane to 1.9 ppm.

Note: Some specific experiments were conducted using a 3.2 mm rotor (outside diameter) in a magic-angle spinning probe at a spin rate of 20 kHz at either ambient temperature or – 20 °C. This was the only deviation from the standard experimental procedure and was used to provide line sharpening to the acquired spectrum. This deviation will be referred to at the relevant spectra.

^{1}H–^{29}Si ssNMR Spectroscopy WISE experimental method

^{1}H–^{29}Si ssNMR WISE experiments were conducted using a Bruker Avance III HD spectrometer operating at 400 MHz. They were obtained using a 4mm rotor (outside diameter) in a magic-angle spinning probe at a spin rate of 10 kHz at ambient temperature. Spectra were obtained using the wideline separation (WISE) sequence, which uses correlation between a high-resolution nucleus (^{29}Si) and low-resolution nucleus (^{1}H) to demonstrate different relaxation behaviours contained within a sample.[3] WISE experiments used a recycle delay of 1 s, a contact time of 1 ms and 1792 repetitions. Spectral referencing is with respect to external, neat tetramethylsilane (TMS), carried out by setting the signal from an external sample of adamantane to 1.9 ppm.

3.3 Chapter Three Bibliography

1 P. J. Hore, in *Encyclopedia of Spectroscopy and Spectrometry*, ed. J. C. Lindon, Elsevier, Oxford, 1999, pp. 1545–1553.

2 B. Reif, S. E. Ashbrook, L. Emsley and M. Hong, *Nat. Rev. Methods Prim.*, Solid-state NMR spectroscopy, 2021, **1**, 2.

3 D. C. Apperley, R. K. Harris and P. Hodgkinson, *Solid-State NMR: Basic Principles and Practice*, Momentum Press, New York, 2012.

4 R. K. Harris, E. D. Becker, S. M. Cabral de Menezes, R. Goodfellow and P. Granger, *Solid State Nucl. Magn. Reson.*, NMR Nomenclature: Nuclear Spin Properties and Conventions for Chemical Shifts: IUPAC Recommendations 2001, 2002, **22**, 458–483.

5 A. McNaught, A. D., Wilkinson, Ed., *IUPAC, Compendium of Chemical Terminology, the 'Gold Book'*, Blackwell Scientific Publications, 2014.

6 Z. Li, D. Dittmann, C. Rieg, M. Benz and M. Dyballa, *Catal. Sci. Technol.*, Hydronium ion and water complexes vs. methanol on solid catalyst surfaces: how confinement influences stability and reactivity, 2022, **12**, 5189–5202.

7 M. Wang, N. R. Jaegers, M.-S. Lee, C. Wan, J. Z. Hu, H. Shi, D. Mei, S. D. Burton, D. M. Camaioni, O. Y. Gutiérrez, V.-A. Glezakou, R. Rousseau, Y. Wang and J. A. Lercher, *J. Am. Chem. Soc.*, Genesis and Stability of Hydronium Ions in Zeolite Channels, 2019, **141**, 3444–3455.

8 C. Schroeder, V. Siozios, M. Hunger, M. R. Hansen and H. Koller, *J. Phys. Chem. C*, Disentangling Brønsted Acid Sites and Hydrogen-Bonded Silanol Groups in High-Silica Zeolite H-ZSM-5, 2020, **124**, 23380–23386.

9 H. Windeck, F. Berger and J. Sauer, *Angew. Chemie Int. Ed.*, Spectroscopic Signatures of Internal Hydrogen Bonds of Brønsted-Acid Sites in the Zeolite H-MFI, 2023, **62**, e202303204.

10 E. Dib, I. M. Costa, G. N. Vayssilov, H. A. Aleksandrov and S. Mintova, *J. Mater. Chem. A*, Complex H-bonded silanol network in zeolites revealed by IR and NMR spectroscopy combined with DFT calculations, 2021, **9**, 27347–27352.

11 T. Baba, Y. Iwase, K. Inazu, D. Masih and A. Matsumoto, *Microporous Mesoporous Mater.*, Catalytic properties of silver-exchanged zeolites for propene production by conversion of methane in the presence of ethene, 2007, **101**, 142–147.

12 M. V Luzgin, A. A. Gabrienko, V. A. Rogov, A. V Toktarev, V. N. Parmon and A. G. Stepanov, *J. Phys. Chem. C*, The 'Alkyl' and 'Carbenium' Pathways of Methane Activation on Ga-Modified Zeolite BEA: 13C Solid-State NMR and GC-MS Study of Methane Aromatization in the Presence of Higher Alkane, 2010, **114**, 21555–21561.

13 M. V Luzgin, A. V Toktarev, V. N. Parmon and A. G. Stepanov, *J. Phys. Chem. C*, Coaromatization of Methane with Propane on Mo-Containing Zeolite H BEA: A Solid-State NMR and GC-MS Study, 2013, **117**, 22867–22873.

14 A. A. Gabrienko, S. S. Arzumanov, I. B. Moroz, A. V Toktarev, W. Wang and A. G. Stepanov, *J. Phys. Chem. C*, Methane Activation and Transformation on Ag/H-ZSM-5 Zeolite Studied with Solid-State NMR, 2013, **117**, 7690–7702.

15 S. Raynes, M. A. Shah and R. A. Taylor, *Dalt. Trans.*, Direct conversion of methane to methanol with zeolites: towards understanding the role of extra-framework d-block metal and zeolite framework type, 2019, **48**, 10364–10384.

16 M. A. Shah, S. Raynes, D. C. Apperley and R. A. Taylor, *Chemphyschem*, Framework Effects on Activation and Functionalisation of Methane in Zinc-

Exchanged Zeolites, 2020, **21**, 673.

17 A. A. Gabrienko, S. S. Arzumanov, M. V Luzgin, A. G. Stepanov and V. N. Parmon, *J. Phys. Chem. C*, Methane Activation on Zn^{2+}-Exchanged ZSM-5 Zeolites. The Effect of Molecular Oxygen Addition, 2015, **119**, 24910–24918.

18 M. Ravi, V. L. Sushkevich and J. A. van Bokhoven, *Chem. Sci.*, On the location of Lewis acidic aluminum in zeolite mordenite and the role of framework-associated aluminum in mediating the switch between Brønsted and Lewis acidity, 2021, **12**, 4094–4103.

19 R. Liu, B. Fan, Y. Zhi, C. Liu, S. Xu, Z. Yu and Z. Liu, *Angew. Chemie Int. Ed.*, Dynamic Evolution of Aluminum Coordination Environments in Mordenite Zeolite and Their Role in the Dimethyl Ether (DME) Carbonylation Reaction, 2022, **61**, e202210658.

20 M. Jin, M. Ravi, C. Lei, C. J. Heard, F. Brivio, Z. Tošner, L. Grajciar, J. A. van Bokhoven and P. Nachtigall, *Angew. Chemie Int. Ed.*, Dynamical Equilibrium between Brønsted and Lewis Sites in Zeolites: Framework-Associated Octahedral Aluminum, 2023, **62**, e202306183.

21 Z. Wang, Y. Jiang, A. Baiker and J. Huang, *Acc. Chem. Res.*, Pentacoordinated Aluminum Species: New Frontier for Tailoring Acidity-Enhanced Silica–Alumina Catalysts, 2020, **53**, 2648–2658.

22 A. Omegna, J. A. van Bokhoven and R. Prins, *J. Phys. Chem. B*, Flexible Aluminum Coordination in Alumino−Silicates. Structure of Zeolite H−USY and Amorphous Silica−Alumina, 2003, **107**, 8854–8860.

23 M. Ravi, V. L. Sushkevich and J. A. van Bokhoven, *Nat. Mater.*, Towards a better understanding of Lewis acidic aluminium in zeolites, 2020, **19**, 1047–1056.

24 A. G. Stepanov, in *Zeolites and Zeolite-Like Materials*, eds. B. F. Sels and L. Kustov, Elsevier, Amsterdam, 2016, pp. 137–188.

25 K. Chen, S. Horstmeier, V. T. Nguyen, B. Wang, S. P. Crossley, T. Pham, Z. Gan, I. Hung and J. L. White, *J. Am. Chem. Soc.*, Structure and Catalytic Characterization of a Second Framework $Al^{(IV)}$ Site in Zeolite Catalysts Revealed by NMR at 35.2 T, 2020, **142**, 7514–7523.

26 C. Lei, A. Erlebach, F. Brivio, L. Grajciar, Z. Tosner, C. J. Heard and P. Nachtigall, *Chem. Sci.*, The need for operando modelling of 27Al NMR in zeolites: the effect of temperature, topology and water, 2023, **14**, 9101–9113.

27 G. Paul, C. Bisio, I. Braschi, M. Cossi, G. Gatti, E. Gianotti and L. Marchese, *Chem. Soc. Rev.*, Combined solid-state NMR, FT-IR and computational studies on layered and porous materials, 2018, **47**, 5684–5739.

28 H. Sammoury, J. Toufaily, K. Cherry, T. Hamieh, Y. Pouilloux and L. Pinard, *Microporous Mesoporous Mater.*, Desilication of *BEA zeolites using different alkaline media: Impact on catalytic cracking of n-hexane, 2018, **267**, 150–163.

29 M. K. Wardani, G. T. M. Kadja, A. T. N. Fajar, Subagjo, I. G. B. N. Makertihartha, M. L. Gunawan, V. Suendo and R. R. Mukti, *Rsc Adv.*, Highly crystalline mesoporous SSZ-13 zeolite obtained via controlled post-synthetic treatment, 2019, **9**, 77–86.

30 L. Qi, Y. Zhang, M. A. Conrad, C. K. Russell, J. Miller and A. T. Bell, *J. Am. Chem. Soc.*, Ethanol Conversion to Butadiene over Isolated Zinc and Yttrium Sites Grafted onto Dealuminated Beta Zeolite, 2020, **142**, 14674–14687.

31 P. Sazama, B. Wichterlova, J. Dedecek, Z. Tvaruzkova, Z. Musilova, L. Palumbo, S. Sklenak and O. Gonsiorova, *Microporous Mesoporous Mater.*, FTIR and 27Al MAS NMR analysis of the effect of framework Al- and Si-defects in micro- and micro-mesoporous H-ZSM-5 on conversion of methanol to hydrocarbons, 2011,

143, 87–96.

32 J. E. Olszowka, M. Lemishka, K. Mlekodaj, P. Kubat, D. Rutkowska-Żbik, J. Dedecek and E. Tabor, *J. Phys. Chem. C*, Determination of Zn Speciation, Siting, and Distribution in Ferrierite Using Luminescence and FTIR Spectroscopy, 2021, **125**, 9060–9073.

33 J. K. Plischke, A. J. Benesi and M. Albert Vannice, *J. Catal.*, A ^{13}C NMR study of ethylene adsorbed on reduced and oxygen-covered ag surfaces, 1992, **138**, 223–239.

34 M. Hunger, in *Handbook of Heterogeneous Catalysis*, eds. G. Ertl, F. Knözinger, F. Schüth and J. Weitkamp, 2008, pp. 1163–1178.

35 A. M. Zheng, S. B. Liu and F. Deng, *Chem. Rev.*, P-31 NMR Chemical Shifts of Phosphorus Probes as Reliable and Practical Acidity Scales for Solid and Liquid Catalysts, 2017, **117**, 12475–12531.

36 E. Grifoni, G. Piccini, J. A. Lercher, V.-A. Glezakou, R. Rousseau and M. Parrinello, *Nat. Commun.*, Confinement effects and acid strength in zeolites, 2021, **12**, 2630.

37 W. Yang, Z. Wang, J. Huang and Y. Jiang, *J. Phys. Chem. C*, Qualitative and Quantitative Analysis of Acid Properties for Solid Acids by Solid-State Nuclear Magnetic Resonance Spectroscopy, , DOI:10.1021/acs.jpcc.1c01887.

38 R. E. Dinnebier and S. J. L. Billinge, *Powder Diffraction: Theory and Practice*, Royal Society of Chemistry, 2008.

39 K. D. M. Harris and P. A. Williams, in *Structure from Diffraction Methods*, 2014, pp. 1–81.

40 J. A. Kaduk, S. J. L. Billinge, R. E. Dinnebier, N. Henderson, I. Madsen, R. Cerný, M. Leoni, L. Lutterotti, S. Thakral and D. Chateigner, *Nat. Rev. Methods Prim.*, Powder diffraction, 2021, **1**, 77.

41 M. T. Weller and N. A. Young, *Characterisation Methods in Inorganic Chemistry*, Oxford University Press, Oxford, 2017.

42 U. Holzwarth and N. Gibson, *Nat. Nanotechnol.*, The Scherrer equation versus the ‘Debye-Scherrer equation’, 2011, **6**, 534.

43 A. Vorokh, *Nanosyst. Physics, Chem. Math.*, Scherrer formula: estimation of error in determining small nanoparticle size, 2018, 364–369.

44 R. Comparelli, E. Fanizza, M. Striccoli and M. L. Curri, in *Synthesis and Characterization*, eds. A. Dibenedetto and M. Aresta, De Gruyter, pp. 157–198.

45 W. Wan, J. Su, X. D. Zou and T. Willhammar, *Inorg. Chem. Front.*, Transmission electron microscopy as an important tool for characterization of zeolite structures, 2018, **5**, 2836–2855.

46 W. Kühlbrandt, *Science*, The Resolution Revolution, 2014, **343**, 1443–1444.

47 D. Lei, A. E. Marras, J. Liu, C.-M. Huang, L. Zhou, C. E. Castro, H.-J. Su and G. Ren, *Nat. Commun.*, Three-dimensional structural dynamics of DNA origami Bennett linkages using individual-particle electron tomography, 2018, **9**, 592.

48 A. Yoshida, Y. Kaburagi and Y. Hishiyama, in *Materials Science and Engineering of Carbon*, eds. M. Inagaki and F. Kang, Butterworth-Heinemann, Oxford, 2016, pp. 71–93.

49 P. J. D. Whiteside, J. A. Chininis and H. K. Hunt, *Coatings*, 2016, 6, 35.

50 A. Jentys and J. A. Lercher, in *Introduction to Zeolite Science and Practice*, eds. H. van Bekkum, E. M. Flanigen, P. A. Jacobs and J. Jansen, Elsevier, Amsterdam, 2nd edn., 2001, vol. 137, pp. 345–386.

51 L.-H. Chen, M.-H. Sun, Z. Wang, W. Yang, Z. Xie and B.-L. Su, *Chem. Rev.*, Hierarchically Structured Zeolites: From Design to Application, 2020, **120**, 11194–11294.

52 Z.-S. Duma, T. Sihvonen, J. Havukainen, V. Reinikainen and S.-P. Reinikainen, *Micron*, Optimizing energy dispersive X-Ray Spectroscopy (EDS) image fusion to Scanning Electron Microscopy (SEM) images, 2022, **163**, 103361.

53 D. E. Newbury and N. W. M. Ritchie, *J. Mater. Sci.*, Performing elemental microanalysis with high accuracy and high precision by scanning electron microscopy/silicon drift detector energy-dispersive X-ray spectrometry (SEM/SDD-EDS), 2015, **50**, 493–518.

54 T. Arai, in *Handbook of Practical X-Ray Fluorescence Analysis*, eds. B. Beckhoff, B. Kanngiesser, N. Langhoff, R. Wedell and H. Wolff, Berlin, Heidelberg, 2006, pp. 1–26.

55 J. A. van Bokhoven, A. M. J. van der Eerden and D. C. Koningsberger, *J. Am. Chem. Soc.*, Three-Coordinate Aluminum in Zeolites Observed with In situ X-ray Absorption Near-Edge Spectroscopy at the Al K-Edge: Flexibility of Aluminum Coordinations in Zeolites, 2003, **125**, 7435–7442.

56 S. Bordiga, E. Groppo, G. Agostini, J. A. van Bokhoven and C. Lamberti, *Chem. Rev.*, Reactivity of Surface Species in Heterogeneous Catalysts Probed by In Situ X-ray Absorption Techniques, 2013, **113**, 1736–1850.

57 C. Prestipino, G. Berlier, F. X. Llabrés i Xamena, G. Spoto, S. Bordiga, A. Zecchina, G. Turnes Palomino, T. Yamamoto and C. Lamberti, *Chem. Phys. Lett.*, An in situ temperature dependent IR, EPR and high resolution XANES study on the NO/Cu+–ZSM-5 interaction, 2002, **363**, 389–396.

58 I. E. Wachs, *Catal. Today*, Recent conceptual advances in the catalysis science of mixed metal oxide catalytic materials, 2005, **100**, 79–94.

59 K. Nakamura, K. Okumura, E. Tsuji, S. Suganuma and N. Katada, *ChemCatChem*, Reactivity of Methane and Benzene over Metal/MFI Zeolite Analyzed with Temperature-Programmed Reaction Technique, 2020, **12**, 2333–2340.

60 V. Marchuk, X. Huang, J.-D. Grunwaldt and D. E. Doronkin, *Catal. Sci. Technol.*, Structure sensitivity of alumina- and zeolite-supported platinum ammonia slip catalysts, 2023, **13**, 2946–2965.

61 A. A. Gabrienko, S. S. Arzumanov, A. V Toktarev, I. G. Danilova, I. P. Prosvirin, V. V Kriventsov, V. I. Zaikovskii, D. Freude and A. G. Stepanov, *Acs Catal.*, Different Efficiency of Zn^{2+} and ZnO Species for Methane Activation on Zn-Modified Zeolite, 2017, **7**, 1818–1830.

62 G. E. Cutsail, M. O. Ross, A. C. Rosenzweig and S. DeBeer, *Chem. Sci.*, Towards a unified understanding of the copper sites in particulate methane monooxygenase: an X-ray absorption spectroscopic investigation, 2021, **12**, 6194–6209.

63 E. Coutino-Gonzalez, W. Baekelant, D. Grandjean, M. B. J. Roeffaers, E. Fron, M. S. Aghakhani, N. Bovet, M. Van der Auweraer, P. Lievens, T. Vosch, B. Sels and J. Hofkens, *J. Mater. Chem. C*, Thermally activated LTA(Li)-Ag zeolites with water-responsive photoluminescence properties, 2015, **3**, 11857–11867.

64 J. Nölte, *ICP Emission Spectrometry: A Practical Guide*, Wiley, Hoboken, New Jersey, 2021.

65 A. Palčić and V. Valtchev, *Appl. Catal. A Gen.*, Analysis and control of acid sites in zeolites, 2020, **606**, 117795.

66 V. Zholobenko, C. Freitas, M. Jendrlin, P. Bazin, A. Travert and F. Thibault-

Starzyk, *J. Catal.*, Probing the acid sites of zeolites with pyridine: Quantitative AGIR measurements of the molar absorption coefficients, 2020, **385**, 52–60.

67 L. Treps, C. Demaret, D. Wisser, B. Harbuzaru, A. Méthivier, E. Guillon, D. V. Benedis, A. Gomez, T. de Bruin, M. Rivallan, L. Catita, A. Lesage and C. Chizallet, *J. Phys. Chem. C*, Spectroscopic Expression of the External Surface Sites of H-ZSM-5, 2021, **125**, 2163–2181.

68 A. S. Medin, V. Y. Borovkov, V. B. Kazansky, A. G. Pelmentschikov and G. M. Zhidomirov, *Zeolites*, On the unusual mechanism of Lewis acidity manifestation in HZSM-5 zeolites, 1990, **10**, 668–673.

69 A. G. Pelmenschikov, R. A. van Santen, J. Janchen and E. Meijer, *J. Phys. Chem.*, Acetonitrile-d3 as a probe of Lewis and Broensted acidity of zeolites, 1993, **97**, 11071–11074.

70 J. Zou, C. Fan, Y. Jiang, X. Liu, W. Zhou, H. Xu and L. Huang, *Microporous Mesoporous Mater.*, A preliminary study on assessing the Brunauer-Emmett-Teller analysis for disordered carbonaceous materials, 2021, **327**, 111411.

71 J. W. M. Osterrieth, J. Rampersad, D. Madden, N. Rampal, L. Skoric, B. Connolly, M. D. Allendorf, V. Stavila, J. L. Snider, R. Ameloot, J. Marreiros, C. Ania, D. Azevedo, E. Vilarrasa-Garcia, B. F. Santos, X.-H. Bu, Z. Chang, H. Bunzen, N. R. Champness, S. L. Griffin, B. Chen, R.-B. Lin, B. Coasne, S. Cohen, J. C. Moreton, Y. J. Colon, L. Chen, R. Clowes, F.-X. Coudert, Y. Cui, B. Hou, D. M. D'Alessandro, P. W. Doheny, M. Dincă, C. Sun, C. Doonan, M. T. Huxley, J. D. Evans, P. Falcaro, R. Ricco, O. Farha, K. B. Idrees, T. Islamoglu, P. Feng, H. Yang, R. S. Forgan, D. Bara, S. Furukawa, E. Sanchez, J. Gascon, S. Telalović, S. K. Ghosh, S. Mukherjee, M. R. Hill, M. M. Sadiq, P. Horcajada, P. Salcedo-Abraira, K. Kaneko, R. Kukobat, J. Kenvin, S. Keskin, S. Kitagawa, K. Otake, R. P. Lively, S. J. A. DeWitt, P. Llewellyn, B. V Lotsch, S. T. Emmerling, A. M. Pütz, C. Marti-Gastaldo, N. M. Padial, J. García-Martinez, N. Linares, D. Maspoch, J. A. Suarez del Pino, P. Moghadam, R. Oktavian, R. E. Morris, P. S. Wheatley, J. Navarro, C. Petit, D. Danaci, M. J. Rosseinsky, A. P. Katsoulidis, M. Schröder, X. Han, S. Yang, C. Serre, G. Mouchaham, D. S. Sholl, R. Thyagarajan, D. Siderius, R. Q. Snurr, R. B. Goncalves, S. Telfer, S. J. Lee, V. P. Ting, J. L. Rowlandson, T. Uemura, T. Iiyuka, M. A. van der Veen, D. Rega, V. Van Speybroeck, S. M. J. Rogge, A. Lamaire, K. S. Walton, L. W. Bingel, S. Wuttke, J. Andreo, O. Yaghi, B. Zhang, C. T. Yavuz, T. S. Nguyen, F. Zamora, C. Montoro, H. Zhou, A. Kirchon and D. Fairen-Jimenez, *Adv. Mater.*, How Reproducible are Surface Areas Calculated from the BET Equation?, 2022, **34**, 2201502.

72 F. Ambroz, T. J. Macdonald, V. Martis and I. P. Parkin, *Small Methods*, Evaluation of the BET Theory for the Characterization of Meso and Microporous MOFs, 2018, **2**, 1800173.

73 M. Lorenz, C. Paganini, G. Storti and M. Morbidelli, *Materials (Basel).*, Macroporous Polymer–Protein Hybrid Materials for Antibody Purification by Combination of Reactive Gelation and Click-Chemistry, 2019, **12**, 1580.

74 L. M. Blumberg, in *Gas Chromatography*, ed. C. Poole, Elsevier, Amsterdam, 2012, pp. 19–78.

75 W. Engewald, K. Dettmer-Wilde and H. Rotzsche, eds. K. Dettmer-Wilde and W. Engewald, Springer Berlin Heidelberg, Berlin, Heidelberg, 2014, pp. 59–116.

76 J. H. Gross, *Mass Spectrometry: A Textbook*, Springer Berlin Heidelberg, Berlin, Heidelberg, 2nd edn., 2011.

77 J. Texter, R. Kellerman and T. Gonsiorowski, *J. Phys. Chem.*, Formation of charged silver clusters and their reversible silver ion desorption in zeolite A, 1986, **90**, 2118–2124.

78 T. Sun and K. Seff, *Chem. Rev.*, Silver Clusters and Chemistry in Zeolites, 1994,

94, 857–870.

79 T. Baba, N. Komatsu, H. Sawada, Y. Yamaguchi, T. Takahashi, H. Sugisawa and Y. Ono, *Langmuir*, H-1 magic angle spinning NMR evidence for dissociative adsorption of hydrogen on Ag^{+}-exchanged A- and Y-zeolites, 1999, **15**, 7894–7896.

80 R. Seifert, R. Rytz and G. Calzaferri, *J. Phys. Chem. A*, Colors of Ag+-Exchanged Zeolite A, 2000, **104**, 7473–7483.

81 T. Baba, H. Sawada, T. Takahashi and M. Abe, *Appl. Catal. a-General*, Chemisorption study of hydrogen and methane by H-1 MAS NMR and conversion of methane in the presence of ethylene on Ag-Y zeolite, 2002, **231**, 55–63.

82 O. Fenwick, E. Coutino-Gonzalez, D. Grandjean, W. Baekelant, F. Richard, S. Bonacchi, D. De Vos, P. Lievens, M. Roeffaers, J. Hofkens and P. Samori, *Nat. Mater.*, Tuning the energetics and tailoring the optical properties of silver clusters confined in zeolites, 2016, **15**, 1017–1022.

83 L. A. Ageev and V. K. Miloslavsky, *Opt. Eng.*, Photoinduced effects in light-sensitive films, 1995, **34**, 960–972.

84 A. Nahal, V. K. Miloslavsky and L. A. Ageev, *Opt. Commun.*, Influence of photoinduced gyrotropy on the formation of spontaneous periodic structures in light-sensitive AgCl–Ag thin films, 1998, **154**, 234–242.

85 A. Krol-Gracz, E. Michalak, P. Nowak and A. Dyonizy, Photo-induced chemical reduction of silver bromide to silver nanoparticles, 2011, **9**, 982–989.

86 C. A. Schneider, W. S. Rasband and K. W. Eliceiri, *Nat. Methods 2012 97*, NIH Image to ImageJ: 25 years of image analysis, 2012, **9**, 671–675.

87 P. Zimmermann, S. Peredkov, P. M. Abdala, S. DeBeer, M. Tromp, C. R. Müller and J. A. Bokhoven, *Coord. Chem. Rev.*, Modern X-ray spectroscopy: XAS and XES in the laboratory, 2020, **423**, 213466.

88 W. M. Holden, O. R. Hoidn, A. S. Ditter, G. T. Seidler, J. Kas, J. L. Stein, B. M. Cossairt, S. A. Kozimor, J. Guo, Y. Ye, M. A. Marcus and S. Fakra, *Rev. Sci. Instrum.*, A compact dispersive refocusing Rowland circle X-ray emission spectrometer for laboratory, synchrotron, and XFEL applications., 2017, **88**, 73904.

89 B. Ravel and M. Newville, *J. Synchrotron Radiat.*, ATHENA, ARTEMIS, HEPHAESTUS: data analysis for X-ray absorption spectroscopy using IFEFFIT, 2005, **12**, 537–541.

Chapter Four – Project Aims

4.1 Project Aims

Before embarking upon this project, the literature surrounding the use of silver-exchanged zeolites for methane upgrading was found to be sparse. More often than not, co-processing of methane with another feedstock was utilised for silver-exchanged zeolites, including co-feeds such as ethylene,[1] propylene[2] and ethanol.[3] Therefore, this project set out with goals to improve the understanding around the ability of silver to activate methane in silver-mediated methane upgrading reactions over silver-exchanged zeolites, further the understanding around the stability of silver under upgrading reaction conditions, determine the effect of the framework itself on methane upgrading reactions, and to determine any enhancement effects observed from methane co-processing.

The first goals set out to improve the understanding of silver-mediated methane upgrading using silver-exchanged zeolites, however, this cannot be separated from the need to understand both the effect of the zeolite framework on both the reaction and on the stability of silver during upgrading reactions. Gaining insight into how the changing framework properties such as pore size, pore shape and framework dimensionality, which lead to the observation of size exclusion effects all directly affect all upgrading reactions, with regards to diffusion through the framework, confinement effects from the framework on products and subsequent product selectivity and overall catalyst lifetime. In addition, investigating changed levels of silver loading, to determine whether increased loading leads to proportionally increased activity or improved catalyst lifetime was to be decided.

An extension of understanding the role of the framework is understanding the effect of framework acidity and the type of acid sites present, which in themselves can determine changes in reaction pathway, catalyst activity and product selectivity. This can be achieved through the use of Lewis acidic zincosilicates in place of identical topology Brønsted acidic zeolites. In addition, changed co-counterions can provide a large enough change in framework acidity that could prove beneficial to both the product distribution and catalyst lifetime, making the sodium-exchanged form preferable to the protic form of zeolites.[4]

Outlined in Section 1.4 and Section 2.3 are some valuable and some limiting properties towards the usefulness of silver as a catalyst, and through the use of multiple factors outlined here, such as changing framework acidity, diffusion and co-counterions, it was

envisaged that the lifetime of silver-exchanged materials could be extended over those reported in literature, where complete catalyst deactivation occurs through carbonaceous deposition[5] or no methane conversion was reported at and beyond 5 hours on-stream.[1]

One aspect that is crucial to understanding the effect of changes on a silver-exchanged catalyst during upgrading reactions will be to characterise the as prepared material, as well as the spent material. This would be carried out to gain valuable insight into which aspects positively or negatively affect catalyst lifetime and activity, product selectivity and distribution, and to determine any chemical changes, such as carbonaceous deposition, framework damage or silver sintering. As discussed in Section 2.3, silver redox chemistry can lead to the formation of charged silver clusters, with reduction leading ultimately to silver metallic species. The growth of these species arises from silver sintering and migration to the surface, leading to premature deactivation of the catalyst. Understanding the deactivation conditions of silver allows for the designing of catalysts or reaction conditions to negate or reduce the unwanted effects that shorten catalyst lifetimes.

From this, we aim to design reactions which include oxygen as part of the feed. This approach has been used in literature for the partial oxidation of methane to produce carbon monoxide, rather than direct conversion of methane to higher hydrocarbons.[6] However, the inclusion of oxygen should theoretically improve both catalyst lifetime and catalyst activity, as it negates the reductive conditions found during upgrading reactions that lead to framework damaging effects, silver sintering and premature deactivation. This would also be suited to catalyst regeneration as a post-reaction treatment.

The final aim would be achieved through isolating the individual upgrading reactions prior to the running of co-processing, highlighting whether methane upgrading is enhanced through the use of change conditions. Through isolating each of the reaction conditions, we can observe any distinguishable differences in product selectivity through a changed reaction pathway facilitated by co-processing.

4.2 Chapter Four Bibliography

1 K. Inazu, T. Koyama, A. Miyaji and T. Baba, *J. Japan Pet. Inst.*, 2008, **51**, 205–216.

2 T. Baba and H. Sawada, *Phys. Chem. Chem. Phys.*, 2002, **4**, 3919–3923.

3 P. He, A. Wang, S. Meng, G. M. Bernard, L. Liu, V. K. Michaelis and H. Song, *Catal. Today*, 2019, **323**, 94–104.

4 G. De Cremer, E. Coutino-Gonzalez, M. B. J. Roeffaers, B. Moens, J. Ollevier, M. Van der Auweraer, R. Schoonheydt, P. A. Jacobs, F. C. De Schryver, J. Hofkens, D. E. De Vos, B. F. Sels and T. Vosch, *J. Am. Chem. Soc.*, 2009, **131**, 3049–3056.

5 A. G. Wang, P. He, M. Yung, H. B. Zeng, H. Qian and H. Song, *Appl. Catal. B-Environmental*, 2016, **198**, 480–492.

6 Y. Kuroda, T. Mori, H. Sugiyama, Y. Uozumi, K. Ikeda, A. Itadani and M. Nagao, *J. Colloid Interface Sci.*, 2009, **333**, 294–299.

Chapter Five – Hydrothermal Synthesis of Zeolites and Silver Ion-exchange

Introducing new counterions to zeolite frameworks using aqueous media is a common technique used for zeolite modification.[1–3] The experimental procedures used in this project are covered in the aqueous ion-exchange of materials, section 3.2.4. Zeolite properties can be tuned through the use of changed extra-framework cations. In this project, metals were chosen to enhance catalytic activity, with silver chosen due to the highly dispersed cations displaying a propensity towards methane activation at raised temperatures, facilitating direct upgrading through hydrocarbon co-processing reactions.[4–8] To both emulate and improve on prior art for the reported methane conversion observed during methane co-processing reactions is an overarching goal for the project. Additionally, achieving comparable levels for methane conversion using milder conditions would be advantageous, especially with respect to energy consumption.

5.1 Silver Ion-exchange of Zeolites

5.1.1 Aqueous Ion-exchange with Silver

Establishing a baseline of how readily exchangeable zeolites were with silver cations required investigation of the silver source, ion-exchange method, silver solution molarity, exchange temperature and exchange duration. Dwyer assessed the affinity of ZSM-5 towards a series of cations introduced using aqueous ion-exchange, reporting the series of least to most favourable as below.[9]

$$H^+ > NH_4^+ > Ag^+ > Na^+$$

Initial aqueous ion-exchanges to produce silver-exchanged zeolites were carried out using NH_4/ZSM-5(15), NH_4/ZSM-5(12.5) and Na/MOR(6.5). The nomenclature used represents the counterbalancing ion, the framework and its silicon-to-aluminium ratio. For example, NH_4/ZSM-5(15) is an ammonium-exchanged form of ZSM-5, an MFI topology zeolite, with a silicon-to-aluminium ratio of 15. All materials will be referred to in this style. The results for aqueous ion-exchange of NH_4/ZSM-5(15) using varied molarity silver nitrate solutions for 16 hours are shown in Table 5.1. Alongside this, ion-exchanges using 0.1M silver nitrate solution were carried out three and five times, each ion-exchange was 16 hours, to highlight the effect of repeated exchange. The excess moles of silver cations introduced during aqueous ion-exchange compared against the

estimated moles of exchangeable framework counterbalancing sites, were calculated for each ion-exchange entry in Table 5.1. This helped us determine the exchange with the highest molar efficiency.

Table 5.1: Results for aqueous ion-exchange of NH_4/ZSM-5(15) with varied silver nitrate solution molarities at 20 °C for 16 hours, alongside repeated ion-exchange using 0.1M silver nitrate solution.

Sample ID	$AgNO_{3\,(aq)}$ Molarity (M)	No. of Exchanges	Excess moles of Ag used[a]	Final Ag:Al ratio
RK-1-17D	0.02	1	0.36	0.12
RK-1-17C	0.05	1	0.90	0.19
RK-1-1	0.1	1	1.79	0.30
RK-1-2		3	5.37	0.43
RK-1-3		5	8.95	0.43
RK-1-17B	0.2	1	3.59	0.28
RK-1-17A	0.5	1	8.98	0.35
RK-1-24B	1.0	1	17.96	0.44
RK-1-24A	2.0	1	35.92	0.44

[a] the excess moles of silver used in the ion-exchange compared with estimated moles of exchangeable framework counterbalancing sites.

From Table 5.1 entries 1 thru 3, a trend was observed showing that the resultant silver-exchange level was directly proportional to silver reagent concentration, although this effect soon reached a plateau. This shows that the exchange isotherm cannot be forced solely by concentration when using a single ion-exchange, so different reaction conditions are required in order to reach complete exchange of silver.

However, NH_4/ZSM-5(15) was found to demonstrate poor exchangeability, not only in this work but in that of others in the research group, whereas other ZSM-5 topology materials, albeit with a slightly different Si:Al ratio, materials were found to display ratios approaching 1:1 following repeated ion exchange. Therefore, NH_4/ZSM-5(15) was dropped from further study. Additionally, prior art widely reported that silver auto reduction can occur when silver-exchanged zeolites are exposed to raised temperatures, so materials were not calcined post ion-exchange with silver during this

project. This meant we could avoid undesirable framework damage occurring at this stage from silver sintering, framework oxidation and subsequent silver clustering.[10–15]

Further ion-exchanges with silver were carried out using NH_4/ZSM-5(12.5) and Na/MOR(6.5) using different exchange conditions. Aqueous ion-exchange of NH_4/ZSM-5(12.5) with 0.1M silver nitration solution was carried out at four temperatures. Exchange at 0 °C used a duration of 4 hours, as it was found that extending the exchange duration produced negligible changes and the required equipment to exchange overnight was not available. Exchanges at 20 °C, 50 °C and 80 °C were conducted over 16 hours. The results are shown in Table 5.2. In each exchange, a 1.5x molar excess of silver to exchangeable framework site was used.

Table 5.2: Results for aqueous ion-exchange of NH_4/ZSM-5(12.5) with 0.1M silver nitrate solution at 0 °C, 20 °C, 50 °C and 80 °C, for which higher exchange was observed with reduced temperature. Errors calculated from averaged results acquired over three acquisitions using Panalytical Epsilon 1 benchtop ED-XRF.

Sample ID	Temp (°C)	Al (wt%)	Si (wt%)	Ag (wt%)	Ag:Al	Si:Al
RK-1-30	0	3.72±0.12	38.75±1.52	6.16±0.04	0.41±0.02	10.02
RK-1-13	20	3.73±0.07	38.57±0.67	5.89±0.05	0.40±0.01	9.94
RK-1-36	50	3.93±0.10	41.58±1.17	5.95±0.05	0.38±0.01	10.17
RK-1-19	80	4.38±0.06	47.86±0.09	5.92±0.01	0.34±0.01	10.51

It was observed that the final exchange level increased with decreasing temperature. To make sense of the relationship observed here, we have to hypothesize that silver nitrate solubility in water would be decreased at lower temperatures. At lower temperatures, an larger pH gradient between solution and acidic zeolite micropores would facilitate the migration and subsequent exchange of silver and ammonium cations, produce a silver-exchanged ZSM-5 with a higher loading level whilst ammonium nitrate would be the byproduct in solution.

Na/MOR(6.5) underwent a series of aqueous ion-exchanges using silver nitrate solution of varying molarity, each exchange carried out over 16 hours at 20 °C, with the results shown in Table 5.3. Results showed that for silver nitrate concentrations of 0.1 M and below, a directly proportional increase in silver-exchange level was observed with increased silver nitrate solution molarity. For concentrations of silver nitrate solutions

beyond 0.25 M, a diminishing effect for silver loading was observed with increased silver ion excess in exchange, reaching a plateau beyond 0.5 M, as shown in Figure 5.1.

Table 5.3: Results for aqueous ion-exchange of Na/MOR(6.5) with varying silver nitrate solution molarity, carried out over 16 hours at 20 °C. Errors calculated from averaged results acquired over three acquisitions using Panalytical Epsilon 1 benchtop ED-XRF.

Sample ID	$AgNO_{3\,(aq)}$ Molarity (M)	Excess moles of Ag[a]	Al (wt%)	Si (wt%)	Ag (wt%)	Ag:Al	Si:Al
RK-1-90B	0.005	0.05	5.52 ±0.29	34.51 ±2.20	1.16 ±0.01	0.05±0.00	6.01
RK-1-90A	0.01	0.09	5.53 ±0.22	34.81 ±1.93	1.96 ±0.01	0.09±0.00	6.05
RK-1-50B	0.02	0.18	5.99 ±0.12	34.93 ±0.82	3.76 ±0.02	0.16±0.00	5.60
RK-1-50A	0.05	0.45	5.54 ±0.08	31.95 ±0.502	8.45 ±0.04	0.38±0.01	5.54
RK-1-27	0.10	0.91	5.60 ±0.72	30.54 ±0.44	14.08 ±0.09	0.57±0.01	5.24
RK-1-42	0.25	2.27	5.55 ±0.62	29.71 ±0.30	16.22 ±0.14	0.73±0.09	5.18
RK-1-57A	0.50	4.54	4.98 ±0.06	28.80 ±0.27	16.69 ±0.04	0.84±0.01	5.56
RK-1-57B	1.0	9.08	5.04 ±0.03	29.12 ±0.20	17.07 ±0.12	0.85±0.01	5.55

[a] the excess moles of silver used in the ion-exchange compared with estimated moles of exchangeable framework counterbalancing sites.

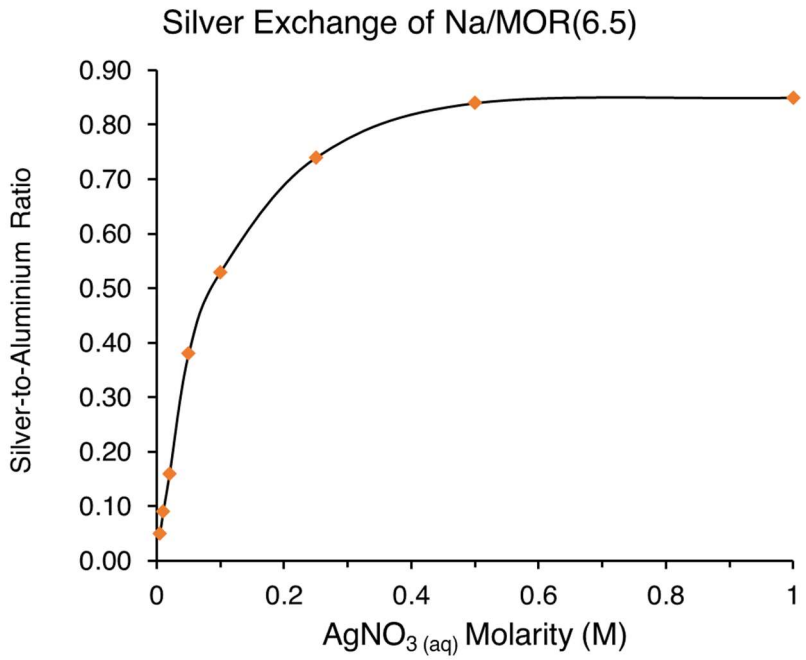

Figure 5.1: Graph of the silver-to aluminium ratio following ion-exchange of Na/MOR(6.5) with varying concentration silver nitrate solutions at 20 °C for 16 hours.

Due to the high level of exchange observed following aqueous ion-exchange of Na/MOR(6.5), an experiment was designed using three one-hour ion-exchanges with 0.25 M silver nitrate solution to achieve complete exchange, as shown in Figure 5.2. These exchange conditions were sufficient in achieving complete exchange of Na/MOR(6.5), giving a 1:1 ratio of silver-to-aluminium.

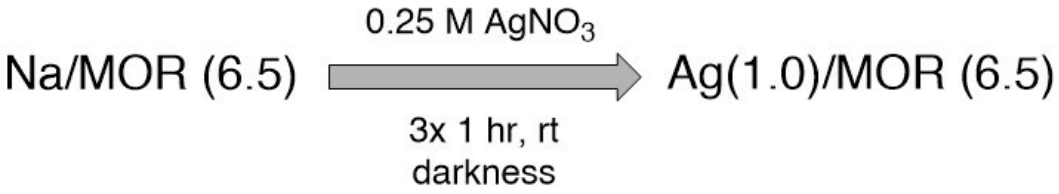

Figure 5.2: Graphic showing an aqueous ion-exchange of Na/MOR (6.5) using three one-hour ion-exchanges with 0.25 M silver nitrate solution leading to complete exchange with a silver-to-aluminium ratio of 1:1.

The aqueous ion-exchange outlined in Figure 5.2 was repeated using 0.25M silver sulfate solution. This time, the resultant silver-exchanged mordenite material was found to be significantly over-exchanged, Ag(5.57)/MOR(6.5), 57.3 wt%. There were on profound effects of the silver over-exchange on material characterisation, however, both SEM-EDS and TEM revealed profound silver clustering had occurred.

5.1.2 Solid Mixing for Ion-exchange with Silver

Many silver compounds are insoluble in aqueous media. Aqueous ion-exchange allows for the simple separation of zeolite and aqueous media through centrifugation, however, with silver nitrate solutions it was found that multiple ion-exchanges were required to reach complete exchange and each exchange used excess moles of silver. Experiments were devised using silver chloride and silver carbonate for ion-exchange through solid mixing to investigate if this method was more atom efficient than aqueous ion-exchange.

H/ZSM-5(13.5) (1 g) and silver chloride (200 mg, 1.4 mmol) were loaded into a black 50 mL centrifuge tube, to protect the mixture from light and mixed on a tube roller at room temperature for 16 hours. The solids were suspended in boiling DI water (40 mL), before being applied to a filter and washed using Büchner filtration. Approx. 400 ml boiling DI water was used to dissolve the remaining silver chloride. Zeolite was initially pale yellow on the filter, returning to a white powder once the residual silver chloride was removed. Material was dried overnight in the oven at 80 °C. Resultant material was determined by ED-XRF to be Ag(0.03),H/ZSM-5(13.5), 0.4 wt% Ag. This showed there was very little exchange between the zeolite and silver reagent during the solid mixing phase using silver chloride. A 1.3x molar excess of silver to exchangeable framework site was used.

H/ZSM-5(13.5) (1 g) and silver carbonate (384 mg, 1.4 mmol) were loaded into a black 50 mL centrifuge tube, to protect the mixture from light and mixed on a tube roller at room temperature for 16 hours. The solids were suspended in boiling DI water (40 mL), before being applied to a filter and washed using Büchner filtration. Approx. 400 ml boiling DI water was used to dissolve the remaining silver carbonate. Zeolite was grey with no colour change observed during the initial wash. A second wash was conducted returning the material to a white powder. Material was dried overnight in the oven at 80 °C. Resultant material was determined by ED-XRF to be Ag(0.74),H/ZSM-5(13.5), 9.4 wt% Ag.

5.1.3 Analysis of Silver-exchanged Materials

Several different characterisation techniques were used on freshly prepared silver-exchanged zeolites. As alluded to earlier, materials with a high silver-loading level were reported to exhibit peaks in their pXRD patterns indicating the presence of bulk silver.[17] De Cremer *et al.* reported that silver-exchanged zeolites displayed little to no change in their pXRD pattern irrespective of silver-exchange level, and only contained silver clusters in their pXRD if a sufficient amount of larger silver clusters were present.[18]

Whilst we have acquired STEM-BF images for silver-exchanged zeolites of varying topology and silver loading level, we conclude that for even the most over-exchanged materials, the silver cluster dimensions must not be sufficiently large enough to be observed by pXRD.

TEM and Energy Dispersive X-Ray Spectroscopy-Transmission electron microscopy (EDS-TEM) were used to acquired STEM-BF images and EDS-TEM maps of our silver-exchanged materials, giving an insight into silver clustering. Silver clusters were observed for a wide range of framework topologies with varied silver-loading levels and with different secondary counterions, as shown in Figure 5.3. Regardless of silver loading level, topology or the secondary counterion, silver clusters were present in the STEM-BF images acquired for each of the silver-exchanged zeolites observed in this project.

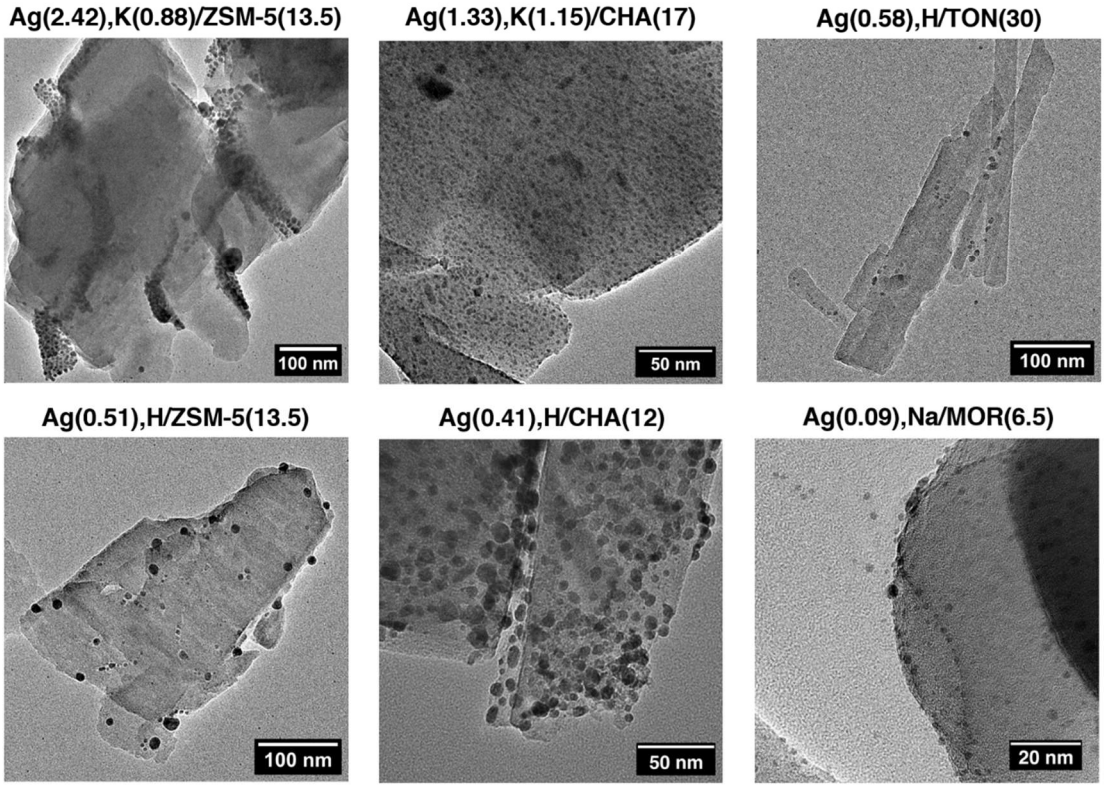

Figure 5.3: STEM-BF images acquired for various silver-exchanged materials that were produced using aqueous ion-exchange with silver nitrate solution during this project, with varied topology, secondary counterion and silver loading level.

In each case, silver clustering was evident for these materials following aqueous ion-exchange and drying of the materials at 80 °C, both conducted whilst protected from

light and handling of materials was kept to a minimum to avoid light exposure. Different solvents were explored for the dispersal of silver-exchanged materials onto TEM grids, with it determined that there was no appreciable difference to materials following the use of water, methanol and IPA.

EDS-TEM maps were acquired for Ag(2.42),K(0.88)/ZSM-5(13.5), shown in Figure 5.4. Silicon, aluminium and oxygen displayed good elemental distribution throughout the zeolite crystals. Both silver and potassium displayed a propensity to co-cluster around the edges of the crystal. No reports in prior art for the co-clustering of silver and potassium together in zeolites at present, although potassium clusters are known in both FAU and LTA topology zeolites.[19,20] Ge *et al.* reported how potassium atoms and potassium clusters were observed to become localised at tungsten grain boundaries, highlighting a strong trapping effect through electronic stabilisation.[21]

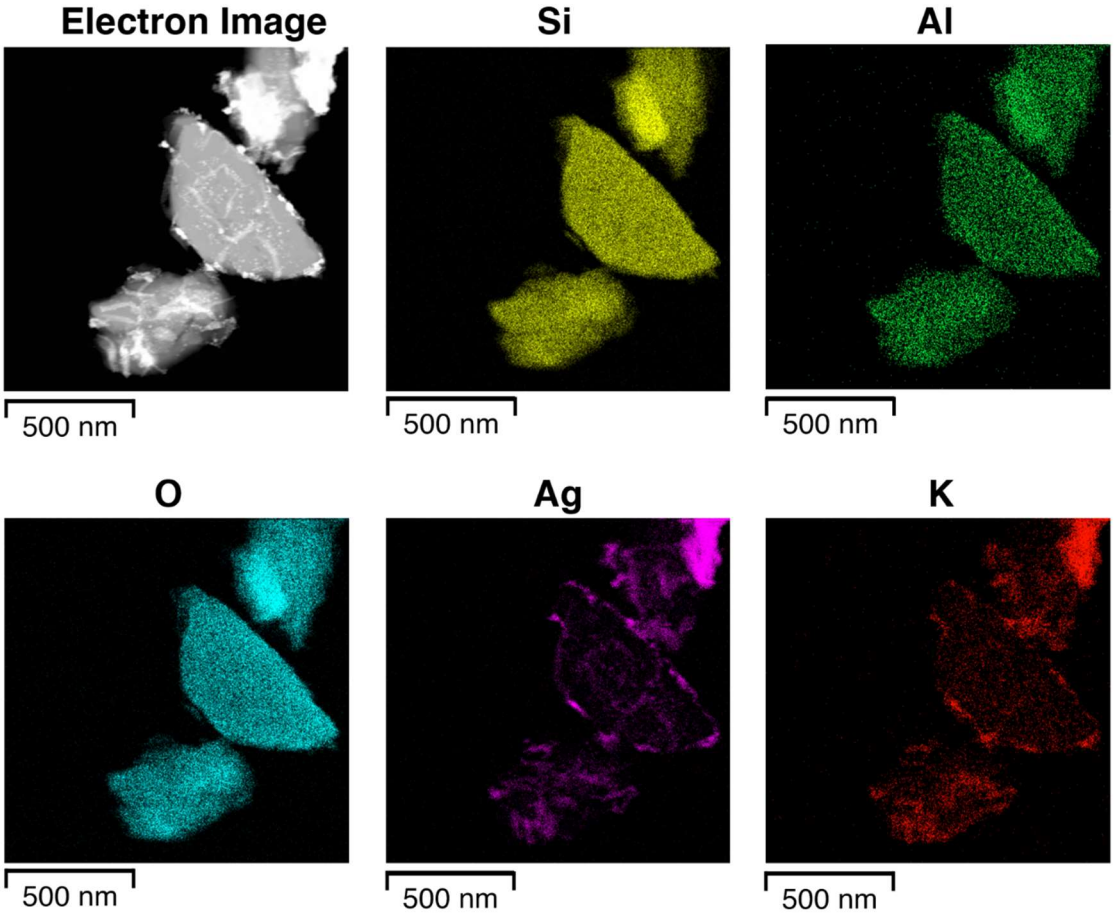

Figure 5.4: EDS-TEM maps acquired for Ag(2.42),K(0.88)/ZSM-5(13.5), showing good elemental distribution of silicon, aluminium and oxygen, but co-clustering for silver and potassium at the surfaces of the zeolite crystal.

Prior art reported Ag/ZSM-5(25) with 15wt% Ag, prepared from incipient wetness impregnation using silver nitrate solution, led to the acquired pXRD pattern containing reflections indicating silver clusters.[4] In comparison with over-exchanged

Ag(2.42),K(0.88)/ZSM-5(13.5) 14.6 wt%, there were no reflections for silver clusters in the acquired pXRD pattern. We therefore conclude that incipient wetness impregnation leads to the formation of larger silver clusters than aqueous ion-exchange, due to the absence of clusters in our material with similar Ag wt%. Ag(2.42),K(0.88)/ZSM-5(13.5) is an over-exchanged material, so EDS-TEM maps were acquired on silver-exchanged ZSM-5 with a lower silver loading and also the absence of potassium counterions.

EDS-TEM maps acquired for Ag(0.51),H/ZSM-5(13.5) are shown in Figure 5.5. For silicon, aluminium and oxygen, there was good elemental distribution throughout the zeolite crystal. However, it was again evident that silver clustering had occurred from the electron image, with silver unevenly distributed, with clusters localised towards the edges of the zeolite crystal in the EDS map.

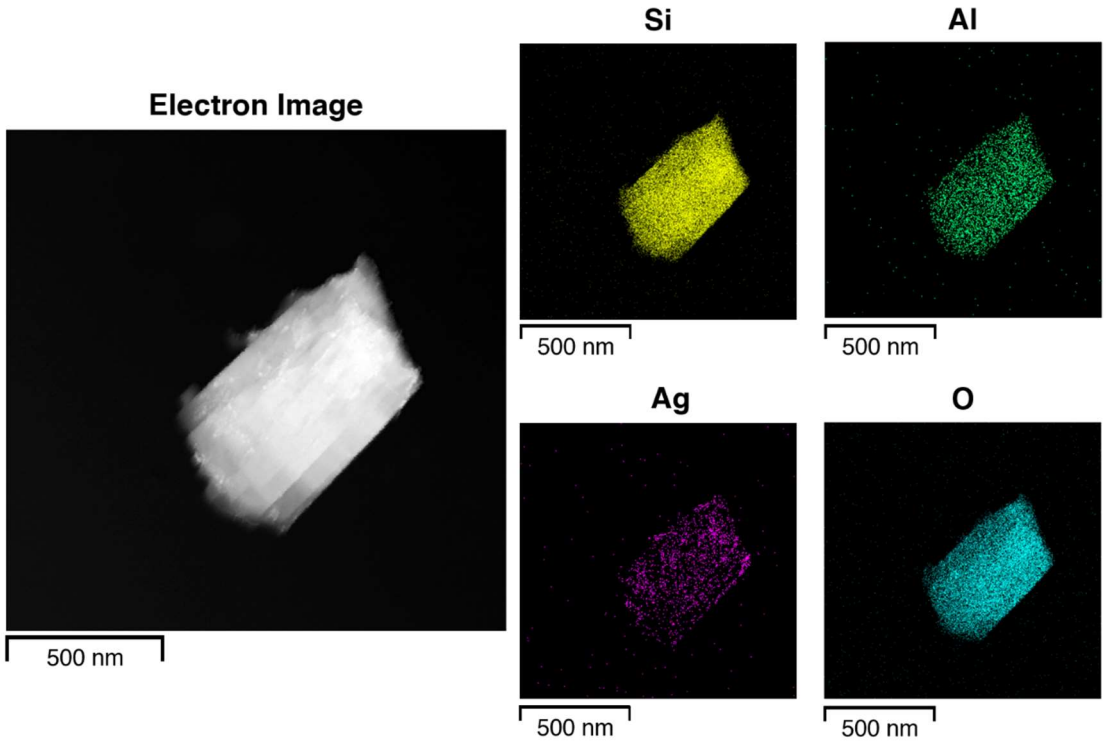

Figure 5.5: EDS-TEM maps acquired for Ag(0.51),H/ZSM-5(13.5), showing good elemental distribution of silicon, aluminium and oxygen, but clustering of silver in the electron image and at the surface of the zeolite crystal in the EDS map.

Through the acquired STEM-BF images of silver exchanged zeolites, we could measure the silver cluster size and determine the distribution of clusters in the material. A STEM-BF image acquired for Ag(0.44),K(0.23)/CHA(18) is shown in Figure 5.6, from which the size distribution of silver clusters was measured, with results included in Figure 5.7. The average silver cluster size was determined to be 7.1 nm (± 2.0 nm), calculated from a total of 197 particles measured.

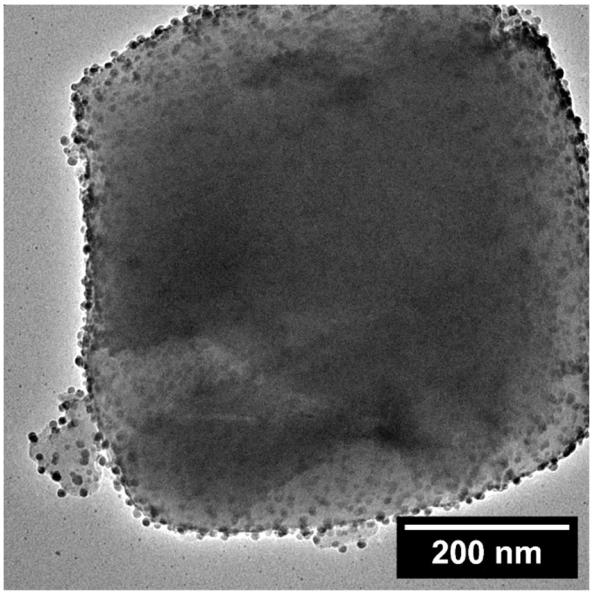

Figure 5.6: BF-STEM images of silver-exchanged chabazite, Ag(0.44),K(0.23)/CHA(18), showing the surface of the material covered by silver nanoparticles that have formed following aqueous ion-exchange with silver nitrate solution.

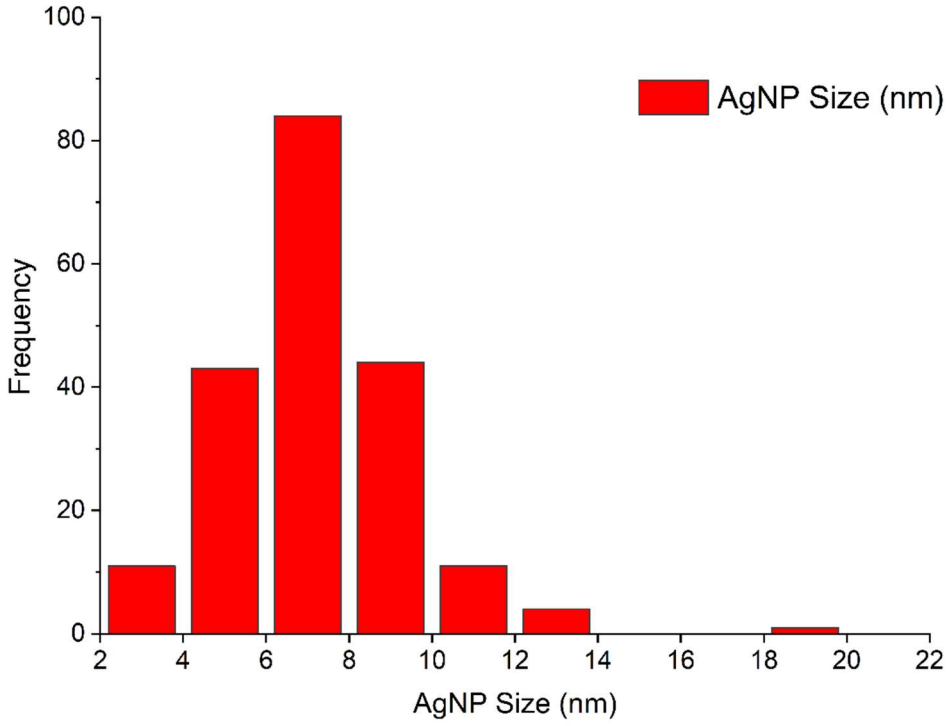

Figure 5.7: Graph showing the size distribution of silver nanoparticles on Ag(0.44),K(0.23)/CHA(18) that have formed following aqueous ion-exchange with silver nitrate solution.

EDS-TEM maps were acquired for Ag(0.44),K(0.23)/CHA(18), shown in Figure 5.8. Silicon, aluminium and oxygen show good elemental distribution throughout the zeolite crystal. However, both silver and potassium show a propensity for localisation of the elements. Whilst silver clustering was evident in the electron image, the EDS map for both silver and potassium displayed localisation around the edge and in the centre of the zeolite crystal. Co-clustering of potassium and silver was also evident for Ag(2.42),K(0.88)/ZSM-5(13.5), shown in Figure 5.4, although that material was over-exchanged.

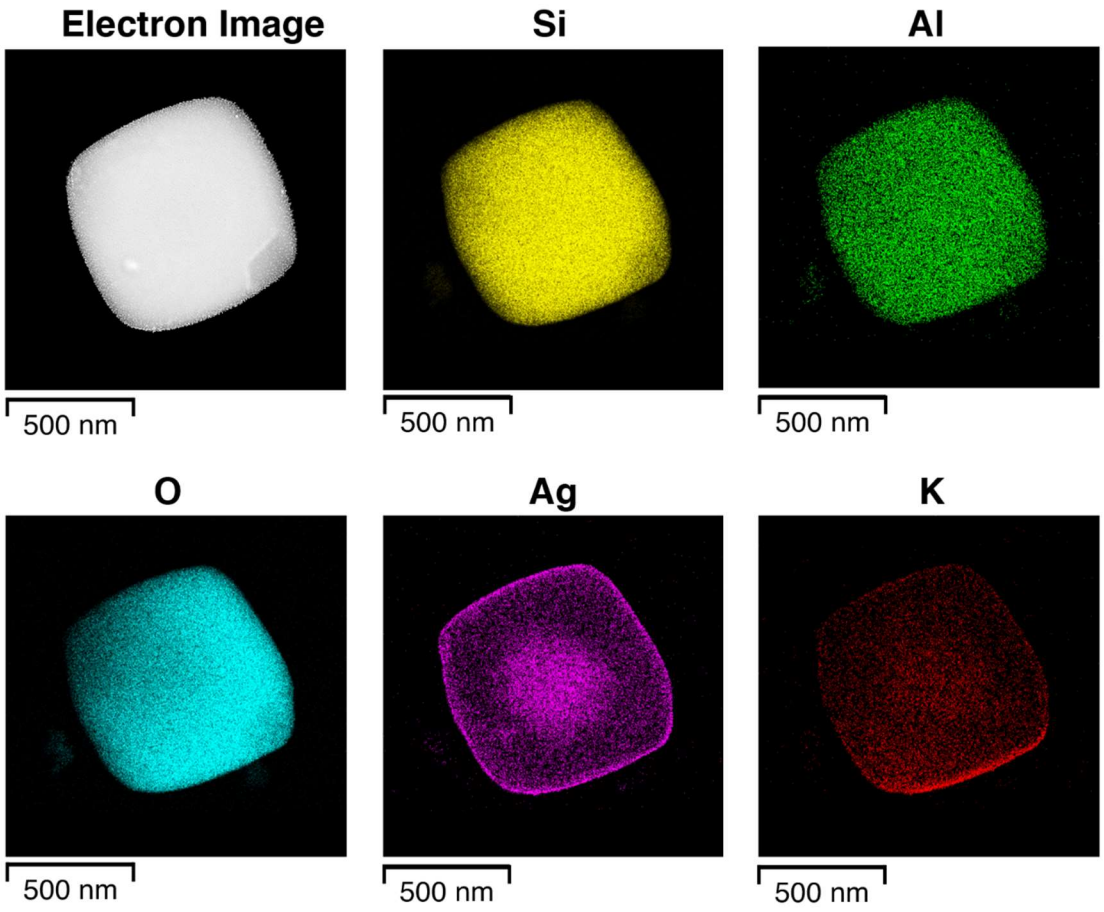

Figure 5.8: EDS-TEM maps acquired for Ag(0.44),K(0.23)/CHA(18), showing good elemental distribution of silicon, aluminium and oxygen, although clustering of silver was evident in the electron image and both silver and potassium are located towards the edge and centre of the zeolite crystal in their EDS maps.

Solid-state NMR spectroscopy was used to both characterise silver-exchanged materials, as well as determine their ability to activate methane at raised temperatures whilst also detecting upgrading products. Prior to analysis, silver-exchanged materials

were dehydrated at 400 °C, either under reduced pressure (lower than 1 x10^{-1} mbar) or under the flow of a dry, inert gas, such as nitrogen. Dehydration was carried out using a quartz u-tube fitted with two Young's taps, where a specific mass of material was loaded into the tube and held in place by two quartz wool plugs. The Young's taps were connected to a Schlenk line and a gas bubbler – for gas flow – with the vacuum and gas flow being fed from the Schlenk line. The u-tube would then be placed into a muffle furnace, with the zeolite located in the heating zone. The experimental process is described in detail in section 3.2.1.

Following the dehydration of silver-exchanged zeolites in a quartz u-tube, the tube was transferred into the inert glovebox so the dehydrated and desorbed powder could be recovered. The zeolite was then loaded to a quartz NMR rotor. Ag(1.00)/MOR(6.5), 19.3 wt% Ag was characterised using ssNMR spectroscopy. The acquired ^{1}H NMR spectrum is shown in Figure 5.9. Direct comparison was drawn against the parent material, Na/MOR(6.5). It was evident in the ^{1}H NMR spectrum for Ag(1.00)/MOR(6.5) that a new proton environment had been generated following aqueous ion-exchange with silver nitrate, with a distinct chemical shift at −0.92 ppm. Overall, the ^{1}H NMR spectrum was broadly concordant to the parent material, containing several chemical shifts assignable to environments typical of a zeolite.[22–25] The acquired 1H NMR spectrum contains silanol groups present on the surface or at defect sites (1.81 ppm), non-framework aluminium hydroxyl groups (2.39 ppm), Brønsted acid sites (BAS) in the framework (3.89 ppm) and the presence of silanol groups involved in strong hydrogen bonding (8.22 ppm).[22–25]

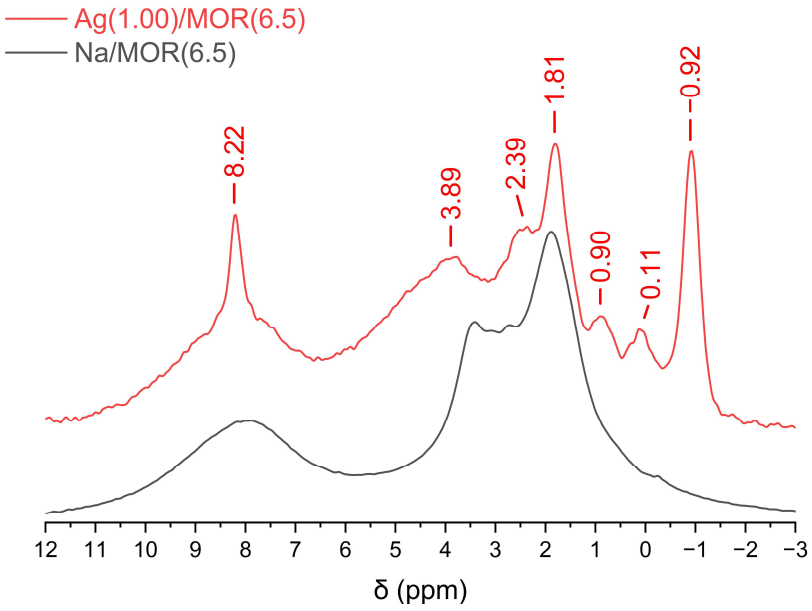

Figure 5.9: ^{1}H NMR spectra acquired for Na/MOR(6.5) (black) and for Ag(1.00)/MOR(6.5) (red), showing the difference in proton environments present in the parent sodium-form and silver-exchanged form. Spectra stacked for clarity.

Further NMR experiments, including a ^{1}H–^{29}Si WISE experiment and a ^{1}H–^{1}H homonuclear DQ-SQ experiment were collected. Unfortunately, the ^{1}H–^{29}Si CP signal that was obtained for Ag(1.00)/MOR(6.5) was very weak, however, the experiments gave resolved proton signals so further line narrowing was not required. As a result, this allowed for a simple ^{1}H–^{29}Si 'WISE' experiment, with the acquired spectrum shown in Figure 5.10. It was evident that no proton-silicon correlation was observed for the chemical shift at −0.92 ppm, implying that either the proton environment was very isolated and unable to achieve efficient CP, or that the chemical shift is likely unrelated to a silicon environment. The results of the DQ-SQ experiment were not plotted, however, they were found to be consistent with the acquired ^{1}H–^{29}Si WISE experiment and contained no chemical shift at −0.9 ppm. Baba *et al.* report a chemical shift for Ag_3-H in Ag(0.54),Na(0.46)/A(4) appearing as a quartet at -1.8 ppm, whilst $Ag_{n>3}$-H in Ag(0.60),Na(0.40)/Y(5) appears as a broad singlet at −0.1 ppm.[12] However, both materials reported by Baba underwent exposure to hydrogen at raised temperature prior to analysis.

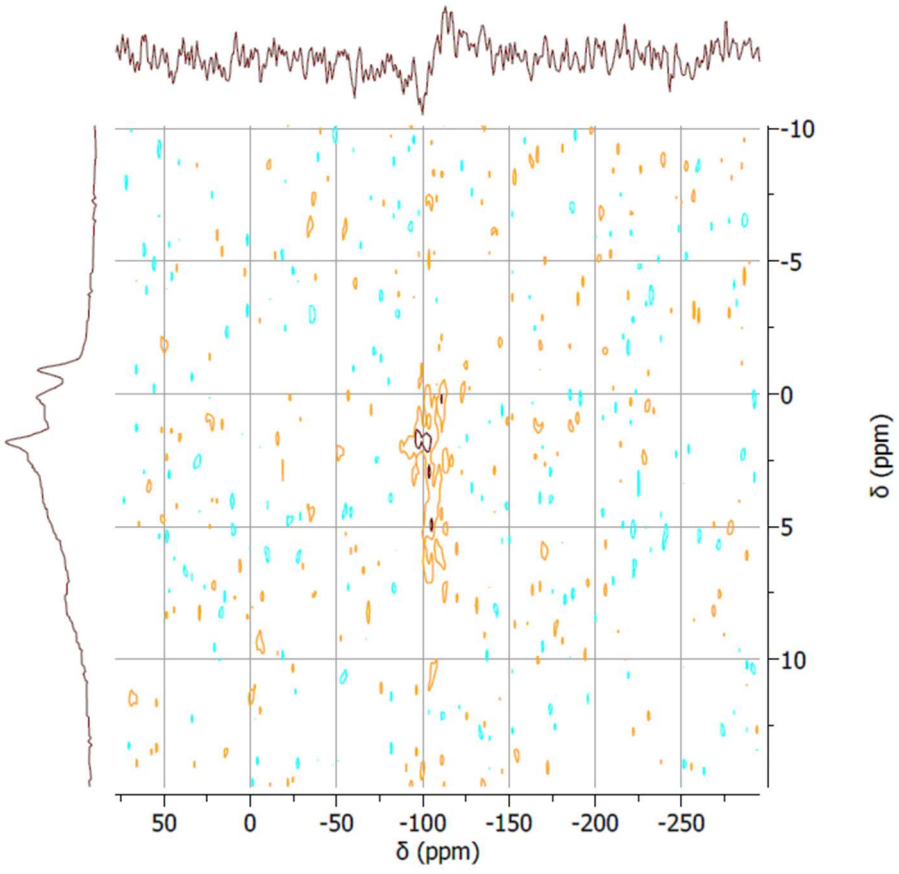

Figure 5.10: ^{1}H–^{29}Si WISE spectrum acquired for the characterisation of Ag(1.00)/MOR(6.5)

Ag(1.00)/MOR(6.5) was exposed to methane at 250 °C to determine the materials propensity to activate methane. Peak deconvolution was conducted on the acquired ^{1}H NMR spectrum, shown in Figure 5.11. In comparison with the parent material. two additional chemical shifts were observed at 0.90 ppm and 0.20 ppm. Stepanov *et al.* reported methane activation over Ag(0.7),H/ZSM-5(13), observing adsorbed methane at 0.94 ppm and methane interacting with BAS in zeolite channels at 0.23 ppm.[26] A subsequent $^{1}H–^{13}C$ CP experiment was conducted, however, the acquired spectrum was featureless.

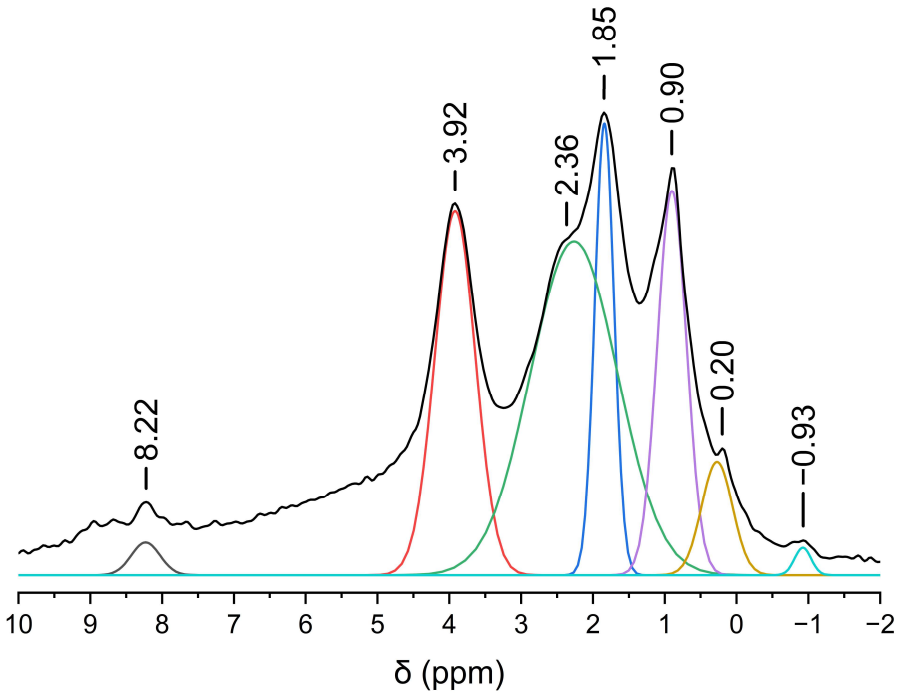

Figure 5.11: Peak deconvolution for the ^{1}H NMR spectrum acquired for Ag(1.00)/MOR(6.5) following exposure to methane at 250 °C.

Another observation following methane activation over Ag(1.00)/MOR(6.5) was the colour change from a white powder to a brown powder, shown in Figure 5.12. A subsequent reaction was also conducted at 350 °C, producing a darker colour powder but no changed species were observed by NMR. Analysis of Ag(1.00)/MOR(6.5) following methane activation by pXRD revealed that no damage had occurred to the framework, which would be facilitated by silver auto reduction and subsequent framework oxidation.[11,27,28] Shown in Figure 5.13, silver cluster formation was observed in the pXRD pattern, with two peaks present at 38.1° and 44.1° (2θ), corresponding to Ag[111] and Ag[200] respectively.[29] An average Ag NP size of 23.7 nm was calculated using the Scherrer equation.

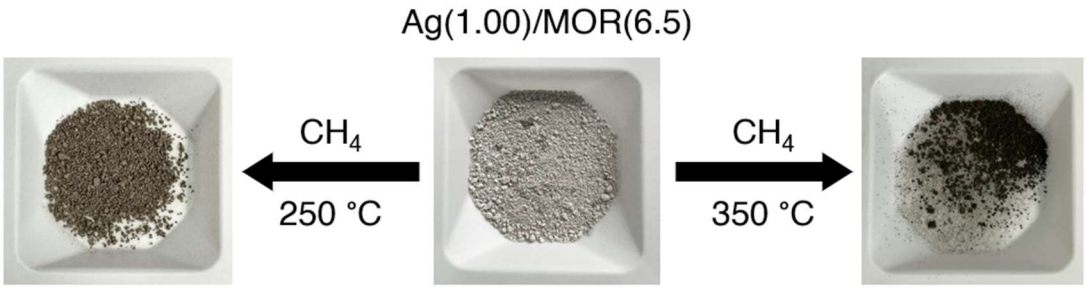

Figure 5.12: Spent Ag(1.00)/MOR(6.5) recovered after methane activation at 250 °C and 350 °C, which exhibited a colour change from a white powder to a brown powder.

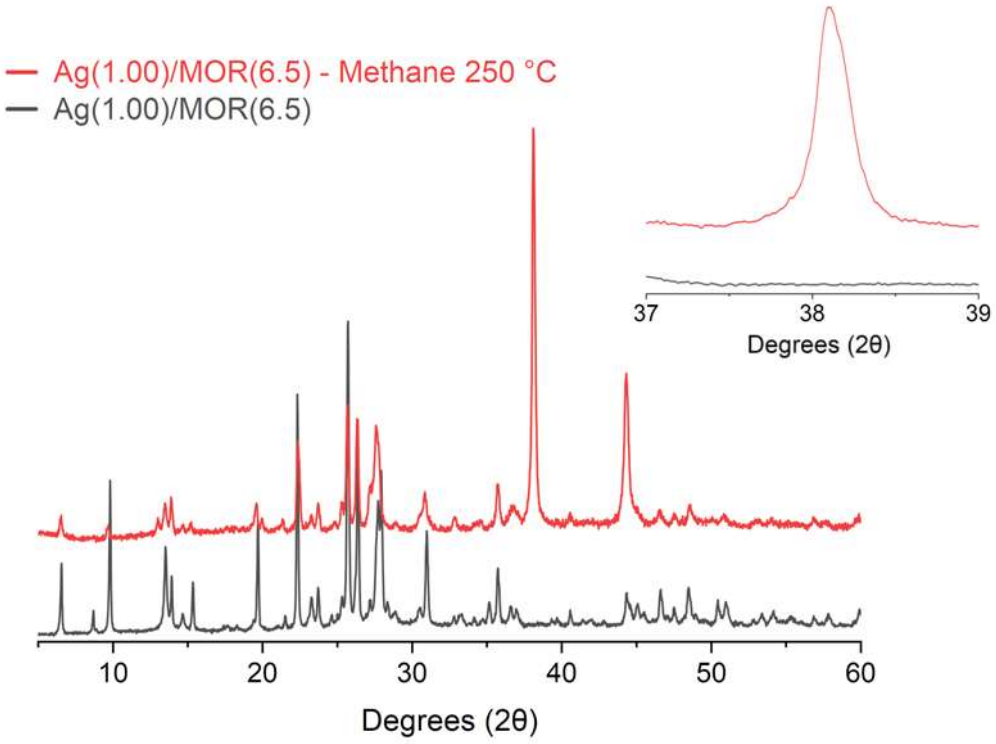

Figure 5.13: pXRD pattern of spent Ag(1.00)/MOR(6.5) recovered after methane activation at 250 °C, compared against the pattern for the fresh material. silver cluster formation was evident with two peaks present at 38.1 and 44.1° (2θ).[29] Patterns stacked for clarity.

A second methane activation experiment was devised for Ag(1.00)/MOR(6.5) using methane-d_4 to determine whether facile H/D exchange would occur for the chemical shift at −0.92 ppm. Overlaid ^{1}H NMR spectra for Ag(1.00)/MOR(6.5) acquired following dehydration and after methane-d_4 exposure at 250 °C are shown in Figure 5.14. Significant changes were observed for the chemical shifts centred at 8.22 ppm and 3.80 ppm respectively. This would suggest that extensive H/D exchange had occurred for the silanol environments with strong hydrogen bonding and BAS present in the framework. A reduction in the intensity of the chemical shift at −0.92 ppm was also

observed, suggesting H/D exchange was taking place. The increase in intensity of the chemical shift at 0.84 ppm indicates the presence of adsorbed methane-d_4. A ^{2}H ssNMR experiment was conducted, with the acquired spectrum containing a single chemical shift at 0.57 ppm, indicating physisorbed methane-d_4. A subsequent ^{1}H–^{2}H CP experiment was featureless, however.

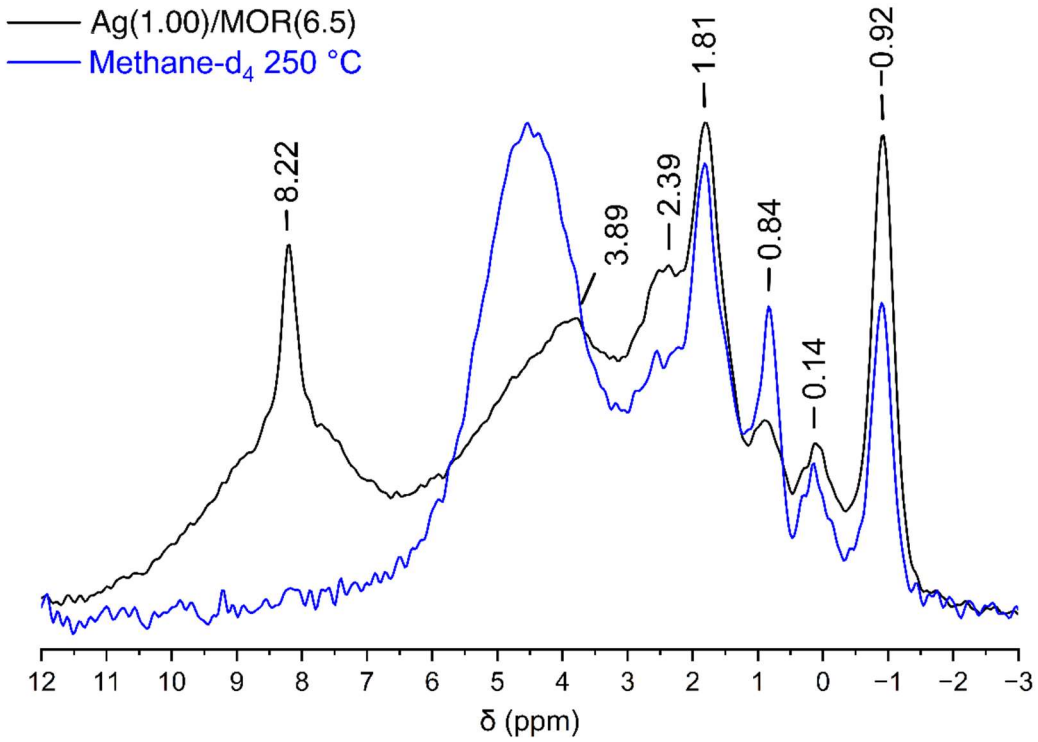

Figure 5.14: Overlaid ^{1}H NMR spectra acquired following the exposure of Ag(1.00)/MOR(6.5) to methane methane-d_4 (blue) to determine lability of the chemical shift at −0.92 ppm to H/D exchange.

The results of the NMR experiments for Ag(1.00)/MOR(6.5) indicate that the chemical shift at −0.92 ppm is highly isolated from other protons, evident from no proton-silicon correlation in the acquired ^{1}H–^{29}Si WISE spectrum, shown in Figure 5.10. We conclude that the chemical shift is unrelated to a silicon environment and could indicate the presence of a silver hydride species situated on a multinuclear silver cluster. Previous reports for zeolites A and Y show that Ag_3-H in Ag/A appeared as a quartet at -1.8 ppm, whilst $Ag_{n>3}$-H in Ag/Y appeared as a broad singlet at −0.1 ppm.[12] Other chemical shifts present were associated with silanol groups present on the surface or at defect sites (1.81 ppm), non-framework aluminium hydroxyl groups (2.39 ppm), Brønsted acid sites (BAS) in the framework (3.89 ppm) and the presence of silanol groups involved in strong hydrogen bonding (8.22 ppm).[22–25]

Methane activation was conducted over Ag(0.83)-NH_4/ZSM-5(12.5), with ^{1}H ssNMR spectroscopy used to characterise and determine its propensity for methane activation and determine the species present. The acquired ^{1}H NMR spectra for Ag(0.83)-NH_4/ZSM-5(12.5) before and after methane exposure at 250 °C is shown in Figure 5.15. Ag(0.83)-NH_4/ZSM-5(12.5) was dehydrated under a flow of nitrogen at 400 °C prior to methane exposure.

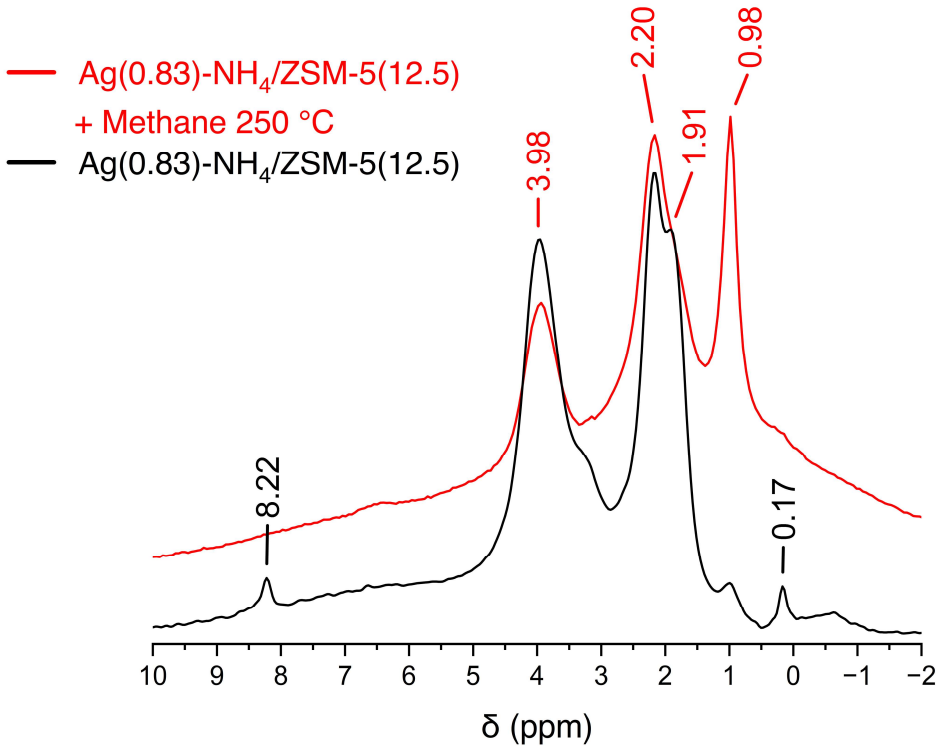

Figure 5.15: ^{1}H NMR spectra acquired for Ag(0.83)-NH_4/ZSM-5(6.5) (black) and after carrying out methane activation at 250 °C.

We observed chemical shifts associated with silanol groups present on the surface or at defect sites (1.91 ppm), extra-framework aluminium hydroxyl groups (2.20 ppm), Brønsted acid sites (BAS) in the framework (3.98 ppm) and the presence of silanol groups involved in strong hydrogen bonding (8.22 ppm).[22–25] Following methane exposure at 250 °C, a chemical shift at 0.98 ppm was observed, associated with adsorbed methane.[26]

A difference spectrum was obtained for Ag(0.83)-NH_4/ZSM-5(12.5), to highlight the species present following methane activation at 250 °C. The spectrum is shown in Figure 5.16 and contains two chemical shifts at 2.18 ppm and 0.96 ppm. Whilst the chemical shift at 0.96 ppm indicates the presence of adsorbed methane,[26] the chemical shift at 2.18 ppm is believed to be water present in the sample. Both nitrogen and methane

used for dehydration and methane activation were dried over a column of calcium sulfate. However, rehydration of the framework may have occurred following prolonged acquisition of several NMR experiments and the inherent unsealed nature of quartz ssNMR rotors.

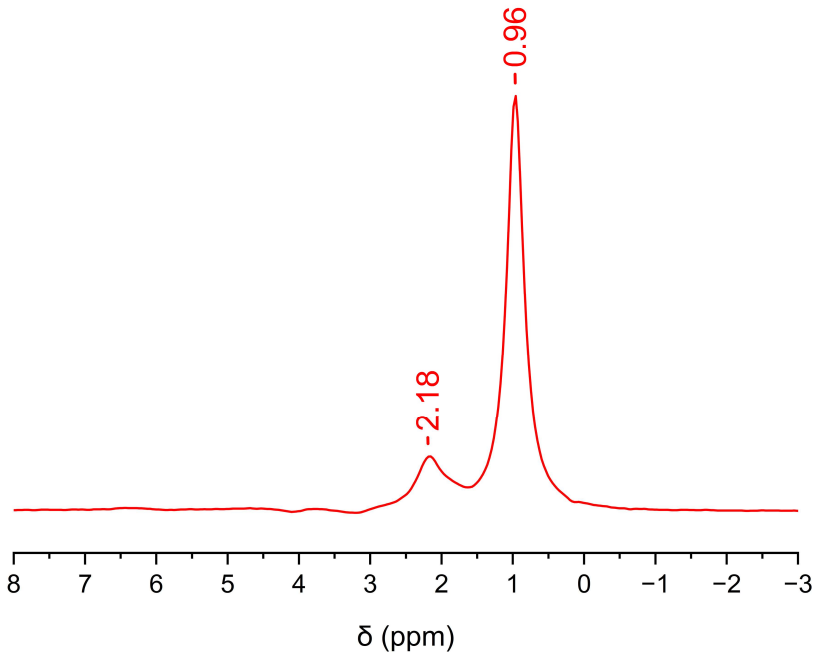

Figure 5.16: ^{1}H NMR difference spectrum acquired for Ag(0.83)-NH_4/ZSM-5(6.5), achieved by removing chemical shifts present in the framework from those observed following methane activation at 250 °C.

Ag(0.83)-NH_4/ZSM-5(12.5) was exposed to methane-d_4, with both ^{1}H and ^{2}H ssNMR experiments conducted. In the acquired ^{1}H ssNMR spectrum, a single chemical shift was observed at 0.70 ppm, indicating adsorbed methane-d_4. The ^{2}H ssNMR experiment was conducted using 'solidecho' sequence, utilising a second inverted pulse with a time delay. The second pulse quenched the signal for any mobile species, such as methane-d_4, with two chemical shifts observed in the acquired spectrum, shown in Figure 5.17. The broad chemical shift at 4.23 ppm indicates H/D exchange of BAS, whilst the chemical shift at 0.65 ppm indicates exchange of extra-framework aluminium hydroxy groups located within the microporous channels.[22]

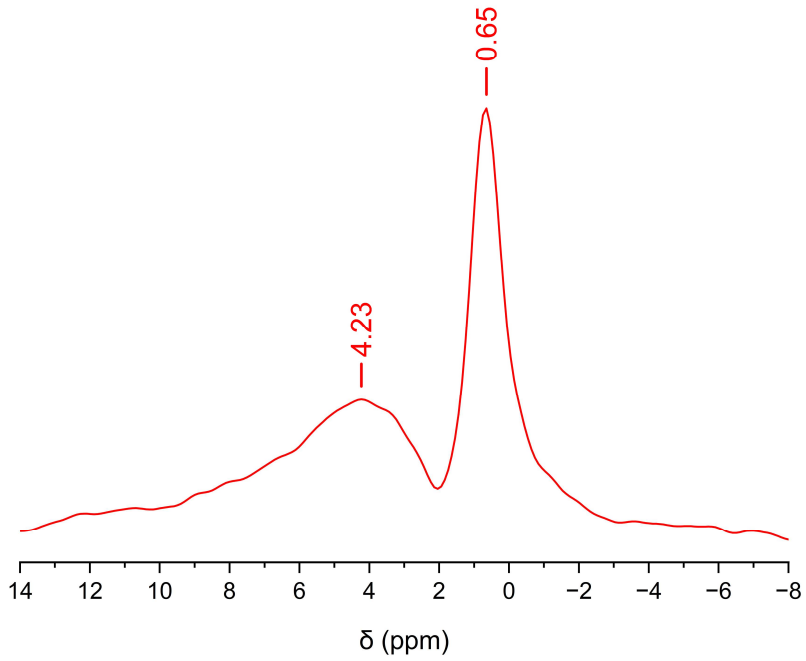

Figure 5.17: ^{1}H NMR spectra acquired following the exposure of Ag(0.83)-NH_4/ZSM-5(12.5) to methane methane-d_4 to determine lability of the chemical shifts towards H/D exchange.

Unlike Ag(1.00)/MOR(6.5), there was no evidence of silver clustering for spent Ag(0.83)-NH_4/ZSM-5(12.5) after methane activation at 250 °C by pXRD, as shown in Figure 5.18. In addition, there were no observable changes to the framework crystallinity in the acquired pattern. TEM images were acquired for spent Ag(0.83)-NH_4/ZSM-5(12.5) which did show evidence of surface silver clustering, shown in Figure 5.19. We observe significant silver clustering on the surface of the zeolite crystals, however, the pXRD pattern contains no reflections indicating the presence of silver clusters.[29] De Cremer claims that for silver to be observed by pXRD the clusters must be sufficiently large.[18] Our findings here are in line with these claims.

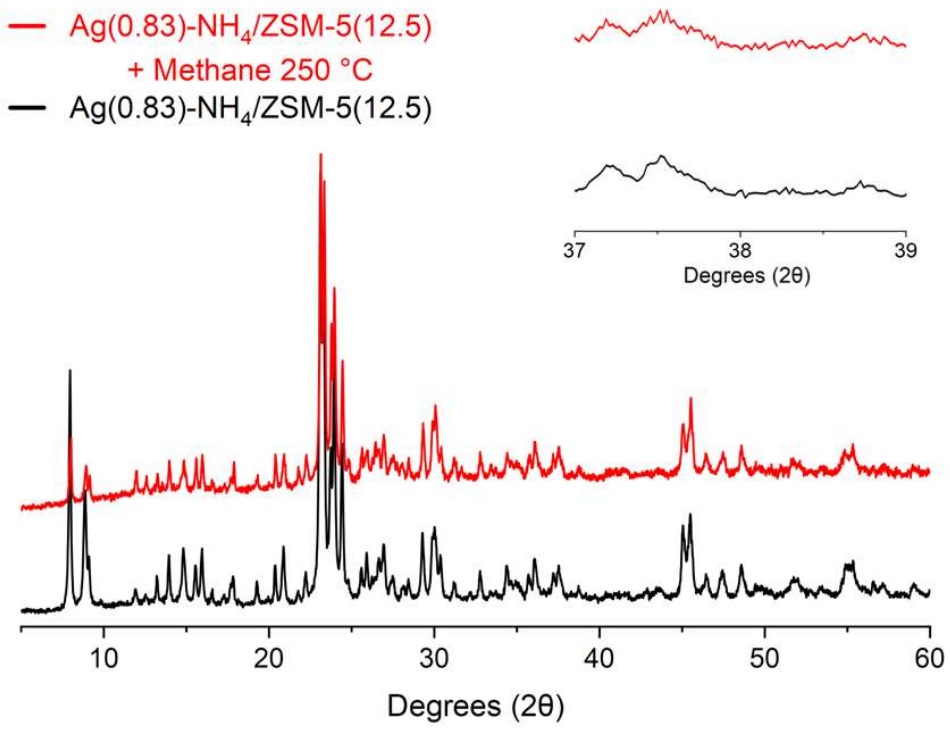

Figure 5.18: pXRD pattern of spent Ag(0.83)-NH_4/ZSM-5(12.5) recovered after methane activation at 250 °C, compared against the pattern for the fresh material. Patterns stacked for clarity.

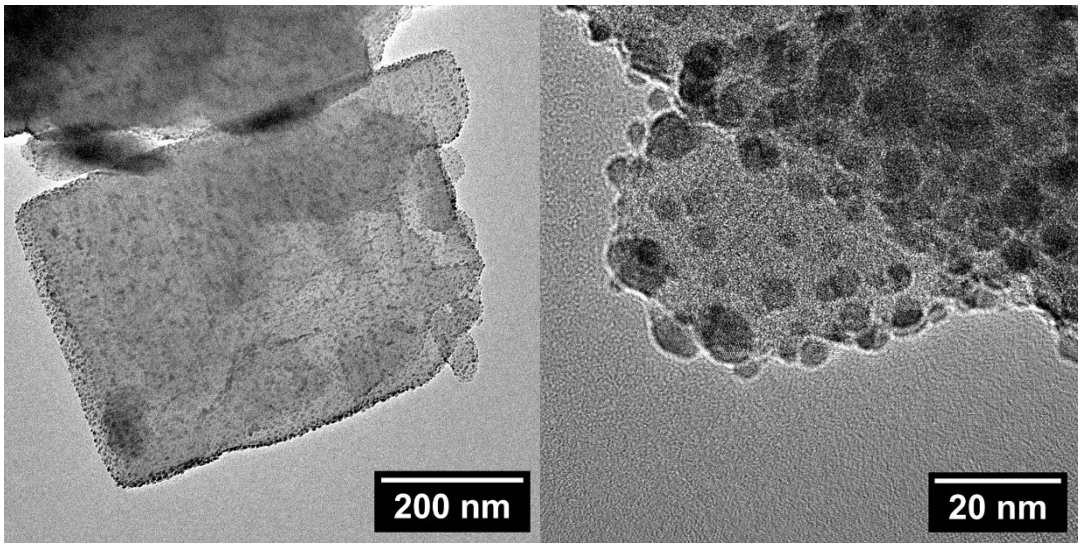

Figure 5.19: TEM images acquired for spent Ag(0.83)-NH_4/ZSM-5(12.5) recovered after methane activation at 250 °C, showing silver clustering over the zeolite crystal surface.

Baba carried out ^{1}H NMR spectroscopy of both Ag(0.54),Na/A(4) and Ag(0.6),Na/Y(5). After reduction of Ag(0.54),Na/A(4) using H_2, a quartet was observed at – 1.8 ppm which was attributable to Ag_3−H, the generation of this species was found to be reversible.[12] Ag(0.6),Na/Y(5) was exposed to both H_2 and CH_4 independently, with the chemical shift

at -0.1 ppm observed in both acquired spectra, with a lack of defined splitting. This chemical shift was attributed to a silver hydride species adsorbed onto cationic silver clusters, albeit larger in size than the defined Ag_3−H clusters found in Ag/A, hence a lack of peak splitting. Prior art and acquired experimental data lead us to postulate that the species present at −0.92 ppm in Ag(1.00)/MOR(6.5) was also a silver hydride, adsorbed onto a cationic multinuclear silver cluster.

5.1.4 Conclusion of Silver Ion-exchange

Silver ion-exchange has been routinely conducted using aqueous ion-exchange with silver nitration solutions of varying molarity, determining that repeated ion-exchange is the most effective way to reach complete silver exchange of materials. ED-XRF has been the characterisation method employed to determine elemental composition of exchange materials.

Regardless of silver loading level, STEM-BF images acquired for silver-exchanged zeolites demonstrated silver clustering, however, their pXRD patterns have shown no indication of silver clustering. Prior art reported silver clustering in the pXRD pattern of Ag/ZSM-5(25) with 15wt% Ag, prepared from incipient wetness impregnation.[4] No silver clusters were apparent in the pXRD pattern for Ag(2.42),K(0.88)/ZSM-5(13.5), leading us to conclude that incipient wetness impregnation generated larger silver clusters on the material surface than aqueous ion-exchange.[18] EDS-TEM maps acquired for silver exchanged zeolites highlighted the localisation of silver towards the edges of zeolite crystals. Co-clustering of silver and potassium was also observed. Whilst potassium clusters in both FAU and LTA topology zeolites are reported,[19,20] no examples of silver and potassium co-clustering are known. We propose that silver and potassium co-clustering arises through an electronic stabilisation effect.[21]

It was apparent for Ag(1.00)/MOR(6.5) that a novel proton containing species was present as a result of aqueous ion-exchange with silver nitrate. The species present in the ^{1}H NMR spectrum displayed a chemical shift at −0.92 ppm as a broad singlet, that was comparable to silver-hydrides observed in Ag/A (-1.8 ppm, quartet) and Ag/Y (−0.1 ppm, broad singlet).[12] We determined that the species readily undergoes H/D exchange, following exposure of methane-d_4 at 250 °C. Methane activation over Ag(1.00)/MOR(6.5) at 250 °C led to the observation of adsorbed methane and methane interacting with BAS in the channels.[26]

5.2 Hydrothermal Synthesis and Characterisation of CHA Zeolites

Chabazite (CHA) is one of the most widely used zeolite framework topologies throughout industry for widespread applications. CHA is commonly found in emissions control applications for their gas adsorption properties, particularly in deNOx selective catalytic reduction (SCR) in the automotive industry.[30–34] Whilst a naturally occurring zeolite, chabazite is often produced by hydrothermal synthesis to give targeted properties that enhance its performance.[35–39] Chabazite is a small-pore, three-dimensional zeolite framework outlined in section 2.2.1, which contains CHA cages connected by channel openings with accessible dimensions of 3.8 Å by 3.8 Å, as shown in Figure 5.20. These small but symmetrical openings restrict diffusion through the framework. Molecules larger than the channel opening dimensions cannot freely diffuse out of the micropores, an approach in synthesis that has been exploited in a technique referred to as 'ship-in-a-bottle' catalysis.[40,41]

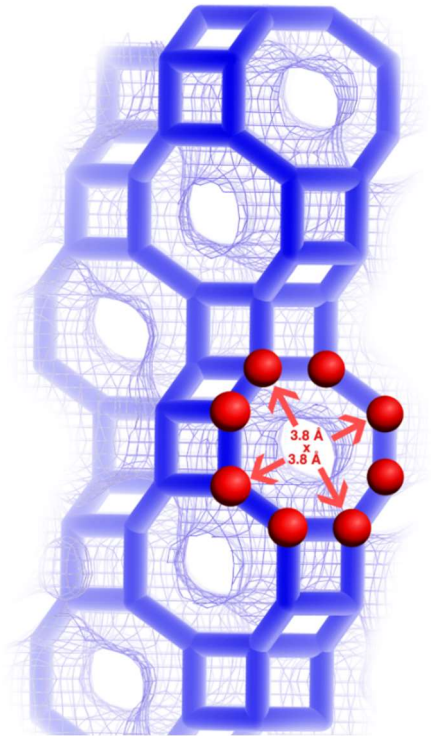

Figure 5.20: Graphic showing the CHA framework topology, with the channel structure depicted using a mesh surface. Symmetrical channel openings connect the CHA cages of the framework and have accessible dimensions of 3.8 Å by 3.8 Å.

The chabazite used in this project was produced through hydrothermal synthesis from three different methods, discussed in section 5.2.1. Synthesis of CHA allowed for direct comparison of the framework effect displayed by small pore zeolites against medium and large pore frameworks. Particularly between CHA and MFI, as the two frameworks have widespread industrial relevance and both contain 3D framework dimensionality.

Hydrothermal syntheses have several changeable conditions that can be adapted to produce frameworks of varying characteristics from synthesis gel. Hydrothermal synthesis has been shown to be sensitive to both time and temperature, the use of a SDA or a seed material, the choice of SDA used, the pH of the solution, the mineralising agent and even the ratio of Si and Al in solution.[42–46]

The use of SDA has been shown as critical for the formation of a zeolite framework from a synthesis gel mixture. Numerous studies assessing the thermodynamic effects exhibited by the SDA during hydrothermal synthesis pathway of a zeolite framework with regards their ability to stabilise and reduce the energy of intermediates that are formed.[47–49] It was postulated that seed-free hydrothermal synthesis could be explored as a route to synthesis of CHA frameworks, however, based on reports by Dusselier it became apparent that better materials were produced in higher yields through seeding or stirring the synthesis gel mixture during synthesis. Dusselier reported yields of up to 90% through the use of stirring, in comparison to 46% for static hydrothermal synthesis.[39,44,46]

Zhang *et al.* evaluated the use of different quantities of SDA and seed in fast chabazite synthesis methods by evaluating the pXRD patterns recorded.[33] pXRD patterns for synthesized materials using higher quantities of SDA or the use of a seed led to better crystallinity and resolution of phases at high 2θ values. Materials synthesised using lower quantities of SDA, SDA-free synthesis or no use of seeding led to materials with reduced crystallinity.

Fan *et al.* highlight how alkali cations introduced through the mineralising agents used in the synthesis gel mixture have influence over the resultant Si/Al ratio of the final material, directly affecting the rate of crystallisation, the crystal morphology and size.[50] The use of sodium cations is extremely common. Sodium cations have been shown to have a co-ordination number of 6 within zeolites and as such they're considered to be a structure-forming cation. This contrasts against other alkali metal elements, which are structure-breaking cations due to their low polarizability and can hinder formation.[51] Guo *et al.* reported that potassium cations displayed a pronounced effect on the rate of crystallisation of ZSM-5, achieved through the dissolution of the amorphous phase due to the improved liquid phase solubility of the gel.[52]

5.2.1 Hydrothermal Synthesis of Chabazite

In this project, CHA topology zeolites were successfully synthesised under hydrothermal synthesis conditions following several different methods, such as an adapted method of the zincosilicate CHA synthesis method reported by Okubo, as well as following the recipes reported by both Lobo and Dusselier.[39,53,54]

Over the project, several iterative changes were made to the original hydrothermal synthesis method reported by Okubo, originally designed for the production of a zincosilicate CHA. One area that attracted greater attention was in the calcination of hydrothermally synthesized materials, which could undergo total loss of framework crystallinity. This was particularly prevalent for zincosilicate CHA, as outlined in section 6.1. Okubo often did not calcine materials they produced following synthesis.[53] Following changes to the calcination profile, materials no longer underwent a complete loss of crystallinity. Over the course of the project, a number of iterative changes were made to improve the reliability. The initial change to the Okubo method involved using aluminium chloride in place of zinc acetate and Ludox HS-40 in place of fumed silica. All other parameters remained identical for the initial hydrothermal synthesis attempt. Post hydrothermal synthesis, the recovered material showed good crystallinity, although extensive framework damage was observed following calcination at 600 °C, as shown in Figure 5.21.

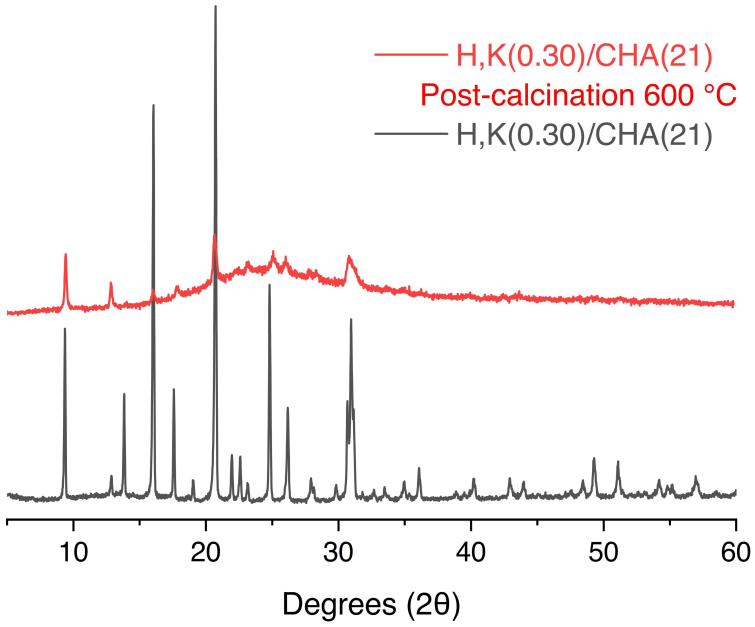

Figure 5.21: pXRD patterns for hydrothermally synthesized H,K(0.30)/CHA(21) post synthesis (black) and post calcination at 600 °C (red), showing significant loss of framework crystallinity. Patterns stacked for clarity.

Further iterative changes were carried out for CHA hydrothermal synthesis as follows:

- Increased mixing times for gel mixtures to 1 hour each. Synthesis gel was aged for 1 hour at ambient temperature. This is an increase from the original method with 5-minute durations for each.
- Seeding synthesis gel mixture loaded to autoclaves with CHA material.
- Aluminium sulfate used as the Al source in place of aluminium chloride.
- Hydrothermal synthesis under static conditions at 150 °C for 7 days, before calcination at 600 °C for 12 hours.
- Use of aluminium nitrate as the Al source.
- Increased mixing times for gel mixtures to 2 hours for each, before aging the synthesis gel at 40 °C for 24 hours. This produced a clear, free-flowing gel.
- Hydrothermal synthesis under static conditions at 150 °C for 5 days, prior to calcination at 600 °C for 10 hours.
- Calcination temperature was reduced from 600 °C to 550 °C and carried out over 24-hours.
- Hydrothermal synthesis using 600 RPM stirring at 160 °C for 5 days, before calcination at 550 °C for 10 hours. Application of stirring used in the synthesis method reported by Dusselier.[39]

Following the iterative changes to the hydrothermal synthesis method, chabazite was repeatedly synthesized with little variance between batches, as shown in Table 5.4. The final hydrothermal synthesis method that we developed consisted of:

Synthesis gel prepared by dissolving potassium hydroxide (510 mg) in 10 mL DI water at room temperature. To this mixture, Ludox HS-40 (16.021 g) was added dropwise using a pressure-equalising dropping funnel. After addition, the solution was heated to 40 °C, with continued stirring overnight. A solution consisting of aluminium nitrate nonahydrate (502 mg) dissolved in tetramethyladamantium hydroxide (46.062 g, 20 wt%) was added dropwise to the silica solution, before allowing the gel to age 24 hours whilst remaining at 40 °C. This caused the gel to change from a white cloudy gel to a clear gel. The synthesis gel was then transferred to a PTFE-lined autoclave, with 20 mg CHA seed added to each autoclave from a previous, successful batch. The autoclaves were heated to 160 ˚C for 5 days with 600 RPM stirring applied to the gel. Recovered solid was then washed until pH ≤ 8, dried at 80 °C for 16 hours before calcination at 150 °C for 1 hour and 550 °C for 10 hours, ramp rate of 1 °C/min.

To compare the chabazite produced in this project with those reported in literature, chabazite was also synthesized using hydrothermal synthesis methods reported by Lobo and Dusselier.[55,56] This allows us to discern whether chabazite produced by a particular method demonstrated superior catalytic properties, greater stability or a higher degree of crystallinity.

ED-XRF results for the chabazite hydrothermally synthesized by the adapted method is shown in Table 5.4. The results show good conformity between batches for the final silicon-to-aluminium ratio of materials, leading to materials with silicon-to-aluminium ratios around 20 from each batch. pXRD patterns were recorded for the materials, shown in Figure 5.22, with the pattern recorded for each in close conformity following calcination. This contrasts heavily with early hydrothermal synthesis where calcination led to extensive crystallinity loss, as shown in Figure 5.21.

Table 5.4: Table containing the ED-XRF results for chabazite synthesized using our developed hydrothermal synthesis method. Errors were calculated from averaged results acquired over three acquisitions using Panalytical Epsilon 1 benchtop ED-XRF. The average crystal size was calculated using the Scherrer equation.

Entry	Al (wt%)	Si (wt%)	K (wt%)	Si / Al ratio	Average Crystal Size (nm)
RK-2-78	0.84±0.01	16.79±0.19	0.25±0.00	19.27	276.8
RK-2-82	1.71±0.03	37.68±0.89	0.51±0.02	21.23	201.5
RK-2-99	1.33±0.05	27.14±0.52	0.44±0.01	19.66	240.2
RK-2-104A	0.92±0.37	19.14±0.83	0.35±0.02	20.06	317.8
RK-2-104B	1.00±0.46	19.99±0.39	0.38±0.01	19.23	282.2
RK-2-113	1.87±0.01	42.43±0.07	0.61±0.00	21.88	289.2

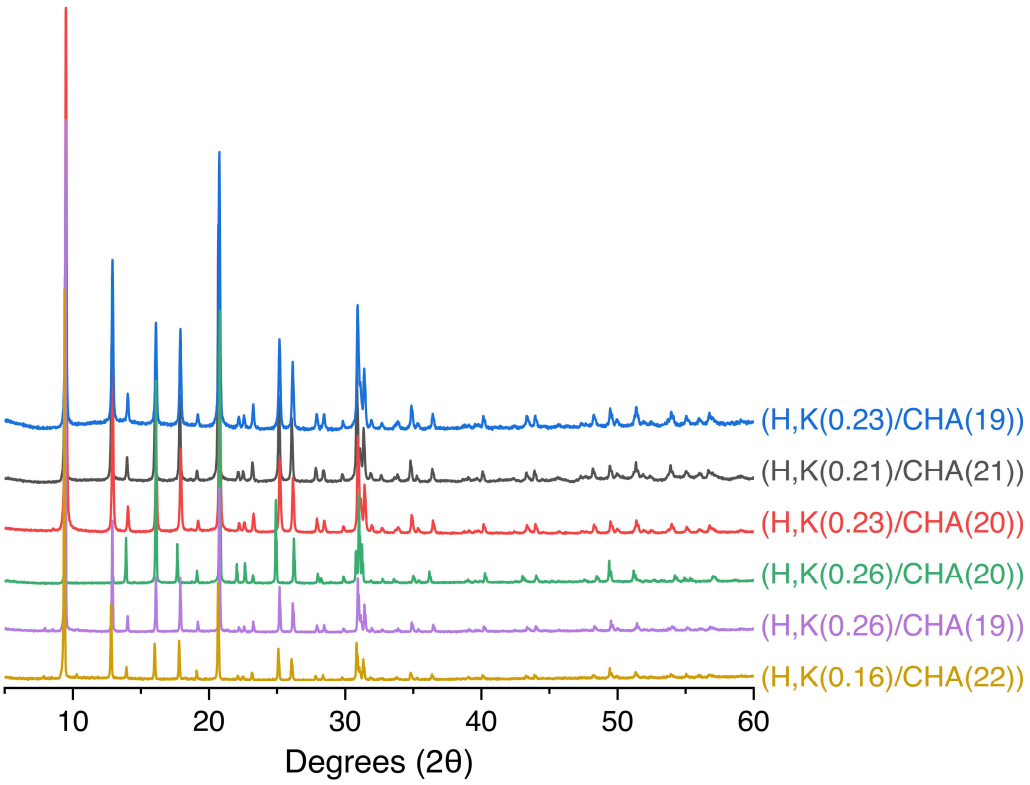

Figure 5.22: pXRD patterns for hydrothermally synthesized CHA materials following calcination at 550 °C, showing good uniformity between repeated batches. Patterns stacked for clarity.

5.2.2 Powder X-ray Diffraction of Hydrothermally Synthesized CHA

Powder X-ray diffraction was a key analytical technique used in the determination of material crystallinity and identity, giving information on the potential crystal size from the broadness of the reflection. Prior art on zeolite hydrothermal synthesis discussed how low angle reflections observed in the pXRD pattern are strongly influenced by extra-framework species, with the intensity of the reflection being directly related to the increasing number of species. This could be used in unison with other analytical techniques to determine whether defects or extra-framework species are present.[57] This is notable for dealumination. The process generates an increased number of terminal Si groups in place of the removed Al T atoms, leading to a decrease in reflection intensity, with the reverse being true for the healing of defect sites, such as a silanol nests. Changes to the long-range crystallinity of the zeolite would also be evident, such as damage caused by silver auto reduction which facilitates undesirable framework damage. One noticeable factor for chabazite was the change between reflection intensities between material with OSDA still present from hydrothermal synthesis and for calcined materials, as shown in Figure 5.23.

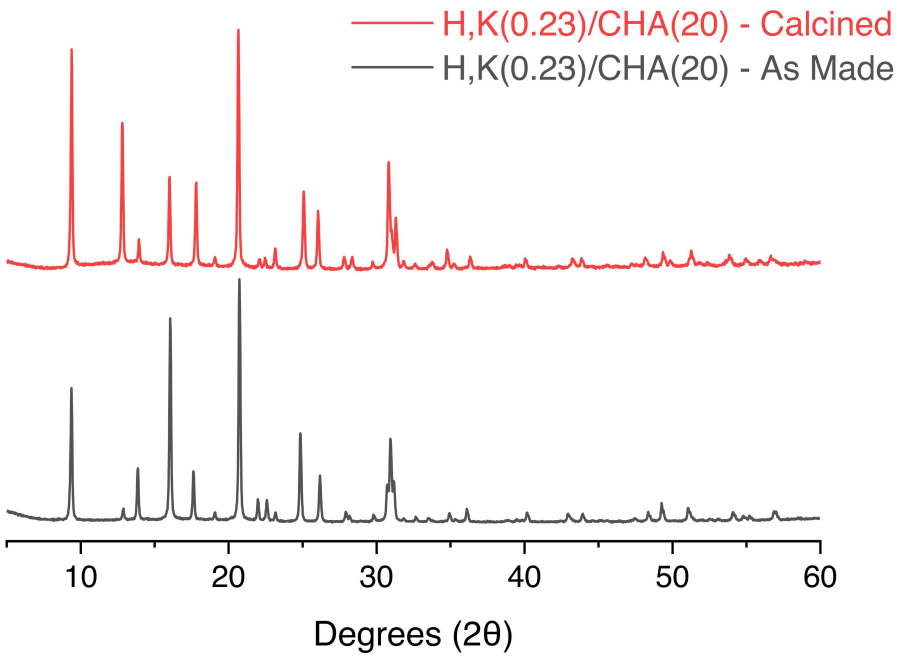

Figure 5.23: Stacked XRD patterns of as made and calcined H,K(0.23)/CHA(20), showing a change in phase intensity for phases at low values of 2θ. Patterns stacked for clarity.

XRD was a crucial technique in producing a reliable calcination method for the CHA materials. Early batches were noted for undergoing total loss of crystallinity and long-range order following calcination, as shown in Figure 5.21.

Calcination of chabazite was conducted using a slower ramp rate than that of medium pore zeolite frameworks, to allow for the slow diffusion rates of water, adsorbents and SDA degradation products out of the micropores. We postulate that this can minimise the effect of steaming from the adsorbed water, as well as avoid the potential build-up of pressure within the microporous channels as the SDA undergoes elimination and subsequent degradation in the channels. To counteract the diffusion limitation, a new calcination profile was devised for chabazite. Calcination used a heating rate of 1 °C/min, with a dwell at 150 °C for 1 hour and at 550 °C for 10 hours. This method proved to be successful in complete removal of SDA from the micropores when analysed by NMR and DRIFTS, whilst pXRD of repeat hydrothermal synthesis, shown in Figure 5.22, displayed good uniformity.

5.2.3 FT-IR spectroscopy of Hydrothermally Synthesized CHA

Lemishka *et al.* investigated whether FTIR spectroscopy could provide information on metal siting and distribution in dehydrated metal-exchanged zeolites.[58] One thing that was investigated was if the wavenumber for T-O-T perturbation was changed by varying metal loading levels, although there was not conclusive evidence to suggest this, they did observe a difference in favourability of the sites within the framework could be observed for each metal.

DRIFTS was chosen to characterise the bulk material and was carried out on chabazite to gain information on the chemical environments present within the framework for both the protic and silver-exchanged forms. We postulated that any undesired framework damage that had occurred due to the presence of silver in the micropores, following ion-exchange or after upgrading reactions, would be observed. DRIFTS was also used in the characterisation of spent catalysts, discussed in section 8.2.2.

The experimental procedure for the acquisition of DRIFTS spectra, using the equipment outlined in section 3.2.12, required ~75 mg of material loaded into the sample cup as a fine powder on top of a fine mesh stainless steel gauze. The top of the sample was lightly pressed to flatten, before being loaded into a Harrick Scientific Praying Mantis cell. The cell was first evacuated to pressures lower than $1x10^{-2}$ mbar, before being heated using a thermal profile outlined in section 3.2.12, where the sample was heated to 500 °C for at least 2 hours and at a heating rate of 5 °C/min. The sample was then cooled at a natural rate to 25 °C, with the pressure in the cell typically reading below $1x10^{-4}$ mbar. This procedure removes any adsorbed atmospheric content and water from the micropores to leave only the framework itself in the collected spectra. For calcined H,K(0.23)/CHA(20), no C–H containing species were present in the acquired DRIFTS spectrum following calcination at 550 °C for 12 hours, as shown in Figure 5.24. This finding was also observed across the repeated synthesis batches. Figure 5.25 shows a DRIFTS spectrum obtained for H,K(0.26)/CHA(20) that underwent incomplete calcination, where C–H containing species were present in the micropores and were observable in the acquired spectrum.

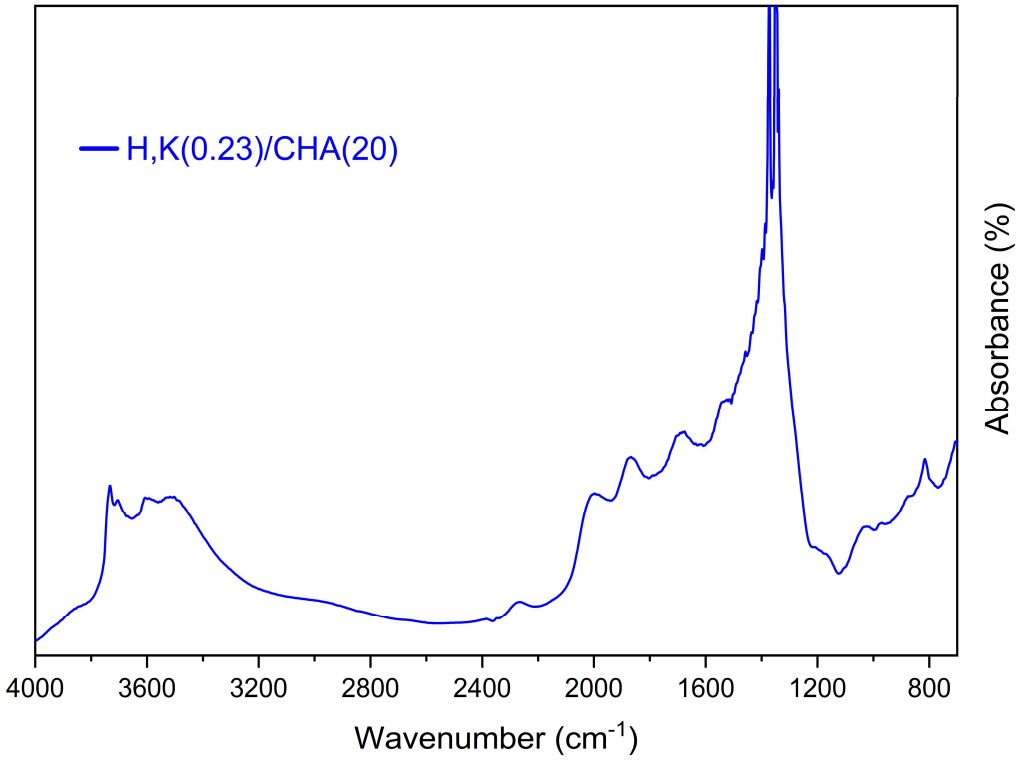

Figure 5.24: DRIFTS spectrum of calcined H,K(0.23)/CHA(20).

DRIFTS spectra were collected for material characterisation at 25 °C to give consistency across materials. This was done to negate any negative effects of the temperature dependence of DRIFTS IR towards signal positioning, broadening and intensity, an effect which is discussed in detail in an excellent report by Zholobenko *et al.*[59]

Signals in the region of 1250 – 1000 cm^{-1} wavenumbers are associated with asymmetric stretching vibrations of Si–O–T, with those in the region of 850 – 650 cm^{-1} wavenumbers are associated with symmetric stretching vibrations of Si–O–T, where T can be Al or Si.[60] The bands observed in this region are often referred to as the zeolite skeletal modes.[59] Changes in this region can be difficult to observe and are often obscured by the framework vibrational modes. The use of an accurate background for the sample minimised noise and maximised signal intensity in the acquired DRIFTS spectrum, allowing for the observation of low intensity signals.

Signals in the region of 2750 – 3200 cm^{-1} wavenumbers are associated to C–H species,[61] typically being organic matter left behind following incomplete calcination, an example of which is shown in Figure 5.25. A portion of H,K(0.23)/CHA (20) underwent calcination for a reduced timeframe, with 4 hours at 550 °C. A series of bands were observed between 2870 cm^{-1} and 3041 cm^{-1}, consistent with SDA remaining in the

micropores and highlighting incomplete calcination of the material. In comparison, no bands were observed in this region for fully calcined H,K(0.23)/CHA(20) shown in Figure 5.24.

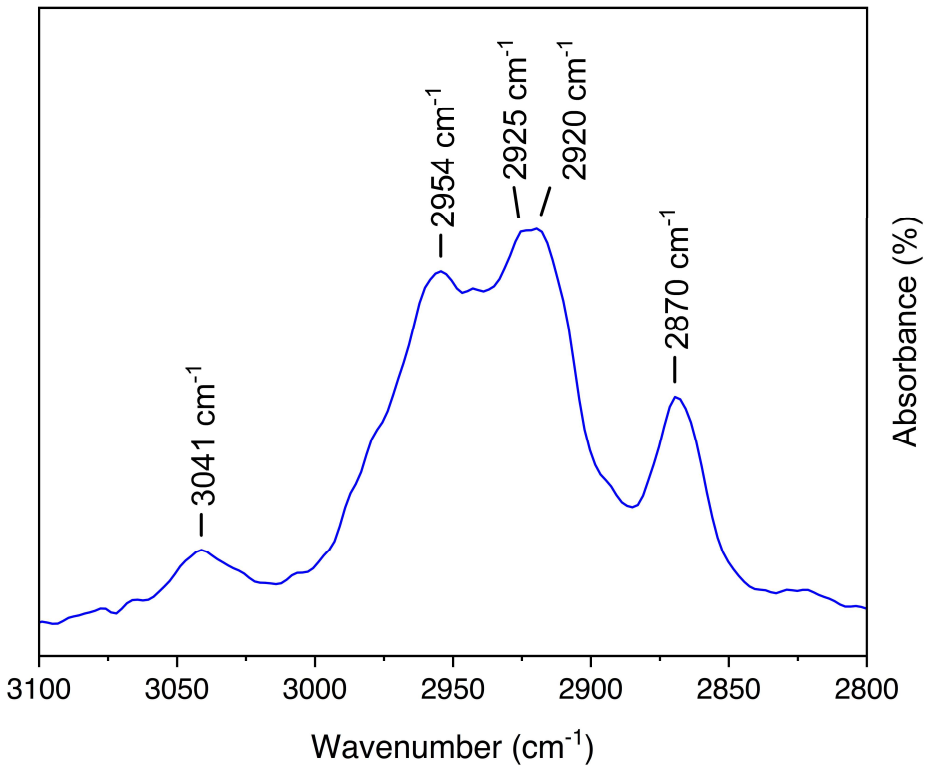

Figure 5.25: DRIFTS IR spectrum highlighting the region of 3150-2750 cm^{-1} wavenumbers for H,K(0.23)/CHA (20) which underwent incomplete calcination, with residual OSDA present in the micropores.

Signals in the region of 3400 – 3800 cm^{-1} wavenumbers are associated to O–H species, whether from Brønsted acid sites, of which there are several possible types. The wavenumber at which their respective band appears has locational dependence, based on whether it is an isolated or perturbed silanol group.[60,62–66]

For synthesized chabazite, two distinct silanol environments were observed, as shown in Figure 5.26. Firstly, an isolated external silanol environment was observed at 3735 cm^{-1}, whilst an internal, perturbed silanol environment at 3705 cm^{-1}.[64] In addition, there was a broad band centred around 3500 – 3600 cm^{-1} indicating the presence of several Brønsted acid environments, with isolated sites at around 3600 cm^{-1} and confined or H-bonded sites centred around 3500 cm^{-1}.

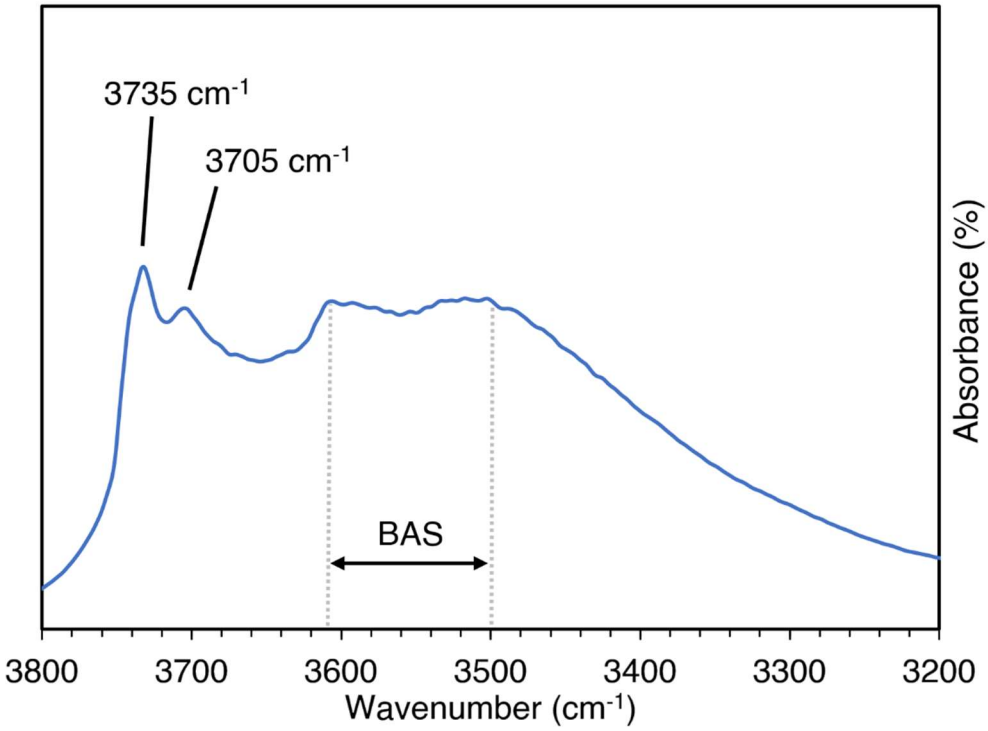

Figure 5.26: DRIFTS IR spectrum for calcined H,K(0.23)/CHA(20), focused on the spectral region of 3800 - 3200 cm^{-1}.

Silver-exchanged chabazite displayed no differences in the acquired DRIFTS spectrum when compared against the parent material, as shown in Figure 5.27. This confirms that there are no undesired effects, such as framework damage and crystallinity loss, took place during the aqueous ion-exchange with silver nitrate. This would be indicated by an increase in the intensity of bands in the 3400 – 3800 cm^{-1} region indicating the generation of new silanol defects, silanol nests and Brønsted acid sites. However, decreased intensity in the BAS region was expected as the protons are exchanged for silver cations.

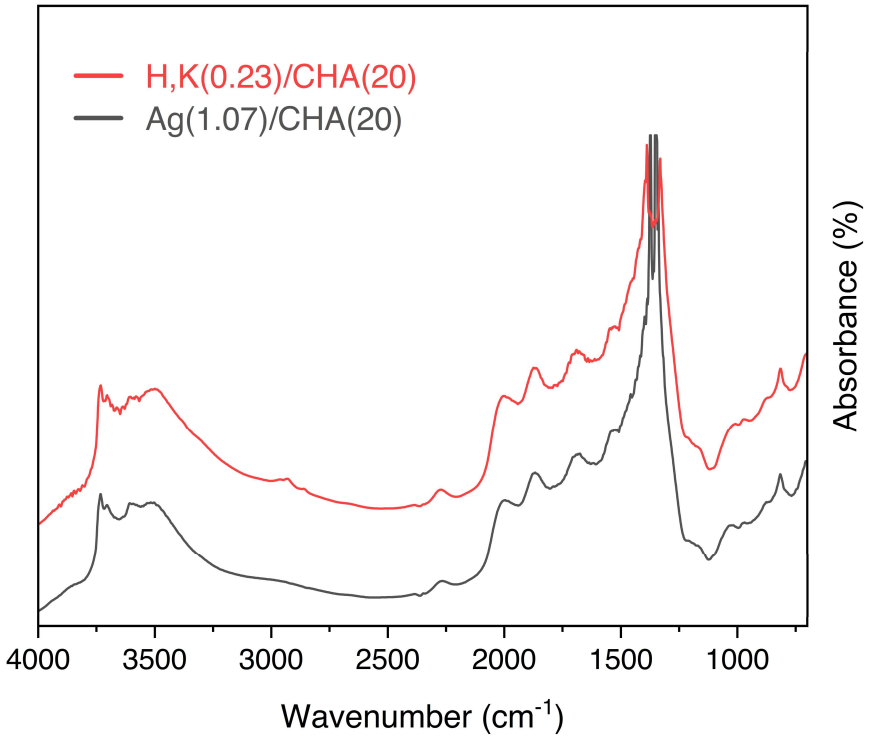

Figure 5.27: Stacked DRIFTS spectra of H,K(0.23)/CHA(20) (red) and Ag(1.07)/CHA(20) (red) displayed no differences between the silver-exchanged and parent materials. Spectra are stacked for clarity.

In addition to the use of DRIFTS for the characterisation of chabazite, vapour phase adsorption was conducted using deuterated acetonitrile to determine both the type and strength of the acid sites present. This was achieved by first dehydrating and desorbing the atmospheric content from the micropores, recording the DRIFTS spectrum for the material, before subsequently dosing deuterated acetonitrile as a vapour to the sample chamber. DRIFTS spectra for H,K(0.23)/CHA(18) before and after vapour phase adsorption of deuterated acetonitrile are shown in Figure 5.28.

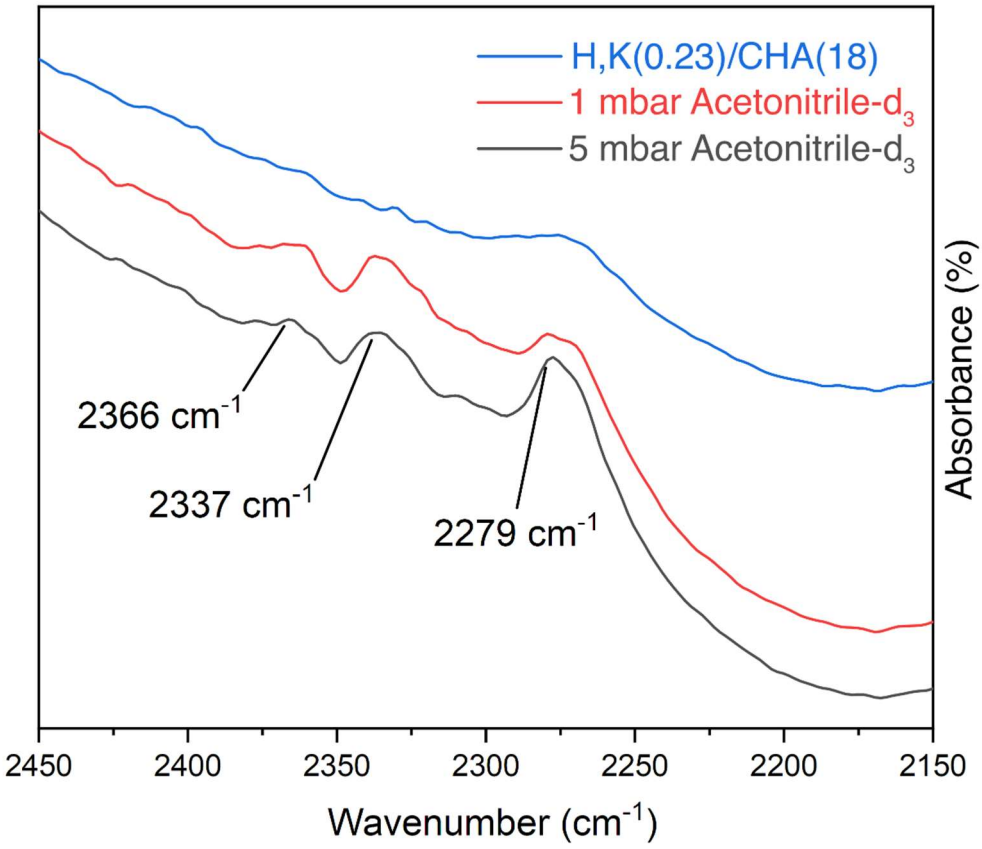

Figure 5.28: Stacked DRIFTS spectra in the spectral region of 2450 – 2150 cm^{-1} for H,K(0.23)/CHA(20) (blue) and after dosing acetonitrile-d$_3$ at 1 mbar (red) and 5 mbar (black). Spectra are stacked for clarity.

Probing the synthesized chabazite with deuterated acetonitrile revealed three distinct environments that the probe molecule could adsorb to. The bands at 2279 cm^{-1} and 2337 cm^{-1} indicate the adsorption on terminal silanol groups and Lewis acidic aluminium environments respectively.[67–70] Assignment of the band at 2366 cm^{-1} however is less straightforward, with the assignments of bridging OH groups and free liquid acetonitrile-d$_3$ able to be ruled out, as they are observed at 2300 cm^{-1} and 2265 cm^{-1} respectively,[70] A second Lewis acidic environment exhibiting stronger acid strength is likely responsible for the band observed at 2366 cm^{-1}.[71] Kazansky *et al.* reported a band at 2370 cm^{-1} that can be assigned to Lewis acid sites in H/ZSM-5 that strongly interact with acetonitrile-d$_3$.[61] This gives strong evidence to suggest that the bands at 2337 cm^{-1} and 2366 cm^{-1} are both Lewis acidic aluminium environments, with the former weakly interacting with the deuterated acetonitrile, and the latter strongly interacting. This would suggest the band at 2337 cm^{-1} corresponds to potassium exchanged sites, whilst the band at 2366 cm^{-1} corresponds to protic sites.[54,72,73]

5.2.4 Solid-state NMR spectroscopy of Hydrothermally Synthesized CHA

Characterisation of the synthesized zeolite chabazite framework was carried out using solid-state NMR spectroscopy observing the following nuclei: ^{1}H, ^{27}Al and ^{29}Si, along with the use of a ^{1}H–^{27}Al REAPDOR experiment, which aimed at providing further evidence for the assignment of species observed in the ^{1}H spectrum. ^{1}H ssNMR spectroscopy gave evidence that corroborated with the DRIFTS spectroscopy, indicating calcination conditions were indeed sufficient for the full removal of the SDA after synthesis. The ^{1}H MAS ssNMR spectrum acquired for H,K(0.23)/CHA(20) contained only two chemical shift environments, as shown in Figure 5.29. Material was calcined post hydrothermal synthesis and dehydrated under flowing nitrogen at 400 °C.

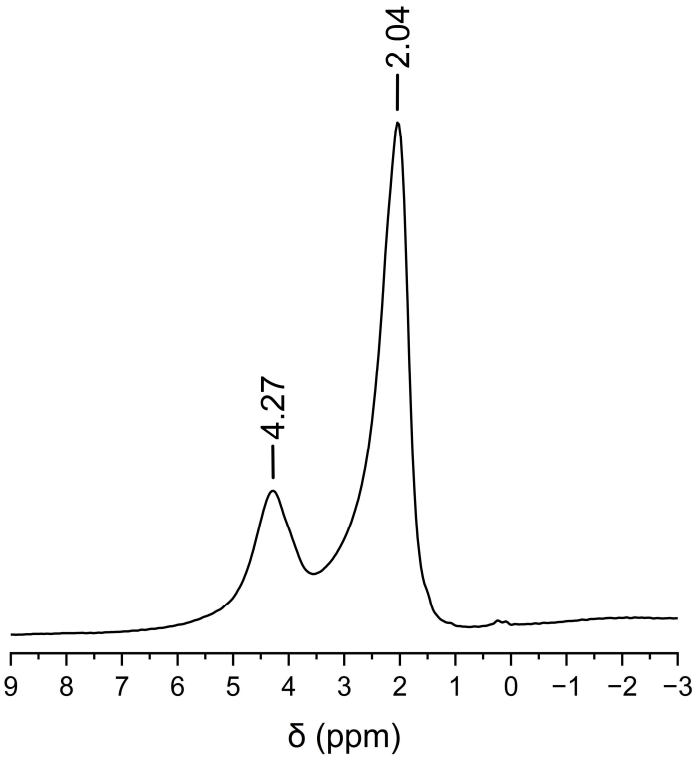

Figure 5.29: ^{1}H MAS ssNMR spectrum of H,K(0.23)/CHA(20) displayed two distinct proton environments present in the framework, although a broad shoulder of the chemical shift at 2.04 ppm appears to mask a third proton environment present in the framework.

^{1}H ssNMR spectrum for H,K(0.23)/CHA(20) contained a chemical shift indicating silanol groups present on the surface or at defect sites (2.04 ppm) and Brønsted acid sites (BAS) in the framework (4.27 ppm).[22–25] No additional chemical shifts were present in the ^{1}H NMR spectrum to indicate the presence of SDA from incomplete calcination, which agrees with the DRIFTS spectrum shown in Figure 5.24 The lower temperature used for calcination contrasts with prior art, where Dusselier *et al.* claim that 580 °C was the minimum temperature required for successful calcination of this particular SDA in

CHA materials.[39] However, a notable shoulder to the chemical shift at 2.04 ppm was observed, indicating a possible third proton environment. Peak deconvolution was conducted, shown in Figure 5.30.

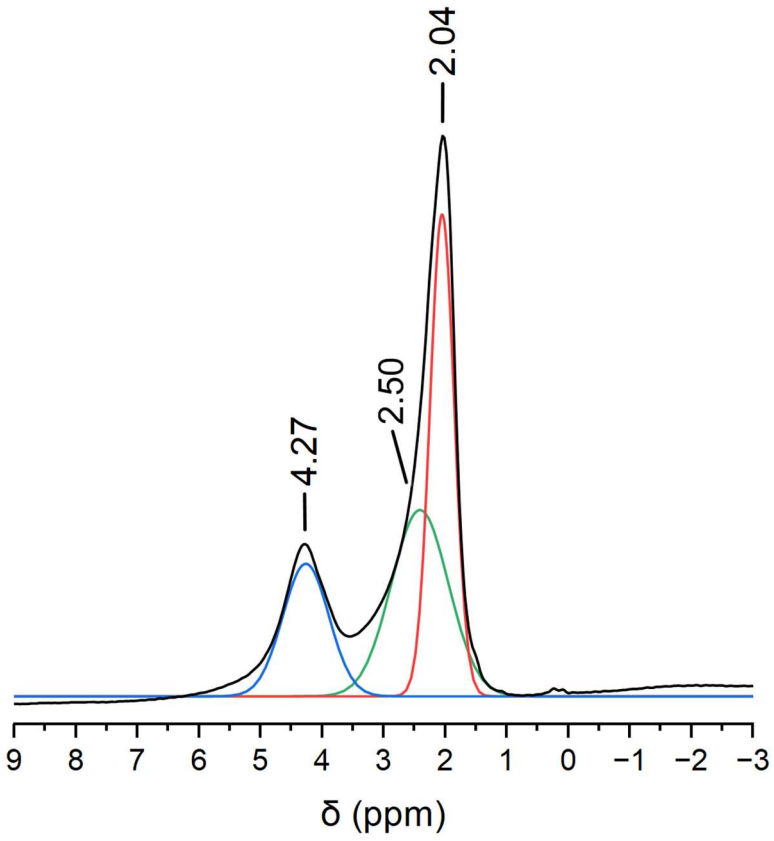

Figure 5.30: Peak deconvolution of the acquired ^{1}H MAS ssNMR spectrum of H,K(0.23)/CHA(20), displaying three distinct proton environments, with chemical shifts at 4.27 ppm, 2.50 ppm and 2.04 ppm.

Peak deconvolution revealed a third proton environment in the ^{1}H ssNMR spectrum for H,K(0.23)/CHA(20), with a chemical shift centred at 2.50 ppm, indicating extra-framework aluminium hydroxyl groups.[22–25]

Subsequently, a ^{27}Al ssNMR experiment was conducted on H,K(0.23)/CHA(20), as shown in Figure 5.31. This material was produced using our developed hydrothermal synthesis method outlined in section 5.2.1 and analysed as synthesised, with the SDA still present in the micropores and after calcination was conducted to remove the SDA from the micropores. This experiment was conducted determine the environments present in the calcined material, whilst determining any changes in the aluminium coordination environment from the as synthesized material that occurred during calcination, caused by Hoffmann elimination of the quaternary amine SDA.

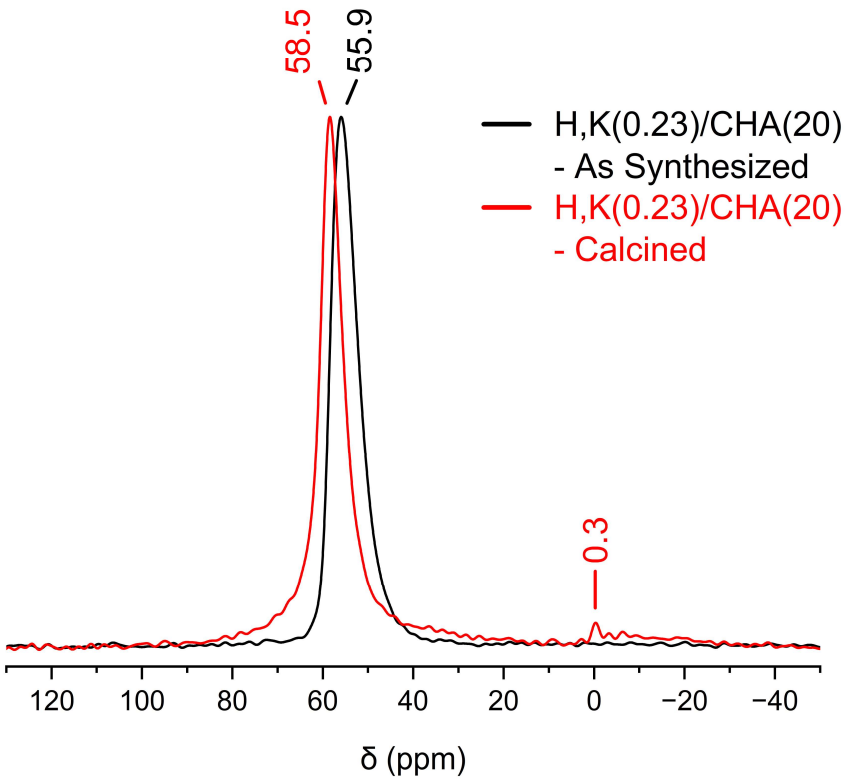

Figure 5.31: Stacked ^{27}Al MAS ssNMR spectra for synthesized H,K(0.23)/CHA(20) and for calcined H,K(0.23)/CHA(20), to display any changes in the aluminium co-ordination environment facilitated by calcination.

^{27}Al ssNMR spectroscopy revealed only a single aluminium environment in the material before calcination, with a chemical shift at 58.5 ppm indicating aluminium present in a tetrahedral environment.[22,74] Calcined H,K(0.23)/CHA(20) was found to contain two distinct aluminium environments, present with a ratio of 100 : 1.4 for tetrahedral aluminium (T_d) (55.9 ppm) to octahedral aluminium (O_h) (−0.3 ppm). The chemical shift attributed to O_h aluminium in the calcined material displayed asymmetry, hinting at the possibility of low number of penta-coordinated aluminium environments present in the framework, which are expected to have a chemical shift centred around 30 ppm.[75,76] Peak deconvolution was applied to the acquired ^{27}Al ssNMR spectrum for calcined H,K(0.23)/CHA(20), shown in Figure 5.32.

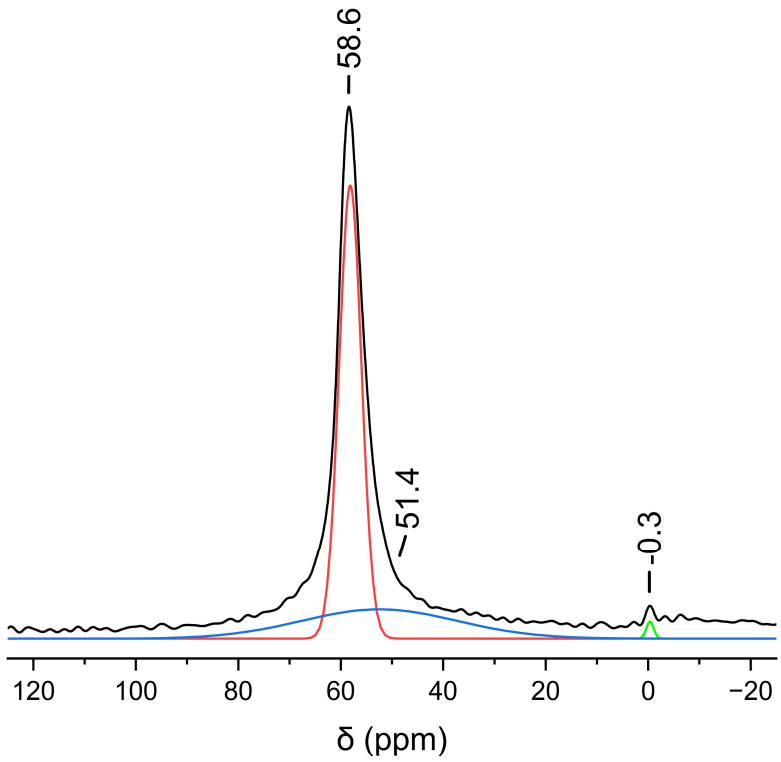

Figure 5.32: Peak fitting has been applied to the ^{27}Al MAS ssNMR spectrum acquired for calcined H,K(0.23)/CHA(20), indicating the presence of three aluminium environments in the framework.

Peak deconvolution revealed a third, broad chemical shift centred at 51.4 ppm. Due to the broad shape of the chemical shift, we postulate a second tetrahedral aluminium environment is present in the framework, arising from defect sites which are highly disordered.[22,74] The chemical shift was observed too far downfield to be associated with pentacoordinated aluminium.[75,76]

A ^{1}H–^{27}Al REAPDOR (rotational-echo adiabatic passage double resonance) experiment was carried out to probe the local environment of species present in the acquired ^{1}H and ^{27}Al ssNMR spectra for H,K(0.23)/CHA(20). REAPDOR NMR experiments are designed to exploit systems containing quadrupolar nuclei, operating through the transfer of magnetisation between the quadrupolar nucleus and the spin-$^{1}/_{2}$ nucleus. The REAPDOR experiment is referred to as a two-step experiment. The first step is the control experiment, for which no dephasing spin pulse was applied, leading to a result very similar to the ^{1}H ssNMR experiment shown in Figure 5.29. The second step was the REAPDOR experiment, a dephased NMR experiment conducted using pulses applied to both the dephased quadrupolar spin and the observed spin. Irradiation from

the radio frequency pulses perturbs the quadrupolar ^{27}Al nucleus leading to dipolar dephasing, which results in a decrease in the echo signal intensity. The difference spectrum, shown in Figure 5.33, displays any discernible changes between the chemical shift intensities in the controlled and dephased experiments. The difference spectrum corroborated with the acquired ^{1}H ssNMR spectrum, which contained a distinct shoulder at 2.50 ppm, indicating a third proton environment at 2.70 ppm.

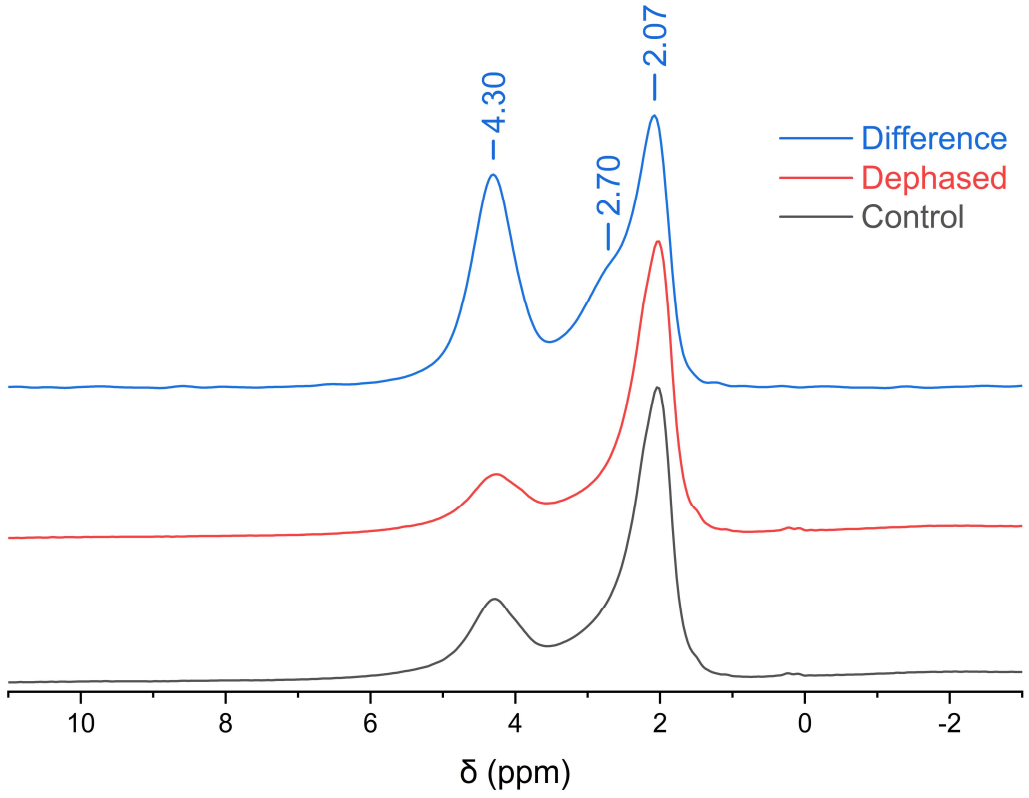

Figure 5.33: Stacked ^{1}H MAS ssNMR spectra representing the ^{1}H–^{27}Al REAPDOR experiment carried out for H,K(0.23)/CHA(20). This consists of a simple direct excitation ^{1}H experiment (control), a dephasing experiment with a second pulse to reduce echo signal intensity and sharpen the peak shape, with a difference spectrum containing the difference between control and dephased spectra.

In the difference spectrum, three distinct chemical shifts were observed for H,K(0.23)/CHA(20), indicating the presence of BAS (4.30 ppm) and extra-framework silanol groups (2.07 ppm), with a third environment observed as a shoulder at 2.70 ppm. We associated this chemical shift (2.70 ppm) with extra-framework aluminium hydroxyl groups,[22–25] corroborating with the chemical shift observed at 2.50 ppm following peak deconvolution, in Figure 5.30. Correlation between ^{1}H–^{27}Al during the REAPDOR experiment facilitated by CP type interactions enhanced the intensity of the shift. Based on previous reports, we conclude that the extra-framework aluminium environment is

located within a cage structure or as a species containing several hydroxyl groups, such as $-Al(OH)_2$.[77–79]

^{29}Si ssNMR spectroscopy was carried out using both CP and HPDEC experiments. The acquired ^{29}Si ssNMR spectra are shown as stacked spectra in Figure 5.34. ^{29}Si CP ssNMR experiment took advantage of ^{1}H coupling to enhance the intensity of the associated chemical shifts for framework moieties containing protons, such as Q^2 and Q^3 silicon environments. HPDEC experiments are quantitative NMR experiments that are used to indicate the quantity of each silicon environment present in the framework. This showed that the silicon in the framework was mostly residing in the Q^4 environment, with a chemical shift value of −110.0 ppm, with a much smaller number of Q^3 sites at −100.9 ppm. There was also a notable shoulder centred at −103.6 ppm, which indicate the presence of Q^4(1Al) sites.[80] Only in the CP spectrum did it become apparent that Q^2 sites were present in the framework, with a low intensity peak appearing at a shift value of −91.2 ppm.

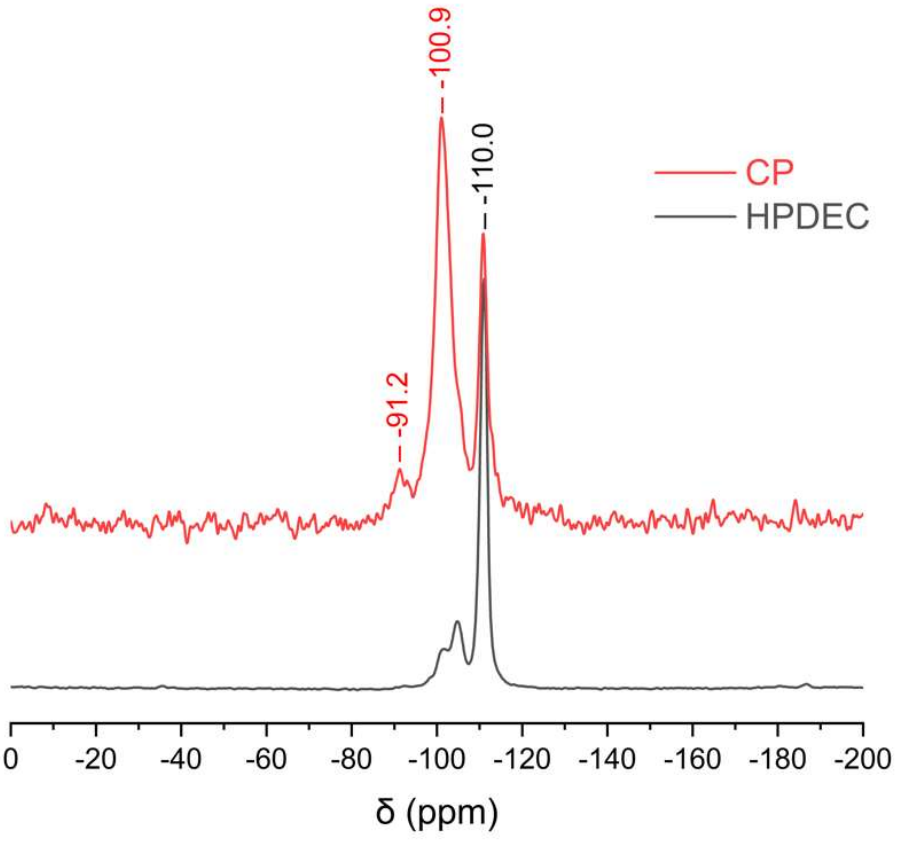

Figure 5.34: A graphic showing two stacked ^{29}Si MAS ssNMR spectra for H,K/CHA acquired from conducting a direct excitation experiment (HPDEC), to attain a quantitative assessment of Si environments present, and the cross-polarisation (CP) experiment, to highlight all Si environments present in the framework.

From the NMR analysis, it could be said with confidence that there is a relatively good degree of order in the synthesized CHA framework with a small quantity of defect sites present. Considering the DRIFT spectrum for the material, it could be argued that the silanol groups present are arranged as silanol nests and that perhaps the data was collected without all adsorbed water having been removed, as a broad band would appear between 3700–3400 cm^{-1} to signify this.[77]

5.2.5 Electron Microscopy of Hydrothermally Synthesized CHA

TEM analysis of chabazite produced using our developed hydrothermal synthesis method gave us great insight into the crystal morphology, for crystal size, shape and distribution, with EDS determining composition of the crystals themselves. Through dispersion of the material onto TEM grids, images were collected of various sections to give us an accurate image of the distribution of crystal size and shape. The distribution of chabazite crystal size is shown in Figure 5.35, with an average crystal size of 246 nm (± 46.1 nm) taken from a total of 202 crystals measured. This value corroborates with the average crystal size calculated using the Scherrer equation of 277 nm.

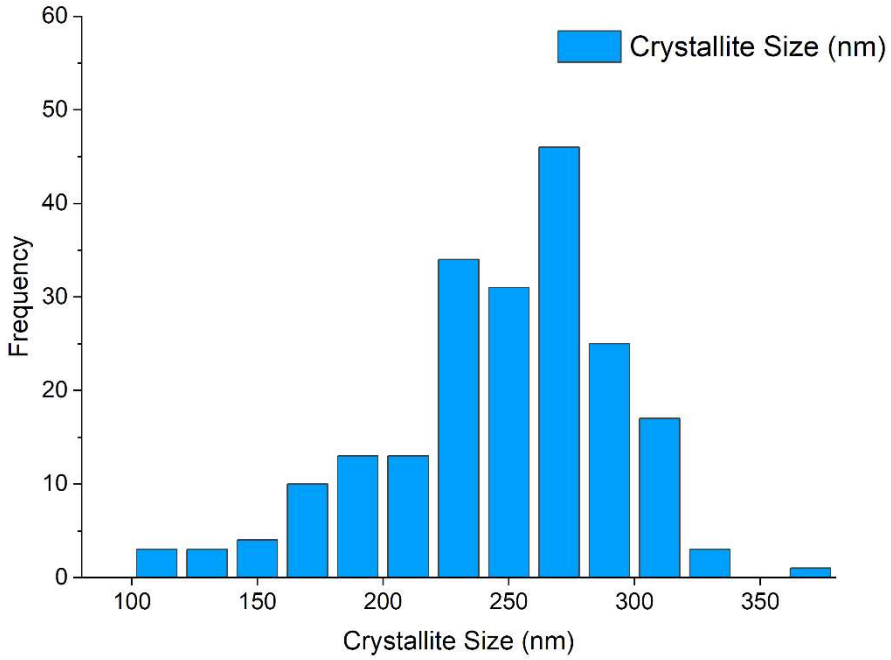

Figure 5.35: Graph showing the size distribution of chabazite crystals, measured from acquired STEM-BF images.

Hydrothermally synthesised chabazite produced using our developed method led to cubic shaped crystals that were on the nanoscale. The acquired STEM-BF images,

shown in Figure 5.36, confirmed that the crystallites were uniform in their size distribution and in their shape. Hydrothermal synthesis was found to be consistent between batches, each noted as having nanosized cubic crystals.

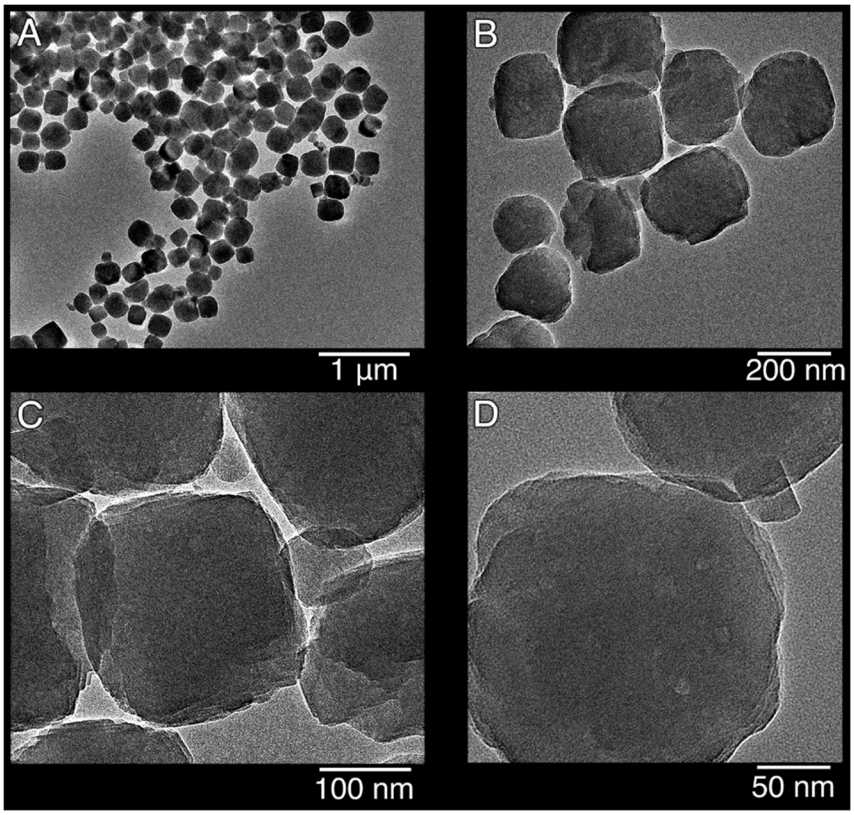

Figure 5.36: A series of STEM-BF images acquired for H,K(0.23)/CHA (20) over a series of magnification: a) 1 µm b) 200 nm c) 100 nm d) 50 nm.

EDS mapping was carried out alongside TEM to give further insight into the elemental distribution of the synthesized material, as well as highlighting the dispersion of exchangeable cations and their position in the framework. As shown in Figure 5.37, there is good elemental distribution throughout the synthesized chabazite crystals.

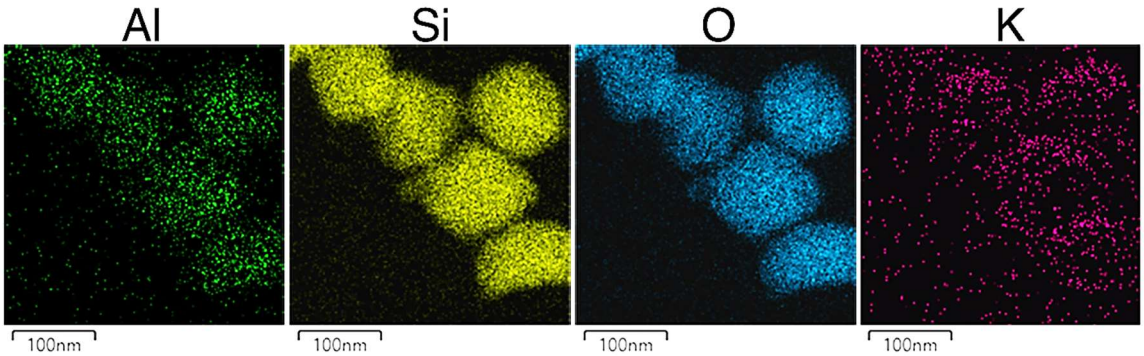

Figure 5.37: EDS-TEM maps acquired for H,K(0.23)/CHA(20) of the elemental distribution of aluminium, silicon, oxygen and potassium in/on the framework.

5.2.6 Brunauer-Emmett-Teller Theory on Hydrothermally Synthesized CHA

To assess the surface area of synthesised chabazite, Brunauer-Emmett-Teller (BET) theory was used. This process first uses N_2 physisorption analysis before BET surface area calculations were undertaken. Using the BET theory as a model to describe adsorption, a gas adsorption isotherm was collected for H,K(0.23)/CHA(20), where the quantity of gas adsorbed per gram of material is plotted against relative pressure, as shown in Figure 5.38. The shape of the isotherm is indicative of how gas adsorption occurs within the material, with diffusion limitations of the small pore material reducing the uptake and desorption of N_2. The observed isotherm is described as being Type I with an H4 hysteresis.[81]

The surface area using BET theory for H,K(0.23)/CHA(20) was calculated to be 682 m^2/g, relative pressure range of P/P_0 = 0.005 – 0.300. In comparison with chabazite materials reported in the literature, the material was noted as having a high surface area and a linear isotherm plot that conforms to those reported for other materials.[81–83] Liu *et al.* reported a surface area between 537 and 569 m^2/g for their chabazite materials,[82] whereas Lillerud reported a range of 463 – 702 m^2/g from their varied hydrothermal syntheses, with an average of 603 m^2/g across their six materials.[81]

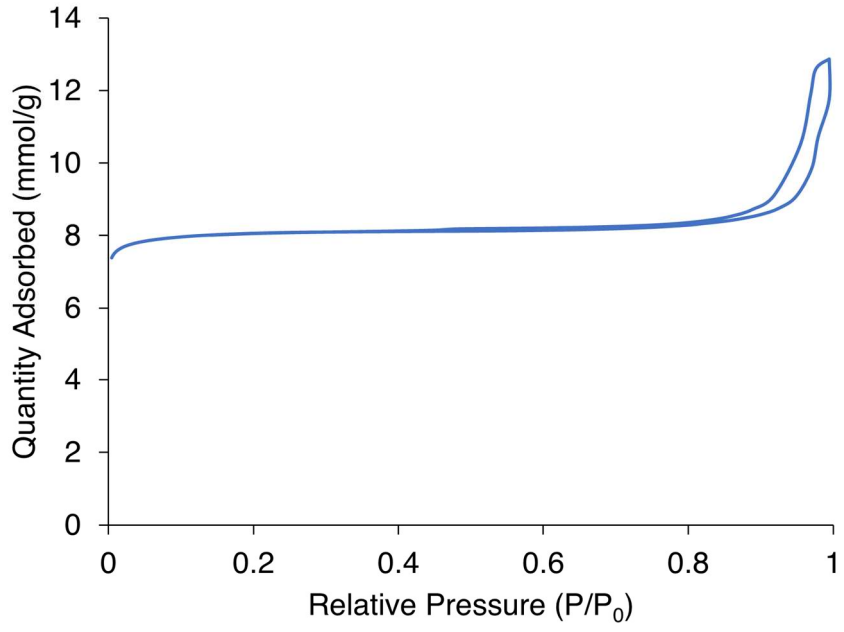

Figure 5.38: Isotherm linear plot for N_2 physisorption analysis of hydrothermally synthesized H,K(0.23)/CHA(20), showing a Type I isotherm with an H4 hysteresis, expected for small pore microporous materials.

5.2.7 Conclusion of Hydrothermal Synthesis of Chabazite

Following the iterative process of making adaptations to the reported Okubo hydrothermal synthesis method for ZnCHA,[53] successful hydrothermal synthesis of nanoscale chabazite zeolite materials was achieved. Repeated generation to synthesize new batches using identical methodology proved our developed method was successful, producing materials with consistent elemental composition and physical zeolite properties. pXRD analysis revealed materials with good crystallinity, and consistent crystal size calculated using the Scherrer equation (277 nm). STEM-BF images acquired revealed uniform cubic crystals with an average size of 246 nm, corroborating with the calculated value. EDS-TEM revealed good elemental distribution throughout the zeolite crystals, with no localisation present for any of the elements. Acquired DRIFTS spectra revealed that calcination conditions were sufficient for complete SDA removal, whilst vapour phase adsorption of deuterated acetonitrile revealed three distinct bands. These revealed a Lewis acidic aluminium environment (2366 cm^{-1}) close in value to a band reported for H/ZSM-5 by Kazansky.[71] A second band indicated a second Lewis acid site (2337 cm^{-1}) present in the framework,[84,85] whilst the third band (2279 cm^{-1}) can be assigned to the asymmetric $\nu(C{\equiv}N)$ stretch of physisorbed deuterated acetonitrile.[54,70,72,73,84–86]

ssNMR analysis highlighted three distinct proton environments, which we assigned to extra-framework silanol groups (2.04 ppm), extra-framework aluminium species (2.50 ppm) and Brønsted acid sites (BAS) in the framework (4.27 ppm).[22–25] Peak association was achieved following peak deconvolution of the acquired ^{1}H ssNMR spectrum and acquisition of a ^{1}H–^{27}Al REAPDOR NMR difference spectrum. ^{27}Al ssNMR spectrum for calcined H,K(0.23)/CHA(20) contained two distinct aluminium environments, with tetrahedral aluminium (T_d) (55.9 ppm) and octahedral aluminium (O_h) (−0.3 ppm) present with a ratio of 100 : 1.4.[22,74] A second T_d aluminium environment was observed (51.4 ppm) indicating the presence of defect sites, whilst no pentacoordinated aluminium was present.[75,76] ^{29}Si ssNMR indicated that silicon in the framework primarily resided in the Q^4 environment, whilst CP experiments highlighted the presence of Q^2, Q^3 and $Q^4(1Al)$ environments.[80] Surface area was calculated using BET theory (682 m^2/g), noted to be a relatively high surface area in comparison with surface areas reported by Liu *(*537 – 569 m^2/g) and Lillerud (463 – 702 m^2/g) for their chabazite materials.[81–83]

5.3 Chapter Five Bibliography

1 A. Dyer and M. Zubair, *Microporous Mesoporous Mater.*, Ion-exchange in chabazite, 1998, **22**, 135–150.

2 R. P. Townsend and E. N. Coker, in *Introduction to Zeolite Science and Practice*, eds. H. van Bekkum, E. M. Flanigen, P. A. Jacobs and J. Jansen, Elsevier, 2001, vol. 137, pp. 467–524.

3 V. Valtchev, G. Majano, S. Mintova and J. Perez-Ramirez, *Chem. Soc. Rev.*, Tailored crystalline microporous materials by post-synthesis modification, 2013, **42**, 263–290.

4 S. Miao, Y. Wang, D. Ma, Q. Zhu, S. Zhou, L. Su, D. Tan and X. Bao, *J. Phys. Chem. B*, Effect of Ag^+ Cations on Nonoxidative Activation of Methane to C2-Hydrocarbons, 2004, **108**, 17866–17871.

5 M. V Luzgin, V. A. Rogov, S. S. Arzumanov, A. V Toktarev, A. G. Stepanov and V. N. Parmon, *Angew. Chem., Int. Ed.*, Understanding methane aromatization on a Zn-modified high-silica zeolite, 2008, **47**, 4559–4562.

6 Q. Zhang, S. Gao and J. Yu, *Chem. Rev.*, Metal Sites in Zeolites: Synthesis, Characterization, and Catalysis, 2023, **123**, 6039–6106.

7 N. Kosinov, C. Liu, E. J. M. Hensen and E. A. Pidko, *Chem. Mater.*, Engineering of Transition Metal Catalysts Confined in Zeolites, 2018, **30**, 3177–3198.

8 H. Wang, L. Wang and F.-S. Xiao, *ACS Cent. Sci.*, Metal@Zeolite Hybrid Materials for Catalysis, 2020, **6**, 1685–1697.

9 P. Chu and F. G. Dwyer, in *Intrazeolite Chemistry*, American Chemical Society, 1983, vol. 218, pp. 4–59.

10 J. Texter, R. Kellerman and T. Gonsiorowski, *J. Phys. Chem.*, Formation of charged silver clusters and their reversible silver ion desorption in zeolite A, 1986, **90**, 2118–2124.

11 T. Sun and K. Seff, *Chem. Rev.*, Silver Clusters and Chemistry in Zeolites, 1994, **94**, 857–870.

12 T. Baba, N. Komatsu, H. Sawada, Y. Yamaguchi, T. Takahashi, H. Sugisawa and Y. Ono, *Langmuir*, H-1 magic angle spinning NMR evidence for dissociative adsorption of hydrogen on Ag^+-exchanged A- and Y-zeolites, 1999, **15**, 7894–7896.

13 R. Seifert, R. Rytz and G. Calzaferri, *J. Phys. Chem. A*, Colors of Ag^+-Exchanged Zeolite A, 2000, **104**, 7473–7483.

14 T. Baba, H. Sawada, T. Takahashi and M. Abe, *Appl. Catal. a-General*, Chemisorption study of hydrogen and methane by H-1 MAS NMR and conversion of methane in the presence of ethylene on Ag-Y zeolite, 2002, **231**, 55–63.

15 O. Fenwick, E. Coutino-Gonzalez, D. Grandjean, W. Baekelant, F. Richard, S. Bonacchi, D. De Vos, P. Lievens, M. Roeffaers, J. Hofkens and P. Samori, *Nat. Mater.*, Tuning the energetics and tailoring the optical properties of silver clusters confined in zeolites, 2016, **15**, 1017–1022.

16 A.-S. Feiner and A. J. McEvoy, *J. Chem. Educ.*, The Nernst Equation, 1994, **71**, 493.

17 N. H. Heo, Y. Kim, J. J. Kim and K. Seff, *J. Phys. Chem. C*, Surprising Intrazeolitic Chemistry of Silver, 2016, **120**, 5277–5287.

18 G. De Cremer, E. Coutino-Gonzalez, M. B. J. Roeffaers, B. Moens, J. Ollevier, M. Van der Auweraer, R. Schoonheydt, P. A. Jacobs, F. C. De Schryver, J. Hofkens, D. E. De Vos, B. F. Sels and T. Vosch, *J. Am. Chem. Soc.*, Characterization of

Fluorescence in Heat-Treated Silver-Exchanged Zeolites, 2009, **131**, 3049–3056.

19 T. Ikeda, T. Kodaira, F. Izumi, T. Kamiyama and K. Ohshima, *Chem. Phys. Lett.*, Neutron powder diffraction study of potassium clusters in zeolite K-LTA, 2000, **318**, 93–101.

20 T. Nakano, S. Araki, N. Hoang Nam, T. Umemoto, K. Tsuchihashi, Y. Kubo, A. Owaki and Y. Nozue, *Soft Condens. Matter*, Origin of magnetic moments and ferromagnetic properties of potassium clusters in zeolite A, 2020, arXiv:2009.04828.

21 M. Wu, W. Lv, Y. Zhang, Y. Yang, Z. Wang, K. Qiu, Y. Shi, B. Zhao and C. Ge, *J. Nucl. Mater.*, Potassium clusters in tungsten grain boundaries: Formation mechanism and strengthening effect, 2023, **573**, 154135.

22 S. Li and F. Deng, in *Zeolites in Sustainable Chemistry: Synthesis, Characterization and Catalytic Applications*, eds. F.-S. Xiao and X. Meng, Springer, Berlin, Heidelberg, 2016, pp. 231–268.

23 H. Koller, R. F. Lobo, S. L. Burkett and M. E. Davis, *J. Phys. Chem.*, SiO-...HOSi Hydrogen Bonds in As-Synthesized High-Silica Zeolites, 1995, **99**, 12588–12596.

24 X. Zhao, J. Xu and F. Deng, *Front. Chem. Sci. Eng.*, Solid-state NMR for metal-containing zeolites: From active sites to reaction mechanism, 2020, Ahead of Print.

25 M. Dyballa, K. Thorshaug, D. K. Pappas, E. Borfecchia, K. Kvande, S. Bordiga, G. Berlier, A. Lazzarini, U. Olsbye, P. Beato, S. Svelle and B. Arstad, *ChemCatChem*, Zeolite Surface Methoxy Groups as Key Intermediates in the Stepwise Conversion of Methane to Methanol, 2019, **11**, 5022–5026.

26 S. S. Arzumanov, D. I. Kolokolov, D. Freude and A. G. Stepanov, *J. Phys. Chem. C*, Methane Mobility in Ag/H-ZSM-5 Zeolite in the Presence of Ethene: A View Based on PFG H-1 MAS NMR Analysis of Methane Diffusivity, 2015, **119**, 18481–18486.

27 P. A. Jacobs, J. B. Uytterhoeven and H. K. Beyer, *J. Chem. Soc. Faraday Trans. 1 Phys. Chem. Condens. Phases*, Redox behaviour of transition metal ions in zeolites. Part 6.—Reversibility of the reduction reaction in silver zeolites, 1977, **73**, 1755–1762.

28 P. A. Jacobs, J. B. Uytterhoeven and H. K. Beyer, *J. Chem. Soc. Faraday Trans. 1 Phys. Chem. Condens. Phases*, Some unusual properties of activated and reduced AgNaA zeolites, 1979, **75**, 56–64.

29 M. Lamoth, T. Jones, M. Plodinec, A. Machoke, S. Wrabetz, M. Krämer, A. Karpov, F. Rosowski, S. Piccinin, R. Schlögl and E. Frei, *ChemCatChem*, Nanocatalysts Unravel the Selective State of Ag, 2020, **12**, 2977–2988.

30 H. V Doan, K. M. Leung, V. P. Ting and A. Sartbaeva, *CrystEngComm*, Effect of mono- and divalent extra-framework cations on the structure and accessibility of porosity in chabazite zeolites, 2021, **23**, 857–863.

31 S. Zhang, L. Pang, Z. Chen, S. Ming, Y. Dong, Q. Liu, P. Liu, W. Cai and T. Li, *Appl. Catal. A Gen.*, Cu/SSZ-13 and Cu/SAPO-34 catalysts for deNOx in diesel exhaust: Current status, challenges, and future perspectives, 2020, **607**, 117855.

32 U. Deka, I. Lezcano-Gonzalez, S. J. Warrender, A. Lorena Picone, P. A. Wright, B. M. Weckhuysen and A. M. Beale, *Microporous Mesoporous Mater.*, Changing active sites in Cu–CHA catalysts: deNOx selectivity as a function of the preparation method, 2013, **166**, 144–152.

33 J. Zhang, J. Liang, H. Peng, Y. Mi, P. Luo, H. Xu, M. He and P. Wu, *Appl. Catal. B Environ.*, Cost-effective fast-synthesis of chabazite zeolites for the reduction of NOx, 2021, **292**, 120163.

34 E. M. Flanigen, R. W. Broach and S. T. Wilson, in *Zeolites in Industrial Separation and Catalysis*, 2010, pp. 1–26.

35 S. Prodinger, R. S. Vemuri, T. Varga, B. Peter McGrail, R. K. Motkuri and M. A. Derewinski, *New J. Chem.*, Impact of chabazite SSZ-13 textural properties and chemical composition on CO2 adsorption applications, 2016, **40**, 4375–4385.

36 S. A. Gomez, A. Campero, A. Martinez-Hernandez and G. A. Fuentes, *Appl. Catal. A Gen.*, Changes in Cu^{2+} environment upon wet deactivation of Cu-ZSM-5 deNOx catalysts, 2000, **197**, 157–164.

37 K. H. Møller, M. Debost, L. Lakiss, S. Kegnaes and S. Mintova, *RSC Adv.*, Interzeolite conversion of a micronsized FAU to a nanosized CHA zeolite free of organic structure directing agent with a high CO2 capacity, 2020, **10**, 42953–42959.

38 L. V Dang, S. T. Le, R. F. Lobo and T. D. Pham, *J. Porous Mater.*, Hydrothermal synthesis of alkali-free chabazite zeolites, 2020, **27**, 1481–1489.

39 J. Devos, M. L. Bols, D. Plessers, C. Van Goethem, J. W. Seo, S.-J. Hwang, B. F. Sels and M. Dusselier, *Chem. Mater.*, Synthesis–Structure–Activity Relations in Fe-CHA for C–H Activation: Control of Al Distribution by Interzeolite Conversion, 2020, **32**, 273–285.

40 A. Ebadi Amooghin, H. Sanaeepur, M. Omidkhah and A. Kargari, *J. Mater. Chem. A*, “Ship-in-a-bottle”, a new synthesis strategy for preparing novel hybrid host–guest nanocomposites for highly selective membrane gas separation, 2018, **6**, 1751–1771.

41 L. Dong, D. Hu, Y. Wang, Z. Sheng, M. Hong and S. Yang, *Nanoscale Adv.*, A zeolite-based ship-in-a-bottle route to ultrasmall carbon dots for live cell labeling and bioimaging, 2020, **2**, 5803–5809.

42 C. S. Cundy and P. A. Cox, *Microporous Mesoporous Mater.*, The hydrothermal synthesis of zeolites: Precursors, intermediates and reaction mechanism, 2005, **82**, 1–78.

43 J. Dedecek, Z. Sobalik and B. Wichterlová, *Catal. Rev.*, Siting and Distribution of Framework Aluminium Atoms in Silicon-Rich Zeolites and Impact on Catalysis, 2012, **54**, 135–223.

44 S. Goel, S. I. Zones and E. Iglesia, *Chem. Mater.*, Synthesis of Zeolites via Interzeolite Transformations without Organic Structure-Directing Agents, 2015, **27**, 2056–2066.

45 J. Zhu, Z. D. Liu, A. Endo, Y. Yanaba, T. Yoshikawa, T. Wakihara and T. Okubo, *Crystengcomm*, Ultrafast, OSDA-free synthesis of mordenite zeolite, 2017, **19**, 632–640.

46 M. Dusselier and M. E. Davis, *Chem. Rev.*, Small-Pore Zeolites: Synthesis and Catalysis, 2018, **118**, 5265–5329.

47 S. I. Zones, K. Jayanthi, J. Pascual, D. Xie and A. Navrotsky, *Chem. Mater.*, Energetics of the Local Environment of Structure-Directing Agents Influence Zeolite Synthesis, 2021, **33**, 2126–2138.

48 P. M. Piccione, S. Yang, A. Navrotsky and M. E. Davis, *J. Phys. Chem. B*, Thermodynamics of Pure-Silica Molecular Sieve Synthesis, 2002, **106**, 3629–3638.

49 A. Jackowski, S. I. Zones, K. Chaudhuri, H. S. Lacheen and S. W. Yeh, *Microporous Mesoporous Mater.*, A hydrothermal synthesis of a 2-dimensional layered silicate followed by a transition to a 3-dimensional aluminosilicate zeolite, 2014, **197**, 33–39.

50 S. Li, J. Li, M. Dong, S. Fan, T. Zhao, J. Wang and W. Fan, *Chem. Soc. Rev.*,

Strategies to control zeolite particle morphology, 2019, **48**, 885–907.

51 D. Vuono, L. Pasqua, F. Testa, R. Aiello, A. Fonseca, T. I. Koranyi and J. B. Nagy, *Microporous Mesoporous Mater.*, Influence of NaOH and KOH on the synthesis of MCM-22 and MCM-49 zeolites, 2006, **97**, 78–87.

52 C. Liu, W. Gu, D. Kong and H. Guo, *Microporous Mesoporous Mater.*, The significant effects of the alkali-metal cations on ZSM-5 zeolite synthesis: From mechanism to morphology, 2014, **183**, 30–36.

53 N. Koike, K. Iyoki, S. H. Keoh, W. Chaikittisilp and T. Okubo, *Chem. – A Eur. J.*, Synthesis of New Microporous Zincosilicates with CHA Zeolite Topology as Efficient Platforms for Ion-Exchange of Divalent Cations, 2018, **24**, 808–812.

54 Y. Yuan and R. F. Lobo, *Chem. Sci.*, Propane dehydrogenation over extra-framework $In^{(I)}$ in chabazite zeolites, 2022, **13**, 2954–2964.

55 A. Deneyer, Q. Ke, J. Devos and M. Dusselier, *Chem. Mater.*, Zeolite Synthesis under Nonconventional Conditions: Reagents, Reactors, and Modi Operandi, 2020, **32**, 4884–4919.

56 B. Ipek and R. F. Lobo, *Chem. Commun.*, Catalytic conversion of methane to methanol on Cu-SSZ-13 using N_2O as oxidant, 2016, **52**, 13401–13404.

57 C. Baerlocher and L. B. McCusker, in *Advanced Zeolite Science and Applications*, eds. J. C. Jansen, M. Stöcker, H. G. Karge and J. Weitkamp, Elsevier, 1994, vol. 85, pp. 391–428.

58 M. Lemishka, J. Dedecek, K. Mlekodaj, Z. Sobalik, S. Sklenak and E. Tabor, *Pure Appl. Chem.*, Speciation and siting of divalent transition metal ions in silicon-rich zeolites. An FTIR study:, 2019, **91**, 1721–1732.

59 V. Zholobenko, C. Freitas, M. Jendrlin, P. Bazin, A. Travert and F. Thibault-Starzyk, *J. Catal.*, Probing the acid sites of zeolites with pyridine: Quantitative AGIR measurements of the molar absorption coefficients, 2020, **385**, 52–60.

60 S. Bordiga, C. Lamberti, F. Bonino, A. Travert and F. Thibault-Starzyk, *Chem. Soc. Rev.*, Probing zeolites by vibrational spectroscopies, 2015, **44**, 7262–7341.

61 A. S. Medin, V. Y. Borovkov, V. B. Kazansky, A. G. Pelmentschikov and G. M. Zhidomirov, *Zeolites*, On the unusual mechanism of Lewis acidity manifestation in HZSM-5 zeolites, 1990, **10**, 668–673.

62 G. P. Heitmann, G. Dahlhoff, J. P. M. Niederer and W. F. Hölderich, *J. Catal.*, Active Sites of a [B]-ZSM-5 Zeolite Catalyst for the Beckmann Rearrangement of Cyclohexanone Oxime to Caprolactam, 2000, **194**, 122–129.

63 V. Bolis, C. Busco, S. Bordiga, P. Ugliengo, C. Lamberti and A. Zecchina, *Appl. Surf. Sci.*, Calorimetric and IR spectroscopic study of the interaction of NH3 with variously prepared defective silicalites: Comparison with ab initio computational data, 2002, **196**, 56–70.

64 P. Bräuer, O. Situmorang, P. L. Ng and C. D'Agostino, *Phys. Chem. Chem. Phys.*, Effect of Al content on the strength of terminal silanol species in ZSM-5 zeolite catalysts: a quantitative DRIFTS study without the use of molar extinction coefficients, 2018, **20**, 4250–4262.

65 G. N. Vayssilov, H. A. Aleksandrov, E. Dib, I. M. Costa, N. Nesterenko and S. Mintova, *Microporous Mesoporous Mater.*, Superacidity and spectral signatures of hydroxyl groups in zeolites, 2022, **343**, 112144.

66 E. Dib, I. M. Costa, G. N. Vayssilov, H. A. Aleksandrov and S. Mintova, *J. Mater. Chem. A*, Complex H-bonded silanol network in zeolites revealed by IR and NMR spectroscopy combined with DFT calculations, 2021, **9**, 27347–27352.

67 P. G. Rouxhet and R. E. Sempels, *J. Chem. Soc. Faraday Trans. 1 Phys. Chem.*

Condens. Phases, Hydrogen bond strengths and acidities of hydroxyl groups on silica–alumina surfaces and in molecules in solution, 1974, **70**, 2021–2032.

68 R. E. Sempels and P. G. Rouxhet, *J. Colloid Interface Sci.*, Infrared study of the adsorption of benzene and acetonitrile on silica—alumina gels: Acidity properties and surface heterogeneity, 1976, **55**, 263–273.

69 P. O. Scokart, F. D. Declerck, R. E. Sempels and P. G. Rouxhet, *J. Chem. Soc. Faraday Trans. 1 Phys. Chem. Condens. Phases*, Evolution of the acidic properties of silica— alumina gels as a function of chemical composition: infrared approach, 1977, **73**, 359–371.

70 A. G. Pelmenschikov, R. A. van Santen, J. Janchen and E. Meijer, *J. Phys. Chem.*, Acetonitrile-d_3 as a probe of Lewis and Broensted acidity of zeolites, 1993, **97**, 11071–11074.

71 D. Pietrogiacomi, M. C. Campa and V. Indovina, *J. Phys. Chem. C*, Location of Isolated Co^{2+} and $[Co{-}O{-}Co]^{2+}$ in Co-MOR as Investigated by Means of FTIR with Acetonitrile and 2,4,5-Trimethylbenzonitrile as Probe Molecules, 2010, **114**, 17812–17818.

72 C. Pazé, A. Zecchina, S. Spera, G. Spano and F. Rivetti, *Phys. Chem. Chem. Phys.*, Acetonitrile as probe molecule for an integrated 1H NMR and FTIR study of zeolitic Brønsted acidity: Interaction with zeolites H-ferrierite and H-beta, 2000, **2**, 5756–5760.

73 T. Sumi, S. Kokuryo, Y. Fujimoto, X. Li, K. Miyake, Y. Uchida and N. Nishiyama, *Catal. Sci. Technol.*, Mg and Zn co-doped mesoporous ZSM-5 as an ideal catalyst for ethane dehydroaromatization reaction, 2022, **12**, 7010–7017.

74 A. G. Stepanov, in *Zeolites and Zeolite-Like Materials*, eds. B. F. Sels and L. Kustov, Elsevier, Amsterdam, 2016, pp. 137–188.

75 M. Ravi, V. L. Sushkevich and J. A. van Bokhoven, *Chem. Sci.*, On the location of Lewis acidic aluminum in zeolite mordenite and the role of framework-associated aluminum in mediating the switch between Brønsted and Lewis acidity, 2021, **12**, 4094–4103.

76 J.-P. Gilson, G. C. Edwards, A. W. Peters, K. Rajagopalan, R. F. Wormsbecher, T. G. Roberie and M. P. Shatlock, *J. Chem. Soc. Chem. Commun.*, Penta-co-ordinated aluminium in zeolites and aluminosilicates, 1987, 91–92.

77 S. Li, A. Zheng, Y. Su, H. Fang, W. Shen, Z. Yu, L. Chen and F. Deng, *Phys. Chem. Chem. Phys.*, Extra-framework aluminium species in hydrated faujasite zeolite as investigated by two-dimensional solid-state NMR spectroscopy and theoretical calculations, 2010, **12**, 3895–3903.

78 P. Paluch, N. Potrzebowska, A. M. Ruppert and M. J. Potrzebowski, *Solid State Nucl. Magn. Reson.*, Application of 1H and 27Al magic angle spinning solid state NMR at 60kHz for studies of Au and Au-Ni catalysts supported on boehmite/alumina, 2017, **84**, 111–117.

79 F. Göltl, A. M. Love, S. C. Schuenzel, P. Wolf, M. Mavrikakis and I. Hermans, *Phys. Chem. Chem. Phys.*, Computational description of key spectroscopic features of zeolite SSZ-13, 2019, **21**, 19065–19075.

80 D. E. Akporiaye, I. M. Dahl, H. B. Mostad and R. Wendelbo, *J. Phys. Chem.*, Aluminum Distribution in Chabazite: An Experimental and Computational Study, 1996, **100**, 4148–4153.

81 Z. Bohström and K. P. Lillerud, *Microporous Mesoporous Mater.*, Preparation of chabazite with mesopores templated from a cationic polymer, 2018, **271**, 295–300.

82 B. Liu, Y. Zheng, N. Hu, T. Gui, Y. Li, F. Zhang, R. Zhou, X. Chen and H. Kita,

Microporous Mesoporous Mater., Synthesis of low-silica CHA zeolite chabazite in fluoride media without organic structural directing agents and zeolites, 2014, **196**, 270–276.

83 B. Liu, R. Zhou, K. Yogo and H. Kita, *J. Memb. Sci.*, Preparation of CHA zeolite (chabazite) crystals and membranes without organic structural directing agents for CO2 separation, 2019, **573**, 333–343.

84 B. Wichterlová, Z. Tvarůzková, Z. Sobalik and P. Sarv, *Microporous Mesoporous Mater.*, Determination and properties of acid sites in H-ferrierite: A comparison of ferrierite and MFI structures, 1998, **24**, 223–233.

85 A. Vimont, J. Lavalley, A. Sahibed-Dine, C. Arean, M. Delgado and M. Daturi, *J. Phys. Chem. B*, Infrared Spectroscopic Study on the Surface Properties of γ-Gallium Oxide as Compared to Those of γ-Alumina, 2005, **109**, 9656–9664.

86 N. Koike, W. Chaikittisilp, K. Iyoki, Y. Yanaba, T. Yoshikawa, S. P. Elangovan, K. Itabashi and T. Okubo, *Dalt. Trans.*, Organic-free synthesis of zincoaluminosilicate zeolites from homogeneous gels prepared by a co-precipitation method, 2017, **46**, 10837–10846.

Chapter Six – Hydrothermal Synthesis of Zincosilicates and Subsequent Silver Ion-exchange

Whilst no work from this thesis has been included, a publication has been prepared for submission on zincosilicate MFI materials. The paper concerns ZnMFI materials that are discussed and compared to the ZnCHA materials hydrothermally synthesised in this project. Publication details:

- I. R. Mazzei, D. C. Apperley, R. Kerrigan and R. A. Taylor, Analysis of Framework Defect Sites in Zn-substituted MFI Zeotypes by Solid-state NMR and Diffuse Reflectance IR Spectroscopies, tbd.

6.1 Hydrothermal Synthesis and Characterisation of Zincosilicate CHA

Zeolites of the chabazite topology (CHA) are some of the most widely used throughout industry, owing to their excellent thermal stability and resistance to steaming.[1,2] As a result, chabazite materials are typically found in applications such as emission control, particularly deNOx selective catalytic reduction (SCR) for the automotive industry.[1,3–6] The catalysts used in these applications are tuned to have a specific composition through targeted hydrothermal synthesis or post-synthetic modifications, maximising their performance for the desired application.[7–11] As outlined in Section 2.2.1, chabazite is a small-pore three-dimensional framework topology consisting of CHA cages connected by channel openings with accessible dimensions of 3.8 Å by 3.8 Å shown in Figure 6.1. The 8MR channel openings can however lead to a restricted rate of diffusion through the micropores, stopping bulkier molecules from freely diffusing through or out of the micropores completely.

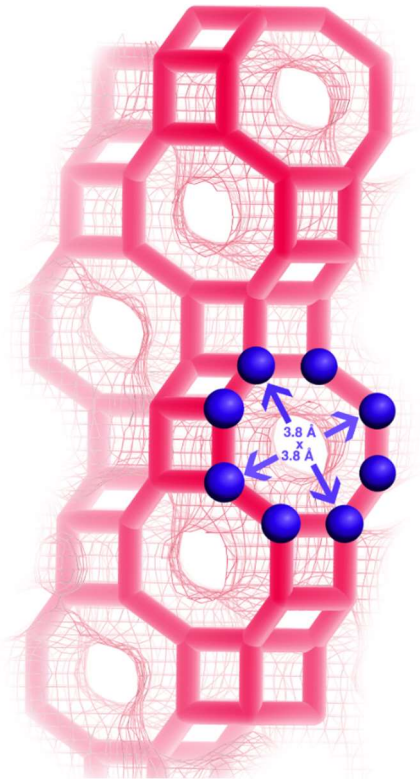

Figure 6.1: Graphic showing the CHA framework topology, with the channel structure depicted using a mesh surface. Symmetrical channel openings connect the CHA cages of the framework and have accessible dimensions of 3.8 Å by 3.8 Å. The synthesis and characterisation of a zincosilicate material was undertaken in this project.

The presence of strong Brønsted acid sites (BAS) facilitates the dehydration of alcohols to alkenes, with the exception of methanol to dimethyl ether.[12–15] Lewis acid sites instead catalyse the dehydrogenation pathway of alcohols, to produce aldehydes.[16] Lewis acidity in zeolites arises from extra-framework moieties, typically extra-framework aluminium species present at channel intersections, channel walls and on the surface.[17] Zincosilicates on the other hand contain Zn^{2+} in place of Al^{3+} within the framework, inherently giving the material Lewis acidity at these sites.[18] However, this opens up the possibility of having potentially several different coordination environments around the Zn^{2+} centres in the framework, as shown in Figure 6.2.

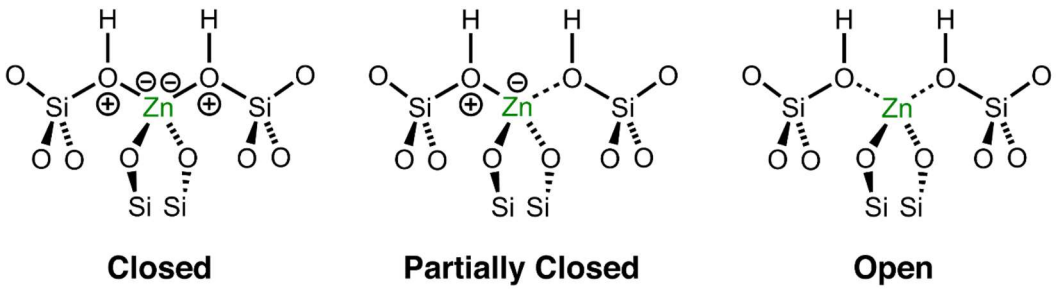

Figure 6.2: Simplified graphic displaying potential coordination environments observed for Zn(II) when incorporated into the framework positions.

For the partially closed configuration, a negative charge centred on the T atom requires the presence of a singly charged cation to restore an overall net neutral charge to the framework. For the closed configuration, a doubly charged cation or two singly charged cations are required for charge neutrality. In addition, it is likely the differing coordination environments shown in Figure 6.2 will impact the reactivity of the M^{2+} species incorporated into the framework. Incorporation of a double negative charge in the framework, should give zeotypes more facile ion-exchange of multivalent cations than their zeolite counterparts.[19]

Davis reported that zincosilicate BEA (CIT-6) was capable of containing multiple distinct zinc environments.[18] Whilst one zinc environment was determined to be in the closed configuration and counterbalanced by two lithium cations, the second zinc was in an open configuration. For the open configuration, zinc was bound to two framework atoms whilst also establishing two dative bonds to two more adjacent framework atoms. It was established that these dative interactions were not strong enough to induce Brønsted acidity to the neighbouring −Si−O(H) groups, determined by the lack of pyridine protonation during DRIFTS spectroscopy.

Therefore, we set out to adapt a bottom-up hydrothermal synthesis method from reported procedures to produce zincosilicate CHA materials, which afforded those used in this project. However, in order to generate a sufficient quantity of material, a reliable hydrothermal synthesis method was required. One important factor of hydrothermal synthesis was to generate zincosilicate CHA with minimal variation in composition between batches. Therefore, we undertook the development of a reliable hydrothermal synthesis method and calcination method. Numerous iterative changes were made, taking inspiration from prior art and from the observations made during zincosilicate chabazite synthesis, outlined in section 6.1.1.

6.1.1 Hydrothermal Synthesis of Zincosilicate Chabazite

During the project, the development of a successful hydrothermal synthesis method for zincosilicate chabazite was achieved following several iterative changes to a hydrothermal synthesis originally reported by Okubo.[20] In parallel with zeolite (aluminosilicate) chabazite synthesis, detailed in Chapter 5.2, the adaptations trialled took into account the effects of changing the duration, temperature, SDA, use of a seed, choice of mineralising agent, gel pH and the silicon to zinc ratio in the gel, all factors for which hydrothermal synthesis of zeolites and related zeotypes are sensitive to.[21–25]

Initial hydrothermal synthesis of zincosilicate CHA materials led to the isolation of amorphous materials, often dark grey in appearance, sometimes directly from hydrothermal synthesis but sometimes as a result of calcination. It was noted that Okubo often did not calcine materials they produced following synthesis.[20] As a result, the following iterative changes were made to the hydrothermal synthesis method reported by Okubo, to derive our own hydrothermal synthesis method:

- Use of sodium hydroxide as the mineralising agent, in place of lithium hydroxide.
- Increased mixing times for gel mixtures to 1 hour each. Synthesis gel was aged for 1 hour at ambient temperature. This is an increase from the original method with 5-minute durations for each.
- Seeding synthesis gel mixture loaded to autoclaves with zeolite CHA material.
- Increased mixing times for gel mixtures to 2 hours for each, before aging the synthesis gel at 40 °C for 24 hours. This produced a clear, free-flowing gel.
- Zinc acetate as the zinc source, in place of zinc chloride.
- Potassium hydroxide as the mineralising agent, in place of lithium hydroxide.
- Increased zinc content of the synthesis gel, making the ratio of silicon to zinc in the gel 14 rather than 28 previously.
- Trialled hydrothermal synthesis at 160 °C instead of 150 °C.
- Ludox AS-40 as the colloidal silica source in place of Ludox HS-40.
- Trialled the use of 600 RPM stirring during hydrothermal synthesis, in place of static conditions. (This was to match the hydrothermal parameters used in the aluminosilicate CHA synthesis method reported by Dusselier.[11])
- Increased hydrothermal synthesis time to 7 days rather than 5 days.
- Shortened calcination time to 10 hours and reduced calcination temperature to 550 °C, from 24 hours at 600 °C.

Initial calcinations did not use the additional step of heating to 90°C and holding for 1 hour. Instead, the calcination process was identical to the profile used for zeolite chabazite, heating to 150 °C and 550 °C described in Section 5.2.1. Some of the initial batches of zincosilicate CHA material were noted to undergo total loss of crystallinity during calcination, as shown in Figure 6.3.

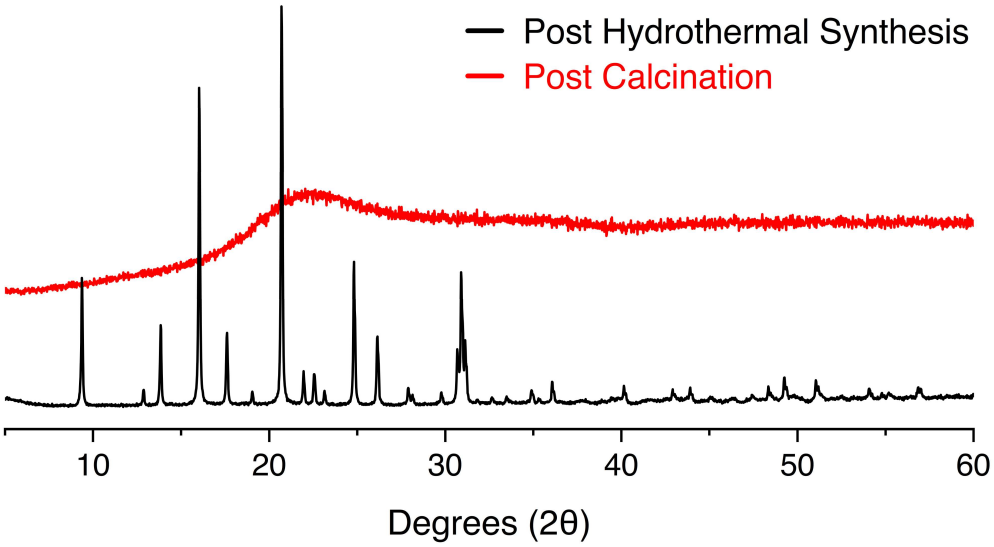

Figure 6.3: Stacked pXRD patterns for H,K(1.61)/ZnCHA(16) following an early attempt at hydrothermal synthesis and calcination, where the material underwent total loss of crystallinity.

This was often immediately evident by the colour change from a white powder to a grey powder, as shown in Figure 6.4. Okubo neglected to mention in the main body of the report for hydrothermal synthesis of zincosilicate CHA that calcination was only conducted 'if needed ' and only stated that it was carried out at 600 °C.[20]

Figure 6.4: Picture showing an early batch of hydrothermally synthesized zincosilicate CHA that underwent total loss of crystallinity following calcination.

The modifications which led to reliable ZnCHA hydrothermal synthesis included changing the mineralising agent (KOH replacing LiOH), where the retained potassium counterion could be observed by ED-XRF, ageing the synthesis gel for 24 hours rather than 5 minutes and stepwise calcination at a reduced temperature. These changes led

to a hydrothermal synthesis method that was not only reliable at producing crystalline materials but also with consistent elemental compositions.

Preparation of the synthesis gel was achieved by dissolving potassium hydroxide (510 mg) in 10 mL DI water at room temperature. To this mixture, Ludox HS-40 (16.02 g) was added dropwise over one hour using a pressure-equalising dropping funnel. After addition, the solution was heated to 40 °C with continued stirring overnight. A solution consisting of zinc acetate (473 mg) dissolved in tetramethyladamantium hydroxide (46.06 g, 20 wt%) was added dropwise over 15 minutes before allowing the gel to age 24 hours at 40 °C. The ageing process leads the gel to change from a thick, white cloudy gel to a fluid, clear gel. The synthesis gel was then transferred to a PTFE-lined autoclave with 20 mg ZnCHA seed added to each autoclave from a previous, successful batch. The autoclaves were heated to 150 °C for 7 days under static conditions, (contrasting with 600 RPM stirring used for CHA synthesis in section 5.2.1, influenced by the CHA synthesis method reported by Dusselier.[11]) A Graphic representation of the hydrothermal synthesis of zincosilicate chabazite is included in Figure 6.5.

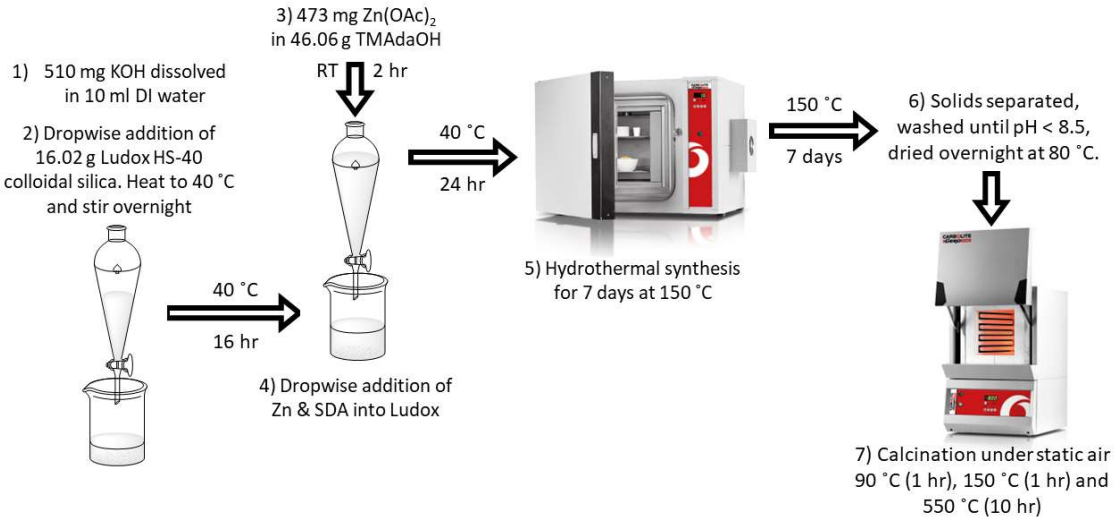

Figure 6.5: Graphic displaying the individual steps of hydrothermal synthesis for zincosilicate chabazite.

Determining the reliability of hydrothermal synthesis was key, with analysis conducted on each batch of zincosilicate chabazite. Initial analysis conducted was ED-XRF to determine the elemental composition of the newly hydrothermally synthesized material. Results are shown in Table 6.1.

Table 6.1: Table containing the ED-XRF results for zincosilicate chabazite synthesized using the final version of our developed hydrothermal synthesis method described above and shown in Figure 6.3.

Entry	Zn (wt%)	Si (wt%)	K (wt%)	Si / Zn ratio	K / Zn ratio
RK-2-81	5.77±0.11	26.35±0.42	2.12±0.05	10.63	0.61
RK-2-97	5.74 ± 0.07	28.60 ± 0.25	2.16 ± 0.04	11.59	0.58
RK-2-102	5.07±0.18	25.49±0.78	1.667±0.08	11.71	0.55
RK-2-103	4.14±0.09	21.40±0.78	1.03±0.03	12.03	0.42
RK-2-118(2)	7.30±0.05	38.64±0.12	2.97±0.01	12.23	0.68
RK-2-118(4)	7.05±0.05	37.15±0.43	3.55±0.01	12.26	0.84
RK-2-118(5)	7.81±0.14	39.86±0.61	5.10±0.08	11.88	1.09

6.2 Characterisation of Synthesized Zincosilicate CHA

Hydrothermally synthesized zincosilicate CHA materials were characterised using the same full suite of analytical techniques as their zeolite counterparts.

6.2.1 Powder X-ray Diffraction of Hydrothermally Synthesized Zincosilicate CHA

Powder X-Ray diffraction (pXRD) was used in the determination of material crystallinity, to identify the CHA topology and provide information on the zincosilicate crystal size based on the broadness of the reflections. Several iterative changes were made to the calcination profile. These included slowing the heating ramp rate from 5 °C/min to only 1 °C/min and adding an additional dwell upon heating at 90 °C. The final calcination profile was as follows:

- Heat to 90 °C, hold for 1 hour (ramp rate of 1 °C/min)
- Heat to 150 °C, hold for 1 hour (ramp rate of 1 °C/min)
- Heat to 550 °C, hold for 10 hours (ramp rate of 1 °C/min)

Following these changes, hydrothermal synthesis and calcination could be carried out to produce a ZnCHA material with a highly crystalline pXRD pattern, as shown in Figure 6.6.

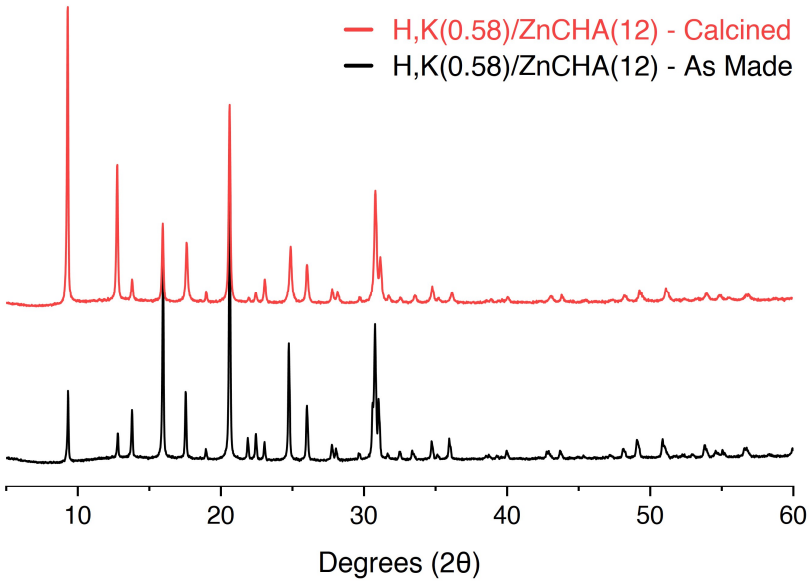

Figure 6.6: Stacked pXRD patterns for hydrothermally synthesised H,K(0.58)/ZnCHA(12) before and after calcination, showing that the material retains crystallinity following calcination under the revised method. Patterns are offset for clarity.

The revised hydrothermal synthesis method, outlined in Figure 6.5, facilitated the successful repeated generation of several batches of zincosilicate CHA materials. Following the preparation of five synthesis gels, hydrothermal synthesis and calcination were conducted using the same procedures, to produce calcined ZnCHA materials that displayed no observable long-range framework crystallinity loss in the acquired pXRD patterns, with good conformity between batches, as shown in Figure 6.7.

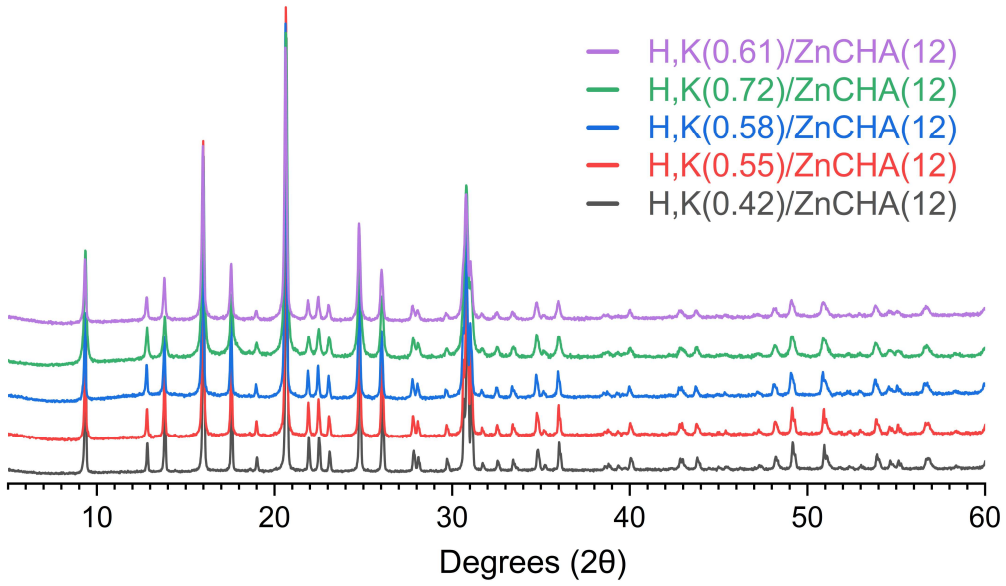

Figure 6.7: Stacked pXRD patterns of calcined zincosilicate CHA showing excellent conformity between repeated batches produced by hydrothermal synthesis. Patterns are offset for clarity.

6.2.2 FT-IR spectroscopy of Hydrothermally Synthesized Zincosilicate CHA

DRIFT spectroscopy was utilised to characterise bulk ZnCHA material and to gain information on the chemical environments present within the framework for both the protic and silver-exchanged forms. It is reported that FTIR spectroscopy provides information on metal siting and distribution in dehydrated metal-exchanged zeolites.[26,27] We applied DRIFTS spectroscopy to provide information on zinc speciation in zincosilicates by directly observing the perturbations of the framework Si−O−Zn bond stretching, whilst also using probe molecules to quantify and identify acid sites.[18,28] Probe molecules such as pyridine and deuterated acetonitrile were used in this project to determine the type of acid site and the acid site strength. DRIFTS was also used in the characterisation of spent catalysts, discussed in section 8.2.2.

The experimental procedure for the acquisition of DRIFTS spectra, using the equipment outlined in section 3.2.12, required ~75 mg of material loaded into the sample cup as a

fine powder on top of a fine mesh stainless steel gauze. The top of the sample was lightly pressed to flatten, before being loaded into a Harrick Scientific Praying Mantis cell. The cell was first evacuated to pressures lower than $1x10^{-2}$ mbar, before being heated using a thermal profile outlined in section 3.2.12, where the sample was heated to 500 °C for at least 2 hours and at a heating rate of 5 °C/min. The sample was then cooled at a natural rate to 25 °C, with the pressure in the cell typically reading below $1x10^{-4}$ mbar. This procedure removes any adsorbed atmospheric content and water from the micropores to give the spectrum of the dehydrated material.

Characterisation of H,K(0.58)/ZnCHA(12) was carried out, with the acquired DRIFTS spectrum stacked against that of H,K(0.23)/CHA(20), shown in Figure 6.8. Comparing the DRIFTS spectra for H,K(0.58)/ZnCHA(12) and H,K(0.23)/CHA(20) highlighted several changes in wavenumber values for several framework bands that arise due to the different T atoms incorporated into the framework (Al vs Zn).[29,30]

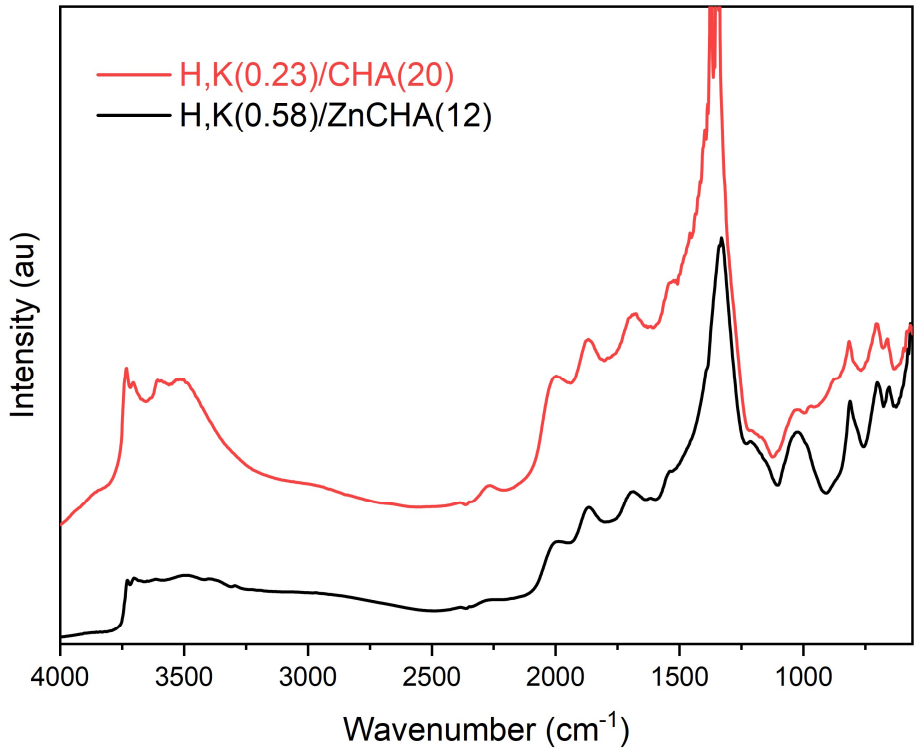

Figure 6.8: DRIFTS IR spectra for calcined H,K(0.58)/ZnCHA(12) and H,K(0.23)/CHA(20) highlight both the similarities and differences between the synthesized zeolite and zincosilicate CHA topology materials. Spectra are offset for clarity.

Symmetric vibrational modes for Si–O–T typically appear between 850 cm^{-1} and 650 cm^{-1} whilst asymmetric vibrational modes appear between 1250 cm^{-1} and

1000 cm^{-1}. Figure 6.9 highlights part of the framework region (1100 cm^{-1} to 520 cm^{-1}) of the stacked DRIFTS spectra of H,K(0.23)/CHA (20) and H,K(0.58)/ZnCHA (12). The labelled peaks display a notable shift to lower wavenumbers for several framework vibrational modes for ZnCHA, a reported observation for successful incorporation of heteroatoms into the framework.[31] The reduced wavenumbers arise from the changed Si–O–T bond length from incorporation of the zinc heteroatom.[29,32] The unlabelled band centred at 569 cm^{-1} corresponds to symmetric Si–O–Si vibrations in both zeolite and zincosilicate CHA materials, whilst the band centered at 1022 cm^{-1} corresponds to asymmetric Si–O–Si vibrations.

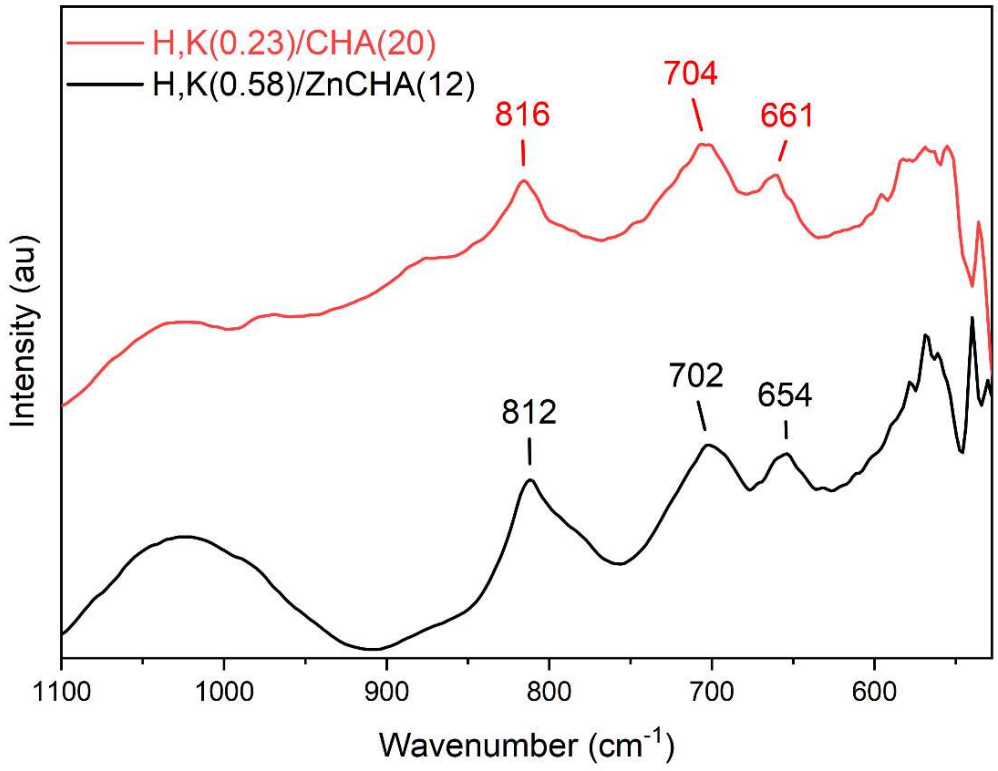

Figure 6.9: Stacked DRIFTS IR spectra highlighting differences in the framework vibrational mode region (1100 to 520 cm^{-1}) for H,K(0.58)/ZnCHA(12) and H,K(0.23)/CHA(20), showing differences between zeolite and zincosilicate chabazite materials. Spectra are offset for clarity.

In order to identify the acid sites present within the zincosilicate CHA framework, vapour phase adsorption of acetonitrile was carried out using deuterated acetonitrile (d_3-acetonitrile) on the vacuum system of the DRIFTS spectrometer. The deuterated form of acetonitrile was used to remove the undesirable Fermi resonances that occur when using acetonitrile, which obscure and alter the observed spectral features through peak broadening and a shift in wavenumber to give an inaccurate representation of the probed acid sites.[33] Dehydration was carried out as outlined previously, reaching a

pressure in the cell of less than $5x10^{-4}$ mbar at room temperature, before pressures of 0.1 – 12 mbar were achieved when exposing materials to d_3-acetonitrile vapour.

H,K(0.58)/ZnCHA(12) was exposed to d_3-acetonitrile at two different pressures at room temperature, which led to the observation of several new bands in the IR spectrum, shown in Figure 6.10. Prior art reports that coordination of deuterated acetonitrile to Lewis acid sites leads to band in the range of 2330 cm^{-1} to 2320cm^{-1} in zeolites.[34] Three distinct bands were observed in the DRIFTS spectrum of H,K(0.58)/ZnCHA(12) following dosing of CD_3CN into the sample cell. The band at 2303 cm^{-1} represents a ν(C≡N) stretch following coordination to Lewis acid zinc in the zincosilicate framework.[35] These bands appear at a lower wavenumber compared to those reported for H/FER(8.4) (2325 cm^{-1} and 2310 cm^{-1}),[36] ZnAPO-5 (2318 cm^{-1}),[37] and CIT-6 (2311 cm^{-1}).[18] The remaining two bands can be assigned to physisorbed deuterated acetonitrile, with the symmetric ν(C≡N) stretch at 2114 cm^{-1} and the asymmetric ν(C≡N) stretch at 2270 cm^{-1}.[34–36,38]

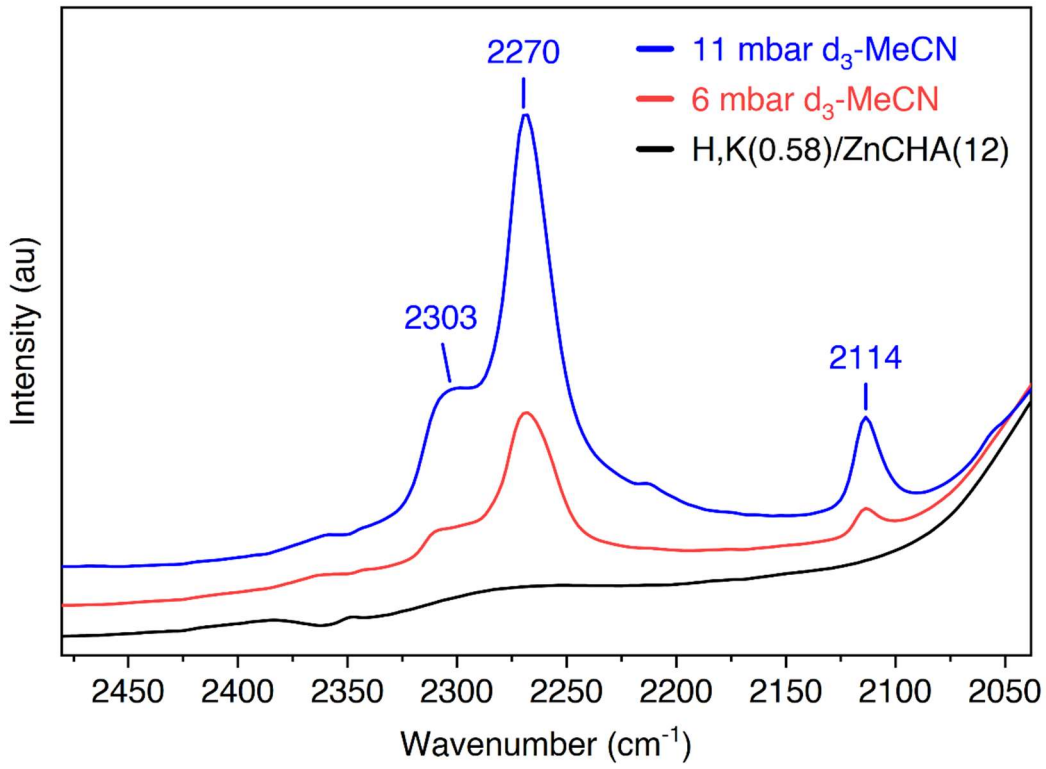

Figure 6.10: Stacked DRIFTS spectra for H,K(0.58)/ZnCHA(12) (black) highlighting the spectral region of 2500 – 2050 cm^{-1} after the introduction of d_3-acetonitrile as a probe molecule at pressures of 6 mbar (red) and 11 mbar (blue), highlighting the different Lewis acid sites present on the framework of the material.

Investigation of how strongly the bound deuterated acetonitrile was to the two distinct Lewis acid sites was achieved by applying both heat and reduced pressure. The initial spectrum was collected at 25 °C after evacuating the cell, with a pressure of $1x10^{-1}$ mbar, to minimise the volume of free d_3-acetonitrile. Heat was then applied, with the

material taken to a final temperature of 500 °C at a ramp rate of 10 °C/min, all whilst remaining at pressures lower than $1x10^{-1}$ mbar. The results are shown in Figure 6.11.

The band observed at 2303 cm^{-1} is associated to deuterated acetonitrile coordinated to Lewis acid sites.[35] Associated acetonitrile coordinated to Lewis acid sites on H,K(0.58)/ZnCHA(12) was observed at temperatures approaching 350 °C. However, the two bands for physisorbed deuterated acetonitrile,[34–36,38] asymmetric ν(C≡N) stretch observed at 2270 cm^{-1} remained visible at temperatures approaching 500 °C, whilst the symmetric stretch at 2114 cm^{-1} was observed at temperatures approaching 350 °C.

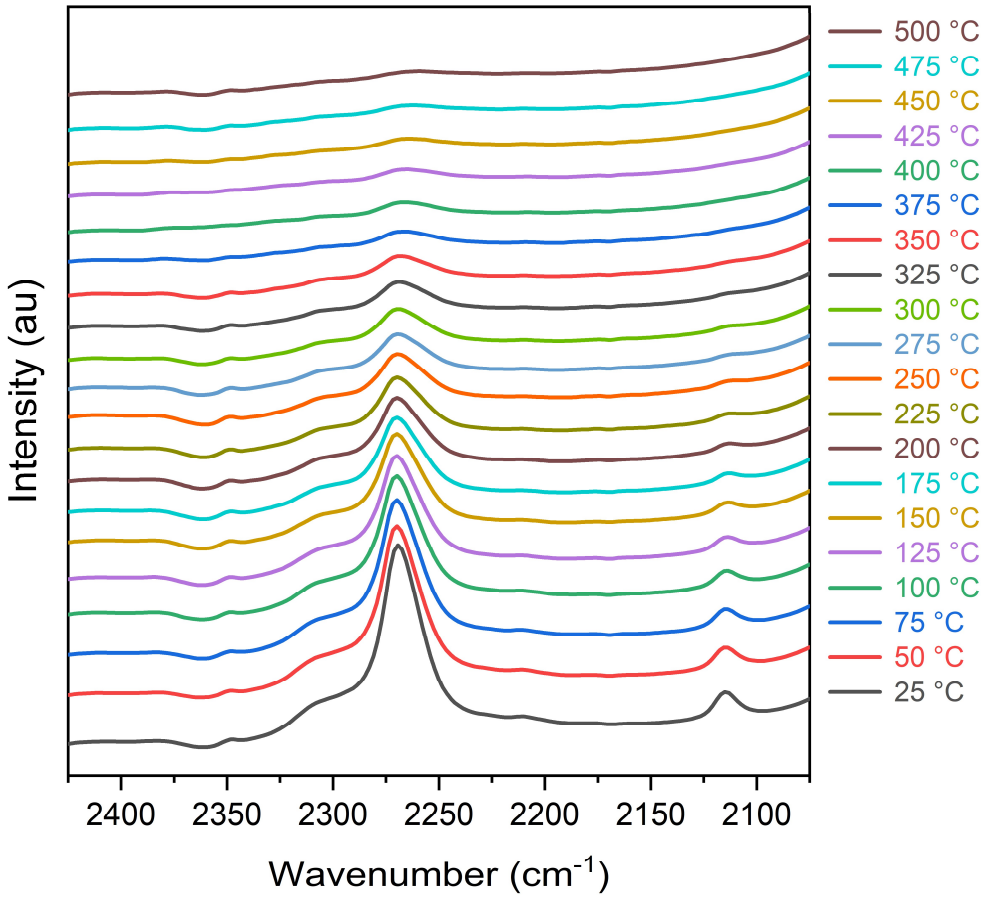

Figure 6.11: Stacked DRIFTS spectra for H,K(0.58)/ZnCHA(12) after exposure to 10 mbar d_3-Acetonitrile vapour, before evacuation of the cell to $1x10^{-1}$ mbar at 25 ˚C and the application of a heat ramp to 500 ˚C (ramp rate of 10 ˚C/min) whilst under reduced pressure.

Pyridine was also used as a probe molecule for DRIFTS spectroscopy to identify the type and strength of acid sites in zincosilicates.[18] Pyridine has a kinetic diameter of 5.7Å,[39] which was deemed too large to enter the small micropores of chabazite (3.8 Å by 3.8 Å). Whilst prior art suggests that minimum molecular diameter more accurately determines which molecules fit in zeolite micropores,[40] we attribute the observed bands

for pyridine to only external sites of the material. Exposing H,K(0.58)/ZnCHA(12) to 15 mbar of pyridine at 150 °C resulted in two low intensity bands centred at 1587 cm^{-1} and 1444 cm^{-1}, shown in Figure 6.12. Prior art reported that bands in this region are associated with hydrogen bonded pyridine to silanol nests (ca. 1575 cm^{-1}) and chemisorption to Lewis acid sites (1446 cm^{-1}).[18] Borgna *et al.* observed pyridine chemisorption to Lewis acid sites on MCM-22 and Zn-MWW at 1455 cm^{-1}, chemisorption to BAS at 1545 cm^{-1} and a third band at 1490 cm^{-1}, indicating adsorption to Lewis acid and BAS.[41] Bell *et al.* report identical assignments to Borgna, but observe four distinct bands over 0.36Zn/DeAlBEA (0.36 Zn:Al), showing several silanol nests were present on their framework.[42]

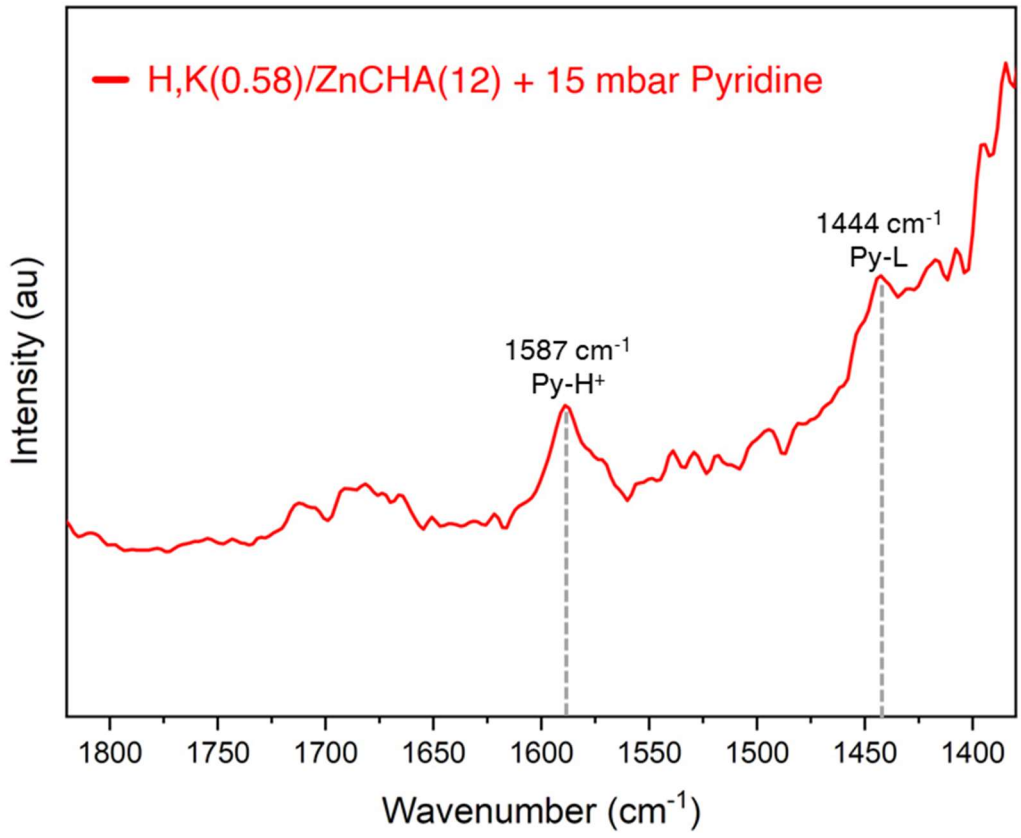

Figure 6.12: DRIFTS IR spectrum for H,K(0.58)/ZnCHA(12) exposed to 15 mbar of pyridine at 150 °C, containing a single band indicating the presence of surface Brønsted acid sites.

We could therefore conclude that the surface of H,K(0.58)/ZnCHA(12) contains BAS alongside Lewis acid sites in very low concentrations. These arise from undesirable extra-framework moieties and fully closed sites, shown in Figure 6.2. Given the low signal to noise only a low concentration of sites were observed, indicating these are located on the surface. Thew low intensity band for silanol nests in the DRIFTS spectrum

of H,K(0.58)/ZnCHA(12) corroborated with the very low concentration observed post adsorption of pyridine.

6.2.3 Solid-state MAS NMR of Hydrothermally Synthesized Zincosilicate CHA

Characterisation of hydrothermally synthesized zincosilicate CHA framework was carried out using solid-state NMR spectroscopy to observe the ^{1}H and ^{29}Si NMR environments present. NMR spectroscopic experiments ranged from single nuclei direct excitation and cross-polarisation experiments to multinuclear ^{1}H–^{29}Si HETCOR experiments to determine the local environment around some of the less common framework moieties that were observed. Experiments were carried out at room temperature using a 4 mm quartz rotor and a 10 kHz spin rate, although some experiments utilised changed parameters such as cooling to - 20 ˚C and the use of a 3.2 mm quartz rotor spun at 20 kHz. These changed experimental parameters were applied as an attempt to sharpen the linewidth of observed chemical shifts in the acquired spectra.

The ^{1}H MAS ssNMR spectrum acquired for H,K(0.58)/ZnCHA(12) contained several chemical shift environments, as shown in Figure 6.13. The material was calcined post hydrothermal synthesis and dehydrated under flowing nitrogen at 400 °C, prior to NMR analysis.

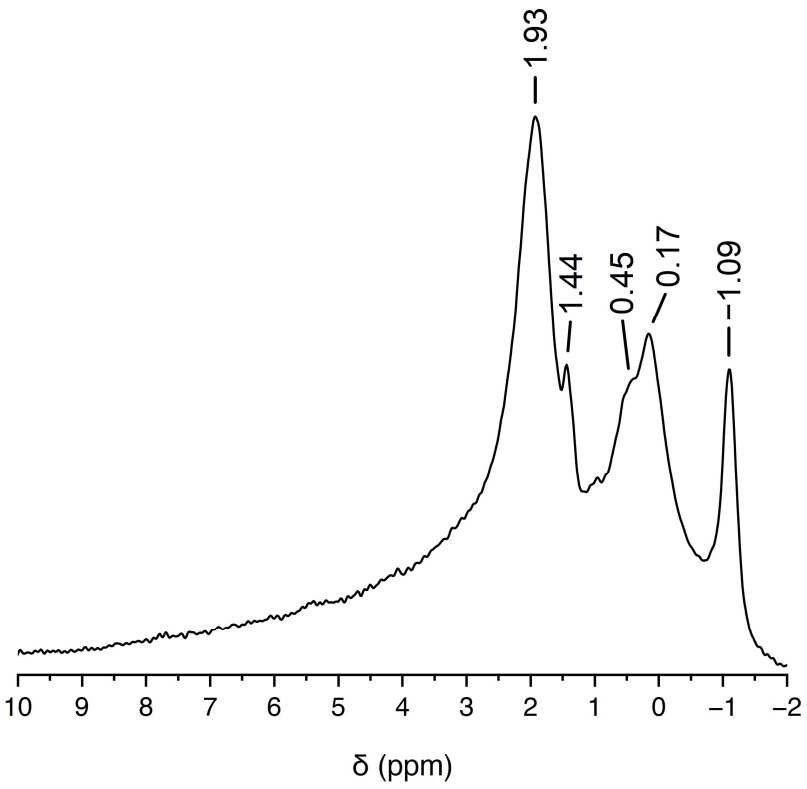

Figure 6.13: ^{1}H MAS ssNMR spectrum of H,K(0.58)/ZnCHA(12) displayed several distinct proton environments present in the framework, with shifts indicating extra-framework species including evidence to suggest the presence of an Si–CH_3 as reported by Copéret et al.[43]

Peak fitting was used on the ^{1}H NMR spectrum, displayed in Figure 6.14, revealing a broad peak centred at 2.70 ppm which rationalizes the raised baseline of the spectrum under the other chemical shifts. This broad peak can be associated to vicinal silanols with extensive hydrogen bonding.[44] The chemical shift identified at 1.93 ppm can be attributed to terminal silanol groups.[45] Whilst peak fitting confirmed the environments in Figure 6.13, it also highlighted an additional chemical shift at 0.98 ppm. The chemical shifts at 1.44 ppm and 0.98 ppm indicate silanol groups, located at the external surface or located at lattice defects. The acquired ^{1}H NMR spectrum gives evidence to suggest that the chosen calcination conditions were sufficient for full removal of the SDA after synthesis, corroborating with the DRIFTS spectrum shown in Figure 6.8. No chemical shifts conforming to adamantane were observed in the expected chemical shift region of 1.7 – 1.8 ppm, with no ammonium species detected around 6.0 ppm. Determining the nature of the species responsible for the shifts at 0.43 ppm, 0.17 ppm and −1.09 ppm required further investigation.

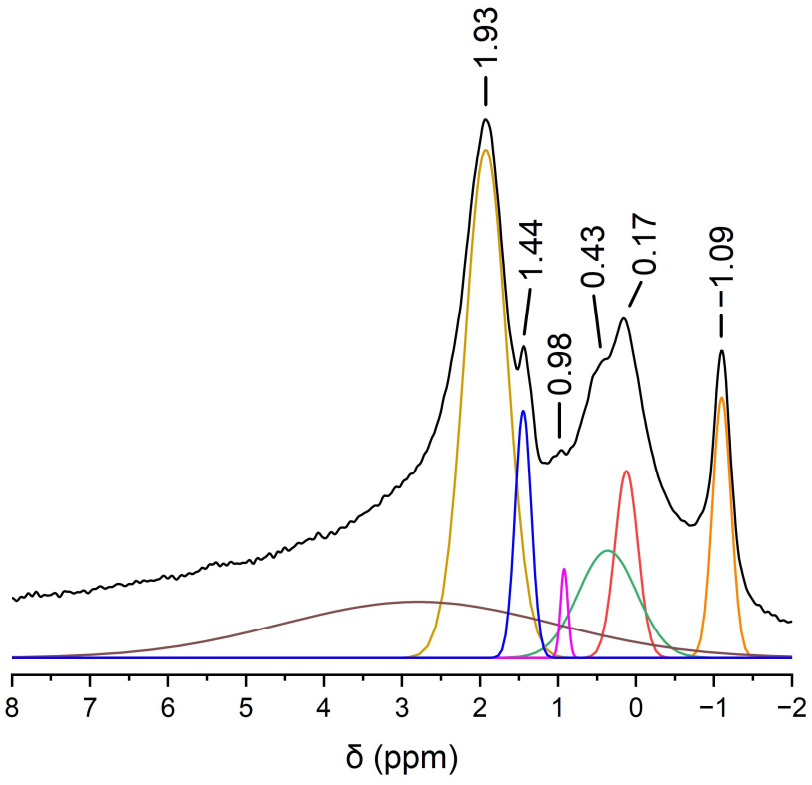

Figure 6.14: ^{1}H MAS ssNMR spectrum of H,K(0.58)/ZnCHA(12) where peak deconvolution has been applied, showing two additional distinct chemical shifts for framework moieties present. Including evidence to suggest the presence of an Si–CH_3 as reported by Copéret et al.[43]

Copéret *et al*. reported that for palladium grafted onto silica, chemical shifts appeared at similar shift values representing methylated species of Pd–Me and Si–Me, which were responsible for chemical shifts at 0.1 ppm and −0.9 ppm respectively.[43] As a result, we associate the shift at −1.09 ppm with Si–Me within H,K(0.58)/ZnCHA(12), whilst the shift at 0.17 ppm was associated with a Zn–Me species, based on NMR investigations in prior art reporting the species at a similar chemical shift value,[46] however, those were a result of methane exposure, which is not the case for ZnCHA materials. The observation of a broad chemical shift at 0.43 ppm could indicate a Zn–Me species, located in a less isolated position of the framework. Prior art report chemical shifts for Zn–OH extra-framework moieties at 1.08 ppm[47] and at ca. 1.20 ppm,[48,49] In addition, significant $Zn(OH)^{+}$ formation is reported to lead to the observation of a new band in the associated DRIFTS spectrum at 3665 cm^{-1},[47] which was not observed for ZnCHA materials, as shown in Figure 6.8.

^{29}Si MAS ssNMR spectroscopy was carried out using CP experiments to enhance the intensity of the associated chemical shift for framework moieties containing protons, such as Q^2 and Q^3 silicon environments. This highlighted interactions that occur between species allowing us to observe a very small quantity of Q^2 sites present in the framework, with a chemical shift value of −93.2 ppm.[50] Whilst the ratio of Q^3 and Q^4 Si sites is not quantitative, their respective shifts were observed at −100.6 ppm and −110.8 ppm.[50] The ^{29}Si CP MAS ssNMR spectrum is shown in Figure 6.15.

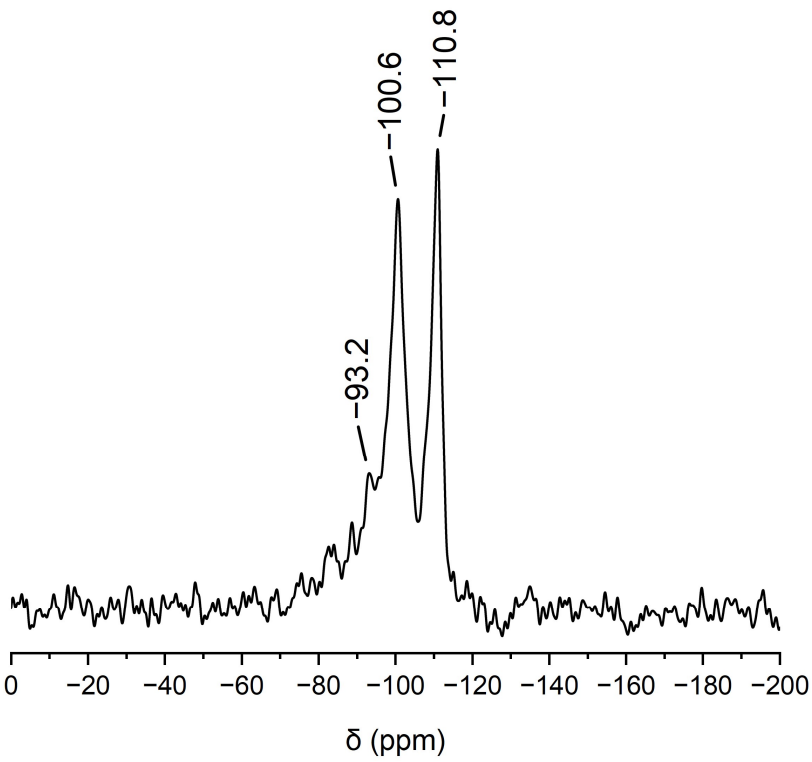

Figure 6.15: A cross-polarisation ^{29}Si MAS ssNMR spectrum for H,K(0.58)/ZnCHA(12) showing the presence of Q^2, Q^3 and Q^4 sites in the zincosilicate CHA framework.

Peak deconvolution was carried out on the acquired ^{29}Si CP MAS ssNMR spectrum acquired for H,K(0.58)/ZnCHA(12), displayed in Figure 6.16. This highlighted a shoulder to the chemical shift at −110.8 ppm which was centred at −107.6 ppm, indicating the presence of Q^4(1Zn) environments in the framework.

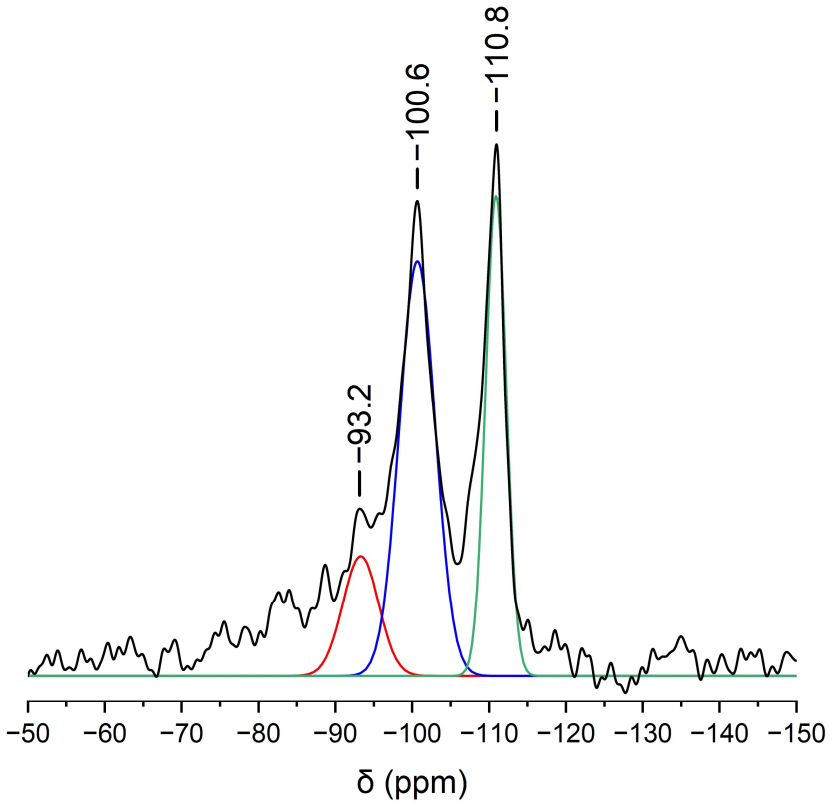

Figure 6.16: Peak deconvolution of a cross-polarisation ^{29}Si MAS ssNMR spectrum for H,K(0.58)/ZnCHA(12) showing the presence of Q^2, Q^3 and Q^4 sites in the zincosilicate CHA framework.

To distinguish which environments were responsible for the signals present in both ^{1}H and ^{29}Si ssNMR spectra for H,K(0.58)/ZnCHA(12), a ^{1}H–^{29}Si HETCOR experiment was conducted. The initial ^{1}H–^{29}Si HETCOR spectrum, shown in Figure 6.17, was conducted at 25 °C using a 4 mm quartz NMR rotor spun at 10 kHz. Experiment was conducted using a frequency switched Lee Goldberg HETCOR (lghetfq sequence) experiment, correlating interactions between the two observed nuclei through single bond spin-spin coupling.[51] This experiment corroborated with the acquired ^{29}Si ssNMR spectrum (Figure 6.15) in determining the presence of distinct Q^2, Q^3 and Q^4 environments in the framework. Correlation between each of the silicon environments and chemical shifts observed between 0.98 ppm and 1.9 ppm (^{1}H) confirmed their identity as silanol groups.[45] Correlation was observed between Q_3 and Q^4 sites with the broad chemical shift centred at 2.70 ppm (Figure 6.14) that we identified as vicinal silanols with extensive hydrogen bonding.[44]

We observe some correlation was observed between Q_2, Q_3 and Q_4 silicon environments and the chemical shift at 0.17 ppm. We postulate the chemical shift at 0.17 ppm indicates Zn–Me based on prior art,[46] however, this correlation would suggest the species is situated in close proximity to all three silicon environments and interacting

through space. The presence of Q^2, Q^3 and Q^4 silicon environments would however be expected at framework defect sites. There was also correlation between the Q^3 and Q^4 sites and the shift at −1.09 ppm, which we associate with Si–Me. Q^4 sites appeared to display more corelation with the chemical shift than Q^3 sites, suggesting that the species is less likely to be present at defect sites, unlike the aforementioned Zn–Me and possibly situated at terminal silanol groups.

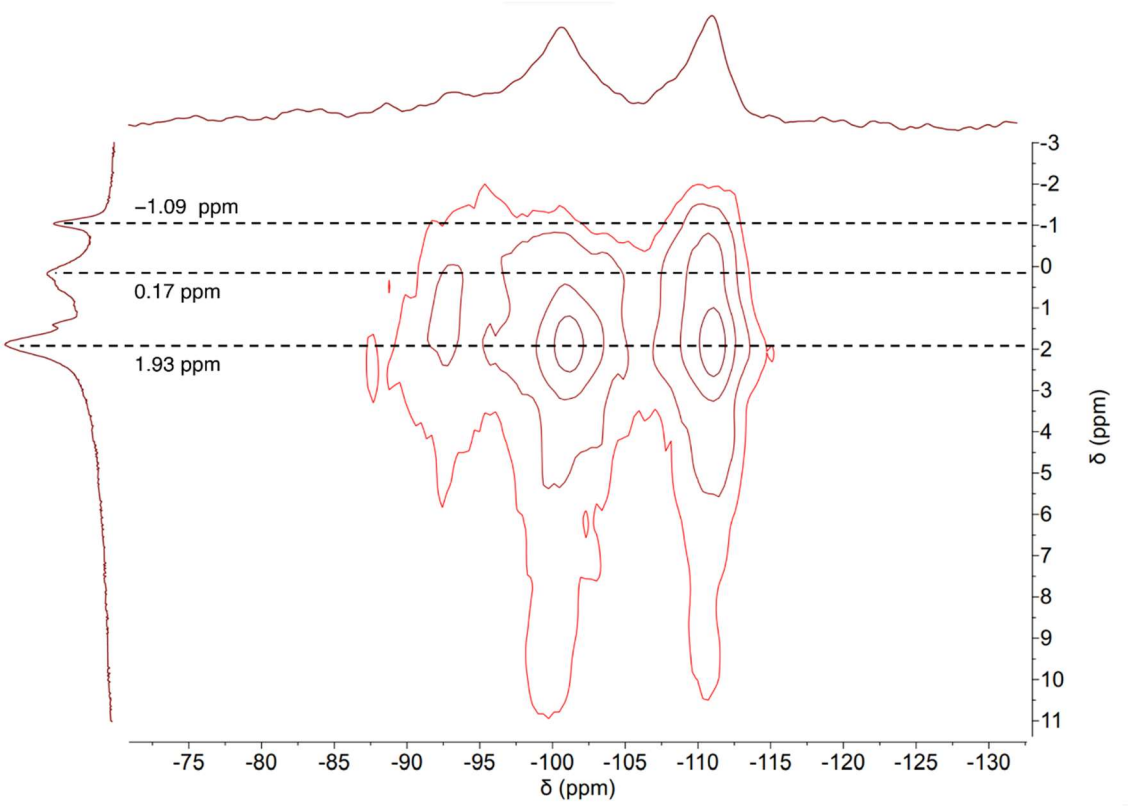

Figure 6.17: ^{1}H–^{29}Si HETCOR MAS ssNMR spectrum (10 kHz, 4 mm rotor, 25 °C) of H,K(0.58)/ZnCHA(12) following dehydration, showing correlation between the shifts observed in both ^{1}H and ^{29}Si ssNMR spectra.

Follow up ssNMR experiments were conducted in order to sharpen the signals acquired for each environment. From these experiments it was hoped we could determine the correlation between signals and identify more accurately the species present within or on the zincosilicate framework. The previous ^{1}H–^{29}Si HETCOR MAS ssNMR spectrum shown in Figure 6.17 was collected at 25 °C. Follow up experiments collecting a ^{1}H ssNMR spectrum, shown in Figure 6.18, and ^{1}H–^{29}Si HETCOR MAS ssNMR spectrum was conducted at −20 °C.

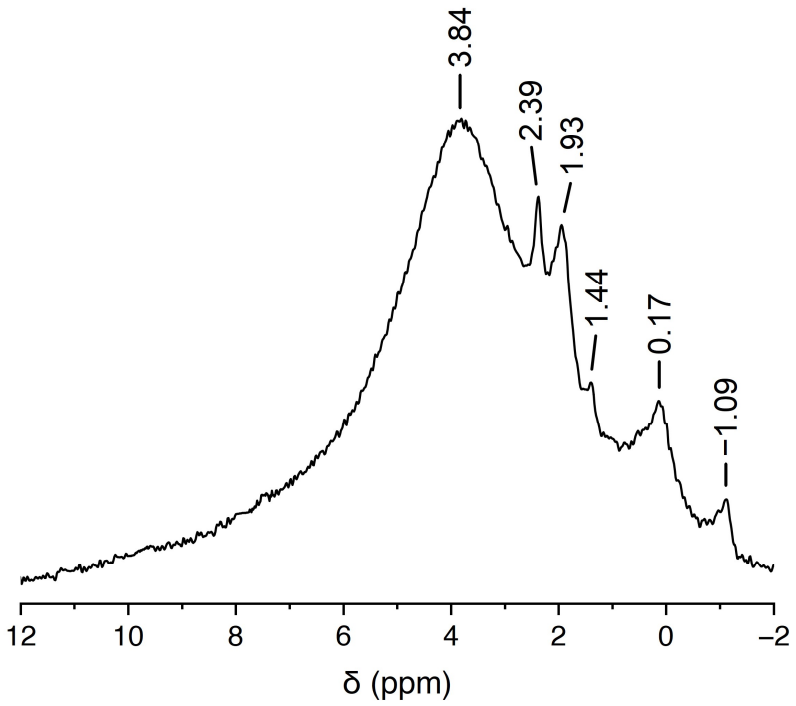

Figure 6.18: ^{1}H MAS ssNMR spectrum (10 kHz, 3.2 mm rotor, −20 °C) of H,K(0.58)/ZnCHA(12) showing excessive amounts of moisture ingress has led to the hydration of the material, with the water peak obscuring the environments present.

These experiments were conducted using a 3.2 mm NMR rotor with a 20 kHz spin rate. This reduced the amount of sample present meant using an extended acquisition time for the experiment. However, since the experiment was conducted at -20 °C, excess condensation was able to build-up on the NMR rotor, which led to moisture ingress into the rotor and hydration of the sample. This therefore negated any potential benefit of the reduced temperature for peak sharpening. The chemical shifts of the environments present were obscured by the broad water peak. Therefore, the experiment would be repeated, this time at 25 °C, to avoid the build-up of condensation on the NMR rotor. A ^{1}H–^{29}Si HETCOR MAS ssNMR spectrum was obtained for H,K(0.58)/ZnCHA(12) using a 3.2 mm NMR rotor with a spin rate of 20 kHz at 25 °C, as shown in Figure 6.19.

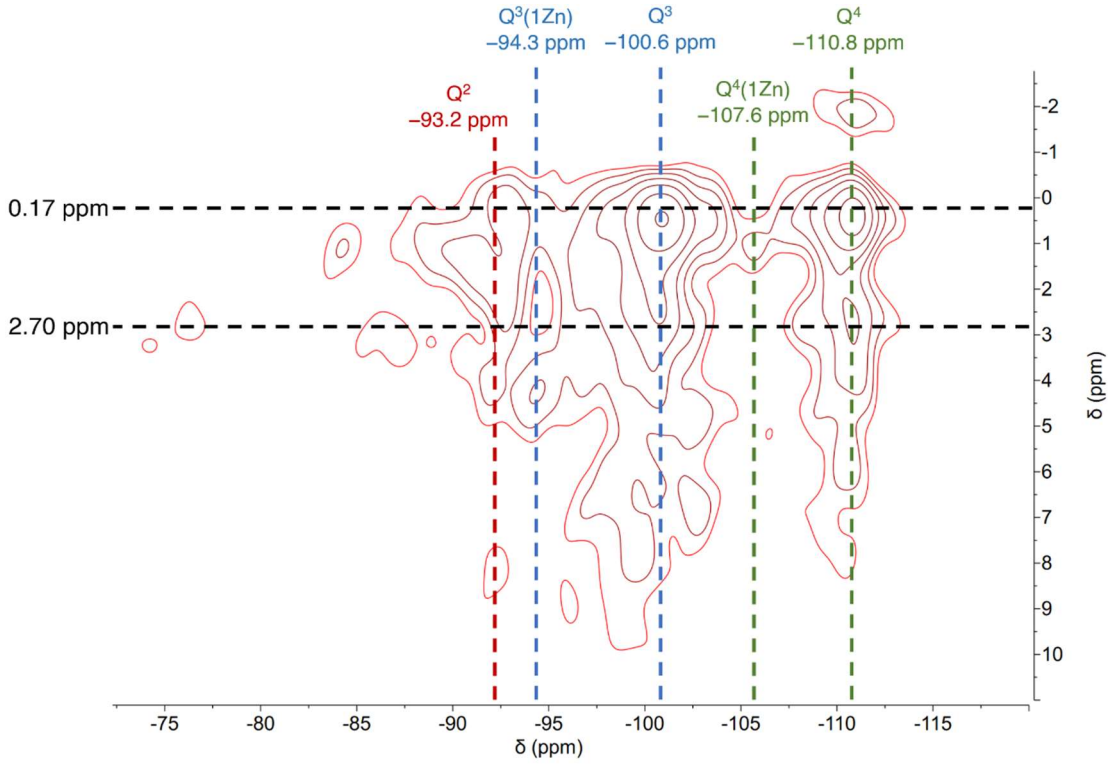

Figure 6.19: ^{1}H–^{29}Si HETCOR MAS ssNMR spectrum (20 kHz, 3.2 mm rotor, 25 °C) of H,K(0.58)/ZnCHA(12) following dehydration, showing correlation between the shifts observed in both ^{1}H and ^{29}Si NMR spectra.

Whilst it is expected that the extended acquisition time led to some degree of hydration of H,K(0.58)/ZnCHA(12) during the acquisition, peaks were no longer obscured by the water peak, as per Figure 6.18. We assume water caused the broad correlation with signals arising from 3 ppm to around 8 ppm, based on the previously acquired proton spectrum of hydrated material. Peak sharpening led us to observe two additional silicon environments, which we assign based on similar chemical shift values for zeolites,[50] with Q^3(1Zn) at −94.3 ppm (^{29}Si) and Q^4(1Zn) at −107.6 ppm (^{29}Si). We assign these environments based on prior art, where Borgna *et al.* observed a chemical shift at −94 ppm (^{29}Si) for Q^3(1Zn) environments in Zn-MWW.[41] Correlation between the chemical shift at 0.17 ppm indicated that Zn–Me is situated in close proximity to Q^3 and Q^4 sites. There was also a clear indication that the Si–Me species at −1.09 ppm was only associated with Q^4 silicon environments, as no correlation was observed to other silicon sites. Correlation with vicinal silanols was present for all silicon environments bar Q^4(1Zn). We could also associate the silanol peak at 0.98 ppm (Figure 6.14) to Q^4(1Zn) silicon environments. The silanol peak at 1.03 ppm can be associated to Q^3 sites.

Observing the presence of Zn–Me and Si–Me in ZnCHA materials led us to determining a possible route of SDA removal following calcination of the hydrothermally synthesised

materials. Copéret *et al*. observed Pd–Me and Si–Me species at similar shift values following the grafting of palladium onto silica,[43] although no post synthetic treatments had been carried out on these materials. While SDAs can be readily removed from zeolite frameworks through calcination, their degradation products are dependent on the SDA used in hydrothermal synthesis. Des Courieres *et al.* reported the products observed following decomposition of tetraethylammonium in a BEA topology material, with the mechanism for SDA elimination consisting of a beta-elimination, leading to the evolution of ethylene, triethyl amine and the formation of a Brønsted acid site on the framework.[52]

Hydrothermal synthesis of CHA topology materials uses trimethyladamantylammonium hydroxide as the SDA. The quaternary amine contains methyl groups which cannot facilitate beta-elimination. Therefore, we postulated that two mechanisms could occur during calcination of zincosilicates under static air at 550 °C. The first mechanism follows convention, with beta-elimination occurring on the adamantane ring at the beta position to the amine. This would proceed on closed zinc sites, leading to the decomposition of trimethyladamantylammonium hydroxide through beta-elimination, to produce trimethylamine and adamantene, as shown in Figure 6.20. Adamantene is known to be a very short-lived species, owing to its highly strained ring structure,[53,54] and whilst a dimeric form is known, we expect decomposition products to be less bulky and able to diffuse from the micropores freely.

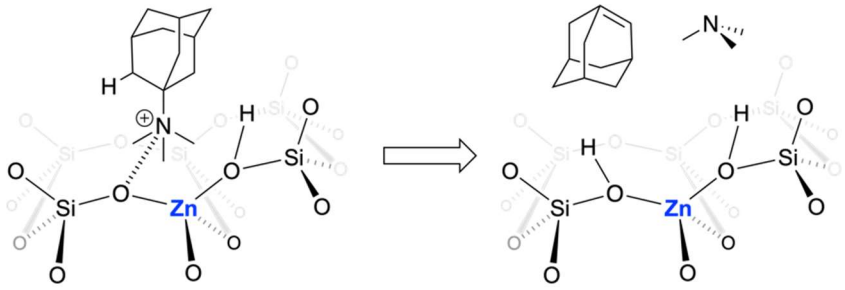

Figure 6.20: A proposed mechanism for the decomposition products from the OSDA during calcination of zincosilicate CHA under static air at 550 ˚C leading to adamantene and a closed site Zn environment.

We postulate that the generation of Zn–Me and Si–Me species observed by ssNMR are a result of calcination of ZnCHA materials, as no post synthetic modifications were conducted to H,K(0.58)/ZnCHA(12). In Figure 6.21 we propose a pathway for the generation of Si–Me (A) and Zn–Me (B). The process would be base catalysed and occur at partially closed or open zinc sites, where an Si–OH is in proximity, generating water and a quaternary amine.

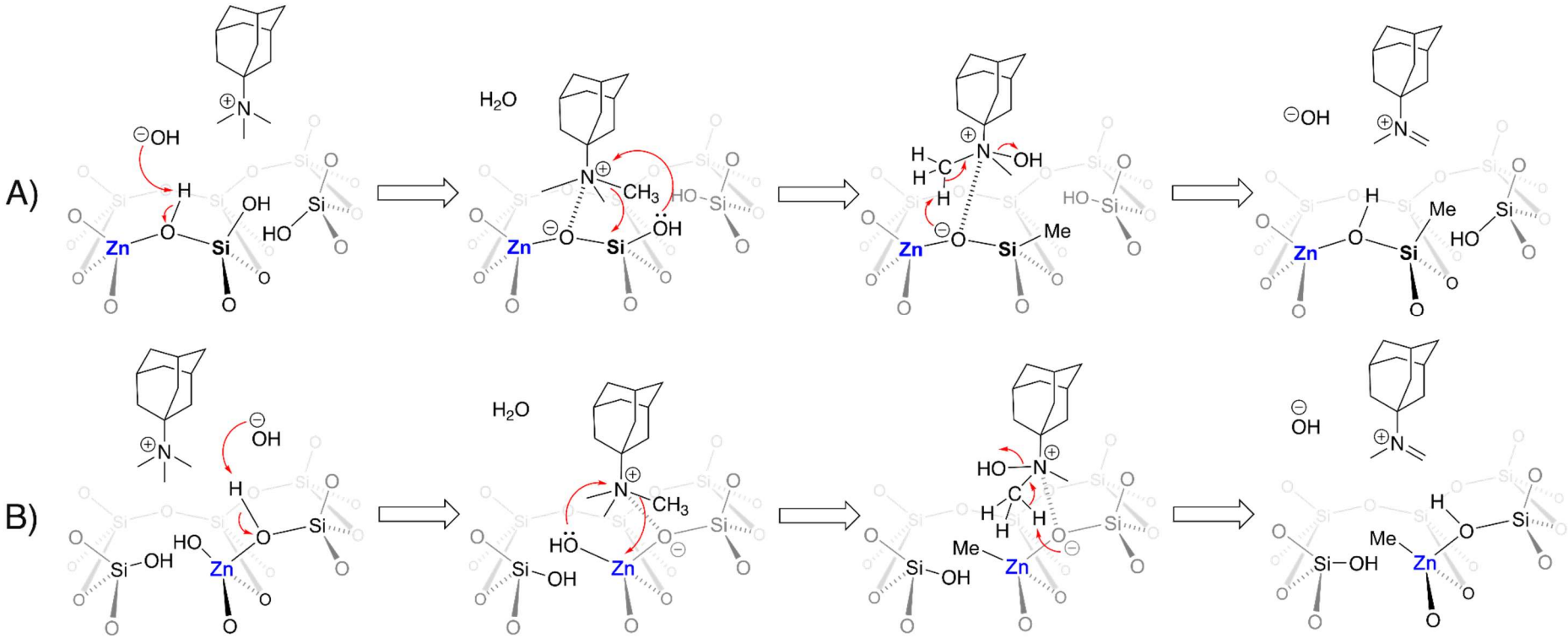

Figure 6.21: A proposed second pathway of OSDA decomposition during calcination under static air at 550 ˚C, leading to the formation of a silicon methyl and zinc methyl species on the zincosilicate framework.

We propose that the second route for elimination of the SDA, shown in Figure 6.21, is what leads to the formation of Si–Me and Zn–Me species within ZnCHA materials with both species observed using solid-state NMR spectroscopy. The presence of defect sites prior to calcination of the materials is critical in facilitating their formation during elimination of the SDA. We observed no evidence of SDA remaining in the micropores post calcination, which would be observed in the acquired BET, DRIFTS and ssNMR spectra. If the formation of highly unstable adamantene does occur during calcination, both it and its derivatives are removed during the process.

6.2.4 Electron Microscopy of Hydrothermally Synthesized Zincosilicate CHA

Scanning Electron Microscopy (SEM) and Tunnelling Electron Microscopy (TEM) have been utilised to gain insight into crystallite size, shape and uniformity for zincosilicate CHA. This was used not only to understand the structural properties of the material following hydrothermal synthesis, but also any observable changes following ion-exchange or with spent materials after carrying out upgrading reactions.

6.2.4.1 Scanning Electron Microscopy (SEM) of Hydrothermally Synthesized Zincosilicate CHA

SEM images were acquired for zincosilicate CHA materials. The SEM images acquired for H,K(0.58)/ZnCHA(12), hydrothermally synthesised using our developed method outlined in Figure 6.5, is shown in Figure 6.22. The zincosilicate crystals displayed a high level of conformity across the individual crystallites, composed of spherical shaped crystals between 3 – 5 μm in length. The crystal size for ZnCHA materials were found to be an order of magnitude larger on average than for hydrothermally synthesised chabazite materials, produced using the method outlined in Section 5.2.1.

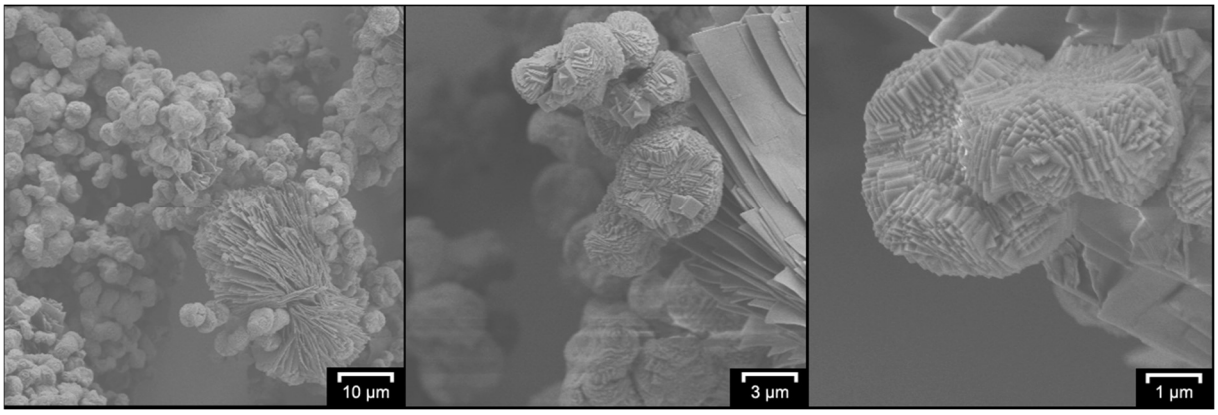

Figure 6.22: SEM images acquired for H,K(0.58)/ZnCHA(12) at 10 μm, 3 μm and 1 μm scales.

6.2.4.2 Tunnelling Electron Microscopy (TEM) of Hydrothermally Synthesized Zincosilicate CHA

Due to their size, zincosilicate CHA materials crystallites proved too large for the minimum magnification of the TEM microscope, however, we could still apply the technique, particularly for acquiring EDS-TEM maps to determine elemental distribution. However, analysis of the hydrothermally synthesised zincosilicate CHA materials corroborated with the findings of SEM, with crystallites being cubic in shape and several times larger than their zeolite counterparts. They were observed to be cubic crystals, with an image acquired containing some smaller crystals of around 500 nm in size shown in Figure 6.23. ZnCHA materials were observed to be consistent in shape and size between the hydrothermally synthesized batches. STEM-BF images allowed us to measure the size and distribution of hydrothermally synthesised chabazite, discussed in Section 5.2.4, however, this technique could not be applied to zincosilicate CHA materials.

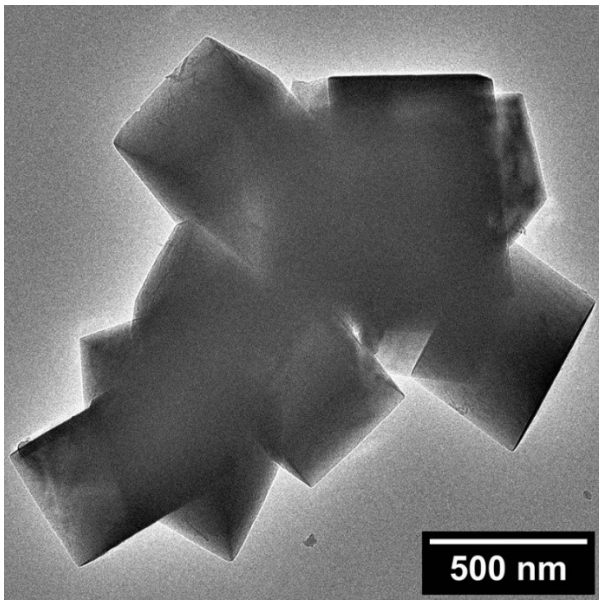

Figure 6.23: STEM-BF images acquired of H,K(0.58)/ZnCHA(12) cubic crystals which averaged around 500 nm in size.

EDS-TEM maps were obtained for H,K(0.58)/ZnCHA(12) alongside STEM-BF imaging, giving insight into the elemental distribution of the calcined material. The elemental maps highlighted the dispersion of exchangeable cations and their position in the framework. The crystallites of H,K(0.58)/ZnCHA(12) which had an average size of around 2.5 μm displayed a high level of uniformity for each of the elements present in the material, as shown in Figure 6.24. For each element, there was no noticeable localisation of any element present for the calcined material.

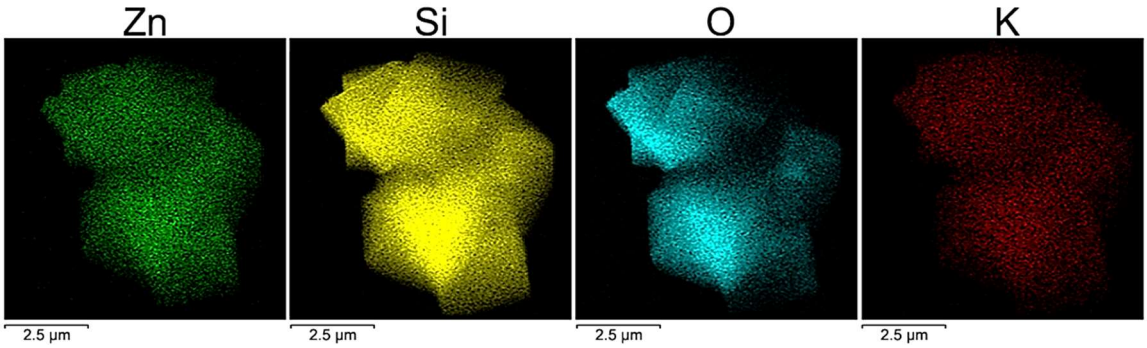

Figure 6.24: EDS-TEM maps acquired for H,K(0.58)/ZnCHA(12) showing the elemental distribution of zinc, silicon, oxygen and potassium in/on the framework.

Some crystallites of H,K(0.58)/ZnCHA(12) were notably smaller than average size, such as those shown in the acquired STEM-BF image in Figure 6.23. EDS-TEM maps were acquired to determine whether any elemental differences were observed between the larger and smaller crystallites. A EDS-TEM map for H,K(0.58)/ZnCHA(12) crystals under 500 nm on average is shown in Figure 6.25, showing a high level of uniformity for each of the elements present. From this observation, we determined there were no differences in elemental distribution for the calcined ZnCHA materials regardless of their crystal size. ZnCHA produced using our hydrothermal synthesis method developed in this project produces materials free of element localisation in the zincosilicate crystals.

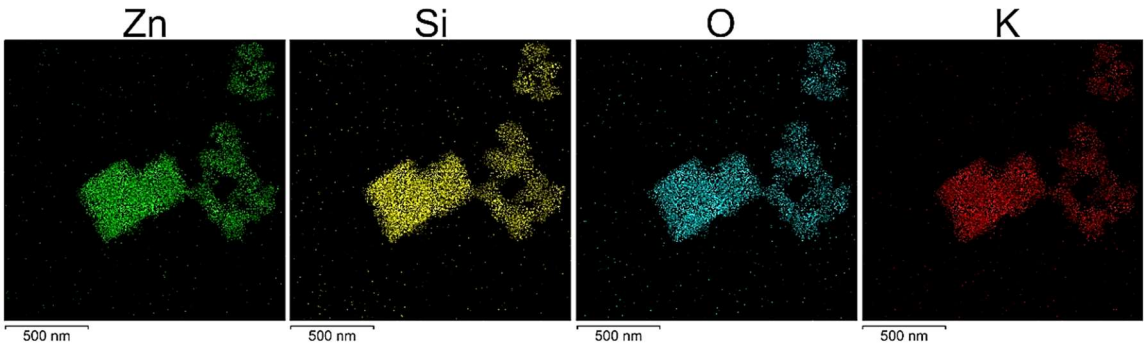

Figure 6.25: EDS-TEM maps acquired for H,K(0.58)/ZnCHA(12), showing the elemental distribution of zinc, silicon, oxygen and potassium in/on the framework of crystallites of smaller than average dimensions.

6.2.5 X-ray Absorption Spectroscopy of Hydrothermally Synthesized Zincosilicate CHA

Understanding the zinc environments present within the framework is critical to comprehending which sites are responsible for the behaviour of the material as a catalyst for hydrocarbon upgrading. XANES was used to highlight the oxidation state of uzinc in the framework, whilst also applying XANES linear combination fitting (LCF) to determine the nature of zinc species present. I must acknowledge Dr Monik Panchal for the acquisition and processing of this data. The materials and experimental parameters used in XAS are reported in Table 6.2.

Table 6.2: Table containing the materials analysed and the experimental parameters for XAS of ZnCHA and zinc reference materials.

Sample ID (Material)	Edge	Experiment	Mass (mg)	Time per sample
H,K(0.68)/ZnCHA(12)	Zn K-edge	XAFS	77	2hr 20m
Reference 1 (zinc oxide)	Zn K-edge	XAFS	10	2hr 20m
Reference 2 (zinc acetate)	Zn K-edge	XAFS	20	2hr 20m
Reference 3 (Zn foil)	Zn K-edge	XAFS	N/A	2hr 20m

6.2.5.1 X-Ray Absorption Near Edge Structure of Zincosilicate CHA

The first XAS technique carried out was X-Ray Absorption Near Edge Structure (XANES), with spectra acquired for H,K(0.68)/ZnCHA(12) and several zinc containing materials as zinc references. These were zinc oxide, zinc acetate and zinc metal foil. XANES was conducted to measure both the oxidation state of zinc and to determine the zinc species present in the framework. Features observed in the XANES region of the edge jump for H,K(0.68)/ZnCHA(12), shown in Figure 6.26, were analogous to those observed for zinc oxide and zinc acetate, with a similar energy position of the absorption edge. This suggested that the primary oxidation state of zinc was the +2 oxidation state. There was little evidence to suggest zinc species of different oxidation states. Features observed in the XANES spectra of H,K(0.68)/ZnCHA(12) were highly similar to those reported for zincosilicates in prior art.[41]

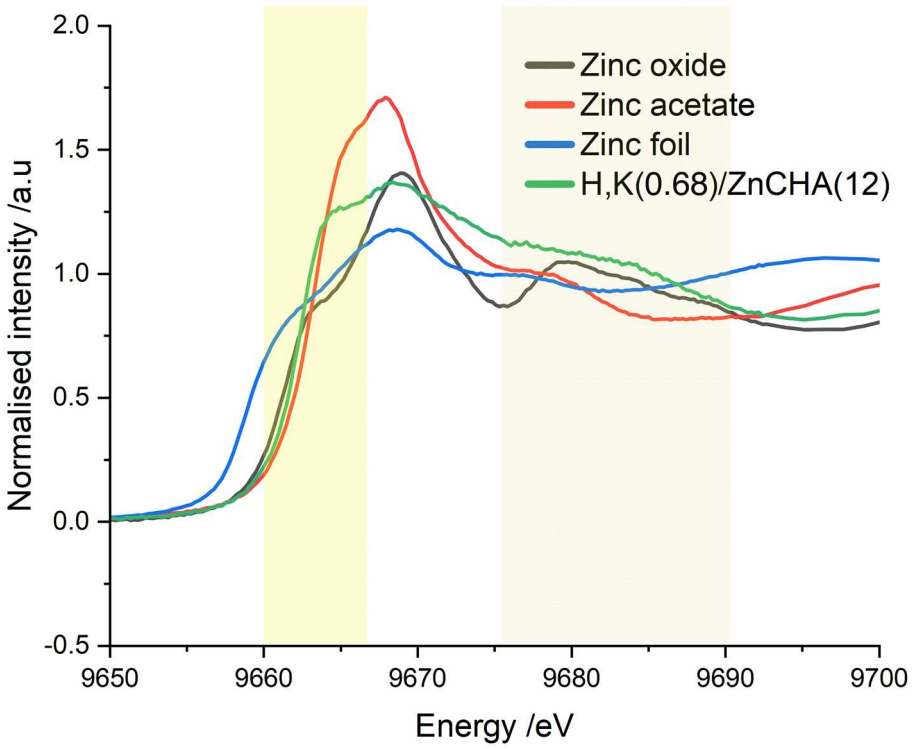

Figure 6.26: Zn K-edge XANES region highlighting the edge jump and common features in the spectra for H,K(0.68)/ZnCHA(12), with zinc references of zinc foil, zinc acetate (zinc source for hydrothermal synthesis of ZnCHA) and zinc oxide.

Linear combination fitting (LCF) was carried out for the XANES spectrum of H,K(0.68)/ZnCHA(12). A poor fit was observed when fitting the acquired XANES spectrum to those of zinc oxide and zinc acetate. This suggested that the zinc environments corresponding to these materials were not present within the zincosilicate framework. This analysis confirms that the zinc acetate used in the hydrothermal synthesis of the material had been completely consumed. However, the use of more sophisticated fitting would be required to determine the exact nature of the zinc species present in the framework with XANES LCF. Prior art reports the use of simulation when determining zinc distribution, which could be of benefit when determining at which positions zinc is located at within the framework.[41,55]

6.2.5.2 Extended X-ray absorption fine structure of Zincosilicate CHA

Extended X-ray absorption fine structure (EXAFS) was acquired for H,K(0.68)ZnCHA(12), shown in Figure 6.27. EXAFS was conducted to determine the average bond lengths for zinc within the framework, giving insight into the potential position of zinc atoms and to corroborate with the previous XANES findings.

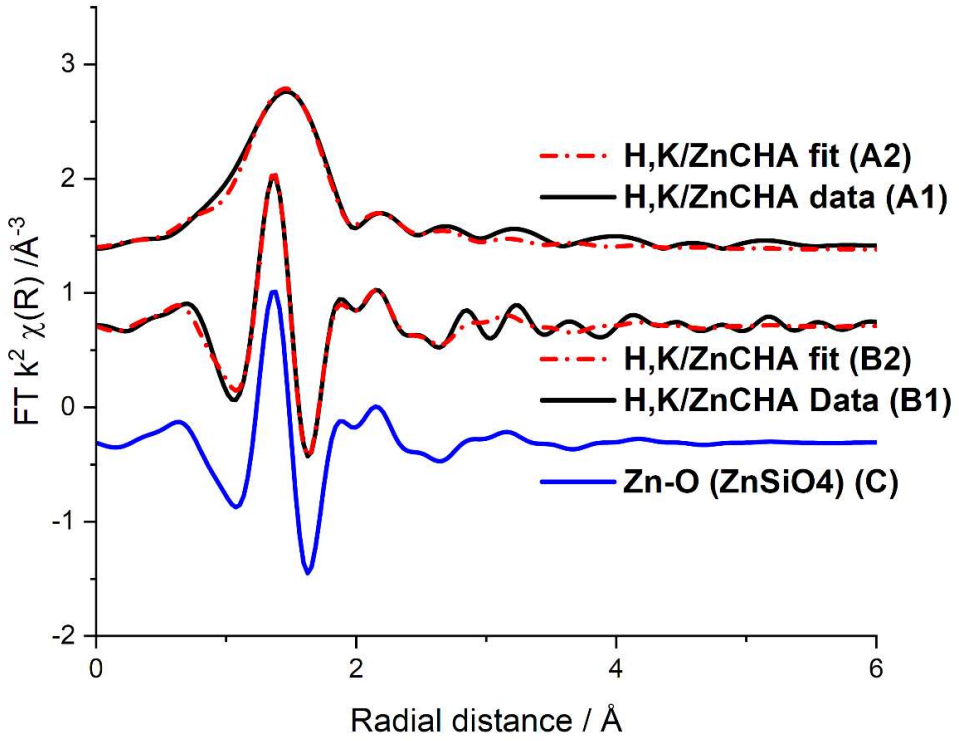

Figure 6.27: Magnitude of the k^2-weighted Fourier transform of the Zn K-edge EXAFS data for H,K/ZnCHA (A and B). The imaginary components of the 1 scattering path used in the fit is shown (C).

The fitting of the EXAFS data made it apparent that zinc was incorporated into the framework of H,K(0.68)ZnCHA(12), with an average bond distance for Zn−O of around 1.93 Å, as shown in Table 6.3. The bond distance for zinc in ZnCHA was consistent with the bond length of H/ZnMFI (1.99 Å).[56] Bond length was also comparable with reported Zn−O bond lengths in prior art for 0.36Zn/DeAlBEA (1.88 Å to 1.95 Å) by Bell *et al.*[42] and by Borgna *et al.* for Zn-MWW (1.98 Å).[41] It was also noted that the Zn−O distance in $ZnSiO_4$ (ca. 1.94 Å) was comparable to ZnCHA.[57] In addition, there was no evidence to suggest that any Zn−O−Zn species were present in the material, which would have an estimated bond length of around 3.02 Å. This provides evidence to suggest that no bulk ZnO is present.

Table 6.3: Average zinc-oxygen bond lengths determined using EXAFS analysis for several zincosilicate materials.

Material	Atom Pair	N	R (Å)	σ^2 (Å^{-2})
H,K(0.68)ZnCHA(12)	Zn−O	4.7 (± 0.4)	1.93 ± (0.02)	0.002
H/ZnMFI	Zn−O	1.8 (± 0.3)	1.99 (± 0.02)	0.009
Zn-MWW[41]	Zn−O	4.7 (± 0.3)	1.98 (± 0.01)	0.008
0.04Pt-0.36Zn-DeAlBEA (as synthesized)[42]	Zn−O	4.3 (± 0.3)	1.95 (± 0.01)	0.008

Attempts to fit a second shell Zn−O−Si scatting path were made for H,K(0.68)/ZnCHA(12), with an estimated bond length of around 2.84 Å. However, accurate values derived from the fitting of the system were unfortunately not achieved, likely due to the low level of signal intensity for the material. Improvements to allow for the measurement of this value from successful fitting would come from either higher signal EXAFS measurements at a synchrotron source or analysing a ZnCHA material that has been hydrothermally synthesised with a higher zinc content.

6.2.6 Brunauer-Emmett-Teller theory of Hydrothermally Synthesized Zincosilicate CHA

To assess the surface area of synthesised zincosilicate chabazite, Brunauer-Emmett-Teller (BET) theory was used. This process first uses N_2 physisorption analysis before BET surface area calculations were undertaken. Using the BET theory as a model to describe adsorption, a gas adsorption isotherm was collected for H,K(0.58)/ZnCHA(12), where the quantity of gas adsorbed per gram of material is plotted against relative pressure, as shown in Figure 6.28. The shape of the isotherm is indicative of how gas adsorption occurs within the material, with diffusion limitations of the small pore material reducing the uptake and desorption of N_2. The observed isotherm is described as being Type I with an H4 hysteresis.[58]

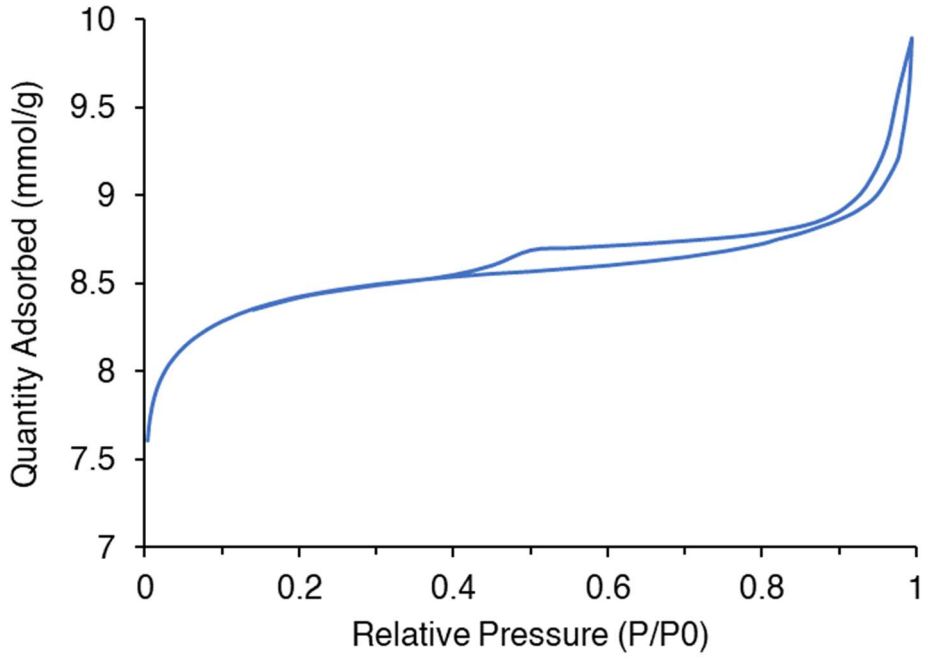

Figure 6.28: Isotherm linear plot for N_2 physisorption analysis of hydrothermally synthesized H,K(0.58)/ZnCHA(12), showing a Type I isotherm with H4 hysteresis, expected for small pore microporous materials.

This is in line with the isotherm type observed for H,K(0.23)/CHA(20) in Figure 5.37. The surface area using BET theory for H,K(0.58)/ZnCHA(12) was calculated to be 580 m^2/g (relative pressure range of P/P_0 = 0.005 – 0.300). This was lower than the calculated surface area for H,K(0.23)/CHA(20) (682 m^2/g, relative pressure range of P/P_0 = 0.005 – 0.300). Comparing the calculated surface area for H,K(0.58)/ZnCHA(12) against zeolite chabazite materials in prior art, showed the material compared favourably. Liu *et al.* reported a surface area between 537 and 569 m^2/g for their chabazite materials,[59] whereas Lillerud reported a range of 463 – 702 m^2/g from their varied hydrothermal syntheses, with an average of 603 m^2/g across their six materials.[58]

6.2.7 Conclusion of Hydrothermal Synthesis of Zincosilicate CHA

Hydrothermal synthesis of zincosilicate CHA materials was successful having made several iterative changes to the reported Okubo method, to produce our own optimised method.[20] Repeated generation of multiple batches of ZnCHA materials observed as having consistent elemental compositions and physical properties, showing that the adaptations made to the hydrothermal synthesis method were successful. Zincosilicate crystals were observed to be cubic and averaged 3 μm in size. EDS-TEM maps observed good uniformity for elemental distribution in the zincosilicate crystals, not only for those of an average size, but also for crystals that were notably smaller.

DRIFTS spectra acquired for ZnCHA showed a shift to lower wavenumbers for several framework bands, indicating zinc incorporation into the framework and leading to changed Si–O–T bond lengths.[29,31,32] DRIFTS spectra post vapour adsorption highlighted the presence of BAS and Lewis acid sites in the framework, whilst also highlighting the low quantity of silanol nests present in the framework.[35–38] ssNMR spectroscopy led to the observation of Zn–Me and Si–Me species, with chemical shifts at 0.17 ppm and −1.09 ppm respectively.[43] Whilst the origin of the species remains unclear, we proposed two possible routes for their generation. Further experimentation could provide us evidence to confirm the pathway for calcination of the SDA, where collection and identification of decomposition products would be crucial in determining the species origin. Experiments using higher spin rates allowed us to observe Q^3(1Zn) at −94.3 ppm (^{29}Si) and Q^4(1Zn) at −107.6 ppm (^{29}Si), with the chemical shift for Q^3(1Zn) closely conforming with prior art for Zn-MWW.[41] XAS of H,K(0.68)ZnCHA(12) highlighted that zinc was present in the +2 oxidation state, with similar XANES spectra features as reported for zincosilicates in prior art.[41] EXAFS also determined that the average bond distance for Zn−O was 1.93 Å, comparable to several zincosilicate materials reporting values between 1.88 Å and 1.99 Å.[41,42,56] ZnCHA was also noted to have a surface area comparable to several zeolite chabazite materials reported in literature.[58–60]

We can therefore conclude that zinc was successfully incorporated into the chabazite framework. The optimised hydrothermal synthesis method reliably produced materials which were highly crystalline, with low quantities of defect sites and with uniform elemental distribution.

6.3 Analysis of Silver-exchanged zincosilicates

The introduction of silver into the micropores of zincosilicate CHA following the methodology employed for zeolite CHA materials, outlined in Section 5.1.1. Conducting ion-exchange meant loading 2 g of material to a black 50 mL centrifuge tube and mixing the material on a tube roller with silver nitrate solution at room temperature for 1 hour. Black centrifuge tubes were used to protect the mixture from light, with the materials dried under darkness at 80 °C overnight. ED-XRF results for several ZnCHA materials are shown in Table 6.4.

There were no notable changes to the elemental ratios for the materials, particularly the Si:Zn ratio post aqueous ion-exchange, even when using more concentrated silver nitrate solutions. This showed that aqueous ion-exchange conditions were mild enough to not facilitate zinc leaching from framework positions.

Table 6.4: Table containing the ED-XRF results for zincosilicate chabazite materials post aqueous ion-exchange to introduce silver to the micropores, with a reversed exchange with potassium also trialled. No evidence to suggest the ion-exchange conditions utilised led to zinc leaching from the framework.

Entry	IE Conditions	Zn (wt%)	Si (wt%)	Ag (wt%)	K (wt%)	Si / Zn ratio	K / Zn ratio	Ag / Zn ratio
RK-2-81	Parent material	5.77±0.11	26.35±0.42	N/A	2.12±0.05	10.63	0.61	N/A
RK-2-89	0.1M $AgNO_3$ 1 hr, RT	8.52±0.25	36.48±1.37	7.46±0.03	0.71±0.04	10.04	0.14	0.53
RK-2-118(2)	Parent material	7.30±0.05	38.64±0.12	N/A	2.97±0.01	12.23	0.68	N/A
RK-2-124	0.25M $AgNO_3$ 1 hr, RT	6.17±0.04	34.00±0.03	10.0±0.51	0.73±0.02	12.82	0.20	0.99
RK-2-124(2)	0.1M KNO_3, 1 hr, RT	6.96±0.04	38.24±0.48	5.9±0.01	2.38±0.12	12.79	0.57	0.51

6.3.1 Powder X-ray Diffraction of Silver-exchanged ZnCHA

Powder X-Ray diffraction (pXRD) was used in the determining the crystallinity of the silver-exchanged ZnCHA materials. Initial observations indicated no pronounced changes to the material crystallinity or crystal size, with the acquired pXRD pattern showing good crystallinity and sharp reflections. Concordant with pXRD patterns obtained for silver-exchanged zeolites, there were no reflections indicating silver clusters. Prior art reports silver-exchanged materials with high silver-loading levels can exhibit reflections indicating the presence of bulk silver,[61] which would be observed at 38.0° and 44.3°(2θ), for Ag [111] and Ag [200] respectively.[62] The pXRD pattern for Ag(0.99),K(0.20)/ZnCHA(12) is shown in Figure 6.29, where no peaks were observed for silver clusters. It was observed to be this way for all silver-exchanged ZnCHA materials in this project post aqueous ion-exchange, regardless of silver loading level.

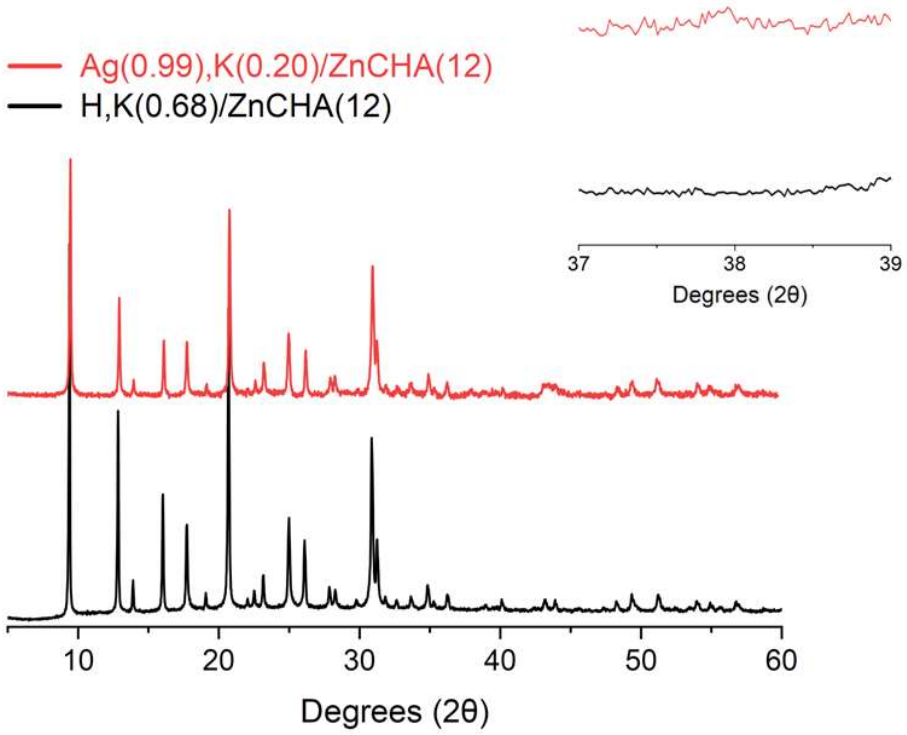

Figure 6.29: Stacked pXRD patterns for the silver-exchanged zincosilicate CHA (red) and the parent material (black), confirming little change in the pattern and no observation of silver clusters.

6.3.2 Transmission Electron Microscopy of Silver-exchanged ZnCHA

TEM imaging was used to gain a greater understanding of ZnCHA materials post silver aqueous ion-exchange, giving insight into the positioning of silver in freshly prepared materials. As discussed in section 6.3.1, pXRD patterns obtained for silver exchanged ZnCHA materials did not contain reflections indicating silver clusters. De Cremer claimed that a lack of silver in the pXRD pattern meant only a negligible quantity of silver clusters with larger dimensions were present on the zeolite surface.[63] STEM-BF images captured for Ag/ZnCHA materials of varying silver loading levels corroborated with their zeolite counterparts regarding silver cluster formation. STEM-BF images acquired for several silver exchanged ZnCHA materials are shown in Figure 6.30, alongside a silver exchanged ZnMFI material. For each of the zincosilicate materials post aqueous ion-exchange, the STEM-BF images acquired highlighted silver clustering on the materials, even though their pXRD patterns did not indicate clustering. Localisation of silver was evident regardless of the silver loading level.

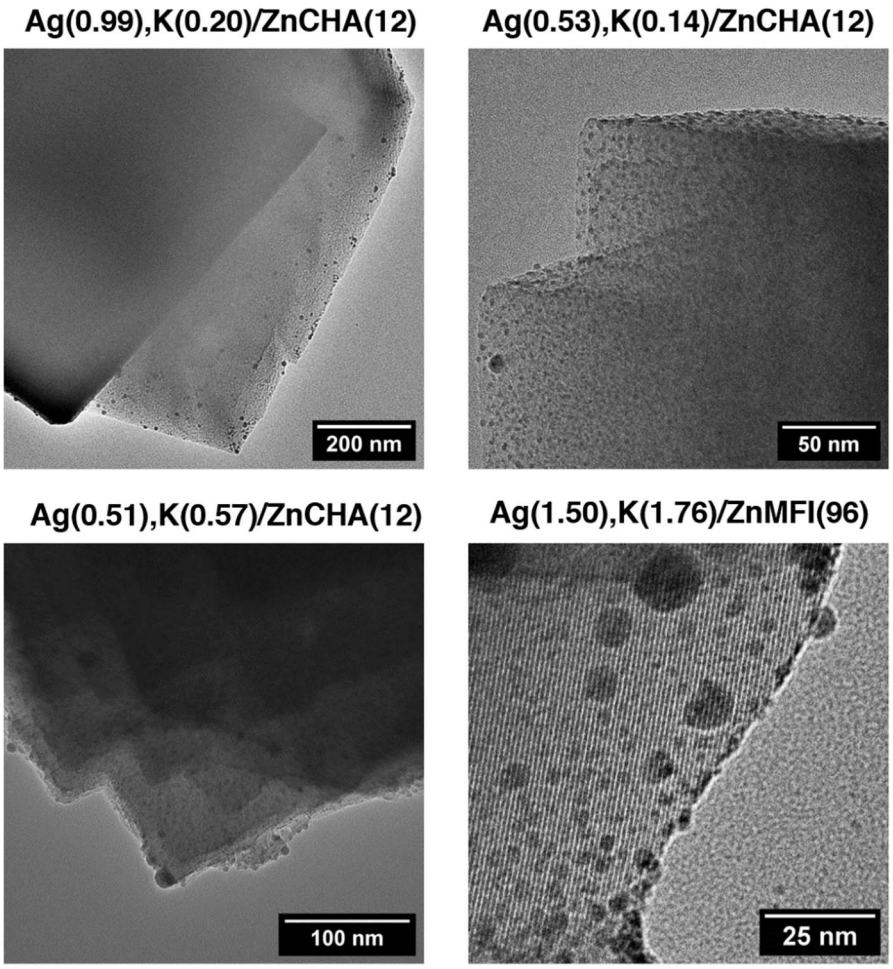

Figure 6.30: STEM-BF images of several silver-exchanged zincosilicate materials, showing the ordered arrangement of the regular channels, as well as the silver clusters that have formed on the materials surface.

Using the STEM-BF images acquired for Ag(0.51),K(0.57)/ZnCHA(12), we could determine the size distribution of silver clusters following aqueous ion-exchange. From the acquired STEM-BF images of Ag(0.51),K(0.57)/ZnCHA(12) (5.8 wt% Ag), displayed in Figure 6.31, the mean silver cluster size was calculated to be 8.7 nm (±6.5 nm), averaged over a total of 238 clusters, with the silver cluster size distribution shown in Figure 6.32.

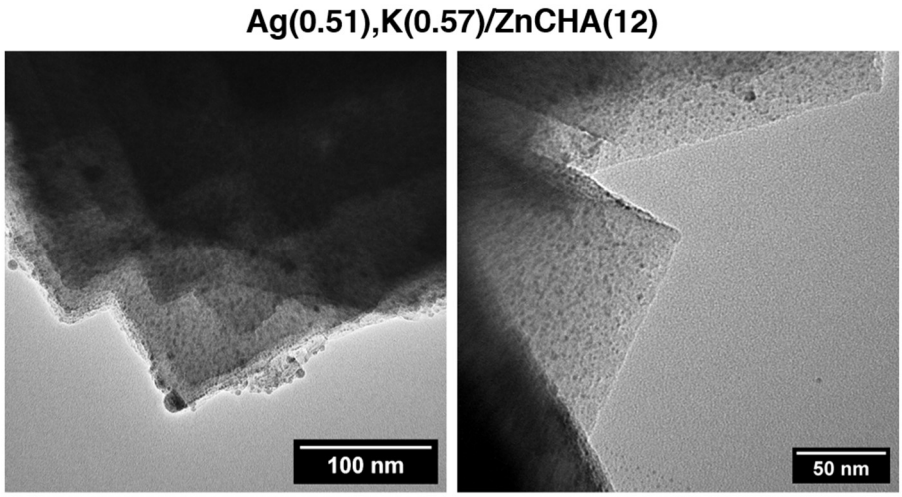

Figure 6.31: STEM-BF images of Ag(0.51),K(0.57)/ZnCHA(12) following aqueous ion-exchange with silver nitrate solution.

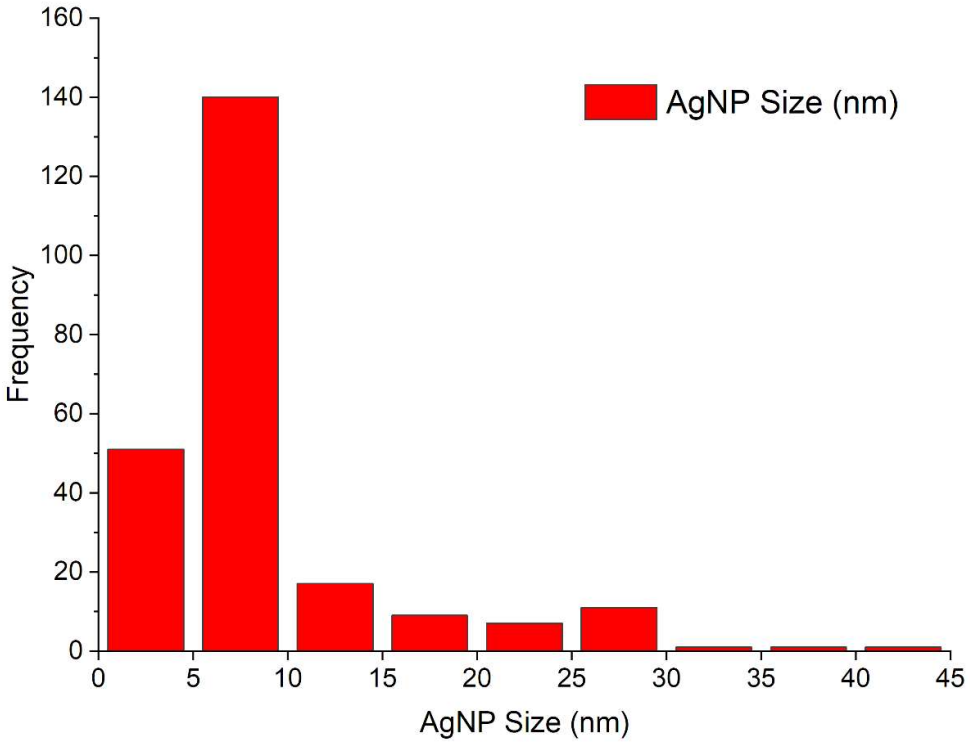

Figure 6.32: Histogram showing the silver cluster dimensions measured for Ag(0.51),K(0.57)/ZnCHA(12) following aqueous ion-exchange with silver nitrate solution.

Whilst silver clusters were observed in the acquired STEM-BF images for Ag(0.51),K(0.57)/ZnCHA(12), EDS-TEM maps included in Figure 6.33 displayed good uniformity across the elements present, with no indication of localisation with the silver clusters not resolved in the acquired EDS map.

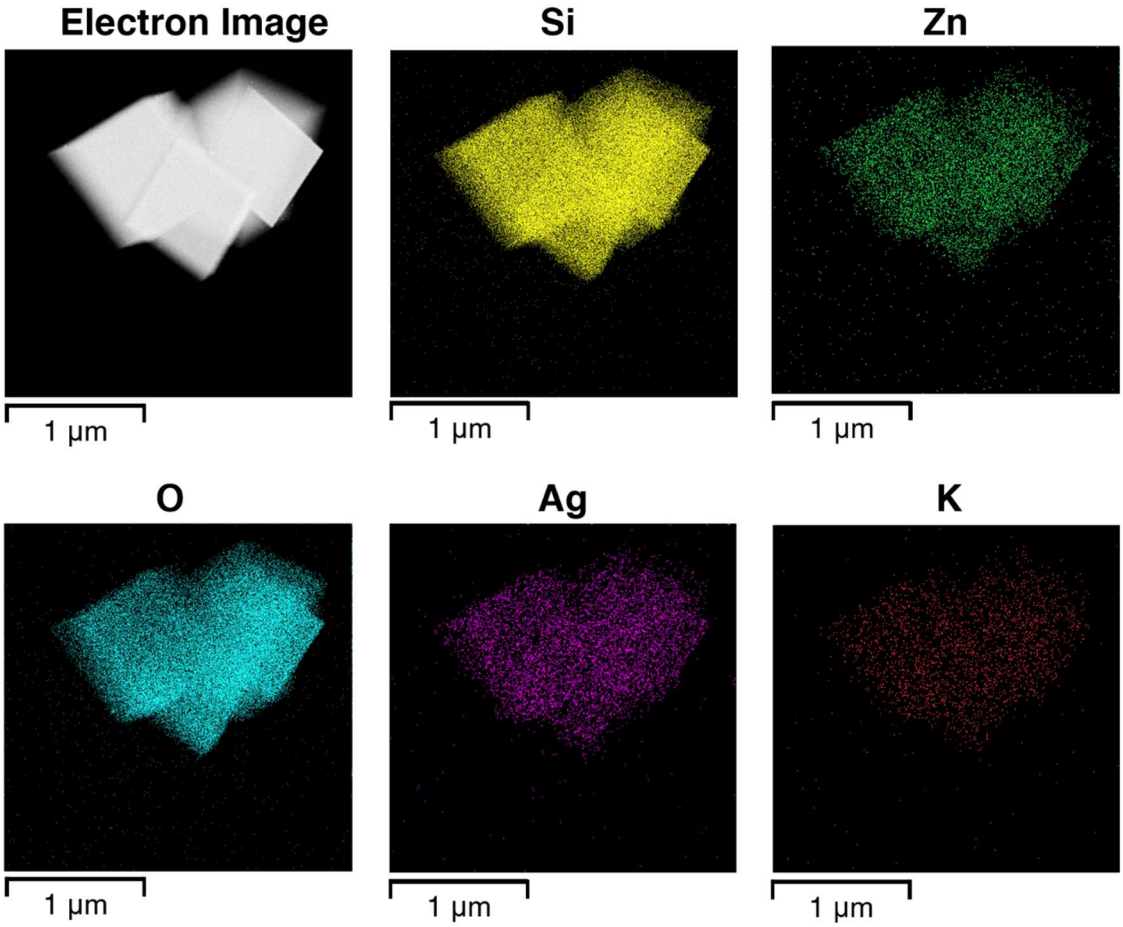

Figure 6.33: EDS-TEM maps acquired for Ag(0.51),K(0.57)/ZnCHA(12).

Minor differences were observed in the propensity of zincosilicates and zeolites to form silver clusters following aqueous ion-exchange, with silver cluster dimensions smaller on average for zincosilicates. The dimensions of silver clusters were measured using acquired STEM-BF images, with cluster size stated as their longest dimension if asymmetric in shape. STEM-BF images were acquired for Ag(0.44),K(0.23)/CHA(18) (4.9 wt% Ag), an example of which is included in Figure 6.34 alongside an acquired image for Ag(0.51),K(0.57)/ZnCHA(12).

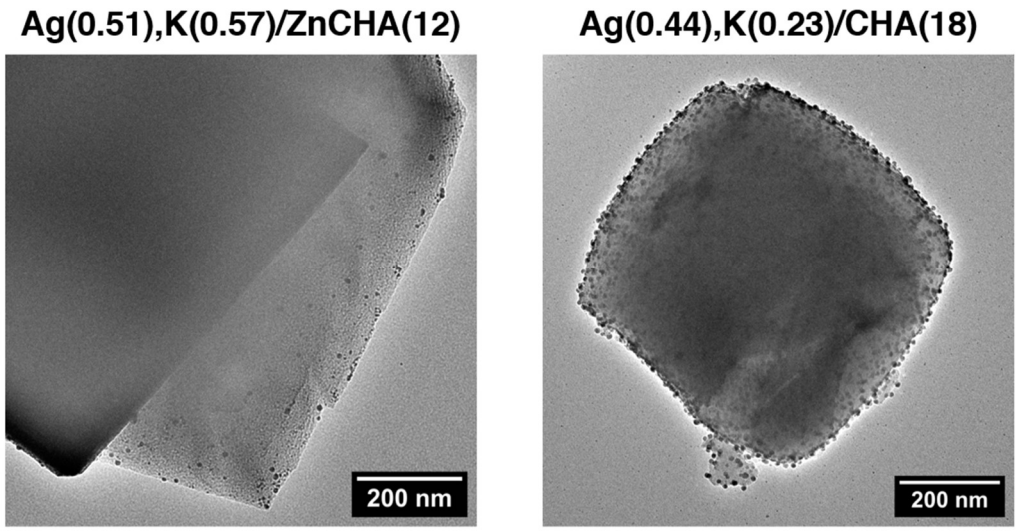

Figure 6.34: STEM-BF images acquired for Ag(0.51),K(0.57)/ZnCHA(12) and Ag(0.44),K(0.23)/CHA(18), providing visual comparison at the 200 nm scale.

The acquired STEM-BF images allowed us to calculate the mean silver cluster size was 7.1 nm (±2.0 nm) for Ag(0.44),K(0.23)/CHA(18), averaged over a total of 197 clusters. This was smaller than that observed for Ag(0.51),K(0.57)/ZnCHA(12) at 8.7 nm (±6.5 nm). A comparison of the silver cluster size distribution observed for the two materials has been included in Figure 6.35.

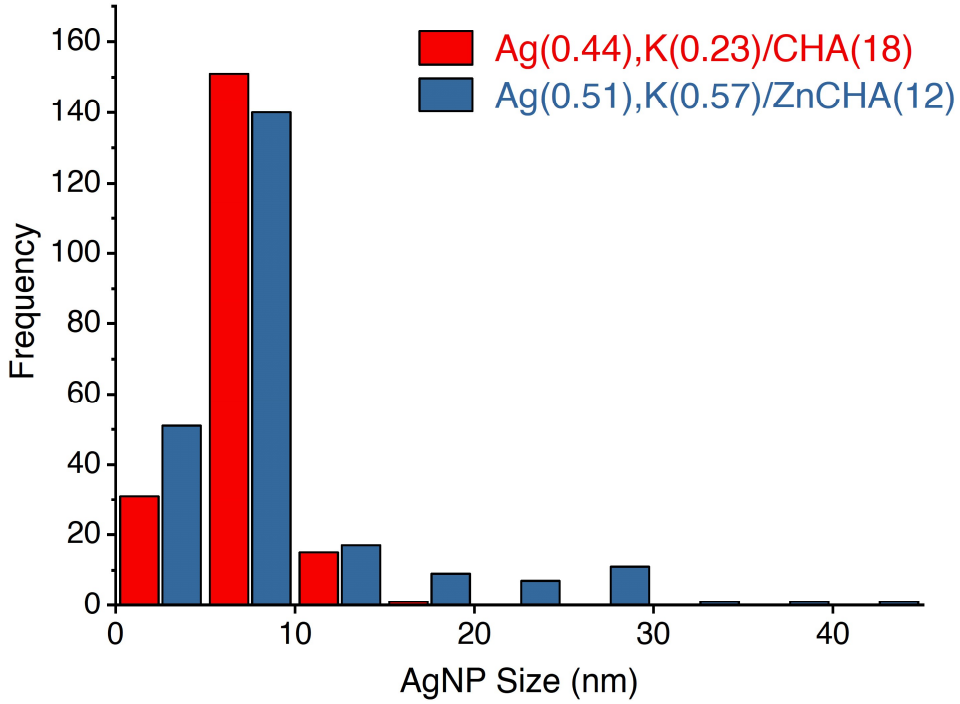

Figure 6.35: Histogram comparing the measured silver cluster dimensions for Ag(0.44),K(0.23)/CHA(18) and Ag(0.51),K(0.57)/ZnCHA(12).

The acquired EDS-TEM map for Ag(0.44),K(0.23)/CHA(18), shown in Figure 6.36, demonstrated a non-uniform elemental distribution for the silver exchanged zeolite. There was a notable level of localisation for silver at the zeolite crystal edges, corroborating with the STEM-BF images included in Figure 6.34. Potassium shows some degree of localisation towards the edges of the zeolite crystal also. However, the distribution of other elements present in the material was highly uniform with no signs of localisation.

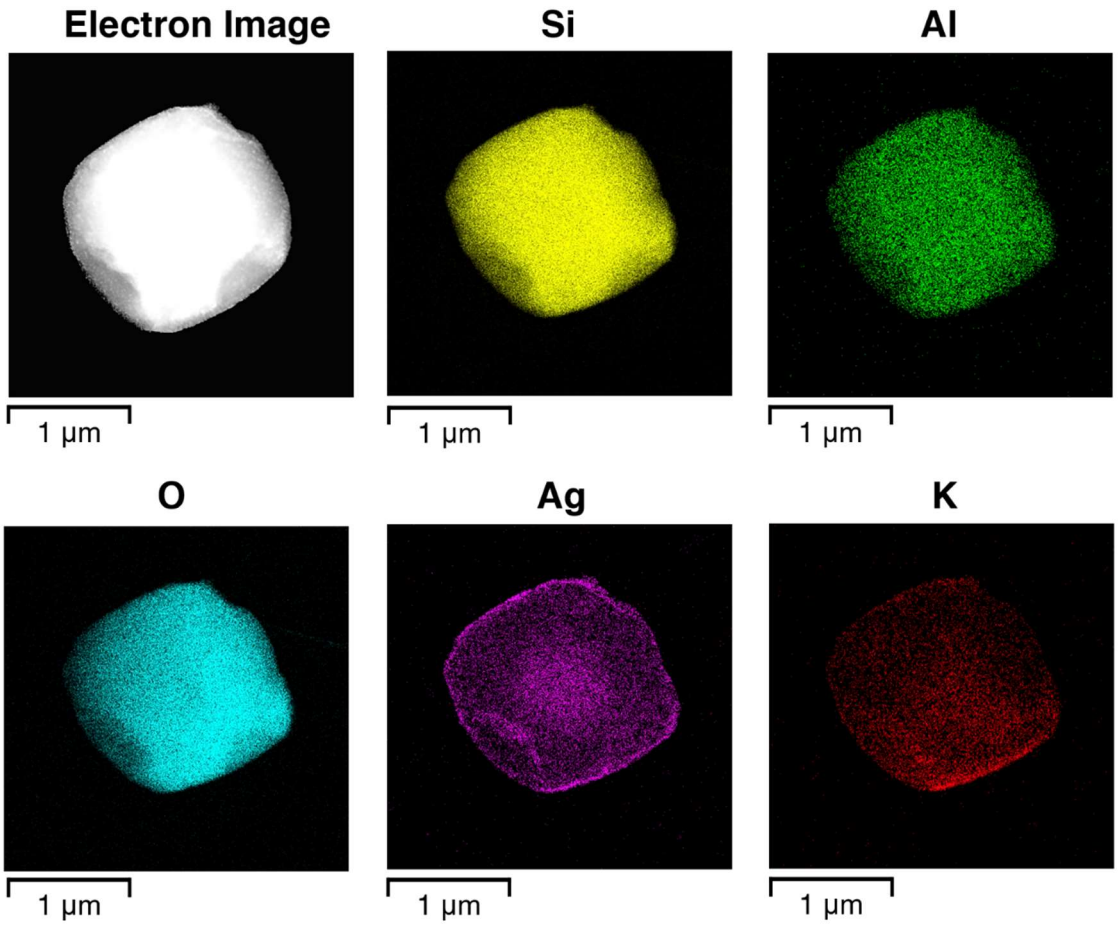

Figure 6.36: EDS-TEM maps acquired for Ag(0.44),K(0.23)/CHA(18).

6.3.3 X-Ray Absorption Spectroscopy of Silver-exchanged ZnCHA

XAS was carried out on hydrothermally synthesized ZnCHA materials to gain understanding of the zinc environments present within the framework. Outlined in section 6.2.5, XAS provided information regarding the zinc environment in H,K(0.68)/ZnCHA(12), determining the oxidation state of zinc as +2 in the parent material, as well as the average bond length and likely environment. We therefore decided to indirectly probe silver using XAS through making a direct comparison between the parent ZnCHA material and a silver exchanged form and observing any differences in the acquired spectra. Whilst obtaining information on silver was highly desirable, directly measuring silver by XAS requires the use of a beamline to generate the required X-ray energy. Silver is a fourth period element, with an X-Ray K-edge energy of 25.5 keV, which is unfortunately too high to measure using an EasyXAFS300+ laboratory-scale spectrometer.[64] Additionally, analysis of ZnMFI materials were conducted alongside to draw comparison between the small pore and medium pore zincosilicate frameworks, with experimental parameters shown in Table 6.5.

Table 6.5: Reports and observations for sample preparation and experimental parameters for XAS of ZnCHA and ZnMFI materials and zinc reference materials.

Sample ID (Material)	Edge	Experiment	Mass (mg)	Time per sample
H,K(0.68)/ZnCHA(12)	Zn K-edge	XAFS	77	2hr 20m
Ag(0.99),K(0.20)/ZnCHA(12) IE 10.0 wt% Ag	Zn K-edge	XAFS	81	2hr 20m
H,K(2.40)/ZnMFI(96)	Zn K-edge	XAFS	106	2hr 20m
Ag(1.50),K(1.76)/ZnMFI(96) IE 5.9 wt%	Zn K-edge	XAFS	106	2hr 20m
Reference 1 (zinc oxide)	Zn K-edge	XAFS	10	2hr 20m
Reference 2 (zinc acetate)	Zn K-edge	XAFS	20	2hr 20m
Reference 3 (Zn foil)	Zn K-edge	XAFS	N/A	2hr 20m

6.3.3.1 X-Ray Absorption Near Edge Structure of Silver-exchanged ZnCHA

XANES was acquired using Ag(0.99),K(0.20)/ZnCHA(12) (10.0 wt% Ag), drawing a direct comparison against its parent material, discussed in section 6.2.5.1. Initial observations of the zinc K-edge region of the XANES spectrum, shown in Figure 6.37, displayed little variance between the parent zincosilicate material and the silver exchanged form. Whilst most features are largely identical, an increase in intensity is

observed for the white line position of Zn^{2+} (9667.7 eV) for Ag(0.99),K(0.20)/ZnCHA(12).[65,66] The higher intensity signifies that more of the transition occurs for the Zn^{2+} from the occupied Zn 1s orbitals to the unoccupied Zn 4p orbitals in the silver-exchanged material.[65] Whilst both parent and silver-exchanged materials contain the same quantity of zinc in the framework, we postulate that aqueous ion-exchange of silver could have facilitated the oxidation of some Zn^{0} and Zn^{1+} species present to Zn^{2+}, with the reduction of monovalent silver cations to silver clusters in the process.

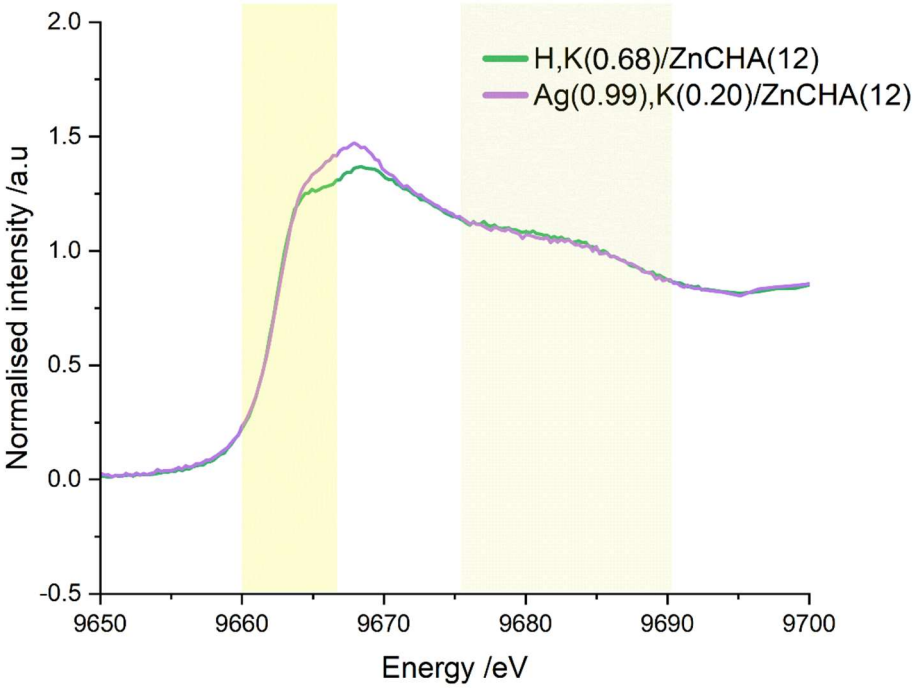

Figure 6.37: Zn K-edge XANES region highlighting the edge jump and common features in the spectra for H,K(0.68)/ZnCHA(12)and Ag(0.99),K(0.20)/ZnCHA(12).

6.3.3.2 Extended X-ray absorption fine structure of Silver-exchanged ZnCHA

Extended X-ray absorption fine structure (EXAFS) was acquired using Ag(0.99),K(0.20)/ZnCHA(12) (10.0 wt% Ag) to again draw direct comparison against the parent material. The EXAFS spectrum is shown in Figure 6.38. No differences were observed between the parent and silver exchanged ZnCHA materials, showing no variance between zinc environments for the two materials in their EXAFS spectra. We can conclude that no changes occurred to the framework with regards to zinc leaching from the aqueous ion-exchange of silver.

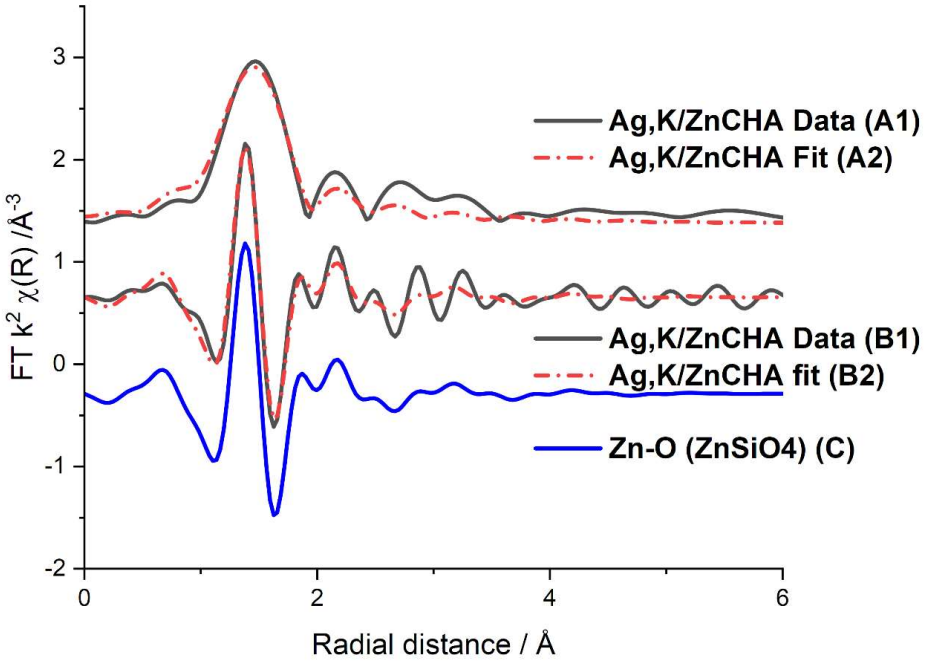

Figure 6.38: Magnitude of the k^2-weighted Fourier transform of the Zn K-edge EXAFS data for Ag(0.99),K(0.20)/ZnCHA(12) (A and B). The imaginary components of the 1 scattering path used in the fit is shown (C).

6.3.3.3 XAS Comparison to Zincosilicate MFI

Hydrothermal synthesis of zincosilicate chabazite was a major focus of this project, for which comparison could be drawn against medium pore zincosilicate MFI hydrothermally synthesized within the research group.[56] Direct comparison could therefore be drawn between both zincosilicate materials for both catalytic activity, discussed in Chapter 7 and their spectral features observed by XAS.

XANES was collected for both protic and silver exchanged ZnMFI material, however, both contain a low wt% of zinc at around 1.2 wt% Zn. In comparison with ZnCHA, which contain 8.0 wt% Zn, a low absorption intensity was acquired for the ZnMFI materials. This made it difficult to observe the features of the zinc K-edge XANES region. However, from the absorption energy of the XANES spectra, shown in Figure 6.39, it is likely that Zn^{2+} is the major zinc species for ZnMFI. This suggests that zinc is in a similar electronic state across both zincosilicate materials.

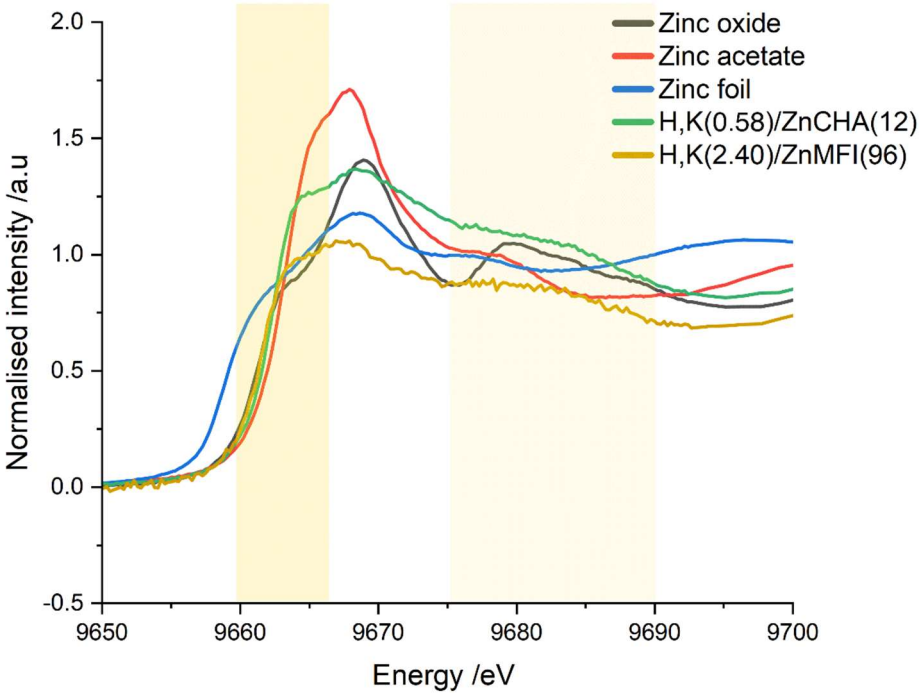

Figure 6.39: Zn K-edge XANES region highlighting the edge jump and common features in the spectra for zincosilicate MFI and silver-exchanged ZnMFI against zinc references.

One notable feature present in the XANES spectrum for Ag(1.50),K(1.57)/ZnMFI(96) was a reduction in intensity at the pre-absorption edge and at 9900 eV, highlighted in Figure 6.40. Both were found to be repeatable measurements from the material and not instrumental artifacts. These reductions in intensity suggest a change had occurred to the zinc in the framework following the introduction of silver by aqueous ion-exchange.

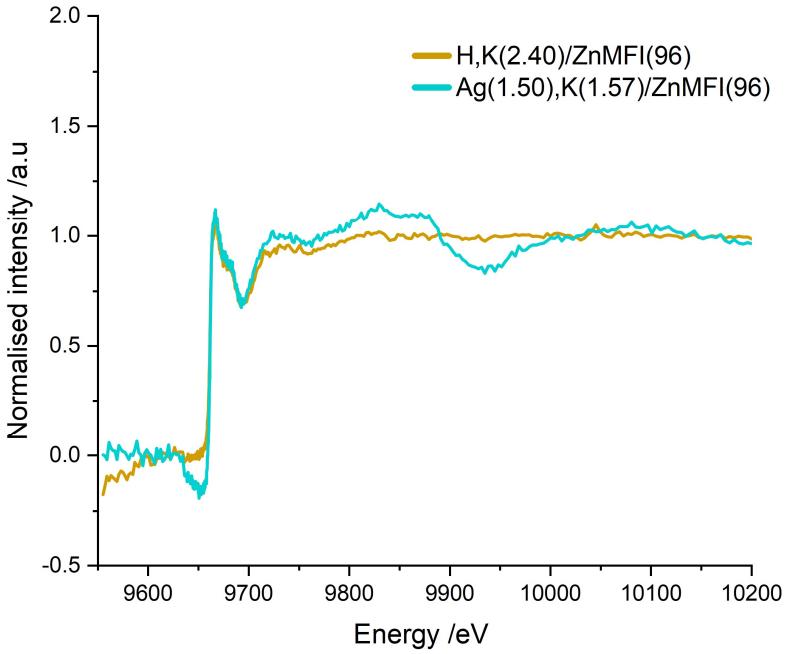

Figure 6.40: XANES spectra overlaid for Ag,K/ZnMFI and H,K/ZnMFI highlighting the differences between parent and silver-exchanged materials, with a drop in signal intensity at pre-absorption edge and at 9900 eV.

6.3.4 Conclusion of Zincosilicate Hydrothermal Synthesis and Characterization

Characterisation of silver exchanged ZnCHA materials highlighted that no zinc leaching occurred from the framework due to the ion-exchange conditions, even when using 0.25M silver nitrate solution. ED-XRF analysis measured the Si/Zn ratio for the parent material (12.23) H,K(0.68)/ZnCHA(12) and silver exchanged form (12.82) Ag(0.99),K(0.20)/ZnCHA(12) and found they remained concordant following aqueous ion-exchange. pXRD patterns indicated good crystallinity for materials, with no broadening of peaks that would indicate loss of long-range order or a significant change in crystallite size. STEM-BF images acquired highlighted silver clustering regardless of silver loading level, however, pXRD patterns did not contain reflections indicating silver clusters.[62] EDS-TEM maps acquired for silver exchanged ZnCHA showed good uniformity for all of the elements present, with no localisation. This contrasted with EDS-TEM maps acquired for Ag/CHA materials, such as Ag(0.44),K(0.23)/CHA(18), where the localisation of silver was notable at the edges and centre of the zeolite crystal. XAS was conducted on Ag(0.99),K(0.20)/ZnCHA(12), with XANES highlighting a greater proportion of zinc in the +2 oxidation state. EXAFS showed no variation between the parent material and the silver exchanged form, indicating that no change to the zinc environment had occurred as a result of aqueous ion-exchange. We can conclude that no leaching of zinc out of framework positions had occurred as a result, as indicated by ED-XRF analysis.

6.4 Chapter Six Bibliography

1 J. Zhang, J. Liang, H. Peng, Y. Mi, P. Luo, H. Xu, M. He and P. Wu, *Appl. Catal. B Environ.*, Cost-effective fast-synthesis of chabazite zeolites for the reduction of NOx, 2021, **292**, 120163.

2 Y. Kunitake, T. Takata, Y. Yamasaki, N. Yamanaka, N. Tsunoji, Y. Takamitsu, M. Sadakane and T. Sano, *Microporous Mesoporous Mater.*, Synthesis of titanated chabazite with enhanced thermal stability by hydrothermal conversion of titanated faujasite, 2015, **215**, 58–66.

3 H. V Doan, K. M. Leung, V. P. Ting and A. Sartbaeva, *CrystEngComm*, Effect of mono- and divalent extra-framework cations on the structure and accessibility of porosity in chabazite zeolites, 2021, **23**, 857–863.

4 S. Zhang, L. Pang, Z. Chen, S. Ming, Y. Dong, Q. Liu, P. Liu, W. Cai and T. Li, *Appl. Catal. A Gen.*, Cu/SSZ-13 and Cu/SAPO-34 catalysts for deNOx in diesel exhaust: Current status, challenges, and future perspectives, 2020, **607**, 117855.

5 U. Deka, I. Lezcano-Gonzalez, S. J. Warrender, A. Lorena Picone, P. A. Wright, B. M. Weckhuysen and A. M. Beale, *Microporous Mesoporous Mater.*, Changing active sites in Cu–CHA catalysts: deNOx selectivity as a function of the preparation method, 2013, **166**, 144–152.

6 E. M. Flanigen, R. W. Broach and S. T. Wilson, in *Zeolites in Industrial Separation and Catalysis*, 2010, pp. 1–26.

7 S. Prodinger, R. S. Vemuri, T. Varga, B. Peter McGrail, R. K. Motkuri and M. A. Derewinski, *New J. Chem.*, Impact of chabazite SSZ-13 textural properties and chemical composition on CO2 adsorption applications, 2016, **40**, 4375–4385.

8 S. A. Gómez, A. Campero, A. Martínez-Hernández and G. A. Fuentes, *Appl. Catal. A Gen.*, Changes in Cu^{2+} environment upon wet deactivation of Cu-ZSM-5 deNOx catalysts, 2000, **197**, 157–164.

9 K. H. Møller, M. Debost, L. Lakiss, S. Kegnæs and S. Mintova, *RSC Adv.*, Interzeolite conversion of a micronsized FAU to a nanosized CHA zeolite free of organic structure directing agent with a high CO2 capacity, 2020, **10**, 42953–42959.

10 L. V Dang, S. T. Le, R. F. Lobo and T. D. Pham, *J. Porous Mater.*, Hydrothermal synthesis of alkali-free chabazite zeolites, 2020, **27**, 1481–1489.

11 J. Devos, M. L. Bols, D. Plessers, C. Van Goethem, J. W. Seo, S.-J. Hwang, B. F. Sels and M. Dusselier, *Chem. Mater.*, Synthesis–Structure–Activity Relations in Fe-CHA for C–H Activation: Control of Al Distribution by Interzeolite Conversion, 2020, **32**, 273–285.

12 C. Chizallet, C. Bouchy, K. Larmier and G. Pirngruber, *Chem. Rev.*, Molecular Views on Mechanisms of Brønsted Acid-Catalyzed Reactions in Zeolites, 2023, **123**, 6107–6196.

13 J. N. Kondo, K. Ito, E. Yoda, F. Wakabayashi and K. Domen, *J. Phys. Chem. B*, An Ethoxy Intermediate in Ethanol Dehydration on Brønsted Acid Sites in Zeolite, 2005, **109**, 10969–10972.

14 P. Pornsetmetakul, S. Klinyod, C. Rodaum, S. Salakhum, P. Iadrat, E. J. M. Hensen and C. Wattanakit, *ChemCatChem*, Fine-Tuning Texture of Highly Acidic HZSM-5 Zeolite for Efficient Ethanol Dehydration, 2023, **15**, e202201387.

15 C. Ortega, M. Rezaei, V. Hessel and G. Kolb, *Chem. Eng. J.*, Methanol to dimethyl ether conversion over a ZSM-5 catalyst: Intrinsic kinetic study on an external recycle reactor, 2018, **347**, 741–753.

16 G. Pomalaza, P. Arango Ponton, M. Capron and F. Dumeignil, *Catal. Sci. Technol.*, Ethanol-to-butadiene: the reaction and its catalysts, 2020, **10**, 4860–4911.

17 A. Palčić and V. Valtchev, *Appl. Catal. A Gen.*, Analysis and control of acid sites in zeolites, 2020, **606**, 117795.

18 M. Orazov and M. E. Davis, *Chem. Sci.*, Catalysis by framework zinc in silica-based molecular sieves, 2016, **7**, 2264–2274.

19 B. D. Wang, N. Koike, K. Iyoki, W. Chaikittisilp, Y. Wang, T. Wakihara and T. Okubo, *Phys. Chem. Chem. Phys.*, Insights into the ion-exchange properties of Zn(ii)-incorporated MOR zeolites for the capture of multivalent cations, 2019, **21**, 4015–4021.

20 N. Koike, K. Iyoki, S. H. Keoh, W. Chaikittisilp and T. Okubo, *Chem. – A Eur. J.*, Synthesis of New Microporous Zincosilicates with CHA Zeolite Topology as Efficient Platforms for Ion-Exchange of Divalent Cations, 2018, **24**, 808–812.

21 C. S. Cundy and P. A. Cox, *Microporous Mesoporous Mater.*, The hydrothermal synthesis of zeolites: Precursors, intermediates and reaction mechanism, 2005, **82**, 1–78.

22 J. Dědeček, Z. Sobalík and B. Wichterlová, *Catal. Rev.*, Siting and Distribution of Framework Aluminium Atoms in Silicon-Rich Zeolites and Impact on Catalysis, 2012, **54**, 135–223.

23 S. Goel, S. I. Zones and E. Iglesia, *Chem. Mater.*, Synthesis of Zeolites via Interzeolite Transformations without Organic Structure-Directing Agents, 2015, **27**, 2056–2066.

24 J. Zhu, Z. D. Liu, A. Endo, Y. Yanaba, T. Yoshikawa, T. Wakihara and T. Okubo, *Crystengcomm*, Ultrafast, OSDA-free synthesis of mordenite zeolite, 2017, **19**, 632–640.

25 M. Dusselier and M. E. Davis, *Chem. Rev.*, Small-Pore Zeolites: Synthesis and Catalysis, 2018, **118**, 5265–5329.

26 M. Lemishka, J. Dedecek, K. Mlekodaj, Z. Sobalik, S. Sklenak and E. Tabor, *Pure Appl. Chem.*, Speciation and siting of divalent transition metal ions in silicon-rich zeolites. An FTIR study:, 2019, **91**, 1721–1732.

27 S. Bordiga, C. Lamberti, F. Bonino, A. Travert and F. Thibault-Starzyk, *Chem. Soc. Rev.*, Probing zeolites by vibrational spectroscopies, 2015, **44**, 7262–7341.

28 J. E. Olszowka, M. Lemishka, K. Mlekodaj, P. Kubat, D. Rutkowska-Żbik, J. Dedecek and E. Tabor, *J. Phys. Chem. C*, Determination of Zn Speciation, Siting, and Distribution in Ferrierite Using Luminescence and FTIR Spectroscopy, 2021, **125**, 9060–9073.

29 S. R. Tomlinson, T. McGown, J. R. Schlup and J. L. Anthony, *Int. J. Spectrosc.*, Infrared Spectroscopic Characterization of CIT-6 and a Family of *BEA Zeolites, 2013, **2013**, 961404.

30 M. Dong, J. Wang and Y. Sun, *Microporous Mesoporous Mater.*, Synthesis of zincosilicate mordenite using citric acid as complexing agent, 2001, **43**, 237–243.

31 R. Szostak and T. L. Thomas, *J. Catal.*, Reassessment of zeolite and molecular sieve framework infrared vibrations, 1986, **101**, 549–552.

32 P. Hu, K. Iyoki, H. Yamada, Y. Yanaba, K. Ohara, N. Katada and T. Wakihara, *Microporous Mesoporous Mater.*, Synthesis and characterization of MFI-type zincosilicate zeolites with high zinc content using mechanochemically treated Si–Zn oxide composite, 2019, **288**, 109594.

33 Y. Kwon, C. Lee and S. Park, *Chem. Phys.*, Effect of ion–molecule interaction on fermi-resonance in acetonitrile studied by ultrafast vibrational spectroscopy, 2014, **445**, 38–45.

34 A. Vimont, J. Lavalley, A. Sahibed-Dine, C. Areán, M. Delgado and M. Daturi, *J. Phys. Chem. B*, Infrared Spectroscopic Study on the Surface Properties of γ-Gallium Oxide as Compared to Those of γ-Alumina, 2005, **109**, 9656–9664.

35 N. Koike, W. Chaikittisilp, K. Iyoki, Y. Yanaba, T. Yoshikawa, S. P. Elangovan, K. Itabashi and T. Okubo, *Dalt. Trans.*, Organic-free synthesis of zincoaluminosilicate zeolites from homogeneous gels prepared by a co-precipitation method, 2017, **46**, 10837–10846.

36 B. Wichterlová, Z. Tvarůžková, Z. Sobalík and P. Sarv, *Microporous Mesoporous Mater.*, Determination and properties of acid sites in H-ferrierite: A comparison of ferrierite and MFI structures, 1998, **24**, 223–233.

37 J. Jänchen, M. J. Haanepen, M. P. J. Peeters, J. H. M. C. van Wolput, J. P. Wolthuizen and J. H. C. Van Hooff, in *Zeolites and Related Microporous Materials: State of the Art 1994 - Proceedings of the 10th International Zeolite Conference, Garmisch-Partenkirchen, Germany, 17-22 July 1994*, eds. J. Weitkamp, H. G. Karge, H. Pfeifer and W. B. T.-S. in S. S. and C. Hölderich, Elsevier, 1994, vol. 84, pp. 373–380.

38 A. G. Pelmenschikov, R. A. van Santen, J. Janchen and E. Meijer, *J. Phys. Chem.*, Acetonitrile-d3 as a probe of Lewis and Broensted acidity of zeolites, 1993, **97**, 11071–11074.

39 P. Bräuer, P. L. Ng, O. Situmorang, I. Hitchcock and C. D'Agostino, *RSC Adv.*, Effect of Al content on number and location of hydroxyl acid species in zeolites: a DRIFTS quantitative protocol without the need for molar extinction coefficients, 2017, **7**, 52604–52613.

40 C. E. Webster, R. S. Drago and M. C. Zerner, *J. Am. Chem. Soc.*, Molecular Dimensions for Adsorptives, 1998, **120**, 5509–5516.

41 W. Yan, S. Xi, Y. Du, M. K. Schreyer, S. X. Tan, Y. Liu and A. Borgna, *ChemCatChem*, Heteroatomic Zn-MWW Zeolite Developed for Catalytic Dehydrogenation Reactions: A Combined Experimental and DFT Study, 2018, **10**, 3078–3085.

42 L. Qi, M. Babucci, Y. Zhang, A. Lund, L. Liu, J. Li, Y. Chen, A. S. Hoffman, S. R. Bare, Y. Han, B. C. Gates and A. T. Bell, *J. Am. Chem. Soc.*, Propane Dehydrogenation Catalyzed by Isolated Pt Atoms in ≡SiOZn–OH Nests in Dealuminated Zeolite Beta, 2021, **143**, 21364–21378.

43 D. Gioffrè, L. Rochlitz, P.-A. Payard, A. Yakimov and C. Copéret, *Helv. Chim. Acta*, Grafting of Group-10 Organometallic Complexes on Silicas: Differences and Similarities, Surprises and Rationale, 2022, **n/a**, e202200073.

44 Z. Wang, Y. Jiang, Y. Zhang, J. Shi, C. Stampfl, M. Hunger and J. Huang, *Ind. Eng. Chem. Res.*, Identification of Vicinal Silanols and Promotion of Their Formation on MCM-41 via Ultrasonic Assisted One-Step Room-Temperature Synthesis for Beckmann Rearrangement, 2018, **57**, 5550–5557.

45 A. A. Gabrienko, I. G. Danilova, S. S. Arzumanov, A. V Toktarev, D. Freude and A. G. Stepanov, *Microporous Mesoporous Mater.*, Strong acidity of silanol groups of zeolite beta: Evidence from the studies by IR spectroscopy of adsorbed CO and 1H MAS NMR, 2010, **131**, 210–216.

46 J.-F. Wu, S.-M. Yu, W. D. Wang, Y.-X. Fan, S. Bai, C.-W. Zhang, Q. Gao, J. Huang and W. Wang, *J. Am. Chem. Soc.*, Mechanistic Insight into the Formation of Acetic Acid from the Direct Conversion of Methane and Carbon Dioxide on Zinc-Modified H–ZSM-5 Zeolite, 2013, **135**, 13567–13573.

47 D. Fu, Y. Park and M. E. Davis, *Angew. Chemie Int. Ed.*, Zinc Containing Small-Pore Zeolites for Capture of Low Concentration Carbon Dioxide, 2022, **61**, e202112916.

48 G. Qi, Q. Wang, J. Xu, J. Trébosc, O. Lafon, C. Wang, J.-P. Amoureux and F. Deng, *Angew. Chemie Int. Ed.*, Synergic Effect of Active Sites in Zinc-Modified ZSM-5 Zeolites as Revealed by High-Field Solid-State NMR Spectroscopy, 2016, **55**, 15826–15830.

49 L. Ye, Q. Song, B. T. W. Lo, J. Zheng, D. Kong, C. A. Murray, C. C. Tang and S. C. E. Tsang, *Angew. Chemie Int. Ed.*, Decarboxylation of Lactones over Zn/ZSM-5: Elucidation of the Structure of the Active Site and Molecular Interactions, 2017, **56**, 10711–10716.

50 G. Paul, C. Bisio, I. Braschi, M. Cossi, G. Gatti, E. Gianotti and L. Marchese, *Chem. Soc. Rev.*, Combined solid-state NMR, FT-IR and computational studies on layered and porous materials, 2018, **47**, 5684–5739.

51 J. A. Wilde and P. H. Bolton, *J. Magn. Reson.*, Suppression of homonuclear couplings in heteronuclear two-dimensional spectroscopy, 1984, **59**, 343–346.

52 E. Bourgeat-Lami, F. Di Renzo, F. Fajula, P. H. Mutin and T. Des Courieres, *J. Phys. Chem.*, Mechanism of the thermal decomposition of tetraethylammonium in zeolite .beta., 1992, **96**, 3807–3811.

53 D. Grant, M. A. McKervey, J. J. Rooney, N. G. Samman and G. Step, *J. Chem. Soc. Chem. Commun.*, Adamantene and its dimer, 1972, 1186.

54 A. H. Alberts, J. Strating and H. Wynberg, *Tetrahedron Lett.*, Adamantene, 1973, **14**, 3047–3050.

55 G. A. Waychunas, C. C. Fuller, J. A. Davis and J. J. Rehr, *Geochim. Cosmochim. Acta*, Surface complexation and precipitate geometry for aqueous Zn(II) sorption on ferrihydrite: II. XANES analysis and simulation, 2003, **67**, 1031–1043.

56 I. R. Mazzei, University of Durham, 2022.

57 ICSD/Retreive Database. ICSD Collection Code: (ZnSiO3) 1860, (Zn2SiO4) 9147, 16172, 20093, (Zinc tectoaluminosilicate) 72065.

58 Z. Bohström and K. P. Lillerud, *Microporous Mesoporous Mater.*, Preparation of chabazite with mesopores templated from a cationic polymer, 2018, **271**, 295–300.

59 B. Liu, Y. Zheng, N. Hu, T. Gui, Y. Li, F. Zhang, R. Zhou, X. Chen and H. Kita, *Microporous Mesoporous Mater.*, Synthesis of low-silica CHA zeolite chabazite in fluoride media without organic structural directing agents and zeolites, 2014, **196**, 270–276.

60 B. Liu, R. Zhou, K. Yogo and H. Kita, *J. Memb. Sci.*, Preparation of CHA zeolite (chabazite) crystals and membranes without organic structural directing agents for CO2 separation, 2019, **573**, 333–343.

61 N. H. Heo, Y. Kim, J. J. Kim and K. Seff, *J. Phys. Chem. C*, Surprising Intrazeolitic Chemistry of Silver, 2016, **120**, 5277–5287.

62 M. Lamoth, T. Jones, M. Plodinec, A. Machoke, S. Wrabetz, M. Krämer, A. Karpov, F. Rosowski, S. Piccinin, R. Schlögl and E. Frei, *ChemCatChem*, Nanocatalysts Unravel the Selective State of Ag, 2020, **12**, 2977–2988.

63 G. De Cremer, E. Coutino-Gonzalez, M. B. J. Roeffaers, B. Moens, J. Ollevier, M. Van der Auweraer, R. Schoonheydt, P. A. Jacobs, F. C. De Schryver, J. Hofkens, D. E. De Vos, B. F. Sels and T. Vosch, *J. Am. Chem. Soc.*, Characterization of Fluorescence in Heat-Treated Silver-Exchanged Zeolites, 2009, **131**, 3049–3056.

64 K. M. Niranjana, N. M. Badiger, D. Joseph and S. Kailas, *X-Ray Spectrom.*, Measurement of K absorption edge energies of silver and tin targets using a weak beta source, 2010, **39**, 359–363.

65 D. Gallach, A. Muñoz-Noval, V. Torres-Costa and M. Manso-Silván, *Phys. Chem. Chem. Phys.*, Luminescence and fine structure correlation in ZnO permeated porous silicon nanocomposites, 2015, **17**, 20597–20604.

66 A. L. Hollings, V. Lam, R. Takechi, J. C. L. Mamo, J. Reinhardt, M. D. de Jonge, P. Kappen and M. J. Hackett, *Metallomics*, Revealing differences in the chemical form of zinc in brain tissue using K-edge X-ray absorption near-edge structure spectroscopy†, 2020, **12**, 2134–2144.

Chapter Seven – Hydrocarbon Upgrading over Metal-Modified Zeolites and Zincosilicates

Direct upgrading reactions of hydrocarbons have attracted widespread attention due to their potential of providing a process to directly valorise cheap and abundant sources of carbon whilst avoiding the energy intensive processes required for indirect upgrading.[1-11]

7.1 Hydrocarbon Upgrading Reactions

Silver-exchanged zeolites show great potential as catalysts for direct methane conversion, in particular when using methane as a C1 feedstock to upgrade other low value feedstocks through C-C bond forming reactions. These co-processing reactions have been reported for methane with methanol,[12,13] ethanol[14] and ethylene.[15,16] C–C bond forming results in the evolution of hydrogen from hydrocarbon upgrading and co-processing reactions, such as methane/ethylene co-processing, or methanol and ethanol upgrading, shown in Equations 7.1 – 7.3.

$$[7.1]\ CH_4 + C_2H_4 \rightarrow C_3H_6 + H_2$$

$$[7.2]\ MeOH \rightarrow CH_2O + H_2$$

$$[7.3]\ EtOH \rightarrow AcH + H_2$$

The generation of hydrogen during upgrading and co-processing reactions produces reducing conditions that facilitates rapid reduction of silver cationic species to silver metallic species. The reduction process causes silver sintering, with the migration of silver to the surface of the zeolite. Formation of a BAS at the charge balancing position of the framework occurs, with silver cluster formation producing multinuclear silver clusters.[17–19] Several different cationic silver clusters have been observed in zeolites, with reports observing Ag_3^+ and Ag_6^{2+} clusters in zeolite cage structures.[20–22]

In this project, the activity of silver-exchanged zeolites and zincosilicates were investigated for several upgrading and co-processing reactions. Across the range of silver-exchanged zeolite and zincosilicate frameworks tested, several conclusions could be drawn relating to the framework effect. This effect arises from framework acidity,

secondary counterions, microporous channel dimensions and the framework dimensionality.

In addition to silver, several other metals such as palladium, platinum and gold, were investigated to compare the activity of the metal-exchanged frameworks to those exchanged with silver in various upgrading reactions. As upgrading reactions involve the evolution of hydrogen, the use of metals that would not be reduced to their metallic state by hydrogen and remaining as a monovalent species, whilst preferentially displaying similar conversion and selectivity to silver were highly desired. Baba *et al.* reported promising results for methane/ethylene co-processing over In(0.17),H/ZSM-5(12).[23] One of the reported benefits of using indium over silver was the high selectivity to produce hydrocarbon products (98.6% In and 68.9% Ag, respectively). Another benefit was the improved selectivity to upgrading products at lower indium loading levels, with higher loading level materials displaying a propensity towards C−H cracking to afford products such as CH_4, giving an apparent reduction in methane conversion.[23] Furthermore, very recent work has shown that cationic indium species supported on CHA are resistant to full reduction to In(0) (unlike cationic indium supported on SiO_2, Al_2O_3 and bulk In_2O_3), resulting in isolated In^+ sites which have been shown to be highly selective for propane dehydrogenation, with minimal (ca. 2.4%) carbon formation.[24] The In^+ cations have been show to reside in the 6MR.[25] Isolated indium hydrides on CHA have also been shown to be active in ethane dehydrogenation,[26] and further work has shown the activity to be diminished when supported on medium and large pore zeolites.[27]

7.2 Accurate Determination of Catalyst Activity by In-Line GC-MS-BID Monitoring

Quantification and determination of a materials propensity to catalyse hydrocarbon upgrading reactions requires reaction monitoring that has been calibrated across the range at which both feed and products will be observed. This ensures the highest accuracy possible when comparing catalysts like-for-like in upgrading reactions. Over the course of the work in this project, the GC-MS system underwent several calibrations. The need for calibrations arose through the requirement of machine maintenance, such as the working lifetime of consumables – often being the MS filaments – meaning that intensity and concentration values required updating in the GC-MS method or adding and removing products quantified for different upgrading reactions.

The GC-MS was setup with split ratio of 5 for the GC and 125 for the MS, both lower than previously used. These parameters allowed for the quantification of trace amounts of upgrading reaction products, assisting in the determination of the upgrading reaction pathway. Over the calibrated range for feedstock and product concentrations, non-linear calibration curves were selected as they gave the highest correlation between peak area and concentration of the analyte. The calibration curve for MeOH, fitted with a nonlinear function, is shown in Figure 7.1. The full calibration is provided in Section 10.2.

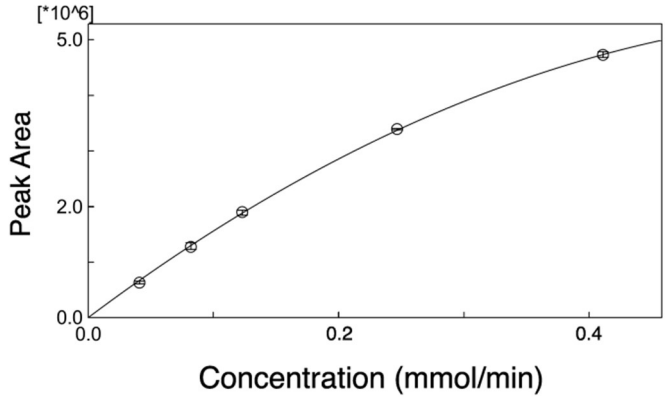

Figure 7.1: Diagram showing the non-linear fitting used for methanol calibration of the MS detector of the GC-MS-BID.

Whilst linear calibration curves are deemed optimal in analytical methodology, non-linear calibration should be used if other factors (e.g. carbon balance) are improved by non-linear calibration. For example, Deem *et al.* reported their observations on requiring non-linear fitting when monitoring a Sonogashira reaction, reflecting that the nonlinear relationship provided the most accurate way to determine the material consumption and

product formation over the course of the reaction.[28] In our case here, the use of a linear fitting for our calibration would have required using a higher split ratio for our GC-MS method, which would have caused a reduction in sample injection volume into the GC-MS. This would in turn lose the ability to detect trace amounts of products produced during the upgrading and co-processing reactions. These trace products could provide key information for us to derive the upgrading reaction pathway, which would otherwise have been lost.

The GC-MS-BID on-line reaction monitoring was fed directly from a HEL FlowCAT unit in which all of our reported upgrading and co-processing reactions took place. The gas feed was fed to the GC-MS through an insulated and trace heated (at 180 °C) line. The standard experimental procedure, as well as the equipment used, is outlined in section 3.2.14 and section 3.2.15.

7.3 Ethanol Upgrading Reactions

Ethanol valorisation has been widely explored, with upgrading reactions carried out over a diverse set of catalysts capable of producing a variety of products.[14,29–33] The widespread availability and low cost of bioethanol provides further emphasis into deriving valorisation processes for this platform chemical.[32] One upgrading product of interest from ethanol is acetaldehyde, produced commercially by ethylene oxidation using the Wacker-Hoechst process.[34,35] Ethanol dehydrogenation to acetaldehyde gives a one-step process to a versatile platform chemical used in the synthesis of carboxylic acids, esters and ketones.[36–38] Renewable bioethanol not only allows the generation of several higher value products from bio-derived means but also generates blue hydrogen in the process.

Ethanol upgrading reactions carried out in this project were explored over a variety of zeolite and zincosilicate materials, facilitating different upgrading reaction pathways due to their changed acidity. Changed temperature, metals and secondary counterions were explored for the majority of the frameworks explored. Ethanol upgrading reactions were carried out using the flow rates and catalyst loading shown in Figure 7.2.

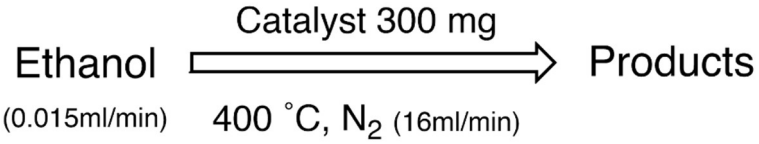

Figure 7.2: Graphic showing the reaction conditions and catalyst loading used for ethanol upgrading at 400 °C

A standard reaction profile was used for ethanol upgrading reactions, shown in Figure 7.3, with temperature, step duration and flow rate labelled for the individual steps. The initial step establishes gas flow through the reactor to ensure no blockages, before undergoing heating to dehydrate and desorb any atmospherics present in the micropores of the catalyst. Figure 7.3 highlights the cooling of the reactor to the reaction temperature of 350 °C. For reactions at 350 °C, a short dwell was used to allow the catalyst bed to equilibrate to the reduced temperature before starting the flow of ethanol. Several reactions were carried out using this profile, such as ethanol upgrading (1), methane/ethanol co-processing (2) and methane/ethanol co-processing with oxygen included in the feed (3).

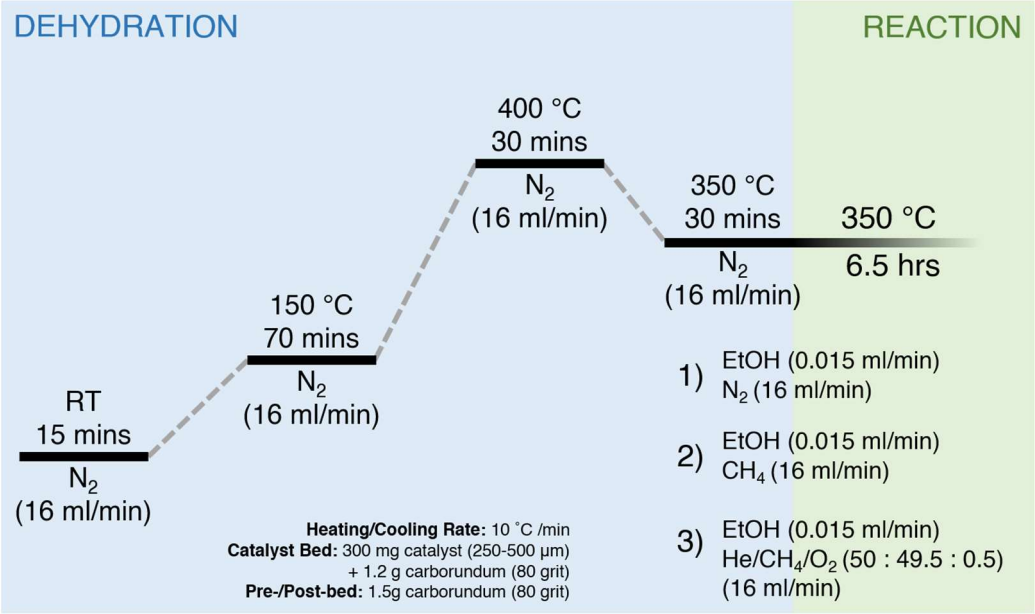

Figure 7.3: Diagram showing the reaction profile for reactions carried out at 350 °C, with the dehydration and desorption steps used prior to the reaction step for ethanol upgrading and methane/ethanol co-processing reactions.

Reaction profiles for reactions at 400 °C, shown in Figure 7.4, were identical for the dehydration steps, with the reaction steps initiating whilst held at 400 °C for the duration of the upgrading reaction.

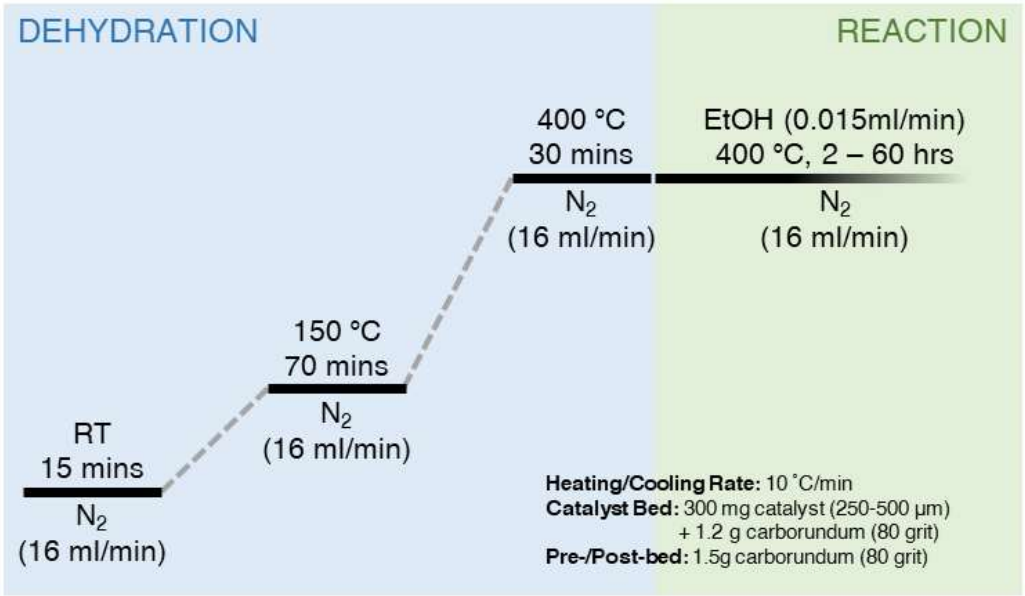

Figure 7.4: Diagram showing the reaction profile for reactions carried out at 400 °C, in this example for ethanol upgrading, with the dehydration and desorption steps used prior to the reaction step.

Ethanol upgrading products and determination of the reaction pathway was of great interest. Over the course of the project, many of the upgrading products shown in Figure 7.5 were observed over various catalysts. The ability to logically determine the upgrading pathway allowed for the potential of refining reaction parameters to enhance particular product selectivity.

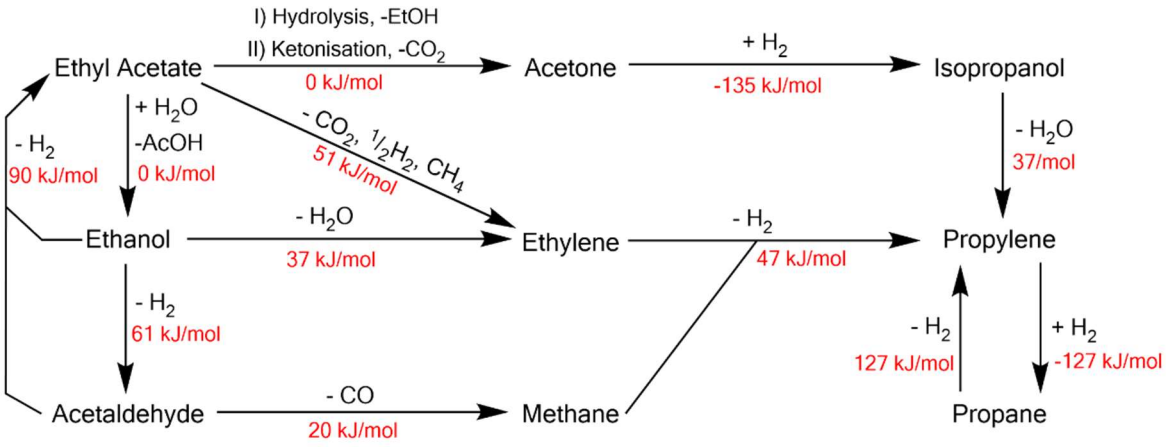

Figure 7.5: Graphic showing ethanol upgrading reaction product pathways to products observed during this project. Enthalpy of reaction values (standard conditions) were calculated for each transformation and highlighted in red.[39]

7.3.1 Ethanol Upgrading Reactions over Metal-exchanged Protic Zeolites

Ethanol upgrading reactions were carried out using various zeolite frameworks, including chabazite, mordenite and ZSM-5, with varied metals and secondary counterions. Product quantification was conducted using on-line GC-MS-BID. Calibration for the GC-MS-BID is provided in full in section 10.4, with the calibrated products listed alongside their detection method in Table 7.1. Aromatic products were not calibrated in the MS as they were not products of interest.

Table 7.1: GC-MS-BID calibrated products and their detection method.

Chemical	Calibrated MS	Calibrated BID
Methanol	✓	X
Ethanol	✓	X
Acetaldehyde	✓	X
Acetone	✓	X
2-Propanol	✓	X
Ethyl acetate	✓	X
1-Butanol	✓	X
Crotonaldehyde	✓	X
Ethylene	✓	✓
Ethane	✓	✓
Propylene	✓	✓
Propane	✓	✓
Isobutane	✓	X
Linear butenes	✓	X
Butadiene	✓	X
Isobutene	✓	X

Ethanol upgrading was carried out at 400 °C over H/ZSM-5(13.5) (Figure 7.6), Ag(0.35),H/ZSM-5(13.5) IE 4.6 wt% Ag (Figure 7.7) and Pt(0.01),H/ZSM-5(13.5) IE 0.2wt% Pt (Figure 7.8). In all cases, the time-on-stream (TOS) graphs show consistent activity, with full ethanol conversion and for the quantified products. Propane was the major product of those quantified. The remaining products (MS trace, unquantified) observed for the ZSM-5 catalysts consisted of various C_3-C_6 olefins alongside BTX products and their derivatives. C_3-C_6 olefins displayed overlapping peaks in the MS trace, giving very poor resolution and making any attempt for accurate quantification difficult.

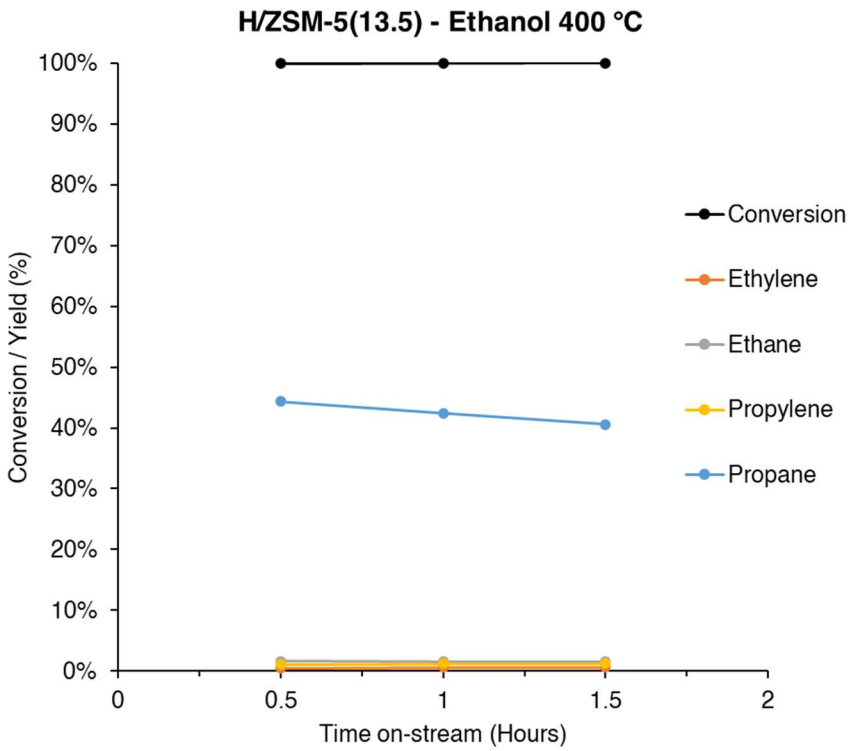

Figure 7.6: Time on-stream graph for ethanol conversion and product yields for ethanol upgrading reaction at 400 °C over H/ZSM-5(13.5).

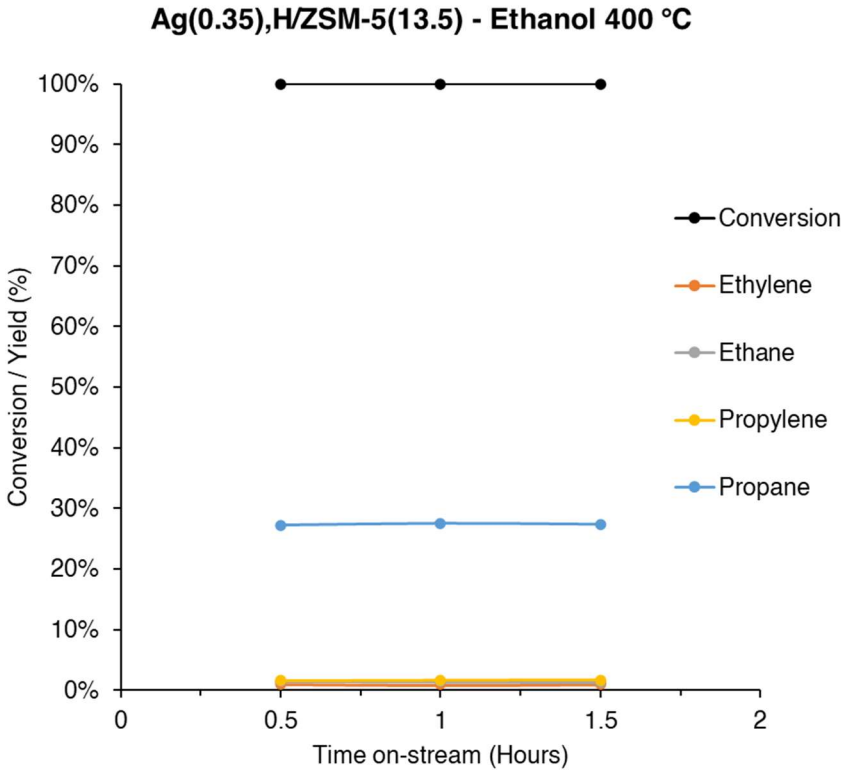

Figure 7.7: Time on-stream graph for ethanol conversion and product yields for ethanol upgrading reaction at 400 °C over Ag(0.35),H/ZSM-5(13.5).

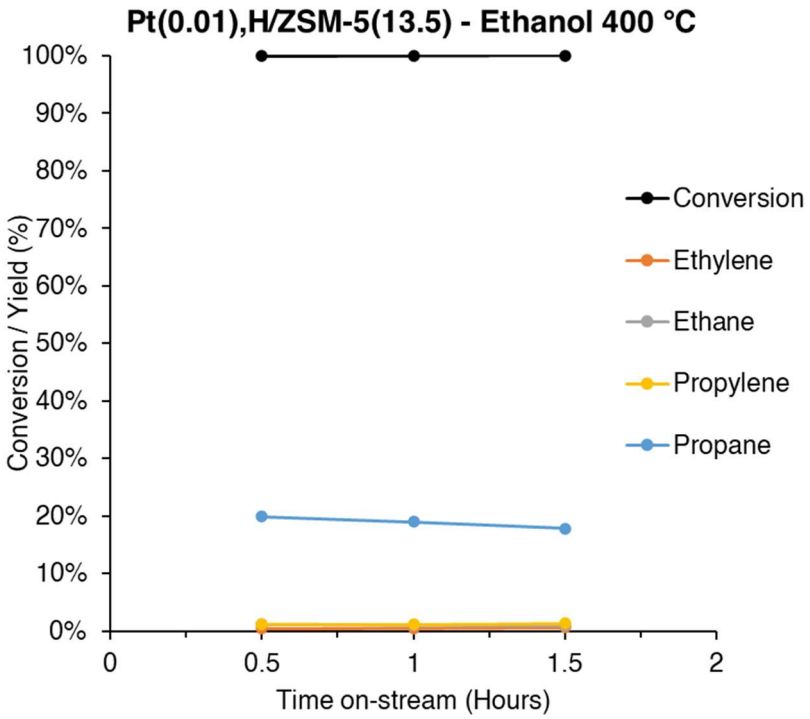

Figure 7.8: Time on-stream graph for ethanol conversion and product yields for ethanol upgrading at 400 °C over Pt(0.01),H/ZSM-5(13.5).

Averaged results over 1.5 hours as shown in Figure 7.9. Whilst all three catalysts displayed complete ethanol conversion, propane yields decreased from parent (42%) to silver (27%) to platinum form (19%) respectively, whilst producing a greater quantity of unquantified C_3-C_6 olefins alongside BTX products. Catalytic activity remained consistent during the reaction for all three catalysts.

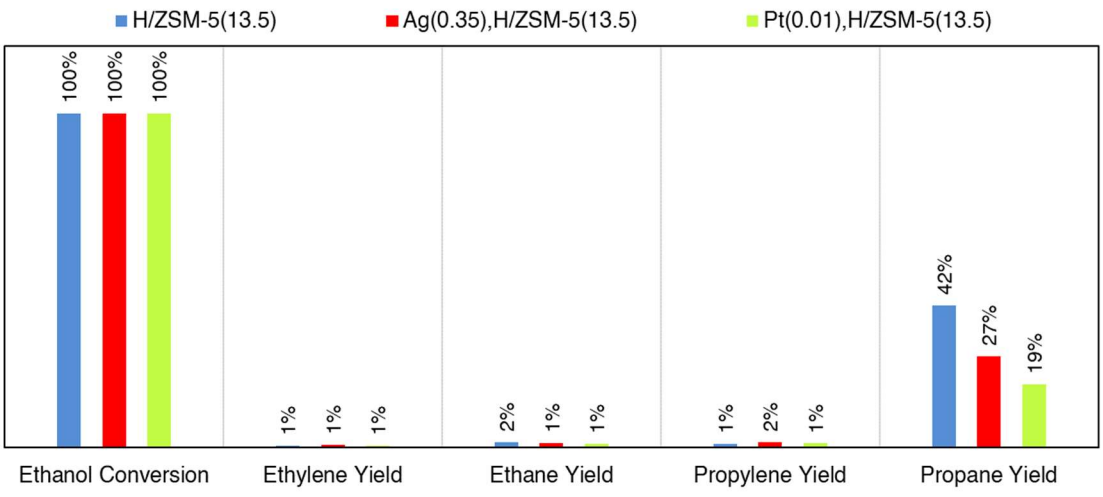

Figure 7.9: Results of ethanol upgrading at 400 °C as an average of 1.5 hours on stream for H/ZSM-5(13.5) (blue), Ag(0.35),H/ZSM-5(13.5) (red) and Pt(0.01),H/ZSM-5(13.5) (lime).

Investigation into the framework effect to highlight differences between small and medium pore frameworks, led to conducting ethanol upgrading at 400 °C over H/CHA(12) (Figure 7.10), Ag(0.41),H/CHA(12) IE 5.7 wt% Ag (Figure 7.11) and Pt(0.01),H/CHA(12) IE 0.3 wt% Pt (Figure 7.12).

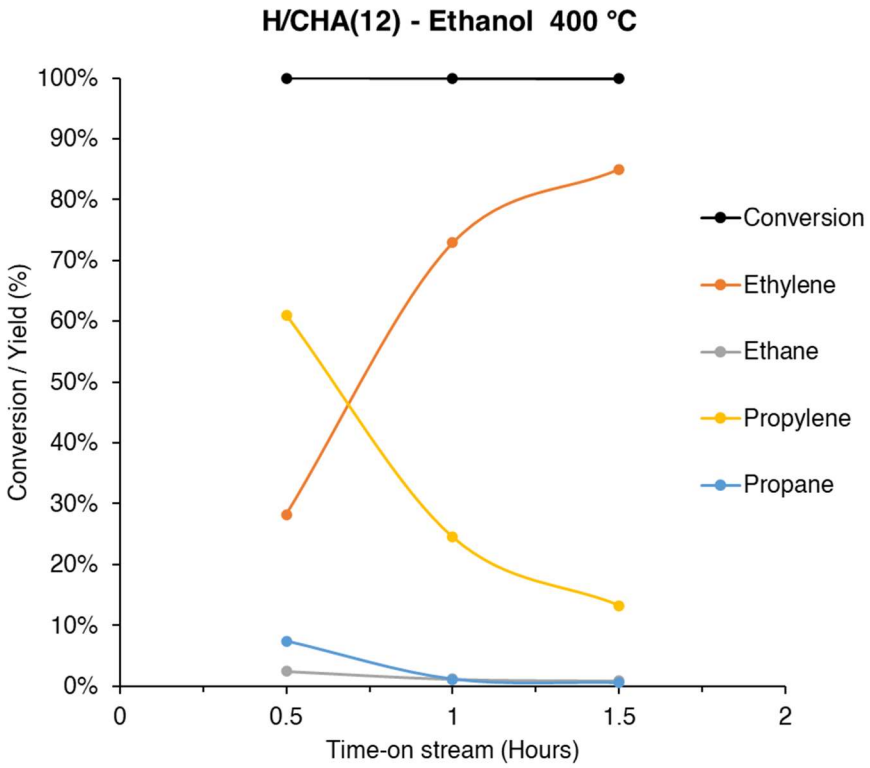

Figure 7.10: Time on-stream graph for ethanol conversion and product yields for ethanol upgrading reaction at 400 °C over H/CHA(12).

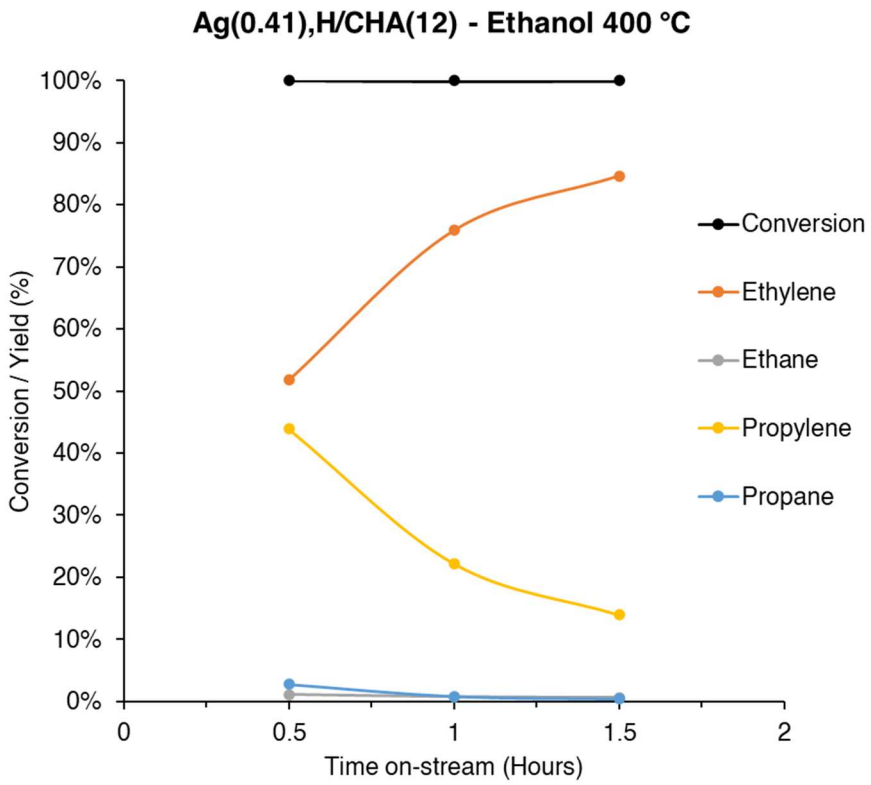

Figure 7.11: Time on-stream graph for ethanol conversion and product yields for ethanol upgrading reaction at 400 °C over Ag(0.41),H/CHA(12).

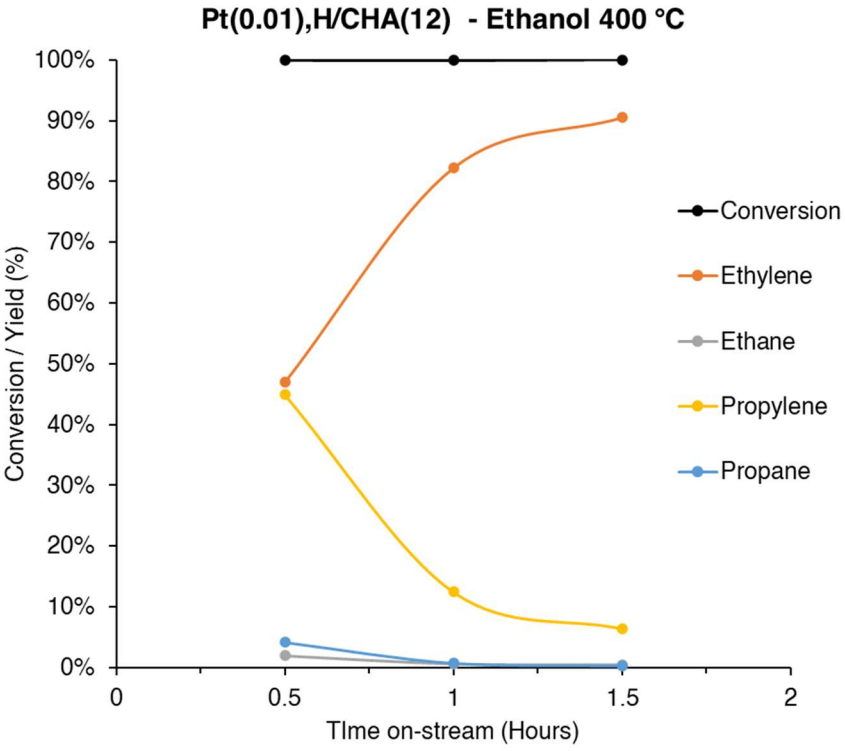

Figure 7.12: Time on-stream graph for ethanol conversion and product yields for ethanol upgrading reaction at 400 °C over Pt(0.01),H/CHA(12).

Averaged results for 1.5 hours of ethanol upgrading at 400 °C are shown in Figure 7.13. Once again, complete ethanol conversion was observed for all catalysts. Ethylene yield was noted to increase from protic (62%) to silver (71%) to platinum (73%) CHA material, whilst propylene yield was noted to decrease from protic (33%) to silver (27%) to platinum (21%) respectively. We postulate that introduction of silver and platinum led to the introduction of more BAS on the framework, hence the increased selectivity towards ethylene from BAS catalysed ethanol dehydration. As the reaction proceeded, ethylene selectivity increased with time as propylene selectivity decreased.

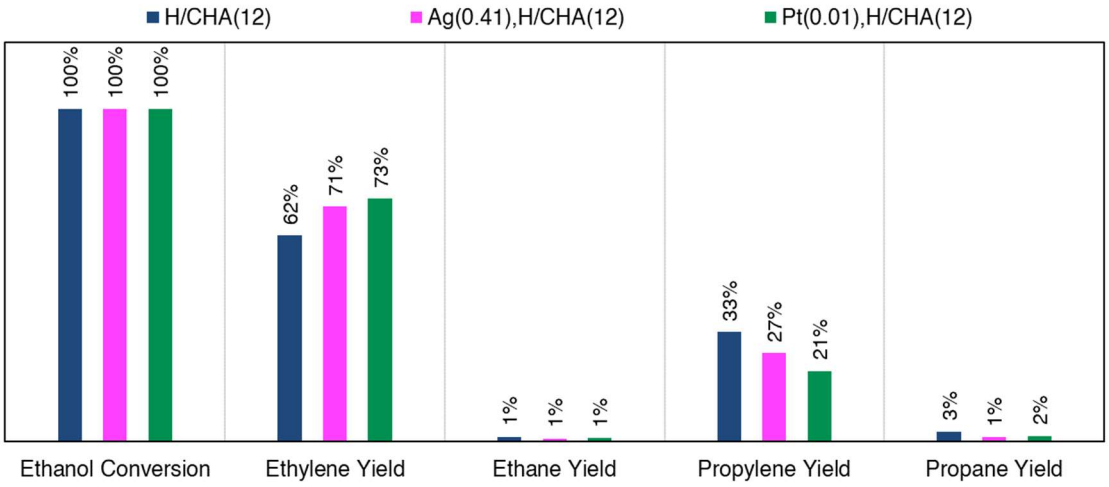

Figure 7.13: Results of ethanol upgrading at 400 °C as an average of 1.5 hours on stream for H/CHA(12) (navy), Ag(0.41),H/CHA(12) (pink) and Pt(0.01),H/CHA(12) (green)

Unlike medium pore ZSM-5, the small pore chabazite catalysts did not produce C_3-C_6 olefins or BTX products and their derivatives. Formation of bulky aromatics and their derivatives are restricted in small pore materials as the necessary transition states (TS) cannot be accessed in the micropores. A drastic change in product selectivity was observed over 1.5 hours for all three chabazite materials. We postulate that aromatic formation (unquantified) and subsequent cracking produces propylene and propane. However, aromatic formation would have to be the rate determining step of ethanol to propylene/propane, with cracking to be rapid since no aromatic products were observed in the MS trace. Blocking of the micropores and cages by either carbonaceous deposition or the production of molecules too large to freely diffuse from the small pore channels could facilitate surface BAS chemistry, with ethanol dehydration being the dominant process at 1.5 hours on-stream for each material. Little effect on product selectivity was observed from the introduction of silver or platinum to the framework.

Both ZSM-5 and CHA catalysts were observed over 1.5 hours on-stream for comparability during ethanol upgrading at 400 °C. Whilst medium-pore ZSM-5 with its propensity to produce BTX products and their derivatives. Continued production of heavy hydrocarbons was highly undesirable due to their inclination to build-up on the internal walls of pipework, hence short run times.

Mordenite was also investigated, with this framework being pseudo 1D with small and large micropores, compared to the 3D frameworks of chabazite (small pore) and ZSM-5 (medium pore). Ethanol upgrading at 400 °C over Ag(0.38),Na/MOR(6.5) (Figure 7.14) and Ag(0.16),Na/MOR(6.5) (Figure 7.15) was conducted over 1.5 hours.

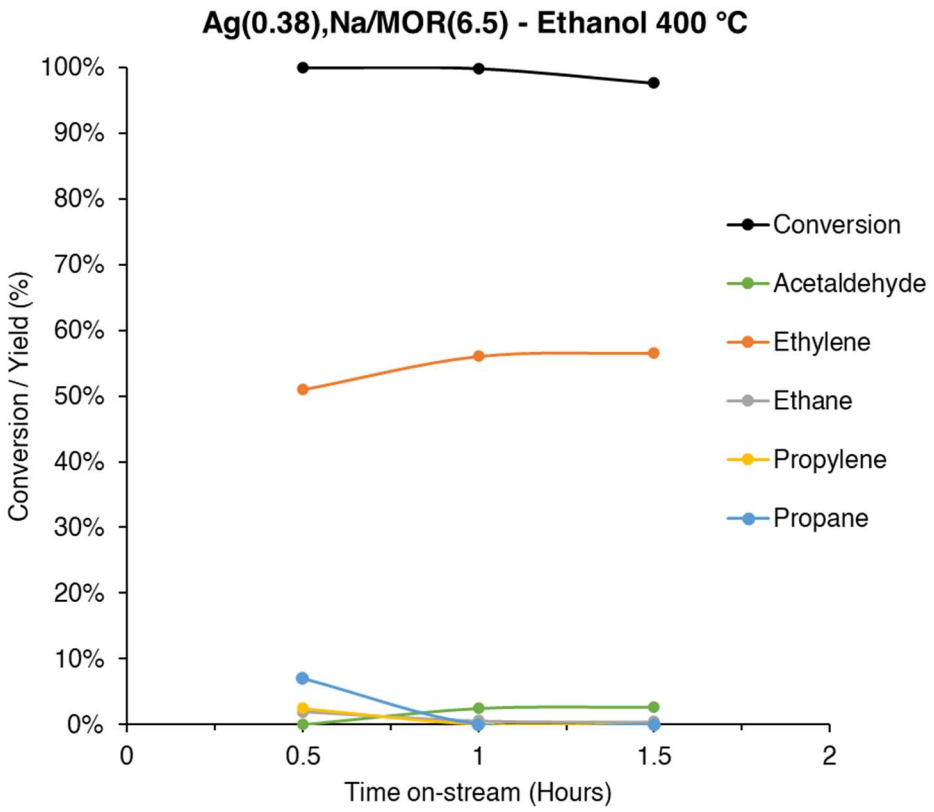

Figure 7.14: Time on-stream graph for ethanol conversion and product yields for ethanol upgrading reaction at 400 °C over Ag(0.38),Na/MOR(6.5).

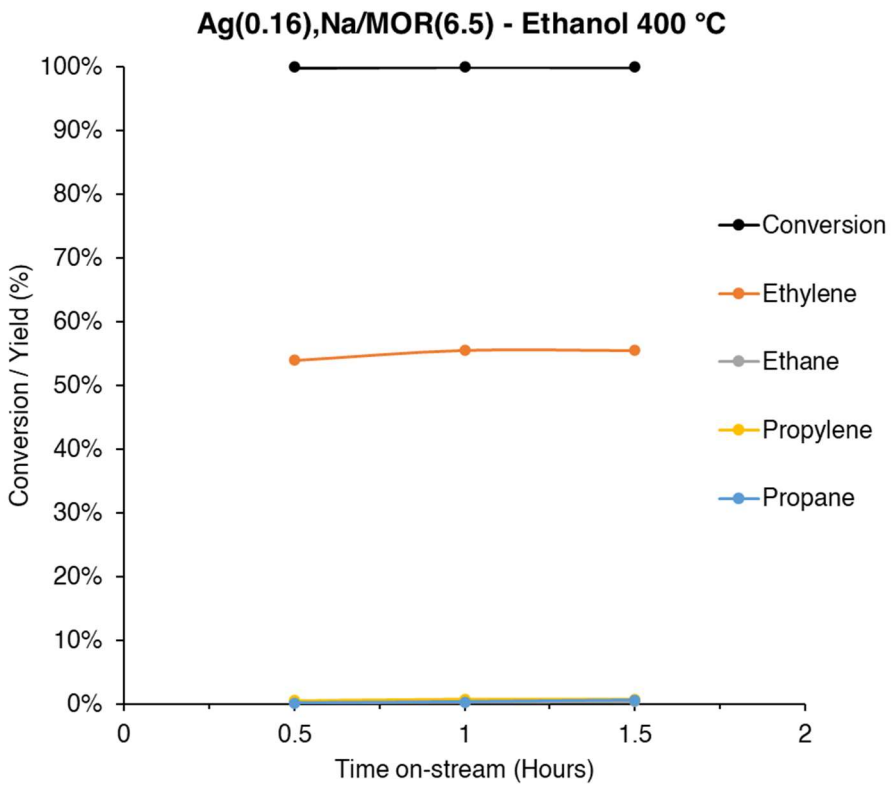

Figure 7.15: Time on-stream graph for ethanol conversion and product yields for ethanol upgrading reaction at 400 °C over Ag(0.16),Na/MOR(6.5).

Both catalysts displayed consistent catalytic activity with TOS, with a small onset observed for mordenite with higher silver loading, likely indicating a change in silver species present. Averaged results of 1.5 hours on-stream are shown in Figure 7.16. Complete ethanol conversion was observed for 1.5 hours on-stream, with Ag(0.38),Na/MOR(6.5) displaying a higher yield of acetaldehyde (2%) and propane (2%) than Ag(0.16),Na/MOR(6.5). However, the time on-stream graph shows the higher loading material product selectivity changes from propylene and propane to acetaldehyde over 1.5 hours. A change in silver species has likely occurred under reaction conditions, to facilitate the changed selectivity.

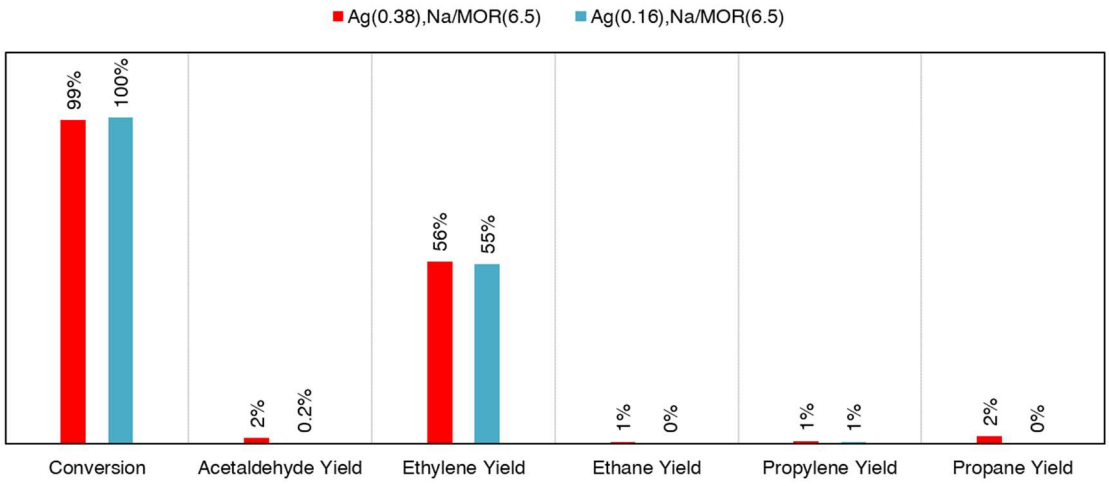

Figure 7.16: Results of ethanol upgrading at 400 °C as an average of 1.5 hours on stream for Ag(0.38),Na/MOR(6.5) (red) and Ag(0.16),Na/MOR(6.5) (blue).

Both mordenite catalysts led to a wide range of C_3-C_6 olefins and BTX being observed, with products unquantified. The presence of residual strong Brønsted acidity of zeolites meant ethanol dehydration (and subsequent conversion steps) was the dominant process. This catalytic pathway was observed across the different zeolite frameworks, with ethanol conversion observed to be close to 100% for all tested. Only mordenite catalysts led to the observation of acetaldehyde as a product. We noted that the inclusion of silver or platinum had little influence on ethanol conversion and product selectivity. Our findings are line with prior reports of ethanol upgrading, with premature deactivation observed for catalysts with BTX selectivity due to excessive coking.[40–47]

7.3.1.1 Ethanol Upgrading over Silver and Potassium-exchanged Zeolites

Carrying out ethanol upgrading over silver-exchanged zeolites showed that the ethanol dehydration pathway would remain dominant if BAS were present in the framework. To avoid this issue and eliminate BAS in the framework, exhaustive ion-exchange of the parent zeolite was conducted with potassium cations, prior to the introduction of Ag^+ via a second ion-exchange step. Potassium aqueous ion-exchanges were carried out using repeated aqueous exchanges as shown in Figure 7.17.

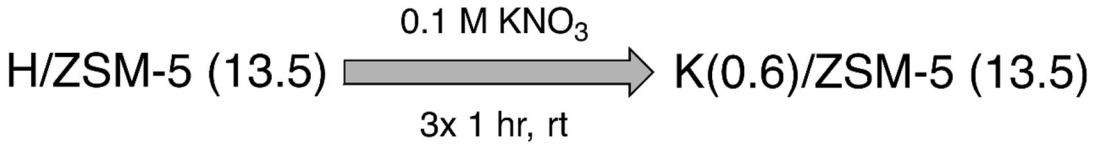

Figure 7.17: Graphic displaying aqueous ion-exchange of zeolites using potassium nitrate solution.

For several materials, 'over-exchange' was observed following potassium and subsequent silver ion-exchange. This was where the ratio of charge balancing cations to aluminium present in the framework exceeded 1:1. An example of this is shown in Table 7.2. All aqueous ion-exchanges with potassium were conducted at room temperature for 1 hour, as shown in Figure 7.17.

Table 7.2: Table showing ED-XRF results for examples of over-exchange of H/ZSM-5(13.5) following potassium ion-exchange and subsequent silver ion-exchange, where the ratio of counterions to aluminium in the framework exceeds 1:1 following aqueous ion-exchange.

Exchange	Al (wt%)	Si (wt%)	Si/Al	K (wt%)	K/Al	Ag (wt%)	Ag/Al
6x KNO3 (0.1M)	2.75 ± 0.06	35.75 ± 0.92	12.50	4.44 ± 0.16	1.12	N/A	N/A
1x AgNO3 (0.1M)	2.28 ± 0.05	29.00 ± 0.70	12.20	1.76 ± 0.04	0.53	8.08 ± 0.07	0.89

Potassium clusters in FAU and LTA topology zeolites are known,[48–50] so over-exchange either indicates cluster formation or potassium counterions were exchanging with sites other than framework charge balancing positions. Corma *et al.* also report potassium exchange with silanol defects and silanol nests, producing Si–O–K^+ species.[51] Over-exchange has also been reported for caesium exchanged zeolites.[52] However, exchanging a significant portion of counterbalancing cations to alkali metals such as potassium or caesium leads to changed acidity within the material itself, producing (weakly) basic zeolites.[52–54] Ethanol upgrading was carried out over potassium-exchanged materials which were fully- or over-exchanged, with no ethanol conversion observed for K(2.70)/ZSM-5(43.5) at 400 °C.

Lower temperatures were also explored for ethanol upgrading, used to decrease selectivity toward aromatic products. These reactions are discussed in section 7.5.2, before investigating methane/ethanol co-processing over a series of silver-exchanged catalysts. In addition, due to a backpressure issue with the FlowCAT system a reduced flow rate for ethanol was used (0.01 ml/min rather than 0.015 ml/min).

Ethanol conversion was carried out at 350 °C over Ag(2.42),K(0.88)/ZSM-5(13.5) IE 14.6 wt% Ag, with time on-stream shown in Figure 7.18. Complete ethanol conversion could be observed over the entire 6.5 hours on-stream. During the ethanol upgrading reaction, product selectivity changed which indicated a change in active species. The yields for propylene, ethane, propane and butanes/butenes all decreased during time on-stream, likely representative of silver deactivation in which the silver cationic species

are reduced causing them to sinter, leaving behind a BAS. The formation of additional BAS would lead to increased ethylene yield over time with fast turnover for ethanol dehydration over BAS, particularly in ZSM-5.[55–58]

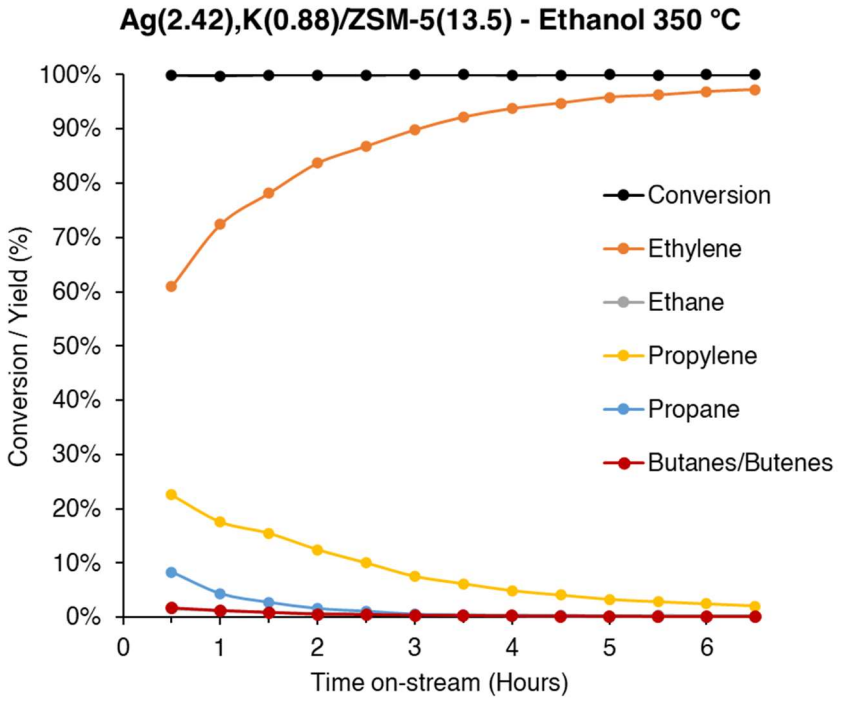

Figure 7.18: Time on-stream graph showing ethanol conversion and product yields for ethanol upgrading reaction at 350 °C over Ag(2.42),K(0.88)/ZSM-5(13.5) Ag 14.6 wt%.

Due to the reduced temperature, a low selectivity towards BTX products were observed over the initial 4 hours, with high selectivity towards gas products After 4 hours, no BTX products were observed. Following the introduction of potassium secondary counterions, BAS chemistry continued to be dominant, with ethylene as the favoured product. Unlike Ag(0.35),H/ZSM-5(13.5), where a significant portion of products at 400 °C were C_3-C_6 olefins and BTX products, these were suppressed at 350 °C over Ag(2.42),K(0.88)/ZSM-5(13.5). Whilst there was a change in secondary counterion from protic to potassium, we must acknowledge the effects of reduced reaction temperature for product selectivity. The delocalised π-system provides stability to aromatics meaning they persist under high temperatures, where aliphatic compounds may not.

Additionally, the lifetime of silver for ethanol upgrading reaction at 350 °C appeared to be around 4 hours. This is in line with prior art, with reported lifetimes for silver in Ag(0.17),H/ZSM-5(12) for methane/ethylene co-processing (400 °C) at 4 hours[16] and in Ag(0.24),H/ZSM-5(10) for ethylene dehydroaromatisation (400 °C) at 5 hours.[59]

7.3.2 Ethanol Upgrading Reactions over Metal-exchanged Zincosilicates

We postulated that changing the Brønsted acidity of zeolites for the Lewis acidity of zincosilicates would avoid undesirable ethanol dehydration. The formation of acid sites should prove less problematic when using zincosilicates, as Lewis acid sites facilitate dehydrogenation rather than dehydration, inclusion of zinc in the framework provides a divalent charge imbalance, which could negate silver sintering by stabilising any multivalent silver clusters that form.

Zincosilicate MFI (ZnMFI) had been produced in-house by Dr Irene Mazzei.[60] Initial observations of ethanol upgrading using K(2.40)/ZnMFI(96) had shown the Lewis acidic material provided a changed upgrading pathway to the Brønsted acidic zeolites. Dehydrogenation of ethanol, to produce acetaldehyde was now the favoured pathway rather than the dehydration of ethanol to ethylene in zeolites, as shown in section 10.4. The ability of zincosilicate zeotypes to effect the dehydrogenation of ethanol to acetaldehyde has recently been reported by a number of groups.[61–64] It was envisaged that silver exchanged ZnMFI could enhance both ethanol conversion and acetaldehyde selectivity, as established catalysts for methanol conversion to formaldehyde are silver based.[65,66] Platinum exchanged ZnMFI was also investigated for its activity towards ethanol upgrading. In addition to this medium-pore zincosilicate, small-pore ZnCHA materials were also investigated to highlight the framework effect on catalytic activity, selectivity and catalyst lifetime.

Ethanol upgrading was carried out at 400 °C over K(2.40)/ZnMFI(96) (Figure 7.19), Ag(1.30),K(0.57)/ZnMFI(96) IE 3.4 wt% Ag (Figure 7.20) and over Pt(0.13),K(0.29)/ZnMFI(96) IE 0.4 wt% Pt (Figure 7.21).

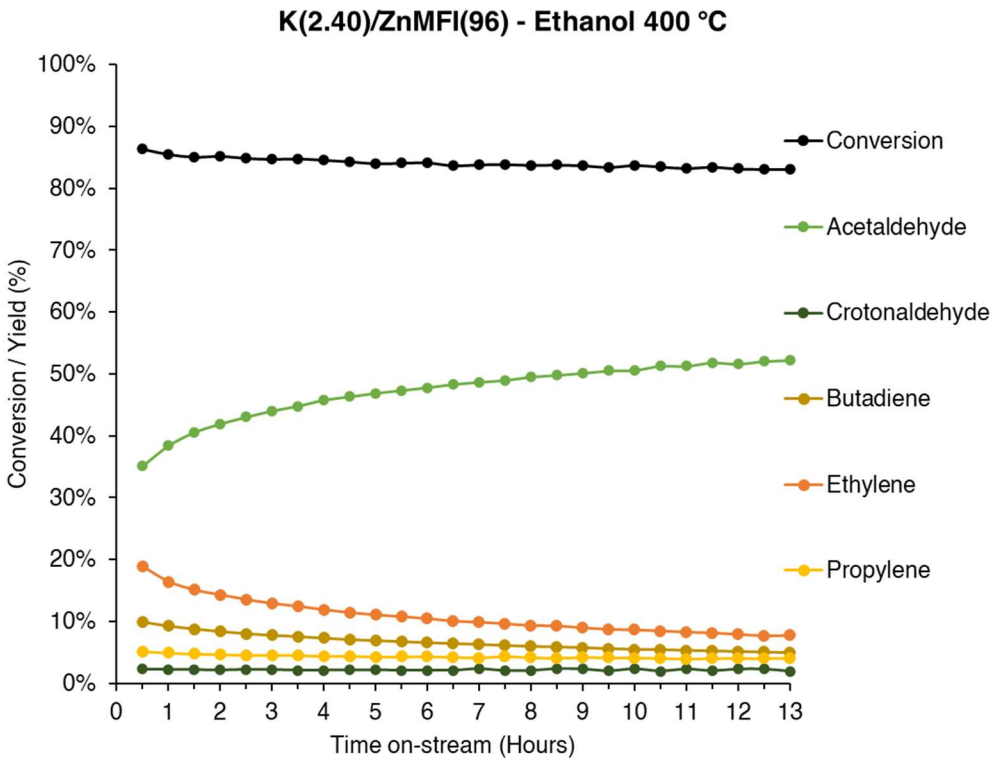

Figure 7.19: Time on-stream graph for ethanol conversion and product yields for ethanol upgrading reaction at 400 °C over K(2.40)/ZnMFI(96).

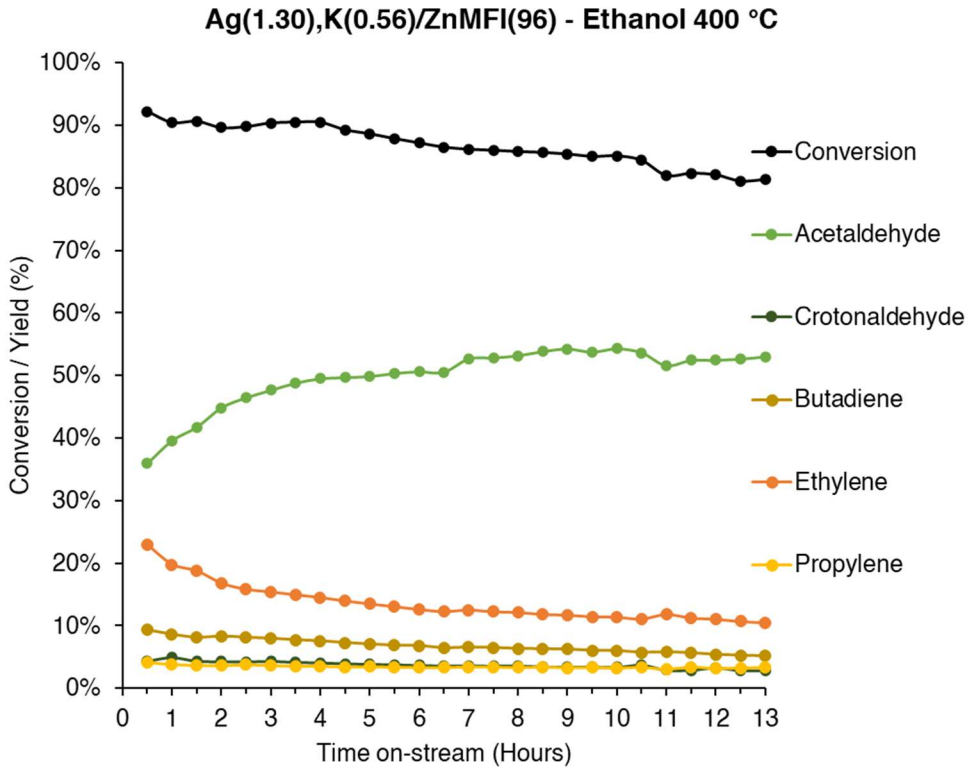

Figure 7.20: Time on-stream graph for ethanol conversion and product yields for ethanol upgrading reaction at 400 °C over Ag(1.30),K0.29)/ZnMFI(96).

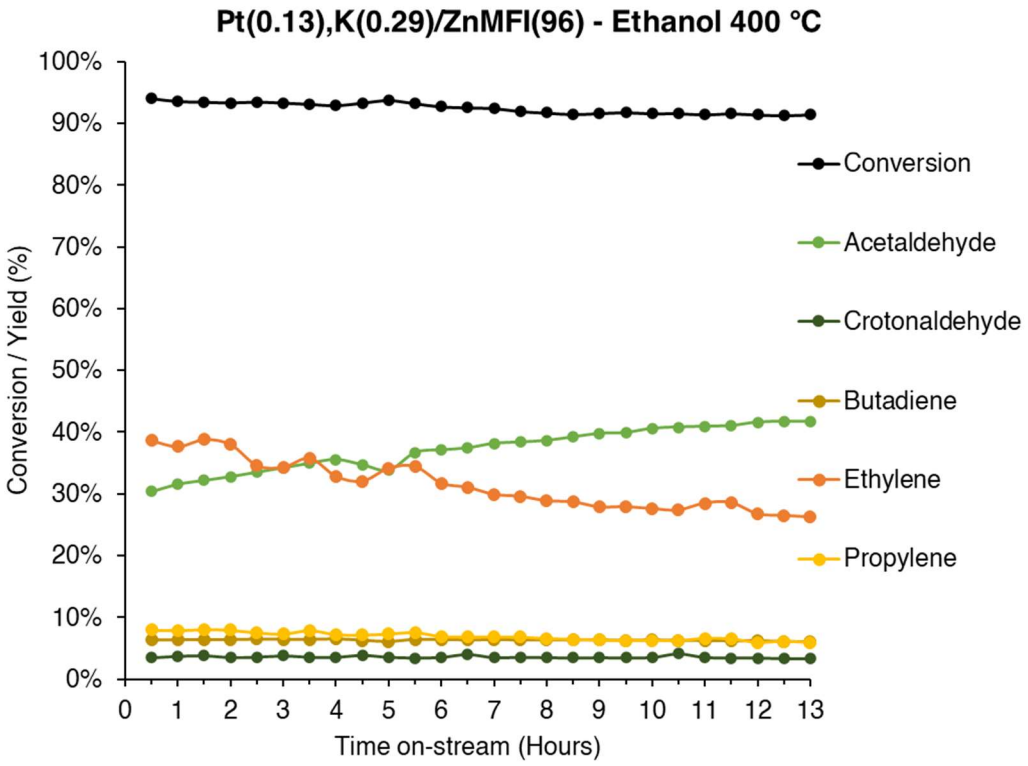

Figure 7.21: Time on-stream graph for ethanol conversion and product yields for ethanol upgrading reaction at 400 °C over Pt(0.13),K(0.29)/ZnMFI(96).

Over 13 hours on stream, reduced selectivity towards ethylene production was observed in comparison with zeolite ZSM-5 catalysts, whilst acetaldehyde becomes the major product for all three ZnMFI catalysts. Conversion and selectivity remained fairly consistent over the TOS for the three catalysts, with only Pt(0.13),K(0.29)/ZnMFI(96) showing a change in major product, changing from ethylene to acetaldehyde after 5 hours. The platinum-exchanged material did not undergo calcination prior to the run, with this change in product distribution likely indicating a changed platinum species present after 5 hours. Averaged results for 13 hours of ethanol upgrading at 400 °C are included in Figure 7.22.

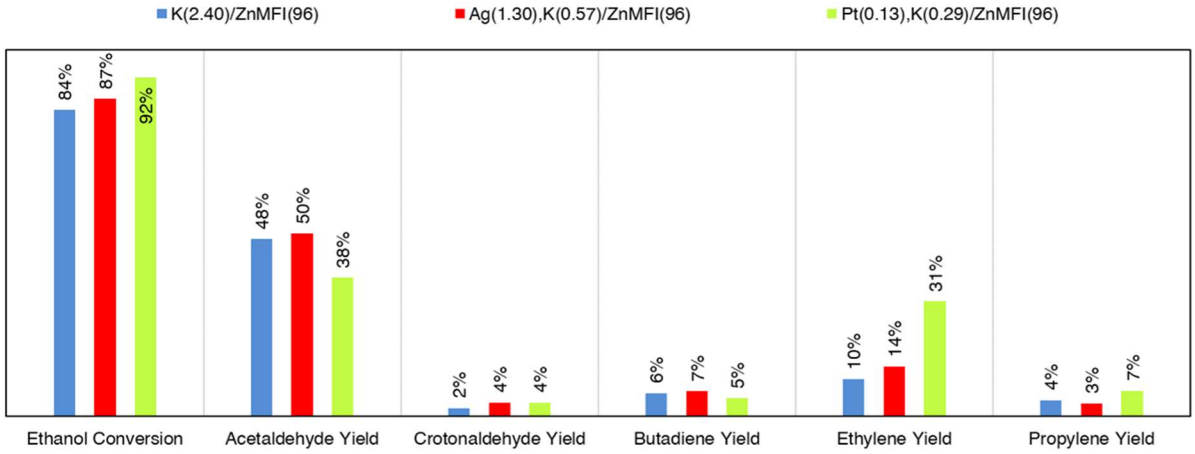

Figure 7.22: Results of ethanol upgrading over ZnMFI materials at 400 °C averaged over 13 hours on-stream, with parent material K(2.40)/ZnMFI(96) (blue), Ag(1.30),K(0.57)/ZnMFI(96) (red) and Pt(0.13),K(0.29)/ZnMFI(96) (lime)

Tabulated results for major product selectivity averaged over 13 hours of ethanol upgrading at 400 °C over zincosilicate MFI is shown in Table 7.3.

Table 7.3: Tabulated results of ethanol upgrading over ZnMFI materials at 400 °C averaged over 13 hours on-stream, showing ethanol conversion, product yield and product selectivity.

		K(2.40)/ZnMFI(96)	Ag(1.30),K(0.57)/ ZnMFI(96)	Pt(0.13),K(0.29)/ ZnMFI(96)
Ethanol Conversion		84%	87%	92%
Acetaldehyde	Yield	48%	50%	38%
	Selectivity	58%	57%	41%
Crotonaldehyde	Yield	2%	4%	4%
	Selectivity	3%	4%	4%
Butadiene	Yield	6%	7%	5%
	Selectivity	7%	8%	5%
Ethylene	Yield	10%	14%	31%
	Selectivity	12%	16%	34%
Propylene	Yield	4%	3%	7%
	Selectivity	5%	4%	7%

Ethanol conversion for K/ZnMFI was 84%, with both Ag/ZnMFI (87%) and Pt/ZnMFI (92%) displaying improved ethanol conversion over the parent material. Ag/ZnMFI displayed unchanged acetaldehyde selectivity (57%) from the parent material (58%), but higher ethylene selectivity (16%) than the parent material (12%). Pt/ZnMFI displayed decreased acetaldehyde selectivity (41%) and increased ethylene selectivity (34%). In both cases, we attribute this changed selectivity to BAS introduced to the material following aqueous ion-exchange of silver and platinum into the parent material. Other product selectivity remained reasonably concordant.

For each ZnMFI material, it was noted that carbon oxides and methane could be observed in their respective BID trace, albeit not quantified here for the results. This would indicate that overoxidation of ethanol had occurred under the reaction conditions. In addition, benzene was observed in the MS trace of Pt(0.13),K(0.29)/ZnMFI(96), a likely byproduct of ethylene oligomerisation as a side reaction.

Ethanol upgrading was carried out at 400 °C over H,K(0.23)/ZnCHA(12) (Figure 7.23), Ag(0.51),K(0.57)/ZnCHA(12) IE 5.8 wt% Ag (Figure 7.24) and Pt(0.02),H/ZnCHA(12) IE 0.35 wt% Pt (Figure 7.25).

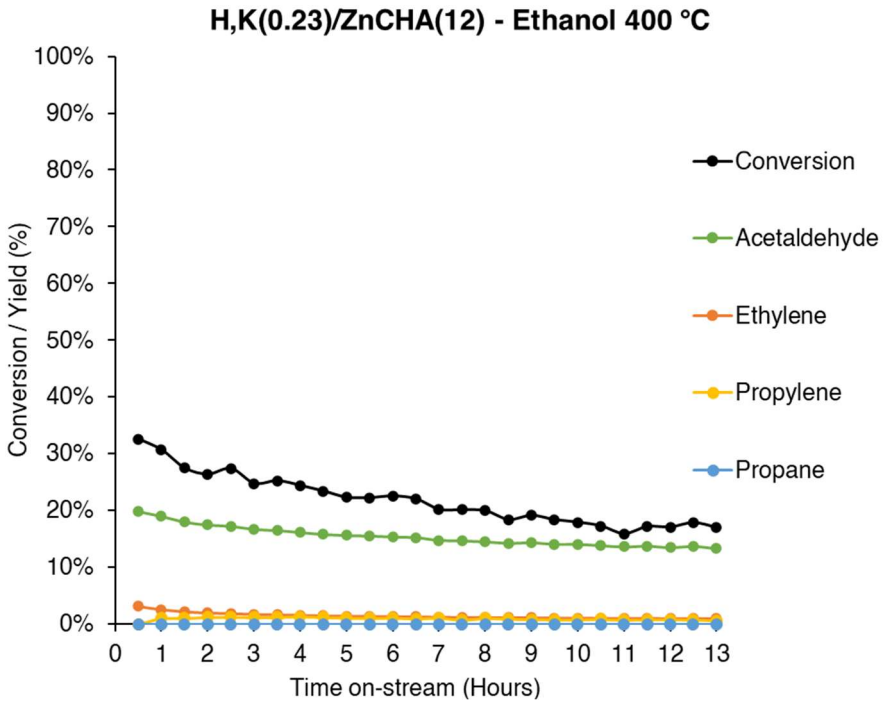

Figure 7.23: Time on-stream graph for ethanol conversion and product yields for ethanol upgrading reaction at 400 °C over H,K(0.23)/ZnCHA(12).

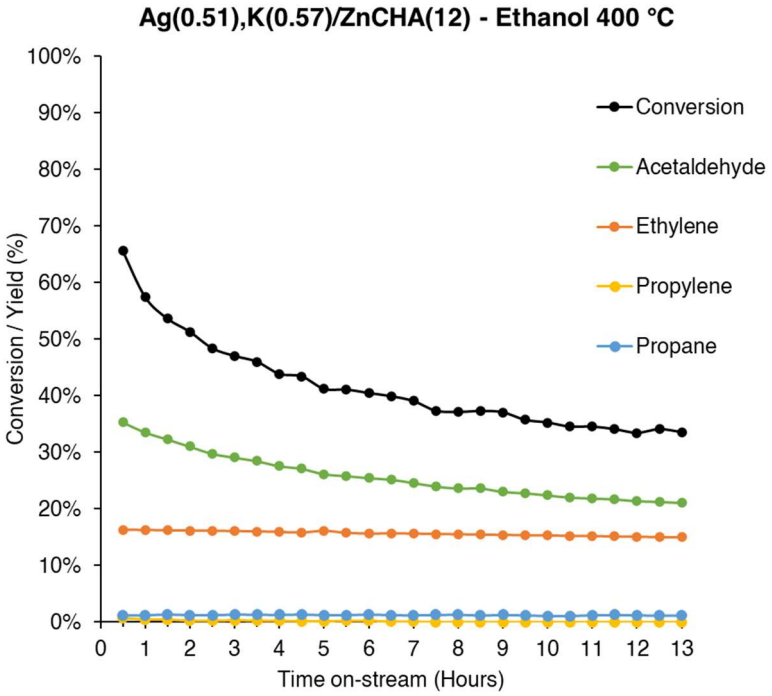

Figure 7.24: Time on-stream graph for ethanol conversion and product yields for ethanol upgrading reaction at 400 °C over Ag(0.51),K(0.57)/ZnCHA(12).

Conversion and product distribution remained consistent for H,K/ZnCHA(12) and Ag,K/ZnCHA(12), with a reduction in conversion and yield over time for the latter.

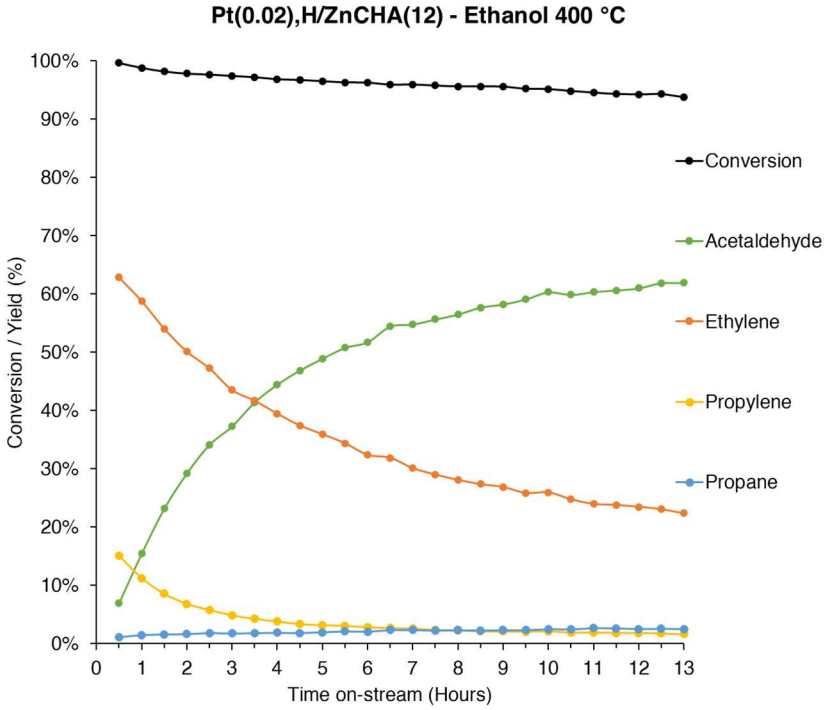

Figure 7.25: Time on-stream graph for ethanol conversion and product yields for ethanol upgrading reaction at 400 °C over Pt(0.02),H/ZnCHA(12).

Pt,H/ZnCHA displayed a distinct change in product distribution over the initial 5 hours on-stream, with ethylene as the initial major product but changing to acetaldehyde. As the catalyst was not calcined prior to its use, we propose that the initial onset was a result of *in situ* calcination of the $PtCl_4$ used as the platinum source.

Averaged results for 13 hours of ethanol upgrading at 400 °C are included in Figure 7.26. Product yields for the parent material, H,K/ZnCHA, and the silver-exchanged form Ag/ZnCHA were largely concordant over 13 hours. Ag/ZnCHA displayed a higher ethylene yield (15%) than the parent material (2%), which in-turn led to higher ethanol conversion (42% vs 29%). Again, we can attribute this to the generation of additional BAS following aqueous ion-exchange to introduce silver. Pt/ZnCHA displayed the highest ethanol conversion (96%), acetaldehyde yield (48%) and ethylene yield (35%) of the three catalysts.

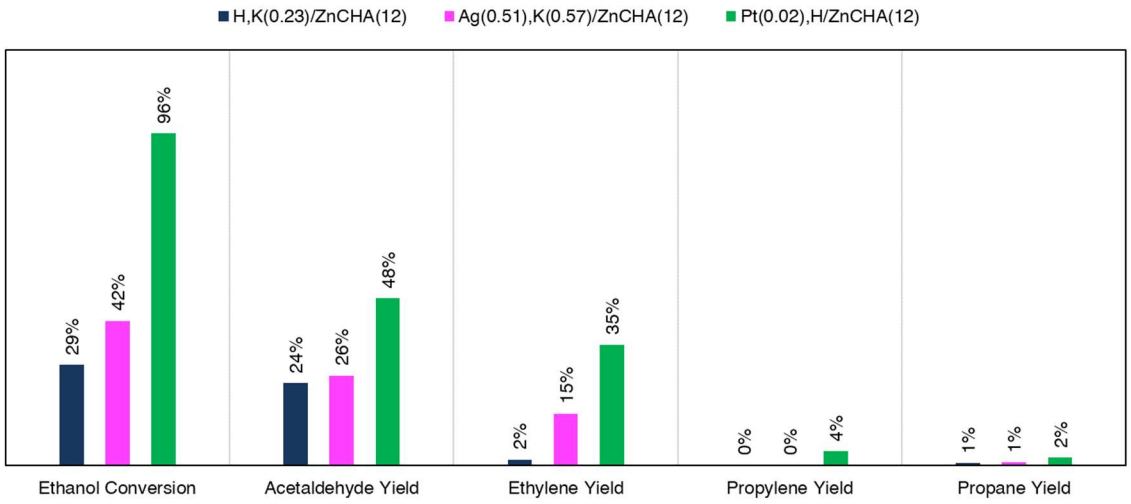

Figure 7.26: Results of ethanol upgrading over ZnCHA materials at 400 °C averaged over 13 hours on-stream, with parent material H,K(0.23)/ZnCHA(12) (navy), Ag(0.51),K(0.57)/ZnCHA(12) (pink) and Pt(0.02),H/ZnCHA(12) (green)

In comparison with ZnMFI materials, conversion for ZnCHA materials was much lower for H,K/ZnCHA (29%) and Ag,K/ZnCHA (42%) compared with K/ZnMFI (84%) and Ag,K/ZnMFI (87%), whereas Pt,H/ZnCHA (96%) displayed higher conversion than even Pt,K/ZnMFI (92%). However, full conversion was observed for their zeolite counterparts. Product distribution was also changed. Whilst acetaldehyde remained the major product followed by ethylene, only trace levels of butadiene and crotonaldehyde were detected for the ZnCHA catalysts. As a result of the changed product selectivity with time on-stream, Pt(0.02),H/ZnCHA(12) and other similar platinum-based catalysts tested following these results were calcined at 550 °C for 6 hours prior to their use. This will be clearly stated by saying the catalyst was calcined.

Ethanol upgrading reactions at 400 °C over ZnCHA was extended to assess the catalytic activity of both Pd and Au exchanged ZnCHA. The time on-stream graphs for freshly calcined Pt(0.03),H/ZnCHA(12) IE 0.7 wt% Pt (Figure 7.27), Pd(0.08),H/ZnCHA(12) IE 0.8 wt% Pd (Figure 7.28) and Au(0.03),H/ZnCHA(12) IE 0.5 wt% Au (Figure 7.29) are shown.

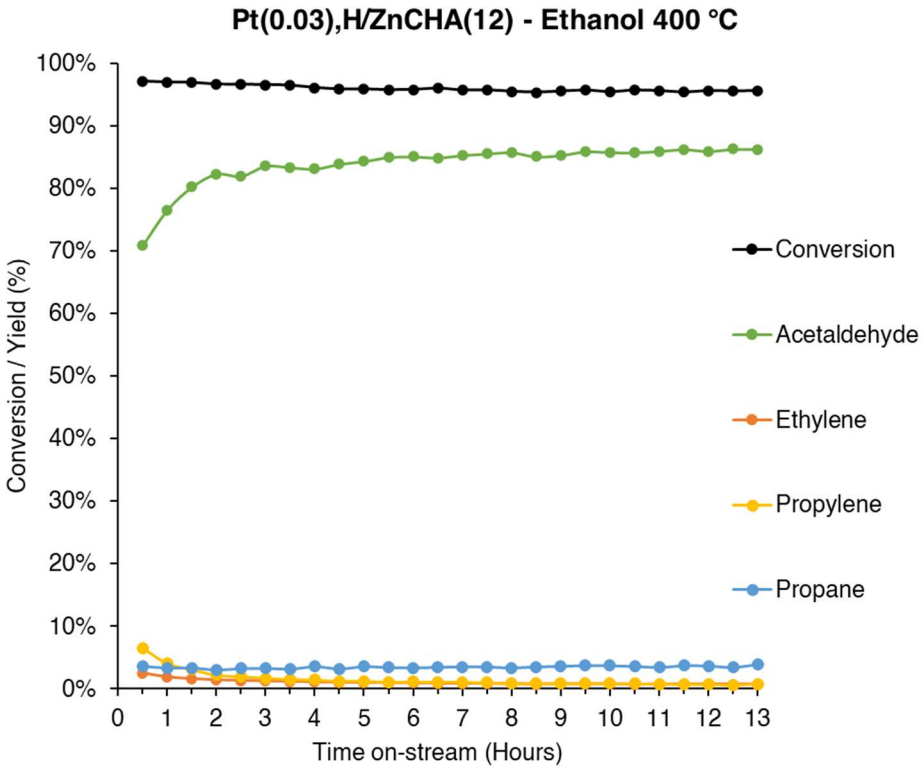

Figure 7.27: Time on-stream graph for ethanol conversion and product yields for ethanol upgrading reaction at 400 °C over Pt(0.03),H/ZnCHA(12).

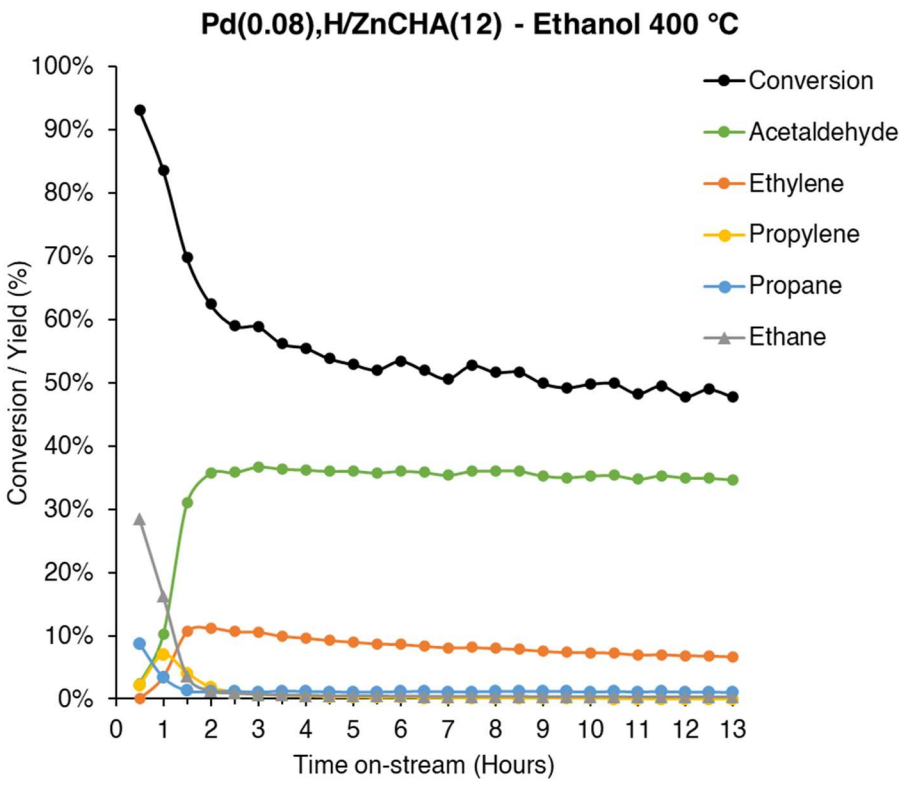

Figure 7.28: Time on-stream graph for ethanol conversion and product yields for ethanol upgrading reaction at 400 °C over Pd(0.08),H/ZnCHA(12).

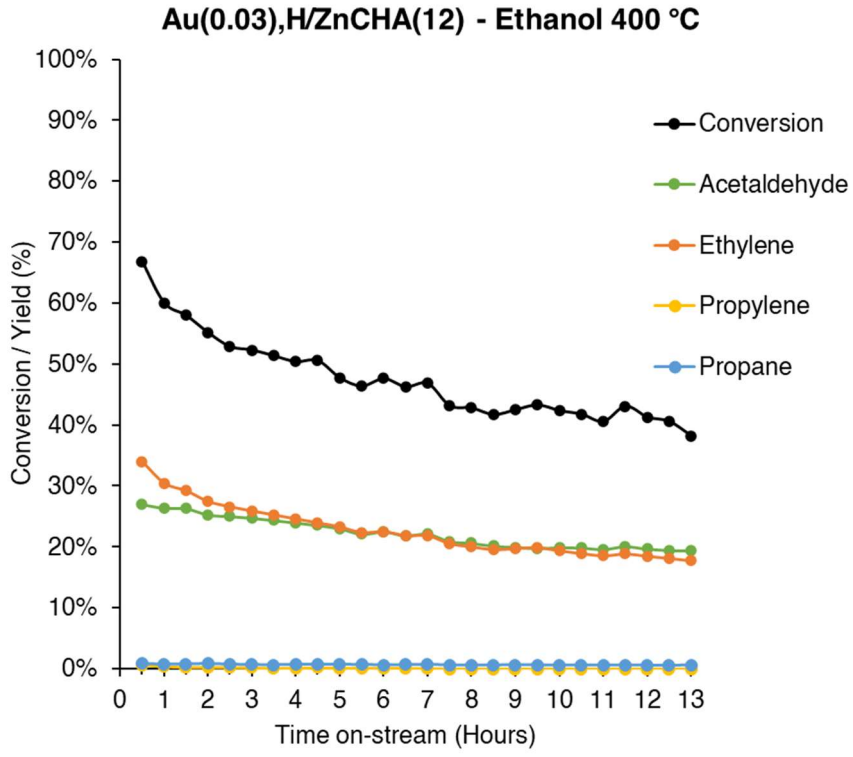

Figure 7.29: Time on-stream graph for ethanol conversion and product yields for ethanol upgrading reaction at 400 °C over Au(0.03),H/ZnCHA(12).

Time on-stream for Pd(0.08),H/ZnCHA(12) displayed ethane selectivity over the initial two hours. Whilst palladium catalysts are known for their intrinsic hydrogenation characteristics, we suspect that the palladium species present facilitated hydrogenation of ethylene due to the presence of hydrogen in the micropores, evolved stoichiometrically from the upgrading reactions. Conversely, whilst platinum is a well-known catalyst for hydrogenation reactions, ethane evolution was not observed during the reaction over Pt(0.03),H/ZnCHA(12).

Averaged results for 13 hours on-stream are shown in Figure 7.30. The observed ethanol conversion and acetaldehyde yield for calcined Pt,H/ZnCHA(12) was unmatched. Ethanol conversion for Pd,H/ZnCHA (55%) and Au,H/ZnCHA (47%) was than parent H,K/ZnCHA (29%) and Ag,K/ZnCHA (42%). Pd/ZnCHA displays higher acetaldehyde yield than Ag/ZnCHA (33% vs 26%) and lower ethylene yield (8% vs 15%), whilst Au/ZnCHA displays a lower acetaldehyde yield than both (22%) and the highest ethylene yield (23%) of all ZnCHA materials tested, the only catalyst where acetaldehyde was not the major product.

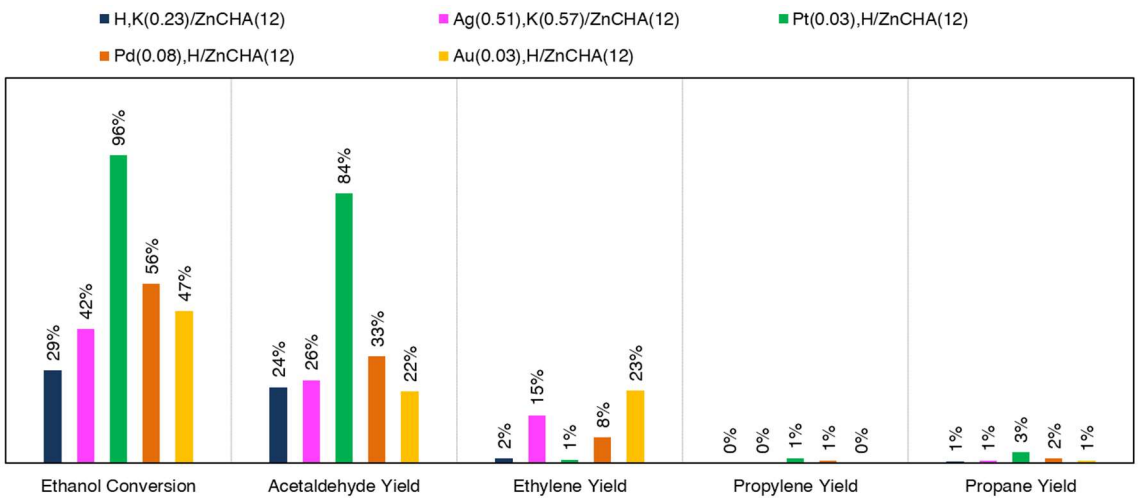

Figure 7.30: Results of ethanol upgrading over ZnCHA materials at 400 °C averaged over 13 hours with parent material H,K(0.23)/ZnCHA(12) (navy), Ag(0.51),K(0.57)/ZnCHA(12) (pink), Pt(0.03),H/ZnCHA(12) (green), Pd(0.08),H/ZnCHA(12) (orange) and Au(0.03),H/ZnCHA(12) (gold).

Tabulated results showing the yield and selectivity for 13 hour averaged ethanol upgrading over ZnCHA materials at 400 °C are shown in Table 7.4.

Table 7.4: Tabulated results of ethanol upgrading over ZnCHA materials at 400 °C averaged over 13 hours on-stream, showing ethanol conversion, product yield and product selectivity.

		H,K(0.23)/ ZnCHA(12)	Ag(0.51),K(0.57)/ ZnCHA(12)	Pt(0.02),H/ ZnCHA(12)	Pt(0.03),H/ ZnCHA(12) (calcined)	Pd(0.08),H/ ZnCHA(12)	Au(0.03),H/ ZnCHA(12)
Ethanol Conversion		29%	42%	96%	96%	56%	47%
Acetaldehyde	Yield	24%	26%	48%	84%	33%	22%
	Selectivity	82%	62%	50%	88%	60%	47%
Ethylene	Yield	2%	15%	35%	1%	8%	23%
	Selectivity	6%	36%	36%	1%	14%	48%
Propylene	Yield	0%	0%	4%	1%	1%	0%
	Selectivity	0%	0%	4%	2%	1%	0%
Propane	Yield	1%	1%	2%	3%	2%	1%
	Selectivity	2%	2%	2%	4%	3%	1%

Comparisons were drawn between protic, silver and platinum exchanged ZnCHA and ZnMFI materials to highlight the differences in activity, selectivity and product distribution between small pore and medium pore frameworks. The averaged results for 13 hours of ethanol conversion at 400 °C are shown in Figure 7.31, for ZnCHA materials of H,K(0.23)/ZnCHA(12), Ag(0.51),K(0.57)/ZnCHA(12), calcined Pt(0.03),H/ZnCHA(12) and ZnMFI materials H,K/ZnMFI(96), Ag(1.30),K(0.57)/ZnMFI(96) and Pt(0.13),K(0.29)/ZnMFI(96).

Comparing the different forms of ZnCHA and ZnMFI highlighted lower ethanol conversion for small pore ZnCHA materials. Whilst overall acetaldehyde yield was lower, acetaldehyde selectivity was higher. The different Si/Zn ratios of ZnCHA (12) and ZnMFI (96) showed that whilst ZnMFI contained less Lewis acid sites, from less zinc in the framework positions, higher ethanol conversion was observed for parent and silver exchanged forms compared to ZnCHA. No crotonaldehyde or butadiene was detected for ethanol upgrading over ZnCHA, whilst both were detected for all three forms of ZnMFI. No carbon oxides were observed in the GC-BID traces collected during ethanol upgrading reactions at 400 °C over any form of ZnCHA. This suggests that the overoxidation of ethanol did not take place in the small pore zincosilicate material.

Prior art for ethanol upgrading at 400 °C over zincosilicates reported ethanol conversion of 65%, acetaldehyde yield of 33% and ethylene yield of 10%. for Zn-MWW, whilst also observing C_{5+} products (15%), which we did not observe.[61] The reported results for ZnO,Rb/MOR(7) showed ethanol conversion of 40% and acetaldehyde yield of 36%, which gives an acetaldehyde selectivity of 90%.[67] For ethanol conversion and acetaldehyde yield, each ZnMFI material had better activity than previously reported zincosilicates. Pt(0.03),H/ZnCHA(12) was our best performing catalyst for this reaction at this temperature. Whilst the observed acetaldehyde selectivity (88%) did not match that reported for ZnO,Rb/MOR(7) (90%),[67] the observed acetaldehyde yield (84%) was far higher than ZnO,Rb/MOR(7) (36%).

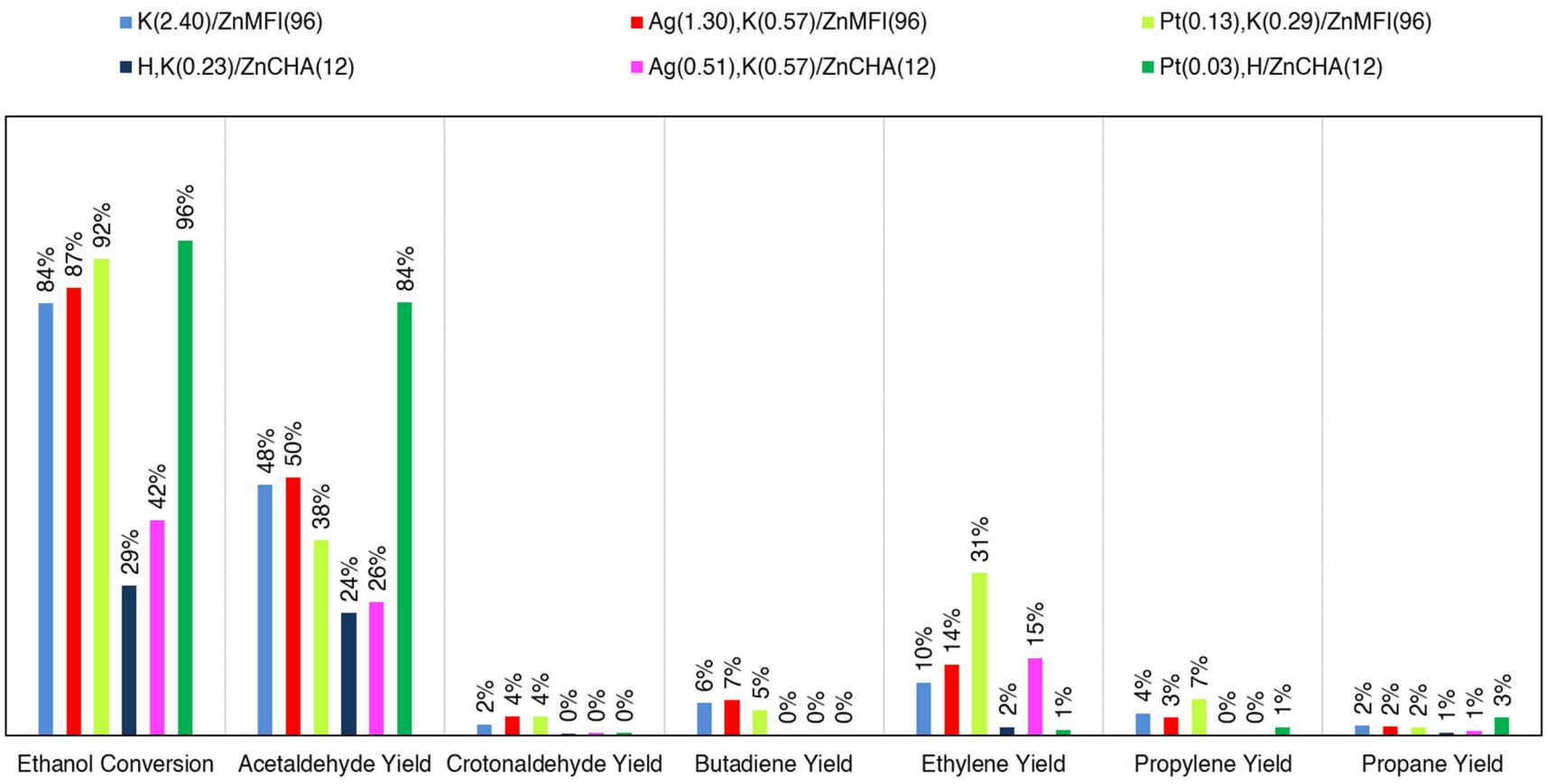

Figure 7.31: Results of ethanol upgrading at 400 °C averaged over 13 hours for various ZnCHA and ZnMFI materials.

7.3.2.1 Silver Stability during Ethanol Upgrading Reactions over Silver-exchanged ZnCHA

Whilst Ag(0.51),K(0.57)/ZnCHA(12) could not match the ethanol conversion and acetaldehyde yield observed for Pt(0.03),H/ZnCHA(12), the catalyst displayed higher ethanol conversion and acetaldehyde conversion when compared against the protic parent form. One major observation of the silver exchanged material was that the increased activity, attributable to the highly dispersed silver cations, could be observed for almost 15 hours on-stream for ethanol upgrading at 400 °C, as shown in Figure 7.32. After 15 hours, acetaldehyde yield was the same value for both catalysts, although Ag(0.51),K(0.57)/ZnCHA(12) continued to display elevated ethanol conversion over H,K(0.23)/ZnCHA(12) for 40 hours, with an average 1.6 times higher (34% vs 21%). We attribute this to the increased ethylene yield, a result of introducing additional BAS following silver exchange.

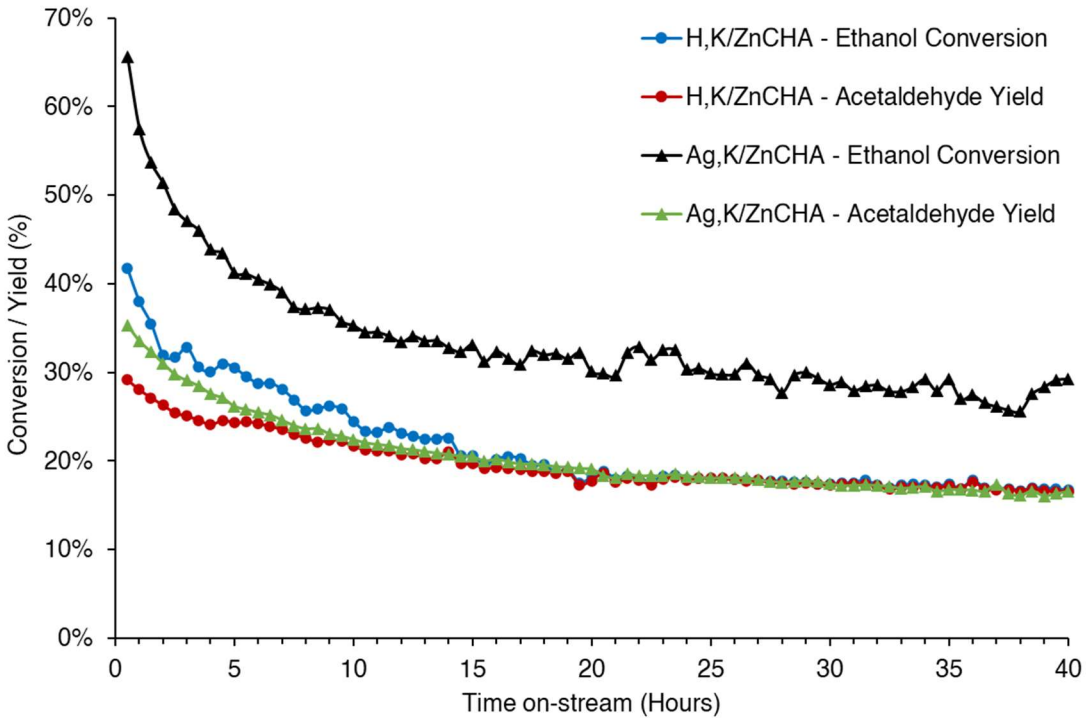

Figure 7.32: Graph displaying the ethanol conversion and acetaldehyde yield for ethanol upgrading reactions at 400 °C over H,K(0.23)/ZnCHA(12) and Ag(0.51),K(0.57)/ZnCHA(12).

7.3.2.2 Investigating Platinum-loading level for Ethanol Upgrading Reactions over Platinum-exchanged Zincosilicates

Following the observation of almost complete ethanol conversion (96%) and high acetaldehyde selectivity (88%) for ethanol upgrading at 400 °C over Pt(0.03),H/ZnCHA(12), we investigated whether changed platinum loading would be beneficial to catalyst activity. In addition, comparison was made with medium pore ZnMFI. The results compared TOS graphs for 13 hours ethanol upgrading at 400 °C over Pt(0.02),H/ZnCHA(12) IE 0.35 wt% Pt (Figure 7.25), calcined Pt(0.03),H/ZnCHA(12) IE 0.7 wt% Pt (Figure 7.27) and Pt(0.13),K(0.29)/ZnMFI(96) IE 0.4 wt% Pt (Figure 7.21). The averaged results are shown in Figure 7.33.

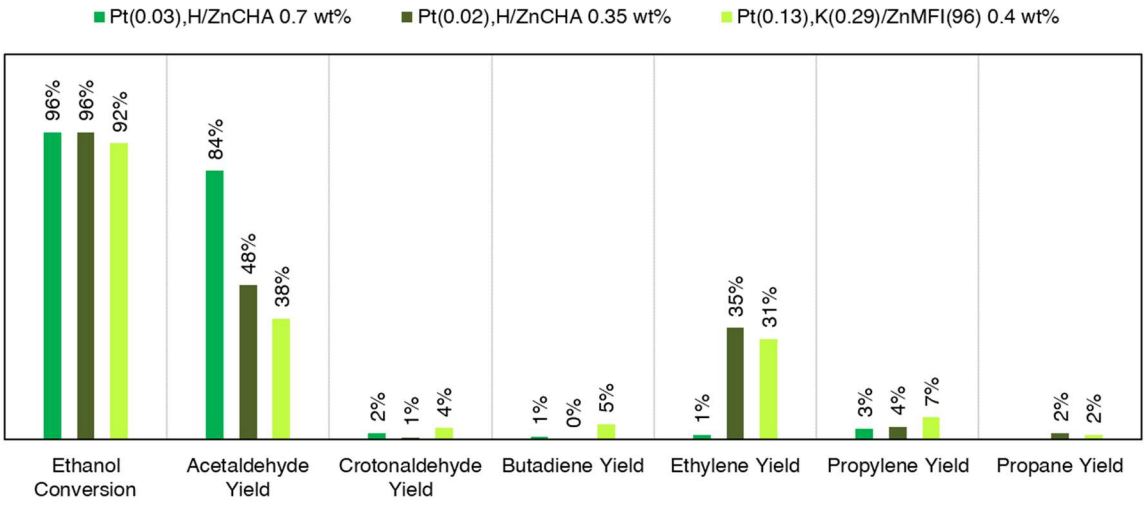

Figure 7.33: Results of ethanol upgrading at 400 °C averaged over 13 hours on-stream over Pt(0.03),H/ZnCHA(12) 0.7wt% (green) and Pt(0.02),H/ZnCHA(12) 0.4wt% (olive), and Pt(0.13),K(0.29)/ZnMFI(96) 0.4 wt% Pt (lime)

Comparing the activity and selectivity of medium pore and small pore platinum-exchanged zincosilicate materials was facilitated by comparison of Pt(0.02),H/ZnCHA(12) and Pt(0.13),K(0.29)/ZnMFI(96), with their similar platinum wt%, with neither catalyst calcined prior to their use. From the results, it was evident that the acetaldehyde yield was higher for small pore Pt/ZnCHA material (64%) when compared to medium pore Pt/ZnMFI (38%). Additionally, Pt/ZnCHA had a lower ethylene yield (20%) than Pt/ZnMFI (31%), showing that the material contained fewer BAS on the framework. Over 13 hours, both catalysts displayed an average of 92% ethanol conversion. There was a notable difference in product selectivity, with crotonaldehyde

and butadiene produced over medium-pore Pt/ZnMFI, whereas neither product was observed for small pore Pt/ZnCHA. This is in-line with previous observations, where bulkier upgrading products were detected for the medium pore zincosilicate. Only short, linear products were detected for the small pore zincosilicate material (ZnCHA), regardless of counterion.

Platinum is an established metal for the dehydrogenation of propane,[68–72] however, we observed high ethanol conversion and acetaldehyde selectivity at 400 °C for Pt(0.02),H/ZnCHA(12) 0.4 wt% Pt and Pt(0.03)/ZnCHA(12) 0.7 wt% Pt, whilst the latter displayed low ethylene selectivity. We conclude that Pt/ZnCHA 0.35 wt% Pt contained BAS, introduced during aqueous ion-exchange, facilitating ethanol dehydration to ethylene. Calcination of Pt(0.03)/ZnCHA(12) could have demonstrated a healing effect and reduced the number of BAS, as a very low ethylene yield (1%) was observed.

The stability of Pt(0.02),H/ZnCHA(12) under reaction conditions was evident following a 55-hour ethanol upgrading reaction carried out at 400 °C, results shown in Figure 7.34. After the initial on-set in activity where a change in active species occurred, consistent ethanol conversion, product distribution and product yield was observed across the following 40 hours of the 55-hour upgrading reaction conducted at 400 °C. To provide a fairer comparison between calcined and uncalcined Pt/ZnCHA materials, we looked at the average values for Pt(0.02),H/ZnCHA(12) activity beyond the initial onset, for 13 to 26 hours on-stream, with results shown in Table 7.5 for the platinum exchanged zincosilicate catalysts tested.

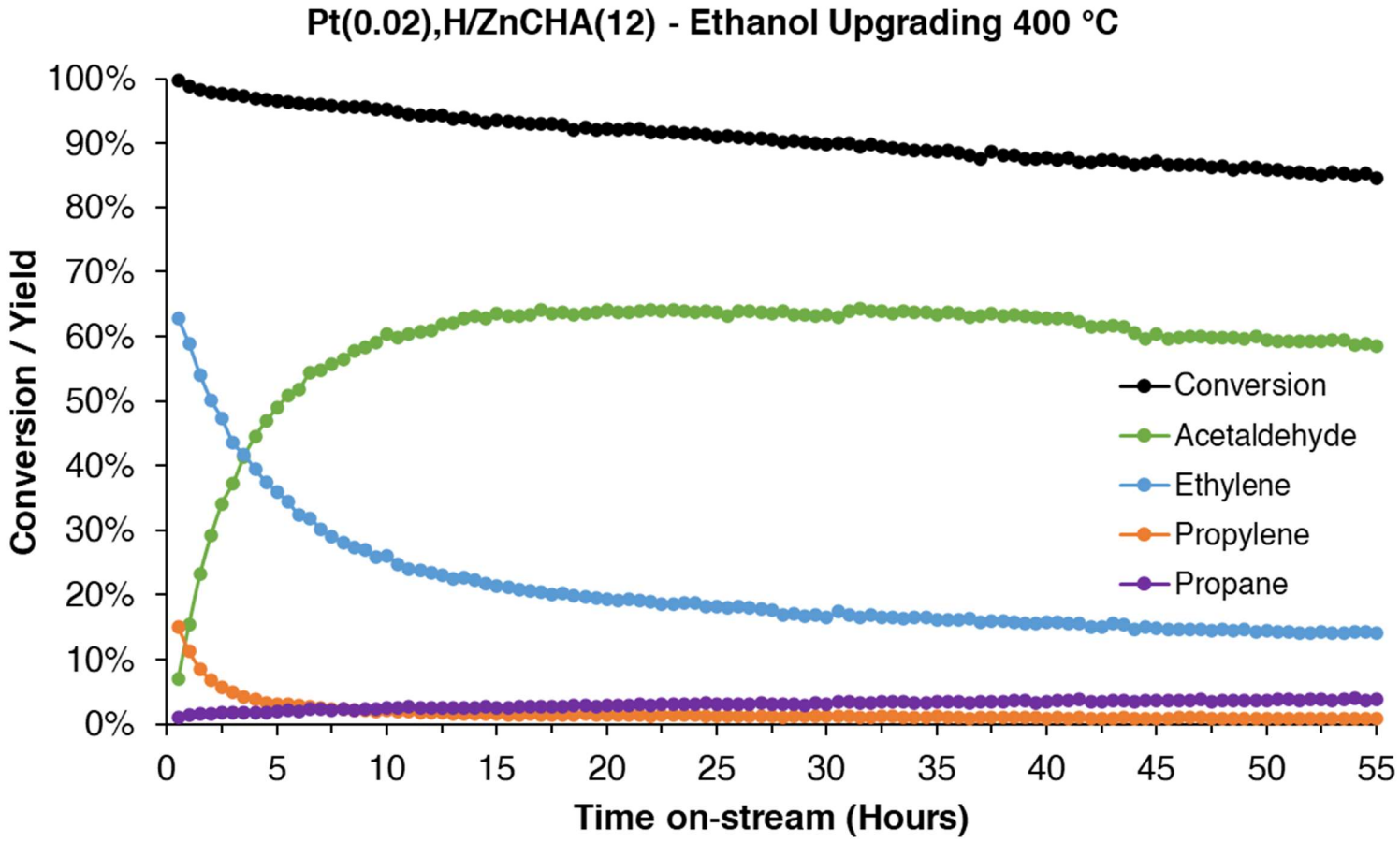

Figure 7.34: Graph showing ethanol conversion and product yields for ethanol upgrading at 400 °C over Pt(0.02),H/ZnCHA(12) 0.35 wt% Pt.

Table 7.5: Tabulated results for ethanol upgrading at 400 °C over platinum exchanged zincosilicates and ZnCHA parent material. Results averaged over 13 hour time period, showing ethanol conversion, product yield and product selectivity.

		H,K(0.23)/ ZnCHA(12)	Pt(0.13),K(0.29)/ ZnMFI(96)	Pt(0.02),H/ ZnCHA(12) (0-13 hours)	Pt(0.02),H/ ZnCHA(12) (13-26 hours)	Calcined Pt(0.03),H/ ZnCHA(12)
Ethanol Conversion		29%	92%	96%	92%	96%
Acetaldehyde	Yield	24%	38%	48%	64%	84%
	Selectivity	82%	41%	50%	69%	88%
Ethylene	Yield	2%	31%	35%	20%	1%
	Selectivity	6%	34%	36%	21%	1%
Propylene	Yield	0%	7%	4%	1%	1%
	Selectivity	0%	7%	4%	2%	2%
Propane	Yield	1%	2%	2%	3%	3%
	Selectivity	2%	2%	2%	3%	4%

When comparing results for Pt(0.02),H/ZnCHA for 13-26 hours on-stream with Pt(0.03),H/ZnCHA, it was evident that higher platinum loading was beneficial to ethanol dehydrogenation. Pt(0.03),H/ZnCHA displayed higher ethanol conversion (96% vs 92%) and acetaldehyde selectivity (84% vs 69%), with a much lower ethylene selectivity (1% vs 21%). No change in product distribution was observed between the materials.

For comparison, ethanol upgrading at 400 °C was conducted over the parent material H,K(0.23)/ZnCHA(12) over 55 hours, with the results showing ethanol conversion and product selectivity shown in Figure 7.35. The parent material demonstrates the effect of the Lewis acidic framework providing a highly selective process to produce acetaldehyde, with peak ethanol conversion (37%, 0.5 hours). However, as shown by the tabulated results in Table 7.5, whilst conversion for the parent ZnCHA material falls short of platinum exchanged forms, high selectivity (82%) is observed, with consistent activity demonstrated over 55 hours on-stream. Trace levels of other products, such as ethyl acetate and crotonaldehyde, were observed but saw less than 1% selectivity across the run.

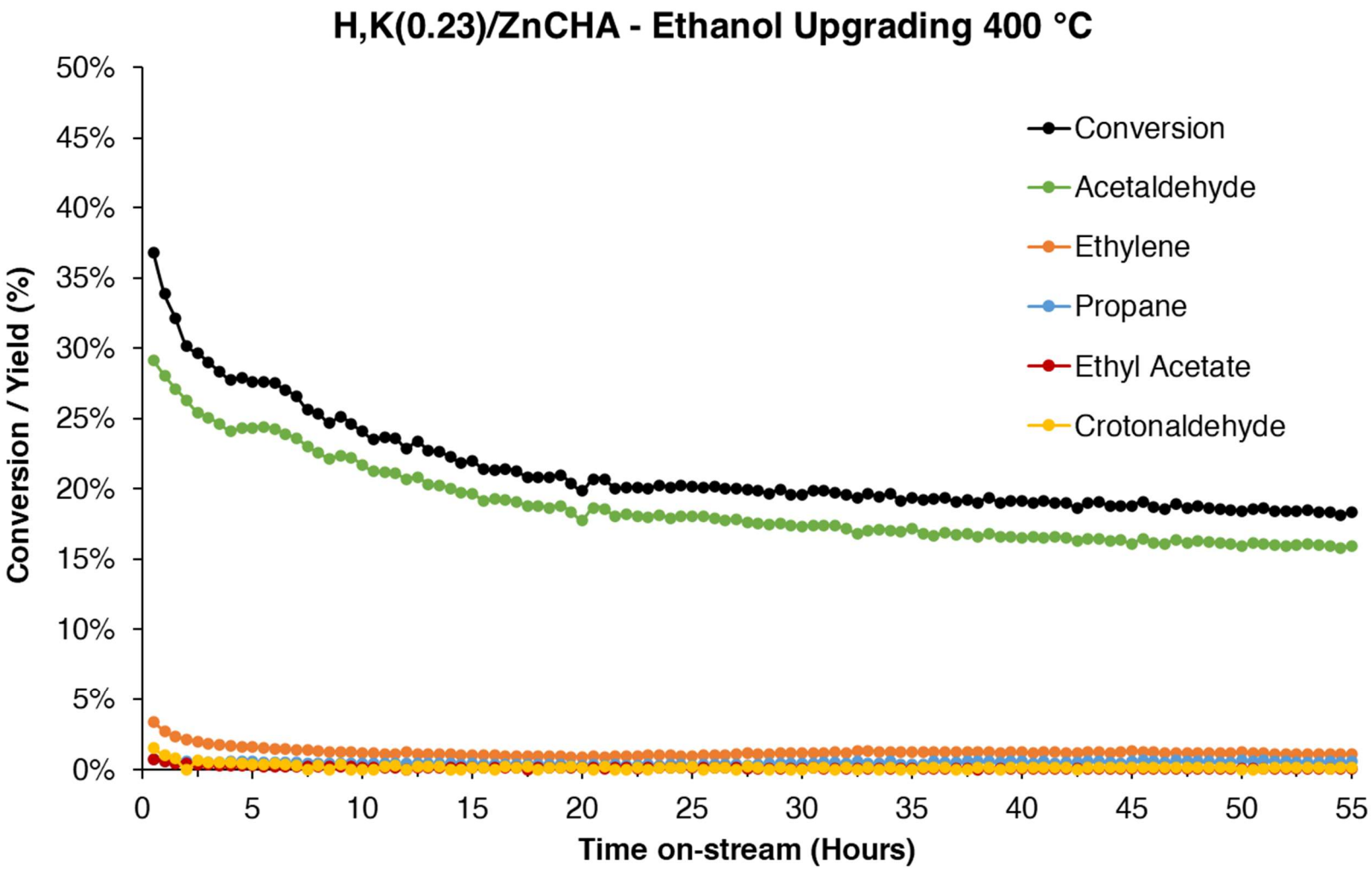

Figure 7.35: Graph showing ethanol conversion and product yields for ethanol upgrading at 400 °C over H,K(0.23)/ZnCHA(12).

7.3.2.3 Investigating Temperature Effect on Ethanol Upgrading Reactions over Platinum-exchanged ZnCHA

Ethanol upgrading reactions at 400 °C over platinum exchanged ZnCHA materials were shown to have high ethanol conversion whilst being highly selective towards acetaldehyde. To determine whether ethanol conversion or selectivity could be improved, or whether similar activity could be achieved at lower temperature, an experiment was devised where the reactor temperature was cycled two times between 300 °C and 400 °C during an ethanol upgrading reaction, with the ethanol conversion and product selectivity monitored by on-line GC-MS-BID. The initial temperature for the temperature cycling of ethanol upgrading over calcined Pt(0.02),H/ZnCHA(12) 0.35 wt% Pt was 300 °C, increasing stepwise by 20 °C until 400 °C had been reached. Each temperature was held for 3 hours before ramping to the next temperature (10 °C/min ramp rate) with a dwell of ca. 20 minutes at the new temperature to allow the catalyst bed to equilibrate to the raised temperature. The reaction profile is shown in Figure 7.36.

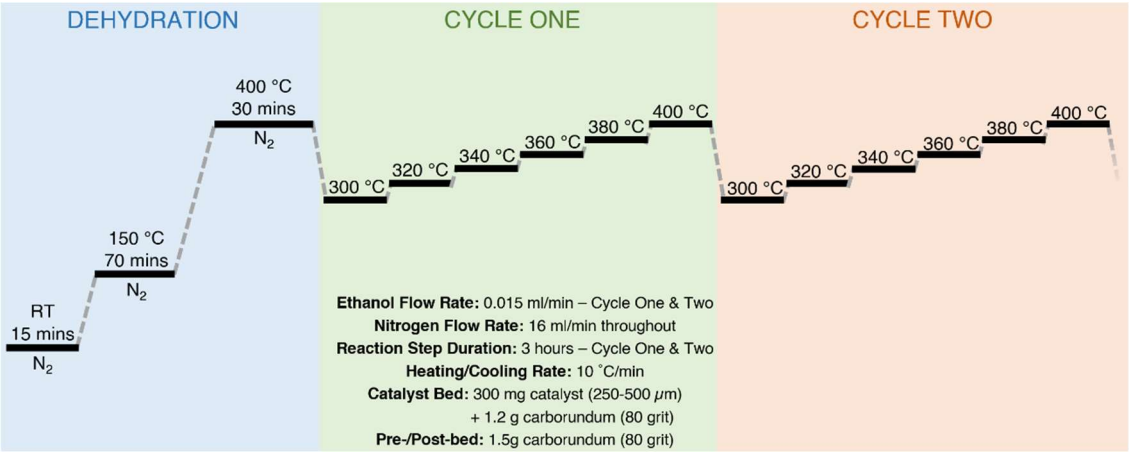

Figure 7.36: Reaction profile for the temperature cycling experiment investigating the effect of temperature on ethanol upgrading reactions conducted over Pt(0.02),H/ZnCHA(12) 0.35 wt% Pt.

The results for temperature cycled ethanol upgrading over Pt/ZnCHA are shown in Figure 7.37, with the results for ethanol conversion and product yield averaged across the multiple GC-MS injections recorded for each temperature step. In the initial temperature cycle, ethanol conversion was observed to increase with increasing temperature. In addition, the yield of ethyl acetate, ethylene, propylene and propane were all observed to increase with increasing reaction temperature. The temperature where acetaldehyde yield was highest was 360 °C on the first temperature cycle. The second temperature cycle was carried out directly after the first temperature cycle. The reactor was cooled from 400 °C to 300 °C at 10 °C/min before immediately repeating

the cycle. Ethanol conversion was again observed to increase with increasing temperature. Again, in parallel with the first temperature cycle, the yields for ethyl acetate, ethylene, propylene and propane all increased with increased reaction temperature. At 360 °C and 380 °C, acetaldehyde yield was at its highest (84%) on the second temperature cycle.

Comparing results obtained during the first temperature cycle against previous results for Pt/ZnCHA 0.35 wt% Pt, both ethanol conversion (98%) and acetaldehyde yield (74%) were higher once the cycle reached 400 °C than for ethanol upgrading at the fixed temperature of 400 °C, which were 92% and 64% respectively (Table 7.5). The reaction data, showing the changes observed for each of the individual temperature steps are included in Figure 7.38.

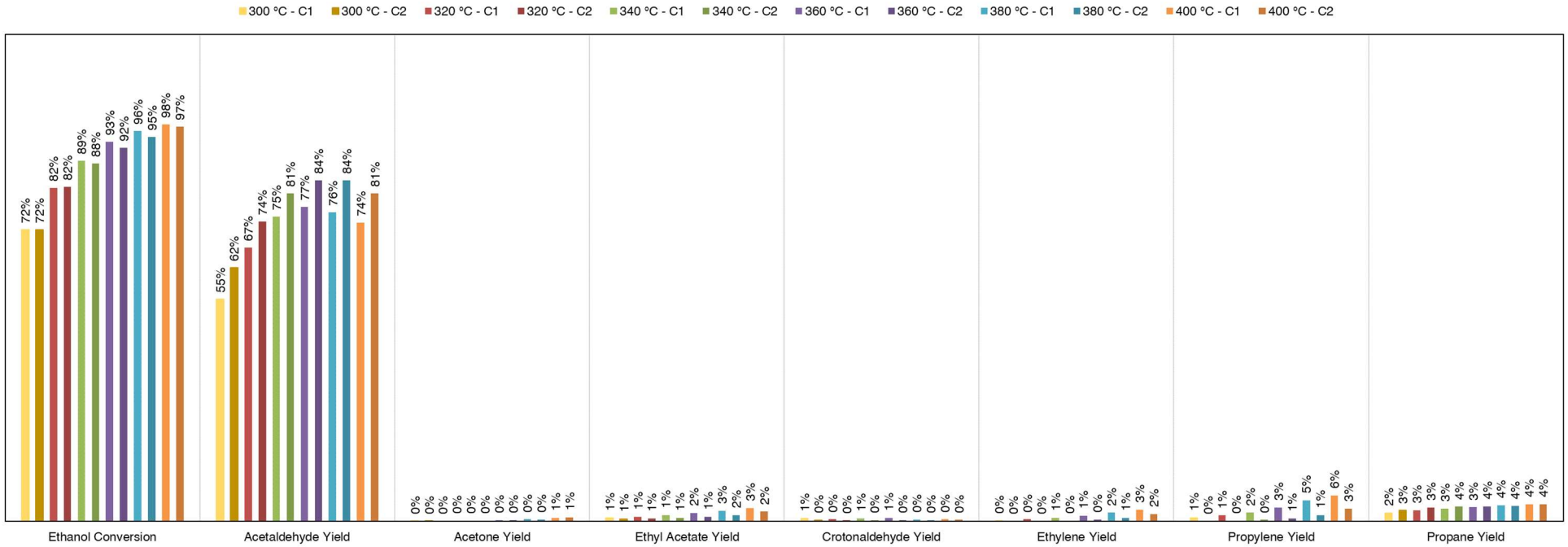

Figure 7.37: Results of ethanol upgrading carried out between temperatures of 300 °C and 400 °C over calcined Pt(0.02),H/ZnCHA(12) 0.35 wt% Pt, with results averaged for each temperature. Lighter colour bars denote results for the first temperature (C1), whilst darker colour bars denote second temperature cycle results (C2).

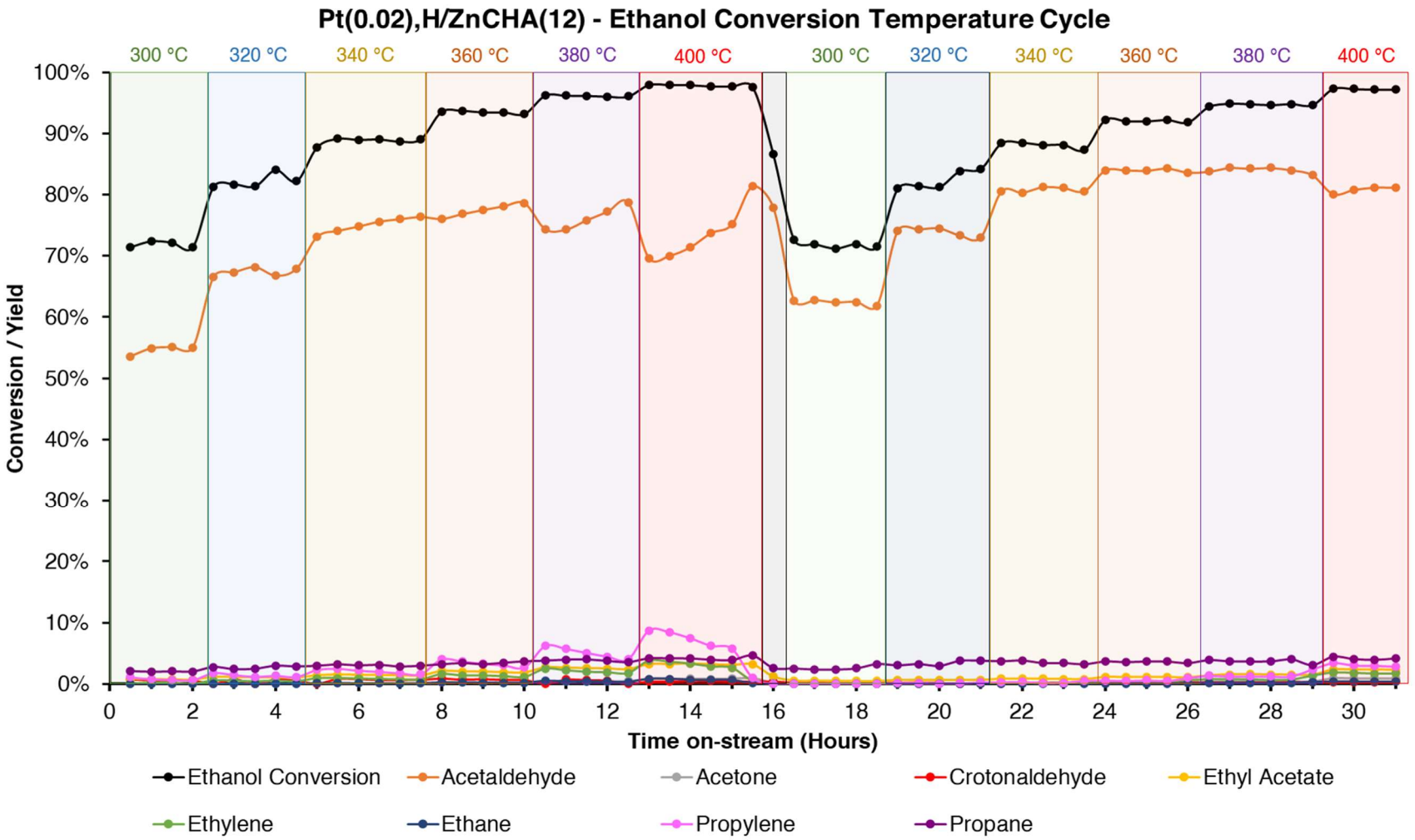

Figure 7.38: Results of ethanol upgrading carried out over calcined Pt(0.02),H/ZnCHA(12) 0.35 wt% Pt between temperatures of 300 °C and 400 °C, showing changed ethanol conversion and product yields with respect to changing temperature.

Tabulated results of the temperature cycling experiment are shown in Table 7.6. Between the first and second temperature cycle, ethanol conversion remained consistent at each temperature step, however, acetaldehyde yield and selectivity was higher for all temperatures in the second cycle. The highest acetaldehyde yield was observed at 360 °C and 380 °C (84%) on the second temperature cycle, however, the highest acetaldehyde selectivity was observed at 340 °C (92%) on the second cycle.

Ethanol conversion at 400 °C over Pt(0.03),H/ZnCHA(12) 0.7 wt% Pt was observed to have achieved almost complete ethanol conversion (96%), with a high acetaldehyde yield (84%) and selectivity (88%). In this experiment, we have observed at 360 °C over Pt(0.02),H/ZnCHA(12) 0.35 wt% Pt, slightly reduced ethanol conversion (92%) with the same high acetaldehyde yield (84%), although we now have achieved higher acetaldehyde selectivity (91%) using a reduced temperature and platinum loading level. However, when the temperature was reduced further to 320 °C, lower ethanol conversion (82%) was observed with reduced acetaldehyde yield (74%), however, a high acetaldehyde selectivity (90%) is observed.

Table 7.6: Tabulated results for ethanol upgrading carried out over calcined Pt(0.02),H/ZnCHA(12) 0.35 wt% Pt at temperatures between 300 °C and 400 °C, showing changed ethanol conversion, product yields and selectivity with respect to the changing temperature.

		300 °C		320 °C		340 °C		360 °C		380 °C		400 °C	
		C1	C2	C1	C2	C1	C2	C1	C2	C1	C2	C1	C2
Ethanol Conversion		72%	72%	82%	82%	89%	88%	93%	92%	96%	95%	98%	97%
Acetaldehyde	Yield	55%	62%	67%	74%	75%	81%	77%	84%	76%	84%	74%	81%
	Selectivity	76%	87%	82%	90%	84%	92%	83%	91%	79%	89%	75%	83%
Ethylene	Yield	0%	0%	0%	0%	1%	0%	1%	0%	1%	0%	2%	1%
	Selectivity	0%	0%	0%	0%	1%	0%	1%	0%	1%	0%	2%	1%
Propylene	Yield	1%	0%	1%	0%	2%	0%	3%	1%	3%	1%	5%	1%
	Selectivity	1%	0%	1%	0%	2%	0%	3%	1%	4%	1%	5%	2%
Propane	Yield	2%	3%	2%	3%	3%	4%	3%	4%	3%	4%	4%	4%
	Selectivity	3%	4%	3%	4%	3%	4%	4%	4%	4%	4%	4%	4%

7.3.2.4 Comparing Metal-Exchanged Zincosilicates Performance for Ethanol Upgrading

In order to draw a direct comparison between previous reports of ethanol upgrading over zincosilicates, an ethanol upgrading reaction was carried out at 320 °C. In this comparison, we compared both H,K(0.23)/ZnCHA(12) and Pt(0.02),H/ZnCHA(12). Bell reported the top-down synthesis of a zincosilicate BEA,[73] which is to be compared directly against our bottom-up synthesized ZnCHA. The Zn/DeAlBEA catalyst used by Bell was generated from zeolite beta and produced in two steps. Firstly, dealumination of zeolite beta and then introduction of zinc from aqueous impregnation. Ethanol upgrading at 320 °C over Zn/DeAlBEA was reported to have an ethanol conversion of 50% and an acetaldehyde selectivity of 60%.[73]

The results reported by Bell have been tabulated in Table 7.7, alongside the results of ethanol upgrading over metal-exchanged zincosilicates at various temperatures that were observed.

Table 7.7: Results of ethanol upgrading reactions carried out over various zincosilicate materials at various reaction temperatures, stating their ethanol conversion and selectivity towards acetaldehyde. Results averaged over 13 hours or longer.

Catalyst	Reaction Temperature	Mass (mg)	GHSV (h^{-1})	Ethanol Conversion	Acetaldehyde Selectivity
Zn(0.3),H/DeAlBEA Bell 2020[73]	320 °C	25	232	50%	60%
Pt(0.02),H/ZnCHA(12) IE 0.35 wt% Pt	320 °C (Table 7.6)	300	112	82%	90%
H,K(0.23)/ZnCHA(12)	320 °C	300	112	5%	82%
Pt(0.02),H/ZnCHA(12) IE 0.35 wt% Pt	360 °C (Table 7.6)	300	112	92%	91%
Pt(0.02),H/ZnCHA(12) IE 0.35 wt% Pt	400 °C	300	112	92%	69%
Pt(0.03),H/ZnCHA(12) IE 0.7 wt% Pt	400 °C	300	112	96%	88%
H,K(0.23)/ZnCHA(12)	400 °C	300	112	29%	82%
Ag(0.51),K(0.57)/ ZnCHA(12) IE 5.8 wt% Ag	400 °C	300	112	42%	62%
Pd(0.08),H/ZnCHA(12) IE 0.8 wt% Pd	400 °C	300	112	56%	60%
Au(0.03),H/ZnCHA(12) IE 0.5 wt% Au	400 °C	300	112	47%	47%
K(2.40)/ZnMFI(96)	400 °C	300	112	84%	58%
Ag(1.30),K(0.57)/ ZnMFI(96) IE 3.4 wt% Ag	400 °C	300	112	87%	57%
Pt(0.13),K(0.29)/ZnMFI(96) IE 0.4 wt% Pt	400 °C	300	112	92%	41%
Zn-MWW(40) Yan 2018[61]	400 °C	500	No Info Given	65%	51%
ZnO,Rb/MOR(7) Raynes 2021[67]	400 °C	300	230	40%	89%
Zn/Silicalite-1 (5wt% Zn) Gao 2022[74]	400 °C	150	750	65%	95%

7.3.3 Conclusion of Ethanol Upgrading Reactions

Ethanol upgrading over zeolites and zincosilicates presented two distinct upgrading pathways. Brønsted acidic zeolites favoured ethanol dehydration, with high ethylene selectivity and heavier products observed, consisting of C_3-C_6 olefins alongside BTX products and their derivatives. Small pore zeolites like chabazite produced linear chain C_3-C_6 olefins, whereas medium and large pore zeolites also generated branched chain C_3-C_6 olefins, showing product distribution was strongly influenced by pore size.

Lewis acidic zincosilicates facilitated ethanol dehydrogenation, with some facilitating high acetaldehyde selectivity. Bell reported ethanol upgrading at 320 °C over 0.3Zn-DeAlBEA, with ethanol conversion (50%), acetaldehyde selectivity (60%) and butadiene selectivity (12%) over 3 hours.[73] In comparison, we observed ethanol upgrading at 400 °C over Ag(1.30),K(0.57)/ZnMFI(96) with ethanol conversion (87%), acetaldehyde selectivity (57%) and butadiene selectivity (8%) averaged over 13 hours. Crotonaldehyde and butadiene were detected for ZnMFI but not small-pore ZnCHA at any temperature, leading us to conclude that the smaller channels of ZnCHA likely restrict the required transition states required for them to form.

Pt(0.03),H/ZnCHA(12) for ethanol upgrading at 400 °C was compared to previously reported zincosilicates Zn-MWW(40),[61] ZnO,Rb/MOR(7)[67] and Zn/Silicalite-1 (5wt% Zn).[74] Pt(0.03),H/ZnCHA(12) displayed both high ethanol conversion (96%) and acetaldehyde selectivity (88%), whilst Zn-MWW(40) displayed lower ethanol conversion (65%) and acetaldehyde selectivity (51%).[61] Both ZnO,Rb/MOR(7) and Zn/Silicalite-1 (5wt% Zn) displayed relatively high acetaldehyde selectivity (89% and 95% respectively), although both displayed a relatively low ethanol conversion (40% and 65% respectively).[67,74] In addition, Pt(0.03),H/ZnCHA(12) displayed relatively low ethylene selectivity (1% vs 5% 0.3Zn-DeAlBEA[73]), highlighting the dominant Lewis acidity of the catalyst. Comparing reaction enthalpies for ethanol upgrading products confirms neither ethylene or acetaldehyde form spontaneously, although the barrier to form ethylene is lower.[75] The reaction enthalpy (standard conditions) per mol of reactant for ethanol to ethylene and water (44.7 kJ/mol) is lower than that of ethanol to acetaldehyde and hydrogen (68.6 kJ/mol).[75] We conclude that the use of strongly Lewis acidic catalysts like the metal-exchanged zincosilicates used here, improved both ethanol conversion and acetaldehyde selectivity over catalysts previously reported. The Lewis acid sites present on the catalysts have sufficiently lowered the energy barrier to acetaldehyde formation to afford 96% ethanol conversion and 88% selectivity (at 400 °C) whilst almost eliminating the production of undesirable ethylene as a byproduct.

7.4 Methanol Upgrading Reactions

Methanol has potential to replace our rapidly diminishing reserves of fossil fuels through the creation of a methanol economy and with this potential, upgrading and valorisation of methanol has been investigated over a wide range of catalysts.[76–80] Electrolytically produced polycrystalline silver catalysts are used industrially for the partial oxidation of methanol (POM) to formaldehyde.[65,81,82] POM requires temperatures in excess of 800 K, facilitating sintering of the polycrystalline silver catalysts and leading to reduced catalytic lifetimes under reaction conditions.[81] It was hoped that small-pore zincosilicates and the use of lower reaction temperatures could supress sintering. In addition, the Lewis acidity of zincosilicates favours dehydrogenation of alcohols.

Methanol upgrading reactions were investigated over a range of silver and indium exchanged zeolites and zincosilicates. Tandem on-line analysis was provided by the GC-MS-BID and proved to be crucial when determining activity, particularly for the accurate identification of products. This was due to multiple product co-elution; propylene and dimethyl ether (DME) in the BID trace and ethylene, methane and CO_2 in the MS trace. DME is considered by many to be dehydrated methanol rather than a product in its own right, with the dehydration process facilitated by Brønsted acidity.[83,84] However, in this section we quantify DME produced as a product to identify differences in activity between catalysts.

Methanol upgrading reactions were carried out using the following conditions: 300 mg catalyst loading (40-60 mesh particle size), methanol (0.009 ml/min flow rate) and nitrogen (24 ml/min) as inert carrier gas, the overall reaction profile is shown in Figure 7.39.

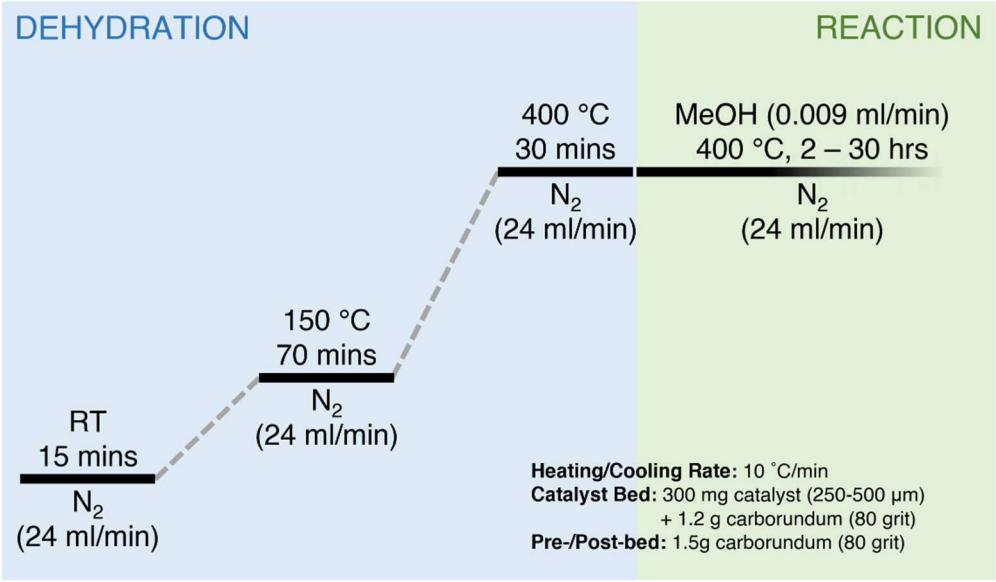

Figure 7.39: Reaction profile for methanol upgrading reactions carried out at 400 °C.

Due to the changed product distribution observed for the methanol upgrading pathway in comparison to ethanol upgrading, new products were added to the calibration to include products such as formaldehyde, methyl formate and dimethoxy methane. To improve our understanding of the upgrading pathway of methanol, a reaction pathway diagram was produced based on reported products for methanol upgrading,[85] shown in Figure 7.40.

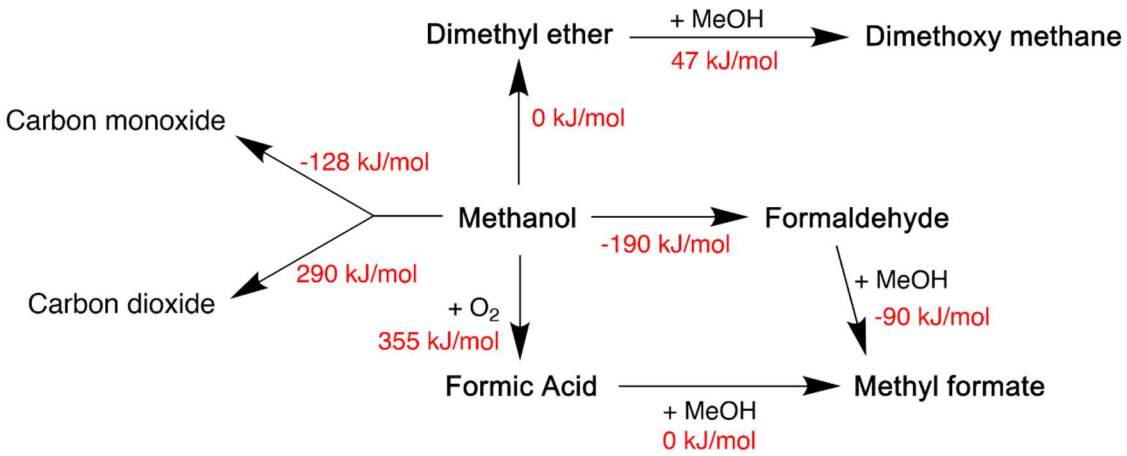

Figure 7.40: Methanol upgrading pathway to commonly reported products.[85] Enthalpy of reaction values (standard conditions) were calculated for each transformation, highlighted in red.[39]

However, in most cases we observed ethylene as a reaction product from methanol upgrading. The process to generate ethylene from methanol contrasts with the simple

dehydration of ethanol to form ethylene, with the requirement of a two-stage process. The first step is the generation of dimethyl ether (DME) from methanol. Over BAS, the acid catalysed condensation of two methanol molecules proceeds to form DME, shown in Equation 7.4. The second stage proceeds when DME interacts with BAS and a chemisorbed methanol, with the process shown in Equation 7.5. Abasov reported that this pathway generates a complex that breaks down to generate ethylene, reform methanol and leads to the transition of a BAS to a Lewis base site on the framework.[86] The overall reaction for methanol to ethylene is shown in Equation 7.6.

$$[7.4]\ 2\ CH_3OH \rightarrow (CH_3)_2O + H_2O$$

$$[7.5]\ (CH_3)_2O + CH_3OH \rightarrow CH_2{=}CH_2 + CH_3OH + H_2O$$

$$[7.6]\ 2\ CH_3OH \rightarrow (CH_3)_2O + 2\ H_2O$$

7.4.1 Methanol Upgrading over Silver-exchanged Zeolites and Zincosilicates

Methanol upgrading was conducted using both zeolite and zincosilicate materials, whilst also comparing small-pore and medium-pore frameworks. We aimed to highlight framework effects from the changed pore sizing and the effect of changed acidity between Brønsted and Lewis acidic materials. Lewis acidic zincosilicates were expected to favour the dehydrogenation of methanol to formaldehyde, rather than the dehydration of methanol to DME as observed for Brønsted acidic materials.

Methanol upgrading was carried out at 400 °C over Ag(2.42),K(0.88)/ZSM-5(13.5) (Figure 7.41), Ag(1.30),K(0.57)/ZnMFI(96) (Figure 7.42) and Ag(2.37),Na/ZnCHA(21) (Figure 7.43).

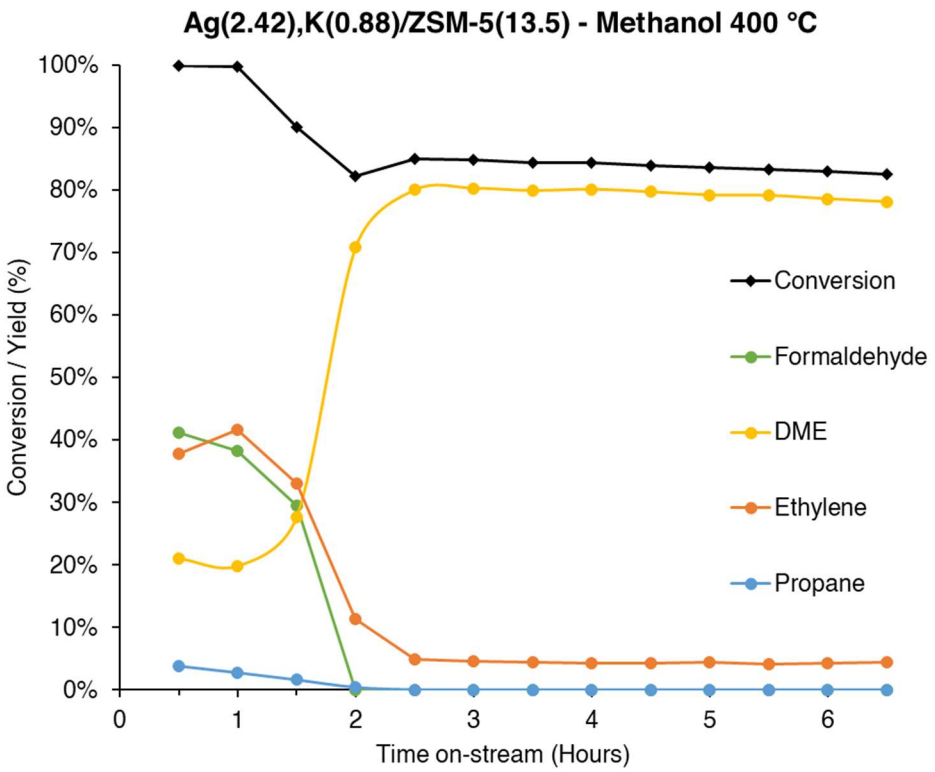

Figure 7.41: Time on-stream graph for methanol conversion and product yields for methanol upgrading reaction at 400 °C over Ag(2.42),K(0.88)/ZSM-5(13.5).

The TOS graph for Ag(2.42),K(0.88)/ZSM-5(13.5) highlighted a rapid change in product distribution after 2 hours. The activity observed in the initial 1.5 hours we associated with silver cations, as methanol to formaldehyde is a well-established transformation conducted over silver based catalysts.[81] This activity remained fairly consistent for 1.5 hours, but product distribution changed completely at 2 hours indicating silver deactivation. The activity observed after 2 hours was attributed to BAS facilitated methanol conversion to DME and ethylene, with both becoming the only products observed after 2 hours. Minimal reduction in methanol conversion and DME yield was observed over the following 4.5 hours. We associate the BAS chemistry with generation of BAS after silver sintering and subsequent silver clustering, facilitated by hydrogen generated during upgrading reactions. Tabulated results showing the change in activity, with product yield and selectivity is included in Table 7.8.

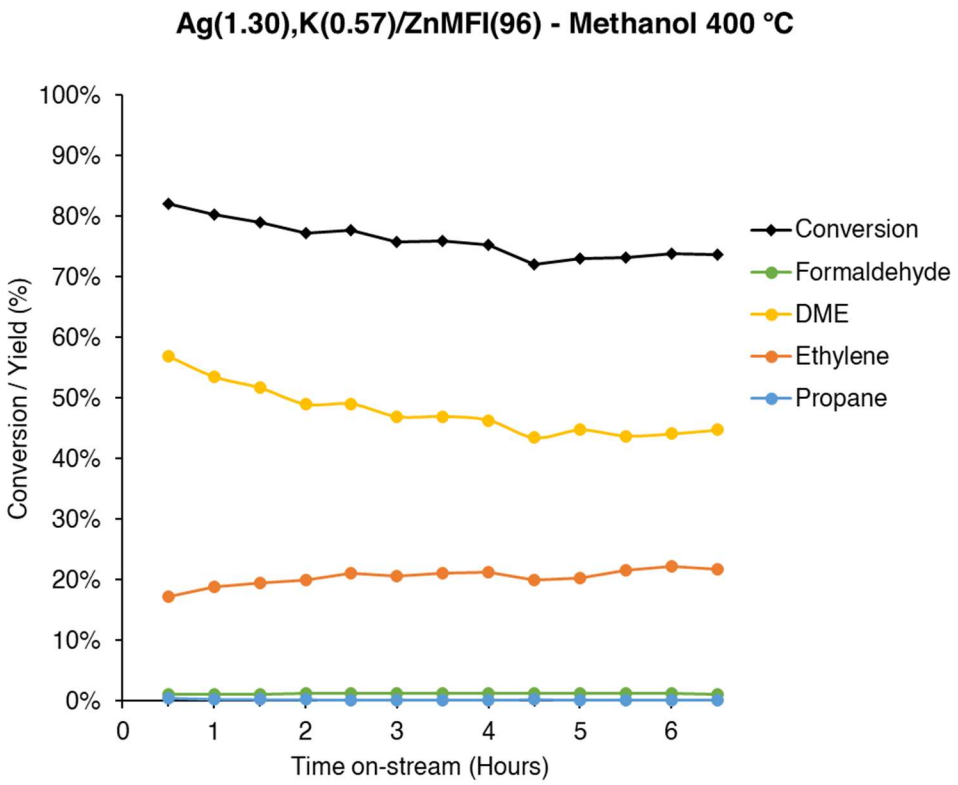

Figure 7.42: Time on-stream graph for methanol conversion and product yields for methanol upgrading reaction at 400 °C over Ag(1.30),K(0.57)/ZnMFI(96).

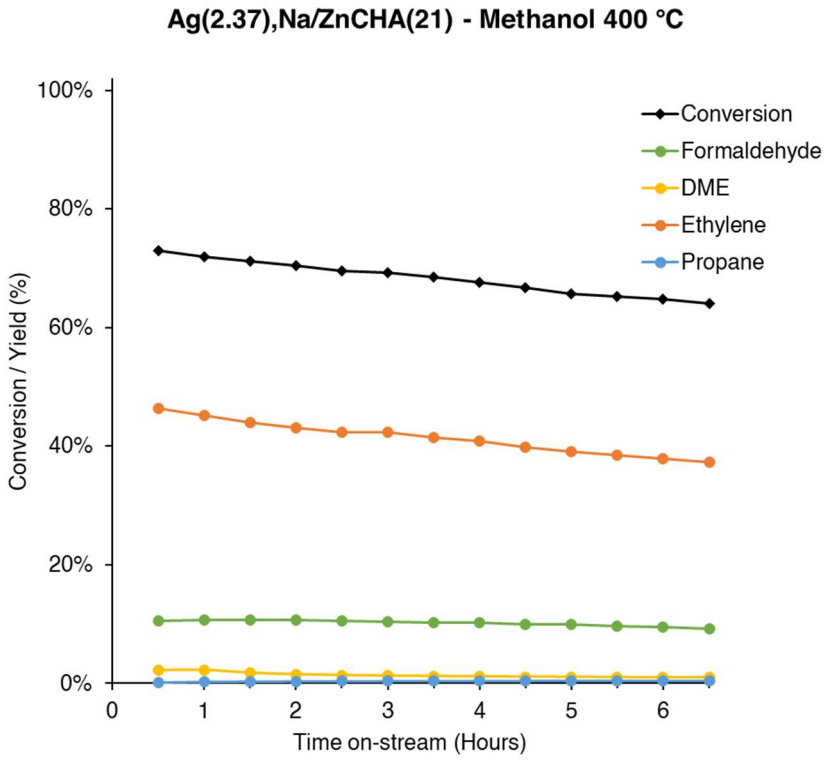

Figure 7.43: Time on-stream graph for methanol conversion and product yields for methanol upgrading reaction at 400 °C over Ag(2.37),Na/ZnCHA(21).

Both zincosilicate catalysts were observed to have consistent catalytic activity and product distribution over 6.5 hours. In both cases, residual framework BAS led to DME and ethylene. However, the major product for medium pore zincosilicate Ag(1.30),K(0.57)/ZnMFI(96) was DME (48% yield), whereas the major product of small pore Ag(2.37),Na/ZnCHA(21) was ethylene (37% yield). Both catalysts displayed reasonable methanol conversion, however, neither catalyst could match the peak formaldehyde yield exhibited by Ag(2.42),K(0.88)/ZSM-5(13.5) (41%).

Average results shown in Table 7.8 conclude that formaldehyde yield (%) was highest for Ag(2.42),K(0.88)/ZSM-5(13.5). However, as shown in the TOS graph the product distribution changed after 2 hours on stream, with no acetaldehyde produced following silver deactivation. Catalytic activity for zincosilicates remained consistent throughout the runs, with ethylene being the dominant product for both zincosilicates. Activity was notably higher for the small pore ZnCHA in comparison to the medium pore ZnMFI, however, the ZnCHA material has a lower framework Si/Zn ratio and higher silver loading.

Table 7.8: Tabulated results for methanol upgrading at 400 °C over silver exchanged ZSM-5, ZnMFI and ZnCHA. Results averaged over 6.5 hour time period unless stated, showing methanol conversion, product yield and product selectivity.

		Ag(2.42),K(0.88)/ ZSM-5(13.5) 0 to 1.5 hours	**Ag(2.42),K(0.88)/ ZSM-5(13.5) 2 to 6.5 hours**	**Ag(1.30),K(0.57)/ ZnMFI(96)**	**Ag(2.37),Na/ ZnCHA(21)**
Methanol Conversion		97%	84%	76%	64%
Formaldehyde	Yield	36%	0%	1%	9%
	Selectivity	37%	0%	1%	14%
DME	Yield	23%	79%	48%	1%
	Selectivity	24%	94%	63%	2%
Ethylene	Yield	37%	5%	20%	37%
	Selectivity	38%	6%	26%	58%
Propane	Yield	3%	0%	0%	0%
	Selectivity	3%	0%	0%	0%

7.4.2 Methanol Upgrading over Indium-exchanged Zeolites

Methanol upgrading was also investigated over indium-exchanged zeolites. Under reaction conditions, silver was noted as prematurely deactivating due to reduction and subsequent sintering and clustering, which indium should avoid. It was also noted that indium can also activate methane[23,87] and facilitate dehydrogenation reactions in zeolites.[24,27] Therefore, methanol upgrading was carried out at 400 °C over several indium-exchanged zeolite catalysts. The TOS graph for In(0.04),H/ZSM-5(13.5) IE is shown in Figure 7.44.

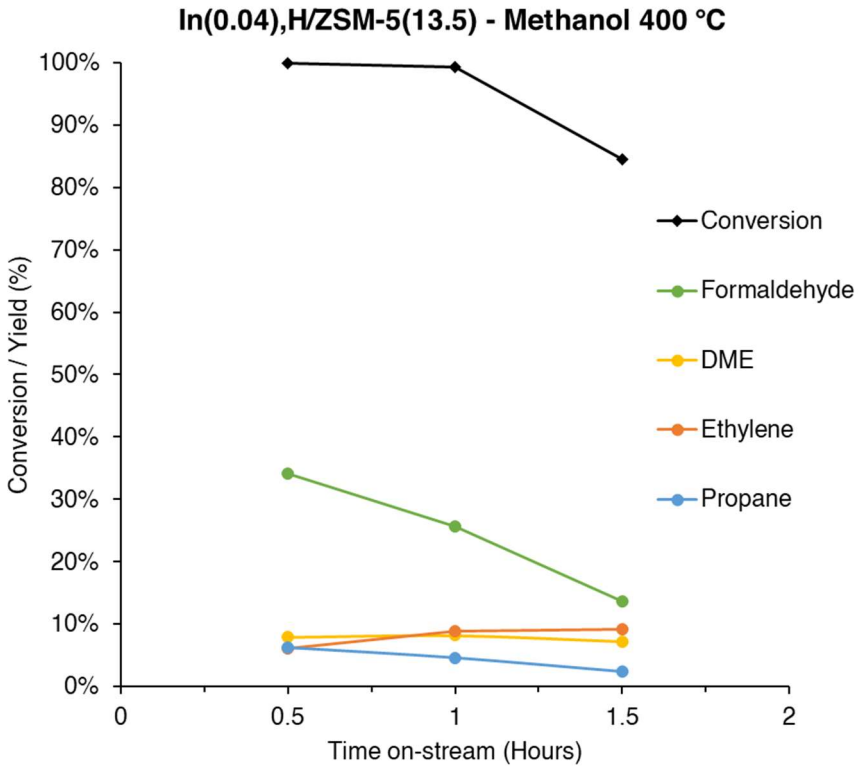

Figure 7.44: Time on-stream graph for methanol conversion and product yields for methanol upgrading reaction at 400 °C over In(0.04),H/ZSM-5(13.5).

Complete methanol conversion was observed for In(0.04),H/ZSM-5(13.5) at 0.5 hours, with methanol conversion and product yields decreasing at 1.5 hours. This drop off in activity can be attributed to the unquantified C_3-C_6 olefins produced alongside BTX products, observed in the MS trace, facilitating pore blocking through carbonaceous deposition. However, peak formaldehyde yield (34%, 0.5 hours) was lower than that observed for Ag(2.42),K(0.88)/ZSM-5(13.5) (41%, 0.5 hours).

The TOS graph for In(0.17),K(0.58)/ZSM-5(13.5) is shown in Figure 7.45.

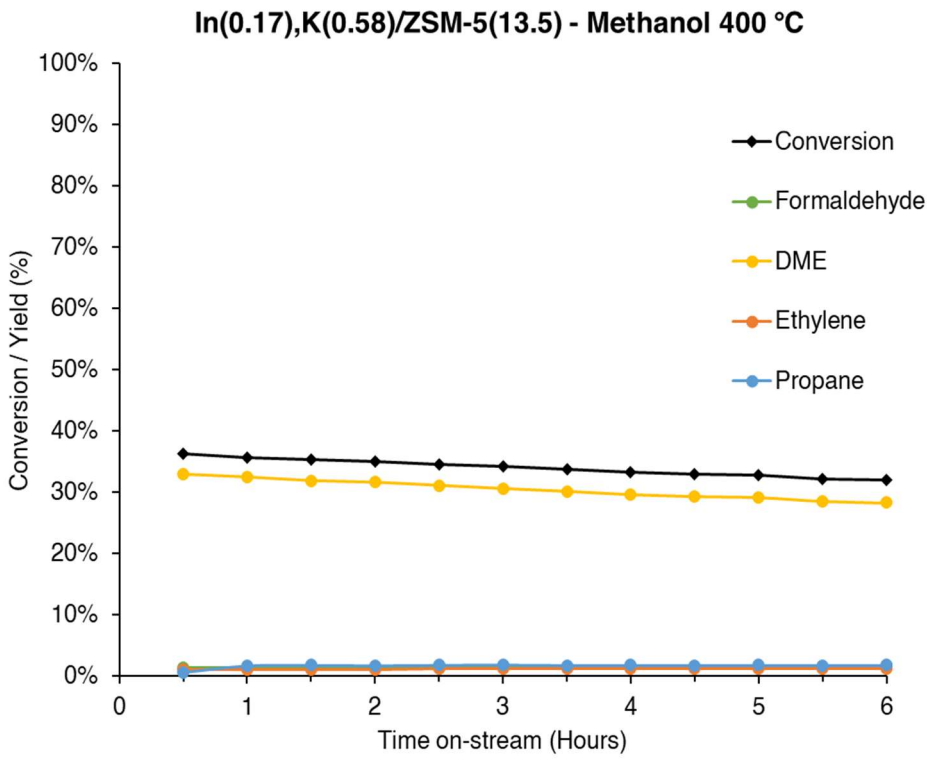

Figure 7.45: Time on-stream graph for methanol conversion and product yields for methanol upgrading reaction at 400 °C over In(0.17),K(0.58)/ZSM-5(13.5).

Consistent catalytic activity was observed for In(0.17),K(0.58)/ZSM-5(13.5), with relatively low methanol conversion and very low product yields compared with In(0.04),H/ZSM-5(13.5). Both catalysts were prepared using indium (III) chloride as the indium source, with neither calcined prior to the reaction. However, the potassium secondary counterion, used to produce basic zeolites,[54] has reduced the inherent framework acidity and appears to have hindered subsequent DME transformation to higher products over BAS. The major product throughout was DME.

The TOS graph for In(0.04),K(0.67)/ZSM-5(13.5) is shown in Figure 7.46.

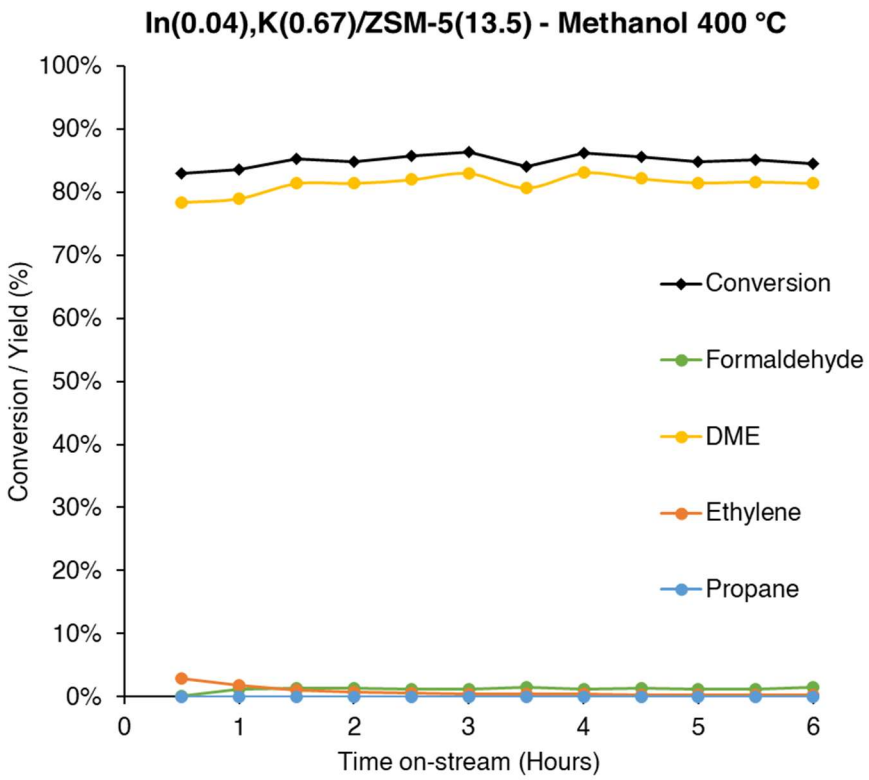

Figure 7.46: Time on-stream graph for methanol conversion and product yields for methanol upgrading reaction at 400 °C over In(0.04),K(0.67)/ZSM-5(13.5).

Consistent catalytic activity was observed for In(0.04),K(0.67)/ZSM-5(13.5), with relatively good methanol conversion and very low product yields. Catalytic activity was very similar to In(0.17),K(0.58)/ZSM-5(13.5), however, higher methanol conversion and DME yields were observed. Indium source was indium (III) nitrate for this catalyst, with a lower indium loading and higher potassium loading. We again associate DME generation to BAS with suppressed upgrading of DME due to the reduced framework acidity. The major product throughout was DME.

The TOS graph for In(0.11),K(0.73)/ZSM-5(13.5) is shown in Figure 7.47.

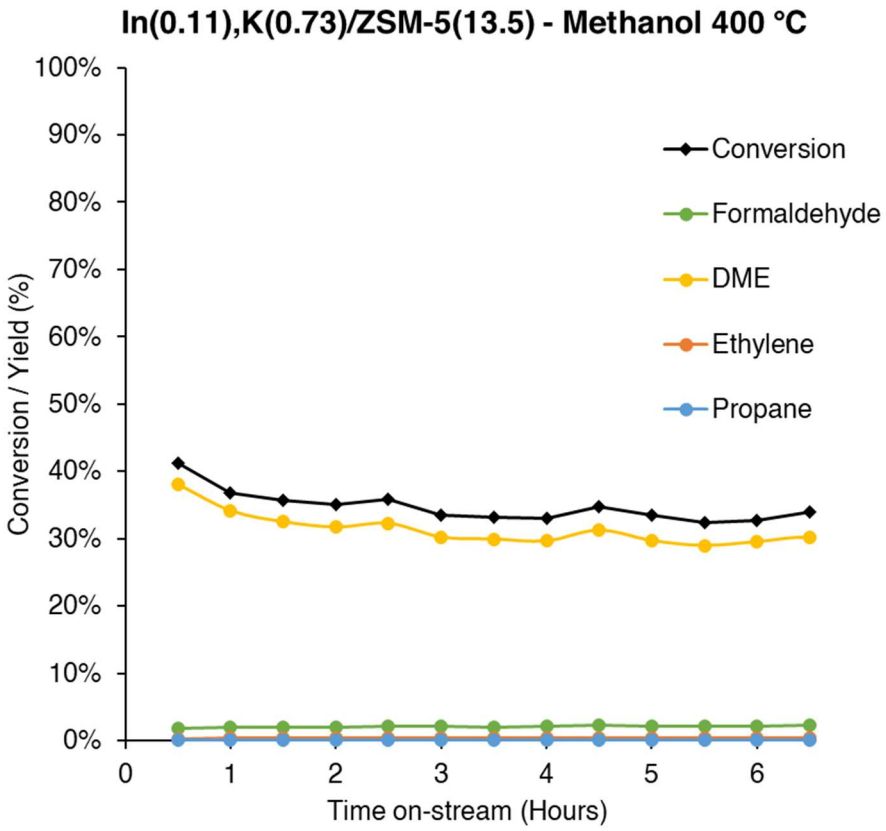

Figure 7.47: Time on-stream graph for methanol conversion and product yields for methanol upgrading reaction at 400 °C over In(0.11),K(0.73)/ZSM-5(13.5).

Consistent catalytic activity was observed for In(0.11),K(0.73)/ZSM-5(13.5), with catalytic activity similar to In(0.17),K(0.58)/ZSM-5(13.5) for methanol conversion, DME yield and low product yields for all others observed. Indium source was indium (III) acetate, and the catalyst had the highest potassium loading of the ZSM-5 catalysts tested. In(0.11),K(0.73)/ZSM-5(13.5) was observed to have the highest formaldehyde yield (2%) out of the indium-exchanged ZSM-5 catalysts with potassium secondary counterions tested, however, acetaldehyde yield was poor for all of the In,K-exchanged catalysts tested.

The TOS graph for In(0.26),H/CHA(28) is shown in Figure 7.48.

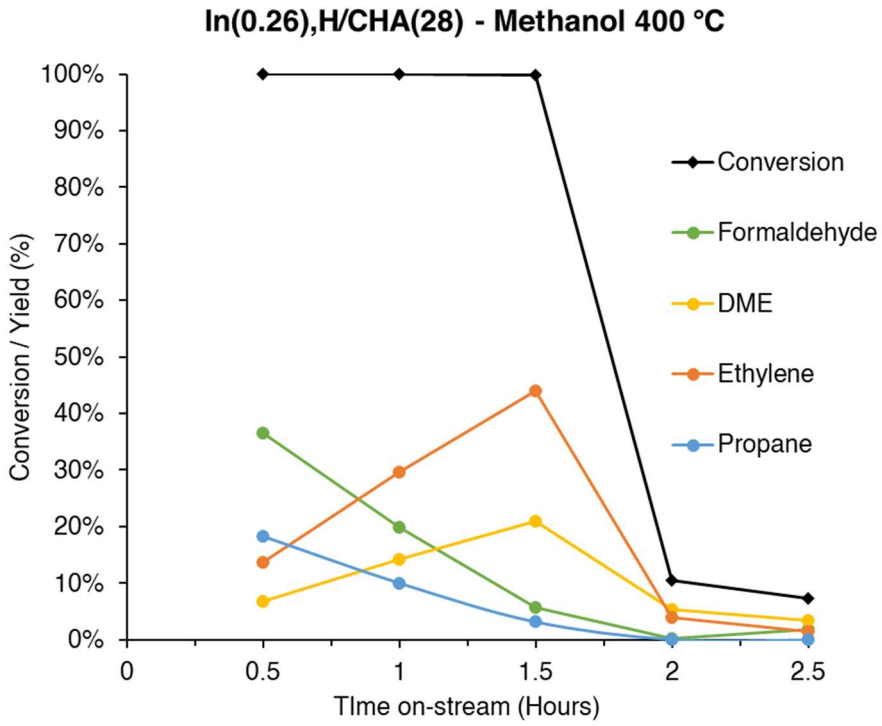

Figure 7.48: Time on-stream graph for methanol conversion and product yields for methanol upgrading reaction at 400 °C over In(0.26),H/CHA(28).

Complete methanol conversion was observed for In(0.26),H/CHA(28) for 1.5 hours, with a sharp drop off observed at 2 hours. Over the initial 1.5 hours, product distribution changed dramatically; initially formaldehyde was the major product (38% yield at 0.5 hours) before changing to ethylene (44% yield at 1.5 hours). BTX products were observed in the MS trace, which can facilitate pore blocking of the small pore material, which we postulate as being the cause of premature deactivation. Indium (III) chloride was the indium source. In comparison against In(0.04),H/ZSM-5 (13.5), both catalysts facilitated complete methanol conversion at the start of reaction before premature deactivation, likely due to excess coking as a result of the strong BAS present in both frameworks. Small pore chabazite was observed to give higher yields for DME, ethylene and propane over the reaction, whereas medium pore ZSM-5 facilitated a larger quantity of C_3-C_6 olefins and BTX products.

The TOS graph for In(0.08),K(0.77)/CHA(18) is shown in Figure 7.49.

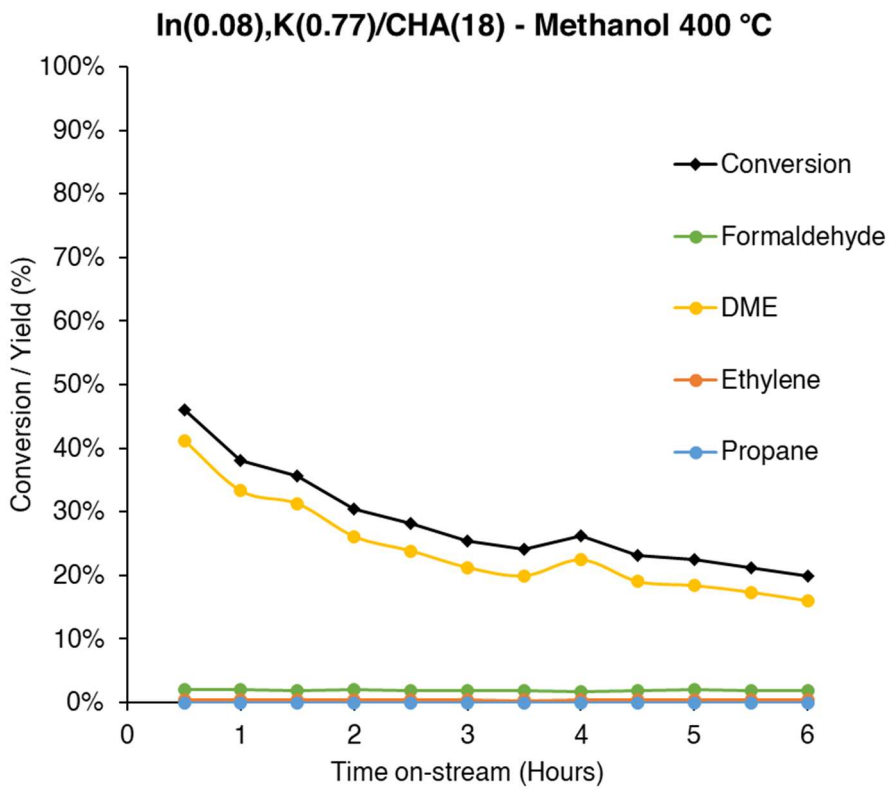

Figure 7.49: Time on-stream graph for methanol conversion and product yields for methanol upgrading reaction at 400 °C over In(0.08),K(0.77)/CHA(18).

Consistent catalytic activity was observed for In(0.08),K(0.77)/CHA(18), with catalytic activity similar to In,K/ZSM-5 catalysts. Methanol conversion and product yields were relatively low, with DME as the major product. Indium (III) chloride was used as a the indium source. In comparison with In(0.26),H/CHA(28), the reduced framework acidity afforded by the presence of potassium has supressed DME upgrading alongside production of BTX products. However, stronger framework acidity appears to be a factor for formaldehyde selectivity, as those with protic secondary counterions led to higher peak formaldehyde yields over indium-exchanged catalysts.

Averaged results of methanol upgrading reaction at 400 °C over indium-exchanged catalysts are shown in Table 7.9.

Table 7.9: Tabulated results for methanol upgrading at 400 °C over indium exchanged zeolites. Results averaged over the given time period, showing methanol conversion, product yield and product selectivity.

		In(0.04),H/ ZSM-5(13.5) 1.5 hours	In(0.17),K(0.58)/ ZSM-5(13.5) 6 hours	In(0.04),K(0.67)/ ZSM 5(13.5) 6 hours	In(0.11),K(0.73)/ ZSM-5(13.5) 6 hours	In(0.26),H/ CHA(28) 2.5 hours	In(0.08),K(0.77)/ CHA(18) 6 hours
Methanol Conversion		95%	34%	85%	35%	64%	28%
Formaldehyde	Yield	24%	1%	1%	2%	13%	2%
	Selectivity	25%	3%	1%	6%	20%	7%
DME	Yield	8%	30%	81%	31%	10%	24%
	Selectivity	8%	88%	95%	89%	16%	86%
Ethylene	Yield	8%	1%	1%	0%	19%	0%
	Selectivity	8%	3%	1%	0%	29%	0%
Propane	Yield	4%	2%	0%	0%	6%	0%
	Selectivity	4%	6%	0%	0%	10%	0%

TOS graphs showed that the indium-exchanged catalysts with potassium secondary counterions had stable catalytic activity with regards to methanol conversion and product distribution. Catalysts with protic secondary counterions saw a drastic reduction in methanol conversion due to their strong Brønsted acidity dominating the catalytic activity and facilitating rapid deactivation of the catalyst after 1.5 hours. Both catalysts were observed to have poor carbon balance and poor selectivity to any single product due to their production of various C_3-C_6 olefins alongside BTX products which were not quantified. Regardless of indium source used to prepare catalysts, catalysts with potassium secondary counterions displayed reduced methanol conversion alongside reduced product yields for several upgrading products. DME was the major product with formaldehyde, ethylene and propane observed as products across all catalysts.

It has been reported that indium chloride as an indium source can have a substantial effect on the catalyst activity. Indium has a strong affinity towards ligands such as chlorine, often meaning that long after impregnation or ion-exchange, chlorine was either still coordinated to the indium centre or still present within the materials.[88,89] Due to this strong affinity, coordination of molecules such as methanol or upgraded products of methanol to the indium centre could be blocked by the retained chloride ligand, reducing overall activity. EDS-TEM was conducted on In(0.17),K(0.58)/ZSM-5(13.5) post methanol upgrading at 400 °C for 6 hours, with the acquired electron image and elemental distribution maps shown in Figure 7.50. What was immediately evident was the presence of chlorine within the material alongside indium, confirming retention of chlorine as a ligand.

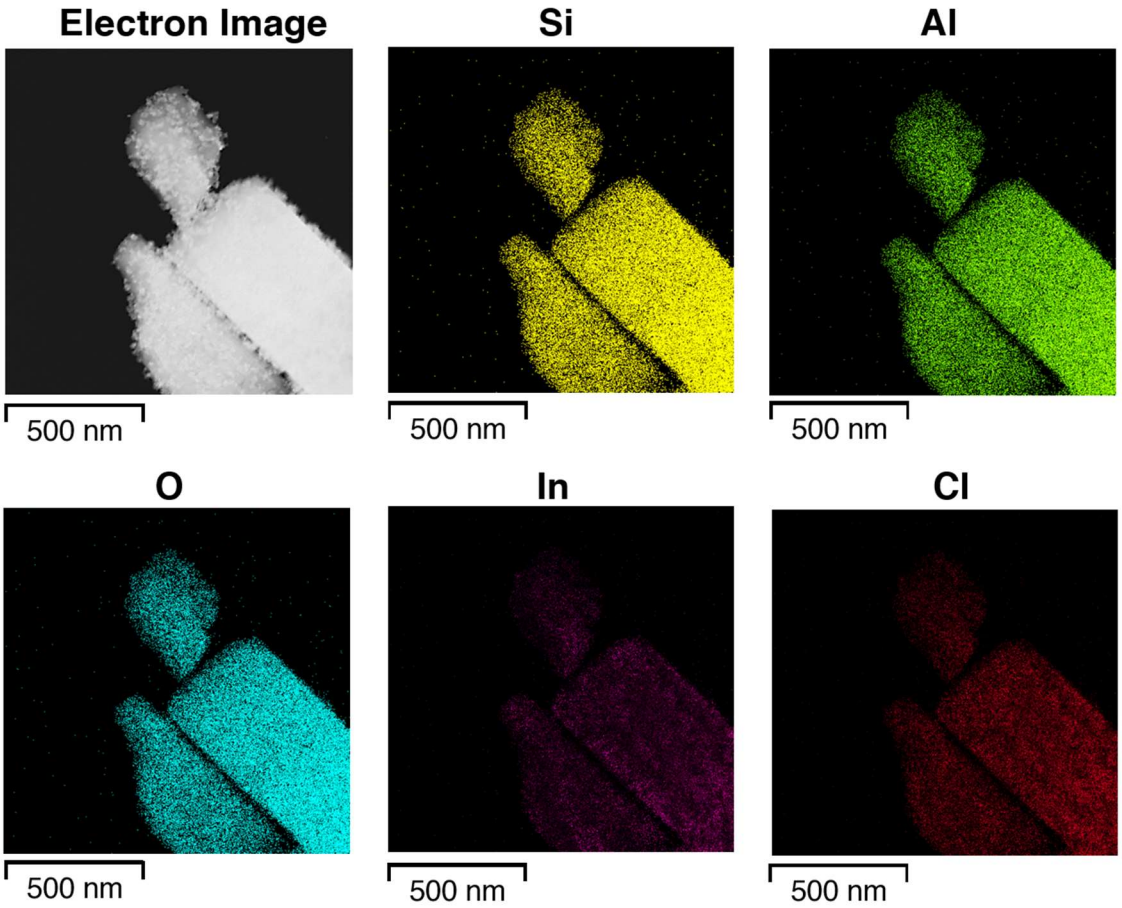

Figure 7.50: EDS-TEM maps acquired for In(0.17),K(0.58)/ZSM-5(13.5) post methanol upgrading at 400 °C for 6 hours.

As a result, indium-exchanged forms of ZSM-5 were prepared using three different indium sources: indium (III) chloride, indium (III) nitrate and indium (III) acetate. Materials were prepared using aqueous ion-exchange, as outlined in section 3.2.4, characterisation in Section 10.6. However, only minor differences were observed between indium (III) chloride and indium (III) acetate, with the material prepared from indium (III) nitrate leading to a lower indium exchange level, with higher methanol conversion and DME yield as a result of a higher number of BAS.

It was postulated that a reductive pre-treatment of indium-exchanged materials using hydrogen flow at raised temperature would reduce the In(III) centres to In(I), activating the materials. However, this process required temperatures beyond 400 °C, which required the use of an external reactor to the FlowCAT to successfully conduct the reductive treatment at sufficient temperature.[24,90] An initial experiment to trial reductive pre-treatment prior to methanol upgrading was conducted at 400 °C, however, ultimately proved futile with the results showing no benefit to catalytic activity following the pre-treatment. Reductive pre-treatment using an external furnace was also proposed,

although this risked the oxidation of In(I) centres under atmospheric conditions when being introduced to the FlowCat. This would lead them to revert to their favoured In(III) state, cancelling out the effect of the pre-treatment. In order to have carried out this work post-reduction of the indium cations, modification to the reactor setup would be required or additional steps to allow for the loading of the catalyst under an inert atmosphere free of oxygen.

7.4.3 Conclusion: Methanol Upgrading Reactions

High methanol conversion was observed initially over materials with protic secondary counterions before premature deactivation of materials, with methanol conversion approaching 0%. MTH has been reported at 400 °C over H/ZSM-5(14) and H/ZSM-5(140), where complete methanol conversion was observed prior to deactivation at ca. 20 hours, whilst higher Si/Al ZSM-5 retained 95% methanol conversion at 40 hours.[91] The reported increase in BTX selectivity for H/ZSM-5(14) was suggested for its deactivation. The detection of BTX led us to conclude that premature deactivation of catalysts has arisen from blocked micropores, with BTX and derivatives known to block medium pore ZSM-5,[46,91] with small pore chabazite even more susceptible.

BTX was not observed for materials with potassium secondary counterions. Indium-modified zeolites with potassium secondary counterions displayed constant activity throughout their time on-stream, although reduced methanol conversion and product yields were observed in comparison with protic zeolites.[91,92]

Methanol dehydration to DME was a major process for each of the catalysts tested. DME generation was initially problematic for product quantification due to its co-elution and initial misidentification as propylene. Through the use of BID and MS traces in tandem, quantification of only trace amounts of propylene was detected for the methanol upgrading reactions carried out here.

7.5 It's a Gas, Gas, Gas: Methane Co-processing with Methanol, Ethanol and Ethylene.

Following pioneering research, silver-exchanged zeolites were a leading candidate for direct methane conversion through the use of co-processing reactions.[93] Baba reported over Ag(0.17),H/ZSM-5(12) methane conversion of 13.2% at 1 hour on-stream at 400 °C for methane/ethylene co-processing, using a gas feed consisting of CH_4/C_2H_4/He in equal pressures (33.8 kPa each). In light of methane co-processing being reported with methanol,[12,13,94,95] ethanol,[14] ethylene[15,16] and propylene,[93] methane/ethylene, methane/methanol and methane/ethanol co-processing reactions were undertaken in this study, with methane conversion calculated where possible.

7.5.1 Methane/Methanol Co-processing Reactions

Co-processing reactions were explored to determine whether methanol upgrading reactions could be enhanced through the incorporation of methane. Time on-stream graphs incorporating carbon balancing for methanol upgrading at 400 °C has been included for Ag(1.30),K(0.57)/ZnMFI(96) (Figure 7.51) and Ag(2.37),Na/ZnCHA(21) (Figure 7.52). In both cases, the carbon balance was close to 100%, showing that all products were accounted for. In methane/methanol co-processing reactions, the introduction of methane pushed the carbon balance above 100%, facilitating the calculation to approximate methane conversion.

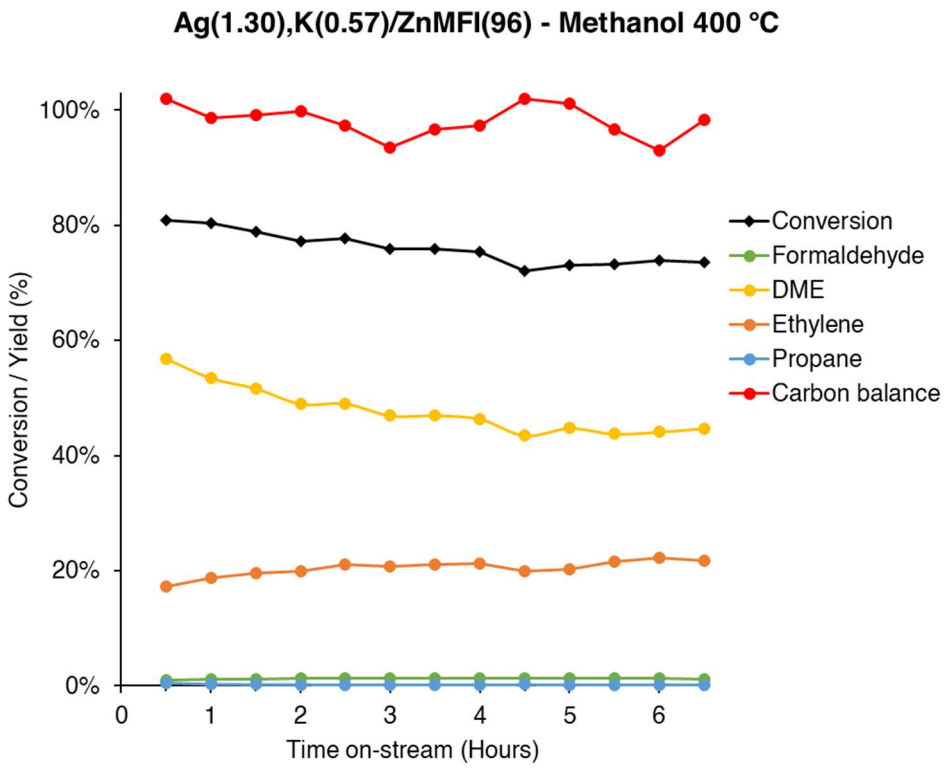

Figure 7.51: Time on-stream graph showing conversion, product yields and carbon balance for methanol co-processing at 400 °C over Ag(1.30),K(0.57)/ZnMFI(96).

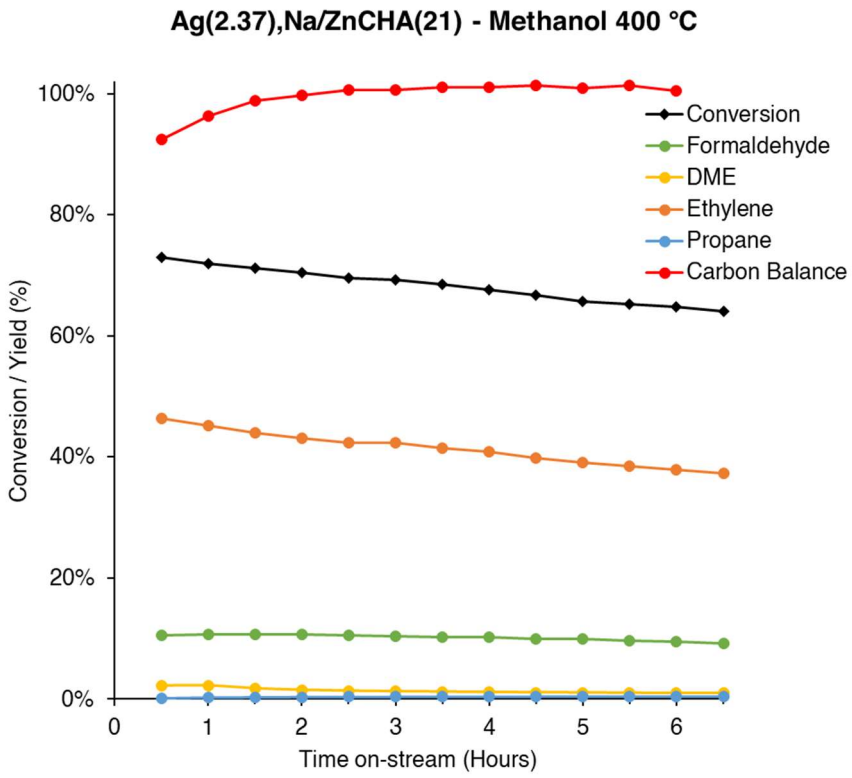

Figure 7.52: Time on-stream graph showing conversion, product yields and carbon balance for methanol co-processing at 400 °C over Ag(2.37),Na/ZnCHA(21).

Both catalysts displayed relatively good methanol conversion, however, DME was the major product for medium pore Ag(1.30),K(0.57)/ZnMFI(96) whilst for small pore Ag(2.37),Na/ZnCHA(21), ethylene was the major product. Catalytic activity remained relatively consistent over TOS for both catalysts.

Experiments were conducted to determine whether using methane as the flow gas facilitated direct methane upgrading through co-processing. Methane/methanol co-processing reactions were carried out using a modified version of the methanol upgrading conditions (Figure 7.39) using: 300 mg catalyst loading (40-60 mesh), methanol (0.009 ml/min flow rate) and methane (24 ml/min) as the carrier gas in place of nitrogen. Methane/methanol co-processing was carried out at 400 °C over Ag(1.30),K(0.57)/ZnMFI(96) (Figure 7.53) and Ag(2.37),Na/ZnCHA(21) (Figure 7.54).

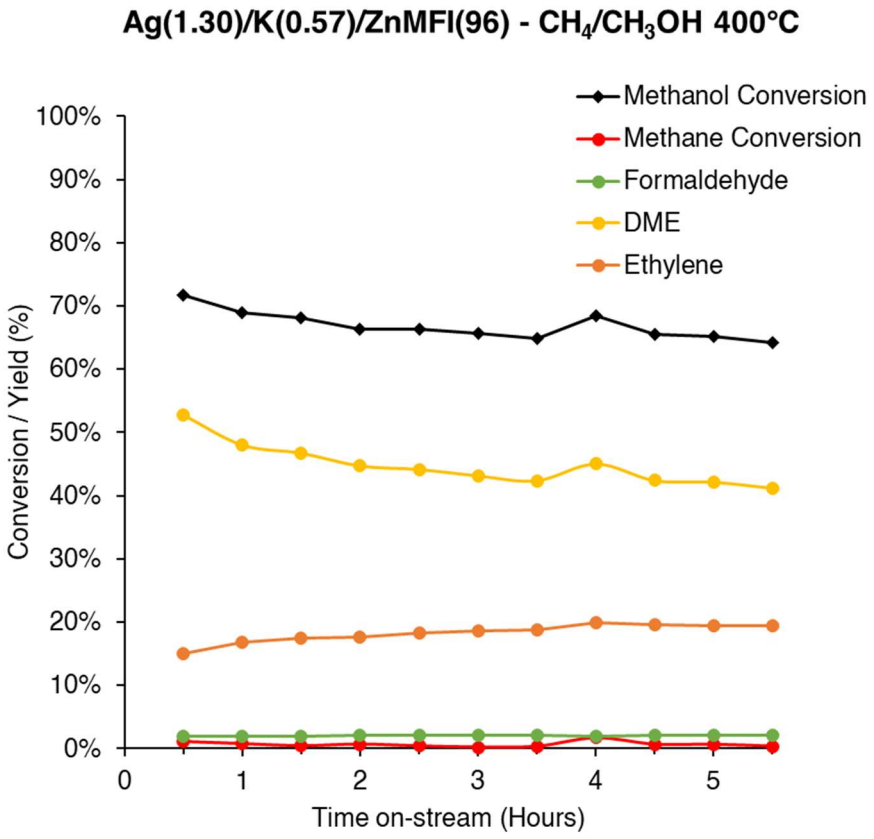

Figure 7.53: Time on-stream graph showing conversion and product yields for methane/methanol co-processing at 400 °C over Ag(1.30),K(0.57)/ZnMFI(96).

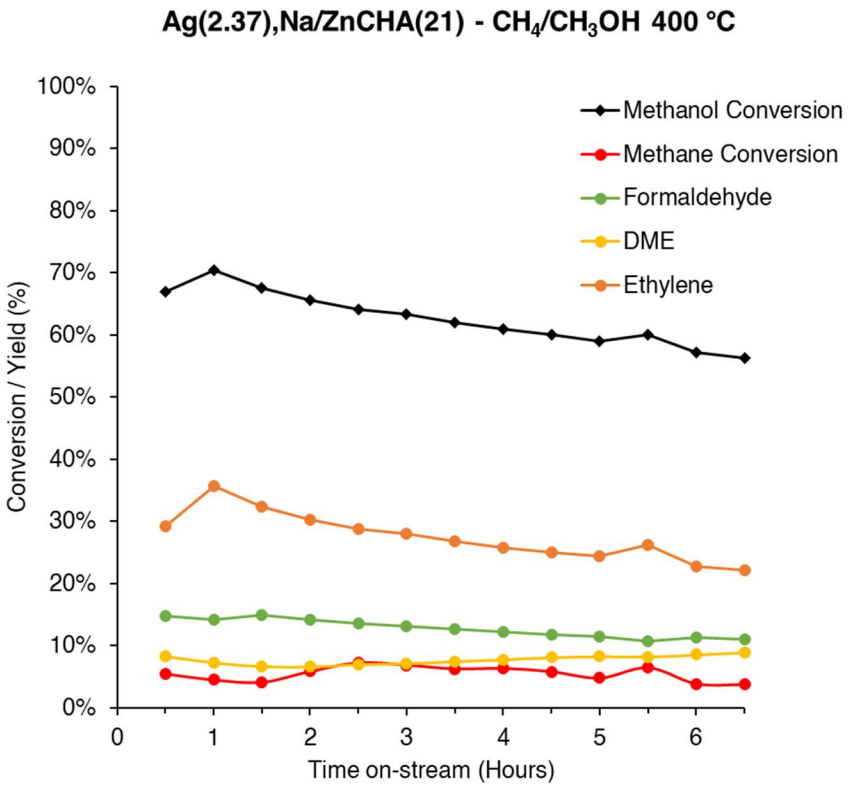

Figure 7.54: Time on-stream graph showing conversion and product yields for methane/methanol co-processing at 400 °C over Ag(2.37),Na/ZnCHA(21).

Averaged results for methanol upgrading and methane/methanol co-processing, both carried out at 400 °C, are shown in Figure 7.55.

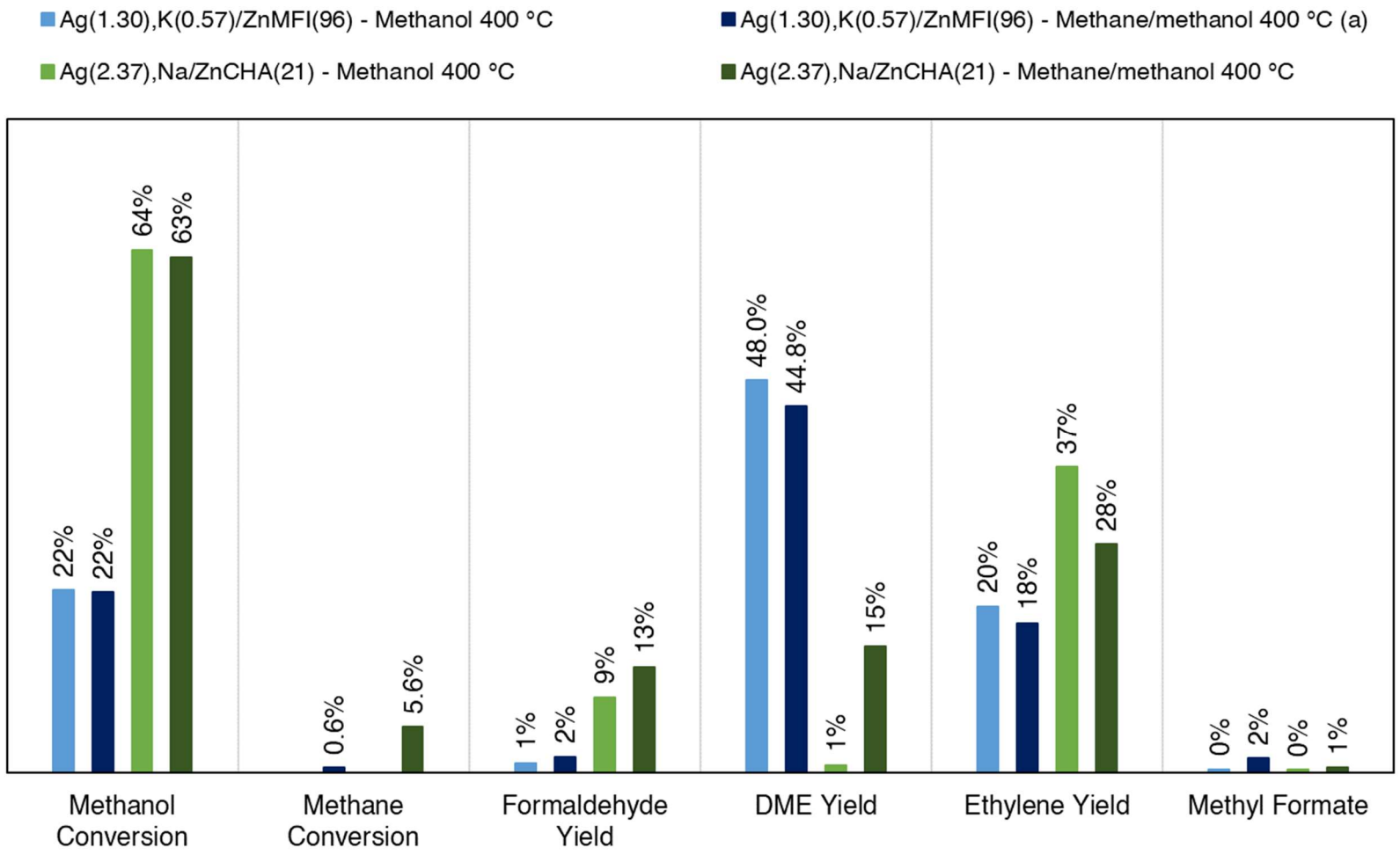

Figure 7.55: Results averaged over 6 hours on-stream for methanol upgrading and methane/methanol coprocessing at 400 °C over Ag(1.30),K(0.57)/ZnMFI(96) and Ag(2.37),Na/ZnCHA(21). (a –average of 5.5 hours)

We observed little variation in methanol conversion and product selectivity during TOS for both catalysts across the reactions, however, formaldehyde and methyl formate yields increased during methane/methanol coprocessing for Ag,K/ZnMFI (2% vs 0%) and Ag,Na/ZnCHA (1% vs 0%). Coprocessing also led to decreased ethylene yield for Ag,K/ZnMFI (18% vs 20%) and for Ag,Na/ZnCHA (28% vs 37%). Formaldehyde yield improved for both materials, doubling yield for ZnMFI (2% vs 1%) and almost 50% greater for ZnCHA (13% vs 9%).

Methane conversion was calculated for Ag(1.30),K(0.57)/ZnMFI(96) (0.6%) and Ag(2.37),Na/ZnCHA(21) (5.6%) for methane/methanol coprocessing at 400 °C. Compared with previous literature, Ag(2.37),Na/ZnCHA(21) was observed to give higher methane conversion at 400 °C. Yang *et al.* reported methane conversion for methane/methanol co-processing at 400 °C over zinc impregnated Zn/ZSM-5(19) (1.3wt% Zn) displayed 3.3%,[13] whilst H/ZSM-5(25) (post 3 hour steaming pre-treatment) displayed 5.4%.[96] Methane conversation that has been reported at values greater than what was observed here have been reported at higher reaction temperatures.[12,13] Yang reported 7.3% methane conversion at 450 °C for Zn/ZSM-5 material, although neglected to state Si/Al.[97] Zhang *et al.* report 26% methane conversion at 600 °C. [94]

7.5.2 Methane/Ethanol Co-processing Reactions

Ethanol upgrading over silver-exchanged zeolites and zincosilicates highlighted a major difference in pathway between Brønsted and Lewis acidic frameworks. It was envisioned that methane could be incorporated into the reaction for methane/ethanol co-processing with methane as a C1 feedstock. Reactions reported here were conducted during a period where additional backpressure was being experienced in the system, likely arisen from a partial blockage of the system.

Ethanol upgrading and methane/ethanol co-processing were conducted at 350 °C, with methane/ethanol co-processing also carried out with oxygen included in the feed. Oxygen was included to negate the reducing effect of hydrogen, produced as a byproduct in upgrading reactions, which should supress silver sintering.[98] Methane/ethanol co-processing reactions were carried out using a modified version of the ethanol upgrading at 350 °C conditions, shown in Figure 7.3, using: 300 mg catalyst loading (40-60 mesh), ethanol (0.015 ml/min flow rate) and methane (16 ml/min) as the carrier gas in place of nitrogen. Co-processing reactions with oxygen used $He/CH_4/O_2$ (50:49.5:0.5) as the carrier gas.

Ethanol conversion was carried out at 350 °C over Ag(2.42),K(0.88)/ZSM-5(13.5) (Figure 7.56) and Ag(0.44),K(0.23)/CHA(17) (Figure 7.57).

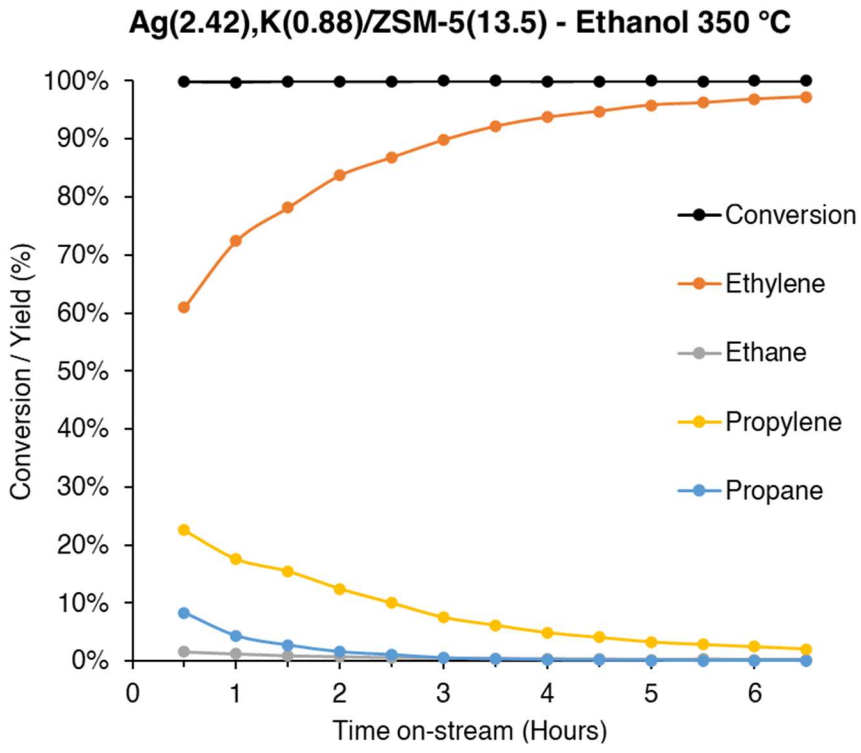

Figure 7.56: Time on-stream graph showing conversion and product yields for ethanol upgrading at 350 °C over Ag(2.42),K(0.88)/ZSM-5(13.5).

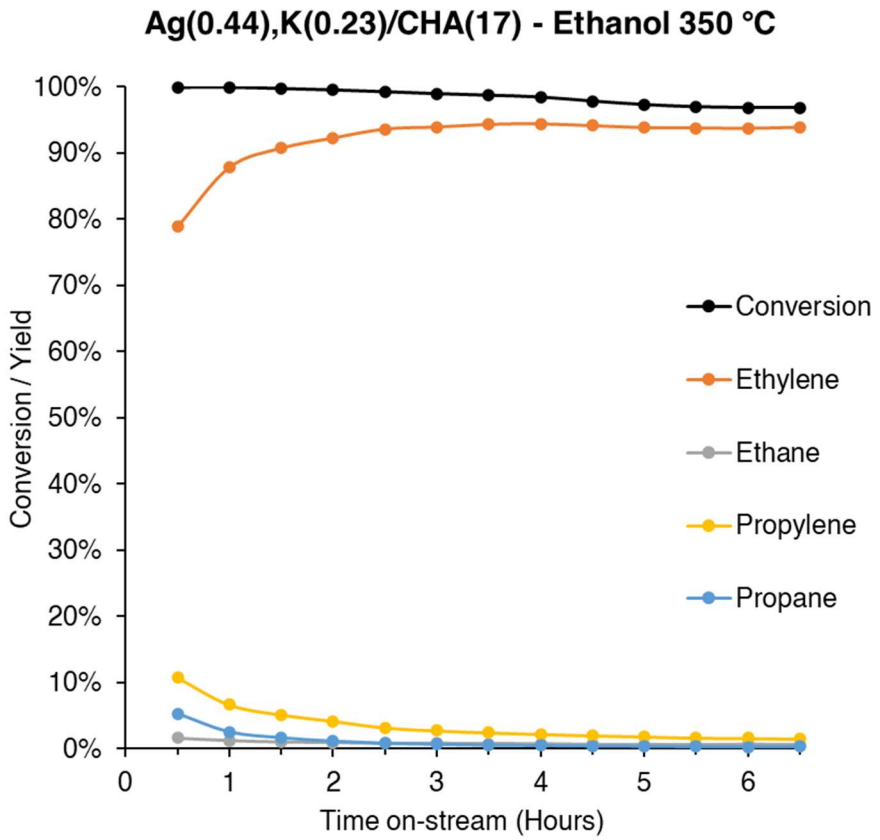

Figure 7.57: Time on-stream graph showing conversion and product yields for ethanol upgrading at 350 °C over Ag(0.44),K(0.23)/CHA(17).

Both catalysts led to almost complete ethanol conversion throughout the reaction, with ethylene the major product. It was evident that ethanol dehydration to form ethylene over BAS was the dominant process. Initial activity highlighted the production of propylene, propane and ethane in descending yields, which were observed to reduce in selectivity as the reaction proceeded.

TOS graphs are included for methane/ethanol co-processing at 350 °C over Ag(2.42),K(0.88)/ZSM-5(13.5) (Figure 7.58) and CH_4/EtOH/O_2 co-processing at 350 °C (Figure 7.59).

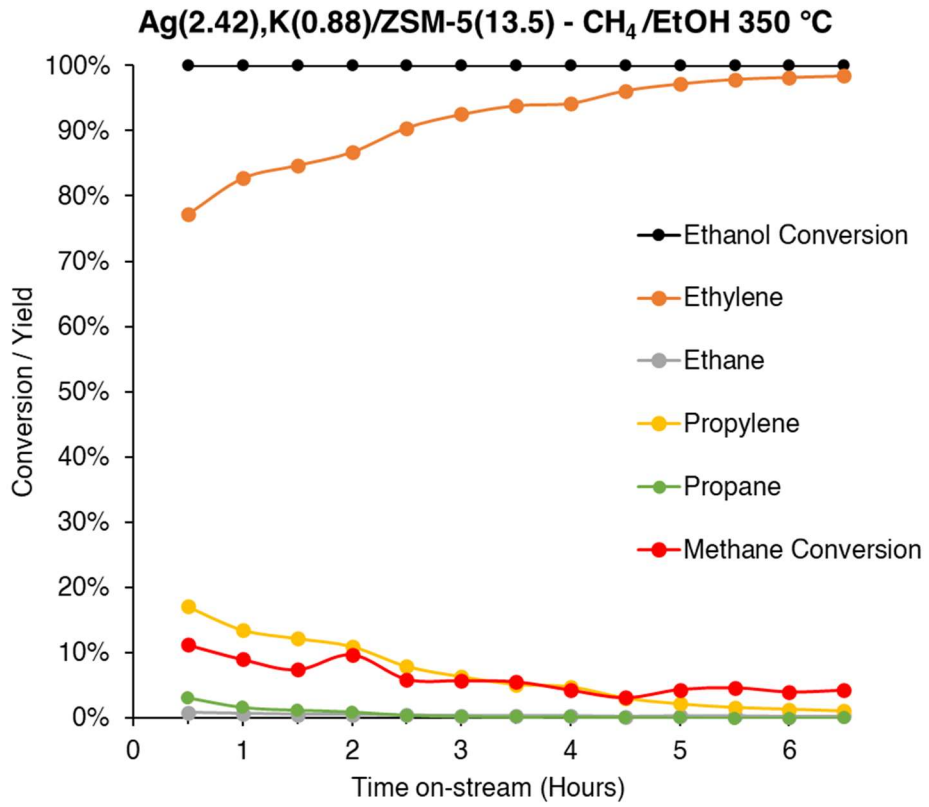

Figure 7.58: Time on-stream graph showing conversion and product yields for methane/ethanol co-processing at 350 °C over Ag(2.42),K(0.88)/ZSM-5(13.5).

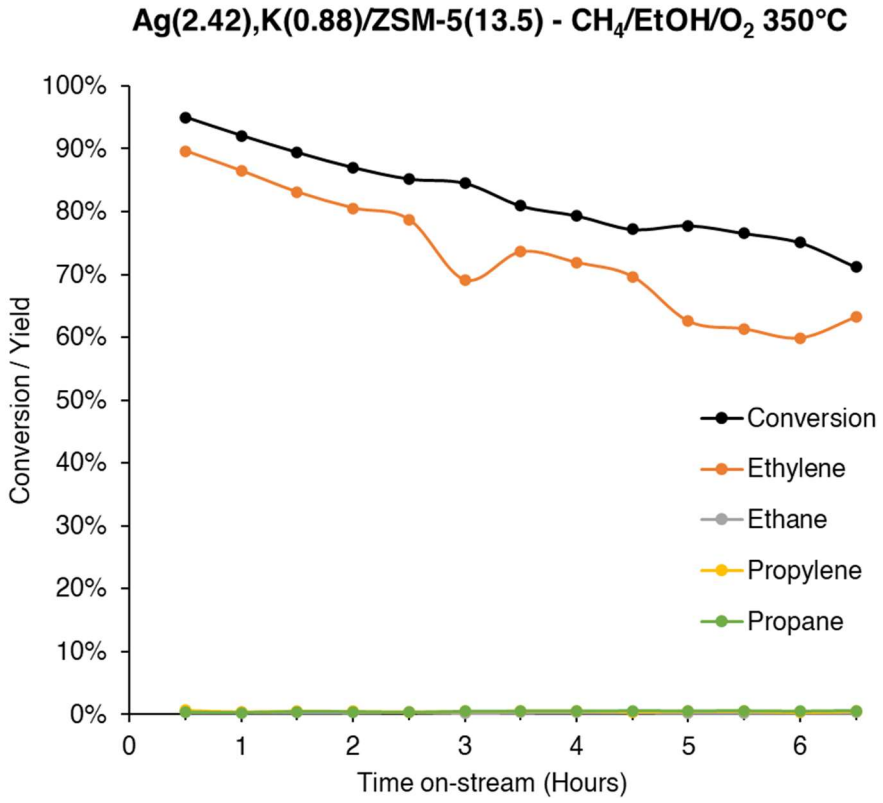

Figure 7.59: Time on-stream graph showing conversion and product yields for methane/ethanol co-processing with oxygen at 350 °C over Ag(2.42),K(0.88)/ZSM-5(13.5).

The inclusion of oxygen as part of the feed led to reduced ethanol conversion (82% vs 100%) during methane/ethanol co-processing. Greater ethylene yield was observed when methane was included (92% vs 88%) but lowered with oxygen in the feed (73%). Relatively low propylene yield (9% vs 6% vs 1%) and propane yield (2% vs 1% vs 0%) were observed for each reaction. Methane conversion (6%) was calculated during methane/ethanol co-processing, with higher methane conversion observed than is reported for Ag(1wt%),Ga(1wt%)/ZSM-5(40) (4.7%) at 400 °C.[14] Methane conversion peaked at 11.2% after 0.5 hours on-stream and remained reasonably consistent throughout the reaction, slowly decreasing as the reaction proceeded. We associate this with the deactivation of silver.

TOS graphs are included for methane/ethanol co-processing at 350 °C over Ag(0.44),K(0.23)/CHA(17) (Figure 7.60) and CH_4/EtOH/O_2 co-processing at 350 °C (Figure 7.61).

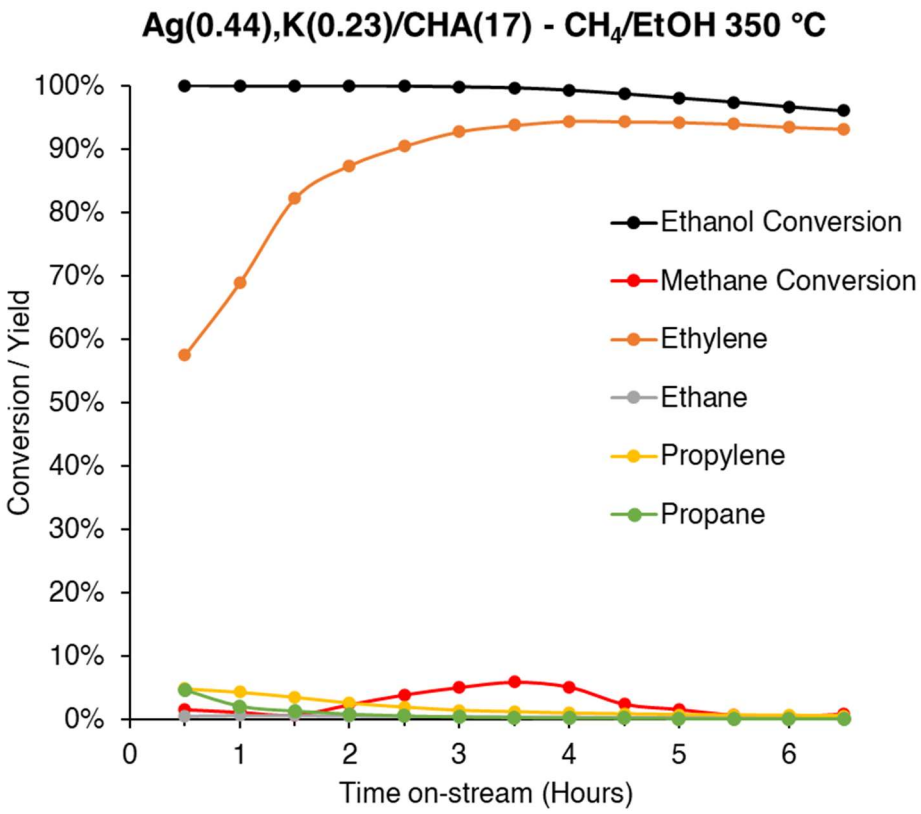

Figure 7.60: Time on-stream graph showing conversion and product yields for methane/ethanol co-processing at 350 °C over Ag(0.44),K(0.23)/CHA(17).

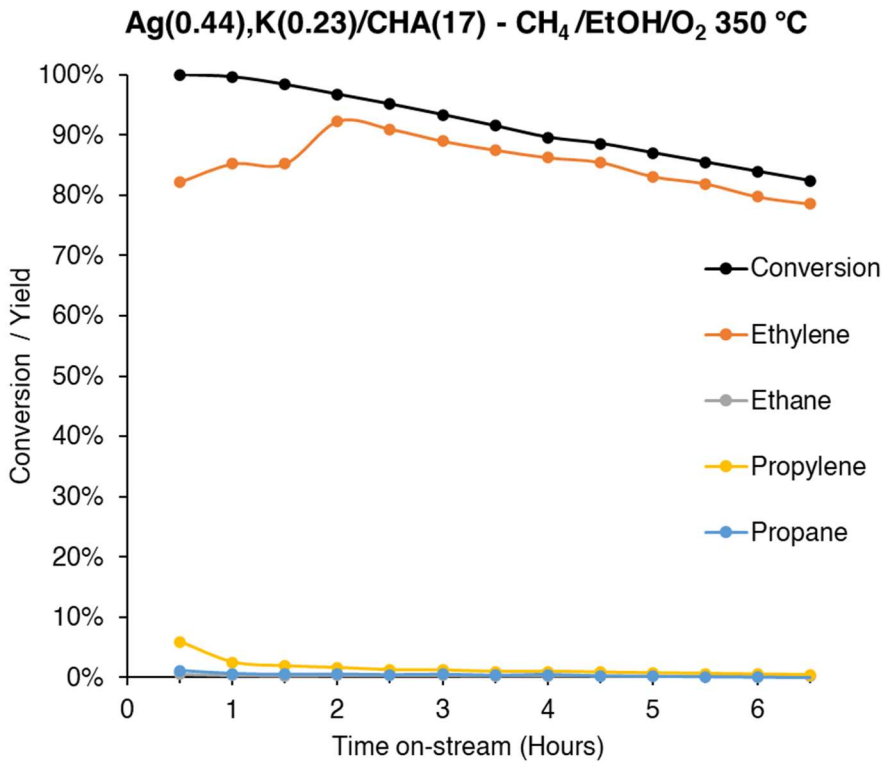

Figure 7.61: Time on-stream graph showing conversion and product yields for methane/ethanol co-processing with oxygen at 350 °C over Ag(0.44),K(0.23)/CHA(17).

Complete ethanol conversion was observed for both ethanol upgrading and methane/ethanol co-processing over Ag(0.44),K(0.23)/CHA(17) (Figure 7.60) but was reduced for CH_4/EtOH/O_2 co-processing (92%) (Figure 7.61). Ethylene yield remained fairly constant for each reaction condition (89% vs 87% vs 85%). This was also the case for the relatively low propylene yield (5% vs 2% vs 2%) and propane yield (2% vs 1% vs 0%). Methane conversion (2%) was calculated during methane/ethanol co-processing, although conversion was at a maximum around 3 to 4 hours on-stream. Prior art tells us that no methane conversion was observed for methane/ethylene co-processing at 400 °C over zeolites with protic counterions, so we associate this activity with the silver cations present on the framework. After around 1 hour, methane conversion increases to a maximum of 5.9% at 3.5 hours before reducing over the following 3 hours.

Averaged results for ethanol upgrading, methane/ethanol co-processing and CH_4/EtOH/O_2 co-processing are shown in Figure 7.62.

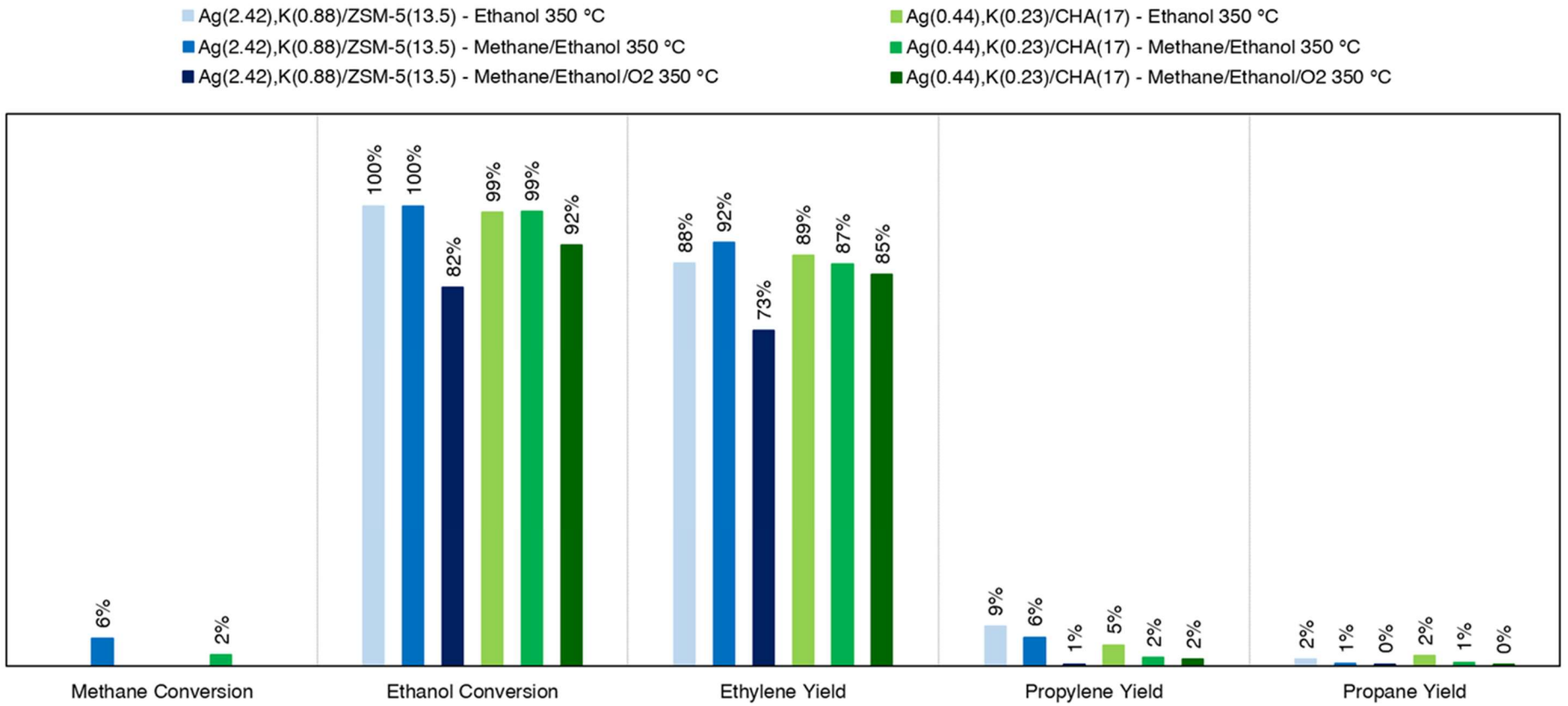

Figure 7.62: Results averaged over 6.5 hours on-stream for ethanol conversion, methane/ethanol co-processing and $CH_4/EtOH/O_2$ co-processing at 350 °C for Ag(2.42),K(0.88)/ZSM-5(13.5) and Ag(0.44),K(0.23)/CHA(17).

For the methane/ethanol co-processing reactions carried out under oxidative conditions, issues accurately controlling gas flow with the MFC made it difficult to calculate the carbon balance, so methane conversion could not be approximated for these co-processing reactions. Whilst not quantified, it is worth noting that ethylene oxide (EO) was observed during CH_4/EtOH/O_2 co-processing reactions. EO was successfully identified following additional work to elucidate EO and acetaldehyde in the MS trace. Whilst EO and acetaldehyde are known to have an almost identical mass spectrum fragmentation pattern, our GC-MS-BID could successfully resolve the two compounds with distinct retention times that were well resolved.

Ethanol conversion was carried out at 350 °C over Ag(1.50),K(1.76)/ZnMFI(96) (Figure 7.63) and Ag(0.51),K(0.57)/ZnCHA(12) (Figure 7.64).

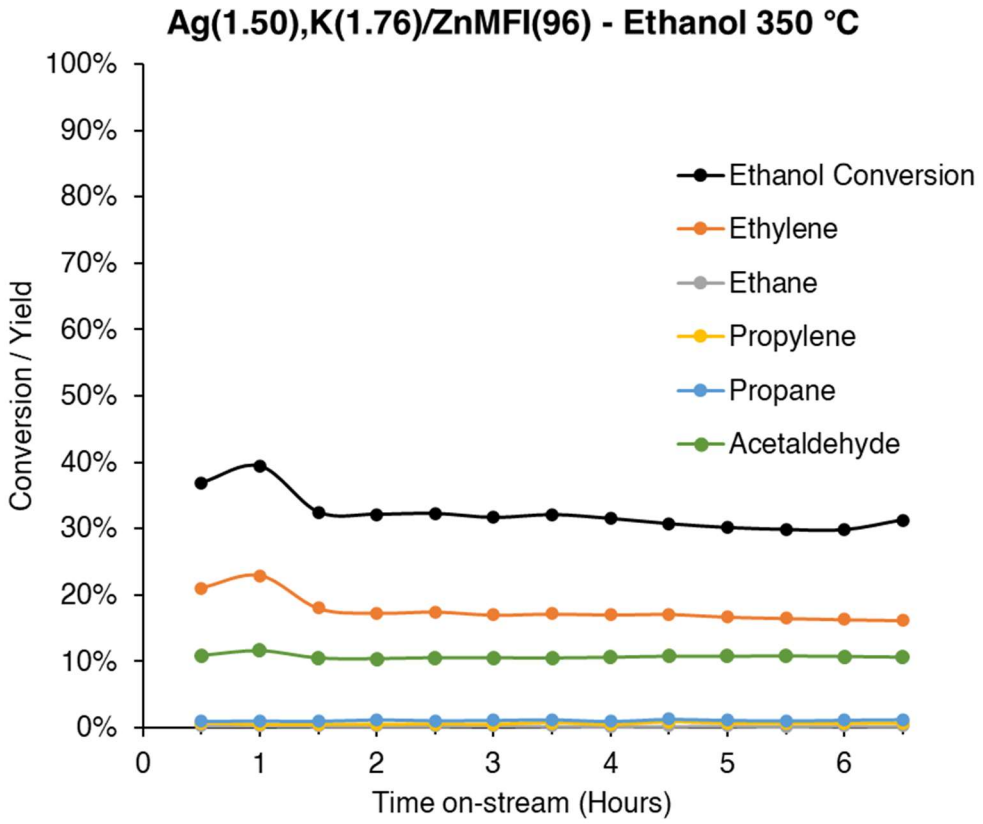

Figure 7.63: Time on-stream graph showing conversion and product yields for ethanol upgrading at 350 °C over Ag(1.50),K(1.76)/ZnMFI(96).

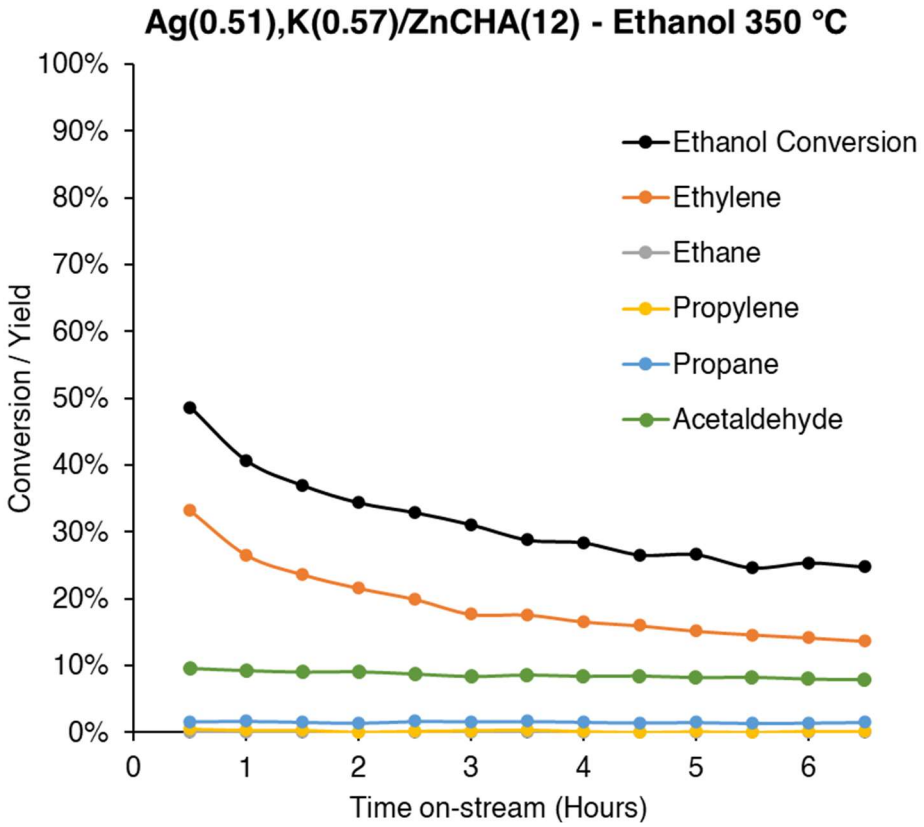

Figure 7.64: Time on-stream graph showing conversion and product yields for ethanol upgrading at 350 °C over Ag(0.51),K(0.57)/ZnCHA(12).

Zincosilicate catalysts displayed relatively low ethanol conversion in comparison to their zeolite counterparts, however, activity remained consistent during the reaction. Ethylene remained the major product, owing to the presence of framework BAS, but now the Lewis acidic frameworks facilitated ethanol upgrading to acetaldehyde.

TOS graphs have been included for methane/ethanol co-processing (Figure 7.65) and CH_4/EtOH/O_2 co-processing (Figure 7.66) at 350 °C over Ag(1.50),K(1.76)/ZnMFI(96).

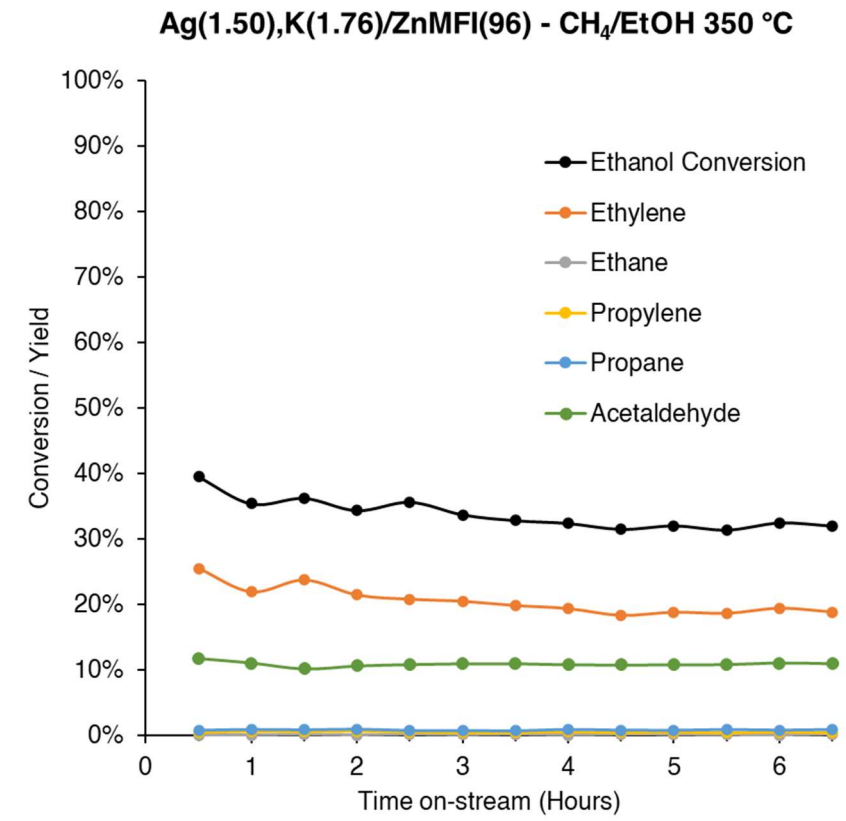

Figure 7.65: Time on-stream graph showing conversion and product yields for methane/ethanol co-processing at 350 °C over Ag(1.50),K(1.76)/ZnMFI(96).

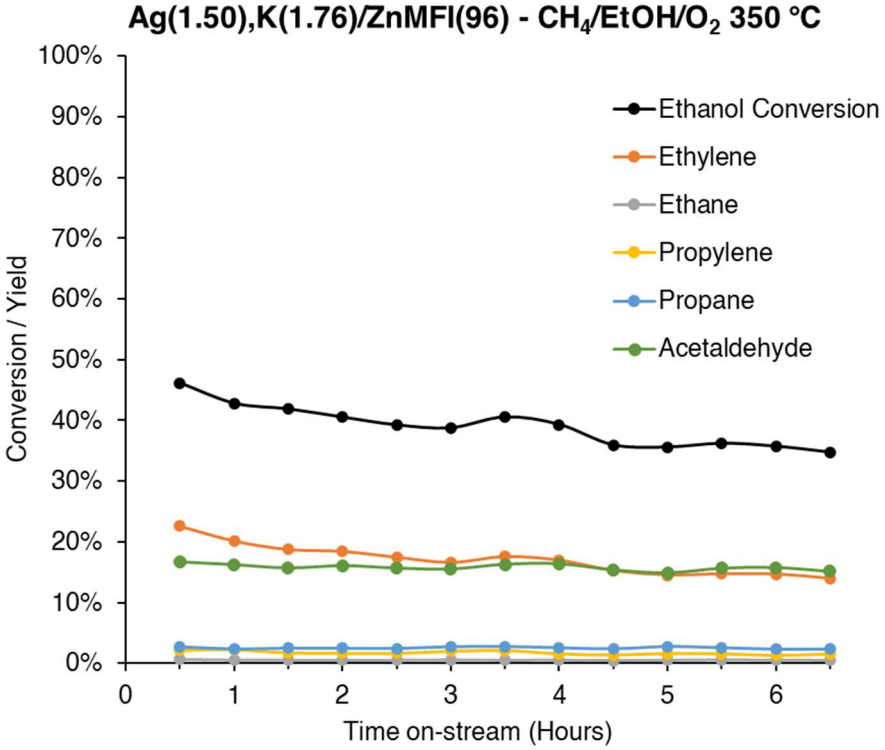

Figure 7.66: Time on-stream graph showing conversion and product yields for methane/ethanol co-processing with oxygen at 350 °C over Ag(1.50),K(1.76)/ZnMFI(96).

Comparing the three reactions conducted over Ag(1.50),K(1.76)/ZnMFI(96) showed that ethanol conversion remained relatively consistent across reactions but was highest for oxidative co-processing (32% vs 34% vs 39%). This was also observed for ethylene yield (18% vs 21% vs 17%), with consistent and relatively low propylene yield (1% vs 0% vs 2%) and propane yield (1% vs 1% vs 3%). Acetaldehyde yield was highest for co-processing with oxygen in the feed (16%), whereas reactions without oxygen led to a lower acetaldehyde yield being observed (11%).

TOS graphs have been included for methane/ethanol co-processing (Figure 7.67) and CH_4/EtOH/O_2 co-processing (Figure 7.68) at 350 °C over Ag(0.51),K(0.57)/ZnCHA(12).

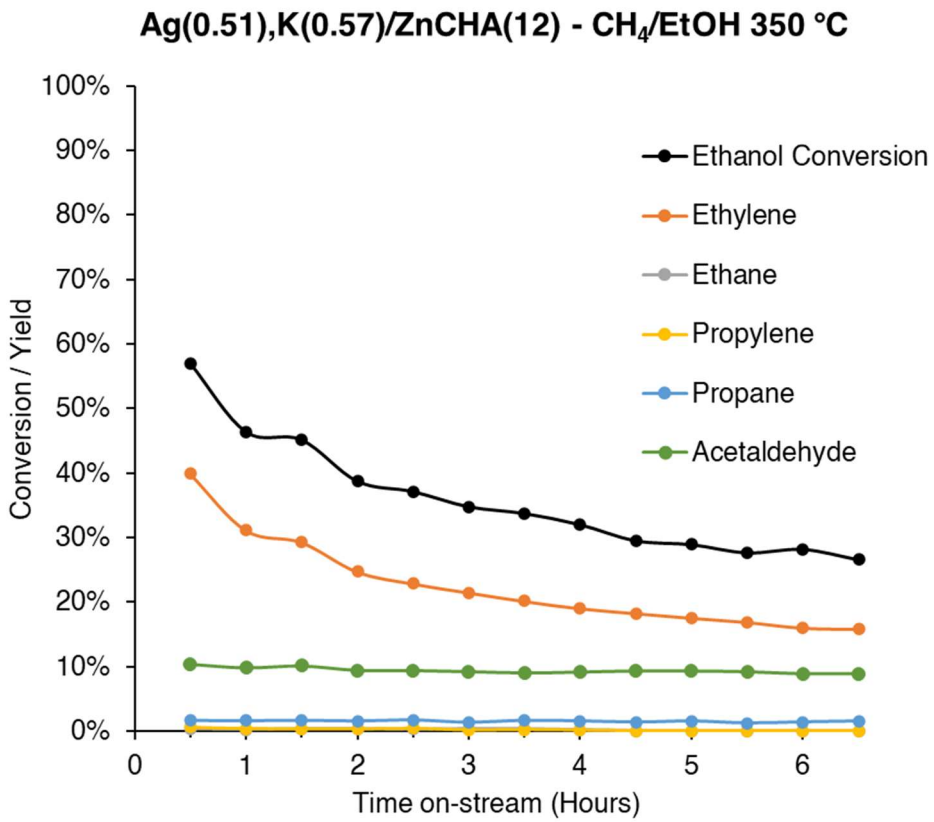

Figure 7.67: Time on-stream graph showing conversion and product yields for methane/ethanol co-processing at 350 °C over Ag(0.51),K(0.57)/ZnCHA(12).

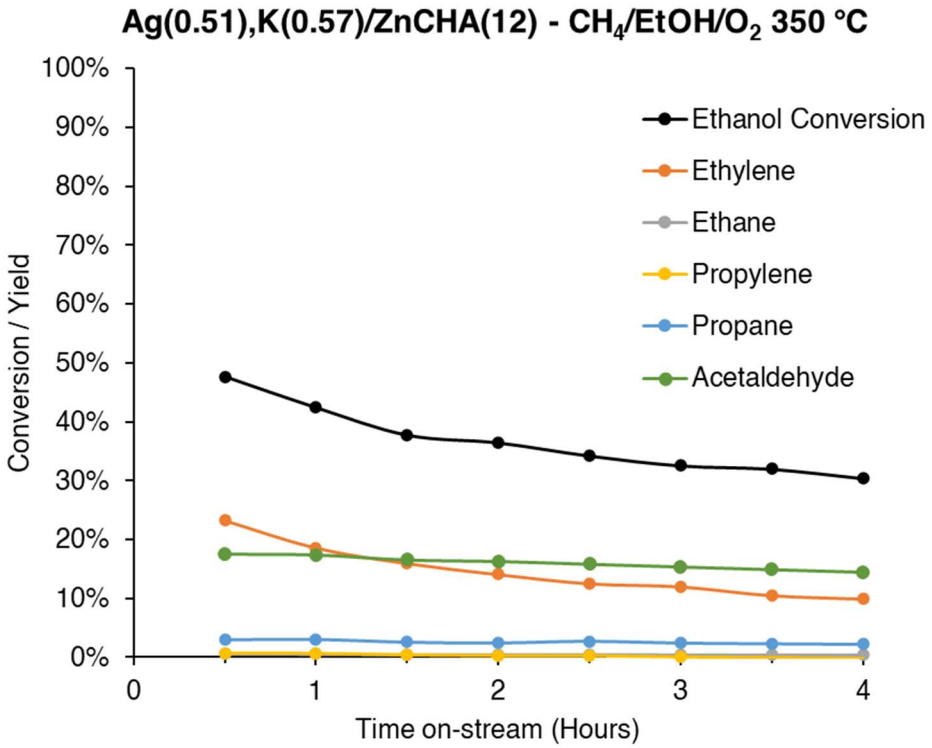

Figure 7.68: Time on-stream graph showing conversion and product yields for methane/ethanol co-processing with oxygen at 350 °C over Ag(0.51),K(0.57)/ZnCHA(12).

Ethanol conversion for Ag(0.51),K(0.57)/ZnCHA(12) increased for co-processing reactions (32% vs 36% vs 37%). Ethylene yield was similar across reaction, although lowest for oxidative co-processing (19% vs 23% vs 15%), with a relatively low propylene yield (0% vs 0% vs 1%) and propane yield (2% vs 2% vs 3%) that were both increased for oxidative co-processing. Acetaldehyde yield was greatest for co-processing with oxygen in the feed (16%), whereas reactions without oxygen led to a lower acetaldehyde yield being observed (9%).

In comparison with the zeolite materials tested, ethanol conversion was far lower across all reaction conditions (ca. 35% vs ca. 99%) and with much lower ethylene yield (ca.18% vs ca. 85%), owing to the Lewis acidity of zincosilicates facilitating ethanol dehydrogenation to produce acetaldehyde, which was not detected for the zeolite catalysts. Averaged results for ethanol upgrading, methane/ethanol co-processing and CH_4/EtOH/O_2 co-processing are shown in Figure 7.69.

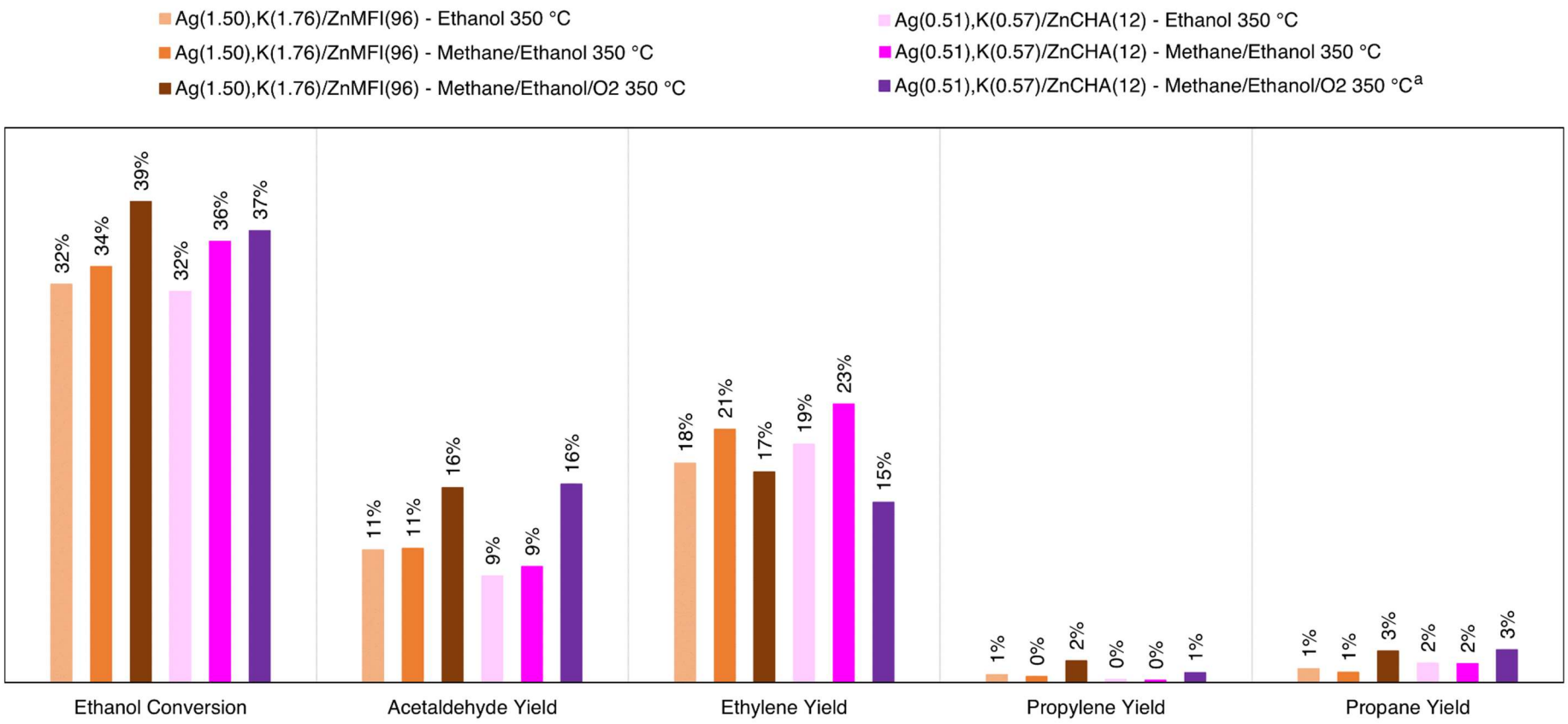

Figure 7.69: Results averaged over 6.5 hours on-stream for ethanol conversion, methane/ethanol co-processing and methane/ethanol/O_2 co-processing at 350 °C for Ag(1.50),K(1.76)/ZnMFI(96) and Ag(0.51),K(0.57)/ZnCHA(12). (a –average of 4 hours)

Characterisation of the spent catalysts was conducted in Section 8.2.1 to highlight changes between fresh catalyst and spent catalyst following the reaction conditions tested. This facilitated the determination of which frameworks provided a stabilising effect on the silver cations, through measuring which led to the smallest increase in silver cluster size by pXRD and TEM, as well as determining changes in elemental distribution through the use of EDS-TEM.

7.5.3 Methane/Ethylene Co-processing Reactions

Influenced by prior art reporting 13.2% methane conversion over silver-exchanged zeolites during methane/ethylene co-processing,[93] several modifications were made to the FlowCAT setup to allow for the permanent attachment of different gas feeds. These changes are outlined in Section 7.2. Initiating the reactions proved challenging, as the mass flow controller (MFC) controls the flow rate of the gas fed into the FlowCAT reactor using a specific thermal mass flow conversion factor that is unique to each gas. This was calculated for the mixed gas cylinder used here, consisting of equal parts methane, ethylene and helium (inert carrier), replicating the gas flow of reported work.[16] Even so, the flow rate of the input gas did not appear to be controlled by the MFC at the chosen flow rate. Reactions were carried out following the ethanol upgrading profile for 400 °C, shown in Figure 7.4, albeit without a liquid feed, with the reaction parameters as: 300 mg catalyst loading (40-60 mesh) and CH_4/C_2H_4/He, in equal pressures (33.8 kPa) (16 ml/min) as carrier gas in place of nitrogen.

Tentatively, reactions were initially carried out to emulate those reported previously.[93] Methane/ethylene co-processing was carried out for 6 hours at 400 °C over H/ZSM-5(13.5) (Figure 7.70) and Ag(0.35),H/ZSM-5(13.5) (Figure 7.71).

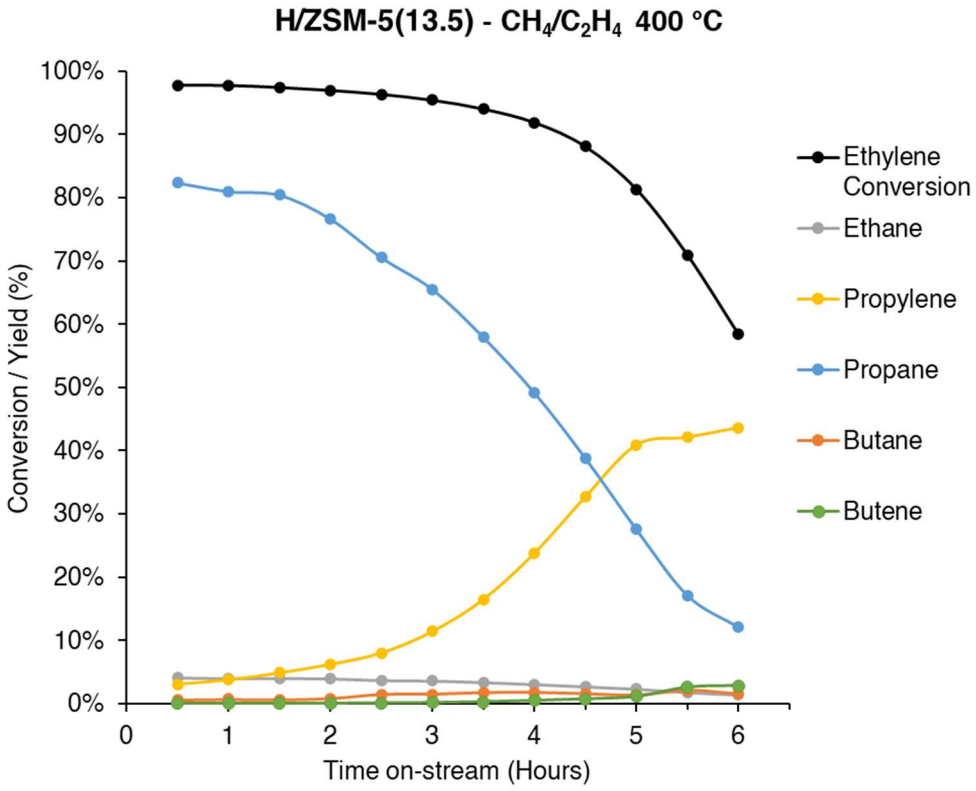

Figure 7.70: Time on-stream graph for methane/ethylene co-processing at 400 °C over H/ZSM-5(13.5).

Whilst complete ethylene conversion was observed at the start, after 4 hours conversion rapidly began to decrease (57% at 6 hours). Product distribution also changed after 4 hours, with propylene replacing propane as the major product. A wide range of C_3-C_6 olefins and BTX products and their derivatives were also observed in the MS trace. Propane dehydrogenation to propylene is well known over metal-modified ZSM-5 catalysts,[99,100] however, in absence of metals here we postulate that activity arises through ethylene oligomerisation and subsequent cracking to C_3 products, the latter emulating FCC applications that utilise ZSM-5.[101]

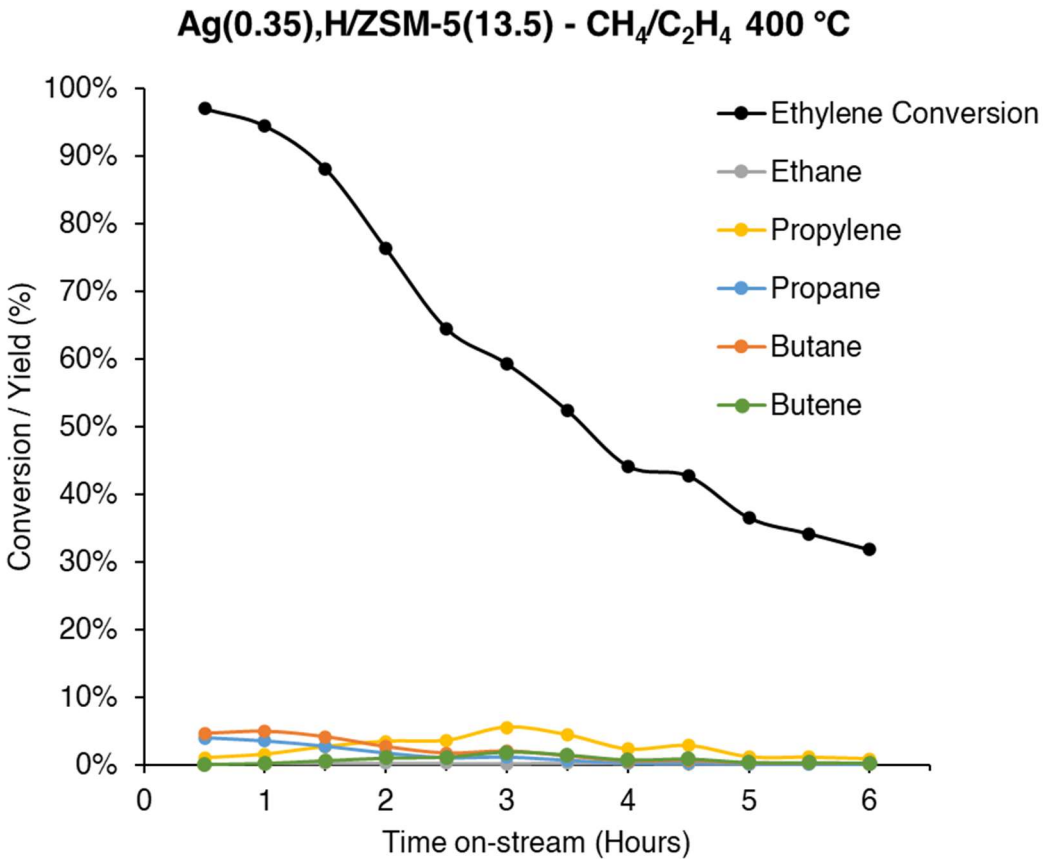

Figure 7.71: Time on-stream graph for methane/ethylene co-processing at 400 °C over Ag(0.35),H/ZSM-5(13.5).

Ag(0.35),H/ZSM-5(13.5) exhibited almost complete ethylene conversion at 0.5 hours, but the drop off in activity was more pronounced than for the protic parent H/ZSM-5(13.5). The silver-exchanged form led to a pronounced change in product distribution, with a wide range of C_3-C_6 olefins and BTX products and their derivatives being observed, although unquantified.

Averaged results of 6 hours are shown in Figure 7.72. For all quantified products, the yield was much lower for Ag(0.35),H/ZSM-5(13.5) than the protic parent material. For both catalysts, the yields for butane and butene were concordant, with H/ZSM-5(13.5) displaying higher ethane yield (3%), propane yield (52%) and propylene yield (22%). The remaining products (MS trace, unquantified) observed for both catalysts were various C_3-C_6 olefins alongside BTX products and their derivatives.

Prior art conducting methane/ethylene co-processing at 400 °C over Ag(0.17)/ZSM-5(12) reported ethylene conversion (86%) comparable to H/ZSM-5(13.5), with a lower propane yield (12%) and lower propylene yield (20%).[102] However, they report a greater butene yield (10%) and butane yield (14%), whilst observing 13.2% methane conversion.[102] Methane conversion could not be quantified here, due to the

low carbon balance, as a result of generating various C_3-C_6 olefins and BTX products across both catalysts.

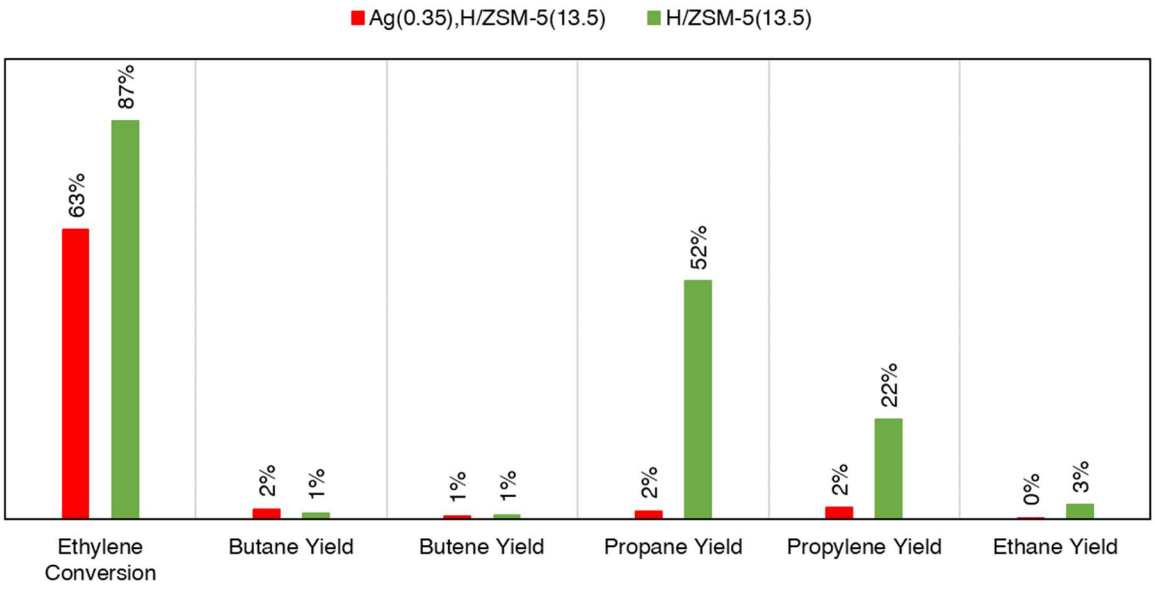

Figure 7.72: Results averaged over 6.5 hours on-stream for methane/ethylene co-processing at 400 °C over Ag(0.35),H/ZSM-5(13.5) (red) and H/ZSM-5(13.5) (green).

7.6 Conclusion of Upgrading Reactions

Ethanol upgrading for its valorisation to higher value products was explored,[14,29–33] using catalysts with a variety of metals and secondary counterions. Zeolites led to complete ethanol conversion (100%), with BAS facilitating ethanol dehydration to ethylene.[55–58] Whilst unquantified, we detected various C_3-C_6 olefins and BTX products for medium pore ZSM-5 catalysts, but not for small pore CHA catalysts, demonstrating that selectivity was driven by framework pore size. Zincosilicates facilitated dehydrogenation to acetaldehyde.[61–64] Ethanol upgrading was conducted over various ZnMFI and ZnCHA materials at varying temperatures. Pt(0.02),H/ZnCHA(12) displayed greater ethanol conversion (72%) and acetaldehyde selectivity (68%) at 320 °C than reported Zn(0.3),H/DeAlBEA (50% and 60% respectively) at the same temperature.[73] Pt(0.03),H/ZnCHA(12) displayed greater ethanol conversion (96%) and acetaldehyde selectivity (88%) at 400 °C, both far greater than reported ethanol conversion (65%) and acetaldehyde selectivity (51%) for Zn-MWW(40).[61] Whilst acetaldehyde selectivity is lower than that reported for ZnO,Rb/MOR(7) (89%)[67] and Zn/Silicalite-1 (5wt% Zn) (95%),[74] both display lower ethanol conversion (40% and 65% respectively) at 400 °C.

Pt(0.02),H/ZnCHA(12) was observed to be highly stable and highly catalyst for ethanol upgrading over a range of temperatures. During a temperature cycling experiment, we observed a relatively high ethanol conversion (92%) and recorded our highest acetaldehyde selectivity (91%) at 360 °C. Material also displayed consistent activity and product distribution after 55 hours.

Methanol upgrading over zeolites with protic secondary counterions displayed methanol conversion approaching 100% before premature deactivation, with our findings in line with reports of blocked micropores following the generation of BTX and derivatives.[46] Zeolites with potassium secondary counterions displayed consistent activity, albeit with reduced methanol conversion and DME selectivity around 90%.

Direct methane upgrading where methane was the lone feed into the reactor resulted in no activity, which is in line with reports in literature.[13] Methane/methanol coprocessing at 400 °C over Ag(1.30),K(0.57)/ZnMFI(96) and Ag(2.37),Na/ZnCHA(21) led to methane conversion of 0.6% and 5.6% respectively. Reports of methane/methanol co-processing over zinc impregnated Zn/ZSM-5(19) (1.3wt% Zn) was 3.3% methane conversion at 400 °C,[13] whilst H/ZSM-5(25) (post 3 hour steaming pre-treatment) was reported as 5.4%.[96] During methane/ethanol co-processing at 350 °C, we recorded 6% methane conversion for Ag(2.42),K(0.88)/ZSM-5(13.5), greater than reported for Ag(1wt%),Ga(1wt%)/ZSM-5(40) (4.7%) at 400 °C.[14]

7.7 Chapter Seven Bibliography

1 S. Miao, Y. Wang, D. Ma, Q. Zhu, S. Zhou, L. Su, D. Tan and X. Bao, *J. Phys. Chem. B*, Effect of Ag^+ Cations on Nonoxidative Activation of Methane to C2-Hydrocarbons, 2004, **108**, 17866–17871.

2 J. A. Labinger, *J. Mol. Catal. A Chem.*, Selective alkane oxidation: hot and cold approaches to a hot problem, 2004, **220**, 27–35.

3 A. I. Olivos-Suarez, A. Szecsenyi, E. J. M. Hensen, J. Ruiz-Martinez, E. A. Pidko and J. Gascon, *Acs Catal.*, Strategies for the Direct Catalytic Valorization of Methane Using Heterogeneous Catalysis: Challenges and Opportunities, 2016, **6**, 2965–2981.

4 M. Ravi, M. Ranocchiari and J. A. van Bokhoven, *Angew. Chemie Int. Ed.*, The Direct Catalytic Oxidation of Methane to Methanol—A Critical Assessment, 2017, **56**, 16464–16483.

5 N. F. Dummer, D. J. Willock, Q. He, M. J. Howard, R. J. Lewis, G. Qi, S. H. Taylor, J. Xu, D. Bethell, C. J. Kiely and G. J. Hutchings, *Chem. Rev.*, Methane Oxidation to Methanol, 2023, **123**, 6359–6411.

6 L. Liu and A. Corma, *Chem*, Isolated metal atoms and clusters for alkane activation: Translating knowledge from enzymatic and homogeneous to heterogeneous systems, 2021, **7**, 2347–2384.

7 R. Horn and R. Schlögl, *Catal. Letters*, Methane Activation by Heterogeneous Catalysis, 2015, **145**, 23–39.

8 B. L. Farrell, V. O. Igenegbai and S. Linic, *ACS Catal.*, A Viewpoint on Direct Methane Conversion to Ethane and Ethylene Using Oxidative Coupling on Solid Catalysts, 2016, **6**, 4340–4346.

9 P. Schwach, X. Pan and X. Bao, *Chem. Rev.*, Direct Conversion of Methane to Value-Added Chemicals over Heterogeneous Catalysts: Challenges and Prospects, 2017, **117**, 8497–8520.

10 A. Blankenship, M. Artsiusheuski, V. Sushkevich and J. A. van Bokhoven, *Nat. Catal.*, Recent trends, current challenges and future prospects for syngas-free methane partial oxidation, 2023, **6**, 748–762.

11 P. del Campo, C. Martínez and A. Corma, *Chem. Soc. Rev.*, Activation and conversion of alkanes in the confined space of zeolite-type materials, 2021, **50**, 8511–8595.

12 V. R. Choudhary, K. C. Mondal and S. A. R. Mulla, *Angew. Chemie Int. Ed.*, Simultaneous Conversion of Methane and Methanol into Gasoline over Bifunctional Ga-, Zn-, In-, and/or Mo-Modified ZSM-5 Zeolites, 2005, **44**, 4381–4385.

13 Z. Xi, B. Zhou, B. Jiang, J. Wang, Z. Liao, Z. Huang and Y. Yang, *Mol. Catal.*, Efficient conversion of methane to aromatics in the presence of methanol at low temperature, 2019, **475**, 110493.

14 P. He, R. Gatip, M. Yung, H. B. Zeng and H. Song, *Appl. Catal. B-Environmental*, Co-aromatization of olefin and methane over Ag-Ga/ZSM-5 catalyst at low temperature, 2017, **211**, 275–288.

15 K. Inazu, T. Koyama, A. Miyaji and T. Baba, *J. Japan Pet. Inst.*, Propene production from ethene and methane using silver- and proton-exchanged zeolite catalysts, 2008, **51**, 205–216.

16 Y. Ono and T. Baba, *Phys. Chem. Chem. Phys.*, Unique properties of silver cations in solid-acid catalysis by zeolites and heteropolyacids, 2015, **17**, 15637–15654.

17 T. Sun and K. Seff, *Chem. Rev.*, Silver Clusters and Chemistry in Zeolites, 1994,

94, 857–870.

18 N. S. Flores-Lopez, J. Castro-Rosas, R. Ramirez-Bon, A. Mendoza-Cordova, E. Larios-Rodriguez and M. Flores-Acosta, *J. Mol. Struct.*, Synthesis and properties of crystalline silver nanoparticles supported in natural zeolite chabazite, 2012, **1028**, 110–115.

19 M. Lamoth, T. Jones, M. Plodinec, A. Machoke, S. Wrabetz, M. Krämer, A. Karpov, F. Rosowski, S. Piccinin, R. Schlögl and E. Frei, *ChemCatChem*, Nanocatalysts Unravel the Selective State of Ag, 2020, **12**, 2977–2988.

20 N. H. Heo, Y. Kim, J. J. Kim and K. Seff, *J. Phys. Chem. C*, Surprising Intrazeolitic Chemistry of Silver, 2016, **120**, 5277–5287.

21 A. Mayoral, T. Carey, P. A. Anderson, A. Lubk and I. Diaz, *Angew. Chemie Int. Ed.*, Atomic Resolution Analysis of Silver Ion-Exchanged Zeolite A, 2011, **50**, 11230–11233.

22 T. Altantzis, E. Coutino-Gonzalez, W. Baekelant, G. T. Martinez, A. M. Abakumov, G. Van Tendeloo, M. B. J. Roeffaers, S. Bals and J. Hofkens, *ACS Nano*, Direct Observation of Luminescent Silver Clusters Confined in Faujasite Zeolites, 2016, **10**, 7604–7611.

23 T. Baba, Y. Abe, K. Nomoto, K. Inazu, T. Echizen, A. Ishikawa and K. Murai, *J. Phys. Chem. B*, Catalytic transformation of methane over in-loaded ZSM-5 zeolite in the presence of ethene, 2005, **109**, 4263–4268.

24 Y. Yuan and R. F. Lobo, *Chem. Sci.*, Propane dehydrogenation over extra-framework In(i) in chabazite zeolites, 2022, **13**, 2954–2964.

25 J. Pan, J. Lee, M. Li, B. A. Trump and R. F. Lobo, *J. Catal.*, Comparative investigation of Ga- and In-CHA in the non-oxidative ethane dehydrogenation reaction, 2022, **413**, 812–820.

26 Z. Maeno, S. Yasumura, X. Wu, M. Huang, C. Liu, T. Toyao and K. Shimizu, *J. Am. Chem. Soc.*, Isolated Indium Hydrides in CHA Zeolites: Speciation and Catalysis for Nonoxidative Dehydrogenation of Ethane, 2020, **142**, 4820–4832.

27 Z. Maeno, X. Wu, S. Yasumura, T. Toyao, Y. Kanda and K. Shimizu, *Catalysts*, 2020, 10.

28 M. C. Deem, I. Cai, J. S. Derasp, P. L. Prieto, Y. Sato, J. Liu, A. J. Kukor and J. E. Hein, *ACS Catal.*, Best Practices for the Collection of Robust Time Course Reaction Profiles for Kinetic Studies, 2023, **13**, 1418–1430.

29 I. Takahara, M. Saito, M. Inaba and K. Murata, *Catal. Letters*, Dehydration of Ethanol into Ethylene over Solid Acid Catalysts, 2005, **105**, 249–252.

30 C. R. V. Matheus, L. H. Chagas, G. G. Gonzalez, E. Falabella S. Aguiar and L. G. Appel, *ACS Catal.*, Synthesis of Propene from Ethanol: A Mechanistic Study, 2018, **8**, 7667–7678.

31 C.-Y. Liu, K. Struwe, C.-H. Lee, H.-Y. Chuang, J. Sauer, J. C.-C. Yu, V.-H. Nguyen, C.-W. Huang and J. C. S. Wu, *Catal. Commun.*, Ethanol conversion to selective high-value hydrocarbons over Ni/HZSM-5 zeolite catalyst, 2020, **144**, 106067.

32 H. Xiang, R. Xin, N. Prasongthum, P. Natewong, T. Sooknoi, J. Wang, P. Reubroycharoen and X. Fan, *Resour. Chem. Mater.*, Catalytic conversion of bioethanol to value-added chemicals and fuels: A review, 2022, **1**, 47–68.

33 J. Sun and Y. Wang, *ACS Catal.*, Recent Advances in Catalytic Conversion of Ethanol to Chemicals, 2014, **4**, 1078–1090.

34 J. M. Church and H. K. Joshi, *Ind. Eng. Chem.*, Acetaldehyde by Dehydrogenation of Ethyl Alcohol, 1951, **43**, 1804–1811.

35 M. Eckert, G. Fleischmann, R. Jira, H. M. Bolt and K. Golka, in *Ullmann's Encyclopedia of Industrial Chemistry*, 2006.

36 C. M. Moore, O. Staples, R. W. Jenkins, T. J. Brooks, T. A. Semelsberger and A. D. Sutton, *Green Chem.*, Acetaldehyde as an ethanol derived bio-building block: an alternative to Guerbet chemistry, 2017, **19**, 169–174.

37 J. C. Gebers, A. F. Bin Abu Kasim, G. J. Fulham, K. Y. Kwong and E. J. Marek, *ACS Eng. Au*, Production of Acetaldehyde via Oxidative Dehydrogenation of Ethanol in a Chemical Looping Setup, 2023, **3**, 184–194.

38 G. Pampararo, G. Garbarino, P. Riani, V. Vykoukal, G. Busca and D. P. Debecker, *Chem. Eng. J.*, Ethanol dehydrogenation to acetaldehyde with mesoporous Cu-SiO2 catalysts prepared by aerosol-assisted sol–gel, 2023, **465**, 142715.

39 T. L. Cottrell, *The Strengths of Chemical Bonds*, Butterworths, London, 2nd ed., 1958.

40 S. Taco-Vasquez, M. Salinas, H. Murillo and W. Oñate, *IOP Conf. Ser. Earth Environ. Sci.*, Ethanol to high-octane hydrocarbons using HZSM-5 as catalyst, 2022, **1094**, 12005.

41 A. Galadima and O. Muraza, *J. Ind. Eng. Chem.*, Zeolite catalysts in upgrading of bioethanol to fuels range hydrocarbons: A review, 2015, **31**, 1–14.

42 E. G. Derouane, J. B. Nagy, P. Dejaifve, J. H. C. van Hooff, B. P. Spekman, J. C. Védrine and C. Naccache, *J. Catal.*, Elucidation of the mechanism of conversion of methanol and ethanol to hydrocarbons on a new type of synthetic zeolite, 1978, **53**, 40–55.

43 M. Inaba, K. Murata, M. Saito and I. Takahara, *React. Kinet. Catal. Lett.*, Ethanol conversion to aromatic hydrocarbons over several zeolite catalysts , 2006, **88**, 135–141.

44 F. F. Madeira, N. S. Gnep, P. Magnoux, S. Maury and N. Cadran, *Appl. Catal. A Gen.*, Ethanol transformation over HFAU, HBEA and HMFI zeolites presenting similar Brønsted acidity, 2009, **367**, 39–46.

45 I. M. S. Anekwe, B. Oboirien and Y. M. Isa, *Biofuels, Bioprod. Biorefining*, Catalytic conversion of bioethanol over cobalt and nickel-doped HZSM-5 zeolite catalysts, , DOI:https://doi.org/10.1002/bbb.2536.

46 D. Dittmann, E. Kaya and M. Dyballa, *ChemCatChem*, Desilicated ZSM-5 Catalysts: Properties and Ethanol to Aromatics (ETA) Performance, 2023, **15**, e202300716.

47 E. Catizzone, G. Ferrarelli, P. Bruno, G. Giordano and M. Migliori, *Catal. Today*, Simultaneous catalytic dehydration of methanol and ethanol: How ZSM-5 acidity addresses conversion and products distribution, 2024, **427**, 114436.

48 T. Ikeda, T. Kodaira, F. Izumi, T. Kamiyama and K. Ohshima, *Chem. Phys. Lett.*, Neutron powder diffraction study of potassium clusters in zeolite K-LTA, 2000, **318**, 93–101.

49 T. Nakano, S. Araki, N. Hoang Nam, T. Umemoto, K. Tsuchihashi, Y. Kubo, A. Owaki and Y. Nozue, *Soft Condens. Matter*, Origin of magnetic moments and ferromagnetic properties of potassium clusters in zeolite A, 2020, arXiv:2009.04828.

50 J. Michalik, T. Wasowicz, J. Sadlo, E. J. Reijerse and L. Kevan, *Radiat. Phys. Chem.*, Pulsed EPR for studying silver clusters, 1996, **47**, 75–81.

51 L. Liu, M. Lopez-Haro, C. W. Lopes, C. Li, P. Concepcion, L. Simonelli, J. J. Calvino and A. Corma, *Nat. Mater.*, Regioselective generation and reactivity control of subnanometric platinum clusters in zeolites for high-temperature catalysis, 2019, **18**, 866–873.

52 F. Yagi, N. Kanuka, H. Tsuji, S. Nakata, H. Kita and H. Hattori, *Microporous Mater.*, 133Cs and 23Na MAS NMR studies of zeolite X containing cesium, 1997, **9**, 229–235.

53 E. J. Doskocil and R. J. Davis, *J. Catal.*, Spectroscopic Characterization and Catalytic Activity of Zeolite X Containing Occluded Alkali Species, 1999, **188**, 353–364.

54 R. J. Davis, *J. Catal.*, New perspectives on basic zeolites as catalysts and catalyst supports, 2003, **216**, 396–405.

55 M. Seifert, M. S. Marschall, T. Gille, C. Jonscher, O. Busse, S. Paasch, E. Brunner, W. Reschetilowski and J. J. Weigand, *ChemCatChem*, Ethanol to Aromatics on Modified H-ZSM-5 Part I: Interdependent Dealumination Actions, 2020, **12**, 6301–6310.

56 Z. Wang, L. A. O'Dell, X. Zeng, C. Liu, S. Zhao, W. Zhang, M. Gaborieau, Y. Jiang and J. Huang, *Angew. Chemie Int. Ed.*, Insight into Three-Coordinate Aluminum Species on Ethanol-to-Olefin Conversion over ZSM-5 Zeolites, 2019, **58**, 18061–18068.

57 R. Le Van Mao, T. M. Nguyen and J. Yao, *Appl. Catal.*, Conversion of ethanol in aqueous solution over ZSM-5 zeolites: Influence of Reaction Parameters and Catalyst Acidic Properties as Studied by Ammonia TPD Technique, 1990, **61**, 161–173.

58 C. P. Nash, A. Ramanathan, D. A. Ruddy, M. Behl, E. Gjersing, M. Griffin, H. Zhu, B. Subramaniam, J. A. Schaidle and J. E. Hensley, *Appl. Catal. A Gen.*, Mixed alcohol dehydration over Brønsted and Lewis acidic catalysts, 2016, **510**, 110–124.

59 M. F. Hsieh, Y. W. Zhou, H. Thirumalai, L. C. Grabow and J. D. Rimer, *ChemCatChem*, Silver-Promoted Dehydroaromatization of Ethylene over ZSM-5 Catalysts, 2017, **9**, 1675–1682.

60 I. R. Mazzei, University of Durham, 2022.

61 W. Yan, S. Xi, Y. Du, M. K. Schreyer, S. X. Tan, Y. Liu and A. Borgna, *ChemCatChem*, Heteroatomic Zn-MWW Zeolite Developed for Catalytic Dehydrogenation Reactions: A Combined Experimental and DFT Study, 2018, **10**, 3078–3085.

62 L. Qi, M. Babucci, Y. Zhang, A. Lund, L. Liu, J. Li, Y. Chen, A. S. Hoffman, S. R. Bare, Y. Han, B. C. Gates and A. T. Bell, *J. Am. Chem. Soc.*, Propane Dehydrogenation Catalyzed by Isolated Pt Atoms in ≡SiOZn–OH Nests in Dealuminated Zeolite Beta, 2021, **143**, 21364–21378.

63 S. J. Raynes, University of Durham, 2021.

64 J. Zhang, E. C. Wegener, N. R. Samad, J. W. Harris, K. A. Unocic, L. F. Allard, S. Purdy, S. Adhikari, M. J. Cordon, J. T. Miller, T. R. Krause, S. Cheng, D. Liu, M. Li, X. Jiang, Z. Wu and Z. Li, *ACS Catal.*, Isolated Metal Sites in Cu–Zn–Y/Beta for Direct and Selective Butene-Rich C3+ Olefin Formation from Ethanol, 2021, **11**, 9885–9897.

65 A. Nagy, G. Mestl, T. Rühle, G. Weinberg and R. Schlögl, *J. Catal.*, The Dynamic Restructuring of Electrolytic Silver during the Formaldehyde Synthesis Reaction, 1998, **179**, 548–559.

66 P. H. Keijzer, P. E. de Jongh and K. P. de Jong, *ChemCatChem*, Utilization of Silver Silicate for the Formation of Highly Dispersed Silver on Silica Catalysts, 2022, **14**, e202101702.

67 S. J. Raynes and R. A. Taylor, *Sustain. Energy Fuels*, Zinc oxide-modified mordenite as an effective catalyst for the dehydrogenation of (bio)ethanol to acetaldehyde, 2021, **5**, 2136–2148.

68 X. Wei, J. Cheng, Y. Li, K. Cheng, F. Sun, Q. Zhang and Y. Wang, *Nano Res.*, Bimetallic clusters confined inside silicalite-1 for stable propane dehydrogenation, 2023, **16**, 10881–10889.

69 Y. Shan, H. Hu, X. Fan and Z. Zhao, *Phys. Chem. Chem. Phys.*, Recent progress in catalytic dehydrogenation of propane over Pt-based catalysts, 2023, **25**, 18609–18622.

70 N. Kaylor and R. J. Davis, *J. Catal.*, Propane dehydrogenation over supported Pt-Sn nanoparticles, 2018, **367**, 181–193.

71 X. Gao, W. Xu, X. Li, J. Cen, Y. Xu, L. Lin and S. Yao, *Chem. Eng. J.*, Non-oxidative dehydrogenation of propane to propene over Pt-Sn/Al_2O_3 catalysts: Identification of the nature of active site, 2022, **443**, 136393.

72 C. Li and G. Wang, *Chem. Soc. Rev.*, Dehydrogenation of light alkanes to mono-olefins, 2021, **50**, 4359–4381.

73 L. Qi, Y. Zhang, M. A. Conrad, C. K. Russell, J. Miller and A. T. Bell, *J. Am. Chem. Soc.*, Ethanol Conversion to Butadiene over Isolated Zinc and Yttrium Sites Grafted onto Dealuminated Beta Zeolite, 2020, **142**, 14674–14687.

74 K. Gao, J. Mielby and S. Kegnæs, *Catal. Today*, Catalytic dehydrogenation of ethanol over zinc-containing zeolites, 2022, **405**–**406**, 144–151.

75 G. Garbarino, G. Pampararo, T. K. Phung, P. Riani and G. Busca, *Energies*, 2020, 13.

76 Ø. Mikkelsen and S. Kolboe, *Microporous Mesoporous Mater.*, The conversion of methanol to hydrocarbons over zeolite H-beta, 1999, **29**, 173–184.

77 G. A. Olah, *Angew. Chemie Int. Ed.*, Beyond Oil and Gas: The Methanol Economy, 2005, **44**, 2636–2639.

78 Y. Zhao, S. Fan, Q. Ma, J. Zhang and T. Zhao, *J. Fuel Chem. Technol.*, Methanol converting to propylene on weakly acidic and hierarchical porous MFI zeolite, 2022, **50**, 210–217.

79 I. Kaskow, A. Wojtaszek-Gurdak and I. Sobczak, *Catal. Today*, Methanol oxidation on AuAg-Zn/MCM-36 – The effect of catalyst components and pretreatment, 2020, **354**, 123–132.

80 W.-C. Lin, S. Wu, G. Li, P.-L. Ho, Y. Ye, P. Zhao, S. Day, C. Tang, W. Chen, A. Zheng, B. T. W. Lo and S. C. Edman Tsang, *Chem. Sci.*, Cooperative catalytically active sites for methanol activation by single metal ion-doped H-ZSM-5, 2021, **12**, 210–219.

81 G. J. Millar and M. Collins, *Ind. Eng. Chem. Res.*, Industrial Production of Formaldehyde Using Polycrystalline Silver Catalyst, 2017, **56**, 9247–9265.

82 A. W. Franz, H. Kronemayer, D. Pfeiffer, R. D. Pilz, G. Reuss, W. Disteldorf, A. O. Gamer and A. Hilt, in *Ullmann's Encyclopedia of Industrial Chemistry*, 2016, pp. 1–34.

83 P. Cheung, A. Bhan, G. J. Sunley and E. Iglesia, *Angew. Chemie Int. Ed.*, Selective Carbonylation of Dimethyl Ether to Methyl Acetate Catalyzed by Acidic Zeolites, 2006, **45**, 1617–1620.

84 D. Masih, S. Rohani, J. N. Kondo and T. Tatsumi, *Appl. Catal. B Environ.*, Low-temperature methanol dehydration to dimethyl ether over various small-pore zeolites, 2017, **217**, 247–255.

85 J. M. Tatibouët, *Appl. Catal. A Gen.*, Methanol oxidation as a catalytic surface probe, 1997, **148**, 213–252.

86 S. I. Abasov, F. A. Babayeva, B. B. Guliyev, N. N. Piriyev and M. I. Rustamov, *Theor. Exp. Chem.*, Features of Methanol and Dimethyl Ether Conversion to Hydrocarbons on Modified Zeolites Y and ZSM-5, 2013, **49**, 58–64.

87 A. A. Gabrienko, S. S. Arzumanov, I. B. Moroz, I. P. Prosvirin, A. V Toktarev, W. Wang and A. G. Stepanov, *J. Phys. Chem. C*, Methane Activation on In-Modified ZSM-5: The State of Indium in the Zeolite and Pathways of Methane

Transformation to Surface Species, 2014, **118**, 8034–8043.

88 T. Sowade, C. Schmidt, F.-W. Schütze, H. Berndt and W. Grünert, *J. Catal.*, Relations between structure and catalytic activity of Ce-In-ZSM-5 catalysts for the selective reduction of NO by methane: I. The In-ZSM-5 system, 2003, **214**, 100–112.

89 D. Sen, J. J. Kim, H.-C. Kang, N. H. Heo and K. Seff, *Microporous Mesoporous Mater.*, Using InCl vapor to ion exchange indium into zeolite Na–X. II: A single crystal structure containing $(In_8Cl_8)^{16+}$, In_5^{7+}–Cl−In_5^{7+}, and In^+, 2013, **165**, 265–273.

90 C. Schmidt, T. Sowade, E. Löffler, A. Birkner and W. Grünert, *J. Phys. Chem. B*, Preparation and Structure of In−ZSM-5 Catalysts for the Selective Reduction of NO by Hydrocarbons, 2002, **106**, 4085–4097.

91 H.-K. Min, M. B. Park and S. B. Hong, *J. Catal.*, Methanol-to-olefin conversion over H-MCM-22 and H-ITQ-2 zeolites, 2010, **271**, 186–194.

92 T. Liang, J. Chen, S. Wang, P. Wang, Z. Qin, F. Jin, M. Dong, J. Wang and W. Fan, *Catal. Sci. Technol.*, Conversion of methanol to hydrocarbons over H-MCM-22 zeolite: deactivation behaviours related to acid density and distribution, 2022, **12**, 6268–6284.

93 T. Baba and H. Sawada, *Phys. Chem. Chem. Phys.*, Conversion of methane into higher hydrocarbons in the presence of ethylene over H-ZSM-5 loaded with silver cations, 2002, **4**, 3919–3923.

94 Y. Liu, D. Li, T. Wang, Y. Liu, T. Xu and Y. Zhang, *ACS Catal.*, Efficient Conversion of Methane to Aromatics by Coupling Methylation Reaction, 2016, **6**, 5366–5370.

95 S. Liu, K. Bian, H. Yang, M. Sun, X. Nie, X. Zhang, S. Hou, G. Zhang, C. Song and X. Guo, *Chem. Eng. Sci.*, Methane transformation into light olefins using methanol as co-reactant over Mo/HZSM-5, 2024, **283**, 119431.

96 B. Zhou, Z. Xi, Y. Yu, B. Jiang, J. Wang, Z. Liao, Z. Huang and Y. Yang, *J. Zhejiang Univ. A*, Modification of acidity in HZSM-5 zeolite for methane-methanol co-reaction, 2021, **22**, 106–115.

97 Z. Xi, B. Zhou, Y. Yu, B. Jiang, Z. Liao, J. Wang, Z. Huang, Y. Yang, J. Sun and Y. Yang, *Catal. Sci. Technol.*, Enhancing low-temperature methane conversion on Zn/ZSM-5 in the presence of methanol by regulating the methanol-to-aromatics reaction pathway, 2020, **10**, 6161–6172.

98 Y. Kuroda, T. Mori, H. Sugiyama, Y. Uozumi, K. Ikeda, A. Itadani and M. Nagao, *J. Colloid Interface Sci.*, On the possibility of AgZSM-5 zeolite being a partial oxidation catalyst for methane, 2009, **333**, 294–299.

99 S. Zhai, S. Xing, Y. Suo, M. Sun, L. Chen, J. Ren, S. Liang and Z.-Y. Yuan, *Fuel*, Boosting propane dehydrogenation performance over the highly dispersed Co(□) sites on ultra-high silica ZSM-5 zeolite, 2024, **366**, 131429.

100 Y. Yuan and R. F. Lobo, *ACS Catal.*, Zinc Speciation and Propane Dehydrogenation in Zn/H-ZSM-5 Catalysts, 2023, **13**, 4971–4984.

101 T. F. Degnan, G. K. Chitnis and P. H. Schipper, *Microporous Mesoporous Mater.*, History of ZSM-5 fluid catalytic cracking additive development at Mobil, 2000, **35**–**36**, 245–252.

102 T. Baba, *Catal. Surv. from Asia*, Conversion of methane over Ag^+-exchanged zeolite in the presence of ethene, 2005, **9**, 147–154.

Chapter Eight – Pretty Vacant: Silver Auto Reduction, Surface Clustering and Framework Oxidation

Silver auto reduction leads to the evolution of dioxygen due to framework oxidation, generating vacancies in the framework.[1–3] The silver auto reduction process is facilitated by applying reduced pressure or raised temperature to silver-exchanged zeolites and ultimately leads to crystallinity loss through framework damage. Following on from the characterisation of freshly prepared materials, characterisation was conducted on dehydrated and spent materials, in which we paid particular attention to both framework crystallinity and silver cluster formation.

The effects of dehydration on silver-exchanged zeolites and zincosilicates was observed following dehydration under reduced pressure, nitrogen flow or argon flow at raised temperatures. Additionally, we observed the effects of hydrocarbon upgrading, including hydrocarbon co-processing with oxygen included in the stream in an attempt to offset the reducing hydrogen conditions generated during upgrading reactions. The inclusion of oxygen in the gas feed was investigated following reports that the oxidative conditions used in partial-oxidation reactions not only prevented but facilitated the repair of frameworks following undesirable framework damage that arises following framework oxidation.[4–6]

8.1 The Effects of Dehydration on Silver-exchanged Zeolites and Zincosilicates

A range of dehydration experiments were undertaken to determine the effects of raised temperatures and reduced pressure or gas flow on silver exchanged zeolites and zincosilicates. Where appropriate, parent materials, as well as materials exchanged with other metals, have been included for comparison. Dehydration was conducted at temperatures of 200 °C, 400 °C and 600 °C. Nitrogen and argon gases were passed through a celite column to ensure dryness and removing any potential for steaming to occur at the raised temperatures from the presence of moisture. Reduced pressure conditions were all below $5x10^{-2}$ mbar at the peak temperature. Three components were monitored in the analysis of the dehydrated materials, observing for colour change, silver cluster formation and loss of crystallinity by pXRD.[7]

Dehydration was performed in a quartz u-tube, loaded with 300 mg of the specified material between two quartz wool plugs. The material was pressed and sieved to 40-60 mesh. Material was pressed to aid in recovery and allow gas flow without pressure build-up. The quartz u-tube was loaded to a muffle furnace, with one tap connected to a Schlenk line, the other to a gas bubbler (if using flow) or capped if using reduced pressure. Changes were made to the generic dehydration experimental method, reported in Section 3.2.3, heating to 150 °C for 1 hour, before the specified temperature for 12 hours, using a heating ramp rate of 5 °C/min.

Initial dehydrations were carried out using two silver-exchanged ZSM-5 frameworks, with lower and higher silver loading levels to investigate the effect of silver loading. ZSM-5 is a framework commonly used in industry, with pioneering reports for Ag/ZSM-5 for methane conversion.[8,9] Dehydrations conducted at 400 °C were in line with temperatures used previously to demonstrate auto reduction in silver-exchanged zeolites.[2] Table 8.1 displays the key used throughout this Chapter for all results tables.

Table 8.4: Key for all dehydration experiment results tables included in Chapter 8.

No change observed	
Small change observed	
Large change observed	

Select examples have been included for dehydrated Ag(0.35)/NH_4-ZSM-5(43.5) and Ag(0.87)/NH_4-ZSM-5(43.5) in Figure 8.1, with examples of the colour change observed and their designated classification.

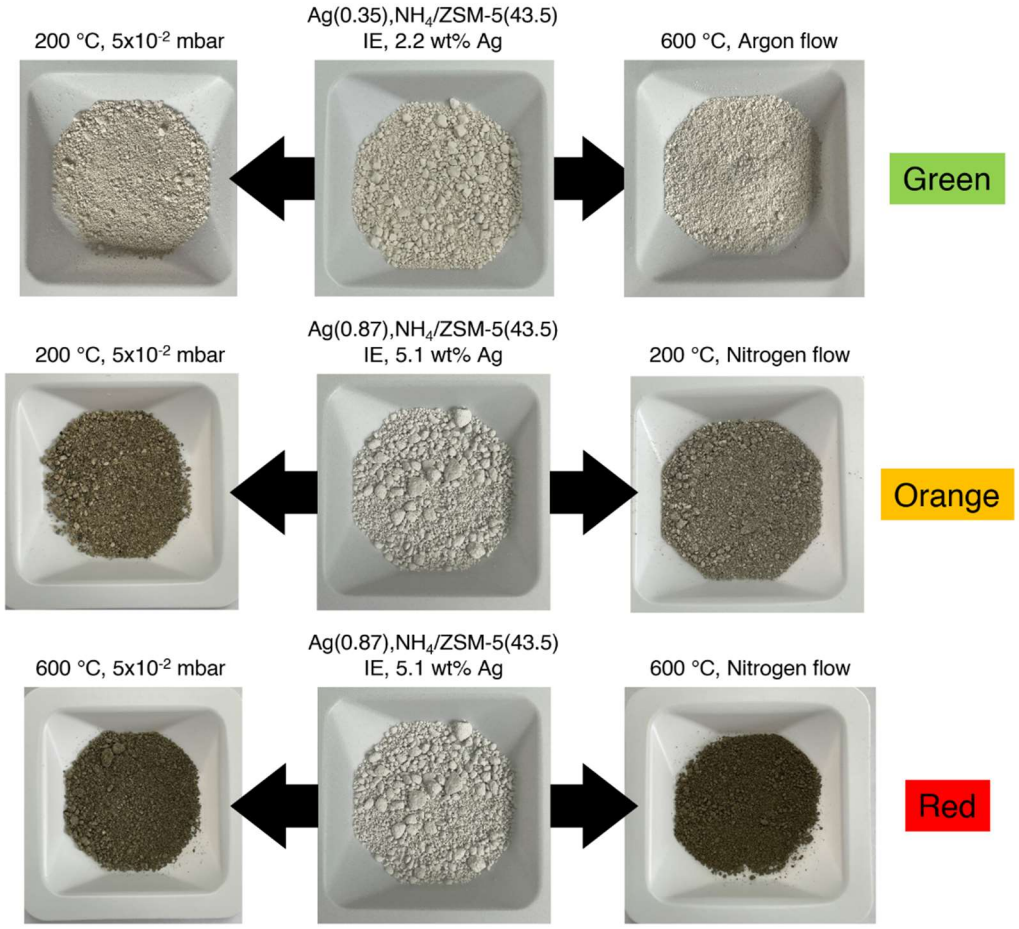

Figure 8.1: Picture showing the observed colour changes for Ag(0.35)/NH_4-ZSM-5(43.5) and Ag(0.87)/NH_4-ZSM-5(43.5) following dehydration under various conditions, with the associated colour designated to the resultant materials.

Results of the initial dehydration experiments of silver-exchanged ZSM-5, to identify differences between two materials with relatively low or high silver loading, are shown in Table 8.2.

Table 8.2: Observations for the initial dehydration experiments under reduced pressure and gas flow for silver-exchanged ZSM-5(43.5) with low and high silver loading levels.

Framework	Dehydration Conditions	Observations by pXRD		
		Colour Change	Ag cluster formation	Loss of Crystallinity
Ag(0.35)/NH_4-ZSM-5(43.5) IE, 2.2 wt% Ag	Vacuum 600 °C			
	Vacuum 400 °C			
	Vacuum 200 °C			
	Nitrogen 600 °C			
	Nitrogen 400 °C			
	Nitrogen 200 °C			
	Argon 600 °C			
	Argon 400 °C			
	Argon 200 °C			
Ag(0.87)/NH_4-ZSM-5(43.5) IE, 5.1 wt% Ag	Vacuum 600 °C			
	Vacuum 400 °C			
	Vacuum 200 °C			
	Nitrogen 600 °C			
	Nitrogen 400 °C			
	Nitrogen 200 °C			
	Argon 600 °C			
	Argon 400 °C			
	Argon 200 °C			

From the initial experiments, Ag(0.35)/NH_4-ZSM-5(43.5) displayed minimal colour change following dehydration under reduced pressure at 400 °C and 600 °C and under nitrogen flow at 600 °C. Images have been included in Table 8.3.

Table 8.3: Images acquired for Ag(0.35)/NH_4-ZSM-5(43.5) as prepared and following a series of dehydration experiments, conducted under the stated atmospheric conditions for 12 hours.

Ag(0.35)/NH_4-ZSM-5(43.5) IE, 2.2 wt% Ag		
Vacuum 200 °C	Vacuum 400 °C	Vacuum 600 °C
Nitrogen 200 °C	Nitrogen 400 °C	Nitrogen 600 °C
Argon 200 °C	Argon 400 °C	Argon 600 °C

Ag(0.87)/NH_4-ZSM-5(43.5) displayed more distinct colour change following dehydration under all conditions. Images have been included in Table 8.4.

Table 8.4: Images acquired for Ag(0.87)/NH_4-ZSM-5(43.5) as prepared and following a series of dehydration experiments, conducted under the stated atmospheric conditions for 12 hours.

Ag(0.87)/NH_4-ZSM-5(43.5) IE, 5.1 wt% Ag		
Vacuum 200 °C	Vacuum 400 °C	Vacuum 600 °C
	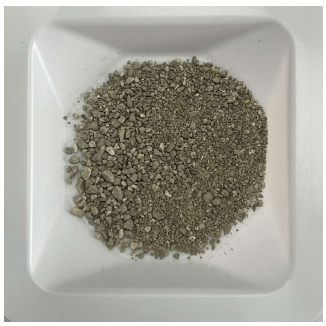	
Nitrogen 200 °C	Nitrogen 400 °C	Nitrogen 600 °C
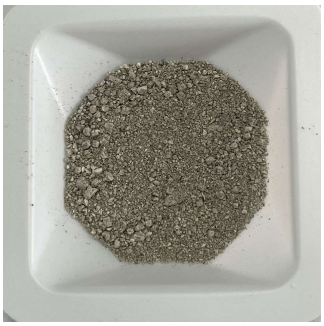		
Argon 200 °C	Argon 400 °C	Argon 600 °C

pXRD patterns for Ag(0.87)/NH_4-ZSM-5(43.5) are shown in Figure 8.2. Silver cluster formation (presence of a peak at 38.1° (2θ) corresponding to Ag [111])[7] was observed at 600 °C under reduced pressure, at all temperatures under nitrogen flow and at 400 °C and 600 °C under argon flow. No loss of crystallinity was observed for any of the materials post dehydration.

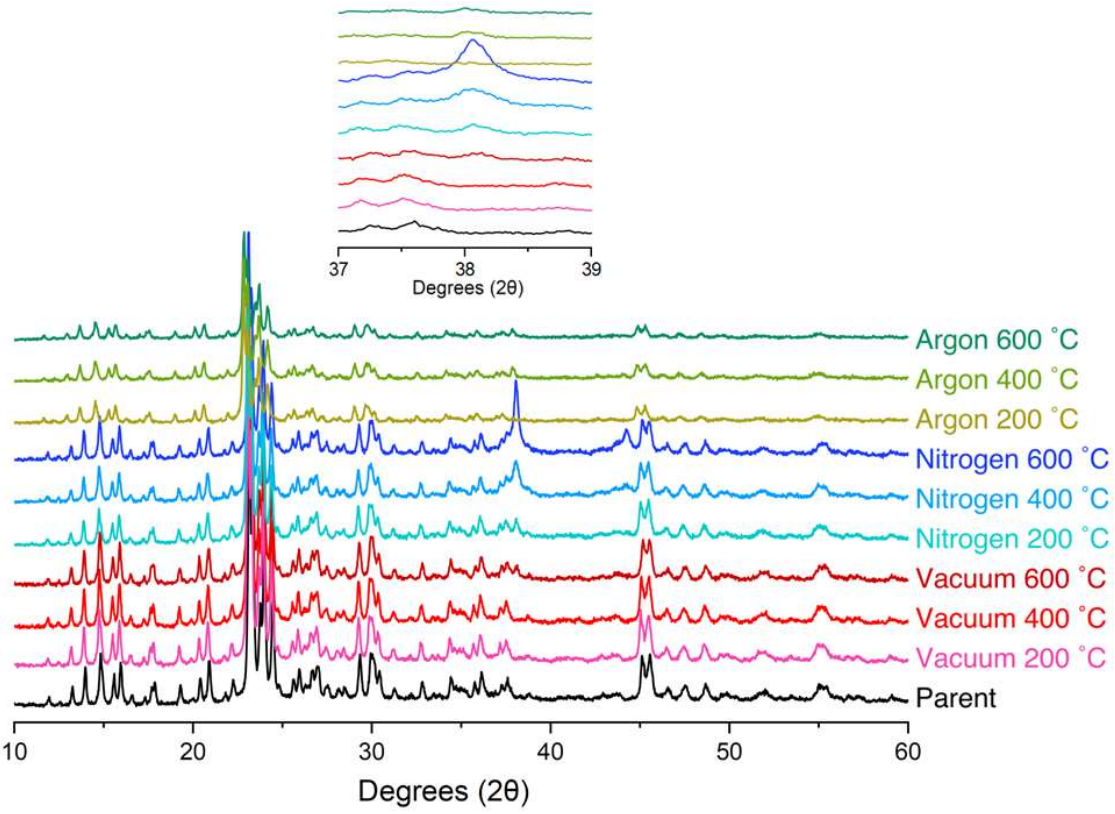

Figure 8.2: Stacked pXRD patterns for Ag(0.87)/NH_4-ZSM-5(43.5) following dehydration under various conditions and temperatures, highlighting no change to the framework crystallinity or silver crystal growth during dehydration. Patterns are offset for clarity.

In contrast with the lower silver loading material, pXRD patterns for Ag(0.35)/NH_4-ZSM-5(43.5), shown in Figure 8.3, displayed good conformity with the parent material. Silver clusters were only observed under reduced pressure at 600 °C. No crystallinity loss was observed across all conditions tested.

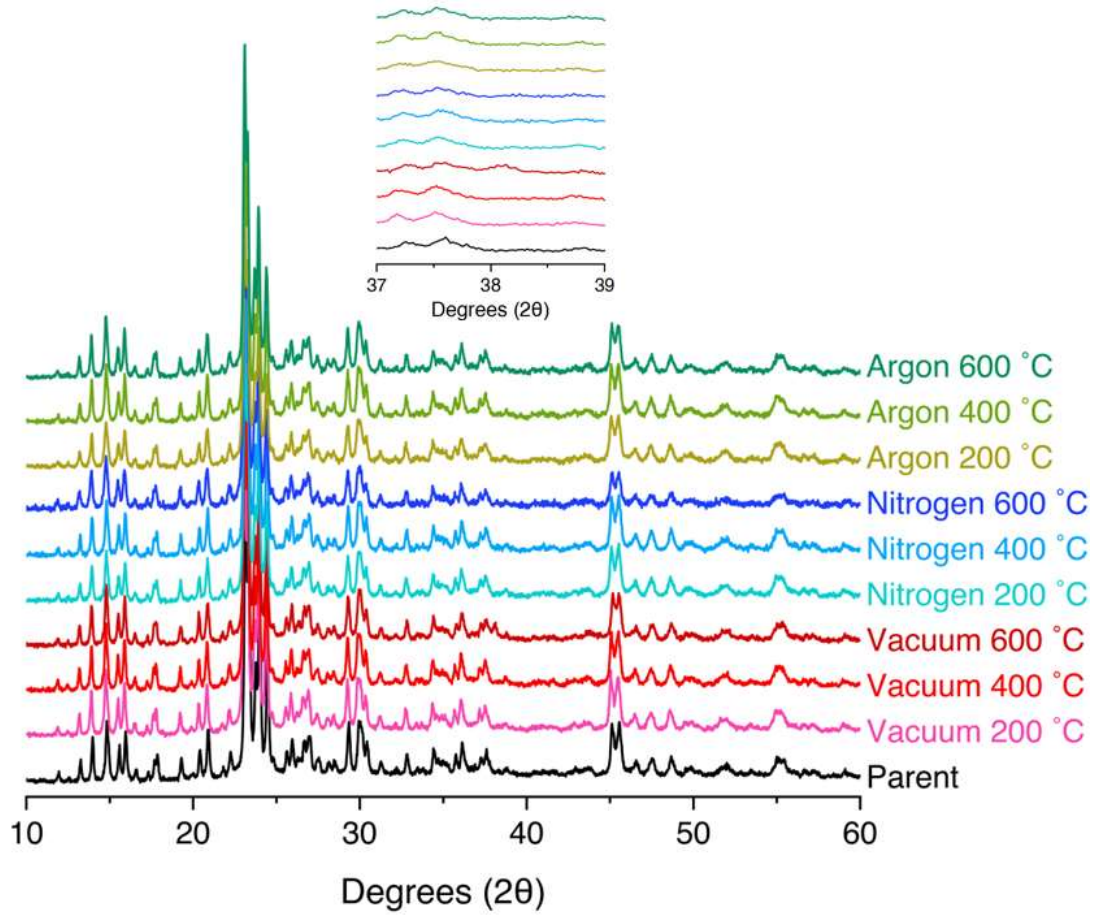

Figure 8.3: Stacked pXRD patterns for Ag(0.35)/NH_4-ZSM-5(43.5) following dehydration under various conditions and temperatures, highlighting no change to the framework crystallinity or silver crystal growth during dehydration. Patterns are offset for clarity.

Silver cluster size could be calculated for the materials post dehydration through the use of the Scherrer equation. This was applied to the acquired pXRD pattern using the peak at 38.1° (2θ), corresponding with the Ag [111] cluster.[7] Results shown in Table 8.5 indicated that the largest silver clusters were observed for Ag(0.87)/NH_4-ZSM-5(43.5) when dehydrating at higher temperatures, with dehydration under flowing nitrogen at 600 °C generating the largest clusters. Dehydrating under argon flow generated small clusters than under nitrogen flow. Dehydration at 600 °C under reduced pressure were the only conditions that led to the observation of silver clusters by pXRD for Ag(0.35)/NH_4-ZSM-5(43.5).

Table 8.5: Characterisation of silver-exchanged ZSM-5 materials with changed silver loading level with silver cluster peaks observed in the pXRD patterns following dehydration under various conditions.

Catalyst	Conditions	Ag NPs present by pXRD	Ag NP size (nm)
			Calculated Scherrer
Ag(0.35)/NH_4-ZSM-5(43.5) IE, 2.2 wt% Ag	Vacuum 600 °C	✓	11.9
Ag(0.87)/NH_4-ZSM-5(43.5) IE, 5.1 wt% Ag	Vacuum 600 °C	✓	13.9
Ag(0.87)/NH_4-ZSM-5(43.5) IE, 5.1 wt% Ag	Nitrogen 600 °C	✓	19.9
Ag(0.87)/NH_4-ZSM-5(43.5) IE, 5.1 wt% Ag	Nitrogen 400 °C	✓	13.6
Ag(0.87)/NH_4-ZSM-5(43.5) IE, 5.1 wt% Ag	Nitrogen 200 °C	✓	12.2
Ag(0.87)/NH_4-ZSM-5(43.5) IE, 5.1 wt% Ag	Argon 600 °C	✓	13.7
Ag(0.87)/NH_4-ZSM-5(43.5) IE, 5.1 wt% Ag	Argon 400 °C	✓	13.0

Ag NP sizes were calculated from the associated pXRD pattern using the Scherrer equation.

Initial observations indicate that no loss of framework crystallinity had occurred for the materials under the conditions tested. This was not in line with the expectations following reports in literature, with Beyer reporting silver auto reduction to generate framework vacancies for both Ag(0.71),Na(0.29)/Y(2.5) and Ag(0.85),Na(0.15)/MOR(5.3).[1,10,11] We postulated that along with the silver exchange level, the silicon-to-aluminium ratio of frameworks could be a factor in the stability of the framework. Further experiments were conducted, targeting the more aggressive conditions for dehydration over a wider range of silver-exchanged frameworks, with the results and observations shown in Table 8.6.

Table 8.6: Observations for dehydration experiments conducted using reduced pressure or inert gas flow at 600 °C over a range of silver-exchanged frameworks with varied silver loading levels.

Framework	Dehydration Conditions	Observations by pXRD		
		Colour Change	Cluster formation	Loss of Crystallinity
Ag(0.87)/NH_4-ZSM-5(43.5) IE, 5.1 wt% Ag	Vacuum 600 °C			
	Nitrogen 600 °C			
	Argon 600 °C			
Ag(0.79),K(0.52)/ZSM-5(13.5) IE, Ag 8.0 wt%	Vacuum 600 °C			
	Nitrogen 600 °C			
	Argon 600 °C			
Ag(1.30),K(0.57)/ZnMFI(96) IE, Ag 3.4 wt%	Vacuum 600 °C			
Ag(0.16),Na/MOR(6.5) IE, Ag 3.8 wt%	Vacuum 600 °C			
Ag(0.38),Na/MOR(6.5) IE, Ag 8.4 wt%	Vacuum 600 °C			
Ag(1.04)/MOR(6.5) IE, Ag 19.3 wt%	Vacuum 600 °C			
Ag(0.58),H/TON(30) IE, Ag 1.1 wt%	Vacuum 600 °C			
	Nitrogen 600 °C			
Ag(0.45),NH_4/FER(10) IE, Ag 7.0 wt%	Vacuum 600 °C			
Ag(1.38),K(0.47)/FER(10) IE, Ag 12.9 wt%	Vacuum 600 °C			
Ag(1.07)/CHA(18) IE Ag 3.0 wt%	Vacuum 600 °C			
Ag(0.51),K(0.57)/ZnCHA(12) IE Ag 5.8 wt%	Vacuum 600 °C			

For comparison, several parent frameworks of the materials included in Table 8.6, as well as indium-exchanged materials for comparison against their silver counterparts, underwent dehydration under reduced pressure at 600 °C. This allowed us to isolate the effect of including silver within the micropores. The results are shown in Table 8.7.

Table 8.7: Observations for dehydration experiments conducted using reduced pressure at 600 °C over several parent frameworks to the materials in Table 8.5, with indium-exchanged CHA and ZnCHA to compare the behaviour of silver and indium under reduced pressure.

Framework	Dehydration Conditions	Observations by pXRD		
		Colour Change	Cluster formation	Loss of Crystallinity
K(1.34),H/ZSM-5(13.5) IE	Vacuum 600 °C		N/A	
Na/MOR(6.5)	Vacuum 600 °C		N/A	
H,K(0.21)/CHA(21)	Vacuum 600 °C		N/A	
In(0.08),K(0.77)/CHA(18) IE In 0.8 wt%	Vacuum 600 °C			
H,K(0.61)/ZnCHA(12)	Vacuum 600 °C		N/A	
In(0.22),H/ZnCHA(12) IE In 2.7 wt%	Vacuum 600 °C			

Colour changes were observed, with silver-exchanged materials all displaying distinct colour changes post dehydration. Examples for chabazite based materials are shown in Table 8.8 and mordenite based materials in Table 8.9.

Table 8.8: Images acquired for chabazite materials post dehydration under reduced pressure at 600 °C, where all materials were off-white powders in their original state.

Vacuum dehydration at 600 °C		
H,K(0.61)/ZnCHA(12)	Ag(0.51),K(0.57)/ZnCHA(12) IE Ag 5.8 wt%	In(0.17),H/ZnCHA(12) IE In 2.7 wt%
H,K(0.21)/CHA(18)	Ag(1.07)/CHA(18) IE Ag 3.0 wt%	In(0.08),K(0.77)/CHA(18) IE In 0.8 wt%

Table 8.9: Images acquired for silver exchanged MOR materials with different silver loading levels post dehydration under reduced pressure at 600 °C. All materials were off-white powders in their original state.

Vacuum dehydration at 600 °C		
Ag(0.16),Na/MOR(6.5) IE, Ag 3.8 wt%	Ag(0.38),Na/MOR(6.5) IE, Ag 8.4 wt%	Ag(1.04)/MOR(6.5) IE, Ag 19.3 wt%

Ag(0.79),K(0.52)/ZSM-5(13.5) was dehydrated alongside its potassium parent, conducted to confirm that the changes observed following dehydration were due to the presence of silver in the micropores. Comparing the observations for Ag/ZSM-5(13.5) and Ag/ZSM-5(43.5) with similar exchange levels, a strong colour change was observed following dehydration, however, no loss of crystallinity was observed showing no obvious effect of silicon-to-aluminium ratio for the chosen conditions. Silver-exchanged mordenite at low exchange levels displayed both colour change and silver cluster formation by pXRD, whilst displaying small changes in the crystallinity observable through phase changes in the pXRD pattern, shown in Figure 8.4. Mordenite with full exchange displayed both a profound colour change and silver cluster growth, with a notable change in crystallinity, indicating a reduction in the long-range order of the material. Silver clusters are observed in the respective pXRD patterns of dehydrated silver-exchanged materials at 38.1° and 44.3°(2θ), for Ag [111] and Ag [200] respectively.[7] An example of this is shown in Figure 8.4, where the stacked pXRD patterns for dehydrated Ag/MOR samples display a pronounced peak for silver clusters.

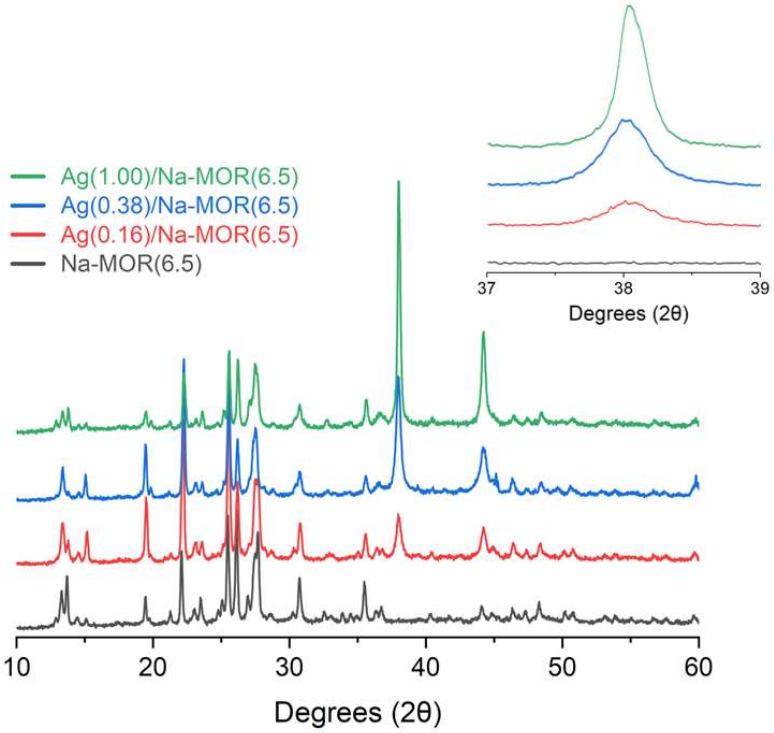

Figure 8.4: Stacked pXRD patterns for silver-exchanged mordenite of varying silver loading levels and their sodium-form parent, following dehydration under reduced pressure at 600 °C. Patterns are offset for clarity.

Silver cluster size could be calculated for the spent silver exchanged mordenite catalysts with varied silver loading through the use of the Scherrer equation. This was applied to the acquired pXRD pattern using the peak at 38.1 ° (2θ), corresponding with the Ag [111] cluster. Results shown in Table 8.10 indicated that a larger average silver cluster size was observed for the spent catalysts with higher silver loading.

Table 8.10: Characterisation of silver-exchanged mordenite materials with varying silver loading levels before and after ethanol upgrading at 350 °C.

Catalyst	Reaction	Ag NPs present by pXRD	Ag NP size (nm)	
			Measured STEM-BF	Calculated Scherrer
Ag(0.16)/Na-MOR(6.5) IE, 3.8 wt% Ag	Ethanol 350 °C	✓	Not Collected	16.0
Ag(0.38)/Na-MOR(6.5) IE, 8.4 wt% Ag	Ethanol 350 °C	✓	Not Collected	17.8
Ag(1.04)-MOR(6.5) IE, 19.3 wt% Ag	Parent Material	X	8.0	N/A
	Ethanol 350 °C	✓	18.4	21.7

Ag NP sizes were calculated from the associated pXRD pattern using the Scherrer equation.

Silver-exchanged chabazite Ag(1.07)/CHA(18) was dehydrated under reduced pressure at 600 °C, alongside its protic parent form. As shown in Figure 8.5, no changes were observed by pXRD, although the dehydrated silver-exchanged material was recovered as a black solid.

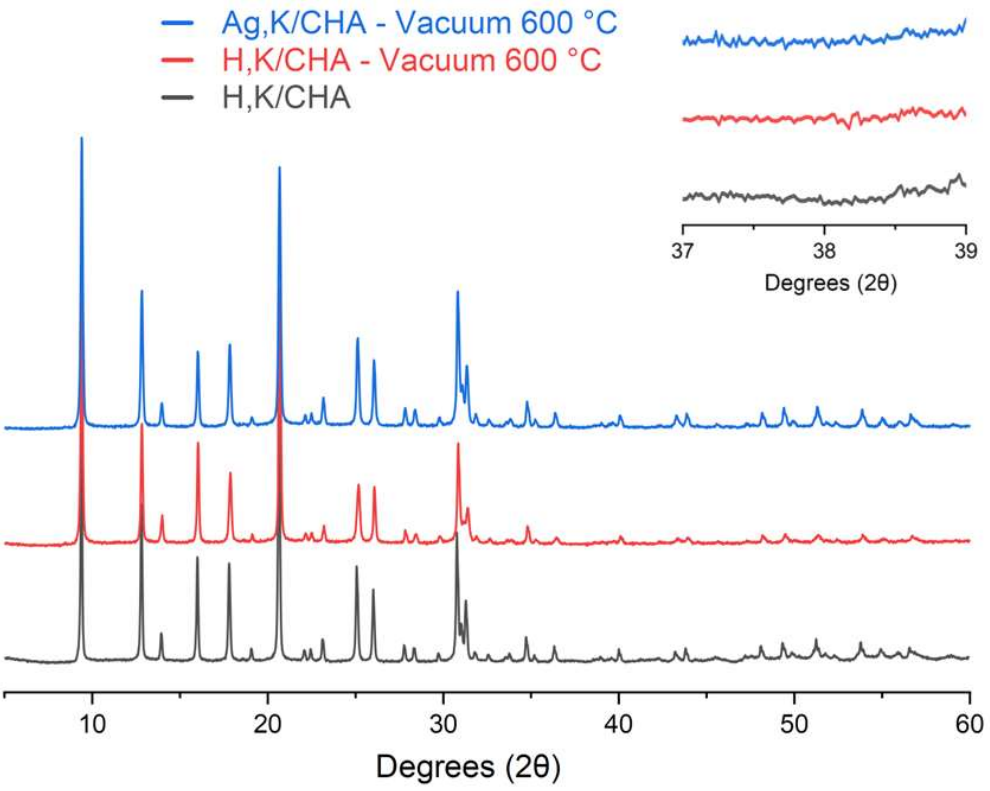

Figure 8.5: Stacked pXRD patterns for Ag(1.07)/CHA(18) (blue) and the protic-form parent H,K(0.23)/CHA(18) (red) following dehydration under reduced pressure at 600 °C, compared against the pattern of the parent H,K(0.23)/CHA(18) (black). Patterns are offset for clarity.

Ferrierite and TON are two frameworks where the smallest ring size are 5MR, whereas the smallest ring size for all other frameworks tested are 4MR. As discussed in Section 2.2.4, we postulated that auto reduction could be more facile for frameworks containing 4MR based on reports that 4MR can be selectively dealuminated over 5MR in MOR.[12] Dehydration of FER and TON was carried out to determine whether auto reduction of silver and the subsequent framework oxidation was more facile in 4MR frameworks than in 5MR frameworks. Dehydration of ferrierite with low silver exchange level displayed only a colour change, whilst over-exchanged material had a marked colour change with silver cluster growth. Silver-exchanged TON, Ag(0.58),H/TON(30), only displayed a change in colour after dehydration, with no silver cluster formation or crystallinity loss by pXRD under both reduced pressure and flowing nitrogen, as shown in Figure 8.6.

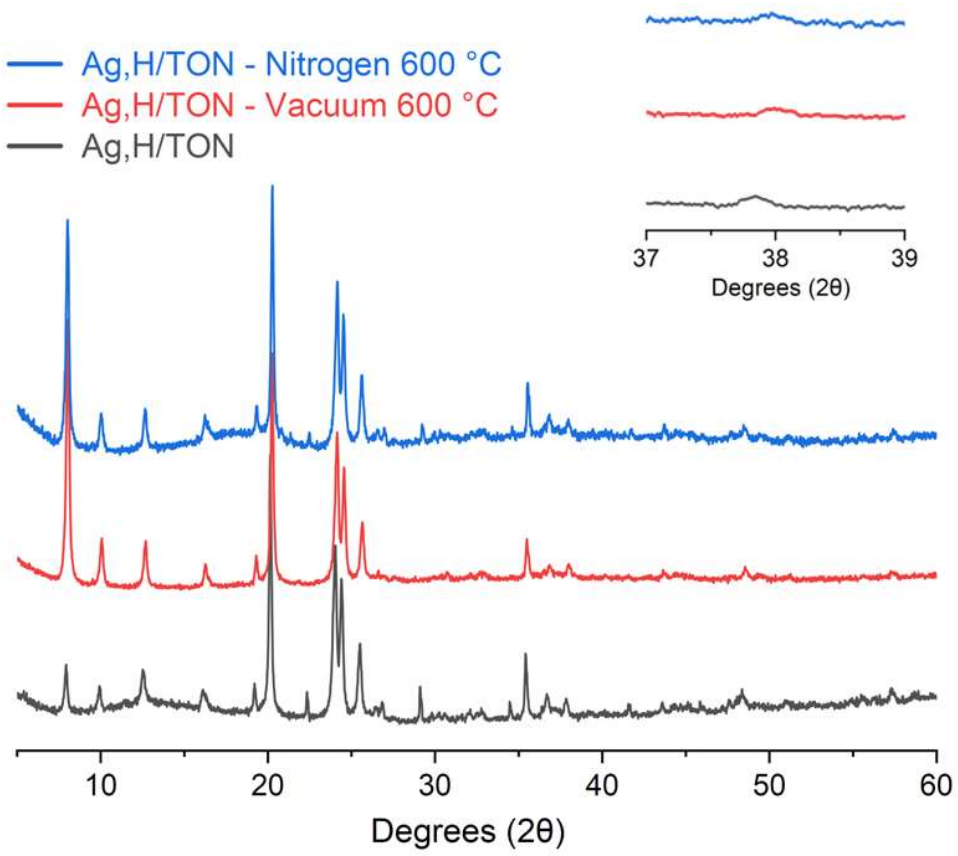

Figure 8.6: Stacked pXRD patterns for Ag(0.58),H/TON(30) as prepared (black), following dehydration under reduced pressure at 600 °C (red) and under flowing nitrogen at 600 °C (blue). Patterns are offset for clarity.

To draw comparison between the behaviour of silver-exchanged forms of zeolite and zincosilicate MFI and CHA topologies, Ag(1.30),K(0.57)/ZnMFI(96) and Ag(0.79),K(0.52)/ZSM-5(13.5) were dehydrated under reduced pressure at 600 °C. Both materials displayed a marked colour change, with the acquired pXRD patterns containing reflections indicating silver cluster growth. Ag/ZnMFI displayed small changes to its crystallinity by pXRD, shown in Figure 8.7, whilst the ZSM-5 material did not show any change to the crystallinity.

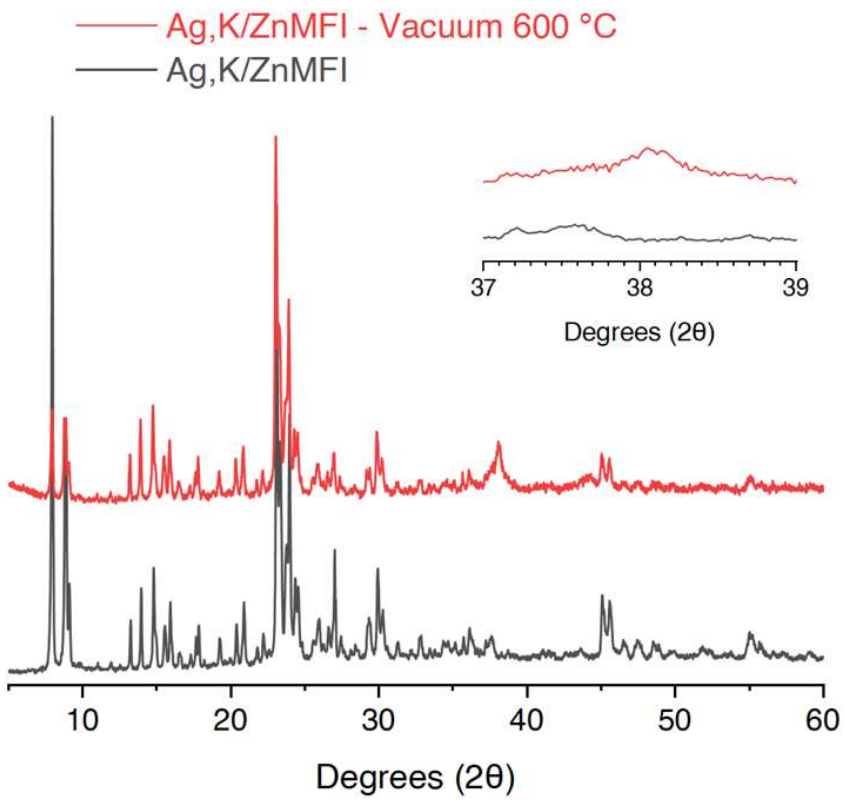

Figure 8.7: Stacked pXRD patterns for Ag(1.30),K(0.57)/ZnMFI(96) as prepared (black) and following dehydration under reduced pressure at 600 °C (red). Patterns are offset for clarity.

Dehydration of Ag(0.53),K(0.14)/ZnCHA(12) under reduced pressure at 600 °C, produced a green coloured powder, shown in Figure 8.8. The pXRD pattern, shown in Figure 8.9, indicated the presence of silver clusters with small peaks at 38.1° and 44.3° (2θ), Ag [111] and Ag [200] respectively.[7] No other differences were observed between the silver-exchanged form and parent protic form. Differences in the pXRD patterns for the dehydrated H,K(0.68)/ZnCHA(12) material (red) and the parent material (black) could have arisen from pressing and sieving the material, with the extra mechanical stress changing the intensity and sharpness of the reflections.

Figure 8.8: Picture showing a sample dish containing Ag(0.53),K(0.14)/ZnCHA(12) dehydrated at 600 °C under reduced pressure.

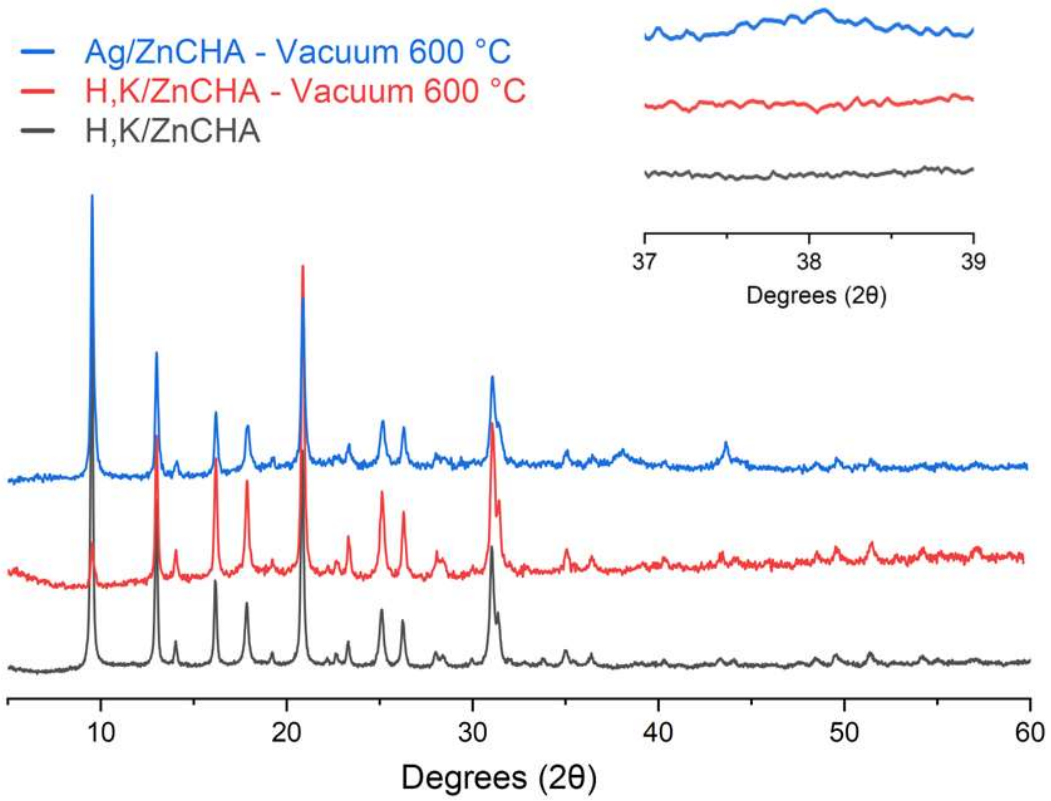

Figure 8.9: Stacked pXRD patterns for H,K(0.68)/ZnCHA(12) as prepared (black) and post dehydration under reduced pressure (red), with Ag(0.53),K(0.14)/ZnCHA(12) following dehydration under reduced pressure (blue). Patterns are offset for clarity.

Silver-exchanged forms of zeolite and zincosilicate CHA underwent a strong colour change following dehydration under reduced pressure at 600 °C. pXRD of Ag(1.07)/CHA(18) indicated no silver clusters or crystallinity loss, whereas the pXRD pattern for Ag(0.53),K(0.14)/ZnCHA(12) indicated silver cluster growth, but no crystallinity loss. STEM-BF images were acquired alongside EDS-TEM maps for Ag(0.53),K(0.14)/ZnCHA(12). The EDS-TEM maps, shown in Figure 8.10, highlighted

silver and potassium co-clustering. Whilst alkali metal clusters,[13] and potassium clusters in FAU and LTA topology zeolites are known,[14–16] there is no prior art showing the co-clustering of silver and potassium. We postulate that potassium atoms and clusters formed in proximity with silver is due to an electronic stabilising effect.[17] Additionally, the over-exchange of materials with silver and/or potassium must arise through the formation of multinuclear ionic clusters in the chabazite cage structure.[18]

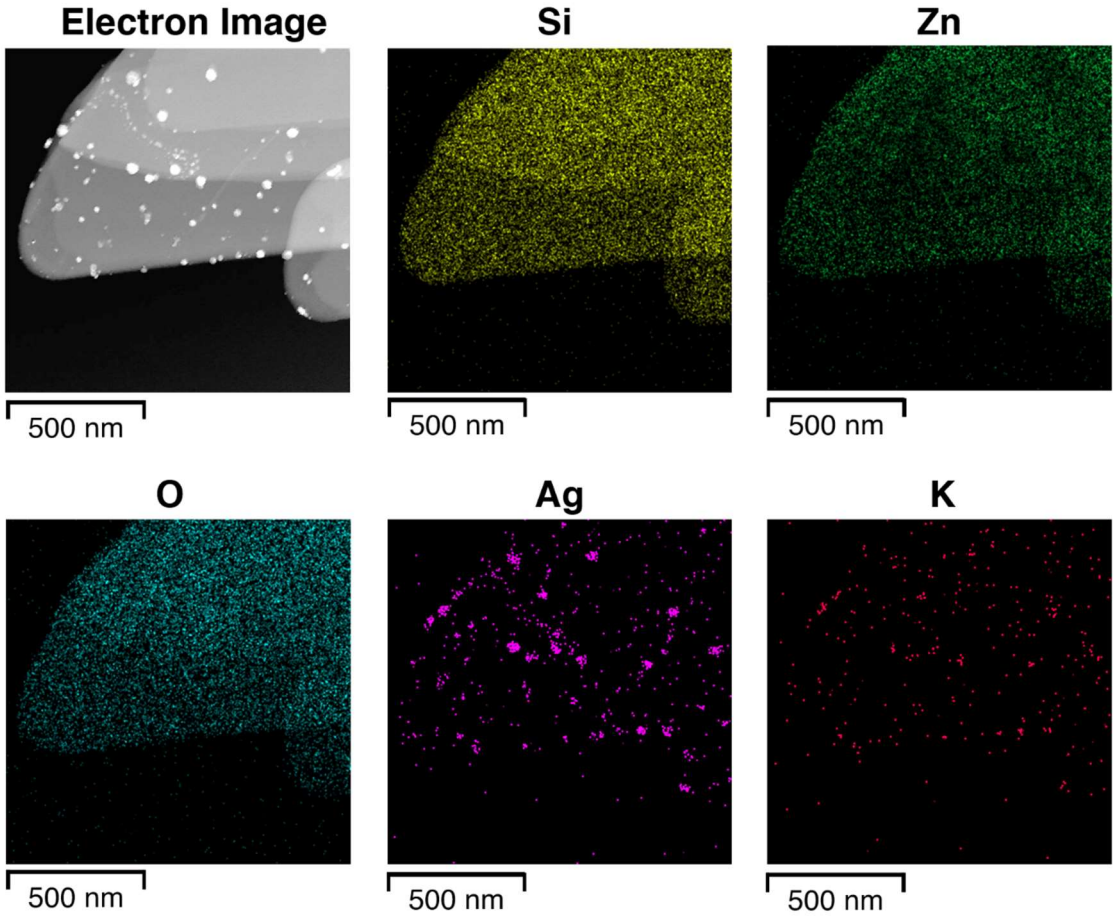

Figure 8.10: EDS-TEM maps acquired for Ag(0.51),K(0.57)/ZnCHA(12) dehydrated under reduced pressure at 600 °C.

8.1.1 Conclusion of Silver Auto Reduction in Silver-exchanged Zeolites and Zincosilicates

Freshly prepared silver-exchanged zeolites and zincosilicates displayed no loss of crystallinity in their acquired pXRD patterns, indicating no structural changes occurred from aqueous ion-exchange.[19] STEM-BF images and EDS-TEM maps indicated silver clusters were present, however, pXRD patterns did not contain reflections for Ag [111] (38.1°) and Ag [200] (44.3°) (2θ). These findings align with prior reports, showing a significant quantity of silver clusters were too small to be observed by pXRD.[20]

Dehydration was conducted for Ag/ZSM-5 materials with relatively low (35%) and high (87%) silver exchange levels. Some recovered materials post dehydration were observed to have undergone a colour change, which was in line with reports,[21,22] although these were permanent and not an indicator of hydration. No changes to crystallinity were observed by pXRD, however, in some materials reflections indicating silver clusters were present.[7] Reported XPS analysis of Ag(0.67)/CHA(6.0) following vacuum treatment at 250 °C confirmed distinct differences between freshly prepared and vacuum treated materials.[23] This suggested a prevalent change in silver species, with changed behaviour between different topologies and frameworks with different Si/Al ratios, implying a sweet spot towards stabilising silver clusters.[23] As a result, dehydration was conducted using the most aggressive conditions of reduced pressure at 600 °C. Under these aggressive conditions, two Ag/ZSM-5 materials of different silicon-to-aluminium ratio (13.5 vs 43.5) but similar silver exchange level (0.79 vs 0.83) were dehydrated, however, we observed little variance between the two materials.

Dehydration of three Ag/MOR materials of varying silver loading levels under reduced pressure at 600 °C led to the observation of colour change, with the acquired pXRD pattern indicating both silver clusters and framework crystallinity loss. No other silver-exchanged zeolite or zincosilicate dehydrated in this study displayed crystallinity loss. This contrasts with prior art, which reported silver-exchanged zeolites readily undergoing crystallinity loss after framework oxidation, facilitated by silver auto reduction.[1–4,6,10,24,25]

Dehydration of Ag(1.07)/CHA(18) and Ag(0.53),K(0.14)/ZnCHA(12) was conducted under reduced pressure at 600 °C. Silver clusters were observed by pXRD for the Ag/ZnCHA material but not for the Ag/CHA material. For both, a colour change was observed and no crystallinity loss. EDS-TEM maps for Ag(0.53),K(0.14)/ZnCHA(12) highlighted silver and potassium co-clustering. There are reports of clusters of alkali metals[13] and potassium in FAU and LTA.[14–16] Although at present, there are no known examples for silver and potassium co-clustering, which has been observed here. We observe silver and potassium co-clustering in freshly prepared materials, which are discussed in Section 5.1.3, in the EDS-TEM maps acquired for both Ag(2.42),K(0.88)/ZSM-5(13.5) and Ag(0.44),K(0.23)/CHA(18). We propose that co-clustering arises through an electronic stabilisation effect.[17]

8.2 Effects of Hydrocarbon Upgrading on Metal-exchanged Zeolites and Zincosilicates

Dehydration of silver-exchanged zeolites and zincosilicates led to a colour change or silver clusters being observed, with only a few cases leading to the loss of crystallinity by pXRD. In this section, we look at spent catalysts that were used for hydrocarbon upgrading reactions, with characterisation to determine changes to the materials with regards to silver clustering and framework crystallinity. Upgrading reactions generate reducing conditions through the evolution of hydrogen, reducing the highly dispersed silver cations present in silver-exchanged materials, generating BAS and forming silver clusters.[1,26] In addition to silver-exchanged materials, materials exchanged with various other metals were investigated for their activity during upgrading reactions. These materials were characterised, with a direct comparison drawn against their silver-exchanged counterparts to determine whether any undesirable effects, such as metal clustering or framework crystallinity loss occurred for these materials.

8.2.1 Spent Catalyst Characterisation Following Hydrocarbon Upgrading Reactions

A variety of characterisation techniques were applied when characterising spent catalysts, including pXRD, DRIFTS and TEM. Silver clusters formed following silver migration could be measured from the acquired STEM-BF images, with cluster size analysis was carried out using ImageJ,[27] with the silver cluster sizes compared between freshly prepared and spent catalysts. DRIFTS was used to determine changes to the framework, observing carbonaceous deposition or the emergence or loss of framework bands.

Several silver-exchanged catalysts were investigated for their activity towards ethanol upgrading and methane/ethanol co-processing at 350 °C. These reactions were carried out using the reaction profile shown in Figure 8.11. Each reaction was carried out for 6.5 hours, prior to the catalysts being isolated and characterized.

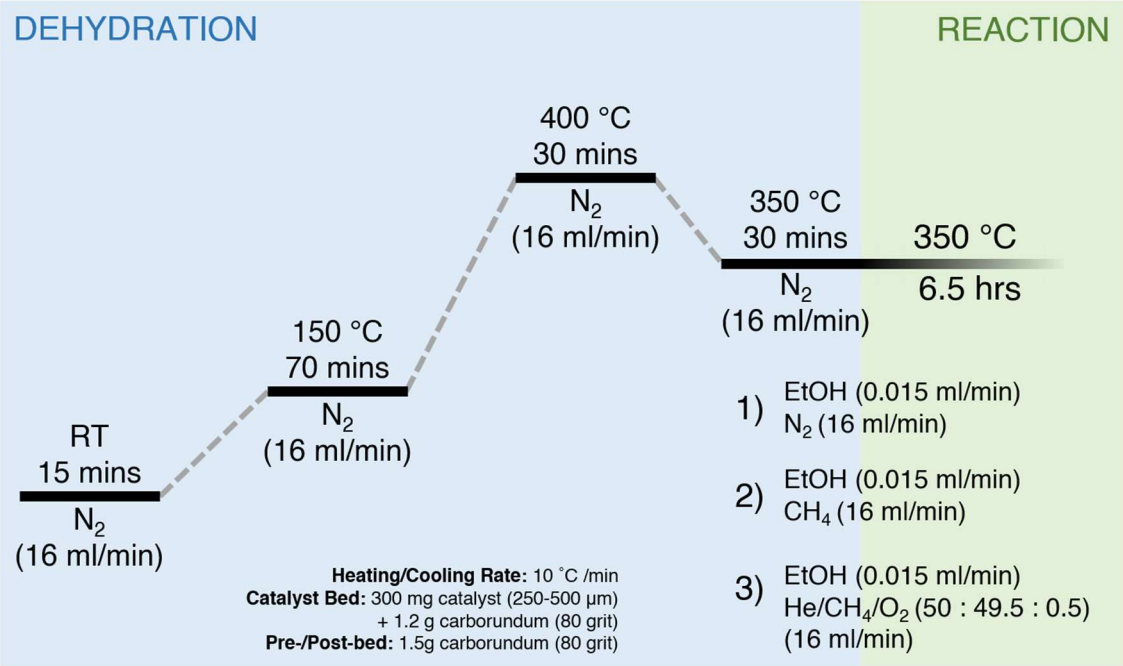

Figure 8.11: Reaction profile for ethanol upgrading (1), methane/ethanol co-processing (2) and methane/ethanol co-processing with oxidative conditions (3) carried out at 350 °C over various silver-exchanged materials.

Song *et al.* reported methane/ethanol co-processing conducted over Ag(0.01),H/ZSM(23) at 300 °C and 400 °C.[28] Whilst ethanol conversion was reportedly identical at both temperatures, selectivity towards ether products was highest at 300 °C, with gas products favoured at 400 °C. Recognising that our silver-exchanged materials had much higher silver loading, a compromise of 350 °C was used, particularly to limit aromatic production as Song reported 33% selectivity towards aromatics at 400 °C for Ag(0.01),H/ZSM-5(23).[28] Additionally, we hoped the reduced temperature would suppress the rate of silver sintering and framework damage, as silver clusters growth was reported for Ag(0.01),Zn(0.05),H/ZSM-5(23) at 400 °C. Spent catalysts following conducting reactions 1 and 2 in Figure 8.11 are discussed here.

ZSM-5 vs ZnMFI - Silver sintering was observed for both Ag(2.42),K(0.88)/ZSM-5(13.5) 14.6 wt% Ag and Ag(1.50),K(1.76)/ZnMFI(96) 3.4 wt% Ag after 6.5 hours on-stream for both ethanol upgrading at 350 °C and methane/ethanol co-processing at 350 °C. This was evident in their respective pXRD patterns, shown in Figure 8.12 and Figure 8.13.

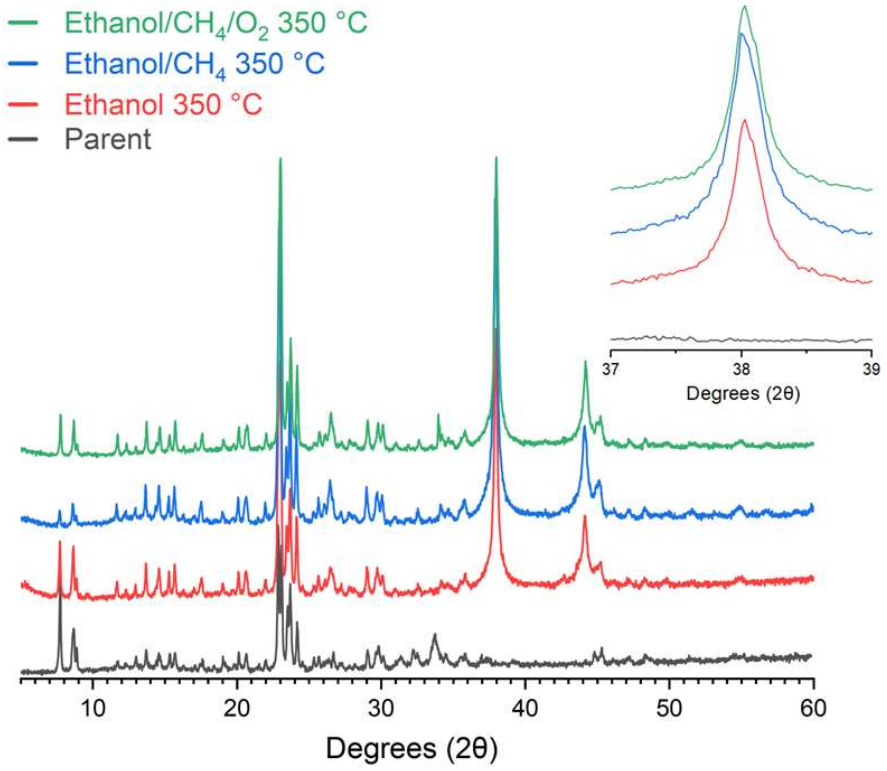

Figure 8.12: pXRD patterns of spent Ag(2.42),K(0.88)/ZSM-5(13.5) following ethanol upgrading, CH_4/EtOH and CH_4/EtOH/O_2 co-processing at 350 °C, with parent material for reference.

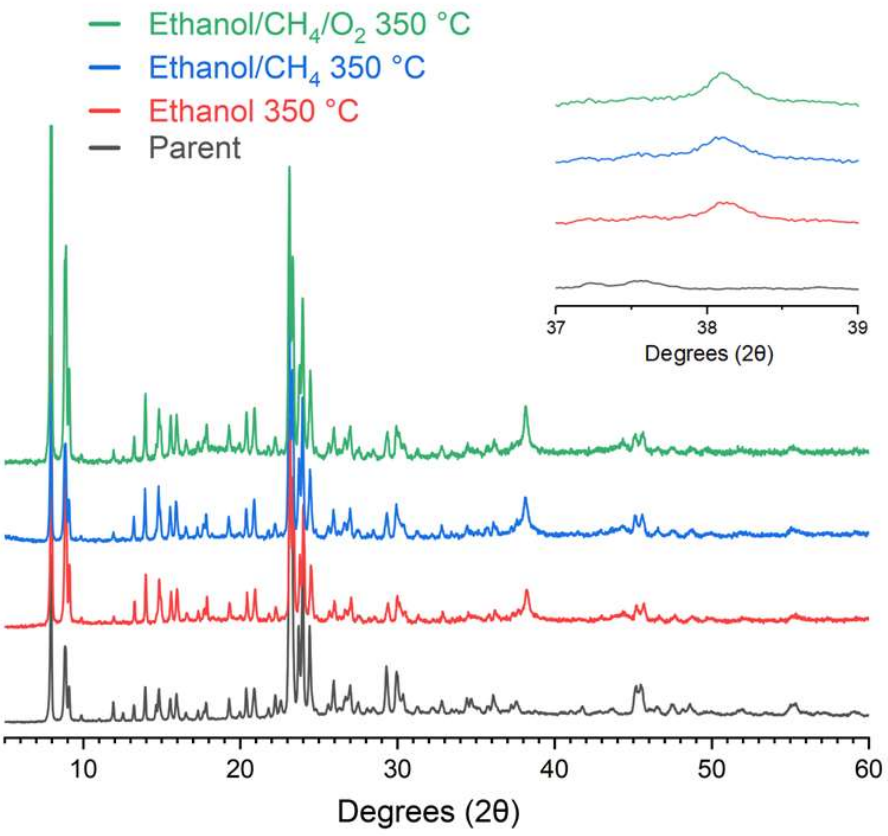

Figure 8.13: pXRD patterns of Ag(1.50),K(1.76)/ZnMFI(96) following ethanol upgrading, CH_4/EtOH and CH_4/EtOH/O_2 co-processing at 350 °C, with parent material for reference.

Colour changes were recorded for the spent catalysts post reaction. In all three reaction conditions, Ag(2.42),K(0.88)/ZSM-5(13.5) was recovered as a black powder, changed from a beige powder, as shown in Table 8.11. Ag(1.50),K(1.76)/ZnMFI(96) was recovered as a brown powder from all three reaction conditions, changed from a white powder, as shown in Table 8.12.

Table 8.11: Images acquired for Ag(2.42),K(0.88)/ZSM-5(13.5) as freshly prepared catalyst and spent following ethanol upgrading, CH_4/EtOH and CH_4/EtOH/O_2 co-processing at 350 °C.

Ag(2.42),K(0.88)/ZSM-5(13.5) IE 14.6 wt% Ag		
Ethanol 350 °C	Methane/Ethanol 350 °C	Methane/Ethanol/O_2 350 °C
	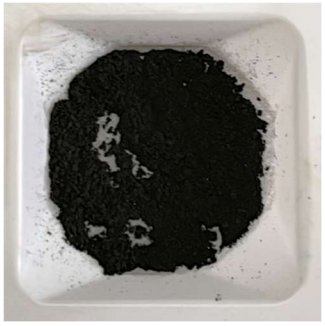	

Table 8.12: Images acquired for Ag(1.50),K(1.76)/ZnMFI(96) as freshly prepared catalyst and spent following ethanol upgrading, CH_4/EtOH and CH_4/EtOH/O_2 co-processing at 350 °C.

Ag(1.50),K(1.76)/ZnMFI(96) IE 3.4 wt% Ag		
Ethanol 350 °C	Methane/Ethanol 350 °C	Methane/Ethanol/O_2 350 °C

STEM-BF images acquired for Ag(2.42),K(0.88)/ZSM-5(13.5) 14.6 wt% Ag following ethanol upgrading at 350 °C for 6.5 hours are included in Figure 8.14. From these images, we calculated that a threefold size increase had occurred with a notable change in the size distribution of silver clusters in the spent material, as shown in Figure 8.15.

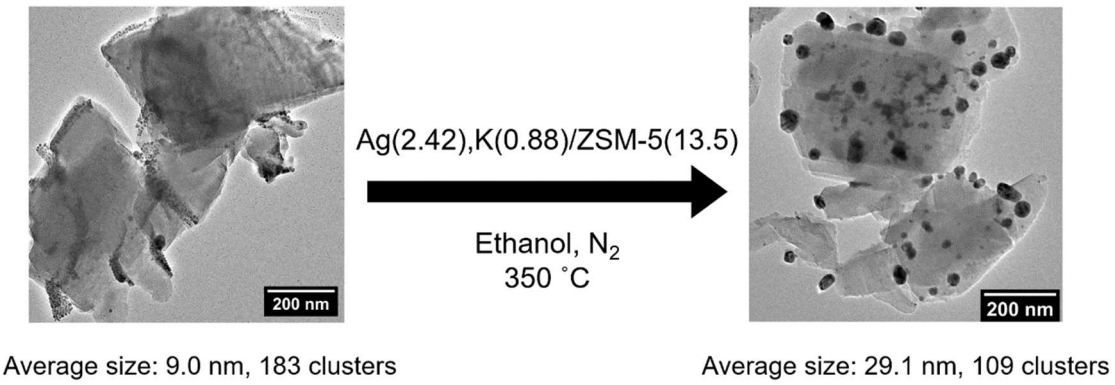

Figure 8.14: STEM-BF images acquired for Ag(2.42),K(0.88)/ZSM-5(13.5) as freshly prepared catalyst and spent catalyst after ethanol upgrading at 350 °C for 6.5 hours, showing the growth of Ag NPs as observed by pXRD.

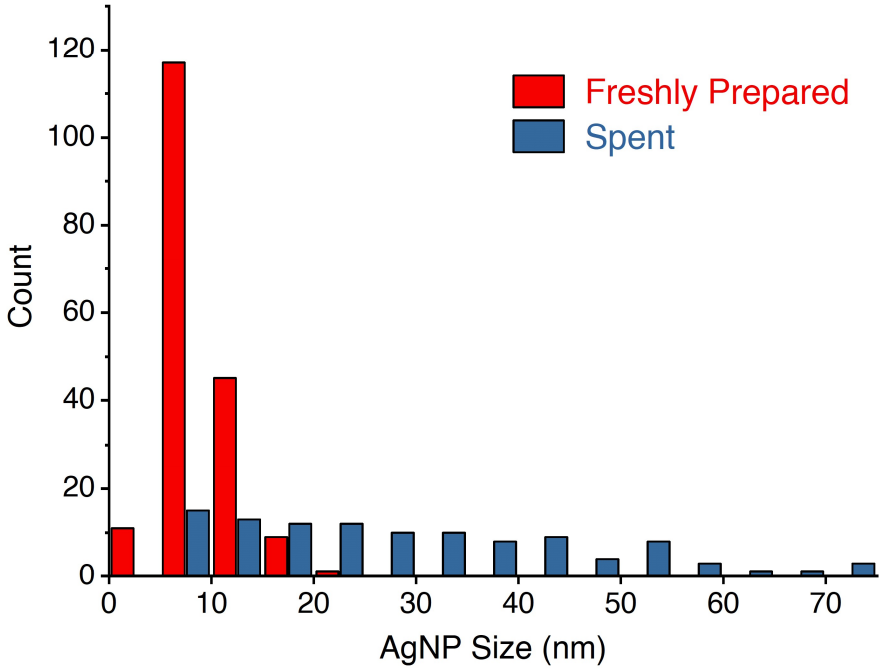

Figure 8.15: Histogram of the silver cluster dimensions measured for Ag(2.42),K(0.88)/ZSM-5(13.5) as freshly prepared material and after ethanol upgrading at 350 °C for 6.5 hours.

Whilst STEM-BF images acquired for Ag(2.42),K(0.88)/ZSM-5(13.5) revealed silver clusters located at the edges of the zeolite crystal for both freshly prepared and spent material. EDS-TEM maps for freshly prepared Ag(2.42),K(0.88)/ZSM-5(13.5), shown in

Figure 8.16, identified that localisation of silver and potassium had occurred following aqueous ion-exchange for the over-exchanged catalyst. Silicon, aluminium and oxygen were observed to have good uniformity throughout the material.

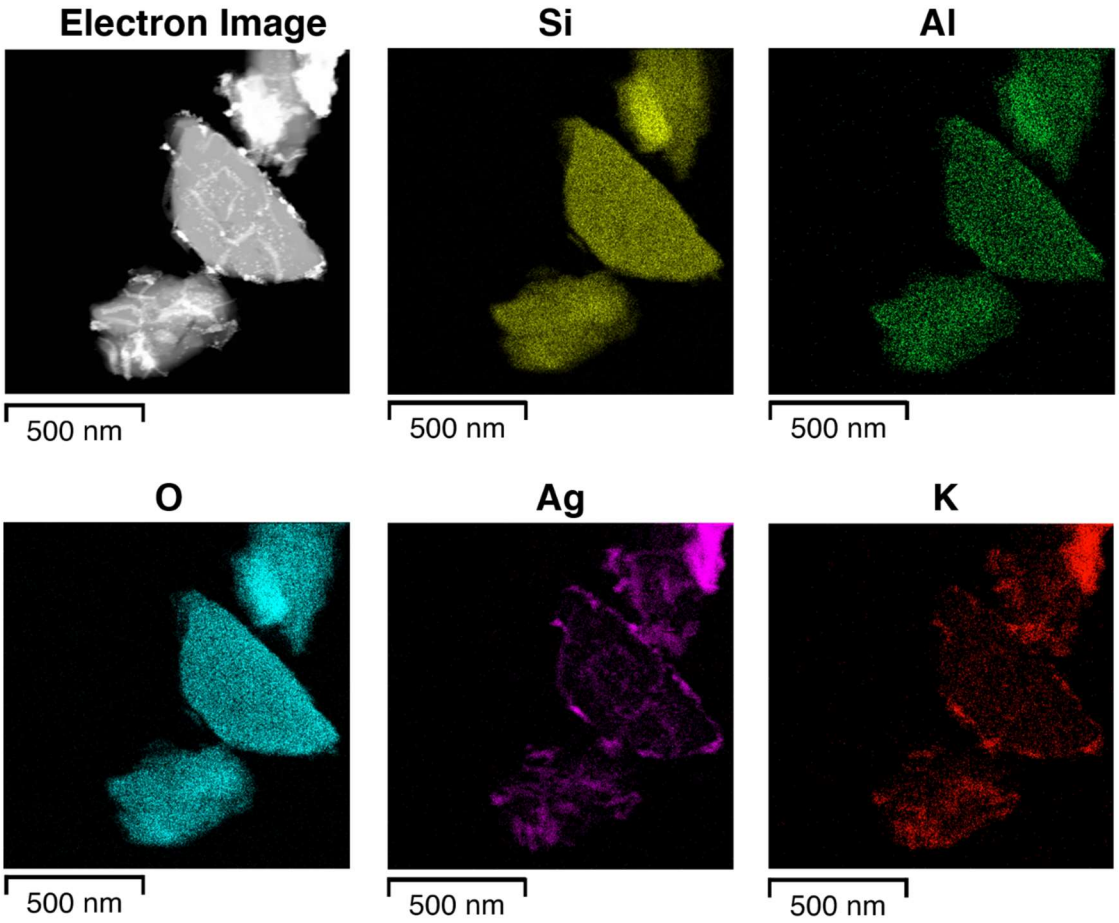

Figure 8.16: EDS-TEM maps acquired for Ag(2.42),K(0.88)/ZSM-5(13.5) as prepared, showing localisation of silver and potassium in the material.

EDS-TEM maps were obtained for Ag(2.42),K(0.88)/ZSM-5(13.5) following ethanol upgrading at 350 °C, shown in Figure 8.17. Localisation was evident for silver and potassium in the as prepared material and the spent material, with silver and potassium co-clustering. A notable change in product selectivity was observed during ethanol upgrading, with increasing selectivity toward ethanol dehydration products, indicating silver deactivation and BAS formation. The corroborates with the silver sintering and cluster growth observed in STEM-BF images. However, silicon, aluminium and oxygen displayed good uniformity throughout the material.

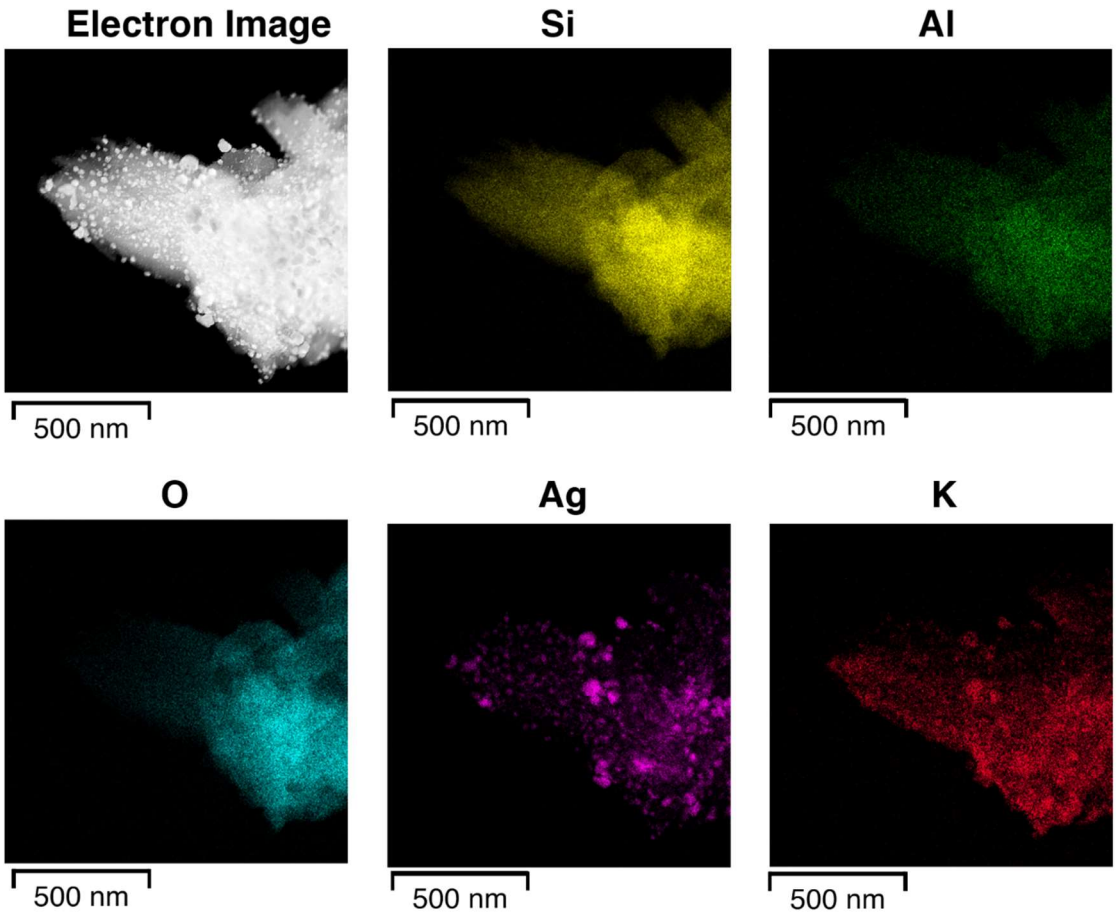

Figure 8.17: EDS-TEM maps acquired for spent Ag(2.42),K(0.88)/ZSM-5(13.5) following ethanol upgrading at 350 °C after 1.5 hours on-stream, showing silver and potassium sintering and co-clustering localised at both a crystal fracture and the crystal edge

STEM-BF images for Ag(1.50),K(1.76)/ZnMFI(96) 3.4 wt% Ag following ethanol upgrading at 350 °C for 6.5 hours are included in Figure 8.18. We calculated a two-fold increase in silver cluster size had occurred with a notable change in the size distribution of silver clusters in the spent material. Additionally, the distribution was also measured following methane/ethanol co-processing at 350 °C for 6.5 hours, with silver clusters measured at 1.6 times larger. Silver cluster size distributions are included in Figure 8.19.

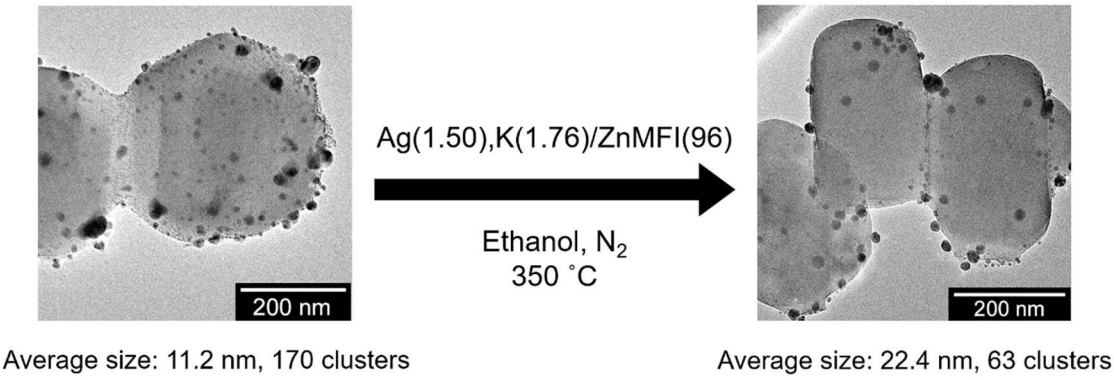

Figure 8.18: STEM-BF images acquired for Ag(1.50),K(1.76)/ZnMFI(96) as freshly prepared catalyst and spent catalyst after ethanol upgrading at 350 °C for 6 hours, showing the growth of Ag NPs as observed by pXRD.

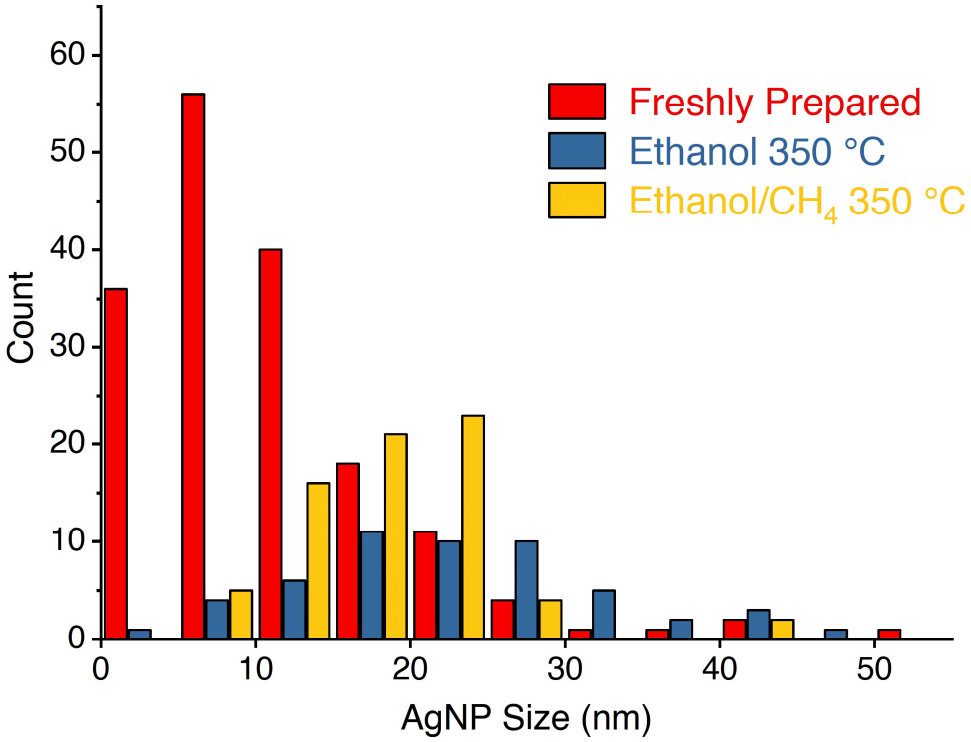

Figure 8.19: Histogram of the silver cluster dimensions measured for Ag(1.50),K(1.76)/ZnMFI(96) as freshly prepared material and after ethanol upgrading at 350 °C for 6.5 hours.

Silver and potassium co-clustering was not observed in the acquired EDS-TEM maps for Ag(1.50),K(1.76)/ZnMFI(96), shown in Figure 8.20.

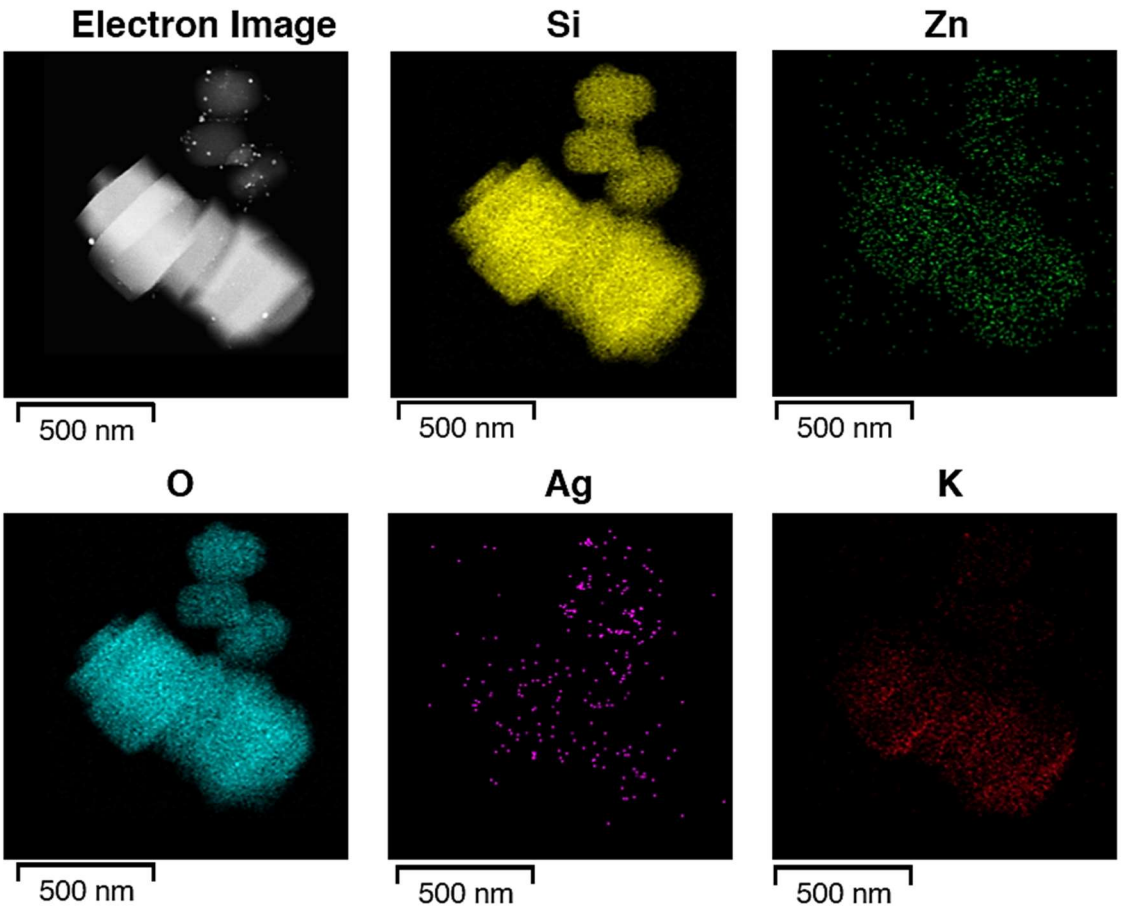

Figure 8.20: EDS-TEM maps acquired for spent Ag(1.50),K(1.76)/ZnMFI(96) following ethanol upgrading at 350 °C after 6.5 hours on-stream, showing silver and potassium sintering and co-clustering localised at both a crystal fracture and the crystal edge

CHA vs ZnCHA – Silver clusters were evident after 6.5 hours of ethanol upgrading or methane/ethanol co-processing at 350 °C over both Ag(0.44),K(0.23)/CHA(17) 3.0 wt% Ag and Ag(0.51),K(0.57)/ZnCHA(12) 5.8 wt% Ag. This was evident in their respective pXRD patterns, shown in Figure 8.21 and Figure 8.22. However, both materials displayed no loss of framework crystallinity by pXRD.

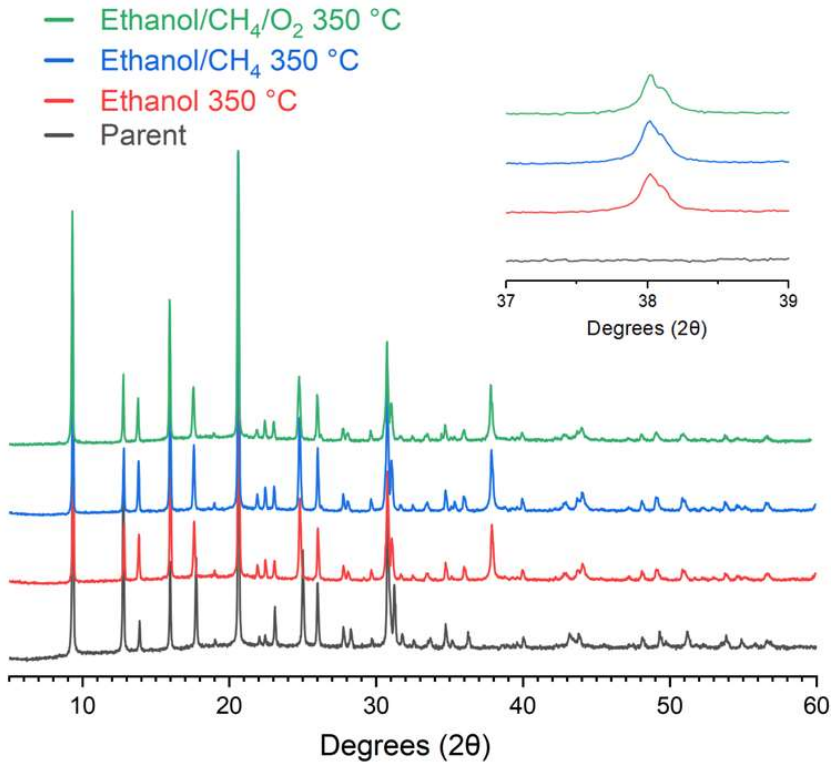

Figure 8.21: pXRD patterns of Ag(0.44),K(0.23)/CHA(17) following ethanol upgrading, CH_4/EtOH and CH_4/EtOH/O_2 co-processing at 350 °C, with parent material for reference.

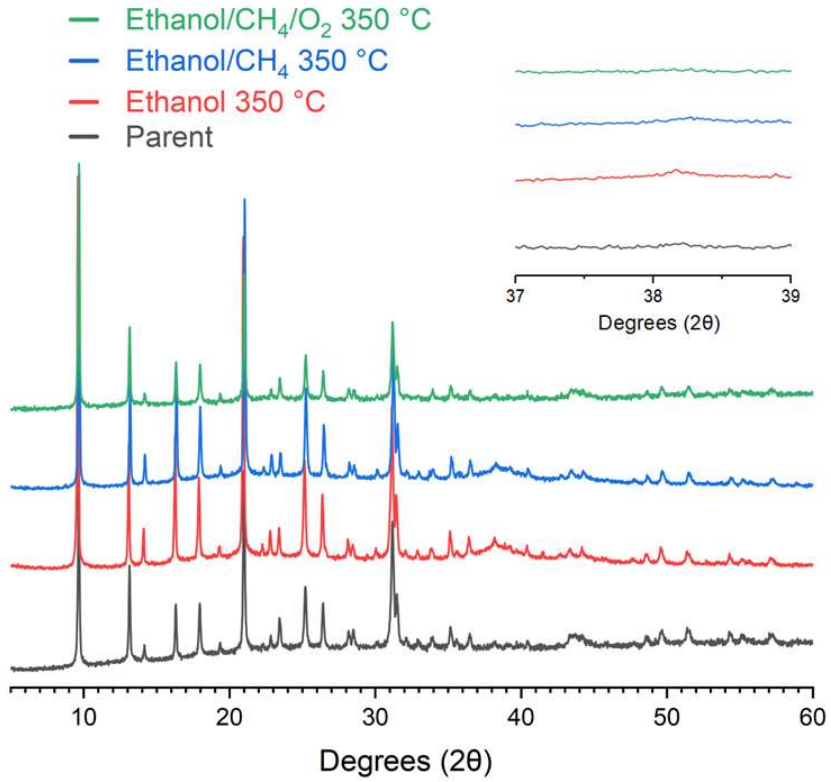

Figure 8.22: pXRD patterns of Ag(0.51),K(0.57)/ZnCHA(12) following ethanol upgrading, CH_4/EtOH and CH_4/EtOH/O_2 co-processing at 350 °C, with parent material for reference.

Colour changes were observed for Ag(0.44),K(0.23)/CHA(17), as shown in Table 8.13. Under all three reaction conditions, the spent material was recovered as a black powder, changed from an off-white powder. This observation was in line with those for spent Ag(2.42),K(0.88)/ZSM-5(13.5), which was a black powder post reaction. Ag(0.51),K(0.57)/ZnCHA(12) was recovered as a brown powder from all three reaction conditions, as shown in Table 8.14, changing from an off-white powder. These findings were in line with those for spent Ag(1.50),K(1.76)/ZnMFI(96), which was a brown powder post reaction.

Table 8.13: Images acquired for Ag(0.44),K(0.23)/CHA(17) as freshly prepared catalyst and spent following ethanol upgrading, CH_4/EtOH and CH_4/EtOH/O_2 co-processing at 350 °C.

Ag(0.44),K(0.23)/CHA(17) IE 3.0 wt% Ag		
Ethanol 350 °C	Methane/Ethanol 350 °C	Methane/Ethanol/O_2 350 °C

Table 8.14: Images acquired for Ag(0.51),K(0.57)/ZnCHA(12) as freshly prepared catalyst and spent following ethanol upgrading, CH_4/EtOH and CH_4/EtOH/O_2 co-processing at 350 °C.

Ag(0.51),K(0.57)/ZnCHA(12) IE 5.8 wt% Ag		
Ethanol 350 °C	Methane/Ethanol 350 °C	Methane/Ethanol/O_2 350 °C

STEM-BF images were acquired for Ag(0.44),K(0.23)/CHA(17) 3.0 wt% Ag following ethanol upgrading at 350 °C for 6.5 hours are included in Figure 8.23. From these images, it was calculated that a sevenfold size increase had occurred with a notable change in the size distribution of silver clusters in the spent material, as shown in Figure 8.24.

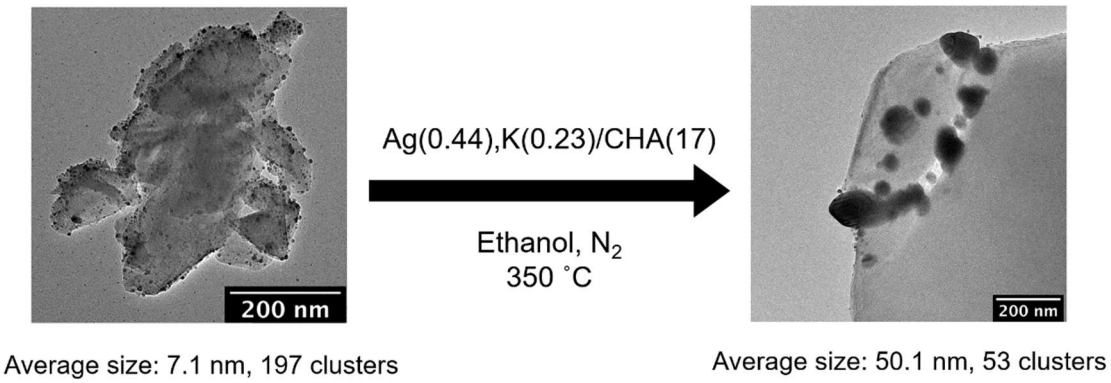

Figure 8.23: STEM-BF images acquired for Ag(0.44),K(0.23)/CHA(17) as freshly prepared catalyst and spent catalyst after ethanol upgrading at 350 °C for 6.5 hours, showing the growth of Ag NPs as observed by pXRD.

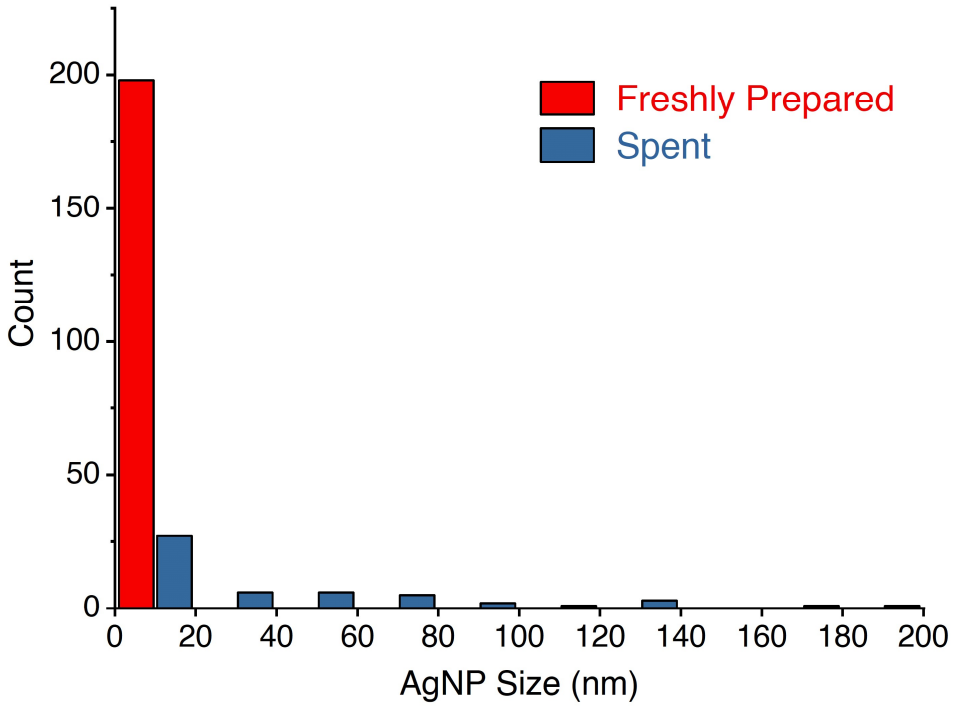

Figure 8.24: Histogram of the silver cluster dimensions measured for Ag(0.44),K(0.23)/CHA(17) as freshly prepared material and after ethanol upgrading at 350 °C for 6.5 hours.

STEM-BF images were acquired for Ag(0.51),K(0.57)/ZnCHA(12) 5.8 wt% Ag following ethanol upgrading at 350 °C for 6.5 hours are included in Figure 8.25. From these images, it was observed that Ag(0.51),K(0.57)/ZnCHA(12) 5.8 wt% Ag was remarkedly less susceptible towards silver sintering, with only a low intensity, broad Ag [111] reflection.[7] Only a slight size increase was observed for the silver clusters, which remained under 10 nm in average size, with their distribution shown in Figure 8.26.

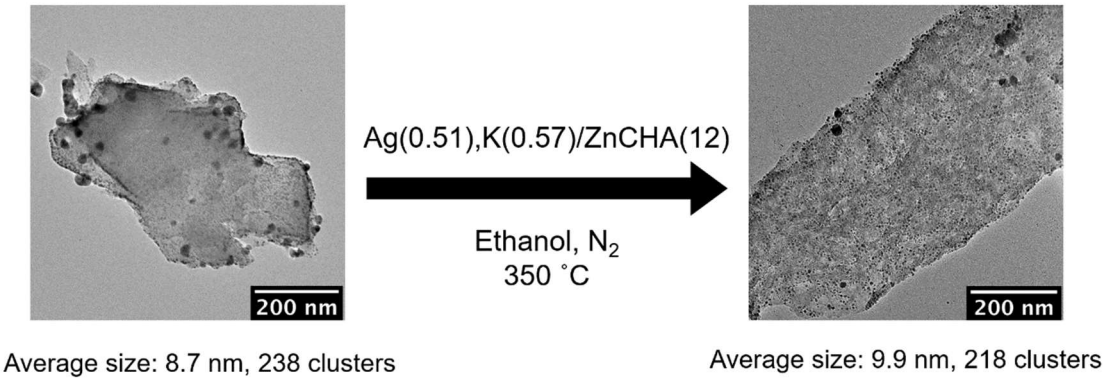

Figure 8.25: STEM-BF images acquired for Ag(0.51),K(0.57)/ZnCHA(12) as freshly prepared catalyst and spent catalyst after ethanol upgrading at 350 °C for 6.5 hours, showing the growth of Ag NPs as observed by pXRD.

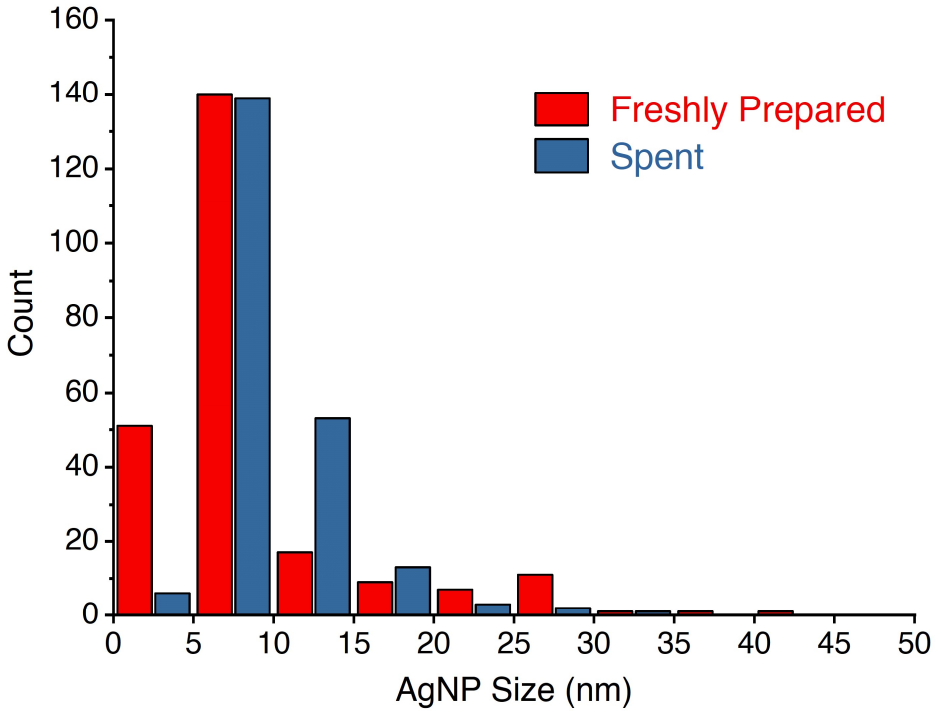

Figure 8.26: Histogram of the silver cluster dimensions measured for Ag(0.51),K(0.57)/ZnCHA(12) as freshly prepared material and after ethanol upgrading at 350 °C for 6.5 hours.

STEM-BF images for Ag(0.44),K(0.23)/CHA(17) revealed several large silver clusters located at the edges of the zeolite crystal, with a large distribution of clusters located at a fracture. EDS-TEM maps were obtained, shown in Figure 8.27, confirming that silver sintering had occurred and led to localisation of silver within the spent catalyst. Co-clustering of potassium could also be observed. TEM-EDS maps obtained for dehydrated Ag(0.53),K(0.14)/ZnCHA(12), included in Figure 8.10, displayed evidence of silver and potassium co-clustering. During ethanol upgrading over Ag(0.44),K(0.23)/CHA(17) there was a notable change in product selectivity toward dehydration products, indicating silver deactivation and BAS formation, evidenced by the dramatic silver cluster growth in the STEM-BF images. No zoning of other elements, such as aluminium, was observed in the collected TEM-EDS maps for spent material.

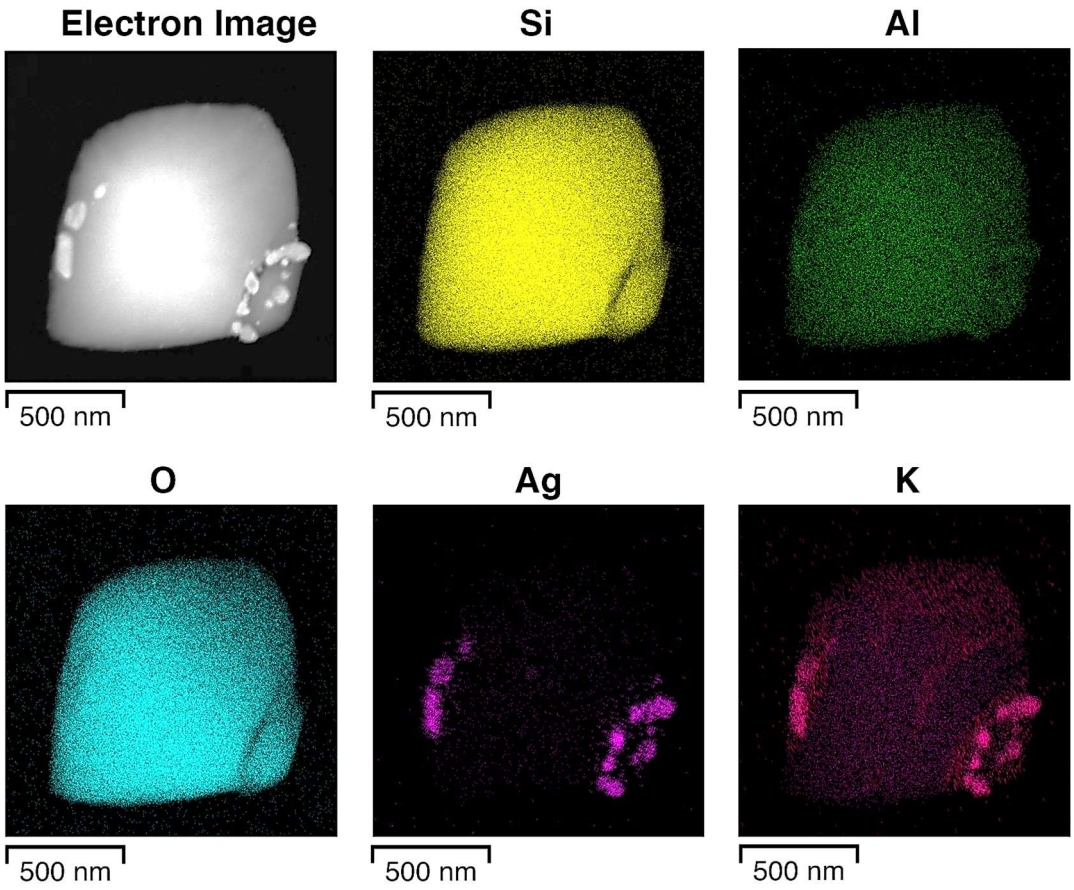

Figure 8.27: EDS-TEM maps acquired for spent Ag(0.44),K(0.23)/CHA(17) following ethanol upgrading at 350 °C after 6.5 hours on-stream, showing silver and potassium sintering and co-clustering localised at both a crystal fracture and the crystal edge.

Methane/ethylene co-processing was also carried out at 350 °C where oxygen was included in the gas feed, outlined in Figure 8.11 as reaction 3. Co-processing was conducted using oxidative conditions to supress undesired premature deactivation of the catalysts.[4,29] The pXRD patterns for the spent materials are shown in Figure 8.28, with the parent material for each included for reference. For each material, there was no observable loss to framework crystallinity under any of the reaction conditions used. Silver cluster formation was observed for all materials under all of the reaction conditions, except for methane/ethanol co-processing over Ag(0.51),K(0.57)/ZnCHA(12) under oxidative conditions. This shows that the use of oxygen in the feed for methane/ethanol co-processing suppressed the rate of silver sintering in the material. STEM-BF images acquired displayed only a slight size increase was observed for the silver clusters, which were 9.3 nm on average, compared to 8.7 nm for the freshly prepared material and 9.9 nm after ethanol upgrading, with their distribution included in Figure 8.29.

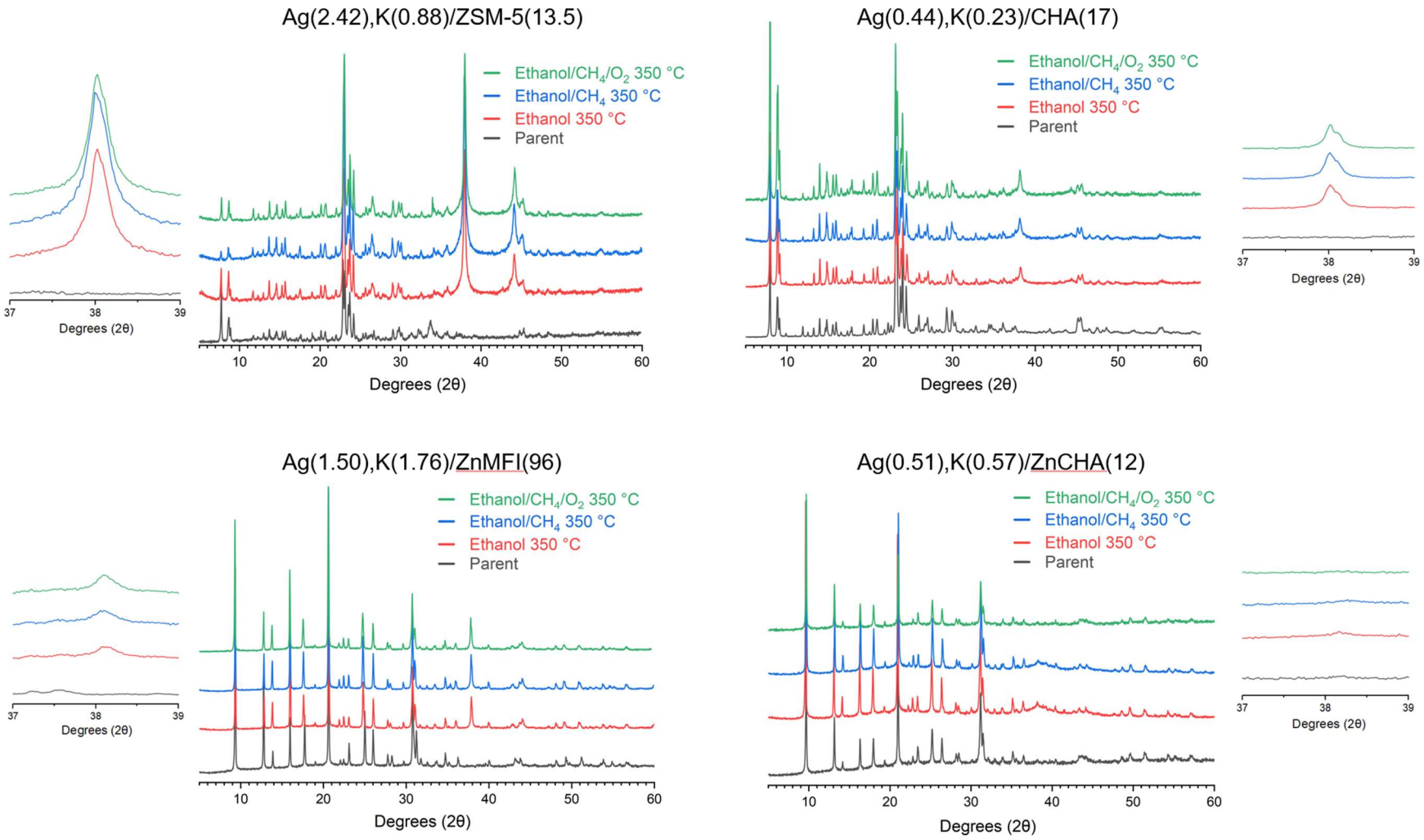

Figure 8.28: pXRD patterns acquired for fresh and spent silver-exchanged catalysts, where the growth of silver NPs were evident from peaks at 38.1° and 44.3° (2θ)[7] for all catalysts except after methane/ethanol co-processing over Ag(0.51),K(0.57)/ZnCHA(12) with and without oxygen. The framework appears to display a stabilising effect on the silver cations, reducing their susceptibility to reduction and subsequent migration. Patterns are offset for clarity.

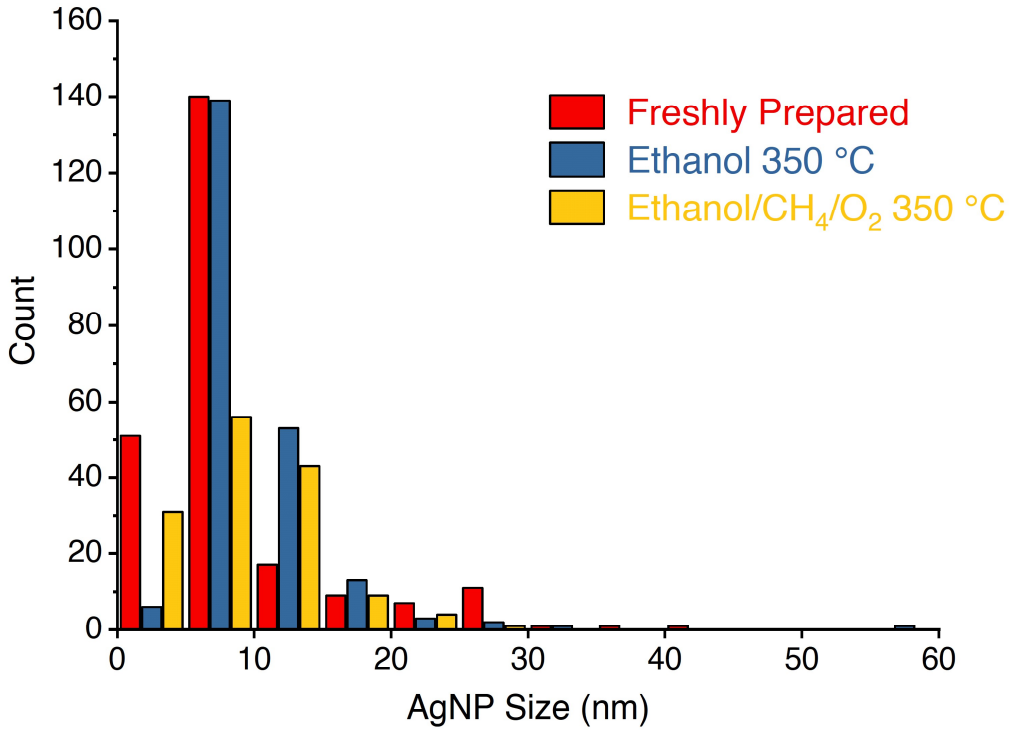

Figure 8.29: Histogram of the silver cluster dimensions measured for Ag(0.51),K(0.57)/ZnCHA(12) as freshly prepared material, after ethanol upgrading at 350 °C for 6.5 hours and after methane/ethanol co-processing with oxidative conditions at 350 °C for 6.5 hours.

It appears that zincosilicate CHA displays a stabilising effect towards the silver cations during upgrading reactions, negating some of the reducing properties of the hydrogen generated during the reaction. Based on prior art,[4,29] we postulate that through the use of a larger portion of oxygen in the feed we can negate undesirable silver sintering completely. Ethanol upgrading was also conducted over Ag(0.51),K(0.57)/ZnCHA(12) at 400 °C, with the enhanced catalytic activity attributed to the silver cations present observed for 20 hours.

For the of the spent catalysts mentioned, we applied the Scherrer equation to the acquired pXRD patterns alongside measuring silver cluster dimensions using STEM-BF imaging. As shown in Table 8.15, the results were found to be concordant between techniques, with co-processing reactions, particularly those undertaken with oxygen included in the feed, generating smaller silver clusters than ethanol upgrading alone. Higher temperature reactions were also observed to produce larger silver clusters.

Table 8.15: Characterisation of silver-exchanged materials before and after ethanol upgrading and co-processing at various temperatures.

Catalyst	Reaction	Ag NPs present by pXRD	Ag NP size (nm)	
			Measured STEM-BF	Calculated Scherrer
Ag(2.42),K(0.88)/ZSM-5(13.5) 14.6 wt% Ag	Parent Material	X	9.0(±3.1)	N/A
	Ethanol 350 °C	✓	29.1(±17.0)	30.6
	CH4/EtOH 350 °C	✓	Not Collected	26.2
	CH4/EtOH/O2 350 °C	✓	Not Collected	22.8
Ag(1.50),K(1.76)/ZnMFI(96) 3.0 wt% Ag	Parent Material	X	11.2(±7.9)	N/A
	Ethanol 320 °C	✓	Not Collected	24.4
	Ethanol 350 °C	✓	22.4(±9.9)	26.2
	Ethanol 400 °C	✓	Not Collected	28.2
	CH4/EtOH 350 °C	✓	18.3(±6.5)	20.5
	CH4/EtOH/O2 350 °C	✓	Not Collected	21.6
Ag(0.44),K(0.23)/CHA(17) 3.0 wt% Ag	Parent Material	X	7.1(±2.0)	N/A
	Ethanol 350 °C	✓	50.1(±62.9)	48.8
	CH4/EtOH 350 °C	✓	Not Collected	40.8
	CH4/EtOH/O2 350 °C	✓	Not Collected	36.2
Ag(0.51),K(0.57)/ZnCHA(12) 5.8 wt% Ag	Parent Material	X	8.7(±5.6)	N/A
	Ethanol 320 °C	X	Not Collected	N/A
	Ethanol 350 °C	✓	9.9(±5.2)	14.3
	Ethanol 400 °C	✓	11.1(±6.3)	16.7
	CH4/EtOH 350 °C	✓	9.8(±5.0)	12.8
	CH4/EtOH/O2 350 °C	X	9.3(±4.6)	N/A

Ag NP sizes were calculated from the associated pXRD pattern using the Scherrer equation.

8.2.2 Spent Metal-Exchanged Zincosilicate CHA following Ethanol Upgrading

Ethanol upgrading at 400 °C was conducted over several metal-exchanged zincosilicate CHA materials, the results of which are discussed in section 7.3.2. Spent catalysts were characterised after 13 hours on-stream. Analysis by pXRD, shown in Figure 8.30, revealed that only Ag(0.51),K(0.57)/ZnCHA(12) 5.8 wt% Ag displayed additional peaks in the XRD pattern, indicating silver sintering and subsequent cluster growth. The pattern acquired for Au(0.03),H/ZnCHA(12) displayed a notable loss of framework crystallinity, with reduced intensity of the pattern coupled with peak broadening, which was attributed to reduced long range order, arising from reduced crystallite dimensions from sintering of the zincosilicate crystals themselves. No other undesirable effects were observed for the spent catalysts by pXRD.

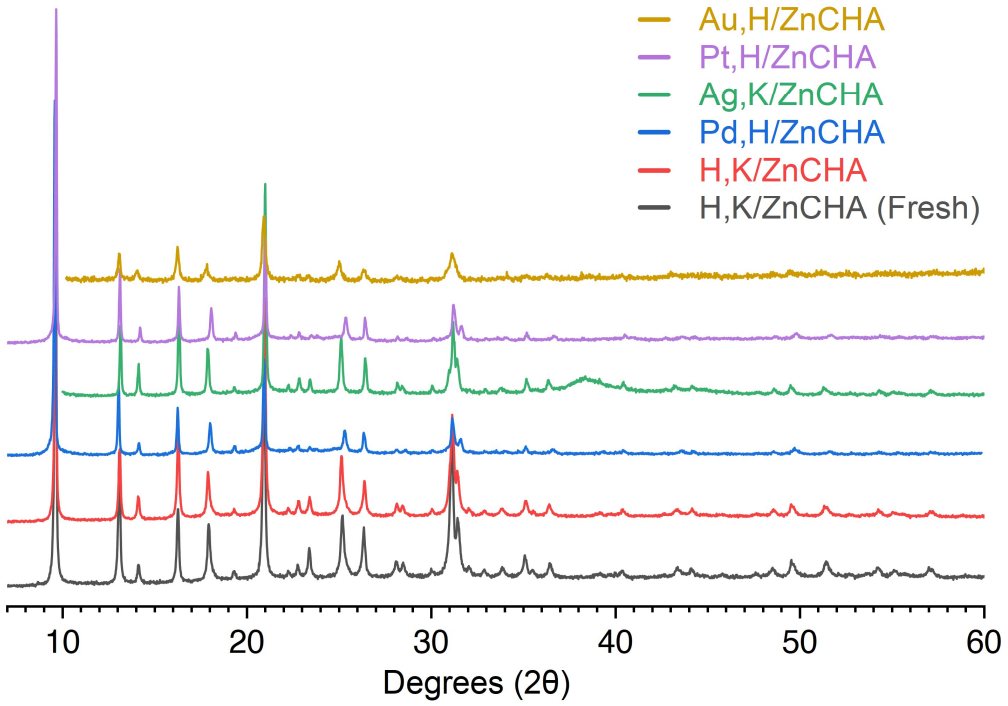

Figure 8.30: XRPD patterns acquired for spent H,K(0.84)/ZnCHA(12) and metal exchanged ZnCHA catalysts after 13 hours on-stream for ethanol upgrading at 400 °C, with the pattern of fresh H,K(0.84)/ZnCHA(12) included for reference. Patterns are offset for clarity.

STEM-BF images were acquired for each of the catalysts tested, employing EDS-TEM mapping to determine changes in elemental distribution. STEM-BF images acquired for select catalysts are shown in Figure 8.31. Silver clusters were present on the surface of Ag(0.51),K(0.57)/ZnCHA(12), as indicated by pXRD. However, metal clusters were also observed for both Pd(0.08),H/ZnCHA(12) and Pt(0.03),H/ZnCHA(12), with metal clusters appearing to be of a comparable size to Ag(0.51),K(0.57)/ZnCHA(12), although not observed by pXRD. No metal clusters were visible on STEM-BF images acquired for

Au(0.03),H/ZnCHA(12), however, the pXRD pattern acquired indicated a significant loss of framework crystallinity. STEM-BF images contained no visual signs indicating widespread framework damage, such as the generation of amorphous content, with generally cubic shaped crystals present.

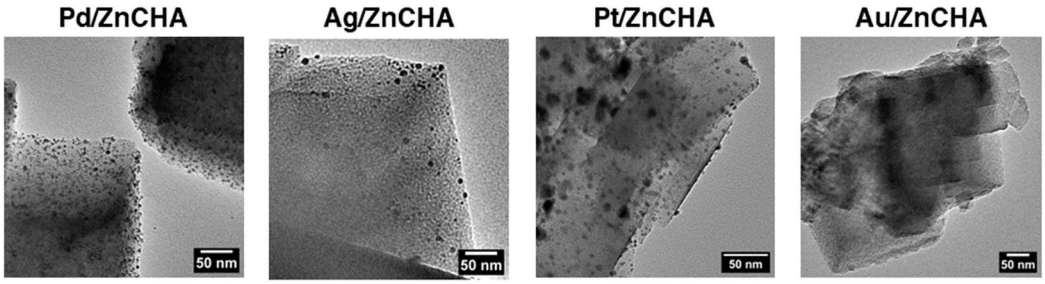

Figure 8.31: STEM-BF images acquired for spent metal-exchanged ZnCHA catalysts following ethanol upgrading at 400 °C after 13 hours.

EDS-TEM maps were acquired for the four metal-exchanged ZnCHA catalysts following ethanol dehydration at 400 °C. Pd(0.08),H/ZnCHA(12) displayed good uniformity across the zincosilicate crystals for each of the elements mapped, as shown in Figure 8.32. Palladium clusters were observed in STEM-BF images for Pd(0.08),H/ZnCHA(12), with localisation of palladium evident the EDS-TEM map. Pd clusters were found to be distributed towards the edges of the zincosilicate crystal and visible in the acquired electron image. No localisation was observed for the other elements present.

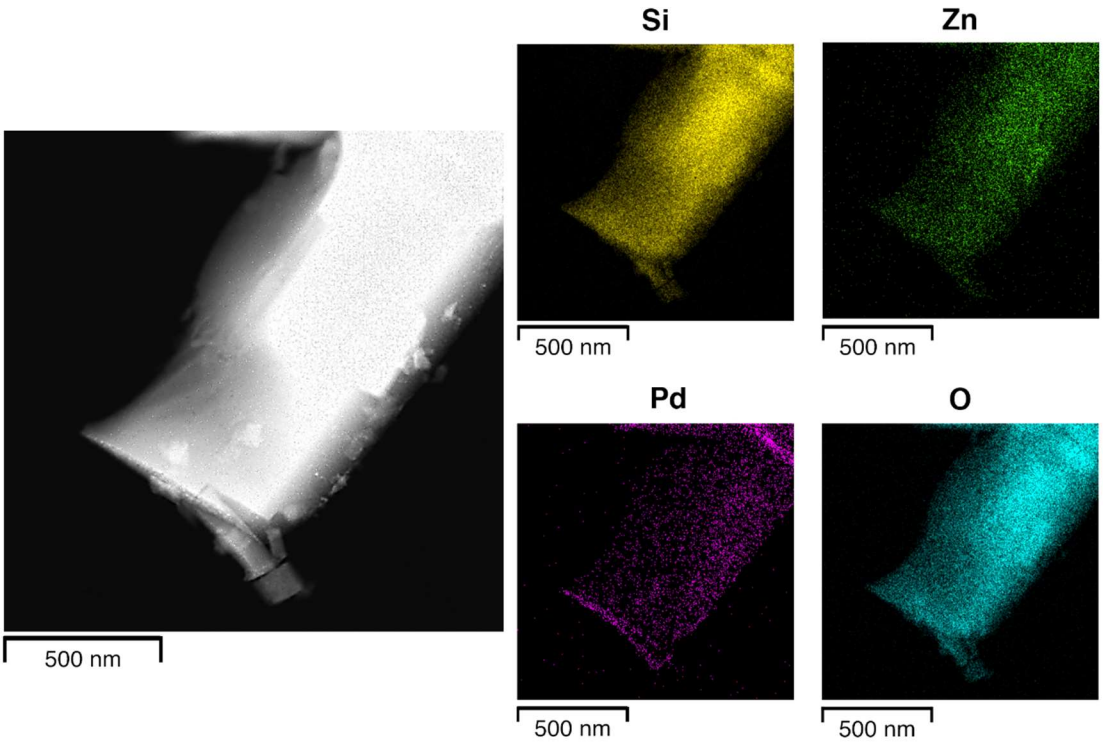

Figure 8.32: EDS-TEM maps acquired for spent Pd(0.08),H/ZnCHA(12) following ethanol upgrading at 400 °C after 13 hours, showing good uniformity of the elements, with some localisation of palladium towards crystal edges.

Silver clusters were observed in the acquired TEM images for Ag(0.51),K(0.57)/ZnCHA(12). The acquired EDS-TEM map for silver displayed a reasonable uniformity across the zincosilicate crystal, as shown in Figure 8.33, showing that widespread silver clusters had formed throughout the material, with some localisation visible at the crystal edges, corroborating with the acquired electron image. Whilst silver clustering was observed in the acquired STEM-BF images for as prepared and spent Ag(0.51),K(0.57)/ZnCHA(12), silver localisation was not observed in EDS-TEM maps for the as prepared material. These findings are reported in section 6.3.2. Good uniformity was observed for the EDS-TEM maps obtained for all other elements present, with no distinct indication of potassium co-clustering occurring.

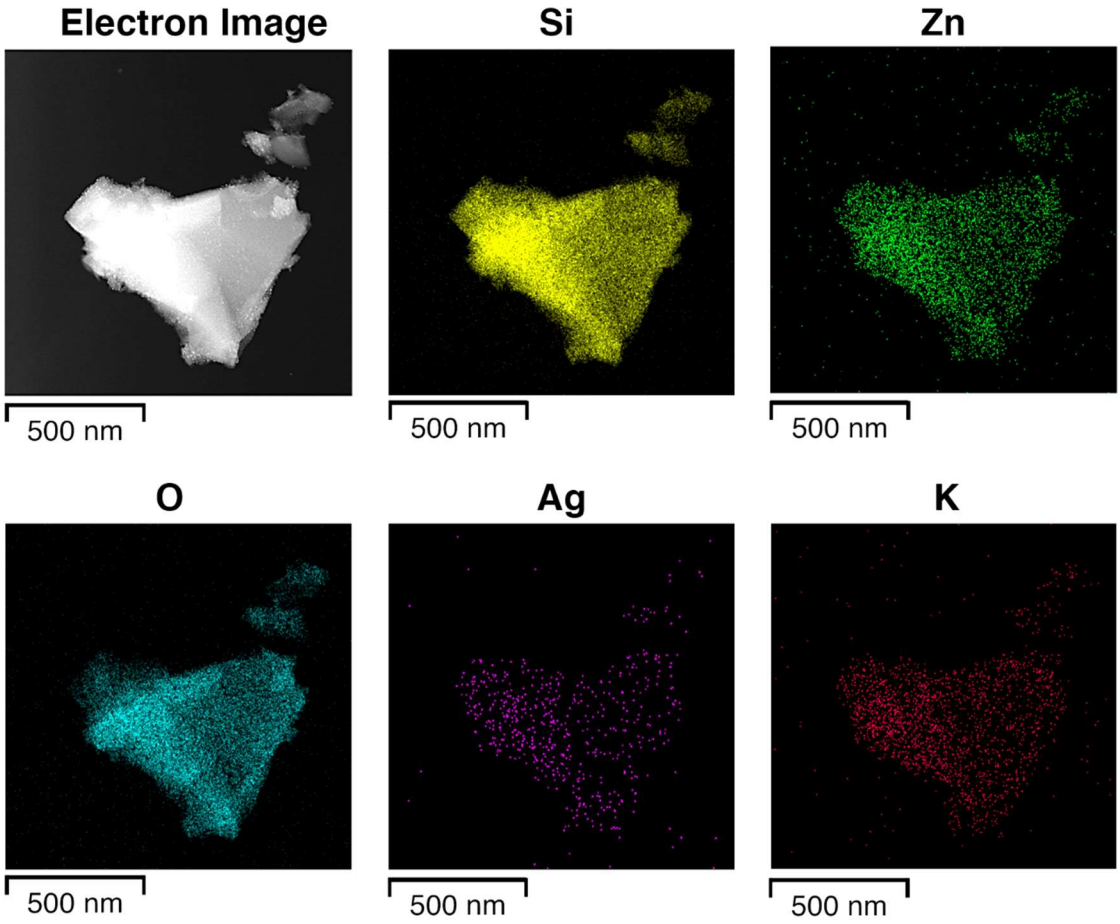

Figure 8.33: EDS-TEM maps acquired for spent Ag(0.51),K(0.57)/ZnCHA(12) following ethanol upgrading at 400 °C after 13 hours, showing a good uniformity across of the elements across the zincosilicate crystals.

EDS-TEM maps were acquired for Pt(0.03),H/ZnCHA(12) alongside STEM-BF images. The acquired STEM-BF images showed no showed no signs of metal clustering on the surface of the material. The EDS-TEM maps showed that there was good uniformity for most elements present throughout the material, with some localisation observed for platinum. This could be observed towards the edges of the zincosilicate crystals, as shown in Figure 8.34.

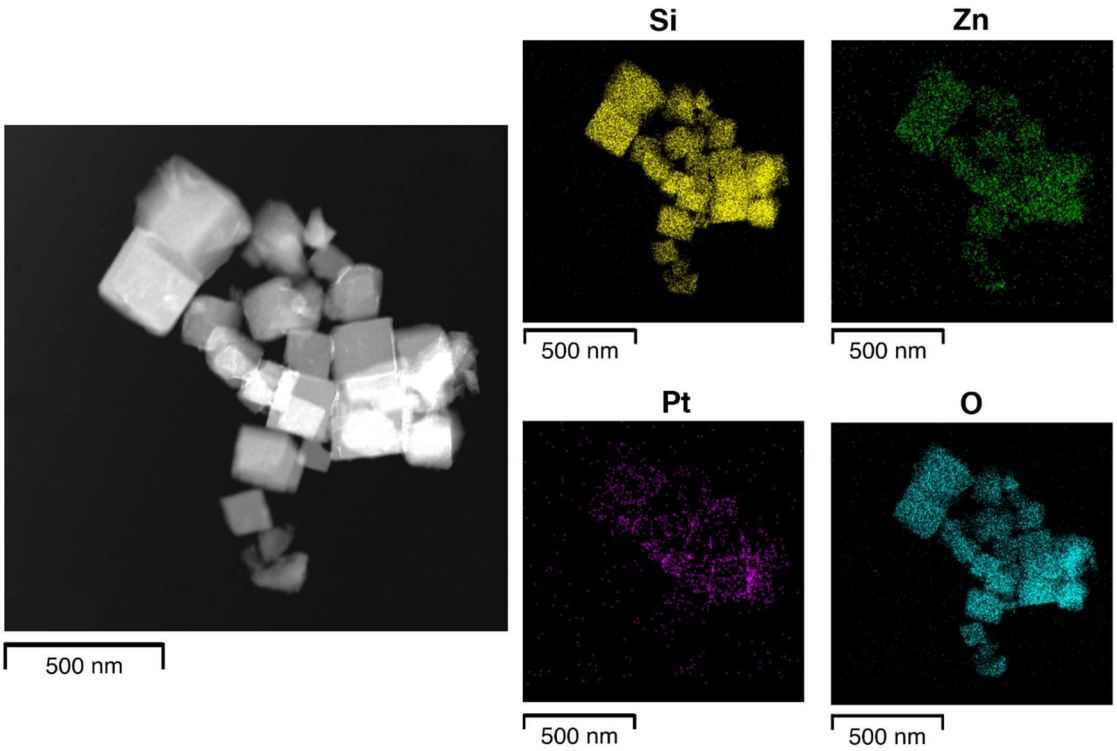

Figure 8.34: EDS-TEM maps acquired for Pt(0.03),H/ZnCHA(12) showing generally good uniformity of elements, albeit with some platinum clusters localised at the crystal edges.

EDS-TEM maps for Pt(0.03),H/ZnCHA(12) after ethanol upgrading at 400 °C displayed good uniformity for silicon, zinc and oxygen as shown in Figure 8.35, although zinc displayed areas with notable clustering. The EDS-TEM map for platinum showed areas of clustering which coincide with areas of clustering in the zinc EDS map. Based on prior art,[30–33] we postulate that this indicates a bimetallic cluster species formed under reaction conditions consisting of platinum and zinc. Clusters were observed in the acquired TEM images for Pt(0.03),H/ZnCHA(12), which corroborated with the bright spots in the electron image, indicating areas of high intensity on the elemental maps. We expect that the localisation of platinum occurred following the sintering of platinum cations during ethanol upgrading at 400 °C, as these observations contrast with the parent material which displayed no obvious signs of platinum localisation, shown in Figure 8.34.

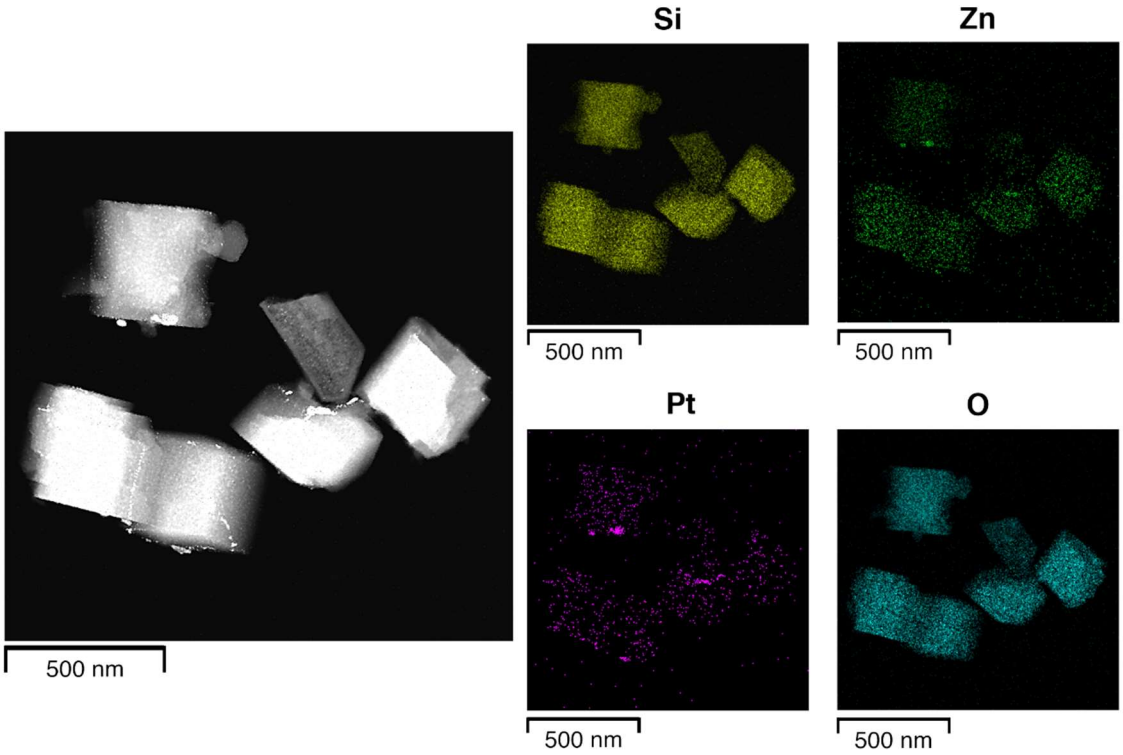

Figure 8.35: EDS-TEM maps acquired for spent Pt(0.03),H/ZnCHA(12) following ethanol upgrading at 400 °C after 13 hours, showing generally good uniformity of elements, albeit with some platinum clusters localised at the crystal edges.

EDS-TEM maps were acquired for Au(0.03),H/ZnCHA(12) alongside STEM-BF images. The acquired STEM-BF images showed no signs of metal clustering on the surface of the material. The EDS-TEM maps showed that there was good uniformity for all elements throughout the zincosilicate crystals, as shown in Figure 8.36. Unfortunately, artifcating occurred during acquisition leading to the production of dark spots in the acquired electron image and all EDS-TEM elemental maps.

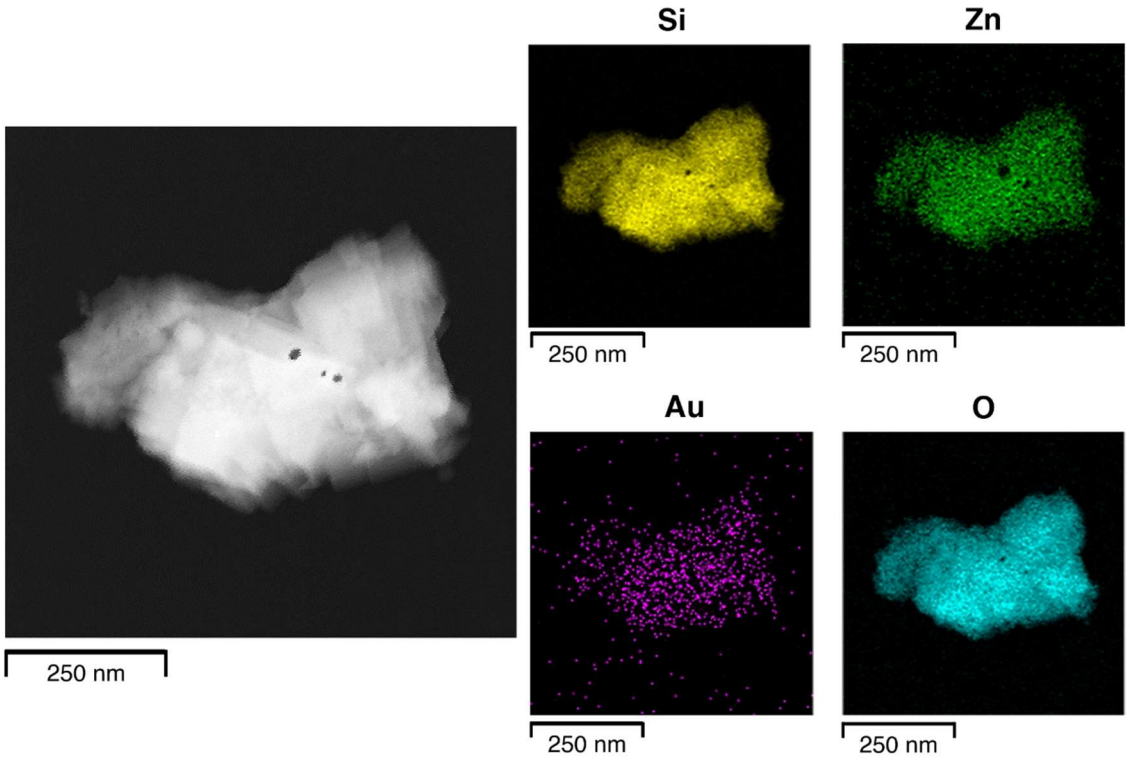

Figure 8.36: EDS-TEM maps acquired for Au(0.03),H/ZnCHA(12)

Au(0.03),H/ZnCHA(12) displayed a reasonably good uniformity across the zincosilicate crystals for each of the elements that were mapped, as shown in Figure 8.37. Clusters were observed in the acquired TEM images for Au(0.03),H/ZnCHA(12), with the electron image showing bright spots which directly correlate with the areas of high intensity in the acquired gold EDS map, signifying that sintering of gold cations had occurred during ethanol upgrading at 400 °C. The localisation of gold indicates that sintering of the gold cations occurred under reaction conditions, as this contrasts with the parent material which contained highly dispersed gold species, as displayed in Figure 8.36.

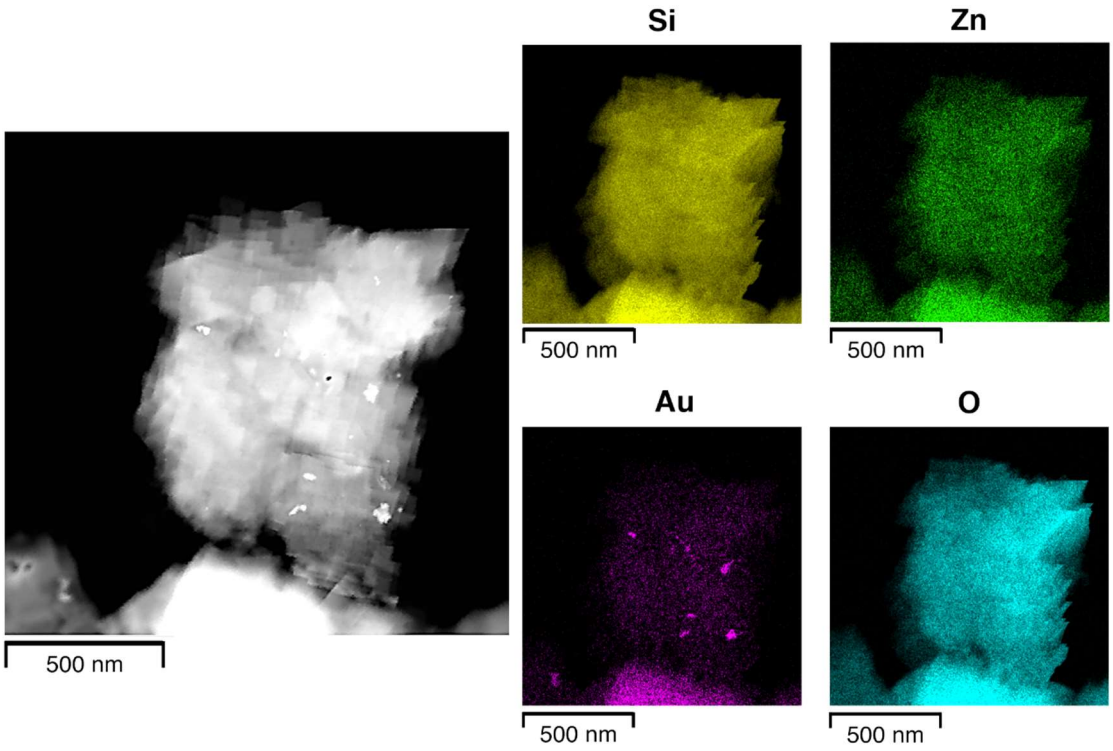

Figure 8.37: EDS-TEM maps acquired for spent Au(0.03),H/ZnCHA(12) following ethanol upgrading at 400 °C after 13 hours, showing uniformity for silicon, zinc and oxygen, with localisation and clustering of gold at several locations.

DRIFTS spectroscopy was carried out on selected spent catalysts following hydrocarbon upgrading and co-processing reactions. One selected example is H,K(0.84)/ZnCHA(12), which was characterised following ethanol upgrading at 400 °C for 13 hours and its spectrum compared against the parent material, displayed in Figure 8.38. External silanols were no longer observed in the spent material (observed at 3750 cm^{-1}), whilst the emergence of C–H stretching bands can be observed between 3100 cm^{-1} and 2800 cm^{-1}. This indicates the presence of carbon containing materials either trapped in the micropores following the upgrading reaction, or as carbonaceous deposits situated on the catalyst surface, which would lead to the loss of the external silanol peak. The spent material was a brown powder rather an off-white powder, as per the parent. These findings were common across metal-exchanged ZnCHA materials.

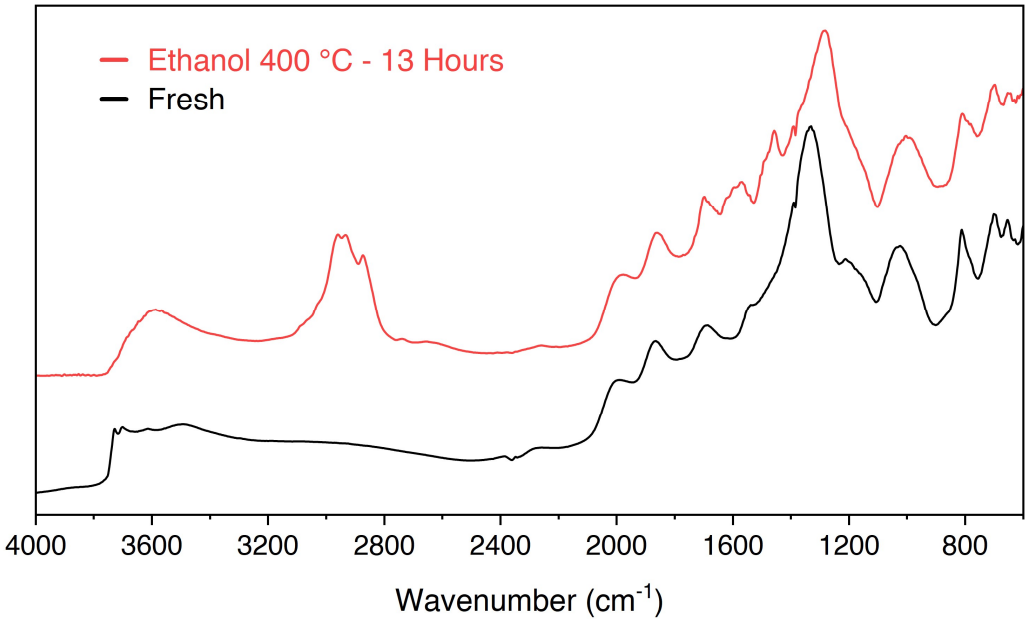

Figure 8.38: DRIFTS spectra for spent H,K(0.84)/ZnCHA(12) following ethanol upgrading at 400 °C for 13 hours, compared against the parent material, showing the presence of carbon containing materials and the loss of the external silanol peak. Spectra are offset for clarity.

8.2.3 Conclusion of the Effects of Hydrocarbon Upgrading on Metal-exchanged Zeolites and Zincosilicates

Initial observations were made for materials post dehydration under a range of different conditions. These were conducted alongside characterisation of spent catalysts to determine the origin of the effects leading to silver clustering and loss of framework crystallinity. Determining changes that occurred to catalysts post hydrocarbon upgrading or co-processing was crucial understanding changes to catalytic activity observed during time on-stream. Where possible, the dimensions of silver clusters were calculated using the Scherrer equation using the silver cluster reflection at 38.1° (2θ), corresponding to Ag [111], in the acquired pXRD patterns.[7] Calculation of cluster size assumed a good fit to particle shape based on the average silver clusters being spherical. The calculated silver cluster sizes was found to corroborate with the measured dimensions from the STEM-BF images acquired for the materials.

We observed that increased reaction temperatures led to larger silver clusters being produced. Ag(0.51),K(0.57)/ZnCHA(12) was the only silver-exchanged material tested which did not have silver clusters present in the pXRD pattern following ethanol upgrading at 320 °C or methane/ethanol co-processing at 350 °C under oxidative conditions. However, each of the spent materials reported here displayed no change in framework crystallinity by pXRD.

In several cases, recovered catalysts displayed a distinct colour change from the freshly prepared material. DRIFTS analysis conducted for H,K(0.84)/ZnCHA(12) following ethanol upgrading revealed the generation of C–H bands in the acquired DRIFTS spectrum, indicating carbonaceous deposition likely led to the brown colouration for these catalysts. For some metal exchanged ZnCHA materials, recovered materials were black powders, changed from white freshly prepared materials. STEM-BF images acquired for metal exchanged ZnCHA materials highlighted sintering on spent materials. We concluded that the black colouration was a result of metal clusters on the surface.

Silver auto reduction facilitates the evolution of oxygen from framework oxidation leading to the subsequent loss of long-range crystallinity.[2] Following ethanol upgrading over Au(0.03),H/ZnCHA(12) at 400 °C, we observed the loss of long range crystallinity in the material. STEM-BF images indicated no clustering of gold on the surface of the material, whilst EDS-TEM maps indicated gold sintering and localisation. Gold cations are reported to be inherently unstable, with poor thermal stability and readily reduced by hydrogen.[34] Reduction would be facilitated by the evolution of hydrogen during hydrocarbon upgrading, so we postulate that gold reduction led to framework oxidation, with analogous consequences to silver auto reduction. Several applications with gold NPs require supports to reduce the rate of deactivation,[35,36] however, no prior art reports framework oxidation following reduction of gold NPs and subsequent framework damage.

8.3 Chapter Eight Bibliography

1 T. Sun and K. Seff, *Chem. Rev.*, Silver Clusters and Chemistry in Zeolites, 1994, **94**, 857–870.

2 N. H. Heo, Y. Kim, J. J. Kim and K. Seff, *J. Phys. Chem. C*, Surprising Intrazeolitic Chemistry of Silver, 2016, **120**, 5277–5287.

3 J. Texter, R. Kellerman and T. Gonsiorowski, *J. Phys. Chem.*, Formation of charged silver clusters and their reversible silver ion desorption in zeolite A, 1986, **90**, 2118–2124.

4 Y. Kuroda, T. Mori, H. Sugiyama, Y. Uozumi, K. Ikeda, A. Itadani and M. Nagao, *J. Colloid Interface Sci.*, On the possibility of AgZSM-5 zeolite being a partial oxidation catalyst for methane, 2009, **333**, 294–299.

5 H. L. Yang, C. Y. Ma, Y. Li, J. H. Wang, X. Zhang, G. Wang, N. L. Qiao, Y. G. Sun, J. Cheng and Z. P. Hao, *Chem. Eng. J.*, Synthesis, characterization and evaluations of the Ag/ZSM-5 for ethylene oxidation at room temperature: Investigating the effect of water and deactivation, 2018, **347**, 808–818.

6 K. Murata, J. Ohyama and A. Satsuma, *Catal. Sci. Technol.*, Kinetic analysis of Ag particle redispersion into ZSM-5 in the presence of coke usingin situXAFS, 2021, **11**, 506–515.

7 M. Lamoth, T. Jones, M. Plodinec, A. Machoke, S. Wrabetz, M. Krämer, A. Karpov, F. Rosowski, S. Piccinin, R. Schlögl and E. Frei, *ChemCatChem*, Nanocatalysts Unravel the Selective State of Ag, 2020, **12**, 2977–2988.

8 T. Baba, H. Sawada, T. Takahashi and M. Abe, *Appl. Catal. a-General*, Chemisorption study of hydrogen and methane by H-1 MAS NMR and conversion of methane in the presence of ethylene on Ag-Y zeolite, 2002, **231**, 55–63.

9 A. A. Gabrienko, S. S. Arzumanov, I. B. Moroz, A. V Toktarev, W. Wang and A. G. Stepanov, *J. Phys. Chem. C*, Methane Activation and Transformation on Ag/H-ZSM-5 Zeolite Studied with Solid-State NMR, 2013, **117**, 7690–7702.

10 P. A. Jacobs, J. B. Uytterhoeven and H. K. Beyer, *J. Chem. Soc. Faraday Trans. 1 Phys. Chem. Condens. Phases*, Redox behaviour of transition metal ions in zeolites. Part 6.—Reversibility of the reduction reaction in silver zeolites, 1977, **73**, 1755–1762.

11 H. Beyer, P. A. Jacobs and J. B. Uytterhoeven, *J. Chem. Soc. Faraday Trans. 1 Phys. Chem. Condens. Phases*, Redox behaviour of transition metal ions in zeolites. Part 2.—Kinetic study of the reduction and reoxidation of silver-Y zeolites, 1976, **72**, 674–685.

12 A. A. C. Reule, J. A. Sawada and N. Semagina, *J. Catal.*, Effect of selective 4-membered ring dealumination on mordenite-catalyzed dimethyl ether carbonylation, 2017, **349**, 98–109.

13 A. Aguado, *Comput. Theor. Chem.*, Structures, relative stabilities, and electronic properties of potassium clusters Kn (13⩽n⩽80), 2013, **1021**, 135–143.

14 T. Ikeda, T. Kodaira, F. Izumi, T. Kamiyama and K. Ohshima, *Chem. Phys. Lett.*, Neutron powder diffraction study of potassium clusters in zeolite K-LTA, 2000, **318**, 93–101.

15 T. Nakano, S. Araki, N. Hoang Nam, T. Umemoto, K. Tsuchihashi, Y. Kubo, A. Owaki and Y. Nozue, *Soft Condens. Matter*, Origin of magnetic moments and ferromagnetic properties of potassium clusters in zeolite A, 2020, arXiv:2009.04828.

16 J. Michalik, T. Wasowicz, J. Sadlo, E. J. Reijerse and L. Kevan, *Radiat. Phys. Chem.*, Pulsed EPR for studying silver clusters, 1996, **47**, 75–81.

17 M. Wu, W. Lv, Y. Zhang, Y. Yang, Z. Wang, K. Qiu, Y. Shi, B. Zhao and C. Ge, *J. Nucl. Mater.*, Potassium clusters in tungsten grain boundaries: Formation mechanism and strengthening effect, 2023, **573**, 154135.

18 M. Kong, Z. Liu, T. Vogt and Y. Lee, *Microporous Mesoporous Mater.*, Chabazite structures with Li^+, Na^+, Ag^+, K^+, NH_4^+, Rb^+ and Cs^+ as extra-framework cations, 2016, **221**, 253–263.

19 A. M. Fonseca and I. C. Neves, *Microporous Mesoporous Mater.*, Study of silver species stabilized in different microporous zeolites, 2013, **181**, 83–87.

20 G. De Cremer, E. Coutino-Gonzalez, M. B. J. Roeffaers, B. Moens, J. Ollevier, M. Van der Auweraer, R. Schoonheydt, P. A. Jacobs, F. C. De Schryver, J. Hofkens, D. E. De Vos, B. F. Sels and T. Vosch, *J. Am. Chem. Soc.*, Characterization of Fluorescence in Heat-Treated Silver-Exchanged Zeolites, 2009, **131**, 3049–3056.

21 M. Rálek, P. Jírů, O. Grubner and H. Beyer, *Collect. Czechoslov. Chem. Commun.*, Molekularsiebe mit farbiger Indizierung des Wassergehaltes, 1962, **27**, 142–146.

22 S. H. Lee, Y. Kim and K. Seff, *Microporous Mesoporous Mater.*, Weak Ag^+–Ag^+ bonding in zeolite X. Crystal structures of $Ag_{92}Si_{100}Al_{92}O_{384}$ hydrated and fully dehydrated in flowing oxygen, 2000, **41**, 49–59.

23 J. G. Min, K. C. Kemp, K. S. Kencana and S. B. Hong, *Microporous Mesoporous Mater.*, Silver-exchanged CHA zeolite as a CO_2-resistant adsorbent for N_2/O_2 separation, 2021, **323**, 111239.

24 P. A. Jacobs, J. B. Uytterhoeven and H. K. Beyer, *J. Chem. Soc. Faraday Trans. 1 Phys. Chem. Condens. Phases*, Some unusual properties of activated and reduced AgNaA zeolites, 1979, **75**, 56–64.

25 H. L. Yang, C. Y. Ma, X. Zhang, Y. Li, J. Cheng and Z. P. Hao, *Acs Catal.*, Understanding the Active Sites of Ag/Zeolites and Deactivation Mechanism of Ethylene Catalytic Oxidation at Room Temperature, 2018, **8**, 1248–1258.

26 N. S. Flores-Lopez, J. Castro-Rosas, R. Ramirez-Bon, A. Mendoza-Cordova, E. Larios-Rodriguez and M. Flores-Acosta, *J. Mol. Struct.*, Synthesis and properties of crystalline silver nanoparticles supported in natural zeolite chabazite, 2012, **1028**, 110–115.

27 C. A. Schneider, W. S. Rasband and K. W. Eliceiri, *Nat. Methods*, NIH Image to ImageJ: 25 years of image analysis, 2012, **9**, 671–675.

28 A. G. Wang, P. He, M. Yung, H. B. Zeng, H. Qian and H. Song, *Appl. Catal. B-Environmental*, Catalytic co-aromatization of ethanol and methane, 2016, **198**, 480–492.

29 M. S. Kim, K. H. Park, S. J. Cho and E. D. Park, *Catal. Today*, Partial oxidation of methane with hydrogen peroxide over Fe-ZSM-5 catalyst, , DOI:https://doi.org/10.1016/j.cattod.2020.07.007.

30 L. Liu, M. Lopez-Haro, C. W. Lopes, C. Li, P. Concepcion, L. Simonelli, J. J. Calvino and A. Corma, *Nat. Mater.*, Regioselective generation and reactivity control of subnanometric platinum clusters in zeolites for high-temperature catalysis, 2019, **18**, 866–873.

31 S. W. Han, H. Park, J. Han, J.-C. Kim, J. Lee, C. Jo and R. Ryoo, *ACS Catal.*, PtZn Intermetallic Compound Nanoparticles in Mesoporous Zeolite Exhibiting High Catalyst Durability for Propane Dehydrogenation, 2021, **11**, 9233–9241.

32 M. Song, B. Zhang, Z. Zhai, S. Liu, L. Wang and G. Liu, *Ind. Eng. Chem. Res.*, Highly Dispersed Pt Stabilized by ZnOx-Si on Self-Pillared Zeolite Nanosheets for Propane Dehydrogenation, 2023, **62**, 3853–3861.

33 V. J. Cybulskis, B. C. Bukowski, H.-T. Tseng, J. R. Gallagher, Z. Wu, E. Wegener,

A. J. Kropf, B. Ravel, F. H. Ribeiro, J. Greeley and J. T. Miller, *ACS Catal.*, Zinc Promotion of Platinum for Catalytic Light Alkane Dehydrogenation: Insights into Geometric and Electronic Effects, 2017, **7**, 4173–4181.

34 J. H. Carter, A. M. Abdel-Mageed, D. Zhou, D. J. Morgan, X. Liu, J. Bansmann, S. Chen, R. J. Behm and G. J. Hutchings, *ACS Nano*, Reversible Growth of Gold Nanoparticles in the Low-Temperature Water–Gas Shift Reaction, 2022, **16**, 15197–15205.

35 E. Eom, M. Song, J.-C. Kim, D. Kwon, D. N. Rainer, K. Gołąbek, S. C. Nam, R. Ryoo, M. Mazur and C. Jo, *JACS Au*, Confining Gold Nanoparticles in Preformed Zeolites by Post-Synthetic Modification Enhances Stability and Catalytic Reactivity and Selectivity, 2022, **2**, 2327–2338.

36 Y.-S. Chi, H.-P. Lin and C.-Y. Mou, *Appl. Catal. A Gen.*, CO oxidation over gold nanocatalyst confined in mesoporous silica, 2005, **284**, 199–206.

9. Chapter Nine – Project Outlook and Conclusions

9.1 Project Conclusion

Silver exchanged zeolites were reported to display higher methane conversion (13.2%) than what was observed for other metal-exchanged ZSM-5, with each having an identical loading level for methane/ethylene co-processing at 400 °C.[1] Rapid deactivation was reported, with no activity at 5 hours, warning of catalyst lifetime issues that were needed to be overcome. Reports for the surprising behaviour of silver in zeolites go back to the 1960's, observing physical colour changes dependent on material hydration.[2,3] Several reports surrounding silver auto reduction highlighted silver cluster formation as a result of reversible redox chemistry.[4–6] Reductive treatments of silver-exchanged zeolites were reported to cause silver sintering, with subsequent migration of the metallic silver species to the surface of the material,[7] generating BAS at charge balancing positions of the framework.[8] However, silver reduction was reported to lead to a loss of framework crystallinity by producing oxygen vacancies in the framework,[4,9,10] with lattice destruction and dealumination facilitated by an interzeolitic process.[4,6,9–11] Oxidative treatments were reported to reverse the damage,[5,12] but were found to not be 100% effective.[4,11]

9.1.1 Hydrothermal Synthesis of CHA and ZnCHA

Hydrothermal synthesis of zeolite and zincosilicate chabazite materials were successfully achieved following a series of iterative changes to optimise a reported method.[13] Changes were made to the synthesis gel composition, using a different silicon source and mineralising agent, with synthesis gel produced using slow addition of the components and aging at raised temperature. Changed hydrothermal synthesis temperatures and conditions were also explored, influenced by prior art.[13–15] An additional calcination step at 90 °C was introduced alongside reduced heating rates (1 °C/min), which stopped materials undergoing crystallinity loss during calcination.

Repeated hydrothermal syntheses of zeolite chabazite produced batches of material that were highly crystalline, comprised of nanosized cubic crystals (ca. 246 nm average crystal size) that were highly uniform in their size and shape. Materials displayed excellent crystallinity by pXRD. Which corroborated with ssNMR spectroscopy which showed that aluminium was predominantly in tetrahedral framework environments,

whilst silicon primarily resided in Q^4 environments. TEM-EDS indicated that the materials had uniform elemental composition, even for the smallest and largest crystallites observed, with no appreciable differences in their associated EDS maps. DRIFTS analysis indicated no organic containing moieties present on the material surface or in the micropores, indicating calcination conditions were sufficient for SDA removal. BET theory indicated that nanosized CHA had a relatively high surface area (682 m^2/g), in comparison with values reported reported by Liu *(*537 – 569 m^2/g) and Lillerud (463 – 702 m^2/g).[16–18]

Zincosilicate chabazite materials were comprised of cubic crystals an order of magnitude larger than their zeolite counterparts and observed to be highly uniform in their size and shape, with excellent crystallinity by pXRD. ssNMR spectroscopy highlighted Q_2 and Q_3 silicon environments present in the framework, whilst experiments at higher spin rates and cooler temperatures highlighted zinc in the framework close to Q_3 and Q_4 environments. Si–Me and Zn–Me moieties were observed by ssNMR,[19] their origin we postulate was a result of calcination. TEM-EDS indicated a highly uniform elemental composition for zincosilicate crystals, even for crystals with smaller than average dimensions. DRIFTS spectroscopy observed only a small quantity of bands attributable to silanol species, indicating a low quantity of defects present. Vapour phase adsorption of pyridine and deuterated acetonitrile highlighted ZnCHA materials contained both BAS and Lewis acid sites, with a low quantity of both sites present on the material surface. XAS determined that zinc was successfully incorporated into the zincosilicate framework, primarily as Zn^{2+}. No indication of bulk ZnO or unreacted zinc source was present. XANES of silver-exchanged ZnCHA highlighted a larger Zn^{2+} contribution, which indicated the presence of more Zn^{2+} in the material .We postulate that aqueous ion-exchange of silver could facilitate the oxidation of Zn^0 and Zn^{1+} species to Zn^{2+}, reducing monovalent silver cations to silver clusters in the process. BET theory also indicated that ZnCHA had a relatively high surface area (582 m^2/g), lower than hydrothermally synthesised chabazite (680 m^2/g) in this project but comparable with values reported by Liu *(*537 – 569 m^2/g) and Lillerud (463 – 702 m^2/g).[16–18]

9.1.2 Silver Exchanged Materials

Routine ion exchange of zeolites was conducted using aqueous media, whilst protecting the mixture from light. It was quickly determined that the molarity of the silver source and the resulting silver loading quickly plateaued, requiring multiple repeat exchanges to achieve complete exchange of a material. Silver clustering was evident in the

acquired STEM-BF images of all silver-exchanged zeolites, regardless of their silver loading level and framework topology, with no exception based on the ion-exchange method or silver source used. Silver clusters are observable through pXRD at 38.1° and 44.3° (2θ)[20] although no pattern acquired for freshly prepared silver-exchanged materials contained the relevant reflections, refuting one claim in literature.[21] Prior art concluded that silver predominantly exists as monovalent silver cations alongside multinuclear silver clusters simultaneously in silver-exchanged zeolites.[8,22–24] Based on our observations of widespread silver clustering post ion-exchange by TEM, temperature programmed oxidation (TPO) of silver exchanged materials would be required to determine the degree of monovalent silver cations present and confirm their claims.

Acquisition of TEM and TEM-EDS data of silver-exchanged materials allowed us to determine the average silver cluster size and their positioning. Several materials with high levels of silver loading, or even materials that displayed over-exchange, there was a notable lack of uniformity for silver throughout the material, with localisation at the crystal edges. ssNMR spectroscopy highlighted a novel proton species in Ag(1.00)/MOR(6.5) introduced following silver ion-exchange, with an apparent chemical shift value similar to a silver hydride moiety reported in prior art.[25] Several NMR experiments were conducted, allowing us to determine the species was isolated, unrelated to a silicon environment and underwent facile H/D exchange.

9.1.3 Hydrocarbon Upgrading and Co-processing

Ethanol to higher value products was explored with catalysts compared to those reported.[26–31] Protic zeolites led to complete ethanol conversion (100%) over BAS that facilitated ethanol dehydration to ethylene,[32–35] alongside various C_3-C_6 olefins and BTX derivatives. However, these products were not observed for small pore catalysts like CHA demonstrating that selectivity was driven by framework pore size. Zincosilicates facilitated dehydrogenation to acetaldehyde.[36–39] Ethanol upgrading was conducted over various ZnMFI and ZnCHA materials with protic, silver, platinum forms tested, with gold and palladium exchanged ZnCHA also tested. We observed displayed greater ethanol conversion (72%) and acetaldehyde selectivity (68%) over Pt(0.02),H/ZnCHA(12) than reported for Zn(0.3),H/DeAlBEA (50% and 60% respectively) at 320 °C.[40] At 400 °C, Pt(0.03),H/ZnCHA(12) displayed high ethanol conversion (96%) and acetaldehyde selectivity (88%) compared with 65% and 51% respectively for Zn-MWW(40).[36] We observed lower acetaldehyde selectivity than reported for ZnO,Rb/MOR(7) (89%)[41] and

Zn/Silicalite-1 (5wt% Zn) (95%),[42] however, both displayed lower ethanol conversion (40% and 65% respectively). Catalytic activity of Pt(0.02),H/ZnCHA(12) was observed to be stable over 55 hours, whilst displaying high ethanol conversion over a range of temperatures (300 – 400 °C). Pt(0.02),H/ZnCHA(12) displayed its highest acetaldehyde selectivity (92%) at 340 °C, with the highest acetaldehyde yield (84%) coming at 360 °C.

Direct methane upgrading with only methane fed into the reactor resulted in no activity being observed, which is in line with prior art.[43] However, methane conversion was observed for methane/methanol coprocessing at 400 °C over Ag(1.30),K(0.57)/ZnMFI(96) (0.6%) and Ag(2.37),Na/ZnCHA(21) (5.6%). Methane conversion was reported for zinc impregnated Zn/ZSM-5(19) (1.3wt% Zn) at 3.3% during methane/methanol co-processing 400 °C,[43] whilst H/ZSM-5(25) (post 3 hour steaming pre-treatment) was reported as 5.4%.[44] During methane/ethanol co-processing at 350 °C over Ag(2.42),K(0.88)/ZSM-5(13.5), we observed 6% methane conversion, greater than reported for Ag(1wt%),Ga(1wt%)/ZSM-5(40) (4.7%) at 400 °C.[28]

9.1.4 Spent Material Characterisation

Characterisation of silver-exchanged materials highlighted that discolouration, crystallinity loss and the observation of silver clusters by pXRD were only apparent for materials that underwent dehydration at raised temperatures or were spent after upgrading reactions. Prior art reported 4MR are selectivity dealuminated over 5MR under selective conditions due to their supposed lower relative stability.[45] Therefore, FER and TON topologies were investigated alongside CHA, MFI and MOR frameworks. Dehydration using aggressive conditions (reduced pressure at 600 °C) was conducted for a range of silver-exchanged materials. Silver clusters were observed in the acquired pXRD pattern for dehydrated MOR and MFI topology materials, over-exchanged ferrierite (Ag(1.38),K(0.47)/FER(10)) and for Ag(0.51),K(0.57)/ZnCHA(12). Silver auto reduction facilitates framework oxidation, generating oxygen vacancies with subsequent silver cluster formation, leading to the observation of reduced long-range order in the material.[5,12] It was also anticipated that high silver loading levels would lead to more profound crystallinity loss.[3] However, only Ag/MOR underwent crystallinity loss following dehydration using aggressive conditions, whilst even over-exchanged materials displayed no notable signs of framework damage.

Spent silver-exchanged materials displayed a notable increase in silver cluster size on the surface of the catalysts, determined by TEM and from applying the Scherrer equation. TEM-EDS maps confirmed silver localisation in spent materials with changed

elemental distribution, indicating co-clustering of silver and potassium in Ag(2.42),K(0.88)/ZSM-5(13.5) and Ag(0.44),K(0.23)/CHA(17) following ethanol upgrading at 350 °C. However, TEM-EDS maps for Ag(1.50),K(1.76)/ZnMFI(96) and Ag(0.51),K(0.57)/ZnCHA(12) indicated that co-clustering of silver and potassium had not occurred following ethanol upgrading at 350 °C. pXRD patterns acquired for Ag(0.51),K(0.57)/ZnCHA(12) post ethanol upgrading at 320 °C and methane/ethanol co-processing with oxidative conditions at 350 °C did not contain reflections indicative of silver clusters.[20] We postulate that the framework must display a stabilising effect on silver cations, leading to supressed silver sintering. Upgrading reactions at higher temperatures, as well as materials with higher silver loadings, displayed more pronounced silver sintering, producing larger silver clusters as calculated using the Scherrer equation and measured acquired STEM-BF images.

Whilst sintering was evident across all spent silver-exchanged materials, it was also observed for Pt/ZnCHA and Pd/ZnCHA following ethanol upgrading at 400 °C. A notable decrease in framework crystallinity was observed for Ag/ZnCHA following ethanol upgrading at 400 °C, which we apportion to the thermally unstable gold NPs undergoing rapid sintering and displaying similar damaging effects to silver auto redution.[46,47] When compared the spent materials against the fresh materials, there was distinct changes in the relevant map for each metal, where localisation was observed in the spent materials. Fresh Pt/ZnCHA displayed localisation, however, this subjectively became more evident for the spent material.

9.2 Future Work

Following the calcination of ZnCHA materials, we observed Si–Me and Zn–Me moieties by ssNMR.[19] Whilst DRIFTS was used to confirm calcination conditions were sufficient for removal of the SDA, ssNMR spectroscopy of ZnCHA prior to calcination should confirm that the moieties are generated through calcination. Isotopic labelling of the SDA would confirm the origin; however, availability and costs prohibit such an experiment. Work to determine a successful route to heal the defect sites in the framework, so zinc is present in closed environments, would also be beneficial in reducing the BAS during upgrading reactions.

Pt/ZnCHA materials were observed to be stable over 55 hours, with high ethanol conversion and acetaldehyde selectivity over a range of temperatures. Reactions to determine their propensity to activate methane could be carried out, introducing a C1 feedstock for methane/ethanol co-processing. Further work to determine activity over a wider temperature range, or with more platinum loading levels, could optimise the process of converting ethanol to acetaldehyde, with the potential of generating greater ethanol conversion and acetaldehyde selectivity than reported here.

Whilst sintering was prevalent for a wide range of metals, the introduction of oxygen into the feed supressed but did not stop the process. Reactions including a greater proportion of oxygen in the feed could negate metal sintering. Adjusted feed rates, as well as varied oxygen levels, could allow for reactions to be conducted where minimal sintering is observed, leading to a drastic improvement in catalyst lifetime.

9.3 Chapter Nine Bibliography

1 T. Baba and K. Inazu, *Chem. Lett.*, Heterolytic dissociation of C-H bond of methane over Ag^+-exchanged ceolites and conversion of methane into higher hydrocarbons in the presence of ethene or benzene, 2006, **35**, 142–147.

2 M. Rálek, P. Jírů, O. Grubner and H. Beyer, *Collect. Czechoslov. Chem. Commun.*, Molekularsiebe mit farbiger Indizierung des Wassergehaltes, 1962, **27**, 142–146.

3 S. H. Lee, Y. Kim and K. Seff, *Microporous Mesoporous Mater.*, Weak Ag^+–Ag^+ bonding in zeolite X. Crystal structures of $Ag_{92}Si_{100}Al_{92}O_{384}$ hydrated and fully dehydrated in flowing oxygen, 2000, **41**, 49–59.

4 P. A. Jacobs, J. B. Uytterhoeven and H. K. Beyer, *J. Chem. Soc. Faraday Trans. 1 Phys. Chem. Condens. Phases*, Some unusual properties of activated and reduced AgNaA zeolites, 1979, **75**, 56–64.

5 H. K. Beyer and P. A. Jacobs, in *Metal Microstructures in Zeolites*, eds. P. A. Jacobs, N. I. Jaeger, P. Jírů and G. Schulz-Ekloff, Elsevier, 1982, vol. 12, pp. 95–102.

6 N. H. Heo, Y. Kim, J. J. Kim and K. Seff, *J. Phys. Chem. C*, Surprising Intrazeolitic Chemistry of Silver, 2016, **120**, 5277–5287.

7 H. Beyer, P. A. Jacobs and J. B. Uytterhoeven, *J. Chem. Soc. Faraday Trans. 1 Phys. Chem. Condens. Phases*, Redox behaviour of transition metal ions in zeolites. Part 2.—Kinetic study of the reduction and reoxidation of silver-Y zeolites, 1976, **72**, 674–685.

8 H. Yoshida, T. Hamajima, Y. Kato, J. Shibata, A. Satsuma and T. Hattori, *Res. Chem. Intermed.*, Active Ag species in MFI zeolite for direct methane conversion in the light and dark, 2003, **29**, 897–910.

9 P. A. Jacobs, J. B. Uytterhoeven and H. K. Beyer, *J. Chem. Soc. Faraday Trans. 1 Phys. Chem. Condens. Phases*, Redox behaviour of transition metal ions in zeolites. Part 6.—Reversibility of the reduction reaction in silver zeolites, 1977, **73**, 1755–1762.

10 T. Sun and K. Seff, *Chem. Rev.*, Silver Clusters and Chemistry in Zeolites, 1994, **94**, 857–870.

11 L. Riekert, *Ber. Bunsenges. Phys. Chem.*, 1973, **73**, 331.

12 K. Murata, J. Ohyama and A. Satsuma, *Catal. Sci. Technol.*, Kinetic analysis of Ag particle redispersion into ZSM-5 in the presence of coke usingin situXAFS, 2021, **11**, 506–515.

13 N. Koike, K. Iyoki, S. H. Keoh, W. Chaikittisilp and T. Okubo, *Chem. – A Eur. J.*, Synthesis of New Microporous Zincosilicates with CHA Zeolite Topology as Efficient Platforms for Ion-Exchange of Divalent Cations, 2018, **24**, 808–812.

14 J. Devos, M. L. Bols, D. Plessers, C. Van Goethem, J. W. Seo, S.-J. Hwang, B. F. Sels and M. Dusselier, *Chem. Mater.*, Synthesis–Structure–Activity Relations in Fe-CHA for C–H Activation: Control of Al Distribution by Interzeolite Conversion, 2020, **32**, 273–285.

15 Y. Yuan and R. F. Lobo, *Chem. Sci.*, Propane dehydrogenation over extra-framework In(i) in chabazite zeolites, 2022, **13**, 2954–2964.

16 B. Liu, Y. Zheng, N. Hu, T. Gui, Y. Li, F. Zhang, R. Zhou, X. Chen and H. Kita, *Microporous Mesoporous Mater.*, Synthesis of low-silica CHA zeolite chabazite in fluoride media without organic structural directing agents and zeolites, 2014, **196**, 270–276.

17 B. Liu, R. Zhou, K. Yogo and H. Kita, *J. Memb. Sci.*, Preparation of CHA zeolite

(chabazite) crystals and membranes without organic structural directing agents for CO_2 separation, 2019, **573**, 333–343.

18 Z. Bohström and K. P. Lillerud, *Microporous Mesoporous Mater.*, Preparation of chabazite with mesopores templated from a cationic polymer, 2018, **271**, 295–300.

19 D. Gioffrè, L. Rochlitz, P.-A. Payard, A. Yakimov and C. Copéret, *Helv. Chim. Acta*, Grafting of Group-10 Organometallic Complexes on Silicas: Differences and Similarities, Surprises and Rationale, 2022, e202200073.

20 M. Lamoth, T. Jones, M. Plodinec, A. Machoke, S. Wrabetz, M. Krämer, A. Karpov, F. Rosowski, S. Piccinin, R. Schlögl and E. Frei, *ChemCatChem*, Nanocatalysts Unravel the Selective State of Ag, 2020, **12**, 2977–2988.

21 G. De Cremer, E. Coutino-Gonzalez, M. B. J. Roeffaers, B. Moens, J. Ollevier, M. Van der Auweraer, R. Schoonheydt, P. A. Jacobs, F. C. De Schryver, J. Hofkens, D. E. De Vos, B. F. Sels and T. Vosch, *J. Am. Chem. Soc.*, Characterization of Fluorescence in Heat-Treated Silver-Exchanged Zeolites, 2009, **131**, 3049–3056.

22 A. A. Gabrienko, S. S. Arzumanov, I. B. Moroz, A. V Toktarev, W. Wang and A. G. Stepanov, *J. Phys. Chem. C*, Methane Activation and Transformation on Ag/H-ZSM-5 Zeolite Studied with Solid-State NMR, 2013, **117**, 7690–7702.

23 Y. Kuroda, T. Mori, H. Sugiyama, Y. Uozumi, K. Ikeda, A. Itadani and M. Nagao, *J. Colloid Interface Sci.*, On the possibility of AgZSM-5 zeolite being a partial oxidation catalyst for methane, 2009, **333**, 294–299.

24 S. Bordiga, G. T. Palomino, D. Arduino, C. Lamberti, A. Zecchina and C. O. Arean, *J. Mol. Catal. a-Chemical*, Well defined carbonyl complexes in Ag^+- and Cu^+-exchanged ZSM-5 zeolite: a comparison with homogeneous counterparts, 1999, **146**, 97–106.

25 T. Baba, N. Komatsu, H. Sawada, Y. Yamaguchi, T. Takahashi, H. Sugisawa and Y. Ono, *Langmuir*, H-1 magic angle spinning NMR evidence for dissociative adsorption of hydrogen on Ag^+-exchanged A- and Y-zeolites, 1999, **15**, 7894–7896.

26 I. Takahara, M. Saito, M. Inaba and K. Murata, *Catal. Letters*, Dehydration of Ethanol into Ethylene over Solid Acid Catalysts, 2005, **105**, 249–252.

27 C. R. V. Matheus, L. H. Chagas, G. G. Gonzalez, E. Falabella S. Aguiar and L. G. Appel, *ACS Catal.*, Synthesis of Propene from Ethanol: A Mechanistic Study, 2018, **8**, 7667–7678.

28 P. He, R. Gatip, M. Yung, H. B. Zeng and H. Song, *Appl. Catal. B-Environmental*, Co-aromatization of olefin and methane over Ag-Ga/ZSM-5 catalyst at low temperature, 2017, **211**, 275–288.

29 C.-Y. Liu, K. Struwe, C.-H. Lee, H.-Y. Chuang, J. Sauer, J. C.-C. Yu, V.-H. Nguyen, C.-W. Huang and J. C. S. Wu, *Catal. Commun.*, Ethanol conversion to selective high-value hydrocarbons over Ni/HZSM-5 zeolite catalyst, 2020, **144**, 106067.

30 H. Xiang, R. Xin, N. Prasongthum, P. Natewong, T. Sooknoi, J. Wang, P. Reubroycharoen and X. Fan, *Resour. Chem. Mater.*, Catalytic conversion of bioethanol to value-added chemicals and fuels: A review, 2022, **1**, 47–68.

31 J. Sun and Y. Wang, *ACS Catal.*, Recent Advances in Catalytic Conversion of Ethanol to Chemicals, 2014, **4**, 1078–1090.

32 M. Seifert, M. S. Marschall, T. Gille, C. Jonscher, O. Busse, S. Paasch, E. Brunner, W. Reschetilowski and J. J. Weigand, *ChemCatChem*, Ethanol to Aromatics on Modified H-ZSM-5 Part I: Interdependent Dealumination Actions, 2020, **12**, 6301–6310.

33 Z. Wang, L. A. O'Dell, X. Zeng, C. Liu, S. Zhao, W. Zhang, M. Gaborieau, Y. Jiang

and J. Huang, *Angew. Chemie Int. Ed.*, Insight into Three-Coordinate Aluminum Species on Ethanol-to-Olefin Conversion over ZSM-5 Zeolites, 2019, **58**, 18061–18068.

34 R. Le Van Mao, T. M. Nguyen and J. Yao, *Appl. Catal.*, Conversion of ethanol in aqueous solution over ZSM-5 zeolites: Influence of Reaction Parameters and Catalyst Acidic Properties as Studied by Ammonia TPD Technique, 1990, **61**, 161–173.

35 C. P. Nash, A. Ramanathan, D. A. Ruddy, M. Behl, E. Gjersing, M. Griffin, H. Zhu, B. Subramaniam, J. A. Schaidle and J. E. Hensley, *Appl. Catal. A Gen.*, Mixed alcohol dehydration over Brønsted and Lewis acidic catalysts, 2016, **510**, 110–124.

36 W. Yan, S. Xi, Y. Du, M. K. Schreyer, S. X. Tan, Y. Liu and A. Borgna, *ChemCatChem*, Heteroatomic Zn-MWW Zeolite Developed for Catalytic Dehydrogenation Reactions: A Combined Experimental and DFT Study, 2018, **10**, 3078–3085.

37 L. Qi, M. Babucci, Y. Zhang, A. Lund, L. Liu, J. Li, Y. Chen, A. S. Hoffman, S. R. Bare, Y. Han, B. C. Gates and A. T. Bell, *J. Am. Chem. Soc.*, Propane Dehydrogenation Catalyzed by Isolated Pt Atoms in ≡SiOZn–OH Nests in Dealuminated Zeolite Beta, 2021, **143**, 21364–21378.

38 S. J. Raynes, University of Durham, 2021.

39 J. Zhang, E. C. Wegener, N. R. Samad, J. W. Harris, K. A. Unocic, L. F. Allard, S. Purdy, S. Adhikari, M. J. Cordon, J. T. Miller, T. R. Krause, S. Cheng, D. Liu, M. Li, X. Jiang, Z. Wu and Z. Li, *ACS Catal.*, Isolated Metal Sites in Cu–Zn–Y/Beta for Direct and Selective Butene-Rich C3+ Olefin Formation from Ethanol, 2021, **11**, 9885–9897.

40 L. Qi, Y. Zhang, M. A. Conrad, C. K. Russell, J. Miller and A. T. Bell, *J. Am. Chem. Soc.*, Ethanol Conversion to Butadiene over Isolated Zinc and Yttrium Sites Grafted onto Dealuminated Beta Zeolite, 2020, **142**, 14674–14687.

41 S. J. Raynes and R. A. Taylor, *Sustain. Energy Fuels*, Zinc oxide-modified mordenite as an effective catalyst for the dehydrogenation of (bio)ethanol to acetaldehyde, 2021, **5**, 2136–2148.

42 K. Gao, J. Mielby and S. Kegnæs, *Catal. Today*, Catalytic dehydrogenation of ethanol over zinc-containing zeolites, 2022, **405**–**406**, 144–151.

43 Z. Xi, B. Zhou, B. Jiang, J. Wang, Z. Liao, Z. Huang and Y. Yang, *Mol. Catal.*, Efficient conversion of methane to aromatics in the presence of methanol at low temperature, 2019, **475**, 110493.

44 B. Zhou, Z. Xi, Y. Yu, B. Jiang, J. Wang, Z. Liao, Z. Huang and Y. Yang, *J. Zhejiang Univ. A*, Modification of acidity in HZSM-5 zeolite for methane-methanol co-reaction, 2021, **22**, 106–115.

45 A. A. C. Reule, J. A. Sawada and N. Semagina, *J. Catal.*, Effect of selective 4-membered ring dealumination on mordenite-catalyzed dimethyl ether carbonylation, 2017, **349**, 98–109.

46 E. Eom, M. Song, J.-C. Kim, D. Kwon, D. N. Rainer, K. Gołąbek, S. C. Nam, R. Ryoo, M. Mazur and C. Jo, *JACS Au*, Confining Gold Nanoparticles in Preformed Zeolites by Post-Synthetic Modification Enhances Stability and Catalytic Reactivity and Selectivity, 2022, **2**, 2327–2338.

47 Y.-S. Chi, H.-P. Lin and C.-Y. Mou, *Appl. Catal. A Gen.*, CO oxidation over gold nanocatalyst confined in mesoporous silica, 2005, **284**, 199–206.

10. Appendix

10.1 Further Characterisation of Hydrothermally Synthesized CHA

Hydrothermal synthesis was carried out to produce chabazite from literature methods reported by Lobo[1] and Dusselier.[2] Characterisation work was undertaken to draw comparison between the hydrothermally synthesised chabazite using our developed method from the originally reported Okubo synthesis method,[3] with modifications and characterisation discussed in section 5.2.

Elemental composition of the hydrothermally synthesised chabazite materials was determined using ED-XRF, with the results shown in Table 10.1.

Table 10.1: Table containing ED-XRF results for hydrothermally synthesised chabazite.

Material	Hydrothermal Synthesis Method	Al (wt%)	Si (wt%)	Si : Al Ratio
H,K(0.23)/CHA(19)	Modified Okubo[3]	0.837±0.007	16.792±0.192	19.27
H/CHA(11)	Lobo[1]	3.988±0.045	47.519±0.679	11.45
H/CHA(19)	Dusselier[2]	2.486±0.017	49.107±0.565	18.98

BET theory was applied to hydrothermally synthesised chabazite materials to determine differences between them for their surface area. Results have been included in Table 10.2. Calculation of the surface area using BET theory was carried out using a relative pressure range of P/P_0 = 0.005 – 0.300.

Table 10.2: Table containing BET theory results for hydrothermally synthesised chabazite.

Material	Hydrothermal Synthesis Method	Surface Area (m^2/g)
H,K(0.23)/CHA(19)	Our method, section 5.2.1	682
H/CHA(11)	Lobo[1]	716
H/CHA(19)	Dusselier[2]	754

Chabazite hydrothermally synthesised from our modified Okubo method was shown to display a Type I isotherm with an H4 hysteresis.[4] The isotherm plot for chabazite produced using the reported Lobo method,[1] shown in Figure 10.1, and the Dusselier method,[2] included in Figure 10.2, were both observed to be a Type I isotherm with an H4 hysteresis.[4]

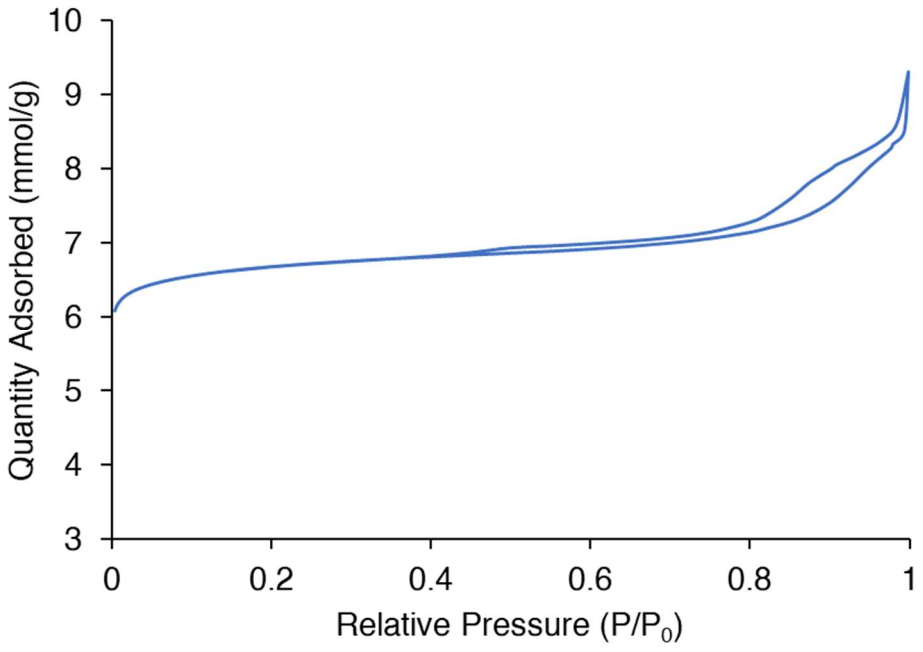

Figure 10.1: Isotherm linear plot for N_2 physisorption analysis of hydrothermally synthesized H/CHA(11), displaying a Type I isotherm with an H4 hysteresis.[4]

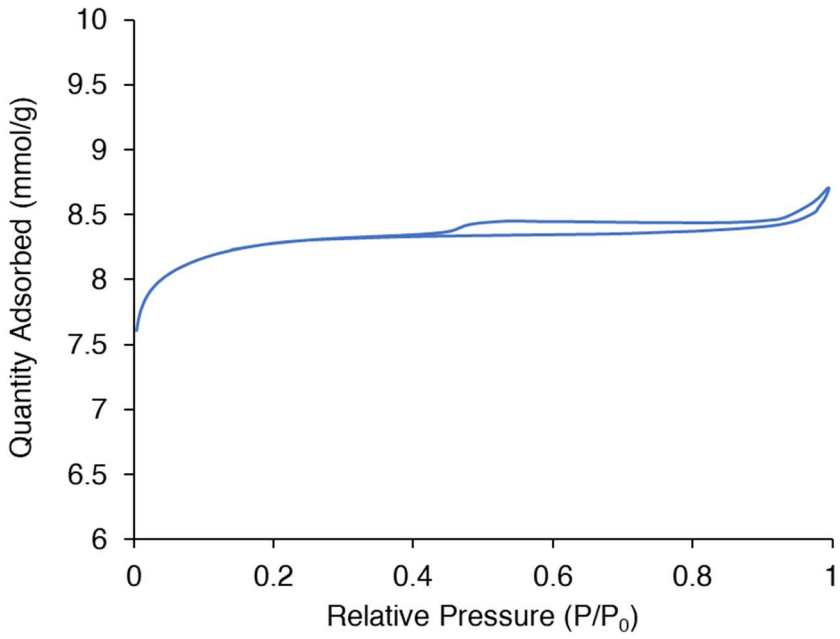

Figure 10.2: Isotherm linear plot for N_2 physisorption analysis of hydrothermally synthesized H/CHA(19), displaying a Type I isotherm with an H4 hysteresis.[4]

10.2 GC-MS-BID Calibration

Accurate calibration was critical for the on-line GC-MS-BID system used to monitor the product stream of upgrading and co-processing reactions. Results discussed in section 7.2 required an accurate representation of catalyst activity and selectivity to allow us to make informed decisions and provide a preliminary ranking of catalysts. Changes were made to the previous GC-MS method, reducing the GC-BID split ratio from 10 to 5 and the MS split ratio from 200 to 125. This provides a larger portion of the injection volume to be sent through the column and to the BID or MS detector, rather than being sent to the purge. This was critical for detecting and quantifying trace amounts of upgrading reaction products, assisting in the determination of the upgrading reaction pathway. Over the calibrated range for reaction products, the calibration curve was fitted with a nonlinear function for concentration to return the most accurate fit. Similar use of nonlinear fitting in prior art reported that a nonlinear relationship was the accurate way of determining material consumption and product formation for their reaction.[5] Through the use of a nonlinear fit, we maximise the amount of information we gather for reactants and products, so we do not miss key information about the upgrading reaction pathway. C_3-C_6 olefins displayed overlapping in the MS trace, with very poor resolution, making accurate quantification difficult. Aromatic products were not calibrated in the MS as they were not products of interest. Calibration was carried out for the following:

- Methanol
- Ethanol
- Acetaldehyde
- Acetone
- 2-Propanol
- Ethyl acetate
- 1-Butanol
- Crotonaldehyde
- Ethylene
- Ethane
- Propylene
- Propane
- Isobutane
- Linear butenes
- Butadiene
- Isobutene

10.2.1 MS Calibration

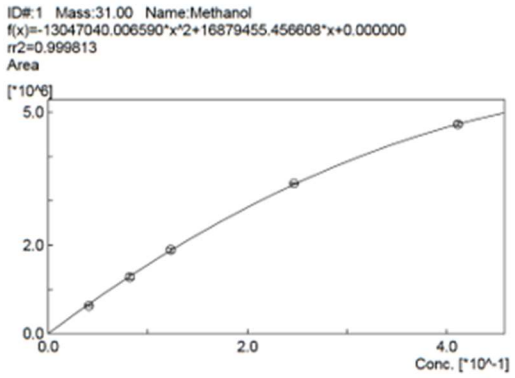

#	Conc. (mmolmin)	Mean Area	Area%RSD
6	0.041	629639.00	3.15
7	0.082	1272926.75	3.98
8	0.123	1898206.20	1.73
9	0.247	3390705.75	0.30
10	0.411	4726850.50	0.98

Figure 10.3: Calibration curve showing the fitting of the methanol peak area at varied concentrations in the MS.

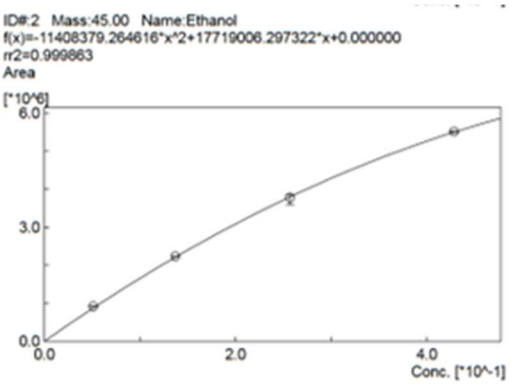

#	Conc. (mmolmin)	Mean Area	Area%RSD
15	0.429	5508385.00	0.22
16	0.257	3771400.00	3.14
17	0.051	914751.00	0.76
18	0.137	2234204.67	0.16

Figure 10.4: Calibration curve showing the fitting of the ethanol peak area at varied concentrations in the MS.

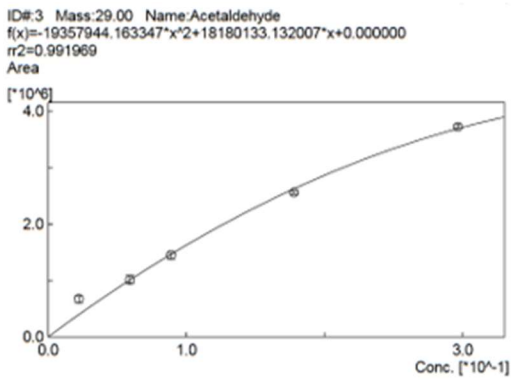

#	Conc. (mmolmin)	Mean Area	Area%RSD
1	0.022	673637.25	7.39
2	0.059	1008174.25	6.84
3	0.089	1452939.50	2.85
4	0.178	2553273.40	1.01
5	0.297	3713777.67	0.68

Figure 10.5: Calibration curve showing the fitting of the acetaldehyde peak area at varied concentrations in the MS.

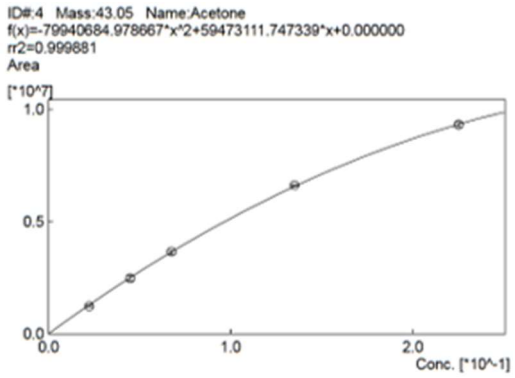

#	Conc. (mmolmin)	Mean Area	Area%RSD
6	0.023	1232965.50	3.13
7	0.045	2471274.00	3.83
8	0.068	3663298.60	1.87
9	0.135	6618775.25	0.40
10	0.225	9322786.25	1.07

Figure 10.6: Calibration curve showing the fitting of the acetone peak area at varied concentrations in the MS.

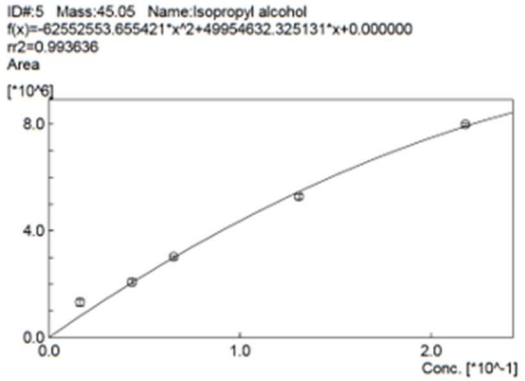

#	Conc. (mmolmin)	Mean Area	Area%RSD
1	0.016	1324151.25	7.90
2	0.044	2064197.25	4.61
3	0.065	3030226.67	1.41
4	0.131	5281734.40	1.33
5	0.218	7976441.50	0.65

Figure 10.7: Calibration curve showing the fitting of the 2-propanol peak area at varied concentrations in the MS.

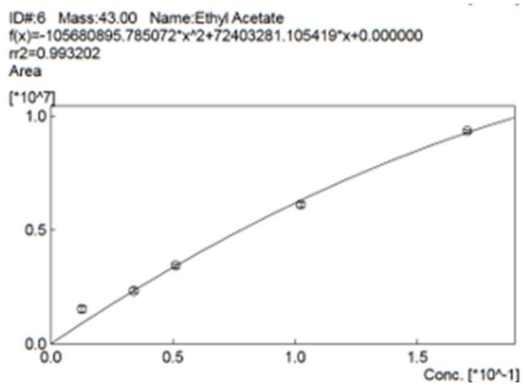

#	Conc. (mmolmin)	Mean Area	Area%RSD
1	0.013	1543969.50	7.44
2	0.034	2326639.00	4.16
3	0.051	3453037.50	1.98
4	0.102	6115224.60	1.37
5	0.171	9340070.33	0.55

Figure 10.8: Calibration curve showing the fitting of the ethyl acetate peak area at varied concentrations in the MS.

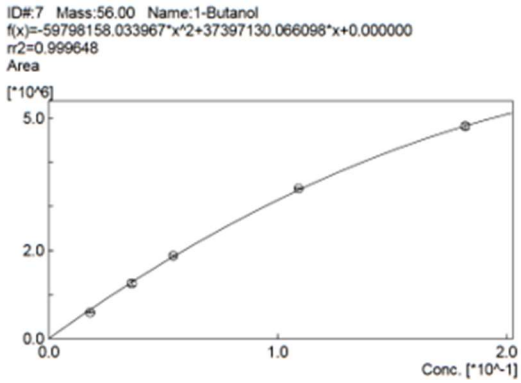

#	Conc. (mmolmin)	Mean Area	Area%RSD
6	0.018	594571.75	3.39
7	0.036	1251075.75	3.86
8	0.055	1879209.80	1.41
9	0.109	3404949.00	0.27
10	0.182	4816118.50	1.30

Figure 10.9: Calibration curve showing the fitting of the 1-butanol peak area at varied concentrations in the MS.

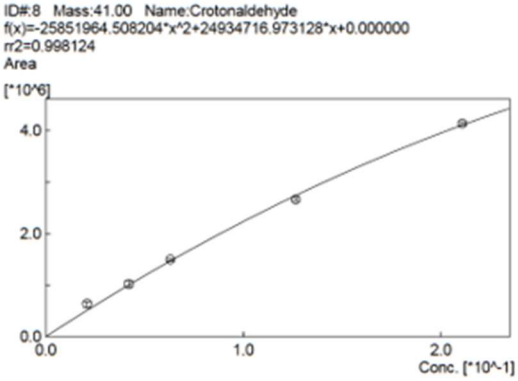

#	Conc. (mmolmin)	Mean Area	Area%RSD
1	0.021	639023.25	7.74
2	0.042	1018558.50	5.23
3	0.063	1498619.67	1.16
4	0.126	2662866.60	1.18
5	0.211	4131360.67	0.65

Figure 10.10: Calibration curve showing the fitting of the crotonaldehyde peak area at varied concentrations in the MS.

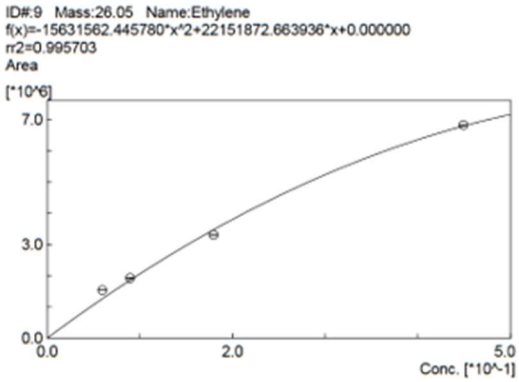

#	Conc. (mmolmin)	Mean Area	Area%RSD
11	0.449	6815958.33	0.20
12	0.180	3310161.33	0.29
13	0.090	1920923.00	0.87
14	0.060	1535319.00	0.30

Figure 10.11: Calibration curve showing the fitting of the ethylene peak area at varied concentrations in the MS.

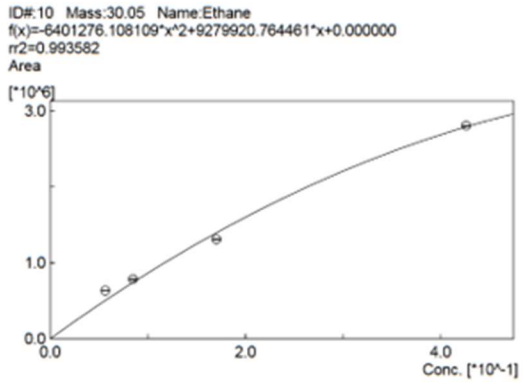

#	Conc. (mmolmin)	Mean Area	Area%RSD
11	0.426	2803009.00	0.27
12	0.171	1309234.33	0.50
13	0.085	783186.33	0.93
14	0.057	634673.67	0.33

Figure 10.12: Calibration curve showing the fitting of the ethane peak area at varied concentrations in the MS.

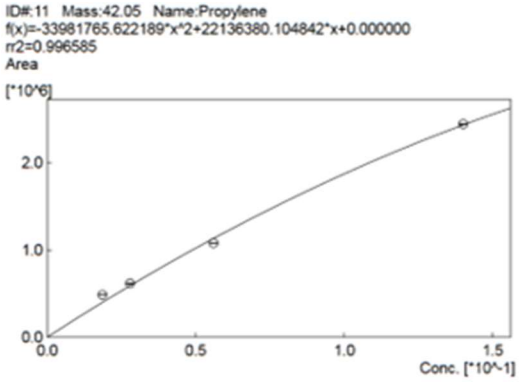

#	Conc. (mmolmin)	Mean Area	Area%RSD
11	0.140	2440628.67	0.18
12	0.056	1078827.00	0.32
13	0.028	614706.00	0.89
14	0.019	486579.00	0.47

Figure 10.13: Calibration curve showing the fitting of the propylene peak area at varied concentrations in the MS.

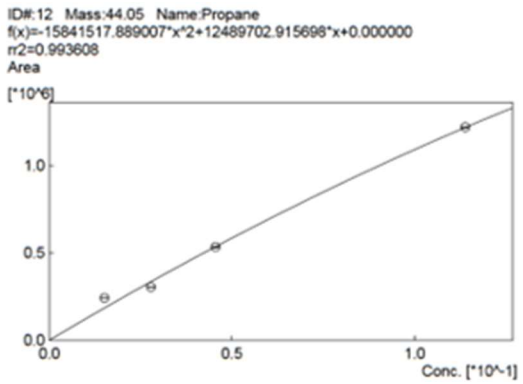

#	Conc. (mmolmin)	Mean Area	Area%RSD
11	0.114	1218661.67	0.28
12	0.046	533633.33	0.64
13	0.028	304081.33	0.64
14	0.015	242806.67	0.46

Figure 10.14: Calibration curve showing the fitting of the propane peak area at varied concentrations in the MS.

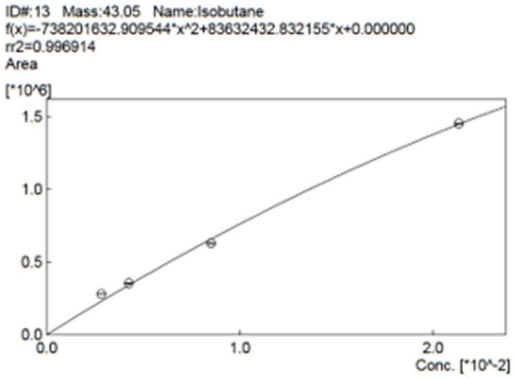

#	Conc. (mmolmin)	Mean Area	Area%RSD
11	0.021	1452141.33	0.15
12	0.009	629066.67	0.49
13	0.004	354233.33	0.72
14	0.003	280533.00	0.25

Figure 10.15: Calibration curve showing the fitting of the isobutane peak area at varied concentrations in the MS.

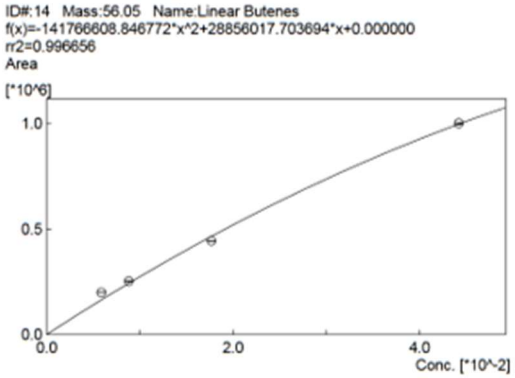

#	Conc. (mmolmin)	Mean Area	Area%RSD
11	0.044	1001086.33	0.53
12	0.018	443585.67	0.34
13	0.009	252501.67	0.94
14	0.006	199564.33	0.15

Figure 10.16: Calibration curve showing the fitting of the linear butenes peak area at varied concentrations in the MS.

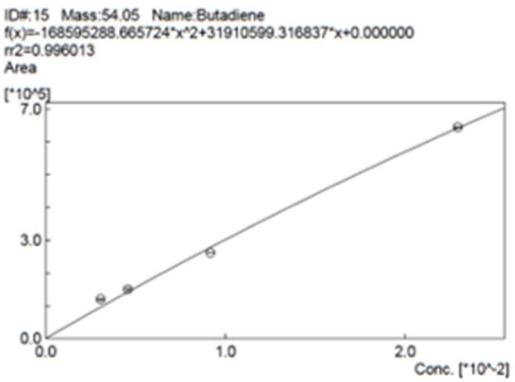

#	Conc. (mmolmin)	Mean Area	Area%RSD
11	0.023	644734.00	0.23
12	0.009	261989.33	0.28
13	0.005	150110.33	2.71
14	0.003	119844.67	2.97

Figure 10.17: Calibration curve showing the fitting of the butadiene peak area at varied concentrations in the MS.

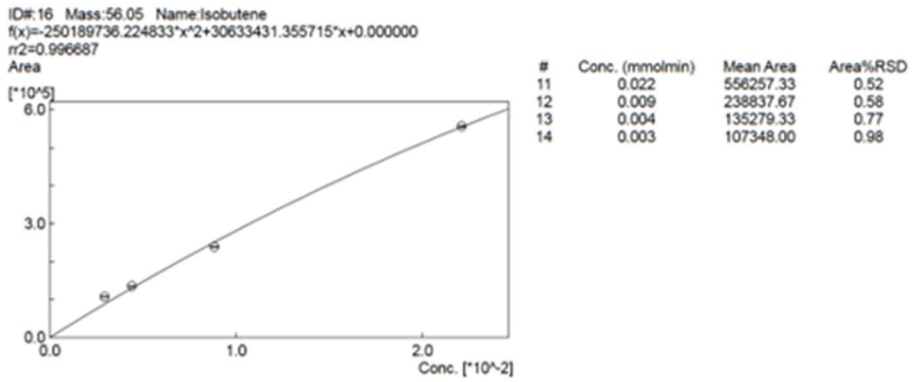

Figure 10.18: Calibration curve showing the fitting of the isobutane peak area at varied concentrations in the MS.

10.2.2 GC-BID calibration

Calibration of the BID was conducted using pre-mixed cylinder of calibration gas in helium, the exact make-up is shown in Table 10.11, with the mixture flowed through the flow cat setup and injected into the GC-BID at four different flow rates, giving the four concentrations of each constituent.

Table 10.10: Gases calibrated in the GC-BID, with the four concentrations for each gas an average of a minimum of three injections, to produce a calibrated range for accurate quantification of upgrading and co-processing products.

Chemical	Retention time (Minutes)	Concentration 1 (mmol/min)	Concentration 2 (mmol/min)	Concentration 3 (mmol/min)	Concentration 4 (mmol/min)
Ethylene	12.735	0.4492	0.17968	0.08984	0.05989
Ethane	13.710	0.4263	0.17054	0.08527	0.05684
Propylene	20.870	0.1401	0.05604	0.02802	0.01519
Propane	21.800	0.1139	0.04557	0.02279	0.01868

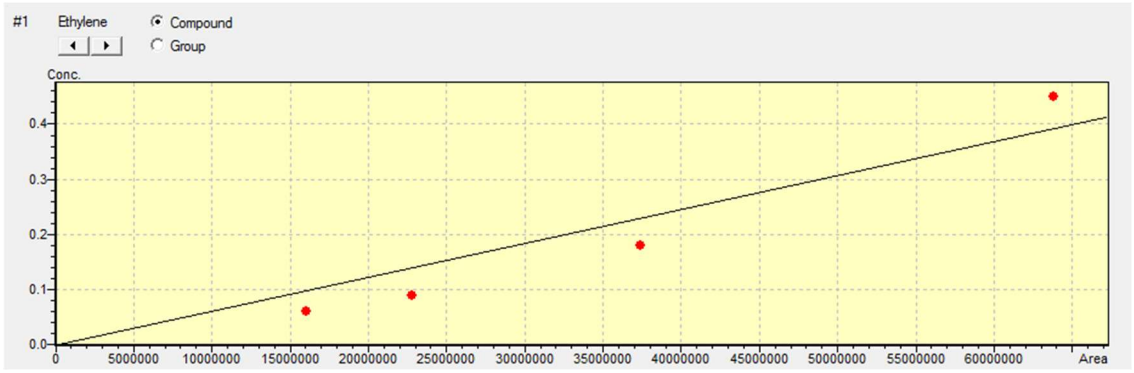

Figure 10.19: Calibration curve showing the fitting for ethylene in the BID.

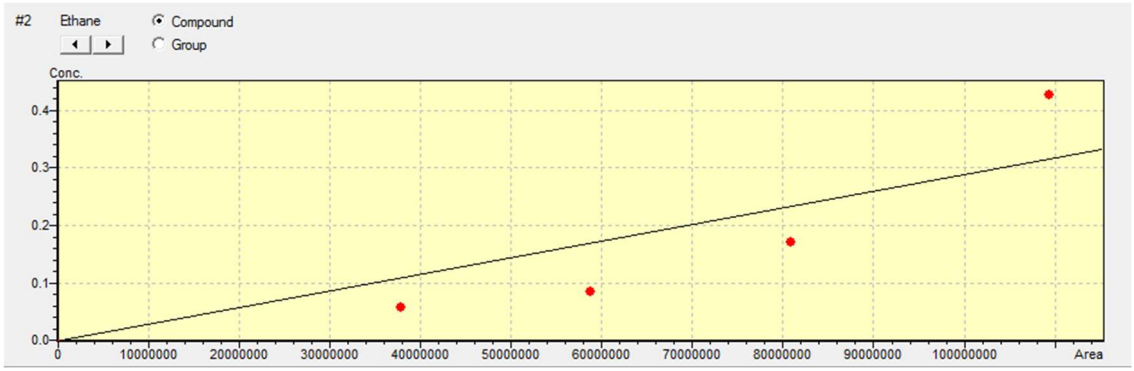

Figure 10.20: Calibration curve showing the fitting for ethane in the BID.

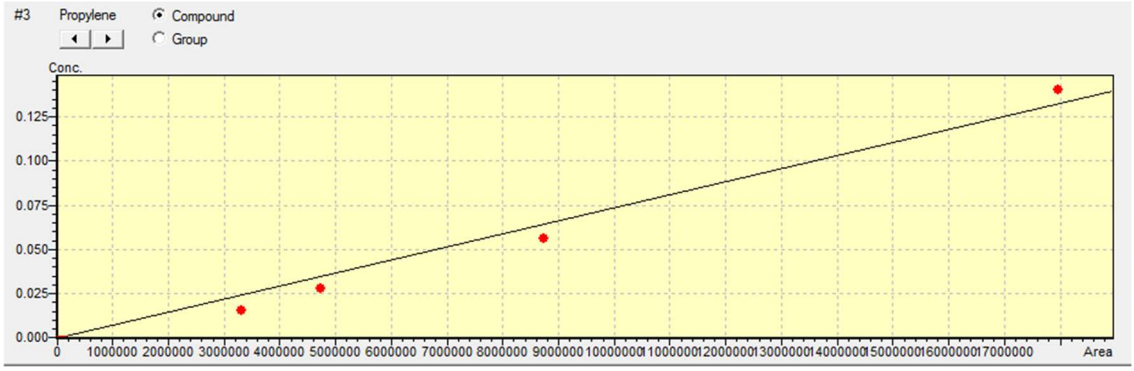

Figure 10.21: Calibration curve showing the fitting for propylene in the BID.

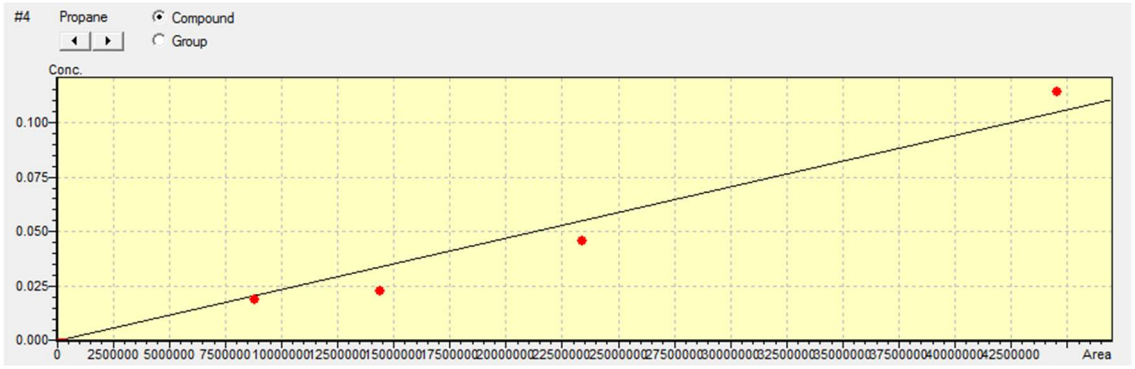

Figure 10.22: Calibration curve showing the fitting for propane in the BID.

Following calibration, an example BID trace where peaks had been integrated would appear as in Figure 10.23.

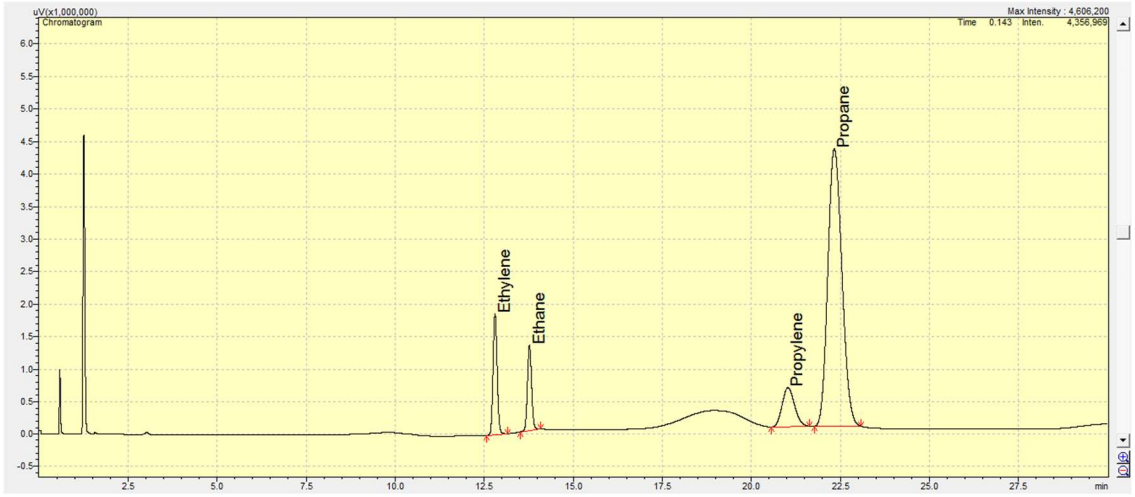

Figure 10.23: BID trace showing the four peaks that have been integrated and identified as ethylene, ethane, propylene and propane.

Whilst not calibrated for as hydrogen, carbon monoxide, carbon dioxide and methane, we could identify the evolution of these gases from their peaks in the collected BID traces, with an example shown in Figure 10.24.

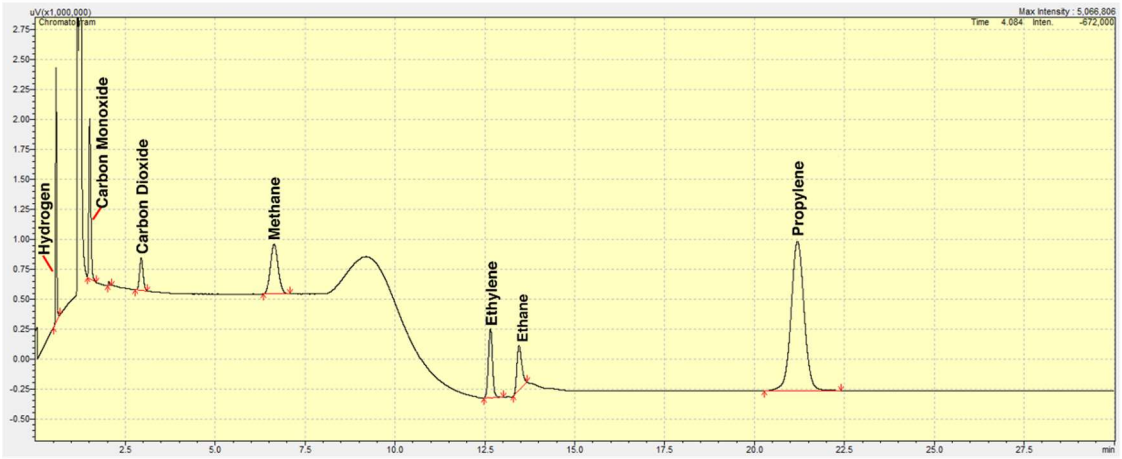

Figure 10.24: BID trace showing unquantified gas products observed during upgrading reactions, such as hydrogen, carbon monoxide, carbon dioxide and methane, alongside ethylene, ethane and propylene.

10.3 Chemicals Used in Project

Table 10.11: table outlining the array of chemicals used within this project, their chemical purity grade and supplier.

Chemical	Supplier	Chemical Purity / Concentration
Acetaldehyde	ACROS Organics	99.5%
Acetone	Fisher Scientific	99.5%
Acetonitrile-d_3	Thermo Scientific	98.5% min
Aluminium chloride	Thermo Scientific	98.5%
Aluminium ethoxide	Thermo Scientific	99%
Aluminium hydroxide (35% in water)	Fisher Scientific UK	35% $AlOH_3$ in water
Aluminium nitrate nonahydrate	Sigma Aldrich	≥ 98%
Argon (Pureshield)	BOC	99.998%
Caesium nitrate	Alfa Aesar	99.8%
Calibration Gas Mix (in He) • 1,3-Butadiene • Cis-2-Butene • n-Butane • 1-Butene • Ethane • Ethylene • Isobutane • Isobutylene • Propane • Propylene	BOC	1,3-Butadiene: 0.5% Cis-2-Butene: 0.5% n-Butane: 0.5% 1-Butene: 0.5% Ethane: 10% Ethylene: 10% Isobutane :0.5% Isobutylene: 0.5% Propane: 2.5% Propylene: 2.5% Helium: 72%
Chloroform-d_3	Apollo Scientific	99.8%
Crotonaldehyde	ACROS Organics	99%
Dichloromethane	Fisher Scientific UK	99.8%
Dimethylsulfoxide-d_6	Apollo Scientific	99.8%
Dimethoxymethane	Alfa Aesar	98%
Ethanol	Fisher Scientific UK	AR grade
Ethyl acetate	Fisher Scientific UK	AR grade
10% Ethylene (in He)	BOC	9.74% (certified value)
Formaldehyde	Thermo Scientific	37% w/w in water
Helium	BOC	CP Grade, N5.0
Hydrochloric acid	Thermo Scientific	37% in water
Hydrogen peroxide	Fisher Scientific UK	30%, Extra Pure

Chemical	Supplier	Chemical Purity / Concentration
Hydrogen tetrachloroaurate(III) trihydrate	Alfa Aesar	99.99%
Indium (III) acetate, anhydrous	Thermo Scientific	99.99%
Indium (III) chloride	Fluorochem	99.99%
Indium (III) nitrate hydrate	Thermo Scientific	99.99%
Isopropanol	Fisher Scientific UK	AR grade
LUDOX AS-30	Sigma Aldrich	30% SiO_2 in water
LUDOX HS-30	Sigma Aldrich	30% SiO_2 in water
LUDOX HS-40	Sigma Aldrich	40% SiO_2 in water
Methane	BOC	Research Grade 99.995%, N4.5
Methane/O_2 (in He)	BOC	Methane: 49.72% (certified value) Oxygen: 4980 ppm (certified value)
Methane/Ethylene 1:1 (in He)	BOC	Methane: 31.99% (certified) Ethylene: 32.41% (certified)
Methanol	Fisher Scientific UK	HPLC grade
Methyl formate	Thermo Scientific	97%
Nitrogen (Oxygen-free)	BOC	OFN
Palladium (II) nitrate hydrate	ACROS Organics	39 to 46% Pd
Platinum (IV) chloride	ACROS Organics	99%
Potassium carbonate	Thermo Scientific	99%
Potassium hydroxide	Fisher Scientific UK	85%
Potassium nitrate	ACROS Organics	99%
Pyridine	ACROS Organics	99.5%
Silicon carbide (80 grit)	Fisher Scientific UK	Technical Grade
Silver nitrate	ACROS Organics	≥ 99%
Silver sulfate	Thermo Scientific	≥ 98%
Sodium hydroxide	Fisher Scientific UK	98.7%
Sodium nitrate	Alfa Aesar	99% +
Tetramethyladamantylammonium hydroxide	Sachem	25% w/w in water
Zinc acetate	Thermo Scientific	99% pure
Zinc chloride	ACROS Organics	98% +
Zinc oxide	Sigma Aldrich	99.99%

10.4 Project Material ED-XRF Results

For the materials used in this project, the ED-XRF results have been included here, separated by framework topology and secondary counterion.

Table 10.12: ED-XRF results for ZSM-5 materials used in this project with NH_4 secondary counterions.

NH4/ZSM-5 Materials						
Code	**Si/Al**	**Al**	**Si**	**Ag**	**Ag:Al**	**Si:Al**
RK-1-1	15	2.319±0.006	35.643±0.167	2.803±0.013	0.30	14.77
RK-1-2	15	2.486±0.050	38.241±0.834	4.262±0.047	0.43	14.78
RK-1-3	15	2.663±0.003	42.202±0.189	3.606±0.011	0.43	15.23
RK-1-13	12.5	3.729±0.075	38.568±0.674	5.888±0.050	0.40	9.94
RK-1-17A	15	3.042±0.033	41.957±0.419	4.207±0.005	0.35	13.25
RK-1-17B	15	3.217±0.010	44.461±0.216	3.622±0.025	0.28	13.28
RK-1-17C	15	3.234±0.015	44.857±0.649	2.397±0.007	0.19	13.33
RK-1-17D	15	3.548±0.066	50.621±1.370	1.764±0.011	0.12	13.72
RK-1-19	12.5	4.377±0.057	47.862±0.090	5.917±0.013	0.34	10.51
RK-1-24A	15	2.773±0.088	43.995±1.907	4.848±0.009	0.44	15.24
RK-1-24B	15	2.678±0.013	42.161±0.275	4.674±0.028	0.44	15.13
RK-1-26	12.5	3.262±0.041	38.569±0.541	10.855±0.013	0.83	11.36
RK-1-30	12.5	3.715±0.120	38.747±1.517	6.155±0.039	0.41	10.02
RK-1-36	12.5	3.927±0.100	41.578±1.174	5.949±0.049	0.38	10.17
RK-1-63 (crude)	12.5	2.580±0.034	25.734±0.047	13.942±0.317	1.35	9.59
RK-1-63	12.5	3.179±0.170	32.493±2.121	9.441±0.113	0.74	9.82
RK-1-110	43.5	1.564±0.010	46.813±0.586	2.194±0.020	0.35	28.76
RK-1-125	43.5	1.464±0.012	45.916±0.510	5.098±0.017	0.87	30.13
RK-2-134	12.5	2.164±0.020	24.508±0.334	4.665±0.018	0.51	10.88
RK-2-134(2)	13.5	3.137±0.111	37.252±1.591	4.661±0.029	0.35	11.41
RK-2-140A	13.5	3.694±0.076	44.833±1.342	0.403±0.080	0.03	11.66

Table 10.13: ED-XRF results for materials used in this project from Na/MOR(6.5) parent material.

Na/MOR(6.5) Materials					
Code	**Al**	**Si**	**Ag**	**Ag:Al**	**Si:Al**
RK-1-27	5.602±0.068	30.541±0.442	14.084±0.089	0.63	5.24
RK-1-42	5.547±0.620	29.713±0.304	16.218±0.137	0.74	5.18
RK-1-50A	5.538±0.083	31.949±0.502	8.447±0.038	0.38	5.54
RK-1-50B	5.993±0.121	34.931±0.823	3.757±0.015	0.16	5.60
RK-1-57A	4.977±0.059	28.796±0.267	16.690±0.043	0.84	5.56
RK-1-57B	5.037±0.030	29.121±0.199	17.072±0.118	0.85	5.55
RK-1-65	4.883±0.058	27.568±0.364	19.277±0.194	1.00	5.48
RK-1-90A	5.525±0.224	34.812±1.928	1.958±0.013	0.09	6.05
RK-1-90B	5.515±0.288	34.509±2.204	1.158±0.009	0.05	6.01

Table 10.14: ED-XRF results for materials used in this project from different zeolite topologies.

All Other Topology Zeolites						
Code	**Framework**	**Al**	**Si**	**Ag**	**Ag:Al**	**Si:Al**
RK-1-8	K/L (3)	9.618±0.136	26.771±0.389	9.276±0.106	0.24	2.67
RK-1-83	H/FER (10)	3.899±0.061	38.779±0.456	7.025±0.022	0.45	9.56
RK-2-84B	H/TON (30)	0.483±0.013	16.886±0.270	1.118±0.073	0.58	33.59

Table 10.15: ED-XRF results for materials used in this project with potassium secondary counterions, showing their initial ion-exchange before introduction of a metal through a second ion-exchange.

Potassium Secondary Counterion Zeolites										
Code	**Parent Zeolite**	**Al**	**Si**	**Counterion 1**		**Counterion 2**		**C1:Al**	**C2:Al**	**Si:Al**
RK-2-8	H-ZSM-5 (13.5)	3.131±0.066	43.090±1.395	**K**	6.087±0.343			1.34		13.22
RK-2-12	K-ZSM-5 (13.5)	2.535±0.040	32.770±0.584	**Ag**	8.041±0.099	**K**	1.912±0.041	0.79	0.52	12.42
RK-2-22(2)	K-ZSM-5 (13.5) (-2-8(2))	4.025±0.046	43.275±0.579	**In**	2.992±0.011	**K**	3.397±0.082	0.17	10.33	0.58
RK-2-41	H-ZSM-5 (13.5)	2.691±0.023	32.948±0.356	**K**	6.689±0.092			1.72		11.76
RK-2-41 **ICP**	H-ZSM-5 (13.5)	2.65±0.07	31.03±0.14	**K**	6.49			1.69		11.25
RK-2-59	K-ZSM-5 (13.5) (-2-41)	1.509±0.025	22.679±0.214	**Ag**	14.587±0.155	**K**	1.921±0.012	2.42	0.88	14.44
RK-2-59 **ICP**	K-ZSM-5 (13.5)	2.51±0.05	32.07±0.24	**Ag**	13.75±0.07	**K**	2.3	1.29	0.63	12.28
RK-2-77	K-CHA (24) (-2-55B)	1.074±0.029	19.212±0.740	**Ag**	5.691±0.004	**K**	1.787±0.104	1.33	1.15	17.19
RK-2-98	H-ZSM-5 (13.5)	2.351±0.031	32.760±0.135	**In**	0.383±0.038			0.04		13.39
RK-2-125A	K-ZSM-5 (13.5) (-2-8(3))	4.216±0.025	46.487±0.182	**In**	0.790±0.011	**K**	4.116±0.040	0.04	0.67	10.59
RK-2-125B	K-ZSM-5 (13.5) (-2-8(3))	4.059±0.058	44.240±0.550	**In**	1.924±0.024	**K**	4.322±0.028	0.11	0.73	10.47
RK-2-130	ZSM-5 (13.5)	4.055±0.059	44.046±0.863	**K**	2.597±0.084			0.44		10.44

Table 10.16: ED-XRF results for hydrothermally synthesised chabazite materials used in this project.

Chabazite Materials										
Code	**Zeolite**	**Al**	**Si**	**Counterion 1**		**Counterion 2**		**C1 : Al**	**C2: Al**	**Si:Al**
RK-2-78 calc	K-CHA	0.837±0.007	16.792±0.192	**K**	0.246±0.004			0.2		19.27
RK-2-82	CHA	1.705±0.032	37.679±0.891	**K**	0.511±0.019			0.21		21.23
RK-2-86	K-CHA (-2-78)	0.703±0.015	14.015±0.265	**Ag**	3.031±0.012			1.07		19.15
RK-2-96	K-CHA (-2-88)	0.804±0.009	29.721±0.404	**In**	0.873±0.014	**K**	0.433±0.003	0.26	0.37	35.51
RK-2-99	K-CHA	1.326±0.047	27.138±0.517	**K**	0.438±0.009	**H**		0.23		19.66
RK-2-104A	K-CHA	0.917±0.372	19.143±0.827	**K**	0.346±0.018			0.26		20.06
RK-2-104B	K-CHA	0.999±0.458	19.991±0.385	**K**	0.380±0.005			0.26		19.23
RK-2-113	K-CHA	1.868±0.009	42.427±0.067	**K**	0.609±0.000	**H**		0.16		21.88
RK-2-122	K-CHA (-2-109A)	2.494±0.001	49.256±0.040	**In**	0.805±0.002	**K**	2.778±0.030	0.08	0.77	18.97
RK-2-129	K-CHA (-2-109A)	2.595±0.034	46.546±0.702	**Ag**	4.850±0.020	**K**	0.874±0.019	0.44	0.23	17.23
RK-2-138	CHA (-2-135)	3.290±0.067	41.853±1.027	**Ag**	5.675±0.082			0.41		12.22

Table 10.17: ED-XRF results for hydrothermally synthesised zincosilicate chabazite materials used in this project.

Zincosilicate Materials										
Code	**Framework**	**Zn**	**Si**	**Counterion 1**		**Counterion 2**		**C1 : Al**	**C2 : Al**	**Si : Zn**
RK-1-139	ZSM-5	1.573±0.008	52.673±0.190	**Ag**	3.366±0.022	**K**	0.562±0.004	1.30	0.57	77.95
RK-2-16	CHA	1.296±0.022	11.650±0.177	**Ag**	5.072±0.090	**Na**	0.00	2.37	0.00	20.93
RK-2-45	CHA	4.682±0.065	33.118±0.466	**K**	4.506±0.069			1.61		16.47
RK-2-81	CHA	5.772±0.113	26.351±0.417	**K**	2.116±0.047			0.61		10.63
RK-2-89	CHA	8.522±0.247	36.479±1.370	**Ag**	7.461±0.030	**K**	0.709±0.038	0.53	0.14	10.04
RK-2-94	CHA	7.074±0.025	31.586±0.251	**In**	2.745±0.099	**K**	220ppm ±39.1	0.22	< 0.01	10.39
RK-2-97	CHA	5.744±0.074	28.597±0.250	**K**	2.158±0.035	**H**		0.58		11.59
RK-2-100	CHA	6.165±0.145	25.662±0.963	**Au**	0.489±0.010	**K**	0.121±0.006	0.03	0.03	9.69
RK-2-102	CHA	5.069±0.184	25.491±0.777	**K**	1.666±0.075			0.55		11.71
RK-2-103	CHA	4.141±0.089	21.401±0.780	**K**	1.028±0.029			0.42		12.03
RK-2-118(2)	CHA	7.304±0.051	38.636±0.122	**K**	2.972±0.006			0.68		12.23
RK-2-118(4)	CHA	7.052±0.051	37.152±0.431	**K**	3.545±0.011			0.84		12.26
RK-2-118(5)	CHA	7.810±0.144	39.864±0.608	**K**	5.103±0.083			1.09		11.88
RK-2-124	CHA	6.172±0.041	34.001±0.028	**Ag**	10.047±0.512	**K**	0.729±0.019	0.99	0.20	12.82
RK-2-124(2)	CHA	6.960±0.044	38.240±0.478	**Ag**	5.874±0.014	**K**	2.381±0.117	0.51	0.57	12.79
RK-2-132	ZnMFI	1.192±0.097	49.451±1.601	**Ag**	2.953±0.286	**K**	1.255±0.037	1.50	1.76	96.58
RK-2-142	CHA	6.398±0.127	44.116±1.016	**Pd**	0.782±0.021	**K**	12.2ppm	0.08	<0.01	16.05
RK-2-143	CHA	7.887±0.154	50.704±0.062	**Pt**	0.728±0.037	**K**	50.2±7.2ppm	0.03	<0.01	14.97
RK-2-143(3)	CHA	8.140±0.011	50.403±0.013	**Pt**	0.376±0.085	**K**	49.4±2.7ppm	0.02	<0.01	14.42
RK-2-146	ZnMFI	1.149±0.041	51.153±1.762	**Pt**	0.447±0.030	**K**	0.201±0.011	0.13	0.29	105.67
IM153(5)	ZnMFI	1.693±0.075	53.996±2.050	**K**	2.430±0.117			2.4		74.25

10.5 Appendix Bibliography

1 Y. Yuan and R. F. Lobo, *Chem. Sci.*, Propane dehydrogenation over extra-framework In(i) in chabazite zeolites, 2022, **13**, 2954–2964.

2 J. Devos, M. L. Bols, D. Plessers, C. Van Goethem, J. W. Seo, S.-J. Hwang, B. F. Sels and M. Dusselier, *Chem. Mater.*, Synthesis–Structure–Activity Relations in Fe-CHA for C–H Activation: Control of Al Distribution by Interzeolite Conversion, 2020, **32**, 273–285.

3 N. Koike, K. Iyoki, S. H. Keoh, W. Chaikittisilp and T. Okubo, *Chem. – A Eur. J.*, Synthesis of New Microporous Zincosilicates with CHA Zeolite Topology as Efficient Platforms for Ion-Exchange of Divalent Cations, 2018, **24**, 808–812.

4 Z. Bohström and K. P. Lillerud, *Microporous Mesoporous Mater.*, Preparation of chabazite with mesopores templated from a cationic polymer, 2018, **271**, 295–300.

5 M. C. Deem, I. Cai, J. S. Derasp, P. L. Prieto, Y. Sato, J. Liu, A. J. Kukor and J. E. Hein, *ACS Catal.*, Best Practices for the Collection of Robust Time Course Reaction Profiles for Kinetic Studies, 2023, **13**, 1418–1430.